
THE MINERALOGICAL DEPARTMENT OF RADIONUCLIDES IN
SOUTH AUSTRALIAN CU-AU-(U) ORES

Nicholas Daniel Owen

This thesis is submitted for the degree of Doctor of Philosophy

in the

School of Chemical Engineering and Advanced Materials,

Faculty of Engineering, Computer and Mathematical Sciences

at

The University of Adelaide



THE UNIVERSITY
of ADELAIDE

September 2019

TABLE OF CONTENTS

ABSTRACT	vi
Declaration.....	viii
Acknowledgements	ix
Preface	x
CHAPTER 1: INTRODUCTION	1
1. Introduction	3
2. Background.....	3
2.1. The Olympic Cu-Au Province	3
2.2. The Olympic Dam IOCG(U) deposit	5
2.3. The Prominent Hill deposit	7
2.4. Uranium and stable radiogenic lead	7
2.5. Deposition and mineralogical expression of Intermediate RN from the ^{238}U decay series, fractionation and decoupling	9
2.6. Lead chalcogenides	11
2.7. Scavenging of ^{210}RN	12
3. Research objectives and thesis structure	14
References	16
CHAPTER 2: LEAD ISOTOPE DATA FOR Pb-CHALCOGENIDES	25
1. Introduction	27
2. Sampling and Analytical Methodology	28
2.1. Scanning Electron Microscopy	28
2.2. Laser Ablation Inductively Coupled Mass Spectrometry	28
3. Results	29
3.1. Sample mineralogy.....	29
3.2. Mineral Textures	30
3.3. Pb-isotope analysis by LA-ICP-MS.....	31
4. Discussion.....	34
5. Conclusions	37

References.....	38
-----------------	----

CHAPTER 3: NANOSCALE STUDY OF CLAUSTHALITE-BEARING SYMPLECTITES IN CU-AU-(U) ORES: IMPLICATIONS FOR ORE GENESIS..... 43

Abstract.....	47
1. Introduction	47
2. Background	48
3. Sampling and Analytical Methodology.....	51
4. Results	51
4.1. Characterisation of Symplectite Textures	51
4.2. Compositional Data for Pb-Chalcogenides and Host Cu-(Fe)-Sulphides ...	54
4.3. Nanoscale Characterisation (TEM Data)	54
5. Discussion	68
5.1. Evolution of Sulphide Assemblages.....	68
5.2. Formation of Clausthalite in Cu-(Fe)-Sulphides	68
6. Conclusions and Implications	71
References.....	72

CHAPTER 4: REE-, SR- CA-ALUMINUM-PHOSPHATE-SULFATE MINERALS OF THE ALUNITE SUPERGROUP AND THEIR ROLE AS HOSTS FOR RADIONUCLIDE 76

Abstract.....	81
1. Introduction.....	81
2. Background.....	82
2.1. APS crystal chemistry	82
2.2. Olympic Dam	82
3. Samples and Methods	83
4. Results.....	83
4.1. Textural Characterization and Mineral Associations	83
4.2. Compositional Data.....	84
4.3. NanoSIMS Isotope Mapping of APS and Associated Minerals.....	86
5. Discussion.....	87

5.1. Composition of APS Minerals	87
5.2. Alteration and APS Mineralogy at Olympic Dam	91
5.3. APS Minerals as RN Scavengers	92
7. Implications	93
References	93
CHAPTER 5: A SPONGE FOR RADIONUCLIDES: A STUDY ON THE DYNAMIC UPTAKE OF LEAD BY SYNTHETIC ALUMINIUM-PHOSPHATE-SULPHATES	96
Abstract.....	100
1. Introduction	101
2. Background.....	102
2.1. APS crystallography.....	102
2.2. Evidence for radionuclide scavenging by natural APS minerals	103
3. Materials and methods.....	105
3.1. Synthesis of APS minerals	105
3.2. Pb-sorption experiments.....	105
3.3. Characterisation of solids and solutions.....	106
3.4. XAS data collection and analysis.....	107
4. Results	107
4.1. Composition of synthesised APS phases	107
4.2. Pb-sorption by synthetic APS phases.....	109
4.3. Composition of Pb-sorbed APS phases.....	110
4.4. Pb incorporation in natural woodhouseite.....	113
4.5. X-ray absorption spectroscopy of Pb in APS minerals	114
5. Discussion.....	116
6. Conclusions and implications.....	120
References	122
CHAPTER 6: SUMMARY, RECOMMENDATIONS AND CONCLUDING REMARKS	128
1 Summary.....	130
1.1. Migration of radiogenic Pb within Cu-Au-(U) deposits of the Olympic Cu-Au Province	130

1.2. Aluminium-phosphate-sulphates and RN deportment during metallurgical processing	132
2 Recommendations.....	133
2.1. Recommendations for work on natural mineral phases	134
2.2. Evidence for radionuclide scavenging by natural APS minerals	136
3 Concluding remarks.....	137
References.....	138
CHAPTER 7: SUPPLEMENTARY MATERIAL.....	144
Supplementary Material A: Appendix for Chapter 2	146
Supplementary Material B: Appendix for Chapter 3.....	152
Supplementary Material C: Appendix for Chapter 4.....	154
Supplementary Material D: Appendix for Chapter 5	159
Supplementary Material E: Co-authored paper	175
Supplementary Material F: Conference abstract	205
Supplementary Material G: Conference abstract.....	208
Supplementary Material H: Conference abstract.....	212
Supplementary Material I: Co-authored conference abstract	216
Supplementary Material J: Co-authored conference poster.....	221
CHAPTER 8: REFERENCES	224

ABSTRACT

Iron-oxide copper gold (IOCG)-uranium deposits represent South Australia's primary resource base for copper production. The presence of daughter radionuclides (RN) from the ^{238}U decay series within the ores necessitates a detailed understanding of their mineralogical deportment as a pre-requisite for attempts to remove or reduce RN concentrations. Research presented in this thesis contributes towards this knowledge by identifying and characterising potential RN-carriers, migration of radiogenic lead via geological processes, and provides evidence for RN sorption during processing. Novel approaches to RN reduction are proposed based on mineralogical-geochemical results.

Evidence for migration of Pb within the deposit and during processing is relevant for any assessment of RN deportment, especially since the Pb-chalcogenides galena, clausthalite (PbSe) and altaite (PbTe) are often hosted within Cu-(Fe)-sulphides. Lead isotope values measured in-situ by laser ablation inductively coupled plasma mass spectrometry suggest an overwhelmingly radiogenic origin for Pb and thus extensive decoupling of radiogenic Pb from parent U- and Th-minerals. Calculated $^{207}\text{Pb}/^{206}\text{Pb}$ ratios suggest Pb mobilisation during an event that postdates the initial Mesoproterozoic Fe-Cu-Au-U mineralisation event, an interpretation consistent with other studies in the Olympic Cu-Au province which indicate cycles of replacement-remobilization-recrystallization.

A nanoscale study of the most common of the three Pb-chalcogenide minerals, clausthalite, by high-angle annular dark field scanning transmission electron microscopy, proved highly instructive for identifying mechanisms of remobilization and overprinting. Characteristic symplectite textures involving clausthalite and host Cu-(Fe)-sulphides are indicative of formation via reaction between Se that pre-existed in solid solution within Cu-(Fe)-sulphides and migrating Pb. Observed superstructuring of clausthalite nanoparticles within chalcopyrite provides a direct link between solid solution and symplectite formation.

Sr-Ca-REE-bearing aluminium-phosphate-sulphates (APS) of the alunite supergroup are a minor component of the Olympic Dam orebody. They appear paragenetically late, often replacing earlier REE-minerals. Characterisation of these compositionally zoned phases allowed them to be defined as minerals that span the compositional fields of woodhouseite and svanbergite, and also a REE- and phosphate-dominant group displaying solid solution towards florencite. A nanoscale secondary ion mass spectrometry study of RN distributions in APS minerals in acid-leached copper concentrate revealed that APS minerals readily sorb products of ^{238}U decay, notably ^{226}Ra and ^{210}Pb , whereas U remains in solution. Many APS phases, particularly those that are Pb-bearing, are stable over a wide range of pH and Eh conditions and at temperatures up to 450 °C. As such, synthetic APS phases represent viable candidates not only for the removal of radionuclides from metallurgical streams, but also for their safe storage and isolation from surrounding environments.

Ca-Sr-dominant phases display preferential enrichment by Pb (notably ^{210}Pb) during flotation. ^{210}Pb uptake then increases during subsequent acid leaching.

Mixed Ca- and Sr-bearing APS phases were synthesised by modifying existing recipes to test the role of compositional variability of APS phases on the sorption rate of Pb from dilute $\text{Pb}(\text{NO}_3)_2$ solution. Lead incorporation by the synthetic APS phases was confirmed, whereby Pb replaces Ca, but not Sr, within the APS crystal structure. Extended X-ray absorption fine structure analysis of the resulting solids reveals the nature of Pb sorption by the synthesized material. The data showed that the dynamic incorporation of Pb by APS phases occurred overwhelmingly at pH 3.5, thus verifying that uptake of Pb by synthetic APS phases may represent a robust mechanism to achieve both reduction and immobilisation of ^{210}Pb within metallurgical processing streams.

DECLARATION

I certify that this work contains no material which has been accepted for the award of any other degree or diploma in my name, in any university or other tertiary institution and, to the best of my knowledge and belief, contains no material previously published or written by another person, except where due reference has been made in the text. In addition, I certify that no part of this work will, in the future, be used in a submission in my name, for any other degree or diploma in any university or other tertiary institution without the prior approval of the University of Adelaide and where applicable, any partner institution responsible for the joint-award of this degree.

I acknowledge that copyright of published works contained within this thesis resides with the copyright holder(s) of those works.

I also give permission for the digital version of my thesis to be made available on the web, via the University's digital research repository, the Library Search and also through web search engines, unless permission has been granted by the University to restrict access for a period of time.

Signed:

Date: 29/08/2019

ACKNOWLEDGEMENTS

Many people have contributed towards the work contained within this dissertation with particular thanks towards my academic supervisors. Firstly, I would like to extend my deepest and heartfelt gratitude towards my primary academic supervisor, Prof. Nigel Cook, for his tireless hours of work, ceaseless encouragement and unending support toward the completion of this PhD dissertation. His extensive knowledge of ore mineralogy and microanalytical characterisation of mineral phases proved invaluable at many points throughout my candidature. I would also like to thank my secondary academic supervisor, Prof. Joel Brugger, for his hospitality and support in my role as an affiliate researcher at Monash University in the second half of my candidature. His guidance and assistance in geochemical and synchrotron experiments were essential for the success of the second half of my PhD. My thanks also to my other secondary academic supervisor, Prof. Stephen Grano, for providing encouragement and focus along the journey. Additional thanks are required for Dr. Cristiana Ciobanu, who helped with many of the ideas and provided much expertise during the first half of my candidature.

A special mention is needed for Dr. Kathy Ehrig, without whom the ARC Research Hub for Australian Copper Uranium would not be possible. Dr. Kathy Ehrig's exhaustive knowledge of the Olympic Dam Cu-U-Au-Ag deposit and strong industry focus on scientific research has steered much of what is contained within this dissertation, and indeed, within the Hub in general.

The analytical and support staff at Adelaide Microscopy are thanked for their patience and expertise. Though it is a large team at Adelaide Microscopy, I would like to extend particular thanks towards Dr. Benjamin Wade, Dr. Sarah Gilbert, Dr. Ashley Slattery, Dr. Animesh Basak and Mr. Ken Neubauer for their enthusiasm in sharing their extensive knowledge of microanalytical characterisation methods.

I would like to thank all members of the ARC Research Hub for Australian Copper Uranium for their dedication to the research and openness to interdisciplinary collaboration. The opportunity to work with a group of people with such diverse skill sets has enabled an extra level of applied focus for the research conducted within my candidature. While there are too many members to name individually, I would like to extend my warm gratitude to the two central organisers within the Hub, Prof. Stephen Grano and Dr. Ruth Shaw, and my fellow 'Node 1' collaborators Dr. Danielle Schmandt, Mark Rollog and Dr. Rahul Ram.

Last but not least, I would like to extend a heartfelt thanks to all of my peers, family and friends who provided their support and friendship throughout my candidature with a special mention for my University of Adelaide research colleagues Danielle, Liam, Max V-I, Marija, Will, Urs, Nau, Mark, Wei Li, Zhiyong, Wenyuan Gao, Wenyuan Liu and Jing.

PREFACE

This thesis is comprised of manuscripts which are published in, accepted, or submitted to international peer-reviewed journals, and an as yet unpublished manuscript presented as stand-alone supplementary research. All of the research contained within this thesis is a contribution toward the ARC Research Hub for Australian Copper-Uranium. Research by the 30+ members of the Hub has been conducted with the goal of identifying pathways for removal of deleterious components from South Australian Cu-Au ores via a large-scale interdisciplinary approach. This thesis dissertation supports this goal by contributing towards a fundamental mineralogical approach combined with the investigation of geochemical pathways for the removal of non-target metals from Cu-processing streams.

Chapters 2 (unpublished) and 3 (published) form a comprehensive study on the movement of radiogenic Pb within an economically mineralised zone of the Mt. Woods Inlier over geological time, and its intimate relationship with the Cu-(Fe)-sulphides through the formation of intragranular Pb-chalcogenides which are often hosted within the Cu-(Fe)-sulphides at the very finest scale. Chapter 4 (accepted for publication) contains the first part of a study on aluminium-phosphate-sulphate (APS) minerals within the Olympic Dam Cu-processing circuit and the observed ability of naturally occurring APS mineral phases to scavenge radionuclides of ^{238}U decay from ^{226}Ra onwards. The second part of this study (Chapter 5, submitted for publication) pursues a geochemical approach for the reduction of Pb from solution by the addition of synthetic APS phases at varying pH and Pb concentration. The final chapter (Chapter 6) summarises all of the research contained within this dissertation, makes recommendations for the direction of future work and makes some concise concluding remarks.

The papers which form the basis of this dissertation include:

Chapter 2. Pb isotope data for Pb-chalcogenides in the Mt Woods Inlier

Chapter 3. Owen, N., Ciobanu, C., Cook, N., Slattery, A., and Basak, A. (2018) Nanoscale study of clausthalite-bearing symplectites in Cu-Au-(U) ores: Implications for ore genesis. *Minerals*, 8(2), 67.

Chapter 4. Owen, N.D., Cook, N.J., Rollog, M., Ehrig, K., Schmandt, D.S., Ram, R., Brugger, J., Ciobanu, C.L., Wade, B. and Guagliardo, P. (2019) REE-, Sr-, Ca-aluminum-phosphate-sulfate minerals of the alunite supergroup and their role as hosts for radionuclides. *American Mineralogist*, 104, 1806–1819.

Chapter 5. Owen, N.D., Brugger, J., Ram, R., Eschmann, B., Cook, N.J., Ehrig, K.J., Schmandt, D.S., Rollog, M., and Guagliardo, P. (2020) A sponge for radionuclides: a study on the dynamic

uptake of lead by synthetic aluminium-phosphate-sulphates. Applied Geochemistry, (in review).

A discussion of the key findings and implications for this collection of research, and recommendations for future work are included in Chapter 6.

Chapter 7 contains all of the supplementary material not otherwise included in the previous chapters as well as co-authored publications and conference abstracts. These include:

- A. Supplementary material for Chapter 2
- B. Supplementary material for Chapter 3
- C. Supplementary material for Chapter 4
- D. Supplementary material for Chapter 5

Co-authored full-length papers

- E. Cook, N.J., Ehrig, K.J., Rollog, M., Ciobanu, C.L., Lane, D.J., Schmandt, D.S., Owen, N.D., Hamilton, T. & Grano, S. (2018) ^{210}Pb and ^{210}Po in geological and related anthropogenic materials: implications for their mineralogical distribution in base metal ores. Minerals. 8, 211. doi: 10.3390/min8050211.

Peer-reviewed conference abstracts

- F. Owen, N., Ciobanu, C., Cook, N. and Basak, A. (2017) Nanoscale study of clauthalite-bearing symplectites in Cu-Au-(U) ores from South Australian deposits: Implications for ore genesis. Goldschmidt 2017, 13-18 August, Paris, France. Goldschmidt Abstracts, 3017.
- G. Owen, N.D., Cook, N.J., Rollog, M., Ehrig, K.J., Schmandt, D.S. and Ciobanu, C.L. (2018) REE-, Sr-, Ca-aluminium-phosphate-sulphate minerals of the woodhouseite series and their role as hosts for radionuclides. 15th Quadrennial IAGOD Symposium, Salta, Argentina, 28-31 August 2018. Symposium Proceedings Volume, SegemAR, 187-188.
- H. Owen, N.D., Cook, N.J., Ram, R., Brugger, J., Rollog, M., Ehrig, K., Schmandt, D.S., Ciobanu, C.L., Wade, B. and Guagliardo, P. (2019) Natural and synthetic aluminium-phosphate-sulphates under acid leach conditions: Pathways to radionuclide reduction in copper processing. TIGeR 2019, 11-13 September, Perth, Australia.

Co-authored peer-reviewed conference abstracts

- I. Cook, N.J., Ehrig, K.J., Ciobanu, C.L., Courtney-Davies, L., Verdugo-Ihl, M.R., Rollog, M., Schmandt, D.S., Owen, N.D., Macmillan, E., Kontonikas-Charos, A., Krneta, S. & Dmitrijeva, M. (2018) Why detailed mineralogy is important: Understanding evolution of the giant Olympic Dam iron-oxide copper-gold system, South Australia. 15th Quadrennial IAGOD Symposium, Salta, Argentina, 28-31 August 2018. Symposium Proceedings Volume, SegemAR, 371-372.

- J. Schmandt, D.S., Cook, N.J., Ciobanu, C.L Ehrig, K.J., Owen, N.D., Wade, B.P. & Gilbert, S.E. (2018) Rare Earth Element mineralogy at Olympic Dam, South Australia. Gordon Research Seminar and Conference, Geochemistry of Mineral Deposits: Mineralizing Processes Across All Scales, August 5-10, 2018, Waterville Valley, NH, USA.

The final chapter (Chapter 8) contains a reference list of all of the publications cited within this thesis dissertation including publications, chapters, and supplementary material.

CHAPTER 1

INTRODUCTION

1 INTRODUCTION

Australia is the fourth largest copper producer globally with almost 75% of Australia's economic Cu resource in South Australia. Despite this, South Australia only makes up for ~30% of national Cu production (www.ga.gov.au). The main style of Cu-mineralising systems in South Australia are Iron Oxide Copper Gold (IOCG) deposits (http://www.energymining.sa.gov.au/minerals/mineral_commodities/copper), a relatively newly described class of magmatic-hydrothermal deposit in which Fe-oxides are the dominant components (Hitzman et al. 1992; Hitzman 2000; Groves et al. 2010; Barton 2014). The South Australian Government is committed to boosting copper production three-fold by 2030. The ARC Research Hub for Australian Copper and Uranium, to which the research in this thesis contributes, was established to develop new knowledge and innovation to address one challenging technical issue, the presence of uranium and its short- to medium half-life daughter radionuclides (RN). A sound understanding of the physical distribution of these non-target components, notably ^{226}Ra , ^{210}Po and ^{210}Pb , and their geochemical behaviour in ore and during processing is a critical first step for the development of innovative process designed to reduce or eliminate them in final products.

As one project among several inter-related research projects within the broader Research Hub, the research questions addressed in this thesis fall into two main research areas, as follows:

(1) Can minor phases, notably the Pb-chalcogenides, galena, clausthalite and altaite, host significant concentrations of radiogenic Pb, and can the mobility and chemical affiliation of radiogenic lead be modelled from a combination of quantitative isotope analysis and examination of mineralogical relationships at the nano- to micron-scales?

(2) The second phase of the research combines mineralogy and geochemistry to target one group of minerals in South Australian IOCG ores shown to harbour significant concentrations of RN, and which may represent a fresh approach towards novel ways of extracting RN from metallurgical processing streams. Aluminium-phosphate-sulphate (APS) minerals of the alunite supergroup are indicated as potential hosts of RN from ^{226}Ra onward with particular compatibility between ^{210}Pb and (Ca,Sr)-bearing APS phases. The mechanism of Pb-uptake by the synthetic phases is investigated via Extended X-ray Absorption Fine Structure (EXAFS) analysis to determine the bonding environments of Pb that arise from Pb-bearing solutions under different conditions.

2 BACKGROUND

2.1 *The Olympic Cu-Au Province*

The Olympic Cu-Au Province forms a ~500 km-long belt, striking approximately N-S along the eastern margin of the Gawler Craton ([Figure 1.1](#)). The province hosts a number of iron-oxide copper gold (IOCG) deposits including the world-class Olympic Dam deposit, as well as the

Prominent Hill and Carrapateena deposits, and the historic Cu-Au mining regions at Moonta and Wallaroo (Ferris et al. 2002; Skirrow et al. 2007; Conor et al. 2010; Reid 2019). Mineralisation throughout the Olympic Domain is broadly considered to be associated with emplacement of the 1600-1580 Ma Hiltaba Suite granites, coeval with the Gawler Range Volcanics. Mineralisation related to this event has resulted in the largest known concentration of iron oxide, copper, gold and uranium of any geological province world-wide. While Cu is the primary economic commodity in the IOCG deposits, with by-product Au and Ag also exploited, most deposits contain some uranium. Olympic Dam is, however, is the only deposit containing U at economic concentrations within the ore.

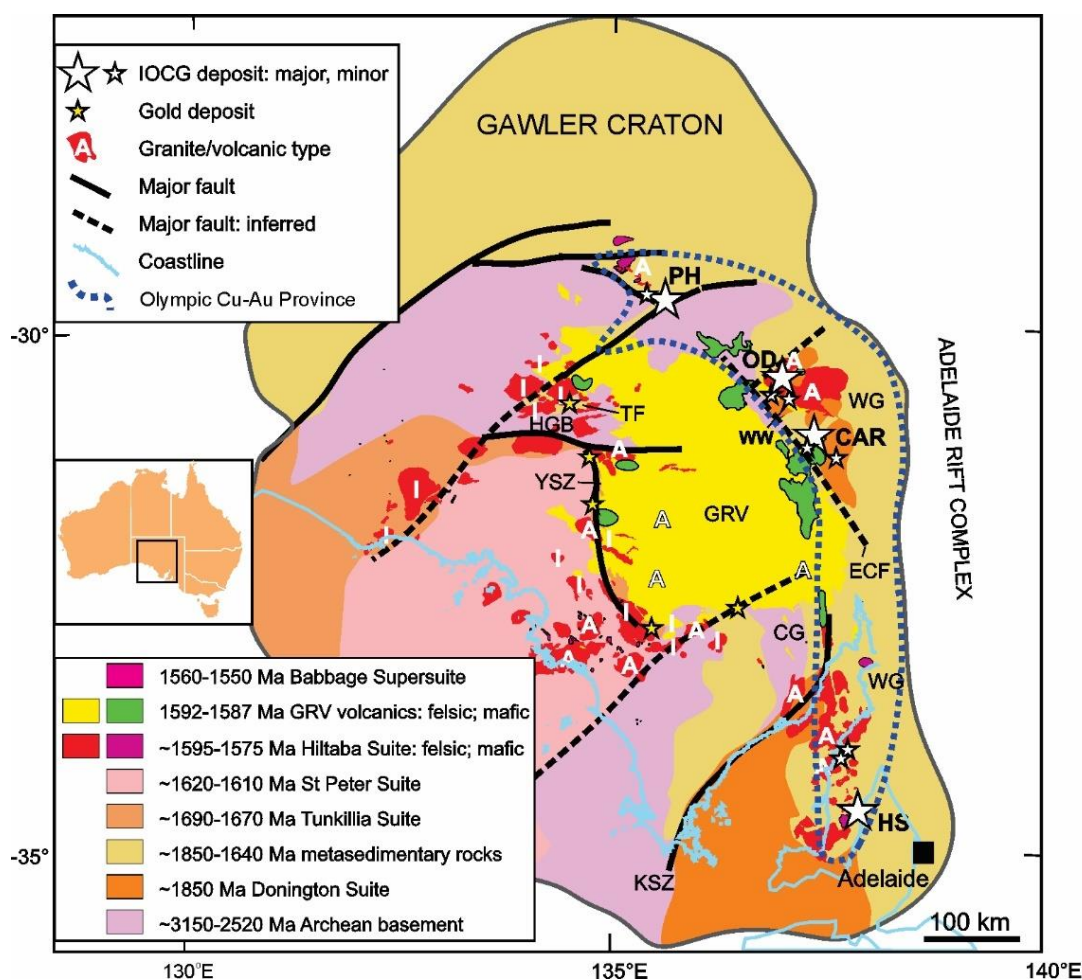


Figure 1.1: Simplified geological map showing the location of the Olympic Cu-Au Province within the Gawler Craton. The Olympic Cu-Au Province is host to the largest concentration of IOCG style mineralisation world-wide and includes Prominent Hill (PH), Olympic Dam (OD), Carrapateena (CAR) and the southern part of the district, encompassing Moonta-Wallaroo and Hillside (HS). Modified after Skirrow et al. (2018).

Economic mineralisation in the Olympic Cu-Au Province is related to the Hiltaba Suite granites and associated Gawler Range Volcanics, which were emplaced during a major magmatic event (Hand et al. 2007; Reid and Hand 2012; Reid 2019), collectively termed the Gawler Siliceous

Large Igneous Province (Allen et al. 2008). Hand et al. (2007) suggest the Hiltaba Suite granites were intruded into an overall compressional regime, suggested to be driven by Orogenic events. However, observations from a seismic reflection transect across the Olympic Dam region indicates that the magmatic event was accommodated by a transpressional and locally extensional regime (Skirrow and Davidson 2007) during the development of the Olympic Dam Cu-Au Province, and at least partially negates the compressional environment proposed by Hand et al. (2007). Within some parts of the Olympic Cu-Au Province, Hiltaba Suite magmatism was associated with high metamorphic grades, reaching upper amphibolite to granulite facies in restricted areas in the southern part of the province (Hand et al. 2007; Reid and Hand 2012; Reid, 2019). Importantly, however, rocks of lower-grade metamorphic facies, i.e. Moonta-Wallaroo-aged metasedimentary and -volcanic rocks are widespread. There are also no high metamorphic-grade rocks observed in the Olympic Dam district (including Wirrda Well, Acropolis, Oak Dam, and Carrapateena). Varying tectonic and alteration environments are expressed within the Olympic Cu-Au Province, resulting in the formation of the Mt Woods Inlier in the north, which contains the Prominent Hill deposit, the Olympic District, which hosts Olympic Dam, Carrapateena, and a dozen or more smaller prospects, and the Moonta-Wallaroo Cu-Au region in Yorke Peninsula, that includes the Hillside deposit.

Some of the research described in this thesis was based on sample material from the Prominent Hill (Chapters 2 and 3) and Olympic Dam deposits (Chapter 4), necessitating a brief introduction to the two deposits.

2.2 *The Olympic Dam IOCG(U) deposit*

The giant Olympic Dam Deposit (Ehrig et al. 2012) is considered as the archetypal example of IOCG(U) mineralisation and is by far the largest in the Olympic Domain. The deposit has an estimated resource of 10,727 Mt @ 0.72% Cu, 0.3 g/t Au, 1.0 g/t Ag, 0.23 kg/t U₃O₈ (BHP Billiton 2018). Although copper is the prime commodity of interest, the deposit contains sufficient concentrations of uranium for economic recovery of the element.

The deposit is hosted by the Olympic Dam Breccia Complex, which is largely though not exclusively derived from the Roxby Downs Granite (RDG), a member of the ca. 1600-1585 Ma Hiltaba Suite. It has been suggested (e.g. Johnson and McCulloch 1995; Pollard 2006, Bastrakov et al. 2007; Ciobanu et al. 2013; Kontonikas-Charos et al. 2017; Verdugo-Ihl et al. 2019a) that the Roxby Downs Granite was a major fluid source for economic mineralisation, as evidenced by its strongly “granitophile” (U, Pb, W, Mo, Sn) signature of the ore and individual minerals (Ciobanu et al. 2013; Verdugo-Ihl et al. 2017, 2019a; Dmitrijeva et al. 2019a), and that initial deposit formation took place immediately following granite emplacement based on comparison of U-Pb ages for zircon and hematite (Cherry et al. 2018a; Courtney-Davies et al. 2019). The mineralogical

zonation of sulphides in the deposit from peripheries to core occurs as sphalerite → galena → pyrite → chalcopyrite → bornite → chalcocite → non-sulphide hematite and quartz rich core (Ehrig et al. 2012). This zoning helps define the geochemical signature of IOCG mineralization at Olympic Dam, which is mirrored by other deposits across the region (Dmitrijeva et al. 2019a, 2019b).

Events recognised at Olympic Dam and adjacent prospects which are suggested to have impacted on the evolution of the Olympic Dam deposit after initial formation include the ca. 1200-1100 Ma Musgravian Orogeny (Lu et al. 1996), emplacement of Gairdner dyke swarms at ca. 830 Ma, and the Delamerian Orogeny at 490-514 Ma. These events are all important as potential contributors to element and isotope mobility, which in turn impacts on radionuclide distributions within Cu-Au ores. Numerous poorly constrained events in the interval 1400-1100 Ma have been identified (e.g. Davidson et al. 2008; Ciobanu et al. 2013). Evidence includes, but is not restricted to a 1370 Ma monazite U-Pb age obtained from the Acropolis prospect, south of Olympic Dam (Cherry et al. 2018b). A hydrothermal event of possible Musgravian age is recorded at Olympic Dam from Re-Os analysis of pyrite-chalcopyrite mineral separates yielding ages of 1258 ± 28 Ma (McInnes et al. 2008). Events of this age (~1300 Ma) are also reported by Mass et al. (2011) by the analysis of Sm-Nd data from step-leached ores from Olympic Dam. Additionally, Pb isotope data taken from isotopically zoned pyrite in mineralized clastic sediments and galena in the ore have common Pb model ages which suggest sediment deposition/diagenesis and U introduction no earlier than 1.3-1.1 Ga (Mass et al. 2011). Further overprinting events within the Olympic Dam district include the emplacement of the Gairdner Dyke Swarms at ca. 830 Ma (Wingate et al. 1998; Huang et al. 2015; Apukhtina et al. 2016; Bowden et al. 2017) and the Delemerian orogeny (~500 Ma) led to extensive faulting and late veining across the region. Recent fission track evidence (Hall et al. 2018) suggests that tectonothermal effects continued until the Tertiary. Each of these events may have had an impact in the remobilisation of U, Pb, and other elements, throughout the Olympic Cu-Au province, leading to the various cycles of replacement, remobilization and recrystallization observed in several mineral groups from Olympic Dam (Macmillan et al. 2016a; Ciobanu et al. 2017; Verdugo-Ihl et al. 2017, 2019b) and elsewhere (Cherry et al. 2018; Owen et al. 2018).

The host Roxby Downs Granite is suggested to be the major source of U, indicated by U isotope ratios from Olympic Dam (Kirchenbauer et al. 2016). Uranium mainly occurs as uraninite, coffinite or brannerite (Macmillan et al. 2016a, 2017). In zones where U concentration is high (U > 500 ppm) the dominant mineral is uraninite while coffinite and brannerite tend to occur mainly in uranium poor (U < 500 ppm) zones (Ehrig et al. 2012, 2017). Macmillan et al. (2016a) identify four broad classes of uraninite evidencing U remobilisation and precipitation events throughout the evolution of the Olympic Dam deposit. Uranium minerals are often associated with zones of high-Fe alteration throughout the deposit and occur as massive aggregates, disseminations and

occasionally as microveinlets which cross-cut earlier lithology. Hematite, by far the most abundant mineral in the deposit, is the fourth most important uranium host (Ciobanu et al. 2013; Ehrig et al. 2017; Verdugo-Ihl et al. 2017). The greater part of the hematite and contained U-minerals report to flotation tails from which uranium is recovered by sulphuric acid leaching. Uranium is also recovered by acid leaching of copper concentrates.

2.3 *The Prominent Hill deposit*

The Prominent Hill deposit is hosted within a large brecciated fault system in the Mount Woods Inlier in the northern part of the Olympic Domain and is overlain by 50-400 m of Mesozoic sediments (Belperio et al. 2007; Schlegel and Heinrich 2015; Schlegel et al. 2018). The deposit contains an estimated resource (as of the 30th of June, 2018) of 130 Mt at 1.1 % Cu, 0.6 g/t Au, 3 g/t Ag (OZ Minerals 2018) and formed within steeply dipping hematite breccias with a Cu barren core at the central and eastern parts of the deposit (Schlegel and Heinrich 2015; Schlegel et al. 2018). The ore-forming process at Prominent Hill is suggested to begin with the onset of Hiltaba and GRV igneous activity at ca. 1600-1575 Ma with related tectonothermal activity possibly continuing until 1570 Ma (Bowden et al. 2017). Economic chalcopyrite, chalcocite and bornite mineralisation is hosted within the brecciated wall rocks and are mainly associated with areas of intense hematite metasomatism. The accessibility and permeability of the brecciated wall rocks allowed for favourable alteration and mineralisation sites for later metasomatic and mineralising hydrothermal fluids. Using $\delta^{34}\text{S}_{\text{V-CTD}}$ values, Schlegel et al. (2017) have shown that the isotopic signature of all sulphur involved with Cu-(Fe)-sulphide mineralisation at Prominent Hill matches that of the Hiltaba Suite and The Gawler Range Volcanics.

2.4 *Uranium and stable radiogenic lead*

Uranium is compatible within a range of mineral crystal structures at multiple oxidation states from U^{2+} to U^{6+} , and as such is able to reside in a large number of mineral species. Christy (2015) records more than 250 different U-bearing mineral species, while 5% of all known minerals contain U as an important structural constituent (Finch and Murakami 1999; Hazen et al. 2009), making it a very diverse element considering its relatively low crustal abundance.

The U grade within an IOCG deposit can largely be related to the composition of the host rocks (Hitzman and Valenta 2005). This relationship can be demonstrated when considering Prominent Hill, which is largely hosted by metavolcanic rocks, and Olympic Dam, hosted almost entirely within the Roxby Downs Granite (Hiltaba Suite equivalent). These host rocks have grades of <5 ppm, and 14 ppm U, respectively (Hitzman and Valenta 2005). In this instance the granitic host rocks of the Olympic Dam deposit are suggested to be major sources of mineralisation, an argument supported by the recognition of U-Pb-bearing hematite at Olympic Dam (Ciobanu et al. 2013) with an age concordant with the host granite. Subsequent work (Courtney-Davies et al.

2016, 2019a, 2019b) has validated the U-Pb hematite geochronometer at Olympic Dam and elsewhere in the region.

Hitzman and Valenta (2005) recognised three main U-bearing minerals, uraninite, coffinite and brannerite, host the bulk of U in IOCG style deposits. Within these three minerals U exists in its tetravalent state (U⁴⁺). Recently however, hematite within the Olympic Dam deposit has also been shown to host significant quantities of U (Ciobanu et al. 2013; Courtney-Davies et al. 2016; Verdugo-Ihl et al. 2017). Uranium minerals, uraninite, coffinite and brannerite, are more easily eliminated from processing streams via acid leaching, thus the relative proportion of U contained by hematite increases with processing.

When high concentrations of U are incorporated into a mineral, the mineral's structure becomes damaged via α -particle decay, in a process known as metamictization (Ewing et al., 2003). The degree of metamictization of a mineral increases systematically with U-Th content up to the point of total metamictization (Woodhead et al. 1991). In a crystal structure such as zircon, largely comprised of tightly bound silicate tetrahedra, metamictization will be preserved for a long time. Minerals such as uraninite, however, with its rapid annealing kinetics, can undergo multiple metamictization events yet be restored to near original form (Janeczek and Ewing 1991). This process makes U and its decay products more easily mobilised from such phases.

Decoupling of parent U and daughter Pb isotopes may occur via the above process, or by dissolution of U-bearing minerals. The most common and most stable isotope resulting from the decay of ²³⁸U within the discussed IOCG systems is ²⁰⁶Pb. Thus, understanding the mineralogy of uranium (Macmillan et al. 2016a, 2017), deposit- and grain-scale U-Pb systematics (Kirchenbaur et al. 2016; Courtney-Davies et al. 2019), and lead isotope ratios of single minerals (Schmandt 2019) provides valuable indirect information on the deportment of radioisotopes throughout the ²³⁸U decay chain. Lead occurs within the Olympic Cu-Au Province as both common and radiogenic Pb. The primary Pb-bearing minerals consist of galena (PbS), clausthalite (PbSe), and altaite (PbTe). Within the Olympic Dam deposit, galena is present in larger quantities than clausthalite or altaite while in the Prominent Hill deposit the prevalence of Pb-bearing minerals occurs in the order clausthalite>galena>altaite (Owen et al. 2018), indicating that areas of the Prominent Hill deposit are slightly more enriched in Se. The majority contribution of radiogenic Pb (i.e. formed post-IOCG mineralisation) within these minerals make them useful not only for tracking radionuclide deportment, but also for identifying deposit-scale overprinting episodes which may have affected the distribution of Cu mineralisation, due to their intimate relationship with the Cu-(Fe)-sulphides (Owen et al. 2018).

Minor amounts of uranium are contained within other accessory phases in Olympic Domain IOCG systems, notably REE-phosphates (monazite), fluorocarbonates (synchysite, bastnäsite), apatite

and baryte. Recent research by [Schmandt et al. \(2017, 2019a, 2019b\)](#) indicate their modest contribution to the overall RN budget within metallurgical processing streams.

2.5 Department and mineralogical expression of Intermediate RN from the ^{238}U decay series, fractionation and decoupling

The ^{238}U decay series comprises 15 decay events from parent to daughter isotopes until it reaches the stable ^{206}Pb isotope ([Figure 1.2](#)). Intermediate RN are those that occur between parent ^{238}U and the stable endmember daughter isotope ^{206}Pb . Secular equilibrium between the parent and their daughter isotopes exists when the daughter isotope concentrations remain at a steady state because loss through decay is matched by formation from their parent isotopes; however, each daughter isotope belongs to a different chemical element than its parent, and hence both physical and chemical properties will differ. The different chemical properties of daughter isotopes, coupled with processes like metamictization, recrystallization or dissolution, may result in decoupling of daughter and parent isotopes. It is possible that decoupling of the daughter isotopes has occurred at multiple times during the evolution of both the Prominent Hill and Olympic Dam deposits as visible by the different phases of U minerals ([Ciobanu et al. 2013](#); [Macmillan et al. 2016a, 2016b, 2016c, 2017](#)) which represent a series of dissolution, remobilization and recrystallization events.

The main isotopes addressed in this review are highlighted based on their physical properties, their mobility, their potential mineralogical hosts, and their ability to interact with each mineral phase. The elements and their respective isotopes are summarised as follows:

^{226}Ra forms from its parent isotope ^{230}Th , which is insoluble in most conditions. When Ra forms the salt radium chloride (RaCl_2), it becomes very mobile ([Coward and Burnett 1994](#)), and is able to migrate from its source quite easily; as such, the mineral phases in which Ra resides are of great importance ([Schmandt et al. 2019b](#)). Radium has many similar properties to Ba, meaning that it can be readily co-precipitated along with Ba within minerals that contain Ba, notably baryte, forming so-called *radiobarite* ([Lehto and Hou 2011](#)). In a ToF-SIMS study in which baryte has been exposed to Ra-bearing solutions for a period of time, baryte has been shown to undergo a homogeneous uptake of Ra into the crystals ([Klinkenberg et al. 2014](#)). Radium also easily incorporates into chlorides, sulphates and carbonates ([Coward and Burnett 1994](#); [Walther and Gupta 2015](#)), however this is only preserved in young strata. ^{226}Ra has a half-life of 1,600 years, after which it decays via alpha-decay to form ^{222}Rn .

When ^{222}Rn forms as a decay product from ^{226}Ra , an alpha particle is ejected which can damage the surrounding structure forming an alpha track ([Semkow 1990](#)). In a study of alpha-recoil damage on mineral structures, [Fleischer \(1982\)](#) shows that Rn, an inert gas, can successfully escape the crystal structure during this process. Accompanied by seismic pumping of fluids within cracks and interconnected pores, Rn may be transported far from its source before further decay. In a

study of a range of alpha-emitting minerals, [Malczewski and Dziurawicz \(2015\)](#) showed that uraninite had the lowest Rn emanation coefficient, despite having the highest U content of the minerals analysed. This could largely be due to the relatively simple crystal structure and chemical composition of uraninite facilitating a high rate of self-annealing ([Janeczek and Ewing 1991](#); [Janeczek et al. 1996](#); [Malczewski and Dziurawicz 2015](#)).

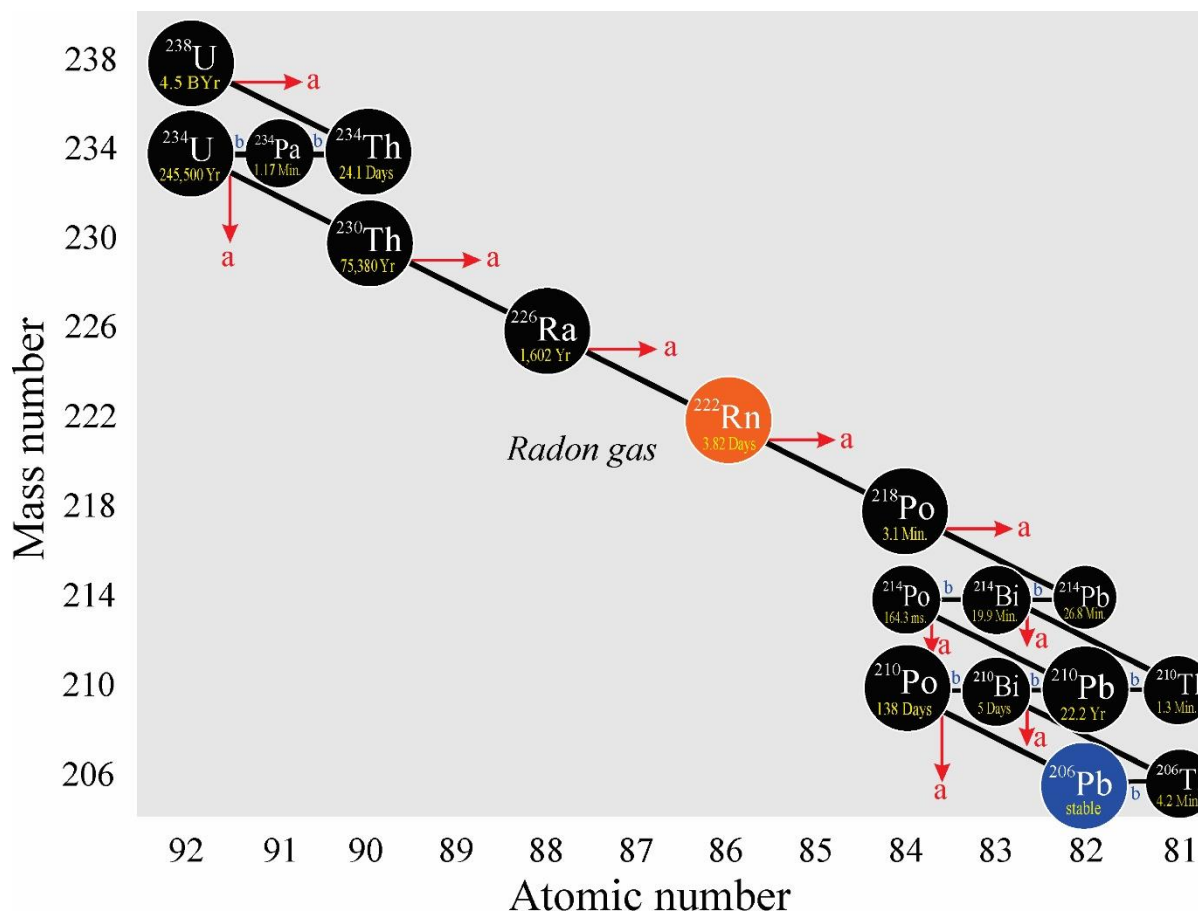


Figure 1.2: The ^{238}U decay series showing the progression of element isotopes from ^{238}U through to stable ^{206}Pb . Each alpha decay results in a decrease in atomic mass by four and atomic number by two; each beta decay results in an increase in atomic mass by one ([Cook et al. 2018](#)).

Polonium occurs as three isotopes following the beta decay of ^{222}Rn in the final stages of the ^{238}U decay series, ^{218}Po , ^{214}Po and ^{210}Po . Unlike Rn, Po is an extremely chemically active element, forming complexes with a large variety of mineral types such as oxides and hydroxides ([Lehto and Hou 2011](#)). ^{210}Po , the most toxic naturally occurring radionuclide ([Maxwell et al. 2013](#)), was discovered by Pierre and Marie Curie in 1898 within the mineral pitchblende and was described to have similar properties to bismuth ([Fry and Thoennesen 2013](#)). ^{210}Po has the longest half-life of the three Po isotopes in the ^{238}U decay chain (138.4 days), while ^{218}Po and ^{214}Po have half-lives of 3.1 min and 0.0002 sec, respectively. As well as its short half-life, it is extremely reactive with acidic solutions and is extremely volatile, meaning that it is extremely difficult to detect. Polonium's electron configuration in its neutral state resembles that of its fellow group members

on the periodic table, Se and Te can be considered analogous to the latter with a similar valence electron configuration ([Ansoborlo et al. 2012](#)).

Like Po, there are three Pb isotopes in the ^{238}U decay series which form from a Po isotope via alpha decay; ^{214}Pb , ^{210}Pb and ^{206}Pb . The natural abundance of common Pb is a subject that has required constant revision over the years. Recent TIMS analysis ([Thirlwall 2000](#)) on the renowned common lead standard, NIST SRM 981 revealed Pb isotope ratios of $^{206}\text{Pb}/^{204}\text{Pb}$ 16.9409(22), $^{207}\text{Pb}/^{204}\text{Pb}$ 15.4956(26), $^{208}\text{Pb}/^{204}\text{Pb}$ 36.722(80), $^{207}\text{Pb}/^{206}\text{Pb}$ 0.91469(7) and $^{208}\text{Pb}/^{206}\text{Pb}$ 2.16770(21) which widely agrees with a summary of NIST SRM 981 values ([Platzner et al. 2001](#)). Minerals containing highly radiogenic lead will be those which contain ratios of ^{206}Pb , ^{207}Pb and ^{208}Pb to ^{204}Pb significantly larger than those stated above. ^{206}Pb , ^{207}Pb and ^{208}Pb are the stable endmembers of the ^{238}U , ^{235}U and ^{232}Th decay series, respectively. ^{210}Pb is perhaps a more important target than its daughter ^{210}Po for ^{210}RN reduction as it has a much longer half-life (22.2 years). Thus, if reduction of ^{210}Pb is achieved, stemming the production of ^{210}Po in the process, the radioactivity of the ore material will naturally decrease within an acceptable time frame.

Prior to the start of research within the ARC Research Hub for Australian Copper-Uranium, much of the understanding of RN distribution in uranium-bearing copper ores and concentrates was based on indirect information, bulk measurement, or inspired guesswork based on known geochemical attributes of the isotopes concerned ([Cook et al. 2018](#)). Clearly, a large part of intermediate RN are hosted within U-bearing minerals capable of retaining the full decay chain (notably uraninite but also other minerals suitable for U-Pb geochronology such as zircon, hematite and apatite). Other potential hosts were more speculative and have been systematically addressed in this thesis and in related work. Development of nanoSIMS isotope mapping to directly visualise RN distributions at the grain-scale ([Rollog et al. 2019a](#)) and subsequent application to different mineral matrices ([Rollog et al. 2019b](#), [2019c](#), [2019d](#)) have proven pivotal for the much-improved knowledge currently available at the time of completing this thesis.

2.6 Lead chalcogenides

Lead forms an unusually large number of different minerals ([Christy 2015](#)). This mineralogical diversity is explained, largely, in terms of its outer electron configuration. Lead is a chalcophile element and as such preferentially forms minerals with heavier chalcogenides and pnictides, only forming oxycompounds upon subsequent oxidation ([Christy 2015](#)). Additionally, in its Pb(II) oxidation state, Pb contains a stereoactive lone pair of electrons, further adding to the variability, and also complexity, of its mineral species. In the context of identifying the potential carriers of radiogenic lead within IOCG deposits, the three most common lead minerals, galena (PbS), clausthalite (PbSe) and altaite (PbTe), are of particular importance. All three are relatively

abundant within ores and their respective concentrates from Olympic Dam and Prominent Hill, and typically – although not exclusively – occur as inclusions within Cu-(Fe)-sulphides.

Galena, clausthalite and altaite display partial solid solution as shown on the PbS-PbSe-PbTe ternary diagram (Figure 1.3). There are extensive miscibility gaps at temperatures below 300 °C but the PbS-PbSe and PbSe-PbTe pairs are miscible above 500°C (Chang and Liu 1994).

Of the three minerals, galena is the more abundant at Olympic Dam. Schmandt (2019) has shown that whereas most of this galena has formed by decay from parent U-minerals, there also exists non-radiogenic galena that was likely crystallised together with other sulphides at the time of initial deposit formation. Within the Prominent Hill deposit, clausthalite is observed to be by far the most common of the three Pb-chalcogenides. Chapter 4 will demonstrate how formation of clausthalite can be linked to reaction between Se-enriched Cu-(Fe)-sulphides and migrating radiogenic lead. Formation of clausthalite over galena is favoured by the greater electronegativity of selenium.

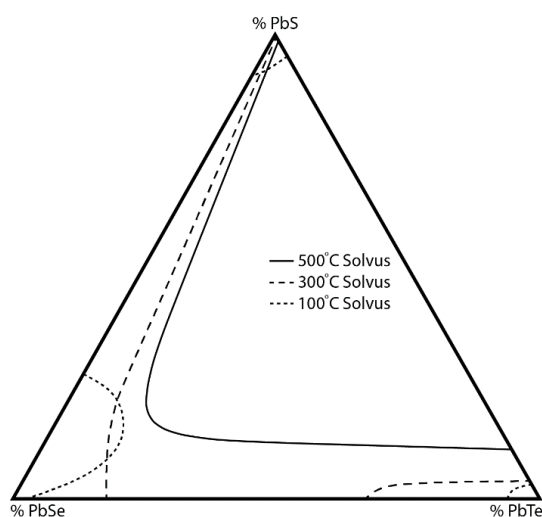


Figure 1.3: PbS-PbSe-PbTe ternary phase diagram with solidus lines between each phase, indicated at 100, 300 and 500 °C, as indicated. Note the larger field for PbSe at 100 °C compared with PbS and PbTe (after Chang and Liu 1994).

2.7 Scavenging of ^{210}RN

The central focus of this work is the occurrence, mobility and interplay between the mineralogy and geochemistry of ^{210}Pb and ^{210}Po (hereafter referred to as ^{210}RN) during the evolution of the ore bodies, as well as evidence for decoupling (secular disequilibrium) during mineral processing. ^{210}RN are relatively enriched in copper concentrates throughout the copper processing cycle at Olympic Dam (Lane et al. 2016; Cook et al. 2018). Sulphuric acid leaching efficiently removes a large part of U but it would appear that RN of concern readily re-adhere onto or diffuse into particles in the concentrate. Smelter feed (i.e. post-concentrate leach) is thus no longer in secular equilibrium. Furthermore, ^{210}RN accumulate within the Cu-sulphate rich smelter dust; this is subsequently recycled into the leach phase of Cu-processing to maximise Cu-recovery.

The mineral hosts for ^{210}RN were very poorly constrained at the start of the present project. It was presumed that they were present within parent U-bearing minerals, which also contain lead, notably uraninite (Macmillan et al. 2016a). They, and the complete decay chain, were also assumed to be contained within other minerals containing non-essential uranium and lead at concentrations of tens of parts-per-million to a few wt.%. Examples include zircon, apatite and hematite, all of which are dateable, albeit with evidence of open system behaviour in some mineral grains (Ciobanu et al. 2013; Krneta et al. 2017; Verdugo-Ihl et al. 2017; Courtney-Davies et al. 2019)

Beyond this, the likely hosts for ^{210}RN were largely speculative (Cook et al. 2018), based on the physical properties of their parent isotopes within the ^{238}U decay series, as well as the geochemical behaviour of each element in the decay chain. This prompted investigation of several key mineral groups: (i) galena, clausthalite and altaite are initially targeted for analysis due to their high radiogenic Pb content; (ii) rare-earth fluorocarbonates and phosphates, since both groups can incorporate U and Pb (Schmandt et al. 2017, 2019a); baryte, known to host Ra and subsequent decay products (Schmandt et al. 2019b). NanoSIMS isotope mapping was identified as an efficient method to screen individual minerals for their potential as RN-carriers (Rollog et al. 2019a), Subsequent work addressed fluorapatite, fluorite, rutile, molybdenite, covellite and many others (Rollog et al. 2019b, 2019c, 2019d) in a focused effort to identify and isotopically map both expected major hosts and also minor minerals that may nevertheless prove surprisingly good RN hosts.

Alongside baryte, aluminium-phosphate-sulphate (APS) minerals of the alunite supergroup stood out as good hosts for, and efficient scavengers for ^{226}Ra and ^{210}RN within the Olympic Dam Cu-processing circuit (Rollog et al. 2019a, 2019b; Owen et al. 2019a, 2019b). This family of minerals had been noted in prior mineralogical studies of the deposit but had not previously been the subject of detailed investigation. They were, however, addressed in the present study due to their ability to host a wide variety of di-, and tri-valent cations, and thus represented potential hosts for RN.

APS minerals of the alunite supergroup follow the general formula $[\text{MA}_3(\text{XO}_4)_2(\text{OH},\text{H}_2\text{O})_6]$. A broad array of solid solutions may be formed with exchange of mono-, di-, or trivalent cations in the M-site. Of great importance to the research reported here are the interplays between Ca, Sr and Pb cations at the M-site, where incorporated Pb may include ^{210}Pb . Ca- and Sr-bearing APS phases have been shown to preferentially incorporate Pb at the expense of Ca and Sr within metallurgical processing streams (Owen et al. 2019).

The crystal structures of APS phases fall within the same $R3m$ or $R\bar{3}m$ space group, accordingly forming almost identical structures with slight deviations. The most significant deviations occur along the c -axis depending largely upon the properties of the M-site cation whereby M^{2+} cations with larger ionic radii cause lengthening whereas smaller cations result in contraction of the

structure. This is especially the case in crandallite-group minerals when considering Ca^{2+} which has a relatively small ionic radius, compared with Sr^{2+} and Pb^{2+} . Its small ionic radius causes contraction of the crystal structure resulting in distortions among the sheets of AlO_6 octahedra, however when Sr^{2+} and Pb^{2+} are substituted at the M-site, the structure becomes more relaxed, hence increasing stability. There is also apparent lengthening along the *c*-axis with addition of SO_4 in Ca-, Sr- and Pb-bearing endmembers which may lead to an increase in thermodynamic stability (Schwab et al. 2005). In Pb(II) compounds the electronic configuration of Pb is $6s^2$, resulting in distortions in the stereochemistry of some compounds, which is known to cause a reduction in crystal symmetry in some Pb-rich alunites (Kolitsch and Pring 2001), adding complexity to substitution of Ca and Sr by Pb. This may also be why we see such variation along the *c*-axis between Sr-, and Pb-bearing APS members, despite their similar ionic radii (Shannon 1976).

3. RESEARCH OBJECTIVES AND THESIS STRUCTURE

The research gaps outlined above provide a context for the research reported in this thesis. Results contribute to a better understanding of radionuclide distributions in ores and copper concentrates and the evolution of those distributions during processing, as well as adding to models for the formation and evolution of IOCG deposits over geological time.

Research described has used different, complementary microanalytical tools to characterise the mineralogy within the ore feed and subsequent phases of the metallurgical processing cycle. Micron- to nanoscale imaging techniques used include backscatter electron imaging on a SEM platform, focused ion beam imaging and high-angle annular dark-field scanning transmission electron microscopy. Quantitative microanalysis using electron microprobe analysis, and laser ablation inductively coupled mass spectrometry. Additional data and interpretations were obtained using nanoscale secondary ion mass spectrometry (nanoSIMS) to provide qualitative information on RN distributions at the sub-micron scale, while a synchrotron Extended X-ray Absorption Fine Structure (EXAFS) study of synthetic Ca-, and Sr-bearing APS phases provided valuable data on the incorporation dynamics of Pb via acidified solution at room temperatures.

Each of the following thesis chapters are written independently as manuscripts for publication within peer reviewed journals. Approach, samples and analytical methods are outlined in the appropriate sections within each chapter:

Chapter 2 (unpublished manuscript) addresses the mobility of and origin of Pb within the Pb-chalcogenide minerals galena, clausthalite and altaite within representative samples from the Prominent Hill deposit. This work was undertaken primarily to track the distribution of the stable endmember isotope of ^{238}U decay, ^{206}Pb , as well as ^{207}Pb and ^{208}Pb from ^{235}U and ^{232}Th decay, with respect to Cu-(Fe)-sulphides within which the Pb-chalcogenides are often hosted. The degree

of decoupling between the radioisotopes between ^{238}U , ^{235}U and ^{232}Th , and the stable Pb isotopes can then be assessed.

Chapter 3 (published paper) describes a micron- to nanoscale study of clausthalite-bearing symplectites hosted within Cu-(Fe)-sulphides from the Prominent Hill deposit, from which a model for radiogenic Pb incorporation into Cu-(Fe)-sulphides is developed. The mechanism of Pb mobilisation within the deposit also adds to a growing body of evidence for one or more large-scale overprints within the Olympic Cu-Au Province, helping to explain the mineralogical heterogeneity observed within South Australian IOCG deposits.

Chapter 4 (submitted manuscript) addresses the petrography and chemistry of aluminium-phosphate-sulphate (APS) phases of the alunite supergroup from the Olympic Dam deposit. Based on nanoSIMS isotope mapping, scavenging of RN by APS phases during mineral processing can be documented. This chapter also provides an interpretation of the genesis and paragenetic position of APS minerals within the ore, and their relationships with other ore minerals. This chapter forms the basis for the synthetic study described in Chapter 5.

Chapter 5 (submitted manuscript) reports the results of an EXAFS study carried out at the Australian Synchrotron on synthetic Ca- and Sr-bearing APS phases and the incorporation dynamics of Pb via acidified solution at room temperature. The results carry significant implications for RN reduction and potential isolation from metallurgical processing streams. Controlled analysis of Pb-sorption by synthetic analogues of the APS phases enables investigation into their potential uses as sorbents for radionuclides within metallurgical processing streams. Here, we propose a method describing the addition of synthetically derived APS minerals to acidic Pb-bearing solutions with the aim of removing dissolved Pb from solution. We discuss how varying the composition of APS minerals, as well as changes to fluid conditions (pH and Pb concentration), effects Pb sorption.

Chapter 6 summarises the key findings presented within the thesis and identifies a number of areas which may be expanded in the future. A series of concluding remarks are made at the end of this section.

Chapter 7 is a compilation of other published material by the author of this thesis such as conference abstracts and co-authored publications. The chapter also contains appended material related to the published/submitted manuscripts in Chapters 2-5.

4 REFERENCES

- Allen, S.R., McPhie, J., Ferris, G., and Simpson, C. (2008) Evolution and architecture of a large felsic Igneous Province in western Laurentia: The 1.6 Ga Gawler Range Volcanics, South Australia. *Journal of Volcanology and Geothermal Resources* 648 172:132–147.
- Ansoborlo, E., Berard, P., Den Auwer, C., Leggett, R., Menetrier, F., Younes, A., Montavon, G., and Moisy, P. (2012) Review of chemical and radiotoxicological properties of polonium for internal contamination purposes. *Chemical Research in Toxicology* 25, 1551–1564.
- Apukhtina, O.B., Kamenetsky, V.S., Ehrig, K., Kamenetsky, M.B., McPhie, J., Maas, R., Meffre, S., Goemann, K., Rodemann, T., Cook, N.J., and Ciobanu, C.L. (2016) Postmagmatic magnetite–apatite assemblage in mafic intrusions: a case study of dolerite at Olympic Dam, South Australia. *Contrib. Mineral. Petrol.* 171:15.
- Barton, M.D. (2014) Iron Oxide(–Cu–Au–REE–P–Ag–U–Co) Systems. In: *Treatise on Geochemistry*, 2nd ed., Elsevier, pp 515–541.
- Bastrakov, E.N., Skirrow, R.G., and Davidson, G.J. (2007). Fluid Evolution and Origins of Iron Oxide Cu-Au Prospects in the Olympic Dam District, Gawler Craton, South Australia. *Economic Geology*, 102, 1415–1440.
- Beiser, A. (2003) *Concepts of Modern Physics* (Tata McGraw-Hill Education).
- Belperio, A., Flint, R., and Freeman, H. (2007) Prominent Hill: A Hematite-Dominated, Iron Oxide Copper-Gold System. *Economic Geology*, 102, 1499–1510.
- Benavides, J. (2010) Paragenesis and Genetic Model for Prominent Hill IOCG Deposit. Implications on Exploration (OZ Minerals Ltd).
- Betts, P.G., Valenta, R.K., and Finlay, J. (2003) Evolution of the Mount Woods Inlier, northern Gawler Craton, Southern Australia: an integrated structural and aeromagnetic analysis. *Tectonophysics*, 366, 83–111.
- Bowden, B., Fraser, G., Davidson, G.J., Meffre, S., Skirrow, R., Bull, S., and Thompson, J. (2017) Age constraints on the hydrothermal history of the Prominent Hill iron oxide copper-gold deposit, South Australia. *Mineralium Deposita*, 52(6), 863–881.
- Chalmers, N.C. (2007) Mount Woods Domain: proterozoic metasediments and intrusives. South Australia. Department of Primary Industries and Resources. Report Book, 20.
- Chang, L.L.Y. and Liu, H. (1994) Phase relations in the system PbS–PbSe–PbTe. *Mineralogical Magazine*, 58, 567–578.
- Cherry, A.R., Ehrig, K., Kamenetsky, V.S., McPhie, J., Crowley, J.L. and Kamenetsky, M.B. (2018a) Precise geochronological constraints on the origin, setting and incorporation of ca. 1.59 Ga surficial facies into the Olympic Dam Breccia Complex, South Australia. *Precambrian. Research* 315, 162–178.

- Cherry, A.R., Kamenetsky, V.S., McPhie, J., Thompson, J.M., Ehrig, K., Meffre, S., Kamenetsky, M.B., and Krneta, S. (2018b) Tectonothermal events in the Olympic IOCG Province constrained by apatite and REE-phosphate geochronology. *Australian Journal of Earth Sciences*, 65, 643–659.
- Christy, A.G. (2015) Causes of anomalous mineralogical diversity in the Periodic Table. *Mineralogical Magazine*, 79, 33–49.
- Ciobanu, C.L., Wade, B.P., Cook, N.J., Schmidt Mumm, A., and Giles, D. (2013) Uranium-bearing hematite from the Olympic Dam Cu–U–Au deposit, South Australia: A geochemical tracer and reconnaissance Pb–Pb geochronometer. *Precambrian Research*, 238, 129–147.
- Ciobanu, C.L., Cook, N.J., Ehrig, K. (2017) Ore minerals down to the nanoscale: Cu-(Fe)-sulphides from the iron oxide copper gold deposit at Olympic Dam, South Australia. *Ore Geology Reviews*, 81, 1218-1235.
- Conor, C., Raymond, O., Baker, T., Teale, G., Say, P., and Lowe, G. (2010) Alteration and Mineralisation in the Moonta-Wallaroo Cu-Au Mining Field Region, Olympic Domain, South Australia. *Hydrothermal Iron Oxide Copper-Gold and Related Deposits: A Global Perspective*, vol. 3, p. 1–24.
- Cook, N., Ciobanu, C., Ehrig, K., Slattery, A., Verdugo-Ihl, M., Courtney-Davies, L., and Gao, W. (2017) Advances and opportunities in ore mineralogy. *Minerals*, 7(12), 233.
- Cook, N., Ehrig, K., Rollog, M., Ciobanu, C., Lane, D., Schmandt, D., Owen, N., Hamilton, T. and Grano, S. (2018) ^{210}Pb and ^{210}Po in geological and related anthropogenic materials: implications for their mineralogical distribution in base metal ores. *Minerals*, 8(5), 211.
- Courtney-Davies, L., Zhu, Z., Ciobanu, C.L., Wade, B.P., Cook, N.J., Ehrig, K., Cabral, A.R., and Kennedy, A. (2016) Matrix-Matched Iron-Oxide Laser Ablation ICP-MS U–Pb Geochronology Using Mixed Solution Standards. *Minerals*, 6, 85–102.
- Courtney-Davies, L., Tapster, S.R., Ciobanu, C.L., Cook, N.J., Verdugo-Ihl, M.R., Ehrig, K.J., Kennedy, A.K., Gilbert, S.E., Condon, D.J., and Wade, B.P. (2019a) A multi-technique evaluation of hydrothermal hematite U-Pb isotope systematics: Implications for ore deposit geochronology. *Chemical Geology*, 513, 54–72.
- Courtney-Davies, L., Ciobanu, C.L., Verdugo-Ihl, M.R., Dmitrijeva, D., Cook, N.J., Ehrig, K. and Wade, B.P. Hematite geochemistry and geochronology resolve genetic and temporal links among iron-oxide copper gold systems, Olympic Dam district, South Australia. *Precambrian Research* (in review)
- Cowart, J.B. and Burnett, W.C. (1994) The Distribution of Uranium and Thorium Decay-Series Radionuclides in the Environment - A Review. *Journal of Environment Quality*, 23, 651.
- Dmitrijeva, M., Ehrig, K.J., Ciobanu, C.L., Cook, N.J., Verdugo-Ihl, M.R., and Metcalfe, A.V. (2019a) Defining IOCG signatures through compositional data analysis: A case study of litho-geochemical zoning from the Olympic Dam deposit, South Australia. *Ore Geology Reviews*, 105, 86–101.

- Dmitrijeva, M., Ciobanu, C. L., Ehrig, K. J., Cook, N. J., Metcalfe, A. V., Verdugo-Ihl, M. R., and McPhie, J. (2019) Mineralization-alteration footprints in the Olympic Dam IOCG district, South Australia: the Acropolis prospect. *Journal of Geochemical Exploration*, 205, 106333.
- Ehrig, K., McPhie, J., and Kamenetsky, V.S. (2012) Geology and mineralogical zonation of the Olympic Dam Iron Oxide Cu-U-Au-Ag deposit, South Australia. In: F. Camus, J.W. Hedenquist, M. Harris (eds.), *Geology and Genesis of Major Copper Deposits and Districts of the World, a Tribute to Richard Sillitoe*. Society of Economic Geologists Special Publication, 16, 237–267.
- Ehrig, K., Kamenetsky V.S., McPhie, J., Cook, N.J., Ciobanu, C.L. (2017) Olympic Dam iron oxide Cu-U-Au-Ag deposit. In *Australian Ore Deposits* (N. Phillips, ed.), AusIMM, Melbourne, Australia, p. 601–610.
- Ewing, R.C., Meldrum, A., Wang, L.M., Weber, W.J., and Corrales, L.R. (2003) Radiation damage in zircon. *Reviews in Mineralogy and Geochemistry*, 53, 387–425.
- Fanning, C. (1997) *Geochronological Synthesis of Southern Australia, Part II, The Gawler Craton*. South Australia Department of Mines and Energy, Open File Envelope 8918.
- Fanning, C., Reid, A., and Teale, G. (2007) *A Geochronological Framework for the Gawler Craton, South Australia* (South Australia: Geological Survey).
- Ferris, G.M., Schwarz, M.P., and Heither, P. (2002) The Geological Framework, Distribution and Controls of Fe-Oxide Cu-Au Mineralisation in the Gawler Craton, South Australia: Part I- Geological and Tectonic Framework. *Hydrothermal iron oxide copper–gold and related deposits: a global perspective*.
- Finch, R.J. and Murakami, T. (1999) Systematics and Paragenesis of Uranium Minerals. *Reviews in Mineralogy and Geochemistry*, 38, 91–180.
- Finlay, J. (1993) *Structural interpretation in the Mount Woods Inlier*. Honours Thesis - Monash University, Department of Earth Sciences.
- Fleischer, R.L. (1982) Alpha-recoil damage and solution effects in minerals: uranium isotopic disequilibrium and radon release. *Geochimica et Cosmochimica Acta*, 46, 2191–2201.
- Foden, J., Elburg, M.A., Dougherty-Page, J., and Burt, A. (2006) The Timing and Duration of the Delamerian Orogeny: Correlation with the Ross Orogen and Implications for Gondwana Assembly. *The Journal of Geology*, 114, 189–210.
- Forbes, C.J., Giles, D., Hand, M., Betts, P.G., Suzuki, K., Chalmers, N., and Dutch, R. (2011) Using P–T paths to interpret the tectonothermal setting of prograde metamorphism: An example from the northeastern Gawler Craton, South Australia. *Precambrian Research*, 185, 65–85.
- Freeman, H. and Hart, J. (2003) Geophysics of the Prominent Hill prospect, South Australia. *ASEG Extended Abstracts 2003*, 93–100.

- Freeman, H. and Tomkinson, M. (2010) Geological setting of iron oxide related mineral-isolation in the Southern Mount Woods Domain, South Australia. *Hydrothermal Iron Oxide Copper–Gold and Related Deposits: A Global Perspective*, 3, 171–190.
- Fry, C. and Thoennessen, M. (2013) Discovery of the thallium, lead, bismuth, and polonium isotopes. *Atomic Data and Nuclear Data Tables*, 99, 365–389.
- Geoscience Australia (2016) Copper – Geoscience Australia. URL: <http://www.ga.gov.au/scientific-topics/minerals/mineral-resources/copper> (accessed 10.09.2016)
- Government of South Australia Department for Energy and Mining (2016) South Australia’s copper strategy. URL: <http://www.energymining.sa.gov.au/minerals> (accessed 10.09.16)
- Hall, J.W., Glorie, S., Reid, A.J., Collins, A.S., Jourdan, F., Danišik, M., and Evans, N. (2018) Thermal history of the northern Olympic Domain, Gawler Craton; correlations between thermochronometric data and mineralising systems. *Gondwana Research*, 56, 90–104.
- Hand, M., Reid, A., and Jagodzinski, L. (2007) Tectonic Framework and Evolution of the Gawler Craton, Southern Australia. *Economic Geology*, 102, 1377–1395.
- Haynes, D.W., Cross, K.C., Bills, R.T., and Reed, M.H. (1995) Olympic Dam ore genesis; a fluid-mixing model. *Economic Geology*, 90, 281–307.
- Hazen, R.M., Ewing, R.C., and Sverjensky, D.A. (2009) Evolution of uranium and thorium minerals. *American Mineralogist*, 94, 1293–1311.
- Hitzman, M.W. (2000) Iron oxide-Cu-Au deposit: What, where, when, and why, in Porter, T.M., ed., *Hydrothermal iron oxide copper-gold and related deposits a global perspective: Adelaide, Australian Mineral Foundation*, p. 9–26.
- Hitzman, M.W., Oreskes, N., Einaudi, M.T. (1992) Geological characteristics and tectonic setting of Proterozoic iron-oxide (Cu–U–Au–REE) deposits. *Precambrian Research* 58, 241–287.
- Hitzman, M.W., and Valenta, R.K. (2005) Uranium in Iron Oxide-Copper-Gold (IOCG) Systems. *Economic Geology*, 100, 1657–1661.
- Huang, Q., Kamenetsky, V.S., McPhie, J., Ehrig, K., Meffre, S., Maas, R., Thompson, J., Kamenetsky, M., Chambefort, I., Apukhtina, O., and Hu, Y. (2015) Neoproterozoic (ca. 820–830 Ma) mafic dykes at Olympic Dam, South Australia: links with the Gairdner large igneous province. *Precambrian Research*, 271, 160–172.
- Johnson, J.P. and McCulloch, M.T. (1995) Sources of mineralising fluids for the Olympic Dam deposit (South Australia): Sm-Nd isotopic constraints. *Chemical Geology*, 121(1-4), 177–199.
- Jagodzinski, E., Reid, A., Chalmers, N.C., Swain, G., Frew, R.A., and Foudoulis, C. (2007) Compilation of SHRIMP U-Pb geochronological data for the Gawler craton, South Australia, 2007. Primary Industries and Resources South Australia, Division of Minerals and Energy Resources.

- Janeczek, J. and Ewing, R.C. (1991) X-ray powder diffraction study of annealed uraninite. *Journal of Nuclear Materials* 185, 66–77.
- Janeczek, J., Ewing, R.C., Oversby, V.M., and Werme, L.O. (1996) Spent Fuels Uraninite and UO₂ in spent nuclear fuel: a comparison. *Journal of Nuclear Materials*, 238, 121–130.
- Johnson, J.P. and McCulloch, M.T. (1995) Sources of mineralising fluids for the Olympic Dam deposit (South Australia) : Sm-Nd isotopic constraints. *Chemical Geology*, 121, 177–199.
- Kirchenbaur, M., Maas, R., Ehrig, K., Kamenetsky, V.S., Strub, E., Ballhaus, C., and Münker, C. (2016) Uranium and Sm isotope studies of the supergiant Olympic Dam Cu–Au–U–Ag deposit, South Australia. *Geochimica et Cosmochimica Acta*, 180, 15–32.
- Klinkenberg, M., Brandt, F., Breuer, U., and Bosbach, D. (2014) Uptake of Ra during the recrystallization of barite: a microscopic and time of flight-secondary ion mass spectrometry study. *Environmental Science & Technology*, 48(12), 6620-6627.
- Kolitsch, U. and Pring, A. (2001) Crystal chemistry of the crandallite, beudantite and alunite groups: a review and evaluation of the suitability as storage materials for toxic metals. *Journal of Mineralogical and Petrological Sciences*, 96(2), 67–78.
- Kontonikas-Charos, A., Ciobanu, C.L., Cook, N.J., Ehrig, K., Krneta, S., and Kamenetsky, V.S. (2017) Feldspar evolution in the Roxby Downs Granite, host to Fe-oxide Cu-Au-(U) mineralisation at Olympic Dam, South Australia. *Ore Geology Reviews*, 80, 838–859.
- Lane, D.J., Cook, N.J., Grano, S.R., and Ehrig, K. (2016) Selective leaching of penalty elements from copper concentrates: A review. *Minerals Engineering*, 98, 110–121.
- Lehto, J. and Hou, X. (2011) *Chemistry and Analysis of Radionuclides: Laboratory Techniques and Methodology*, John Wiley & Sons.
- Lu, J., Plimer, I.R., Foster, D.A., and Lottermoser, B.G. (1996) Multiple post-orogenic reactivation in the Olary Block, South Australia: evidence from ⁴⁰Ar/³⁹Ar dating of pegmatitic muscovite. *International Geology Review*, 38(7), 665–685.
- Macmillan, E., Cook, N.J., Ehrig, K., Ciobanu, C.L. and Pring, A. (2016a) Uraninite from the Olympic Dam IOCG-U-Ag deposit: Linking textural and compositional variation to temporal evolution. *American Mineralogist*, 101, 1295–1320.
- Macmillan, E., Ciobanu, C.L., Ehrig, K., Cook, N.J. and Pring, A. (2016b) Chemical zoning and lattice distortion in uraninite from Olympic Dam, South Australia. *American Mineralogist*, 101, 2351–2354.
- Macmillan, E., Ciobanu, C.L., Ehrig, K., Cook, N.J., and Pring, A. (2016c) Replacement of uraninite by bornite via coupled dissolution-precipitation: Evidence from texture and microstructure. *The Canadian Mineralogist*, 54(6), 1369–1383.

- Macmillan, E., Cook, N.J., Ehrig, K. and Pring, A. (2017) Chemical and textural interpretation of late-stage coffinite and brannerite from the Olympic Dam IOCG-Ag-U deposit. *Mineralogical Magazine*, 81(6), 1323–1366.
- Malczewski, D. and Dziurawicz, M. (2015) ^{222}Rn and ^{220}Rn emanations as a function of the absorbed α -doses from select metamict minerals. *American Mineralogist*, 100, 1378–1385.
- Maxwell, S.L., Culligan, B.K., Hutchison, J.B., Utsey, R.C., and McAlister, D.R. (2013) Rapid determination of ^{210}Po in water samples. *Journal of Radioanalytical and Nuclear Chemistry*, 298, 1977–1989.
- Meffre, S., Ehrig, K., Kamenetsky, V.S., Chambefort, I., Maas, R., and McPhie, J. (2010) Pb isotopes at Olympic Dam: Constraining sulphide growth: Giant ore deposits down under: Proceedings of 13th Quadrennial International Association on the Genesis of Ore Deposits (IAGOD) Symposium, Adelaide, South Australia, 78–79.
- McInnes, B.I.A., Keays, R.R., Lambert, D.D., Hellstrom, J., and Allwood, J.S. (2008) Re–Os geochronology and isotope systematics of the Tanami, Tennant Creek and Olympic Dam Cu–Au deposits. *Australian Journal of Earth Sciences*, 55(6-7), 967–981.
- Owen, N., Ciobanu, C., Cook, N., Slattery, A., and Basak, A. (2018) Nanoscale study of clausenthalite-bearing symplectites in Cu-Au-(U) ores: Implications for ore genesis. *Minerals*, 8(2), 67.
- Owen, N.D., Cook, N.J., Rollog, M., Ehrig, K.J., Schmandt, D.S., Ram, R., Brugger, J., Ciobanu, C.L., Wade, B. and Guagliardo, P. (2019a) REE-, Sr-, Ca-aluminum-phosphate-sulfate minerals of the alunite supergroup and their role as hosts for radionuclides. *American Mineralogist: Journal of Earth and Planetary Materials*, 104(12), 1806-1819.
- Owen, N.D., Brugger, J., Ram, R., Eschmann, B., Cook, N.J., Ehrig, K.J., Schmandt, D.S., Rollog, M., and Guagliardo, P. (2020) A sponge for radionuclides: a study on the dynamic uptake of lead by synthetic aluminium-phosphate-sulphates. *Applied Geochemistry*, (in review).
- OZ Minerals (2018) 2018 mineral resource and ore reserve statement and explanatory notes. OZ Minerals Ltd. URL: <https://www.ozminerals.com/operations/resources-reserves/> (accessed 20.06.2019).
- Platzner, I., Ehrlich, S., and Halicz, L. (2001) Isotope-ratio measurements of lead in NIST standard reference materials by multiple-collector inductively coupled plasma mass spectrometry. *Fresenius' Journal of Analytical Chemistry*, 370, 624–628.
- Pollard, P.J. (2006) An intrusion-related origin for Cu–Au mineralization in iron oxide–copper–gold (IOCG) provinces. *Mineralium Deposita*, 41, 179.
- Reid, A.J. (2019) The Olympic Cu-Au Province, Gawler Craton: A Review of the Lithospheric Architecture, Geodynamic Setting, Alteration Systems, Cover Successions and Prospectivity. *Minerals*, 9(6), 371.

- Reid, A.J. and Hand, M. (2012) Mesoarchean to Mesoproterozoic evolution of the southern Gawler Craton, South Australia. *Episodes*, 35, 216–225.
- Rollog, M., Cook, N.J., Gugliardo, P., Ehrig, K., and Kilburn, M. (2019a) In situ spatial distribution mapping of radionuclides in minerals by nanoSIMS. *Geochemistry: Exploration, Environment, Analysis*; <https://doi.org/10.1144/geochem2018-038>
- Rollog, M., Cook, N.J., Gugliardo, P., Ehrig, K., Ciobanu, C.L., and Kilburn, M. (2019b). Detection of Trace Elements/Isotopes in Olympic Dam Copper Concentrates by nanoSIMS. *Minerals*, 9(6), 336.
- Rollog, M., Cook, N.J., Gugliardo, P., Ehrig, K., and Kilburn, M. (2019c) Radionuclide-bearing minerals in Olympic Dam copper concentrates. *Hydrometallurgy* (accepted subject to minor revision).
- Rollog, M., Cook, N.J., Gugliardo, P., Ehrig, K., and Kilburn, M. (2019d) Radionuclide distributions in Olympic Dam copper concentrates: the significance of minor hosts, incorporation mechanisms, and the role of mineral surfaces. *Minerals Engineering* (in review)
- Schlegel, T.U. and Heinrich, C.A. (2015) Lithology and Hydrothermal Alteration Control of the Distribution of Copper Grade in the Prominent Hill Iron Oxide-Copper-Gold Deposit (Gawler Craton, South Australia). *Economic Geology*, 110, 1953–1994.
- Schlegel, T.U., Wagner, T., Boyce, A., and Heinrich, C.A. (2017) A magmatic source of hydrothermal sulfur for the Prominent Hill deposit and associated prospects in the Olympic iron oxide copper-gold (IOCG) province of South Australia. *Ore Geology Reviews*, 89, 1058–1090.
- Schlegel, T.U., Wagner, T., Wälle, M., and Heinrich, C.A. (2018) Hematite Breccia-Hosted Iron Oxide Copper-Gold Deposits Require Magmatic Fluid Components Exposed to Atmospheric Oxidation: Evidence from Prominent Hill, Gawler Craton, South Australia. *Economic Geology*, 113(3), 597–644.
- Schmandt, D.S. (2019) Mineralogical distributions of radionuclides in copper-uranium ores, Olympic Dam, South Australia. Ph.D. thesis, The University of Adelaide, Adelaide.
- Schmandt, D., Cook, N.J., Ciobanu, C.L., Ehrig, K., Wade, B., Gilbert, S., and Kamenetsky, V. (2017) Rare earth element fluorocarbonate minerals from the Olympic Dam Cu-U-Au-Ag deposit, South Australia. *Minerals*, 7(10), 202.
- Schmandt, D.S., Cook, N.J., Ciobanu, C.L., Ehrig, K., Wade, B.P., Gilbert, S., and Kamenetsky, V.S. (2019a) Rare earth element phosphate minerals from the Olympic Dam Cu-U-Au-Ag deposit, South Australia: Recognizing temporal-spatial controls on REE mineralogy in an evolved IOCG system. *The Canadian Mineralogist*, 57(1), 3–24.
- Schmandt, D.S., Cook, N.J., Ehrig, K., Gilbert, S., Wade, B.P., Rollog, M., Ciobanu, C.L., and Kamenetsky, V.S. (2019b) Uptake of trace elements by baryte during copper ore processing: A case study from Olympic Dam, South Australia. *Minerals Engineering*, 135, 83–94.

- Schwab, R.G., Pimpl, T., Schukow, H., Stolle, A., and Breiter, D.K. (2005) Compounds of the crandallite-type: Synthesis, properties and thermodynamic data of Ca–Sr–Ba–Pb-(arseno)-woodhouseites. *Neues Jahrbuch für Mineralogie Abhandlungen*, 181, 207–218.
- Semkow, T.M. (1990) Recoil-emanation theory applied to radon release from mineral grains. *Geochimica et Cosmochimica Acta*, 54, 425–440.
- Shannon, R.D. (1976) Revised effective ionic radii and systematic studies of interatomic distances in halides and chalcogenides. *Acta Crystallographica A: crystal physics, diffraction, theoretical and general crystallography*, 32(5), 751–767.
- Skirrow, R.G. and Davidson, G.J. (2007) A special issue devoted to Proterozoic iron oxide Cu-Au-(U) and gold mineral systems of the Gawler Craton: preface. *Economic Geology*, 102(8), 1373–1375.
- Skirrow, R.G., van der Wielen, S.E., Champion, D.C., Czarnota, K., and Thiel, S. (2018) Lithospheric Architecture and Mantle Metasomatism Linked to Iron Oxide Cu-Au Ore Formation: Multidisciplinary Evidence from the Olympic Dam Region, South Australia. *Geochemistry, Geophysics, Geosystems*, 19, 2673–2705.
- Thirlwall, M.F. (2000) Inter-laboratory and other errors in Pb isotope analyses investigated using a ^{207}Pb – ^{204}Pb double spike. *Chemical Geology*, 163, 299–322.
- Verdugo-Ihl, M.R., Ciobanu, C.L., Cook, N.J., Ehrig, K.J., Courtney-Davies, L., and Gilbert, S. (2017) Textures and U-W-Sn-Mo signatures in hematite from the Olympic Dam Cu-U-Au-Ag deposit, South Australia: Defining the archetype for IOCG deposits. *Ore Geology Reviews*, 91, 173–195.
- Verdugo-Ihl, M.R., Ciobanu, C.L., Cook, N.J., Ehrig, K.J., and Courtney-Davies, L. (2019a). Defining early stages of IOCG systems: Evidence from iron oxides in the outer shell of the Olympic Dam deposit, South Australia. *Mineralium Deposita*, 1–24.
- Verdugo-Ihl, M.R., Ciobanu, C.L., Slattery, A., Cook, N.J., Ehrig, K., and Courtney-Davies, L. (2019b) Copper-arsenic nanoparticles in hematite: Fingerprinting fluid-mineral interaction. *Minerals*, 9(7), 388.
- Walther, C. and Gupta, D.K. (2015) *Radionuclides in the environment: Influence of chemical speciation and plant uptake on radionuclide migration*, Springer.
- Wingate, M.T., Campbell, I.H., Compston, W., and Gibson, G.M. (1998) Ion microprobe U–Pb ages for Neoproterozoic basaltic magmatism in south-central Australia and implications for the breakup of Rodinia. *Precambrian Research*, 87(3-4), 135–159.
- Woodhead, J.A., Rossman, G.R., and Silver, L.T. (1991) The metamictization of zircon: Radiation dose-dependent structural characteristics. *American Mineralogist*, 76, 1–2.

CHAPTER 2

LEAD ISOTOPE DATA FOR Pb-CHALCOGENIDES

Lead isotope data for Pb-chalcogenides

1. Introduction

Iron-oxide copper gold (IOCG) style deposits of Proterozoic age are among the most complex and enigmatic mineralising systems on Earth (Barton, 2014). Although much evidence has been accumulated to support genetic models and constrain the initial conditions of formation of these enigmatic deposits, less is known about the impacts of post-depositional tectonothermal reactivation on these deposits, and specifically, how an overprinting event or series of events will modify the fundamental mineralogy and geochemistry of the deposits.

Uranium, a common component of many IOCG systems, is a particularly mobile element, especially under oxidising conditions (U^{6+}). Evidence from the Olympic Dam ore system, South Australia, has shown that uranium mineralogy has evolved over time as a response to cycles of replacement, remobilization and recrystallization during the 1.6 Ga since initial formation (Macmillan et al., 2016, 2017). Similar phenomena are recognized among several other mineral groups in the deposit. This redistribution has, however, occurred without obliterating primary deposit-scale mineral zonation.

Within the deepest parts of the cogenetic Olympic Dam Cu-Au-Ag-U deposit, a vein of massive galena has been reported (Meffre et al., 2010), which contains multiple growth zones with less radiogenic Pb occurring in the outer zone and highly radiogenic Pb in the central zone, revealing crustal growth ages of 1200-1400 Ma and 0 Ma respectively. These observations indicate that radiogenic Pb was likely mobile within deep parts of the deposit immediately subsequent to the introduction of U. The Pb-isotope signatures of Pb-chalcogenides have also been investigated in the Olympic Dam deposit (Schmandt, 2019), similarly suggesting highly radiogenic origins for Pb. Here, Pb-chalcogenides are often hosted within Cu-(Fe)-sulphides, thus supplying important information regarding the pervasiveness of cycles of Pb dissolution, remobilisation and recrystallisation throughout the evolution of the deposit following initial formation at ~1.6 Ga.

Whereas the mobility of U within mineralised rocks is relatively well understood and documented in the literature, the comparative behaviour of the intermediate daughter products of uranium decay (i.e. between parent U and the stable daughter isotopes of Pb) during fluid-assisted tectonothermal overprinting is less widely reported due to the difficulty of accurately measuring concentrations of shorter half-life isotopes at extremely low concentrations. Evidence reported elsewhere in this thesis (Owen et al., 2018), and in other publications (Rollog et al., 2019a, 2019b; Schmandt, 2019), has shown that products of uranium decay, notably but not restricted to stable radiogenic lead (^{206}Pb , ^{207}Pb , ^{208}Pb), may migrate from the parent U-mineral over distances ranging from nanometres upwards, and combine with available ligands to form 'new' minerals, or become incorporated into existing minerals. The grain-scale heterogeneity of U/Pb ratios in some hematite

grains from IOCG deposits (Courtney-Davies et al., 2019) is further evidence for mobility of U and/or Pb within individual minerals. Fluid-assisted remobilization occurs at an extremely fine scale, necessitating careful study using a combination of different analytical techniques that can bridge scales of observation.

Galena (PbS) forms a complete solid solution series with clausthalite (PbSe) and also displays limited solid solution towards altaite (PbTe) (Chang and Liu, 1994). All three Pb-chalcogenides, along with a range of other selenides and tellurides, are common minor components of ~1590-1585 Ma IOCG-style mineralization across the Olympic Cu-Au Province, South Australia. This contribution addresses the physical character and Pb-isotope signatures of Pb-chalcogenides in a effort to place constraints on the mobility of ^{238}U -chain radionuclides and the evolution of Pb-isotope systematics during hydrothermal overprinting following the initial mineralisation event.

2. Sampling and analytical methodology

The present study aimed at deriving insights into Pb-isotope ratios in Pb-chalcogenides and associated Cu-(Fe)-sulphides from one representative IOCG system within the Mt Woods Inlier. The sample suite, identical to that used by Owen et al. (2018), consisted of Cu-(Fe)-sulphide rich mineral separates. These laboratory-made concentrates were created via crushing and froth flotation of ore to remove the majority of gangue. Particle size within the samples is in the order of 20-300 μm . Each sample was prepared as a one inch-diameter round for petrographic and compositional analysis.

2.1. Scanning Electron Microscopy

Scanning electron microscopy (SEM) in backscatter electron (BSE) mode was used for basic mineral identification, to evaluate grain morphology and textural relationships between Pb-chalcogenides and their hosts (e.g., sited in cracks or fissures, as inclusions, along mineral boundaries, or as symplectites with host sulphides). SEM study also provided an approximate estimation of the relative abundances of each Pb-chalcogenide. All SEM analysis was undertaken using a FEI Quanta 450 FEG Environmental Scanning Electron Microscope (Adelaide Microscopy, The University of Adelaide) operated in high-vacuum mode at 20 kV and a spot size of 4 to generate high spatial resolution (down to 0.1 μm). Semi-quantitative compositional data was obtained using the built-in energy-dispersive X-ray spectroscopy (EDS) detector.

2.2. Laser Ablation Inductively Coupled Mass Spectrometry

Laser ablation inductively coupled mass spectrometry (LA-ICP-MS) is used for the quantitative analysis of trace elements and of relevant U, Pb and Th isotopes within individual target minerals. LA-ICP-MS analysis was undertaken using an Agilent 7700s mass spectrometer with attached ASI M-50 laser ablation system (Adelaide Microscopy, The University of Adelaide). The following

isotopes were monitored: ^{82}Se , ^{125}Te , ^{204}Pb , ^{206}Pb , ^{208}Pb , ^{232}Th , ^{235}U and ^{238}U , with isotopes of Ag, Sb, Hg, Tl and Bi also being measured to account for any overlapping spectral data.

The main reference material used was a sample of Broken Hill galena for which published isotopic ratios are available (McFarlane et al., 2016), as well as the NIST610 and MASS-1 reference standards. Standards were analysed at the start and end of each batch run, and after every 15-20 unknowns. Total count times for each analysis ran for 30 sec with an additional 30 sec of background measured prior to ablation. Dwell times were 0.1 sec for Pb isotopes, 0.05 sec for Tl and Hg isotopes, 0.02 sec for Th and U isotopes, and 0.01 sec for Bi, Se and Te isotopes. Output data was analysed using correction software Igor and Iolite v3.4 (Paton et al., 2011). The data, comprising individual Pb isotope abundances and their calculated ratios, enables the isotopic fingerprints of each mineral phase to be established.

For high-precision quantitative LA-ICP-MS analysis, a spot size of $\sim 20\ \mu\text{m}$ is desirable. However, many of the minerals targeted in this study ranged in size from $20\ \mu\text{m}$ down to less than $2\ \mu\text{m}$ in diameter, which either precludes their use for analysis, or results in data carrying a greater than ideal error margin due to dilution of the signal by the surrounding host mineral. Some of the data obtained is thus semi-quantitative, and in such cases, LA-ICP-MS counts were interpreted only as a confirmation of the radiogenic/non-radiogenic nature of the target minerals.

3. Results

3.1. Sample mineralogy

The mineralogy of the sample set consists of pyrite, chalcopyrite, bornite and chalcocite, accompanied by the U-minerals coffinite, brannerite and uraninite, and small quantities of gangue, mostly hematite. Baryte was observed in all samples, albeit in small quantities. Analogous to observations by Ciobanu et al. (2017) from Olympic Dam, the ore minerals generally show the following sequence of enrichment/replacement: pyrite \rightarrow chalcopyrite \rightarrow bornite and bornite \rightarrow chalcocite.

Lead-chalcogenides (galena, clausthalite and altaite) occur as inclusions in the Cu-(Fe)-sulphides, infilling cracks in those minerals, along grain boundaries, and, as symplectites within chalcopyrite, bornite and chalcocite (and less commonly within pyrite). Close relationships between baryte and Pb-chalcogenides are rarely observed at the micron-scale. A range of other accessory sulphides and selenides are observed. Although most Co occurs as carrollite and cobaltite, or is incorporated within pyrite, the rare selenides tyrrellite, $(\text{Cu},\text{Co},\text{Ni})_3\text{Se}_4$, and penroseite, $(\text{Ni},\text{Co},\text{Cu})\text{Se}_2$, were observed in trace quantities. Other chalcogenides (e.g. skippenite and hessite) were also observed as sub $5\text{-}\mu\text{m}$ -sized grains.

3.2. Mineral Textures

Lead chalcogenides (galena, clausthalite and altaite) occur within the Cu-(Fe)-sulphides as inclusions down to the sub-micron scale and as such are recognised as intimately related to the evolution of the Pb-chalcogenides. A variety of textures between Pb-chalcogenides and their host minerals are observed. These are summarised in the BSE images shown as [Figure 1](#). The Pb-chalcogenides occur in order of abundance clausthalite > galena > altaite, and do not show any specific preference for any particular host Cu-(Fe)-sulphide. Rather, they display an overall preference for Cu-(Fe)-sulphide hosts in the order chalcopyrite > bornite > chalcocite. The Cu-(Fe)-sulphides incorporate the Pb-chalcogenides as inclusions, along annealed grain boundaries, and, most commonly, as symplectite-type textures formed within the Cu-(Fe)-sulphides ([Figure 1c, d](#)). Structures which are evident of diffusion of Pb into the Cu-(Fe)-sulphides are also noted and have been documented in detail elsewhere ([Owen et al., 2018](#)), and may result in the incorporation of homogeneously spaced nano-inclusions throughout the sulphides, thus attributing to their Pb isotope makeup. Inclusion textures typically involve small ~1 µm-sized grains of Pb-chalcogenides within Cu-(Fe)-sulphides and seemingly randomly located within the host minerals. Crack and grain boundary textures were observed by Pb-chalcogenide formation along annealed cracks and grain boundaries indicating the mobility of Pb within the system. Symplectite textures, usually between clausthalite and the Cu-(Fe)-sulphides, were most common and occur in all Cu-(Fe)-sulphide hosts. These form complex structures with the Cu-(Fe)-sulphides at the sub-micrometre scale, enabling extrapolation on formation environments and mechanisms. The range of textures recorded is diverse ([Figure 1](#)). Textures formed along the grain boundaries ([Figure 1b](#)) record formation history of the Cu-(Fe)-sulphides whereby small grains, in this case of bornite, form into larger aggregates trapping migrating Pb, thus indicating the presence of Pb during the final stages of the grain's formation. Close inspection of clausthalite and altaite symplectite-style textures hosted in chalcopyrite ([Figure 1c, d](#)) indicate their prevalence within highly porous regions of chalcopyrite, indicating Pb incorporation via a reduced fluid phase post Cu-(Fe)-sulphide formation. Symplectite textures formed by altaite were, however, less common than those formed by clausthalite, usually forming as small spotty inclusions at the single micron scale ([Figure 1e](#)).

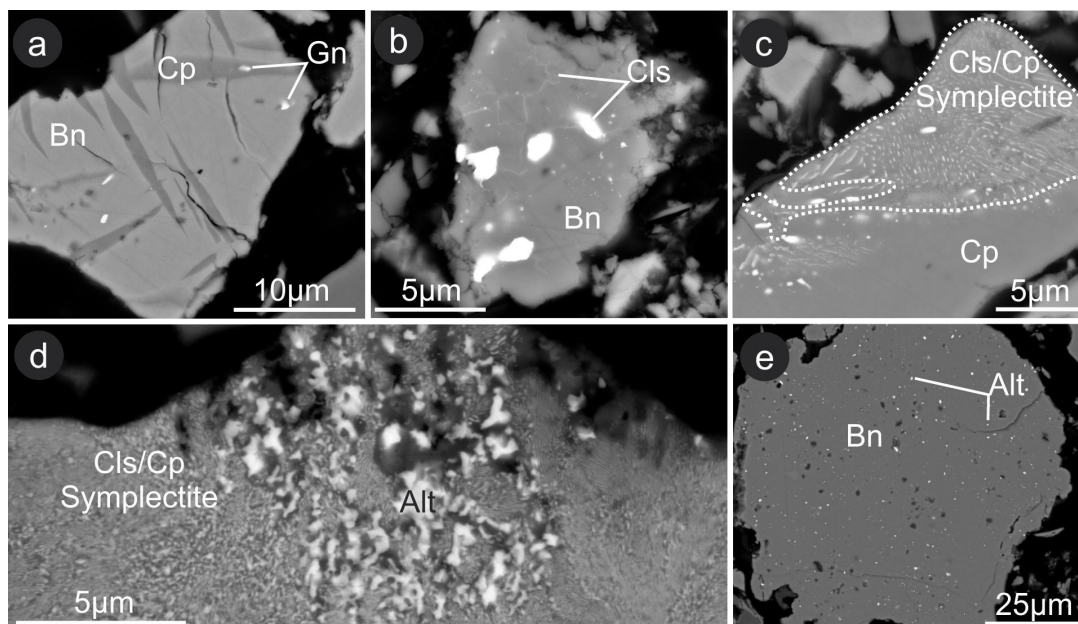


Figure 1: SEM backscatter images of Pb chalcogenides within Cu-(Fe)-sulphides displaying various typical textures; (a) lamellae of chalcopyrite (Cp) in bornite (Bn) and small ‘inclusions’ of galena (Gn) within both minerals; (b) clausthalite (Cls) formed along annealed cracks or grain boundaries of bornite with nucleation points present as bright blebs; (c) clausthalite-bearing symplectite, the most common texture formed between clausthalite and the Cu-(Fe)-sulphides, frequently formed within porous regions (indicated by the dashed line) in chalcopyrite; (d) transition zone between a clausthalite-bearing symplectite and rare altaite (Alt) bearing symplectite in chalcopyrite; (e) rare fine-grained altaite irregularly disseminated within bornite.

3.3. Pb-isotope analysis by LA-ICP-MS

LA-ICP-MS Pb isotope data for each mineral analysed are given in [Appendix A](#). Representative data are presented in [Table 1](#) as geometric means, maxima and minima. Some data points have been removed, due to low counts of ^{204}Pb preventing accurate ratio $^{206}\text{Pb}/^{204}\text{Pb}$, $^{207}\text{Pb}/^{204}\text{Pb}$ and $^{208}\text{Pb}/^{204}\text{Pb}$ calculations. As such, only data points with Pb isotope ratios with 10% or less error (calculated with the 2σ error value) were plotted. For reference, all data is plotted with the [Stacey and Kramers \(1975\)](#) common Pb model values $^{206}\text{Pb}/^{204}\text{Pb} = 18.700$, $^{207}\text{Pb}/^{204}\text{Pb} = 15.628$, and $^{208}\text{Pb}/^{204}\text{Pb} = 38.63$. Larger (~50-60 μm -diameter) spot sizes was used for analysis of the Cu-(Fe)-sulphides as they consistently returned low total Pb counts.

Data points are grouped by their mineralogical species (galena, clausthalite, altaite, or Cu-(Fe)-sulphide) and plotted together to determine any trends in the data ([Figure 2](#)). Each mineral species contained a surprisingly wide variation in Pb isotope signatures making any definitive fingerprinting of an individual mineral species very difficult. In any case, some clustering of the data can, however, be recognized. All analysed Pb-minerals plot away from the primordial Pb signature, indicating degrees of radiogeneity ranging from moderate to strong, possibly via mixing with pre-existing common Pb in various proportions. Although a greater number of clausthalite

analyses are included here (four times as many as for galena), galena returned a wider range of Pb isotope compositions with a small group of analysis recording significantly higher $^{206}\text{Pb}/^{204}\text{Pb}$ and $^{207}\text{Pb}/^{204}\text{Pb}$ values than those seen in any of the clausthalite grains analysed. LA-ICP-MS spots of Cu-(Fe)-sulphides were typically larger, often covering entire grains in order to measure Pb isotope compositions present in trace amounts within solid solution. No differential Pb isotope trends based on textural differences were observed with a homogenous broad range of isotopic signatures resulting from analysis of all textures.

Table 1: Representative Pb isotope data for Pb-chalcogenides hosted within Cu-(Fe)-sulphides and for Cu-(Fe)-sulphides without Pb-chalcogenide inclusions.

Mineral	$^{208}\text{Pb}/^{204}\text{Pb}$	% error	$^{207}\text{Pb}/^{204}\text{Pb}$	% error	$^{206}\text{Pb}/^{204}\text{Pb}$	% error	$^{208}\text{Pb}/^{206}\text{Pb}$	% error	$^{207}\text{Pb}/^{206}\text{Pb}$	% error	$^{204}\text{Pb}/^{206}\text{Pb}$	% error
Cls	54.40	8.3	17.16	4.5	39.60	5.6	1.2780	6.4	0.4270	4.4	0.0253	5.6
Cls	43.40	3.2	16.13	3.3	39.10	3.1	1.1130	1.9	0.4196	2.1	0.0256	3.1
Cls	52.63	1.5	18.60	2.8	51.44	1.8	1.0220	1.8	0.3610	3.3	0.0194	1.8
Cls	57.00	8.4	19.60	8.2	57.90	9.2	1.0180	1.6	0.3393	2.0	0.0173	9.2
Cls	49.60	7.3	16.70	7.8	51.10	9.4	0.9470	4.3	0.3300	6.4	0.0196	9.4
Cls	54.30	3.7	18.77	2.6	61.80	2.6	0.8660	6.2	0.2990	4.7	0.0162	2.6
Cls	56.40	2.3	18.92	1.7	65.08	1.5	0.8620	1.7	0.2916	1.4	0.0154	1.5
Cls	54.20	4.1	19.83	3.4	84.30	2.7	0.6370	2.8	0.2322	1.7	0.0119	2.7
Cls	61.60	7.8	24.50	7.3	135.00	8.1	0.4590	3.7	0.1848	2.5	0.0074	8.1
Cls	54.40	8.6	19.30	8.3	107.10	6.3	0.4980	4.0	0.1783	3.4	0.0093	6.3
Cls	54.20	8.7	37.90	9.5	234.00	9.0	0.2284	3.7	0.1584	2.0	0.0043	9.0
Cls	53.30	9.8	26.20	9.9	177.00	9.0	0.3033	2.5	0.1504	1.8	0.0056	9.0
Cls	56.50	8.7	32.10	8.4	228.00	7.5	0.2458	2.8	0.1376	2.3	0.0044	7.5
Max	61.60	-	37.90	-	234.00	-	1.4700	-	0.4663	-	0.0271	-
Min	43.40	-	15.93	-	36.90	-	0.2284	-	0.1376	-	0.0043	-
GeoMean	54.28	-	18.86	-	57.07	-	0.9514	-	0.3306	-	0.0175	-
Gn	54.60	6.2	17.39	4.9	42.30	3.5	1.2710	2.8	0.4078	1.8	0.0236	3.5
Gn	62.90	5.6	19.21	3.2	61.10	4.1	1.0160	5.2	0.3150	6.0	0.0164	4.1
Gn	50.50	4.2	20.06	3.3	99.30	2.6	0.5100	2.5	0.2040	1.6	0.0101	2.6
Gn	39.30	5.3	40.90	6.1	363.00	6.9	0.1107	5.1	0.1127	1.8	0.0028	6.9
Gn	56.50	3.5	142.4	3.4	1627	3.9	0.0339	3.2	0.0870	1.4	0.0006	3.9
Max	62.90	-	142.4	-	1627	-	1.2710	-	0.4078	-	0.0236	-
Min	39.30	-	16.81	-	42.30	-	0.0339	-	0.0868	-	0.0006	-
GeoMean	53.31	-	24.80	-	118.69	-	0.4519	-	0.2093	-	0.0084	-
Cu-(Fe)-S	50.70	6.5	17.60	6.3	55.80	6.3	0.9350	3.1	0.3200	3.1	0.0179	6.3
Cu-(Fe)-S	49.90	6.2	23.10	6.5	78.60	6.6	0.6390	2.3	0.3007	2.3	0.0127	6.6
Cu-(Fe)-S	56.40	8.7	26.30	8.7	136.00	8.8	0.4150	4.3	0.1881	3.1	0.0074	8.8
Cu-(Fe)-S	61.20	6.9	25.70	6.2	140.70	6.5	0.4250	3.1	0.1824	2.4	0.0071	6.5
Cu-(Fe)-S	56.70	6.0	25.00	6.0	144.80	6.1	0.3888	1.8	0.1736	2.6	0.0069	6.1
Max	61.20	-	26.30	-	144.80	-	0.9350	-	0.3200	-	0.0179	-
Min	49.90	-	17.60	-	55.80	-	0.3862	-	0.1736	-	0.0069	-
GeoMean	55.55	-	22.91	-	99.48	-	0.5609	-	0.2311	-	0.0100	-
Alt	53.20	5.5	17.78	5.5	52.30	5.2	1.0150	1.7	0.3383	1.3	0.0191	5.2
Alt	52.10	4.8	17.59	4.3	56.20	4.4	0.9350	2.2	0.3132	2.4	0.0178	4.4
Alt	53.60	5.0	18.70	5.3	73.80	7.3	0.7440	5.6	0.2569	3.9	0.0136	7.3
Alt	58.00	6.9	22.40	6.7	99.70	4.2	0.5680	2.6	0.2193	2.7	0.0100	4.2
Max	58.00	-	22.40	-	99.70	-	1.0150	-	0.3383	-	0.0191	-
Min	52.10	-	17.59	-	52.30	-	0.5680	-	0.2193	-	0.0100	-

GeoMean	54.18	-	19.02	-	68.19	-	0.7958	-	0.2780	-	0.0147	-
Common Pb	38.64	-	15.63	-	18.70	-	2.0663	-	0.8357	-	0.0535	-

Errors are calculated from the 2σ value and taken as a percentage of the total value for each ratio.

Cls-clausthalite; Gn-galena; Alt-altaite; Cu-(Fe)-S - Cu-Fe-sulphides.

Common Pb values from [Stacey and Kramers \(1975\)](#) are included for reference at the bottom of the table.

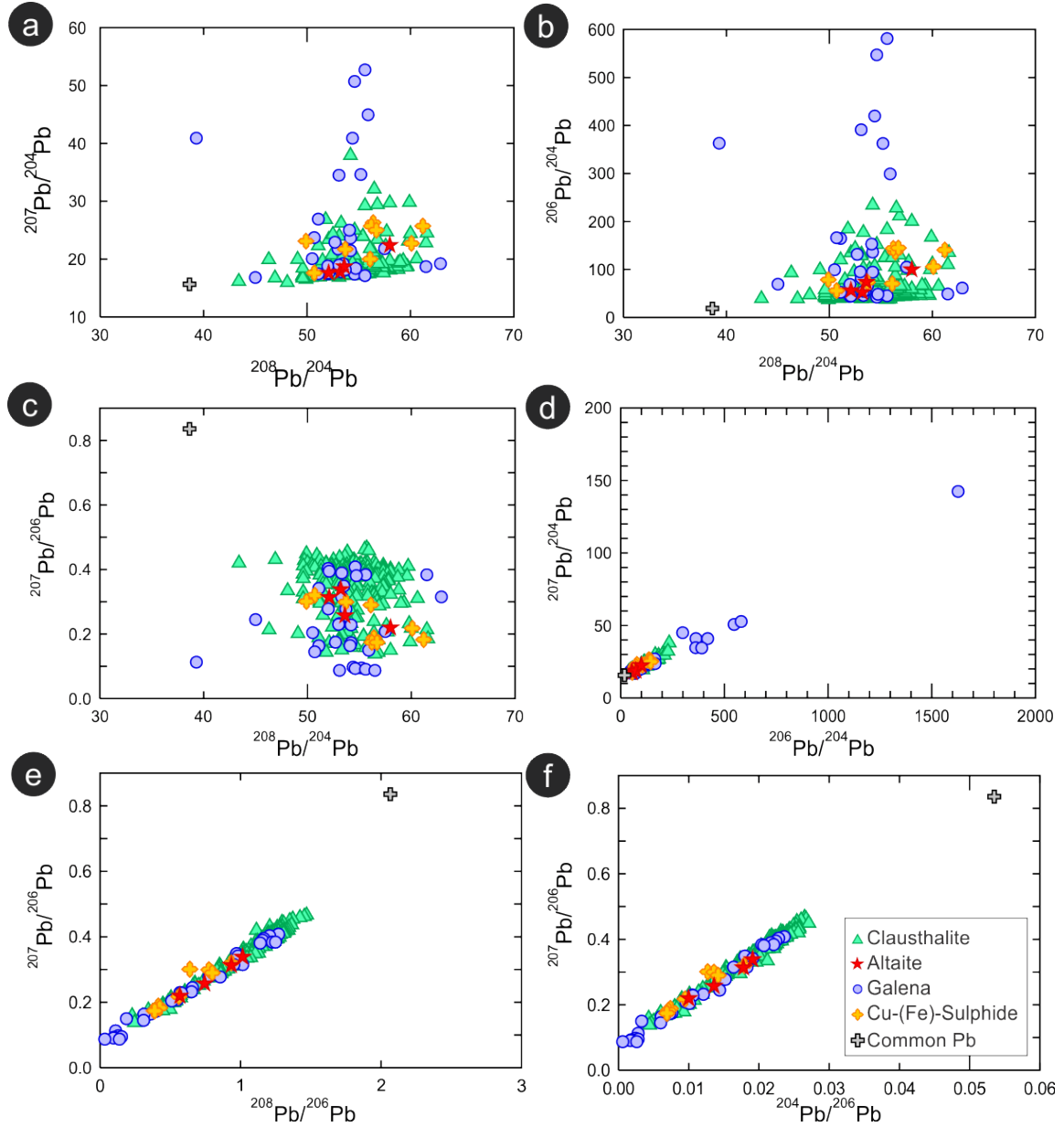


Figure 2: Graphs showing the Pb-isotope composition of clausthalite, altaite, galena and Cu-(Fe)-sulphides. (a), (b) and (c) show $^{207}\text{Pb}/^{204}\text{Pb}$, $^{206}\text{Pb}/^{204}\text{Pb}$ and $^{207}\text{Pb}/^{206}\text{Pb}$ vs. $^{208}\text{Pb}/^{204}\text{Pb}$, respectively. Some outlier values are not plotted for better data viewing (refer to [Table 1](#)); (d) $^{206}\text{Pb}/^{204}\text{Pb}$ vs. $^{207}\text{Pb}/^{204}\text{Pb}$. Note the lack of ^{204}Pb compared to ^{206}Pb and ^{207}Pb in the majority of analyses; (e) and (f) show the variation of uraniumogenic Pb ($^{207}\text{Pb}/^{206}\text{Pb}$) plotted against $^{208}\text{Pb}/^{206}\text{Pb}$ and $^{204}\text{Pb}/^{206}\text{Pb}$, respectively. The x-axis on (f) is set at zero, giving us the purely radiogenic signature of uraniumogenic $^{207}\text{Pb}/^{206}\text{Pb}$; see also [Figure 3](#). The position of common Pb ([Stacey and Kramers, 1975](#)) is plotted for reference.

4. Discussion

Any points straying from the common Pb values indicated in [Figure 2](#) are classed as radiogenic, however some grains show much larger degrees of radiogenicity than others. Such a large difference in variation of isotope values of Pb-bearing minerals can be attributed to varying amounts of mixing between radiogenic Pb with common Pb. Within IOCG deposits in the Olympic Cu-Au Province, only a minority of Pb is common in origin, with the majority of Pb being radiogenic, formed by the release of Pb produced via decay of U and Th in minerals such as uraninite, coffinite, brannerite, thorite, monazite, zircon, hematite, and others. Although some minerals readily reincorporate radiogenic Pb into their crystal structures (the size and charge of daughter radionuclides often differ markedly from parent U), others cannot rapidly self-heal or cannot accommodate larger or differently charged ions. In the presence of fluids, such products may be released and subsequently migrate over nanometres to potentially hundreds of metres where they are deposited as new minerals.

The formation of the largely radiogenic Pb-chalcogenides is suggested to be a consequence of large scale Pb remobilisation. Such Pb remobilisation events, recorded by Pb isotope ratios, have been reported elsewhere, including the following examples: (1) Hydrothermal overprints are recorded in the Tomino and Birgilda deposits (both South Urals, Russia), by distinctly different sets of Pb isotope ratios measured within both Cu-(Fe)-sulphides and Pb-chalcogenides alike ([Plotinskaya et al., 2017](#)); (2) Dating of Pb-isotopes in early stratiform, and later framboidal pyrite, in the Sukhoi Log sediment hosted gold deposit, Russia, indicate events of mobilisation, and concentration of ore minerals, may have continued late into the deposit's history ([Meffre et al., 2008](#)).

The radiogenic signatures presented here, however, do not cluster into individual or distinct groups, but rather form along a single 'mixing trend' with differing amounts of common Pb incorporation. Similar trends, in which Pb isotope ratios vary consistently between samples, are reported in a study attempting to develop origin analysis of yellowcake from various mines ([Varga et al., 2009](#)). The latter authors suggest that mineralogical variability, along with chemical separation of Pb during processing, is one of the main causes of the observed variability in Pb isotope ratios.

Whereas galena is, overall, relatively enriched in ^{206}Pb and ^{207}Pb relative to clausthalite ([Figure 2a, b](#)), altaite or the Cu-(Fe)-sulphides ([Figure 2a, b](#)), there is still a significant degree of overlap between the isotopic signatures for each mineral type. This suggests that the event (or events) responsible for Pb mobilisation was prolonged, and thus achieved a degree of homogenization, but also that differential fluid regimes and variations in fluid/rock ratio driven by permeability may have contributed to the measured variation. The few Pb isotope values for galena which are

strongly uranogenic (Figure 2a, b) likely formed by direct replacement of U-bearing minerals without significant mixing with Pb from other sources.

The isotopic signatures and degree of radiogenicity of Pb-bearing minerals is, in part, dependent on the time at which the contained Pb becomes separated from its parent U and Th decay sources. Minerals formed later should record higher ratios of $^{206}\text{Pb}/^{204}\text{Pb}$ to $^{207}\text{Pb}/^{204}\text{Pb}$. Additionally, fluid mixing and superimposed cycles of dissolution, recrystallization and reprecipitation result in the blending of distinct radiogenic signatures, as well as mixing with common Pb, if available (Figure 2e, f). The relative solubility of uraninite with respect to the other minerals in the ore, and the typically metamict nature of brannerite, which allows Pb to freely migrate from its structure, suggests that such overprinting events need not necessarily be intense, but rather, could occur via the aid of low-temperature hydrothermal fluids. Radiogenic Pb may also be removed from uraninite without its complete dissolution, as shown in samples of Pb-zoned uraninite from Johangeorgenstadt Saxony, Germany (Ram et al., 2013).

Using a nanoscale approach that examined textural relationships between the Pb-chalcogenides and Cu-(Fe)-sulphides, Owen et al. (2018) showed that Pb is likely remobilised during at least one stage after initial hydrothermal deposition. Similarly, within the cogenetic Olympic Dam deposit, Macmillan et al. (2016, 2017) discusses the formation of multiple generations of uraninite and coffinite from remobilised U, indicating a dynamic system of dissolution, remobilisation and precipitation. Given the heat generated by radioactive decay, this may possibly have been semi-continuous over hundreds of millions of years rather than only during specific events. The result is repeated reworking and overprinting of ore mineral assemblages, leading to complex and often varied mineral chemistry, including significant variation of lead concentrations within the U-minerals.

Furthermore, Macmillan et al. (2016) note that primary fine-grained uraninite is observed mainly in relatively deeper parts of the deposit, whereas ‘younger’ uraninite is concentrated within veins representing the most U-rich zones. This apparent zonation does not, however, correspond to patterns of Cu-(Fe)-sulphide distribution, indicating that fluids responsible for uranium mobility and redistribution of uraninite mineralisation did not impact on the zoning of Cu-(Fe)-sulphides in the deposit. The authors suggest that the late generation was migrated by fluids $<250^\circ\text{C}$. Here, we suggest that such low-temperature, oxidizing hydrothermal fluids were probably ubiquitous in all IOCG systems across the province, including those within the Mt Woods Inlier. While a complete reworking of the ore minerals did not take place, they must have been sufficiently strong to result in migration of U and Pb, and ultimately to drive Pb-diffusion into, and recrystallisation of the Cu-(Fe)-sulphides (see also Owen et al., 2018).

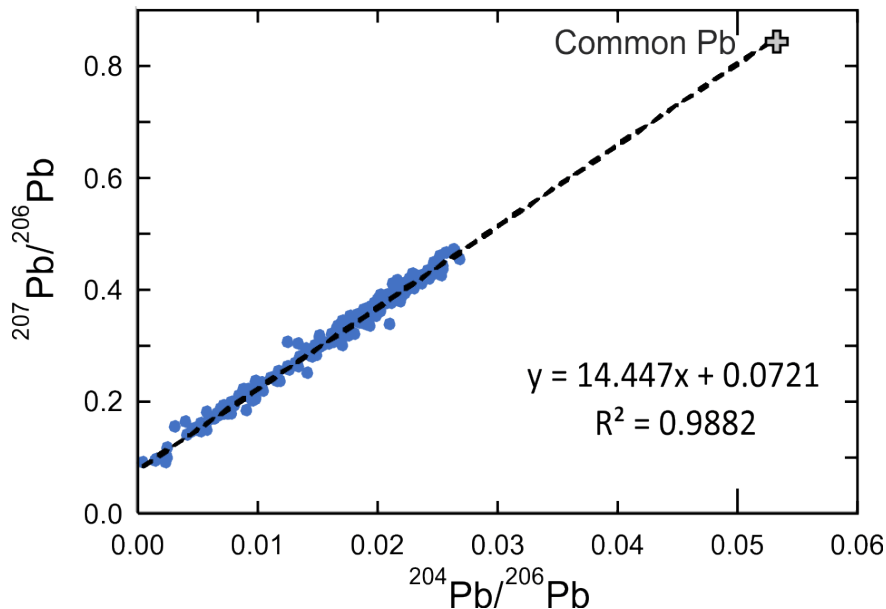


Figure 3: Pb-Pb isochron constructed with Pb isotope data from the Pb-chalcogenides and Cu-(Fe)-sulphides. A line of best fit is anchored through the isotopic composition of common Pb (Stacey and Kramers, 1975), returning a pure radiogenic $^{207}\text{Pb}/^{206}\text{Pb}$ ratio of 0.0721 at the y-intercept.

Further evidence for the mobility of U and radiogenic Pb throughout the Olympic Cu-Au Province comes through an examination of Pb-Pb isochrons shown as Figure 3. By plotting $^{207}\text{Pb}/^{206}\text{Pb}$ for all Pb-chalcogenides against $^{204}\text{Pb}/^{206}\text{Pb}$, we can predict the purely radiogenic signature, i.e. without any common-Pb component. The resulting $^{207}\text{Pb}/^{206}\text{Pb}$ ratio, taken from the y-intercept where ^{204}Pb is zero, is significantly lower, by several hundred million years, than the widely reported ages for igneous and hydrothermal zircon (Reeve et al., 1990; Creaser and Cooper, 1993; Johnson and Cross, 1995; Jagodzinski, 2005, 2014; Courtney-Davies et al., 2019), and U-Pb/Pb-Pb ages for hematite mineralisation (Ciobanu et al., 2013; Courtney-Davies et al., 2016, 2019) reported from the region. This may indicate either an overprinting event, supplying uranium after the initial ~1590-1585 Ma mineralisation event, or alternatively, substantial loss of lead from the system.

It should, however, be pointed out that calculated $^{207}\text{Pb}/^{206}\text{Pb}$ ratios do not allow for derivation of reliable ages, especially when Pb is no longer in equilibrium with parent U. For this reason, no precise geochronological ages are offered here. Confidence in such an interpretation is nevertheless strong as the sample suite and number of analysed points are relatively large, and furthermore that similar results have emerged from a similar study of Pb-isotope systematics in Pb-chalcogenides from Olympic Dam (Schmandt, 2019). Evidence from a variety of sources, including nanoSIMS mapping (Rollog et al., 2019a, 2019b), Pb-isotope mapping of single hematite grains (Courtney-Davies et al., 2019) and characterization of nanoparticles in hematite (Verdugo-Ihl et al., 2019), all pointing to mobility of Pb and/or U at scales from a few nanometres up to centimetres, if not hundreds of metres. The implications of these phenomena for U-Pb geochronology and for ore genesis will be examined elsewhere (Cook et al., in prep).

Several distinct tectonothermal events are suggested to have impacted on the Olympic Cu-Au Province following mineralization associated with intrusion of Hiltaba Suite Granites and eruption of Gawler Range Volcanics. Evidence has come from different geochronometers, on different minerals, and from different deposits across the region.

Firstly, multiple, as-yet poorly-constrained events are recorded in the interval 1400-1100 Ma in several studies from different systems in the Olympic Cu-Au Province (Davidson et al., 2007; Maas et al. 2011 Ciobanu et al., 2013), including the most recent, 1370 Ma age obtained from U-Pb dating of monazite and xenotime inclusions in apatite from the Acropolis prospect (Cherry et al., 2018). These may relate to far-field effects from the Laurentia Orogeny, and to extension following the 1300-1100 Ma Musgravian Orogeny respectively, and are indicated in the central part of the Mt Woods Inlier by northwest striking magnetic anomalies (Betts et al., 2003). A hydrothermal event of Musgravian age is recorded at Olympic Dam via the analysis of pyrite-chalcopyrite mineral separates from a deep, low-Re zone, yielding Re-Os ages of 1258 ± 28 Ma (McInnes et al., 2008).

Secondly, emplacement of the Gairdner LIP (expressed by abundant dyke swarms at Olympic Dam and elsewhere) took place across the northern Olympic Cu-Au Province at ca. 830 Ma (Wingate et al., 1998; Huang et al., 2015; Apukhtina et al., 2017; Bowden et al., 2017).

Thirdly, the Delamerian orogeny (~500 Ma) led to extensive faulting and late veining across the region. Recent fission track evidence (Hall et al., 2018) suggests that tectonothermal effects continued until the Tertiary. In addition to these, the Mount Woods Inlier may display evidence of metamorphism during the late Kararan Orogeny (1565-1540 Ma) via the formation of a weak fabric in the Balta Granite Suite plutons (Betts et al., 2003; Forbes et al., 2011). No recognizable impact of this event is seen at Olympic Dam, however. Each of these events may have had an impact in the remobilisation of U, Pb, and other elements, throughout the Olympic Cu-Au province, leading to the wide range of overprints observed in various mineral groups from Olympic Dam (Ciobanu et al., 2017; Macmillan et al., 2016; Verdugo-Ihl et al., 2017; Schmandt et al., 2019; Owen et al., 2019) and elsewhere in the Olympic Cu-Au Province (e.g., Cherry et al., 2018; Owen et al., 2018).

5. Conclusions

- Pb-isotope ratios in clausthalite, altaite and Cu-(Fe)-sulphides are indistinguishable from one another. All three, however, appear distinct from ratios exhibited by galena, which is relatively enriched, albeit to variable degrees, in (uranogenic) ^{206}Pb and ^{207}Pb .
- The data shows incorporation of minor common Pb within all Pb-bearing minerals. Measured $^{206}\text{Pb}/^{204}\text{Pb}$, $^{207}\text{Pb}/^{204}\text{Pb}$ and $^{208}\text{Pb}/^{204}\text{Pb}$ ratios suggest an overwhelmingly radiogenic origin.

- The purely radiogenic $^{207}\text{Pb}/^{206}\text{Pb}$ ratios calculated from the dataset suggest a scenario involving a remobilisation event (or events) postdating the initial deposition of Cu-Au-U mineralisation, in which radiogenic Pb released by parent U-bearing minerals became incorporated into Cu-(Fe)-sulphides (as included Pb-chalcogenides).
- Homogenisation of Pb-isotope signatures seen in clausthalite, altaite and Cu-(Fe)-sulphides suggests prolonged interaction with hydrothermal fluid, or multiple fluids throughout the post-mineralisation history of the northern Olympic Cu-Au Province.
- The data presented here are consistent with other studies in the Olympic Cu-Au province which record the impact of one or more tectonothermal events younger than the 1600-1585 Ma ‘main’ mineralisation event. The data here suggests that at least one of these tectonothermal events was sufficiently strong to overprint pre-existing Cu-(Fe)-sulphide mineralisation and enable incorporation of radiogenic Pb within existing and new-formed minerals.

Acknowledgements

This is a contribution to the ARC Research Hub for Australian Copper-Uranium, co-funded by BHP Olympic Dam, OZ Minerals, and the Government of South Australia Department of State Development. The staff at Adelaide Microscopy are thanked for their assistance with microanalytical techniques. Kathy Ehrig, Roland Maas and Vadim Kamenetsky are thanked for their contribution towards the ideas formulated in this manuscript.

References

- Apukhtina, O.B., Kamenetsky, V.S., Ehrig, K., Kamenetsky, M.B., McPhie, J., Maas, R., Meffre, S., Goemann, K., Rodemann, T., Cook, N.J., Ciobanu, C.L. (2016) Postmagmatic magnetite–apatite assemblage in mafic intrusions: a case study of dolerite at Olympic Dam, South Australia. *Contributions to Mineralogy and Petrology*, 171, 2.
- Barton, M. (2014) Iron oxide (–Cu–Au–REE–P–Ag–U–Co) systems. In: Holland, H.D., Turekian, K.K., eds., *Treatise on Geochemistry* 2nd ed., vol 13, Elsevier, Amsterdam, 515–541.
- Betts, P.G., Valenta, R., Finlay, J. (2003) Evolution of the Mount Woods Inlier, northern Gawler Craton, Southern Australia: an integrated structural and aeromagnetic analysis. *Tectonophysics*, 366, 83–111.
- Bowden, B., Fraser, G., Davidson, G.J., Meffre, S., Skirrow, R., Bull, S., Thompson, J. (2017) Age constraints on the hydrothermal history of the Prominent Hill iron oxide copper-gold deposit, South Australia. *Mineralium Deposita*, 52, 863–881.
- Chang, L.L.Y., Liu, H. (1994) Phase Relations in the System PbS–PbSe–PbTe. *Mineralogical Magazine*, 58, 567–578.
- Cherry, A.R., Kamenetsky, V.S., McPhie, J., Thompson, J.M., Ehrig, K., Meffre, S., Kamenetsky, M.B., Krneta, S. (2018) Tectonothermal events in the Olympic IOCG Province constrained by apatite and REE-phosphate geochronology. *Australian Journal of Earth Sciences*, 65, 643–659.

- Ciobanu, C.L., Cook, N.J., Ehrig, K. (2017) Ore minerals down to the nanoscale: Cu-(Fe)-sulphides from the iron oxide copper gold deposit at Olympic Dam, South Australia. *Ore Geology Reviews*, 81, 1218–1235.
- Ciobanu, C.L., Wade, B.P., Cook, N.J., Mumm, A.S., Giles, D. (2013) Uranium-bearing hematite from the Olympic Dam Cu–U–Au deposit, South Australia: A geochemical tracer and reconnaissance Pb–Pb geochronometer. *Precambrian Research*, 238, 129–147.
- Courtney-Davies, L., Zhu, Z., Ciobanu, C.L., Wade, B.P., Cook, N.J., Ehrig, K., Cabral, A.R., Kennedy, A. (2016) Matrix-matched iron-oxide laser ablation ICP-MS U–Pb geochronology using mixed solution standards. *Minerals*, 6(3), 85
- Courtney-Davies, L., Tapster, S.R., Ciobanu, C.L., Cook, N.J., Verdugo-Ihl, M.R., Ehrig, K.J., Kennedy, A.K., Gilbert, S.E., Condon, D.J., Wade, B.P. (2019) A multi-technique evaluation of hydrothermal hematite U-Pb isotope systematics: Implications for ore deposit geochronology. *Chemical Geology*, 513, 54–72.
- Creaser R.A., Cooper J.A. (1993) U-Pb geochronology of middle Proterozoic felsic magmatism surrounding the Olympic Dam Cu-Au-U-Ag and Moonta Cu-Au-Ag deposits, South Australia. *Economic Geology*, 88, 186–197.
- Davidson, G.J., Paterson, H., Meffre, S., Berry, R.F. (2007) Characteristics and origin of the Oak Dam East breccia-hosted, iron oxide Cu-U-(Au) deposit: Olympic Dam region, Gawler craton, South Australia. *Economic Geology*, 102, 1471–1498.
- Forbes, C.J., Giles, D., Hand, M., Betts, P.G., Suzuki, K., Chalmers, N., Dutch, R. (2011) Using P–T paths to interpret the tectonothermal setting of prograde metamorphism: an example from the northeastern Gawler Craton, South Australia. *Precambrian Research*, 185, 65–85.
- Hall, J.W., Glorie, S., Reid, A.J., Collins, A.S., Jourdan, F., Danišik, M., Evans, N. (2018) Thermal history of the northern Olympic Domain, Gawler Craton; correlations between thermochronometric data and mineralising systems. *Gondwana Research*, 56, 90–104.
- Huang, Q., Kamenetsky, V.S., McPhie, J., Ehrig, K., Meffre, S., Maas, R., Thompson, J., Kamenetsky, M., Chambefort, I., Apukhtina, O., Hu, Y. (2015) Neoproterozoic (ca. 820–830 Ma) mafic dykes at Olympic Dam, South Australia: links with the Gairdner Large Igneous Province. *Precambrian Research*, 271, 160–172.
- Jagodzinski, E. (2005) Compilation of SHRIMP U-Pb geochronological data, Olympic Domain, Gawler Craton. South Australia, 2001-2003. *Geoscience Australia Record* 2005/020
- Jagodzinski, E. (2014) The age of magmatic and hydrothermal zircon at Olympic Dam. *Proceedings, Australian Earth Sciences Convention, Abstracts*, 110, 260.
- Johnson, J.P., Cross, K.C. (1995) U-Pb geochronological constraints on the genesis of the Olympic Dam Cu-U-Au-Ag deposit, South Australia. *Economic Geology*, 90, 1046–1063.
- Loveless, A.J. (1975) Lead isotopes—a guide to major mineral deposits. *Geoexploration*, 13(1-4), 13–27.
- Maas, R., Kamenetsky, V.S., Ehrig, K., Meffre, S., McPhie, J., Diemar, G. (2011) Olympic Dam U-Cu-Au deposit, Australia: New age constraints: *Mineralogical Magazine, Goldschmidt Conference abstract*, 75, 1375.

- Macmillan, E., Cook, N.J., Ehrig, K., Ciobanu, C.L., Pring, A. (2016) Uraninite from the Olympic Dam IOCG-U-Ag deposit: Linking textural and compositional variation to temporal evolution. *American Mineralogist*, 101, 1295–1320.
- Macmillan, E., Cook, N.J., Ehrig, K., Pring, A. (2017) Chemical and textural interpretation of late-stage coffinite and brannerite from the Olympic Dam IOCG-Ag-U deposit. *Mineralogical Magazine*, 81, 1323–1366.
- McFarlane, C.R., Soltani Dehnavi, A., Lentz, D.R. (2016) Pb-isotopic study of galena by LA-Q-ICP-MS: Testing a new methodology with applications to base-metal sulphide deposits. *Minerals*, 6(3), 96.
- McInnes, B.I.A., Keays, R.R., Lambert, D.D., Hellstrom, J., Allwood, J.S. (2008) Re–Os geochronology and isotope systematics of the Tanami, Tennant Creek and Olympic Dam Cu–Au deposits. *Australian Journal of Earth Sciences*, 55, 967–981.
- Meffre, S., Large, R.R., Scott, R., Woodhead, J., Chang, Z., Gilbert, S.E., Danyushevsky, L.V., Maslennikov, V., Hergt, J.M. (2008) Age and pyrite Pb-isotopic composition of the giant Sukhoi Log sediment-hosted gold deposit, Russia. *Geochimica et Cosmochimica Acta*, 72, 2377–2391.
- Meffre, S., Ehrig, K., Kamenetsky, V.S., Chambefort, I., Maas, R., and McPhie, J. (2010) Pb isotopes at Olympic Dam: Constraining sulphide growth: Giant ore deposits down under: Proceedings of 13th Quadrennial International Association on the Genesis of Ore Deposits (IAGOD) Symposium, Adelaide, South Australia, 78–79.
- Owen, N.D., Ciobanu, C.L., Cook, N.J., Slattery, A., Basak, A. (2018) Nanoscale study of clausthalite-bearing symplectites in Cu-Au-(U) ores: Implications for ore genesis. *Minerals*, 8(2), 67.
- Owen, N.D., Cook, N.J., Rollog, M., Ehrig, K.J., Schmandt, D.S., Ram, R., Brugger, J., Ciobanu, C.L., Wade, B. and Guagliardo, P. (2019) REE-, Sr-, Ca-aluminum-phosphate-sulfate minerals of the alunite supergroup and their role as hosts for radionuclides. *American Mineralogist*, 104(12), 1806–1819.
- Paton, C., Hellstrom, J., Paul, B., Woodhead, J., Hergt, J. (2011) Iolite: Freeware for the visualisation and processing of mass spectrometric data. *Journal of Analytical Atomic Spectrometry*, 26, 2508–2518.
- Plotinskaya, O.Y., Chugaev, A.V., Seltmann, R. (2017) Lead isotope systematics of porphyry–epithermal spectrum of the Birgilda–Tomino ore cluster in the South Urals, Russia. *Ore Geology Reviews*, 85, 204–215.
- Ram, R., Charalambous, F.A., McMaster, S., Pownceby, M.I., Tardio, J., Bhargava, S.K. (2013) Chemical and micro-structural characterisation studies on natural uraninite and associated gangue minerals. *Minerals Engineering*, 45, 159–169.
- Reeve, J.S. (1990). Olympic Dam copper-uranium-gold-silver deposit. *Geology of the Mineral Deposits of Australia and Papua New Guinea*, AusIMM, Melbourne, 1009–1035.
- Rollog, M., Cook, N.J., Guagliardo, P., Ehrig, K., Kilburn, M. (2019a) In situ spatial distribution mapping of radionuclides in minerals by nanoSIMS. *Geochemistry – Exploration, Environment, Analysis*, 19(3), 245–254
- Rollog, M., Cook, N.J., Guagliardo, P., Ehrig, K., Ciobanu, C.L., Kilburn, M. (2019b) Detection of trace elements/isotopes in Olympic Dam copper concentrates by nanoSIMS. *Minerals*, 9(6), 336.
- Schmandt, D.S. (2019) Mineralogical distributions of radionuclides in copper-uranium ores, Olympic Dam, south Australia. Ph.D. thesis, The University of Adelaide, Adelaide.

- Schmandt, D.S., Cook, N.J., Ciobanu, C.L., Ehrig, K., Wade, B.P., Gilbert, S., Kametetsky, V.S. (2019) Rare earth element phosphate minerals from the Olympic Dam Cu-U-Au-Ag deposit, South Australia: Recognizing temporal-spatial controls on REE mineralogy in an evolved IOCG systems. *Canadian Mineralogist*, 57, 1–22.
- Stacey, J.T., Kramers, J.D. (1975) Approximation of terrestrial lead isotope evolution by a two-stage model. *Earth and Planetary Science Letters*, 26, 207–221.
- Varga, Z., Wallenius, M., Mayer, K., Keegan, E., Millet, S. (2009) Application of lead and strontium isotope ratio measurements for the origin assessment of uranium ore concentrates. *Analytical Chemistry*, 81, 8327–8334.
- Verdugo-Ihl, M.R., Ciobanu, C.L., Slattery, A., Cook, N.J., Ehrig, K., Courtney-Davies, L. (2019) Copper-arsenic nanoparticles in hematite: fingerprinting fluid-mineral interaction. *Minerals* 9(7), 388.
- Wingate, M.T., Campbell, I.H., Compston, W., Gibson, G.M. (1998) Ion microprobe U–Pb ages for Neoproterozoic basaltic magmatism in south-central Australia and implications for the breakup of Rodinia. *Precambrian Research*, 87, 135–159.

CHAPTER 3

NANOSCALE STUDY OF CLAUSTHALITE-BEARING SYMPLECTITES IN CU-AU-(U) ORES: IMPLICATIONS FOR ORE GENESIS

Nicholas D. Owen, Cristiana L. Ciobanu, Nigel J. Cook, Ashley Slattery and Animesh Basak

Statement of Authorship

Title of Paper	Nanoscale Study of Clausthalite-Bearing Symplectites in Cu-Au-(U) Ores: Implications for Ore Genesis		
Publication Status	<input checked="" type="checkbox"/> Published	<input type="checkbox"/> Accepted for Publication	
	<input type="checkbox"/> Submitted for Publication	<input type="checkbox"/> Unpublished and Unsubmitted work written in manuscript style	
Publication Details	Minerals, 8(2), 67.		

Principal Author

Name of Principal Author (Candidate)	Nicholas D. Owen		
Contribution to the Paper	Idea conception, performed analytical work, carried out data collection and analysis, wrote the the manuscript.		
Overall percentage (%)	65%		
Certification:	This paper reports on original research I conducted during the period of my Higher Degree by Research candidature and is not subject to any obligations or contractual agreements with a third party that would constrain its inclusion in this thesis. I am the primary author of this paper.		
Signature		Date	26/08/2019

Co-Author Contributions

By signing the Statement of Authorship, each author certifies that:

- i. the candidate's stated contribution to the publication is accurate (as detailed above);
- ii. permission is granted for the candidate to include the publication in the thesis; and
- iii. the sum of all co-author contributions is equal to 100% less the candidate's stated contribution.

Name of Co-Author	Cristiana L. Ciobanu		
Contribution to the Paper	Helped define direction of research, assisted with data collection and interpretation, and aided with writing of the manuscript. 15%		
Signature		Date	27.08.19

Name of Co-Author	Nigel J. Cook		
Contribution to the Paper	Idea conception, supervision of the work, aided in data interpretation and writing of the manuscript. 10%		
Signature		Date	27/8/19


Please cut and paste additional co-author panels here as required.

Name of Co-Author	Ashley Slattery		
Contribution to the Paper	Assisted in operating analytical equipment and data interpretation/processing. 5%		
Signature		Date	02/09/2019

Name of Co-Author	Animesh Basak		
Contribution to the Paper	Assisted in operating analytical equipment and data interpretation/processing. 5%		
Signature		Date	02/09/2019

Article

Nanoscale Study of Clausthalite-Bearing Symplectites in Cu-Au-(U) Ores: Implications for Ore Genesis

Nicholas D. Owen ^{1,*}, Cristiana L. Ciobanu ¹, Nigel J. Cook ¹ , Ashley Slattery ² and Animesh Basak ²

¹ School of Chemical Engineering, The University of Adelaide, Adelaide, SA 5005, Australia; cristiana.ciobanu@adelaide.edu.au (C.L.C.); nigel.cook@adelaide.edu.au (N.J.C)

² Adelaide Microscopy, The University of Adelaide, Adelaide, SA 5005, Australia; ashley.slattery@adelaide.edu.au (A.S.); animesh.basak@adelaide.edu.au (A.B.)

* Correspondence: nicholas.owen@adelaide.edu.au; Tel.: +61-8-8313-4645 Received:

19 January 2018; Accepted: 9 February 2018; Published: 13 February 2018

Abstract: Symplectites comprising clausthalite (PbSe) and host Cu-(Fe)-sulphides (chalcocite, bornite, and chalcopyrite) are instructive for constraining the genesis of Cu-Au-(U) ores if adequately addressed at the nanoscale. The present study is carried out on samples representative of all three Cu-(Fe)-sulphides displaying clausthalite inclusions that vary in size, from a few μm down to the nm-scale (<5 nm), as well as in morphology and inclusion density. A Transmission Electron Microscopy (TEM) study was undertaken on foils prepared by Focussed Ion Beam and included atom-scale High-Angle Annular Dark-Field Scanning TEM (HAADF-STEM) imaging. Emphasis is placed on phase relationships and their changes in speciation during cooling, as well as on boundaries between inclusions and host sulphide. Three species from the chalcocite group (Cu_{2-x}S) are identified as *6a* digenite superstructure, monoclinic chalcocite, and djurleite. Bornite is represented by superstructures, of which *2a* and *4a* are discussed here, placing constraints for ore formation at $T > 265$ °C. A minimum temperature of 165 °C is considered for clausthalite-bearing symplectites from the relationships with antiphase boundaries in *6a* digenite. The results show that alongside rods, blebs, and needle-like grains of clausthalite within the chalcocite that likely formed via exsolution, a second, overprinting set of replacement textures, extending down to the nanoscale, occurs and affects the primary symplectites. In addition, other reactions between pre-existing Se, present in solid solution within the Cu-(Fe)-sulphides, and Pb, transported within a fluid phase, account for the formation of composite, commonly pore-attached PbSe and Bi-bearing nanoparticles within the chalcopyrite. The inferred reorganisation of PbSe nanoparticles into larger tetragonal superlattices represents a link between the solid solution and the symplectite formation and represents the first such example in natural materials. Epitaxial growth between clausthalite and monazite is further evidence for the interaction between pre-existing Cu ores and fluids carrying REE, P, and most likely Pb. In U-bearing ores, such Pb can form via decay of uranium within the ore, implying hydrothermal activity after the initial ore deposition. The U-Pb ages obtained for such ores therefore need to be carefully assessed as to whether they represent primary ore deposition or, more likely, an overprinting event. A latest phase of fluid infiltration is the recognised formation of Cu-selenide bellidoite (Cu_2Se), as well as Fe oxides.

Keywords: lead chalcogenides; symplectites; transmission electron microscopy; HAADF-STEM

1. Introduction

Selenides, often with associated tellurides, are common accessories in a wide variety of base and precious metal mineral deposits [1–3]. Despite their modest proportions, their speciation and mineral

chemistry can be important sources of information that can help constrain conditions and mechanisms of ore genesis.

The lead selenide, clausthalite (PbSe), is the most common selenide mineral [4] and a relatively common accessory phase in copper sulphide and uranium deposits of different genetic types (e.g., [5–7]). In hydrothermally derived ore systems, clausthalite may form synchronous to the initial mineralization event from hydrothermal fluids, or within uranium-bearing deposits, in which clausthalite is formed from Pb, derived from the decay of U, and available selenium within the rock [8]. The occurrence of clausthalite within Cu-(Fe)-sulphides, notably bornite, is generally interpreted as exsolution related to the cooling of broader solid solution fields (e.g., [9]). Liu and Chang [10] described phase relations in the system PbS-PbSe-PbTe, showing the temperature dependence of Pb-chalcogenide compositions, and thus their potential value as indicator minerals that can aid understanding of how an ore formed. Experimental studies of the system Pb-Se-Cu-(Fe)-S are, however, lacking, emphasizing the difficulty in modelling the evolution of observed assemblages in terms of phase relationships.

Clausthalite, as well as other selenides and tellurides, have been noted as trace minerals in iron oxide copper gold (IOCG) deposits (e.g., [11]) and other ore systems with comparable sulphide mineralogy (e.g., the Polish Kupferschiefer) [12]. The Mesoproterozoic Olympic Cu-Au Province of South Australia [13] is arguably the world's largest IOCG province and is host to the 10 billion-tonne Olympic Dam Cu-U-Au-Ag deposit [14]. A dozen or so selenide and telluride mineral species, including clausthalite and altaite (PbTe), are documented from the Olympic Dam. A similar range of minerals are identified in other deposits or prospects within the province, although these are poorly documented in the published literature. Although seldom greater than a few microns in size, selenides and tellurides are typically hosted within Cu-(Fe)-sulphides throughout the province.

In this contribution, we characterize world class examples of nano- to micron-scale symplectite intergrowths between clausthalite and Cu-(Fe)-sulphides (chalcocite, bornite, and chalcopyrite). Their small size necessitates an approach that bridges observations at the micron- and nanoscales. The overarching objective is to document the relationships between Pb-chalcogenides and host Cu-(Fe)-sulphides down to the atomic scale. We demonstrate that Pb-chalcogenide morphology, speciation, and textural relationships with host minerals give valuable insights into processes of ore formation and can also provide information on the fundamental nature of trace element incorporation into minerals. We go on to discuss the implications that the prevailing symplectite textures have for ore evolution.

2. Background

Copper-Au mineralisation in the Olympic Cu-Au Province is suggested to have formed synchronous to the ca. 1600–1585 Ma emplacement of Hiltaba Suite granites and eruption of co-magmatic Gawler Range Volcanics (GRV) [13,15]. This event is associated with initial magmatic-hydrothermal activity leading to the deposition of Cu-Au mineralisation within the region. However, within the Olympic Dam Cu-Au-(U) deposit, there is widespread textural and isotopic evidence for later remobilisation, replacement, and recrystallization of ore-forming minerals, e.g., [16–18]. These phenomena may relate to one or more tectonothermal events, including the intrusion of the regional ~820 Ma Gairdner Dyke Swarm, which are recognised in the region [19,20].

Complete miscibility exists in the system PbS–PbSe–PbTe above 500 °C. Immiscibility between galena-clausthalite and altaite is complete below 300 °C, with the critical temperature at which PbS and PbSe separate calculated at ~100 °C [10]. Hydrothermal origins with temperatures above 100 °C during Pb-chalcogenide mineralisation should therefore result in the preservation of the complete PbS-PbSe series, giving access to both chalcogen elements S and Se, with miscibility gaps appearing below 100 °C [10].

Selenium, substituting for sulphur, is a common minor element in most common sulphides. In some cases, there is complete isomorphous solid solution between the sulphide and analogue selenide, e.g., chalcopyrite-eskebornite (CuFeS₂-CuFeSe₂). Trace element analysis of Cu-(Fe)-sulphides

typically show the presence of hundreds and, locally, thousands of mg/kg of Se within the crystal lattice [21–23]. In contrast, concentrations of lead in common Cu-(Fe)-sulphides are often erratic and readily interpretable in terms of inclusions of galena and other Pb-bearing minerals, rather than lattice-bound lead.

Textural relationships among dominant Cu-(Fe)-sulphides (chalcopyrite, bornite, chalcocite) and the associated phases djurleite, digenite, and covellite at the micron- to nanoscale in Cu ores from the Olympic Dam have been described by Ciobanu et al. [24]. Analogous bornite-chalcocite, bornite-chalcopyrite and chalcopyrite-pyrite assemblages are observed throughout the orebody from which the samples were taken (authors' unpublished data).

A summary of Cu-(Fe)-sulphide and associated species discussed in this contribution and their crystal structure parameters are presented in Table 1. High- and low-temperature species are listed with their corresponding symmetry groups. Within the Cu-(Fe)-sulphides, phase transitions from high to low T are well defined with either cubic (bornite, digenite) or hexagonal (chalcocite) symmetry, indicating the primitive parent structure [24]. Although other minerals listed in Table 1 may display slight variation in their cell parameters *a*, *b*, and *c* because of compositional changes via solid solution of minor elements (e.g., in galena, clausenthalite and altaite [25], and monazite [26]), they do not show changes in overall symmetry and remain within the same crystal system.

Table 1. Crystallographic data for the phases discussed in this contribution.

Mineral Information	Formula	Cu/S Ratio	Symmetry	System	Superstructures	a (Å)	b (Å)	c (Å)	Angle (°)	Reference(s)
Cu-Fe-sulphides										
Chalcopyrite	CuFeS ₂	-	Tetragonal	<i>I42d</i>		5.289	5.289	10.423		[27]
Bornite	Cu ₅ FeS ₄	-	Cubic	<i>F23</i>	(a)	5.47	5.47	5.47		[28]
>265 °C		-	Cubic	<i>Fm3m</i>	2a	10.981	10.981	10.981		[29]
200–265 °C		-	Cubic	<i>F43m</i>	2a	10.71	10.71	10.71		[30,31]
-		-	Cubic		3a	(3 × 5.5)	(3 × 5.5)	(3 × 5.5)		[32]
-		-	Cubic	<i>Fm3m</i>	4a	21.88	21.88	21.88		[30,31]
-		-	Cubic		5a	(5 × 5.5)	(5 × 5.5)	(5 × 5.5)		[32]
-		-	Cubic		6a	(6 × 5.5)	(6 × 5.5)	(6 × 5.5)		[32]
<200 °C		-	Orthorhombic	<i>Pbca</i>	2a4a2a	10.95	21.862	10.95		[33]
Chalcocite	Cu _{2-x} S									
High-T (104–435 °C)	Cu ₂ S	2	Hexagonal	<i>P63/mmc</i>		3.95	3.95	6.72	γ = 120	[34]
Low-T (<104 °C)			Monoclinic	<i>P21/c</i>		15.246	11.884	13.494	β = 116.35	[34]
Pseudo-orthorhombic				<i>ABm2</i>		11.884	27.324	13.494	β = 90.08	[35]
Djurleite	Cu ₃₁ S ₁₆	1.96	Monoclinic	<i>P21/n</i>		26.7	15.72	13.57	β = 90.13	[34]
Digenite										
High-T (>83 °C)	Cu _{1.8} S	1.8	Cubic	<i>Fm3m</i>	(a)	5.57	5.57	5.57		[36,37]
Low-T			Cubic	<i>Fd3m</i>	na	(n × 5.57)	(n × 5.57)	(n × 5.57)		[32,36]
Selenides and monazite										
Clausthalite	PbSe	-	Cubic	<i>Fm3m</i>		6.1054	6.1054	6.1054		[25]
Bellidoite	Cu ₂ Se	-	Tetragonal	<i>P41/m</i>		11.52		11.74		[38]
Monazite	RE(PO ₄)	-	Monoclinic	<i>P21/n</i>		6.7902	7.0203	6.4674	β = 103.38	[26]

3. Sampling and Analytical Methodology

This research was undertaken on a set of 30 different laboratory-prepared sulphide concentrates from representative crushed ore samples. All instrumentation used in this study is housed at Adelaide Microscopy, The University of Adelaide. Each sample was prepared as a polished block, one-inch in diameter. Polished blocks were examined in reflected light and in backscatter electron (BSE) mode using a FEI Quanta 450 Field Emission Gun scanning electron microscope (SEM) (FEI, Eindhoven, The Netherlands) equipped with a silicon-drift energy-dispersive X-ray spectrometer.

Samples were quantitatively analysed using a Cameca SXFive Electron Microprobe running PeakSite software and equipped with 5 WDS X-ray detectors. The beam conditions were set at an accelerating voltage of 20 kV and 20 nA. Because of the small size of the minerals to be targeted, a focussed 1 μm beam was used for the analysis. The calibration and data reduction were carried out in Probe for electron probe microanalyzer (EPMA) (Cameca, Paris, France), distributed by Probe Software Inc. The calibration was performed on certified natural and synthetic standards from Astimex Standards Ltd. (Toronto, ON, Canada) and P & H Associates (Table A1 in Appendix A). The total acquisition time of all elements on a single point was ~ 5 min.

Initially, a set of 16 elements were measured: S K α , Pb M α , Cd L α , Bi M α , As L α , Se L α , Fe K α , Cu K α , Mn K α , Ag L α , Sb L α , Te L α , Hg L α , Zn K α , Ni K α , Co K α . This list was subsequently shorted by removing Cd, Hg, Ni, Co, as these elements were below DL in the samples. The average minimum detection limits (99% CI) in wt % for selenide analysis were: S (0.02), Pb (0.03), Cd (0.05), As (0.05), Se (0.02), Fe (0.02), Cu (0.04), Mn (0.02), Ag (0.06), Hg (0.07), Zn (0.03), Ni (0.03), Co (0.02), Sb (0.03), Te (0.03), Bi (0.07).

Cross-section imaging and TEM sample preparation were performed on a FEI-Helios nanoLab Dual Focused Ion Beam and Scanning Electron Microscope (FIB-SEM). The procedures outlined by Ciobanu et al. [39] were followed in extraction and thinning, to 50–70 nm, of TEM foils by Ga⁺ ion milling. The TEM foils were attached to Cu or Mo grids via Pt welding. Images were obtained in immersion mode to obtain maximum resolution.

High-resolution (HR)-TEM imaging in bright field (BF) mode and electron diffraction were performed using a Philips CM200 TEM. The instrument is equipped with a LaB6 source and operated at 200 kV and utilises a double-tilt holder and a Gatan Orius digital camera (Gatan Inc., Pleasanton, CA, USA). Energy-dispersive X-ray spectra (EDS) were acquired using an Oxford Instruments X-Max 65T SDD detector running the Aztec software.

High-Angle Annular Dark-Field Scanning Transmission Electron Microscope (HAADF-STEM) (FEI, Eindhoven, The Netherlands) imaging was performed using an ultra-high resolution, probe-corrected, FEI Titan Themis S/TEM. This instrument is equipped with the X-FEG Schottky source and Super-XEDS geometry (see also [40–42]) The Super-XEDS detector provides geometrically symmetric EDS detection with an effective solid angle of 0.8 Sr. Probe correction delivered sub-Ångstrom spatial resolution, and an inner collection angle greater than 50 mrad was used for HAADF experiments using the Fischione HAADF detector.

The diffraction measurements were performed using DigitalMicrograph™ 3.11.1 (Gatan Inc., Pleasanton, CA, USA) and Winwulff® 1.4.0 (JCrystalSoft, Livermore, CA, USA) software. Publicly available data from the American Mineralogist Crystal Structure Database [43] were used for indexing of the electron diffractions. Crystal structure simulations were carried out using CrystalMaker® version 9.2.7 (CrystalMaker Software Ltd., Begbroke, Oxon, UK) and STEM™ for xHREM software (HREM Research Inc., Higashimastuyama, Japan).

4. Results

4.1. Characterisation of Symplectite Textures

All three Cu-(Fe)-sulphides (chalcopyrite, bornite, and chalcocite) display symplectitic textures containing clausenthalite. The petrographic relationships within the symplectites were examined in

backscatter electron (BSE) and secondary electron (SE) modes (SEM and FIB-SEM, respectively), and show a wide range of textures with respect to the density of the component phases, size, distribution, etc. In

the absence of other Cu-(Fe)-sulphide host minerals, chalcopyrite displays highly variable relationships with respect to the grain size of clausthalite, with some bleb-like grains of clausthalite as large as 10 μm but others down to fine lamella in the order of 0.01–0.1 μm . Fine lamellae of clausthalite are regularly associated with cracks and pore spaces within the chalcopyrite and tend to radiate from such features (Figure 1a,b). In one sample, chalcopyrite hosts a Cu-selenide phase, which is identified as bellidoite (see below). This appears blotchy and porous on the BSE images (Figure 1a), generally in the presence of coarse clausthalite.

Bornite with coarse chalcopyrite lamellae was regularly observed containing clausthalite, as either relatively coarse (2–10 μm) blebs or fine (<1 μm) lamellae, with both the density of the lamellae and their size varying from grain to grain. In grains containing fine lamellae of clausthalite, these lamellae were roughly parallel to one another within specific domains of the grain but also traversed boundaries between bornite and chalcopyrite without any change in orientation (Figure 1c). The coarser blebs of clausthalite displayed only weak orientation with respect to the crystallographic domains in bornite, typically appearing slightly elongated in the direction of the chalcopyrite lamellae within bornite (Figure 1d). The aforementioned Cu-Se phase was observed in a chalcopyrite-bornite sample where it was associated with a clausthalite, forming a composite bleb (Figure 1d).

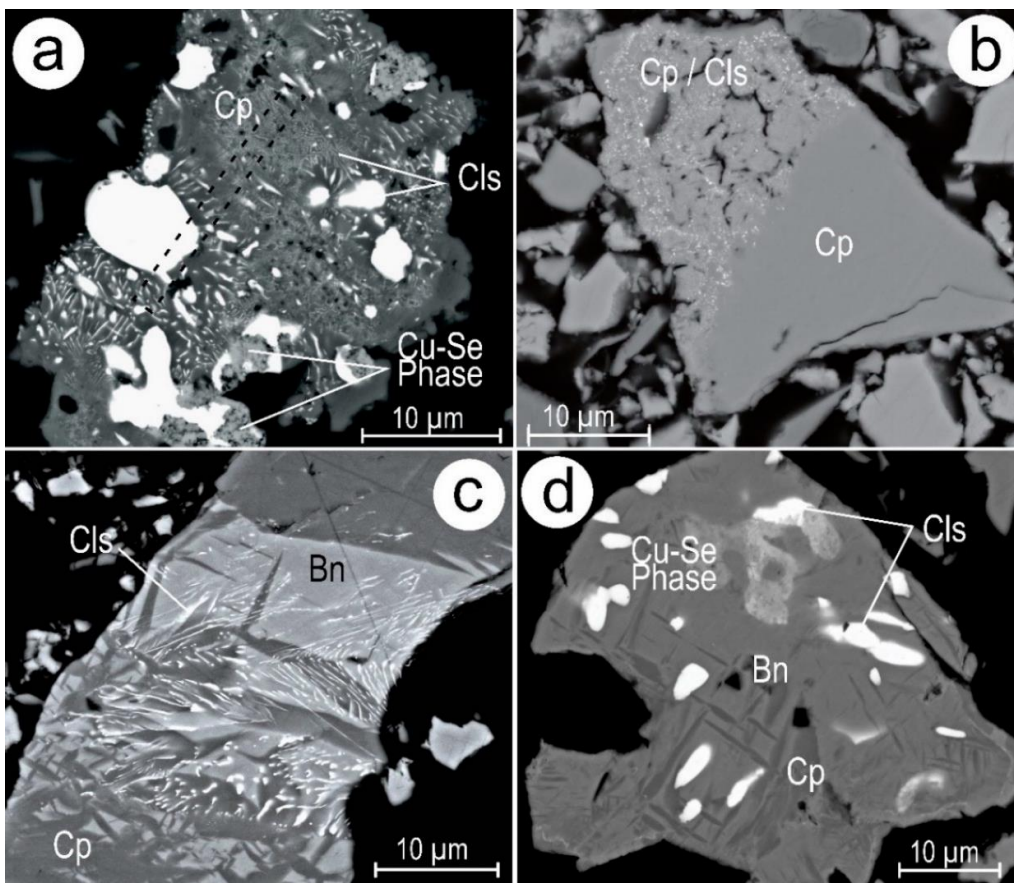


Figure 1. (a,b) Backscatter electron (BSE) images of clausthalite-bearing symplectites hosted within chalcopyrite. The location of the Focused Ion Beam (FIB) cuts for TEM foil preparation is indicated by the dotted line in (a), with clausthalite forming a composite grain with a Cu-Se phase. (c,d) Two varieties of clausthalite-bearing symplectites (fine vs. coarse grained) within coarser chalcopyrite-bornite symplectites. Clausthalite again forms a composite grain with a Cu-Se phase in (d). Abbreviations: Bn—bornite; Cls—clausthalite; Cp—chalcopyrite.

Clausthalite hosted within chalcocite occurs as both fine ($<1\ \mu\text{m}$) blebs and ($<0.1\ \mu\text{m}$ thick) lamellae. Coarser ($>1\ \mu\text{m}$) blebs are less frequent than in chalcocopyrite or bornite and are typically associated with a defect in the chalcocite host, such as cracks or pores. Clausthalite lamellae lie parallel to one another, forming discrete domains within the chalcocite host, identifiable by changes in clausthalite orientation (Figure 2). Symplectites-containing clausthalite are less common in samples containing both bornite and chalcocite than in any of the other host mineral assemblages. Within chalcocite, clausthalite mainly occurs as fine lamellae orientated roughly parallel to one another, forming discrete zones (similar to the clausthalite hosted entirely within chalcocite in the absence of bornite intergrowths, e.g., Figure 2). Clausthalite mainly appears as larger blebs within bornite. At high magnification, bornite is seen to feature nanoscale basket-weave intergrowths of bornite and djurleite and/or chalcocopyrite (Figure 3). The location of the clausthalite blebs is associated with the orientation of the djurleite basket-weave texture, in that clausthalite blebs mostly occur along shifts of the basket-weave textural orientation (Figure 3d). Clausthalite blebs are regularly observed at the mutual boundaries between bornite and chalcocite.

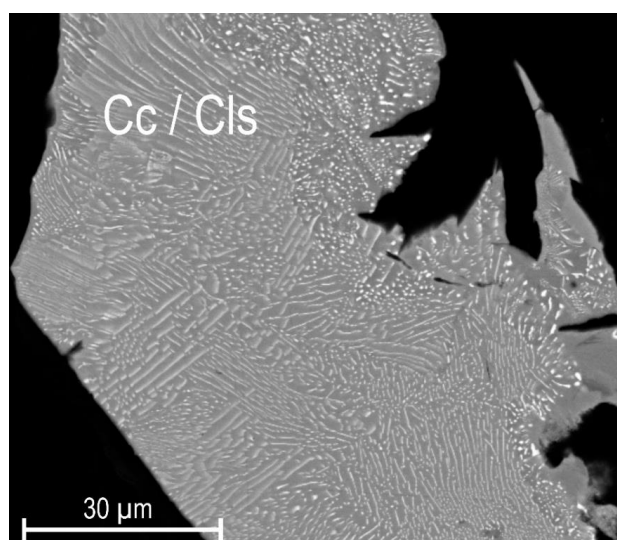


Figure 2. BSE image of clausthalite-bearing symplectite with chalcocite. Note the discrete zones of well-orientated clausthalite lamellae. Abbreviations: Cc—chalcocite; Cls—clausthalite.

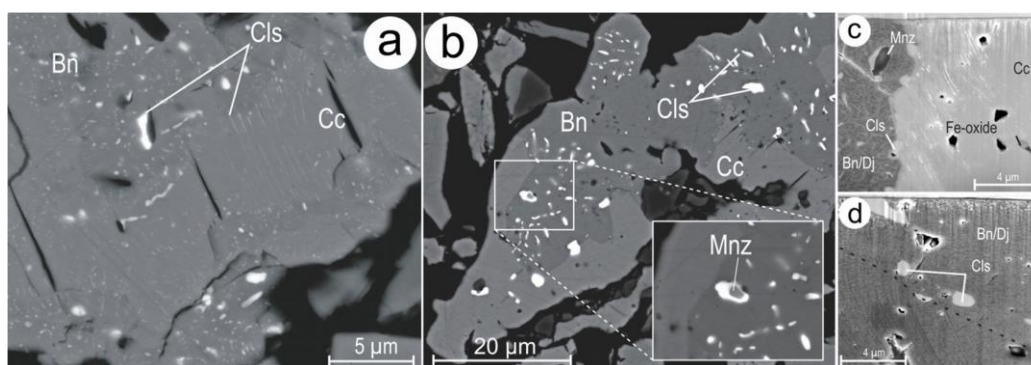


Figure 3. (a,b) BSE images of clausthalite (Cls)-bearing symplectites hosted within coarser bornite (Bn)–chalcocite (Cc) symplectites. The FIB slice taken from (b) (study case BnCcIII, see text below) is imaged in cross section in (c,d), revealing a very fine bornite–djurleite (Dj) symplectic “basket-weave” texture. The dashed line on (d) indicates a change in the orientation of the bornite–djurleite “basket-weave” texture, with clausthalite forming along the boundary. Abbreviations: Bn—bornite; Cc—chalcocite; Cls—clausthalite; Dj—djurleite; Mnz—monazite.

Symplectites preserved in bornite in the absence of either chalcopyrite or chalcocite occur as both randomly orientated and well aligned symplectite structures. Only rarely, however, do they contain clausthalite lamellae as fine as those observed in chalcopyrite or chalcocite.

4.2. Compositional Data for Pb-Chalcogenides and Host Cu-(Fe)-Sulphides

The small size and density of clausthalite within the symplectites makes it difficult to obtain high-quality compositional data by EPMA. Nevertheless, the data show: (1) the large (>5 μm) inclusions are end-member clausthalite without measurable sulphur; (2) the absence, at measurable concentrations, of Ag, Sb, or Bi, the most common minor components of Pb-chalcogenides; (3) the presence of measurable Te in the range 0.06–0.17 wt % within all clausthalite analyses. Inclusions of galena in the same Cu-(Fe)-sulphides outside of the symplectites contained no measurable Se.

Compositional data for the bornite and chalcocite (Figure 4) show that both Cu-(Fe)-sulphides consistently deviate from the ideal stoichiometry. This is attributed to the presence of nanoscale intergrowths of other mineral species such as chalcopyrite (or more rarely djurleite) in bornite (Figure 3c,d) and digenite in chalcocite. A similar non-stoichiometry is reported for Cu-(Fe)-sulphides from the Olympic Dam [24].

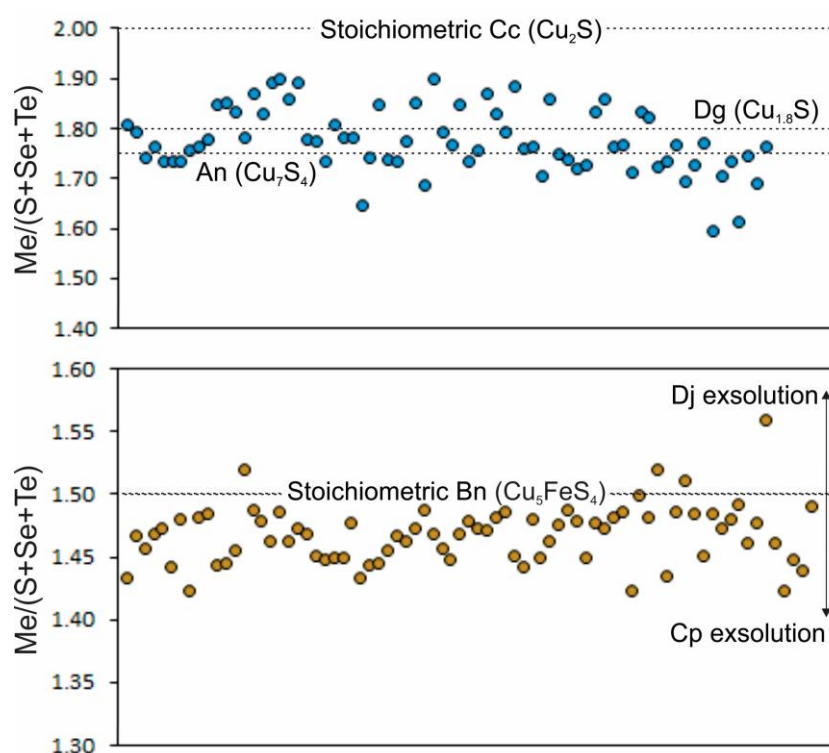


Figure 4. Diagram summarising the stoichiometry of bornite (**brown**) and chalcocite (**blue**). The measurements are presented as the ratio between the total metals measured (Me) and the total chalcogen elements (S, Se, and Te). The data are arranged in order of analysis only. An—ánilite, Bn—bornite, Cc—chalcocite, Cp—chalcopyrite, Dg—digenite, Dj—djurleite.

4.3. Nanoscale Characterisation (TEM Data)

4.3.1. Host Sulphides

Nanoscale studies were carried out on four study cases using bright-field TEM and HAADF-STEM imaging, electron diffraction, and EDS spot analysis and mapping on four FIB-prepared TEM foils (Figure 5).

The four study cases represent: (1) dense symplectites of clausthalite in chalcocite-digenite (CcI; Figure 5a); (2) chalcocopyrite with variable textures with respect to clausthalite inclusions (CpII; Figure 5b); (3) bornite-chalcocite with clausthalite and other mineral inclusions, notably monazite (BnCcIII; Figure 5c); (4) lamellar chalcocopyrite in bornite with lesser clausthalite inclusions (BnCpIV; Figure 5d). The latter contains larger pore fillings comprising Fe oxides and a Cu-selenide (bellidoite). These study cases thus cover clausthalite hosted within both single and binary Cu-(Fe)-sulphides associations, with variability in morphology, size, and phase associations.

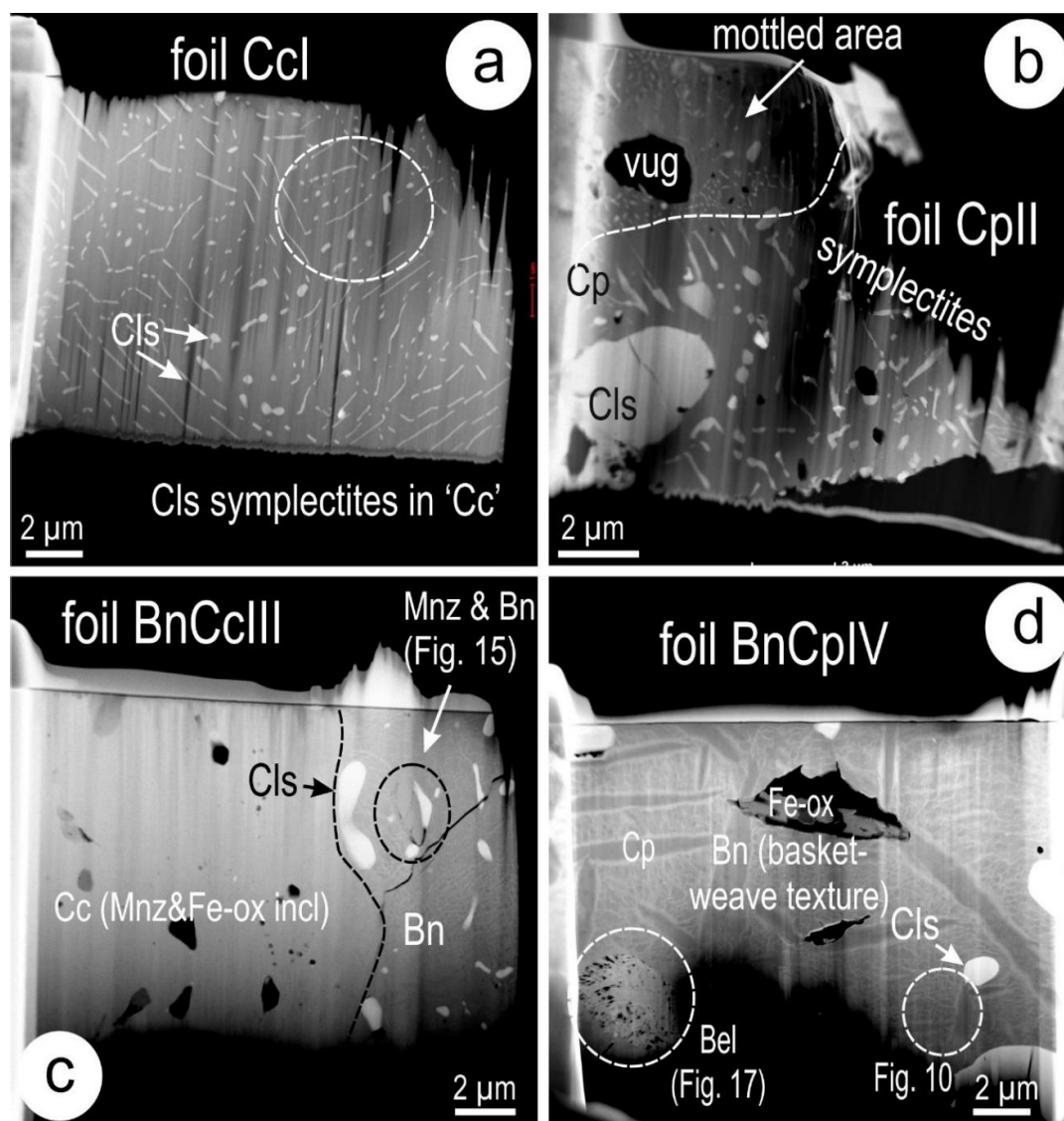


Figure 5. High-Angle Annular Dark-Field Scanning Transmission Electron Microscope (HAADF-STEM) images showing the four analysed TEM foils. (a) Dense field of clausthalite as rods and blebs of variable orientation in chalcocite. (b) Coarse micron-scale clausthalite in chalcocopyrite coexisting with finer swarms of rods and mottled areas of clausthalite inclusions. (c) Clausthalite of variable size mostly in the bornite domain. Monazite and iron oxide are present throughout both chalcocite and bornite. (d) Dense lamellae of chalcocopyrite in bornite, with scattered inclusions of clausthalite. Micron-sized pores are filled by iron oxides and the Cu-selenide bellidoite. Note in both (c,d) the basket-weave appearance of bornite due to the presence of sub-micron-scale djurleite lamellae. Abbreviations: Bel—bellidoite; Bn—bornite; Cls—clausthalite; Cp—chalcocopyrite; Fe-ox—iron-oxides; Mnz—monazite.

The variability in textures throughout the study cases is illustrated in Figure 6. In CcI, this comprises fields of antiphase boundary (APB) domains with variable orientation (Figure 6a). Similar APB domains are observed also in chalcocite in BnCcIII. Fine 30–80 nm-wide clausthalite inclusions are embedded within, or crosscut these domains (Figure 6b,c). Larger (200–500 nm-sized) inclusions of clausthalite also exist outside the APB domains (Figure 6d). In CpII, mottled textures with dense, fine inclusions occur in domains that are outlined by fine fractures and coarser rods of clausthalite, or surrounding micron-sized pores (Figure 6e,f). Symplectites, as in CcI, are developed outside of such mottled areas (Figure 6g). Needles of chalcopyrite inclusions are found in the coarser clausthalite from such areas (Figure 6h). In BnCpIV, rounded, micron-sized blebs of clausthalite are found at the margins of chalcopyrite lamellae in bornite (Figure 6i). The basket-weave texture on the sample develops around the edges of such lamellae and in the surroundings of needles of djurleite (Figure 6j-l). Such needles can be present within the bornite or adjacent to the chalcopyrite lamellae. HAADF-STEM imaging reveals the patchiness in greyscale intensity across foil BnCpIV; some of this is due to the higher alteration in this case (see below) but also to the effect of FIB milling in and around inclusions and lamellae. EDS compositional data for host sulphides was determined in areas free of inclusions (Figure 6m) and indicates the presence of Se throughout the Cu-(Fe)-sulphides and of Pb in those cases where two sulphides are present (BnCcIII and BnCpIV). In the single phases, minor Pb is noted in Cc1, but very little in CpII.

The identity of the species referred to above as “chalcocite” and “bornite”, as well as the characteristics of chalcopyrite in the mottled areas were studied in further detail via TEM imaging down to atomic scale and electron diffractions. In CcI, there are two co-existing species: digenite superstructure and monoclinic chalcocite (Figure 7). Digenite is present in the APB domains, whereas monoclinic chalcocite occurs outside. These domains are outlined in some cases by rods and blebs of clausthalite (Figure 7a) and are marked by different orientation of the sulphides. The APB domains are readily identified by strong contrast in BF-TEM imaging and are observed as dark ripples with variable morphology across internal subdomains (Figure 7b,c). A finer sub-structure develops in such subdomains, particularly at the tip of the coarser clausthalite inclusions (Figure 7d). Selected area of electron diffraction (SAED) representative of the two species are shown in Figure 7e,f. Digenite is attributed to $6a$ superstructure on the basis of SAEDs showing an orthogonal lattice with $\sim 12 \times \sim 12 \text{ \AA}$ repeats, and intensity variation with brighter reflections indicative of a six-fold superlattice. SAEDs obtained over larger clausthalite inclusions (Figure 7g) indicate close-to-coherent orientation between digenite and clausthalite.

Further details of the APB domains and the boundary relationships between clausthalite and digenite are shown as HR BF TEM images in Figure 8. There is a continuation of the lattice fringes across the dark ripples within the APBs on the [001] zone axis of digenite (Figure 8a), but atom-scale defects occur along such ripples (Figure 8b). The two types of boundary (sharp and scalloped) between clausthalite and digenite are clearly observed in BF TEM imaging (Figure 8c). In detail, the scalloped boundaries show a stepwise morphology (Figure 8d).

Atomic-scale imaging of digenite (in CcI) and djurleite (in BnCpIV) is shown in Figure 9. HAADF-STEM imaging was undertaken on [111] zone axis in digenite, showing bright atomic arrays with an arrangement compatible with the $6a$ superstructure, as marked by the green atomic motif shown on Figure 9a. The superstructure is highlighted by the presence of satellite reflections with six-fold periodicity between main spots, as shown on Fast Fourier Transform (FFT) images (Figure 9b). The image in Figure 9a also shows defects (stacking faults?). A portion of the corresponding supercell motif for $6a$ digenite is outlined on Figure 9c. A simplified crystal structural model for high-temperature digenite [37] shows that the distribution of the bright atoms relates to sites with dominant Cu occupancy (Figure 9d). Djurleite down to the [031] zone axis (Figure 9e,f) shows a very different atomic arrangement. The detail in Figure 9g and the crystal model for a single unit cell (Figure 9h) show again that the brighter spots are attributable to Cu atoms, even though the complexity of the crystal structure requires work beyond the scope of the present study.

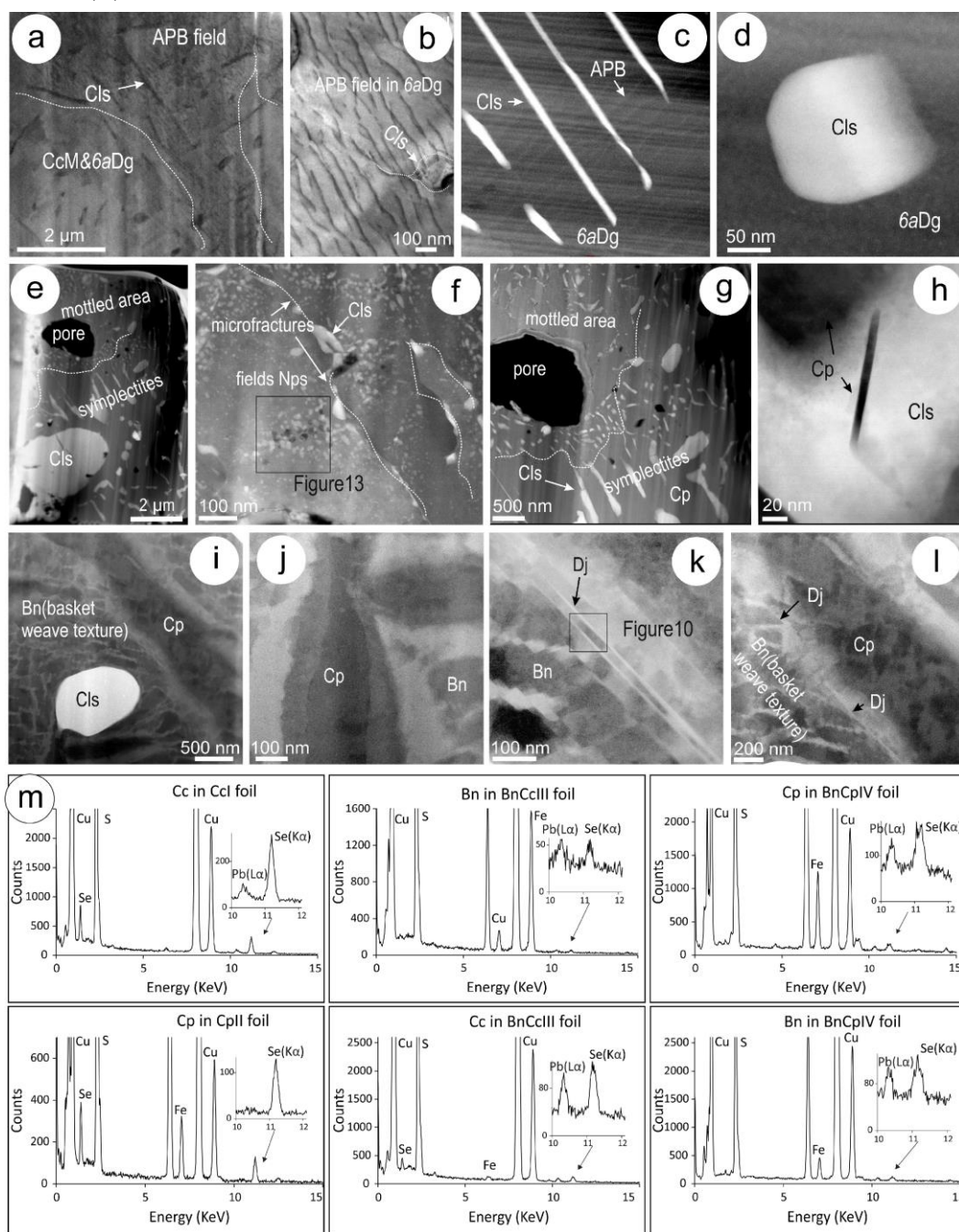


Figure 6. Aspects of host sulphides and their compositions: Bright field (BF)-TEM (a,b); HAADF-STEM (c–l) images; energy-dispersive X-ray spectra (EDS) spectra (m). (a,b) Antiphase boundary (APB) domains with variable orientation in CcI. Note clausenthalite inclusions embedded in (b). (c,d) Fine rods of clausenthalite crosscutting APBs in CcI (c) and a coarser inclusion outside the APBs (d). (e,f) Mottled areas in CpII developed in domains outlined by fine fractures filled by clausenthalite. (g) Boundary between mottled and symplectite areas in CpII. Note the density of inclusions surrounding a micron-sized pore. (h) Needle of chalcopyrite in clausenthalite from an area with the coarser symplectites. (i) Clausenthalite bleb adjacent to chalcopyrite lamellae in bornite (BnCpIV). Note the fine basket-weave texture surrounding the bleb. (j) Chalcopyrite in bornite, displaying marginal intensity variation relating to the development of the basket-weave texture. (k,l) Nanometre-sized needles of djurleite in bornite (k) and on the margin of chalcopyrite (l). (m) EDS spectra of the main sulphides hosting clausenthalite. Abbreviations: APB—AntiPhase Boundaries; Bn—bornite; Cls—clausenthalite; Cp—chalcopyrite; Dg—digenite; Dj—djurleite.

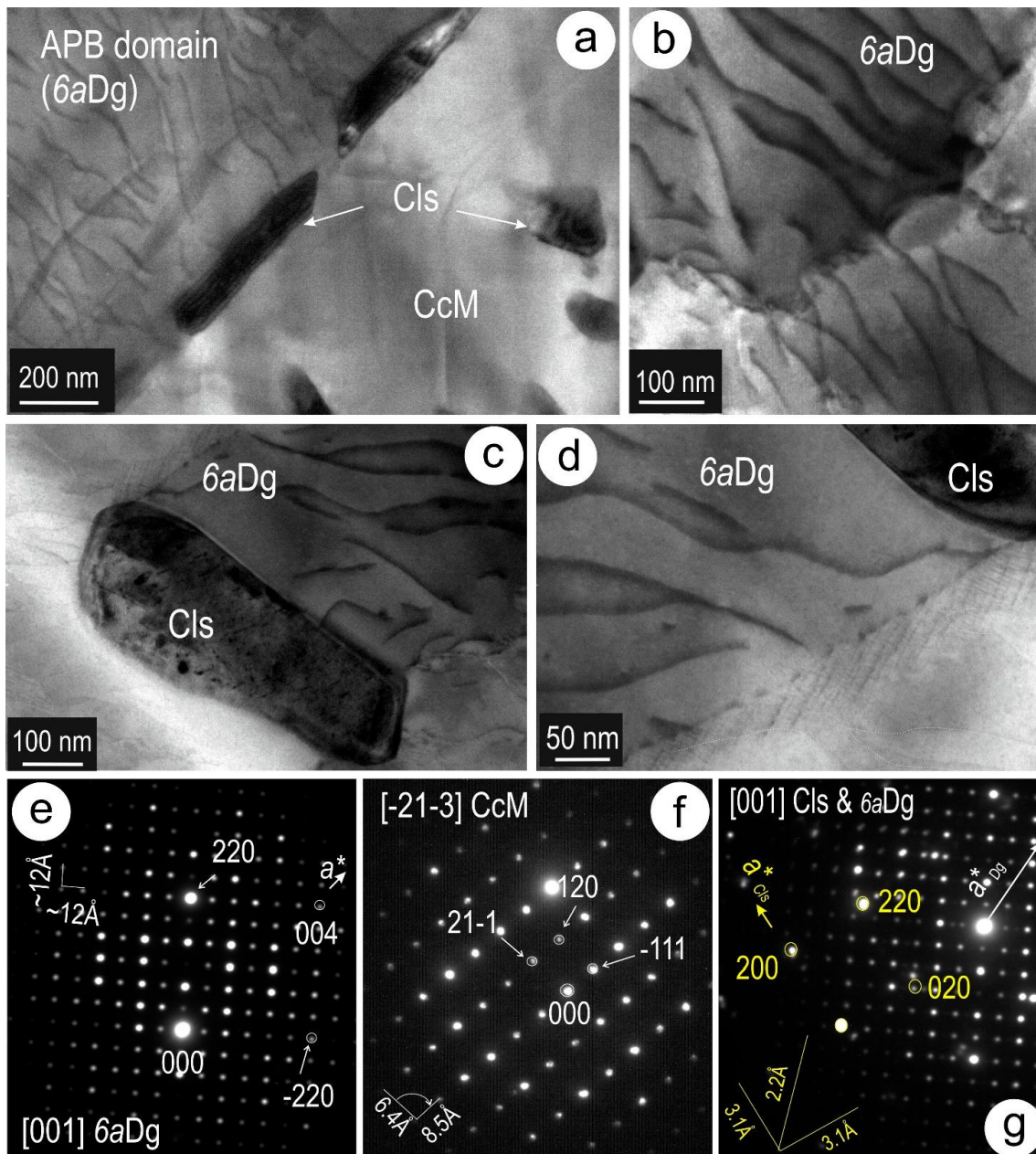


Figure 7. BF-TEM images (a–d) and selected area of electron diffraction (SAEDs) (e–g) showing aspects of sulphide and clausenthalite in Foil Ccl. (a) Rods of clausenthalite along boundaries between APB domains with digenite and monoclinic chalcocite outside the APB domains. (b) Typical aspects of APB domains represented by dark ripples of variable morphology across subdomains. (c) Larger clausenthalite inclusion with marginal variation from straight to slightly scalloped. (d) Internal sub-structure of APBs developed at the tip of clausenthalite shown in (c). (e,f) Representative SAEDs of digenite and monoclinic chalcocite (areas shown in (a)) on zone axes as marked. *6a* digenite is indexed using the *Fd3m* space group of Morimoto and Kullerud [36]. Indexing on (e) refers to the *1a* digenite parent structure. SAEDs in (e,f) were obtained at the same specimen tilt angle indicating different orientation of the sulphides throughout Ccl. (g) Relatively coherent intergrowth between clausenthalite and digenite. Abbreviations: CcM—monoclinic chalcocite; Cls—clausenthalite; Dg—digenite.

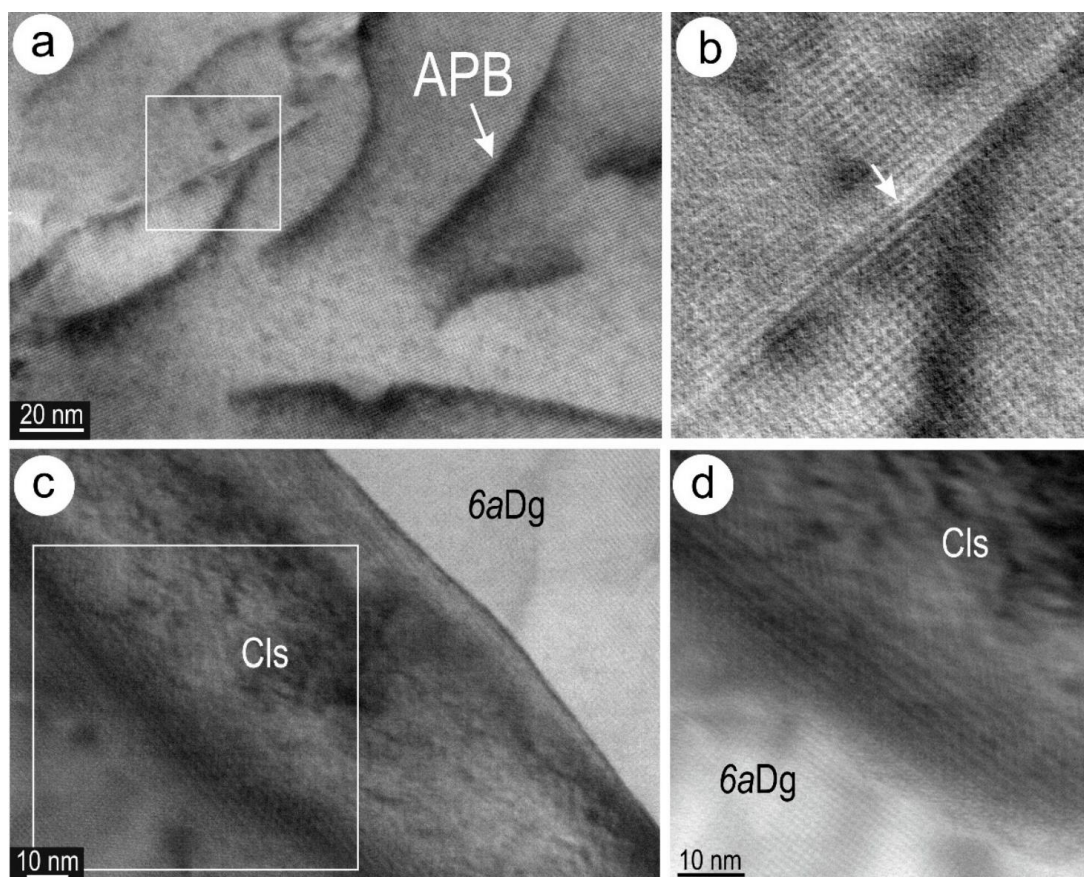


Figure 8. BF-high-resolution (HR)-TEM images of digenite and clausthalite in foil Ccl. (a) APB domain characterised by dark ripples and continuation of lattice fringes across them. (b) Detail of the marked area in (a) showing an atom-wide defect along one of the dark ripples. (c) Sharp and scalloped boundaries of clausthalite (inclusion shown in Figure 7c). (d) Detail of the highlighted area in (c), showing the stepwise character of the scalloped boundary. Abbreviations: APB—AntiPhase Boundaries; Cls—clausthalite; Dg—digenite.

Bornite in the two foils (BnCcIII and BnCpIV) is represented by various superstructures, of which $2a$ and $4a$ are common in both, and $6a$ was only identified in BnCcIII. Bornite superstructures are documented in Figure 10 in an area highlighted in Figure 6k with the specimen titled to the $[101]$ zone axis. These superstructures are imaged from areas outlined by djurelite needles (Figure 10a). Djurelite is coherently intergrown with the bornite, as shown by the FFT (inset on Figure 10a). A close-up of the bornite shows atomic arrays with partitioned spacings (Figure 10b) corresponding to superstructure ordering, as documented by the presence of satellite reflections on the FFTs obtained from such areas. Atomic-scale HAADF-STEM imaging shows subdomains with atom distribution periodicity attributable to the coexistence of $2a$ and $4a$ structures (Figure 10c). Superlattice motifs are highlighted by yellow dots in the figure. A further close-up of the atomic arrangement in $4a$ bornite shows the distribution in a quarter of the unit cell (Figure 10d). Atom distribution arrangements down to $[101]$ zone axis for the two superstructures are shown as STEM simulations and crystal-structural models in Figure 10e–h. The $4a$ superstructure model is based upon eight sites with variable Cu-Fe occupancy ratios as shown, whereas the $2a$ superstructure has distinct Cu and Fe sites (Figure 10f,h). The STEM models clearly show the distinction between the two superstructures (Figure 10e,g), in which the $2a$ superstructure shows variable but high intensity for the Cu atoms relative to Fe atoms. In contrast, the $4a$ superstructure shows relatively even intensity of atoms with higher Cu occupancies (Figure 10e). This is mirrored by the image in Figure 10d for $4a$ bornite analysed here.

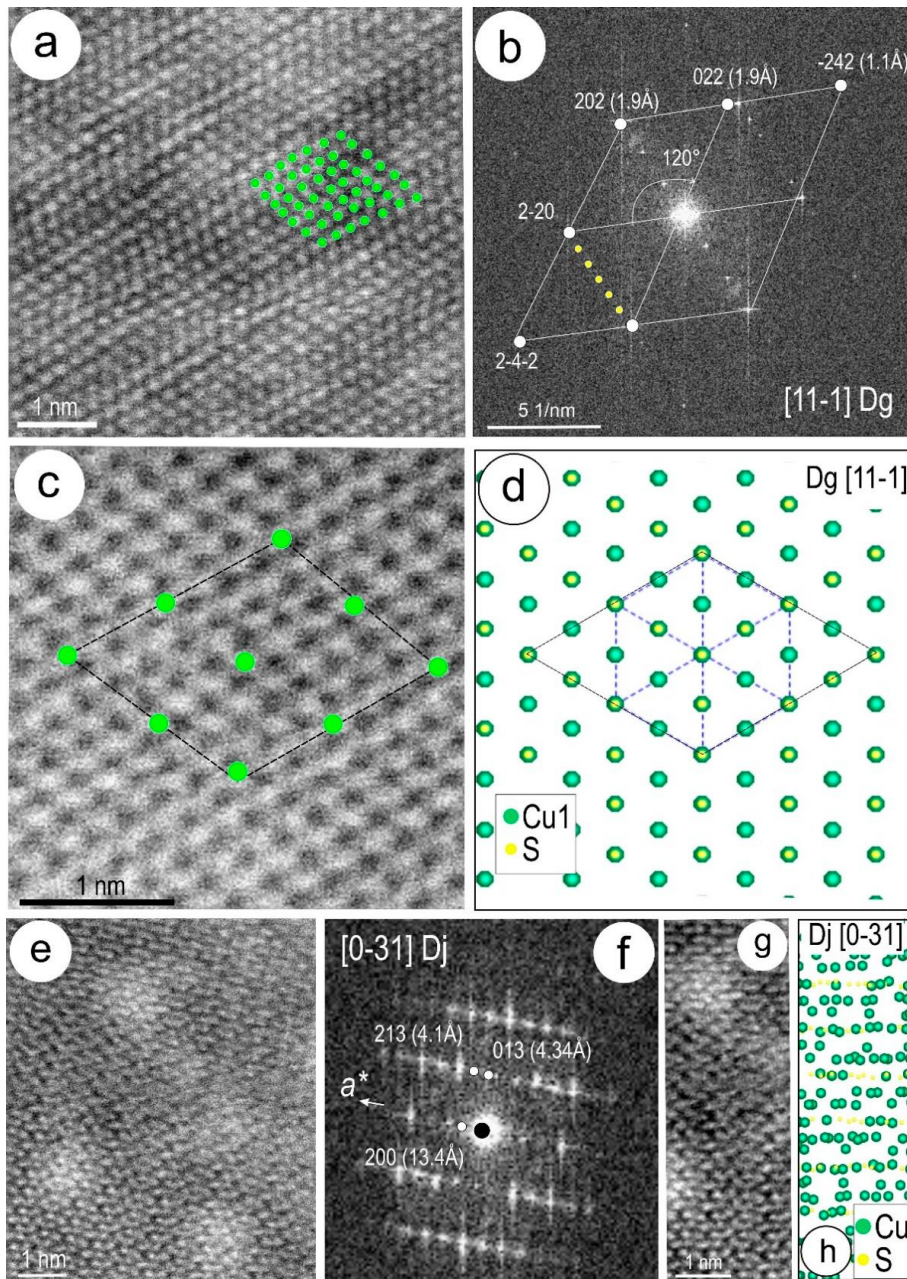


Figure 9. Atomic-scale details images for digenite and djurleite in CcI and BnCpIV, respectively.

(a) HAADF-STEM image showing atom arrangement in digenite on $[11\bar{1}]$ zone axis as calculated from the corresponding Fast Fourier Transform (FFT) in (b). In (a), the structural motif shown by green dots underlines the $6a$ superstructure. Note this is also highlighted by atom-wide defects on the image. The superstructure is clearly highlighted by the six-fold satellite reflections marked in yellow dots on (b). (c) Close-up of an area in (a) showing the structural model consisting of bright atoms with a superstructure motif highlighted by green dots. (d) Simplified model of $1a$ (high-temperature) digenite on the $[11\bar{1}]$ axis using data given in Will et al. [37]. This model includes two Cu sites with different occupancies, of which only Cu1 is shown here (0.3 occupancy). Note the correspondence between the bright spots on the image in (c) and the model in (d) for Cu. (e) HAADF-STEM image showing atom-scale distribution in djurleite down to $[031]$ zone axis as calculated from FFT in (f). (g,h) Atom distribution in a single unit cell on $[031]$ djurleite shown as a cropped image from (e) and a structural model (g) after Evans [34], respectively. Note that the distribution of bright spots resembles those of the Cu sites. Abbreviations: Dg—digenite; Dj—djurleite.

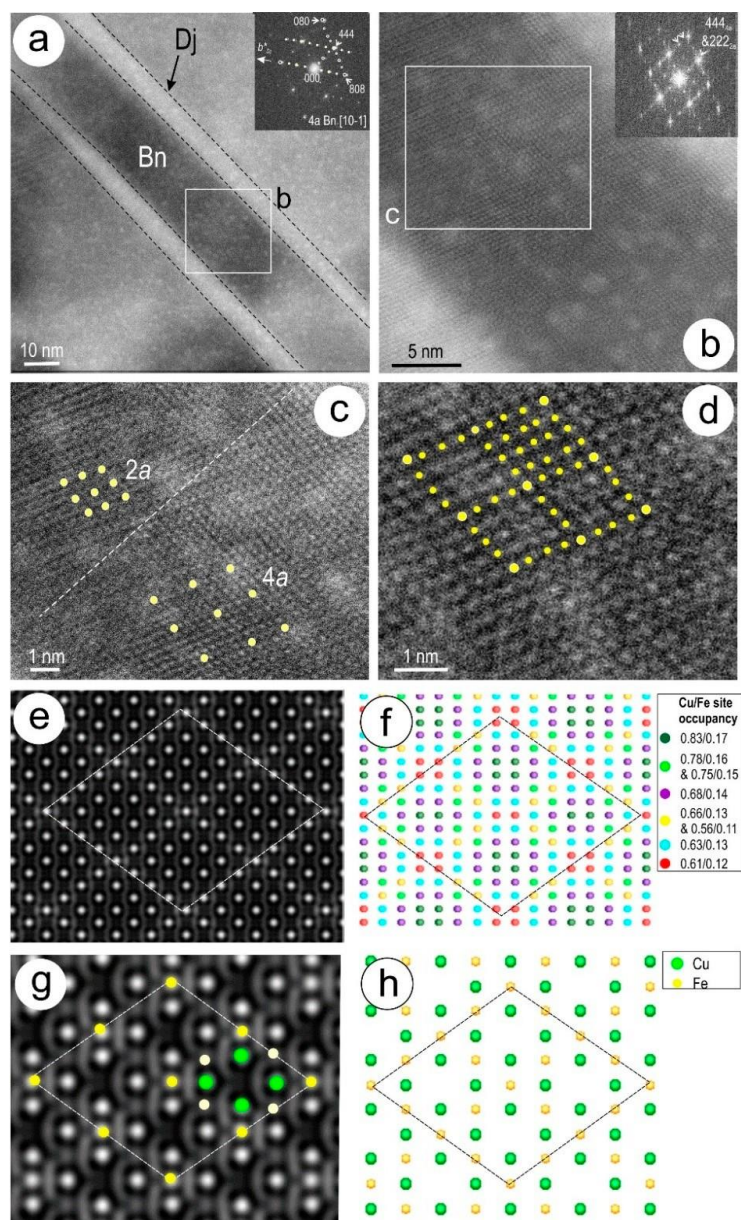


Figure 10. Atomic-scale HAADF-STEM images (a–d) and models (e–h) of bornite superstructures down to the [101] zone axis in $\bar{B}n$ CpIV. (a) Bornite with marginal djurleite from an area highlighted on Figure 6k. FFT in the inset shows coherent intergrowths between $4a$ bornite and djurleite. (b) Close-up of the area marked in (a) showing domain heterogeneity throughout the bornite. Satellite reflections (FFT in inset) shows four-fold periodicity but with variation in intensity indicating the co-existence of $2a$ and $4a$ superstructures. (c) $2a$ and $4a$ superstructure domains in the area marked in (b). The yellow dots highlight the structural motifs for the two species. (d) Detail of the $4a$ superstructure showing atom distribution throughout the superlattice as marked by the yellow dots. Note faint variation in grey-scale intensity of the atoms that make the superstructure unit cell. (e,f) STEM simulation and crystal-structural model for the bornite $4a$ superstructure, respectively, using data for $4aI$ superstructure in Ding et al. [30]. Note the difference in the number of atoms in the STEM simulation relative to the crystal-structural model, whereby the very brightest atoms represent atomic sites with the highest Cu occupancy relative to Fe, and good correspondence between the simulation in (e) and the image in (d). (g,h) STEM simulation and crystal-structural model for the bornite $2a$ superstructure, respectively, using data $2aI$ superstructure in Ding et al. [31]. The yellow and green dots in (g) overlap with the Cu and Fe sites in (h). Sulphur atoms are ignored in both crystal-structural models. Abbreviations: Bn—bornite; Dj—djurleite.

Chalcopyrite was studied in greater detail from mottled areas in foil CpII to better understand the underlying reasons for such textures (Figure 11). SAEDs obtained from such areas show satellite reflections on two zone axes (Figure 11a,b,d). Chalcopyrite down to the $[110]$ zone axis shows an increase in the number of satellite reflections and variable intensity with incommensurate distribution (Figure 11a,b). Image processing of selected areas from such SAEDs with highest density of satellites reveal an ordered pattern (Figure 11c). HAADF-STEM images of chalcopyrite down to the $[221]$ zone axis display bright nm-scale blebs (Figure 11e), whose EDS spectra indicate they are high in Se, yet Pb is at almost negligible concentrations (Figure 6m). Nonetheless, such areas show satellite reflections on both SAEDs and FFTs (Figure 11d and inset on Figure 11e). Bright atoms on the HAADF-STEM image (Figure 11f) correspond to Cu positions on the crystal-structural model (Figure 11g). There is, however, variable intensity in the bright atoms that could represent an overlap between different atom columns, as well as the presence of incipient ordering towards another Se-bearing phase, since the FFTs obtained from such areas show satellite reflections (Figure 11f, inset).

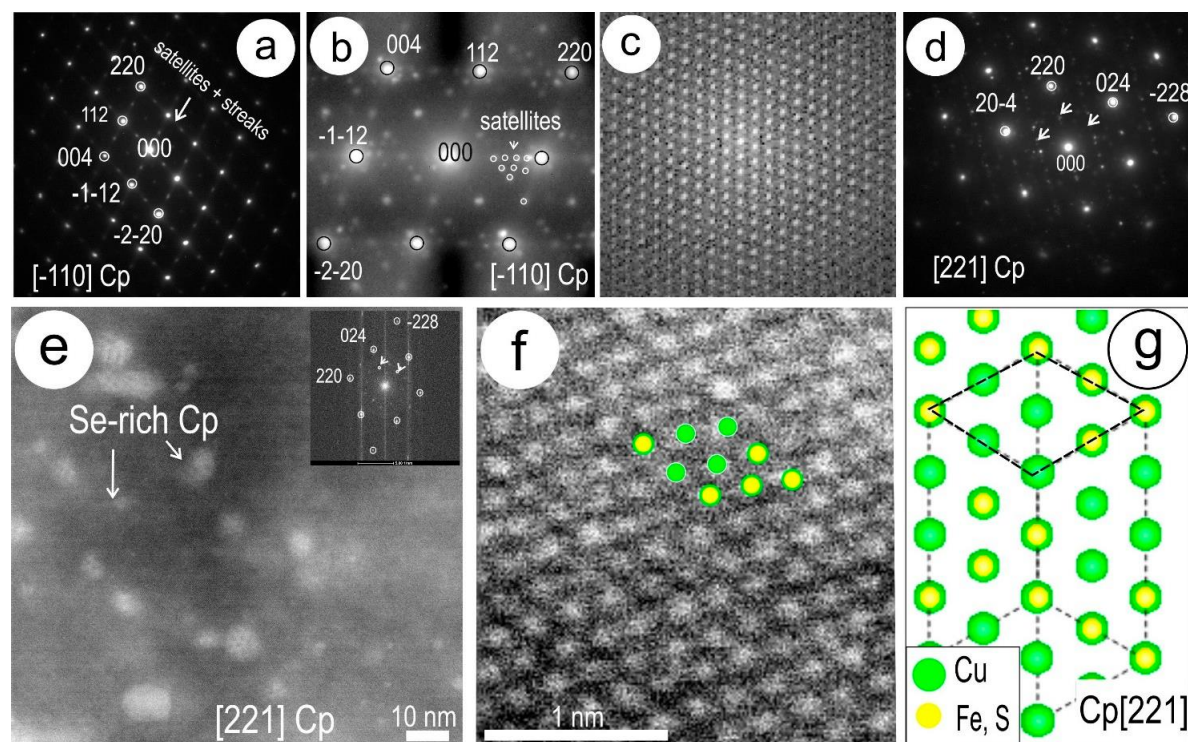


Figure 11. Nanoscale aspects of chalcopyrite from mottled areas in foil CpII. (a) SAED down to the $[110]$ zone axis showing satellite reflections (arrowed). (b) Close-up of SAED in (a), showing detail of satellite reflections and their incommensurate distribution. (c) Inverse FFT image obtained from (b), showing an ordered pattern. (d) SAED down to $[221]$ zone axis, showing satellite reflection (arrowed). (e) HAADF-STEM image of chalcopyrite down to $[221]$ zone axis with bright, nm-scale blebs and corresponding FFT (inset). (f) Atomic-scale HAADF-STEM image down to $[221]$ zone axis, showing brightest atoms attributable to the Cu sites in the crystal-structural model [27] shown in (g). Note, however, the variation in intensity of such atoms and the presence of satellite reflections on FFTs obtained from such areas (inset). Abbreviation: Cp—chalcopyrite.

4.3.2. Clausthalite and other Inclusions

Although clausthalite-bearing symplectites are ubiquitous, their sizes and morphologies in each case described here represent a broad spectrum from simple, dense symplectites in foil Cc1 down to clustered nanoparticles in foil CpII and composite inclusions with other phases in bornite-bearing

samples. The nanoscale investigation is focussed on these three types of inclusions and their speciation in order to better understand the formation of the clausthalite-hosting sulphides.

HAADF-STEM imaging and EDS were undertaken on several clausthalite inclusions (rods and blebs) in foil Cc1 to understand the relationships with host “chalcocite” (particularly in the digenite domains) in terms of orientation and boundary morphologies. Both types of boundaries (sharp and scalloped) shown in Figure 8 were found to be typical throughout the symplectites (Figure 12). The orientation of the clausthalite relative to the [001] zone axis of digenite changes from [001] (Figure 12a–c) to [121] (Figure 12d–f), but retains the relatively coherent orientation between the two species (Figure 12c,f). One case of the scalloped boundaries was imaged at higher magnification (Figure 12g). This shows a ragged interface within the clausthalite edge with a decrease in the intensity of the Se signal, as determined by EDS, from the clausthalite towards digenite. The image shows a darkening correlating with the decrease in Se, as well as well-defined darker strips within the Se-depleted part of the clausthalite (arrowed on Figure 12g). In detail, the clausthalite shows changes in the atomic arrays, from parallel rows of bright atoms (attributable to Pb, see below) in the less affected part of the clausthalite (Figure 12h) to arrays in which some parts markedly miss the bright atoms, suggesting a localised Pb loss (Figure 12i). Altogether, the darkening, Se depletion and the removal of Pb are interpretable as a replacement of clausthalite along scalloped boundaries.

The mottled texture in chalcopyrite shown in Figure 6f consists of clusters of nanoparticles (NPs) with variation in size from ~5 nm up to some tens of nm (Figure 13). Some of the denser fields of inclusions are observed around domain boundaries and, although dominated by PbSe, they also include bismuth-bearing NPs (Bi-NPs) as revealed by EDS mapping (Figure 14). The densest agglomeration of NPs is seen in areas also containing voids (Figure 13a). Peculiar to the PbSe-NPs and clusters is a bright, dotted appearance with rhombic arrangement relative to each cluster (Figure 13b,c). The smallest Bi-NPs are found within clusters of PbSe adjacent to voids (Figure 13c). Notably, such NPs reorganise their atomic arrangement under the electron beam (Figure 13d,e). The rhombic arrangement of the brighter spots in PbSe is associated with the occurrence of satellite reflections on FFTs obtained from such images (Figure 13f). There is a marked coherence between the rhombic arrangement of the bright spots within the PbSe and the atomic arrangement in host chalcopyrite down to the [221] zone axis (Figure 13g). These features suggest that the PbSe-NP clusters undergo ordering towards the formation of large (tens of nm) superstructures. The appearance of PbSe in these NP clusters is clearly distinct from those in symplectites and other coarser textures (e.g., in Figure 12).

The middle part of the NP field in Figure 13a was mapped by STEM EDS (Figure 14) and clearly shows that most of the bright features are PbSe-NPs, whereas the darker features in the middle correlate with depletion in Cu and S. Bismuth is concentrated in the PbSe-NPs but also shows stronger signals indicative of discrete Bi-NPs as that imaged in Figure 13d, e. In contrast to lead, both Se and Bi show signals above background throughout the host chalcopyrite.

In contrast to the single-phase sulphides, inclusions with more varied composition are found in the bornite-bearing sulphide assemblages (Figure 5c,d). These comprise iron oxides (in both BnCcIII and BnCpIV), and numerous nanoinclusions of monazite in BnCcIII and a Cu-selenide in BnCpIV. The smallest monazite inclusions, associated or not with iron oxides, occur throughout the chalcocite domains in BnCcIII (Figure 15a). The coarsest grains of monazite (hundreds of nm in size) are found associated with clausthalite within bornite, near the boundary to chalcocite (Figures 5c and 15b). Similar coarse inclusions are also located close to fractures. Monazite inclusions display a strong relief against the sulphides, with wedged boundaries. HAADF-STEM imaging along the mutual boundary between monazite and clausthalite (Figure 15d,e, respectively) show the occurrence of dark areas in clausthalite. A spectrum obtained with a smaller spot size (5–6 nm, smaller than the inclusion diameter) from such a darker domain (Figure 15c) indicates the presence of both phases, suggesting the presence of monazite inclusions within clausthalite.

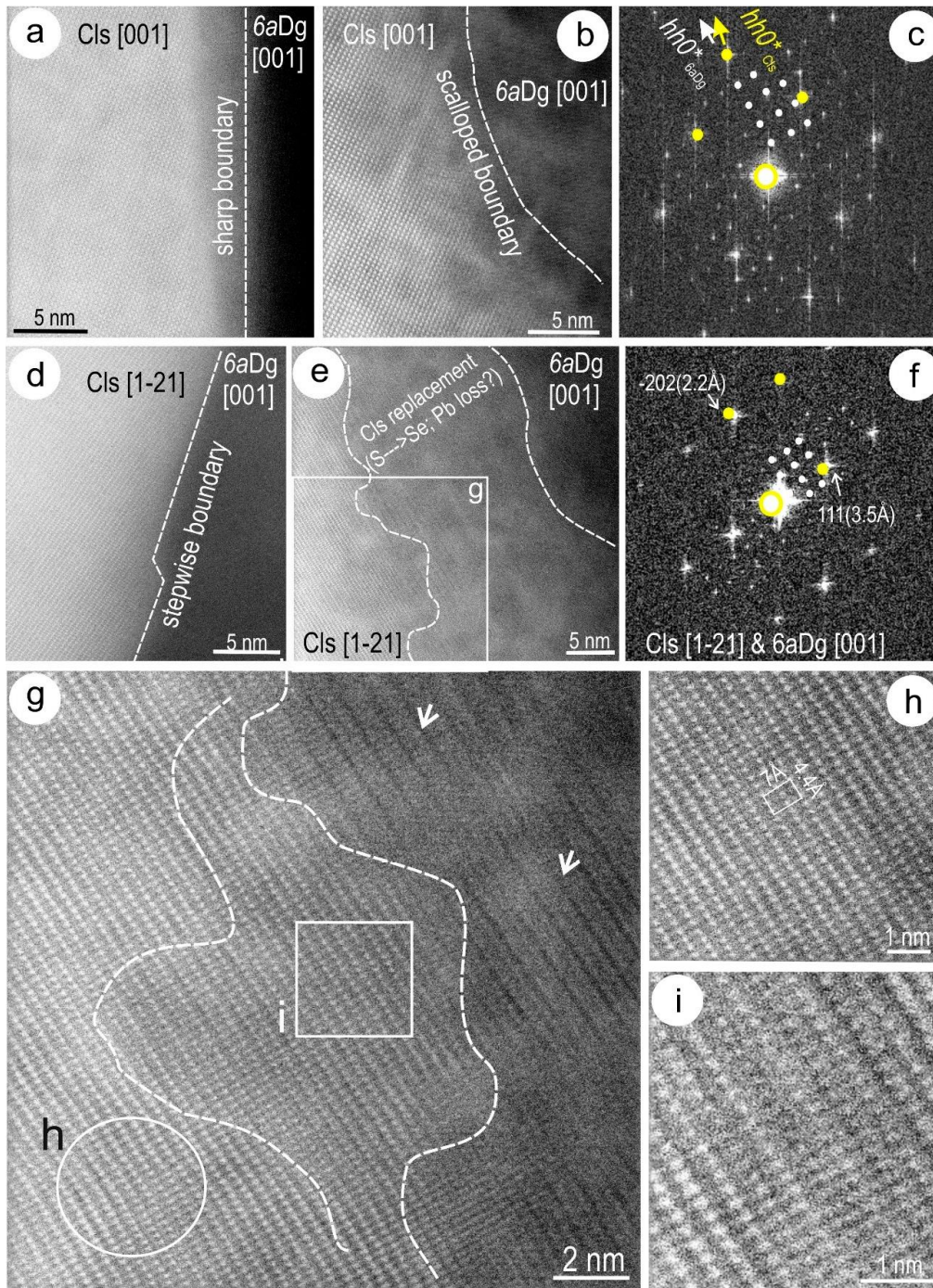


Figure 12. HAADF-STEM imaging and FFTs showing clausenthalite boundaries and the relationship with host digenite in CcI. **(a,b)** Sharp and scalloped boundaries between clausenthalite and digenite with the same [001] orientation, as inferred from the FFT in **(c)**. **(d,e)** Sharp and scalloped boundaries with different orientations to one another, i.e., [121] in clausenthalite and [001] for digenite, as depicted in the representative FFT (shown in **f**). Note the stepwise character of one of the sharp boundaries in **(d)**.

(g) Atom-scale image of clausenthalite (area marked in **e**), showing modification in grey-scale intensity (distinct domains shown by dashed lines). **(h)** Unaffected clausenthalite shows arrays of bright atoms with periodicities at $7 \times 4.4 \text{ \AA}$. **(i)** Parts of the affected clausenthalite show evidence of replacement of these arrays in which the bright atoms are missing. Note (in **g**) that the most affected part of the image also shows dark strips (arrowed) at two-array periodicities. Abbreviations: Cls—clausenthalite; Dg—digenite.

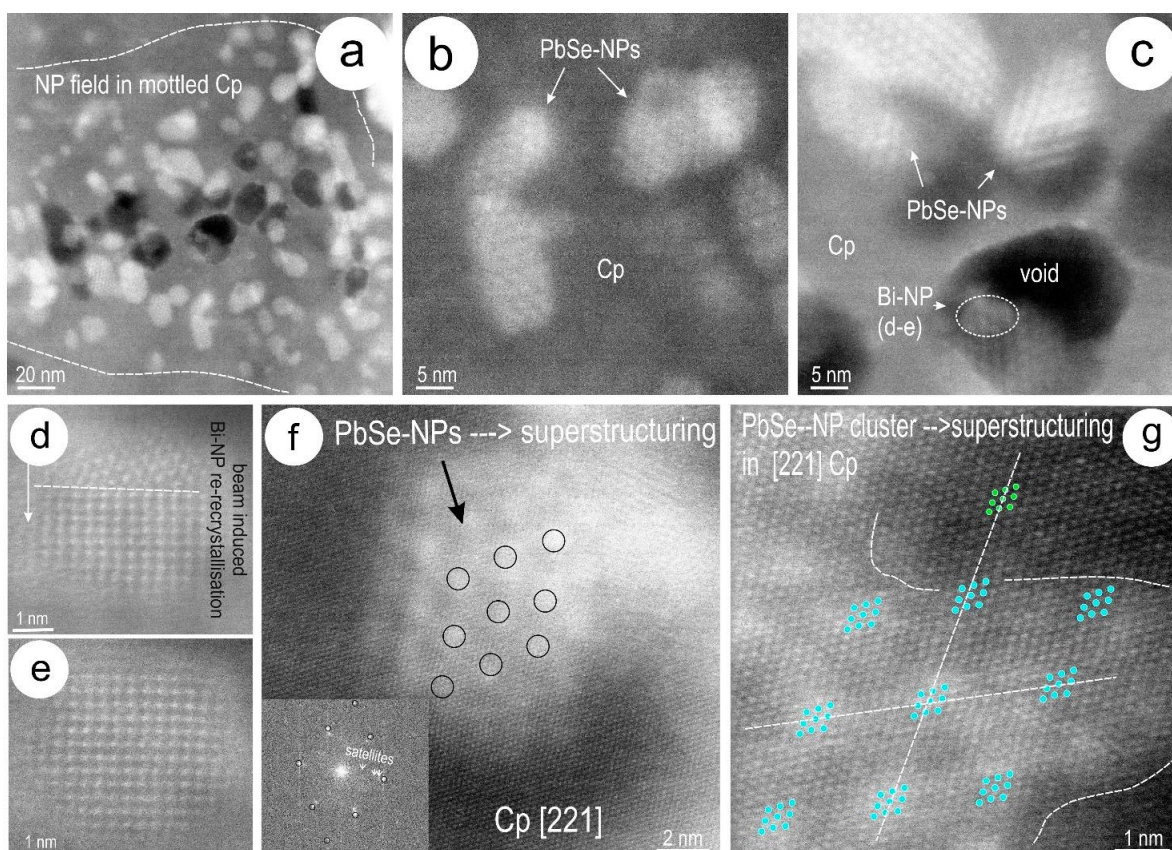


Figure 13. HAADF-STEM images showing NPs present in mottled areas in chalcopyrite from foil CpII. (a) Field of dense NP agglomeration. Note the presence of nanopores (dark) through the middle of the field, whereas the bright dots are the NPs. (b,c) Details of NPs (brighter dots with regular rhombic geometry). Note, in (c), Bi NP highlighted by a dashed outline occurring adjacent to one of the larger voids. (d,e) Square arrangement of bright atoms in Bi-NP, changing the orientation under the electron beam from (d) to (e). (f) Close-up of PbSe NP cluster showing a distribution of bright dots and corresponding FFT (inset). Note that the FFT shows satellite reflections within the chalcopyrite pattern down to the [221] zone axis, instead of reflections attributable to clausthalite structure ($a = 6.1 \text{ \AA}$). This suggests that the brighter dots correspond to a superlattice of clausthalite ordering within the NPs. (g) Atom-scale image of a PbSe-NP cluster showing continuity of atomic arrays from PbSe-NP cluster into chalcopyrite. Rhombic motifs (blue dots) overlap with the brighter dots in NPs arranged in continuation with similar rhombic motifs in chalcopyrite (green dots), suggesting continuity from NP lattice to host chalcopyrite during superstructure development in the clustered NPs. Abbreviations: Bi-NP—bismuth-containing nanoparticle; Cp—chalcopyrite; NP—nanoparticles.

Atomic-scale HAADF-STEM imaging of clausthalite and monazite from the binary inclusions in Figure 15b are shown as different tilts in Figure 16. The atomic arrangement in clausthalite down to the [010] zone axis is compared with crystal-structural models in Figure 16a. The model shows the bright spots correspond to Pb atoms. Tilting the specimen to the [031] zone axis in clausthalite, the image shows continuity between the atomic arrays in clausthalite and monazite (Figure 16b). The atomic arrangement in monazite is compatible with monazite down to the [023] zone axis, as shown in Figure 16c. The crystal-structural model shown for this zone axis in monazite indicates that the bright spots are Ce atoms. This is confirmed by the atomic arrangement in monazite down to the [113] zone axis (Figure 16d), where Ce and P atoms do not overlap on the model. We also note the continuation of atomic arrangements from monazite into clausthalite.

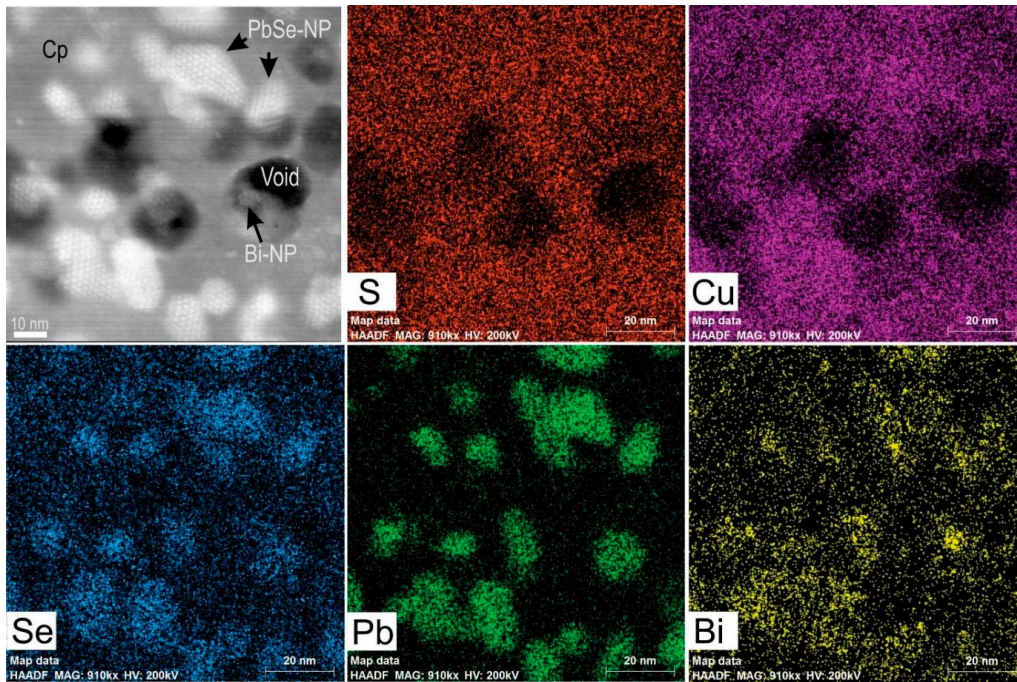


Figure 14. STEM EDS element maps (S, Cu, Se, Pb, and Bi) of the middle part of the NP field shown in Figure 13a. The corresponding HAADF-STEM image is shown top left. Abbreviations: Bi-NP— bismuth-containing nanoparticle; Cp—chalcopyrite; PbSe-NP—PbSe nanoparticle.

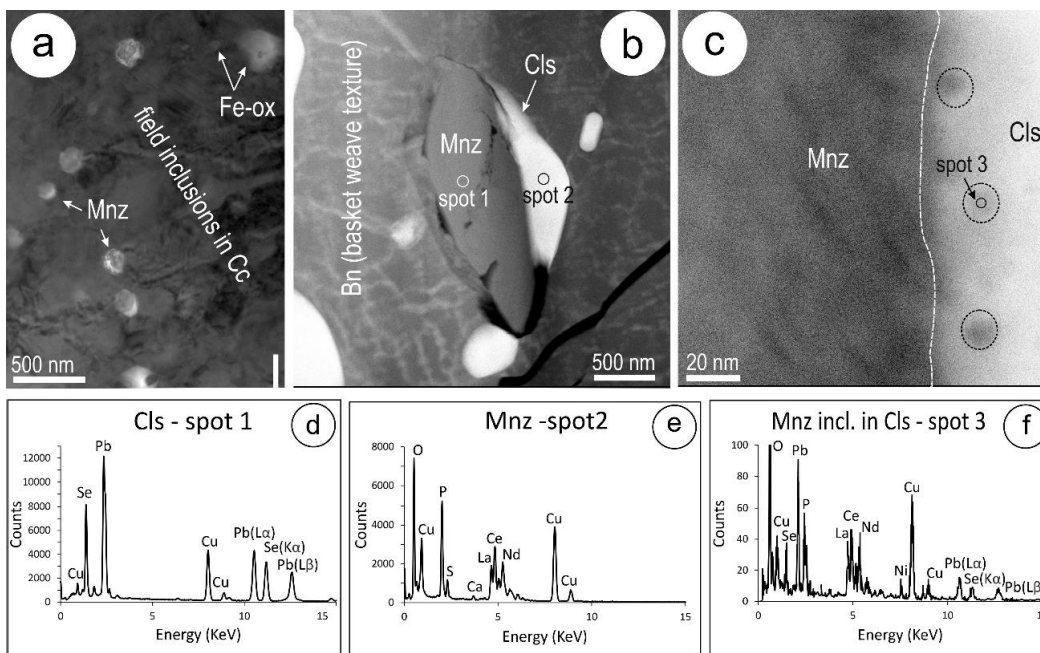


Figure 15. BF-TEM image (a), HAADF images (b,c), and EDS spectra (d–f) of monazite and clausthalite inclusions in BnCcIII. (a) Field with smaller monazite nm-scale inclusions and iron oxides, some of which are attached to pores (arrowed). (b) Coarser monazite-clausthalite composite inclusion in bornite. Note the basket-weave pattern produced by FIB-milling in and around djurleite needles.

(c) Close-up of boundary area between monazite and clausthalite showing the presence of darker spots attributable to monazite. (d–f) EDS spectra from inclusions in (b,c), as marked. In (f), Se and Pb peaks are attributable to the wedged monazite below the surface. Abbreviations: Cls, clausthalite; Fe-ox, iron oxides; Mnz, monazite.

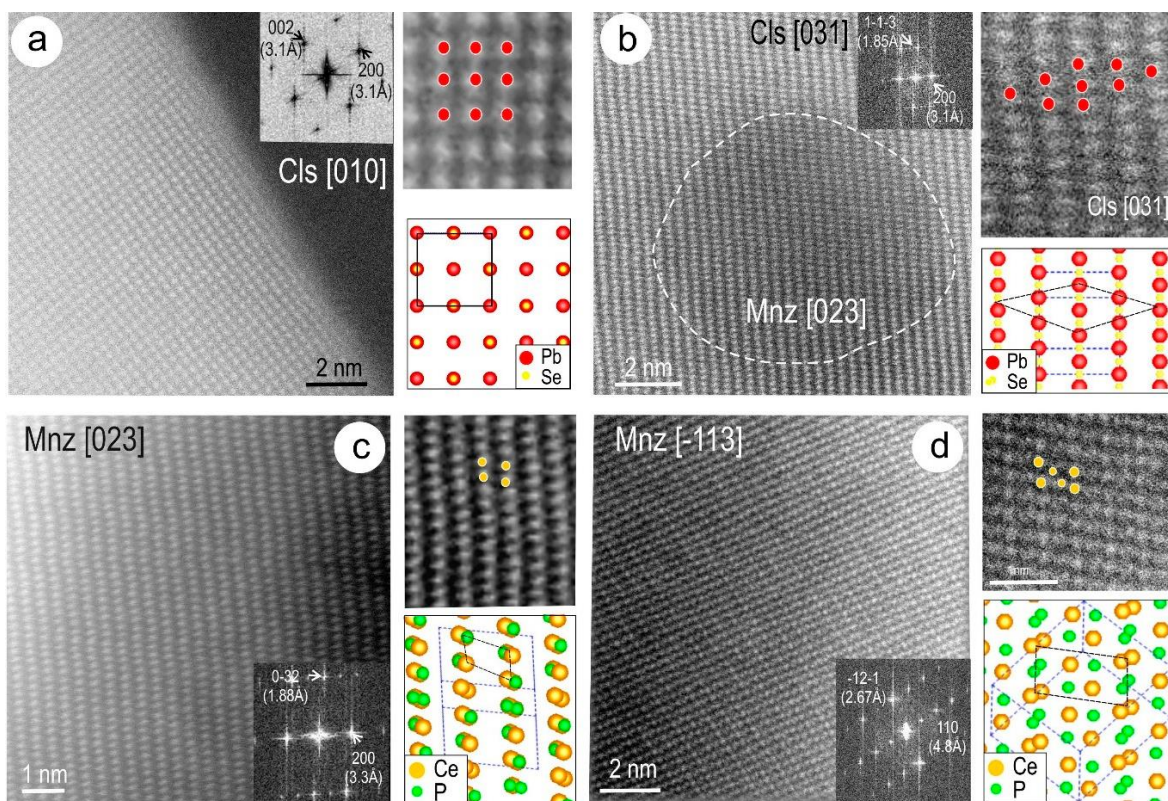


Figure 16. Atomic-scale HAADF-STEM imaging and crystal-structural models for clausenthalite (a,b) and monazite (c,d) on zone axes as marked. (a) Clausenthalite on the [010] zone axis; as shown in FFT (inset), showing bright atoms with square arrangement corresponding to Pb positions in the crystal structure (data from [25]). (b) Clausenthalite on the [031] zone axis (indexed from FFT, inset) and crystal-structural model, showing correspondence between brighter spots and Pb positions. The dashed line outlines the darker inclusions with EDS spectra in Figure 15f, attributable to monazite-(Ce) down to [023], as shown by images and model in (c). Oxygen is excluded from the structural model built for monazite-(Ce) from data given by Ni et al. [26]. (d) Monazite down to the [113] zone axis, as indexed from FFT (inset), showing a good correspondence between the brightest spots (Ce dumbbell site) and the fainter spots corresponding to single Ce atoms. The much lighter P atoms are not visible on the image. Abbreviations: Cls, clausenthalite; Mnz, monazite.

One of the micron-scale vugs in BnCpIV (Figure 5d) is filled with a lamellar aggregate of a Cu-selenide phase with a composition resembling $\sim\text{Cu}_2\text{Se}$ (Figure 14a,b). HR HAADF-STEM imaging shows atom-scale defects at the lamellae boundaries (Figure 17c) or NP inclusions with different orientations to the host (Figure 17d). By tilting the specimen on different zone axes, we obtained HAADF-STEM images (Figure 17e–g) and corresponding FFTs (Figure 17h–j). Assuming the bellidoite crystal structure [38], we could index the FFTs on three distinct zone axes, one of which is a second-order zone axis down to [101] (Figure 17e,h). The other Cu_2Se polymorph (berzelianite) is cubic, with $a = 5.739 \text{ \AA}$, smaller than the 6.7 \AA measured along [111]. The other two zone axes, although not major $\bar{2}31$ and $\bar{2}53$ (FFT in Figure 17i,j), were obtained by rotating the specimen around $(111)^*$ lattice vector, with good spatial resolution of atom arrays on the images (Figure 17f,g).

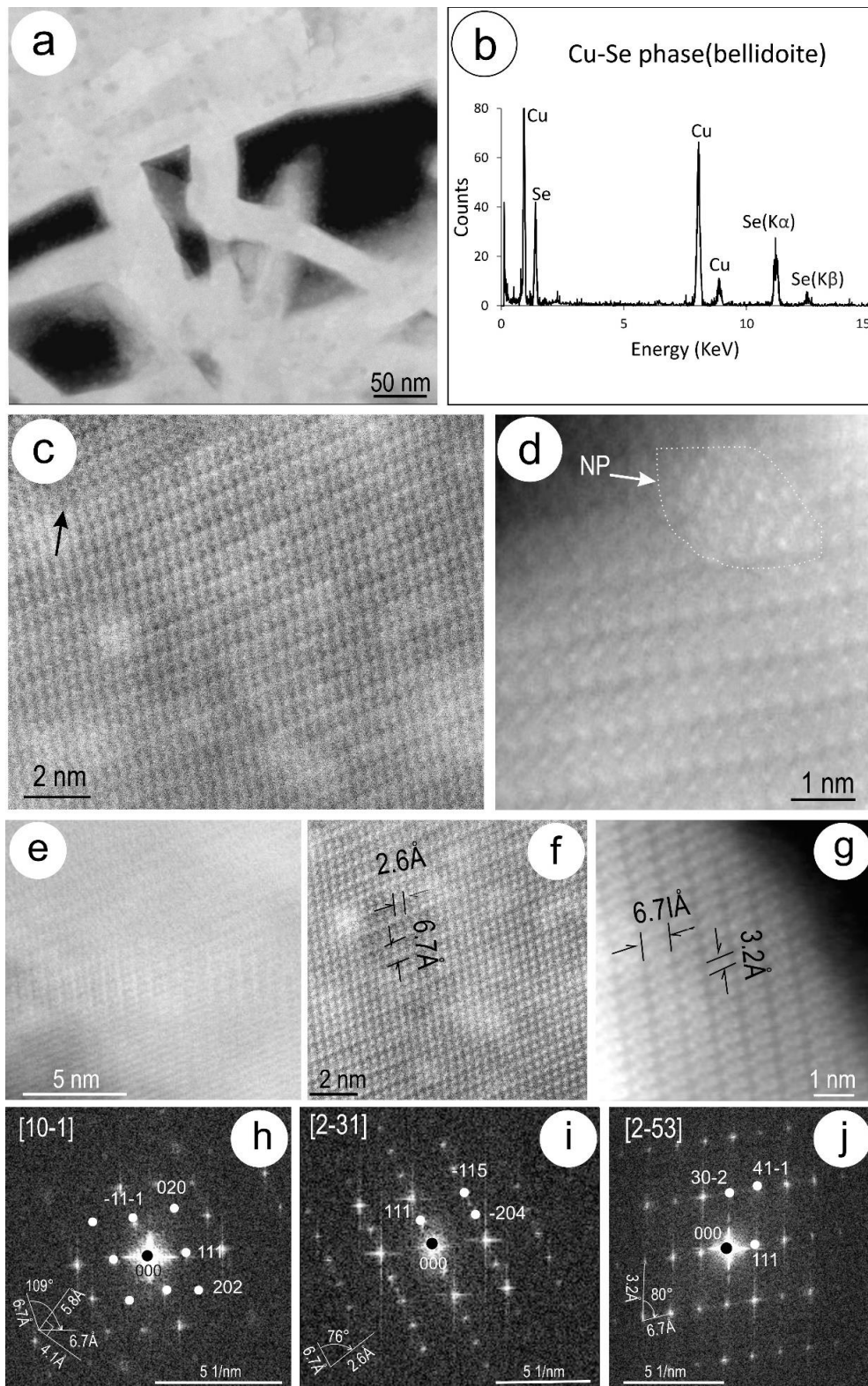


Figure 17. Aspects of Cu-selenide identified as bellidoite from a coarser vug in BnCpIV. **(a)** HAADF-STEM image showing lamellar aggregate. **(b)** Corresponding representative EDS spectra. **(c,d)** HAADF-STEM images showing atom-scale defects between lamellae (arrowed) and NP inclusions (arrowed). **(e-g)** HAADF-STEM images of Cu-selenide on zones axes as indexed in **(h-j)**. FFTs could be indexed using the $P4/m$ space group for bellidoite [38]. Note the good correspondence between the measured distances on the FFT and images.

5. Discussion

Few, if any, HAADF-STEM studies have been carried out previously on Cu-(Fe)-sulphide assemblages. The assemblages and features described here are clearly from ores that can be considered as extremely complex. The observations, however, carry broader applications for features observable in a wide range of copper deposits formed in diverse geological environments. The complexity and presence of different species requires that the intricate associations and relationships are investigated at the nanoscale.

5.1. Evolution of Sulphide Assemblages

The study presented here covers chalcogenide incorporation and release from host Cu-(Fe)-sulphides in ores comprising the three main minerals present in any similar ores (chalcocite, bornite, and chalcopyrite). Both “chalcocite” and bornite show evidence of high-temperature phases that undergo phase transformation and restructuring upon cooling. Bornite solid solutions [44], resulting in bornite-chalcocite and bornite-chalcopyrite assemblages, are comparable to those seen elsewhere [24,45]. The presence of bornite superstructures indicates that the minimum temperatures of formation above 265 °C can be inferred [29]. The co-existence of different bornite superstructure domains at the nanoscale in the same sample (Figure 10) is also reported in natural samples [24,31]. The present study also confirms the widespread presence of lamellar low-temperature djurleite, formed via cooling of bornite solid solutions, as documented elsewhere [24]. The typical basket-weave appearance of bornite containing djurleite in foils prepared for TEM (Figure 6i,k,l) is a characteristic induced by FIB-milling [24].

The type of APBs observed here are constrained within digenite-bearing domains even though monoclinic chalcocite is present beyond these domains. This suggests that the two species derive from a single high-temperature digenite phase undergoing transformation during cooling via changes in the sulphur arrangement from cubic close-packed (ccp) to hexagonal close-packed [46] at temperatures below 120 °C [47]. The observed defects along the APBs (Figure 8b) are evidence in support of low-temperature transformation of the precursor digenite into either monoclinic chalcocite or djurleite at <103.5 °C and <93 °C, respectively [34]. The chalcocite-djurleite transformation may be continuous across lattice fringes and preserves stacking faults in the djurleite, as documented experimentally on Cu_xS films [48].

The intimate relationships between Cu-(Fe)-sulphides that extend down to the nanoscale (Figures 1–3 and 5) account for the non-stoichiometry observed here (Figure 4) and are common in these type of ores [24].

5.2. Formation of Clausthalite in Cu-(Fe)-Sulphides

The data presented here shows a continuum of textural aspects from smallest (<5 nm-sized) Se-rich areas in chalcopyrite, through nanoparticles and their reorganisation via superstructuring, to regular, dense symplectites, and isolated, relatively large blebs. The regular clausthalite rods in chalcocite and chalcopyrite would, at first, be considered as typical products of exsolution. If that is the case, the relationships between clausthalite and APBs in digenite should suggest that such exsolution took place prior to APB development (i.e., above 120 °C) but continued and coarsened thereafter, since the clausthalite rods crosscut the APB boundaries (Figure 6c). The close-to-coherent epitaxial orientation between clausthalite and host digenite is also an argument favouring an exsolution model, even though such symplectites can also occur via coupled dissolution-replacement reactions [49,50]. Nonetheless, the presence of two types of boundaries, expressed both morphologically and chemically (Figure 8c,d and Figure 12), are evidence of distinct processes: primary exsolution (sharp boundaries) and secondary replacement (scalloped boundaries). The latter is mostly observed around larger blebs or rods and is also associated with an increase in the offset in the orientation between clausthalite and the host.

The incorporation of chalcogens, such as Se within Cu-(Fe)-sulphides, and their release are best exemplified through the aspects observed in chalcopyrite, from areas rich in Se to the formation of clustered PbSe nanoparticles and their inferred superstructuring. The epitaxial relationships between the clustered NPs and the chalcopyrite on [221] (Figure 11e,f and Figure 13f,g) are interpretable in terms of a relationship between Se in solid solution and a PbSe superlattice, which in our case takes place via clustering NPs and maturation into coarser inclusions.

Self-assembly of nanocrystals into superlattices has been documented experimentally in PbSe, with three types of atom packing, one of which is tetragonal [51]. However, the superlattices given by Quan et al. [51] are smaller than those observed here in the tetragonal chalcopyrite matrix. None of the FFTs or SAEDs obtained from the mottled areas show the simple lattice of clausthalite (as, for example in the Ccl study case) but instead show satellite reflections on SAEDs, representative of chalcopyrite on different zone axes. We thus infer the reorganisation of PbSe NPs into larger tetragonal superlattices, the first such example in natural materials. As chalcopyrite contains little or no Pb, this infers that the mottled areas represent the products of the interaction between the Se contained within the solid solution in the chalcopyrite with Pb supplied by infiltrating fluids. This leads to dense agglomerated fields of NPs that undergo further epitaxial superstructuring within the chalcopyrite. Further work, beyond the scope of the present report, is required to substantiate the PbSe superlattice(s). The presence of active and annealed microfractures, voids, and pores in the areas are, however, taken as evidence of fluid involvement. The relationships between the mottled areas and symplectites cannot be temporally constrained from the present data, although we point to the fact that it is more likely that the symplectites predate fluid infiltration and associated PbSe-NP formation. Further arguments supporting this hypothesis is the presence of Bi-NPs attached to pores in and around the PbSe. Such fluid-driven chalcogenide NP formation attached to pores is also documented from pyrite in ore systems elsewhere [52].

If such a scenario is feasible, it infers an overprint onto pre-existing symplectites, which can be related to the presence of chemically more complex assemblages, such as the monazite-clausthalite from BnCcIII. The monazite-clausthalite epitaxial relationships are further evidence for (potentially long-lived) overprinting of Cu-(Fe)-sulphide ores, with incoming fluids transporting other components, including Pb, REE, and P (Figure 14). This is exemplified in the relationships between monazite and clausthalite in BnCcIII (Figures 15 and 16). Such aspects can be expected in U-bearing Cu ores in which Pb is produced during the decay of uranium. One significant implication is that attempts to date either monazite or Pb-bearing Cu-(Fe)-sulphides by bulk U-Pb methods (e.g., [53,54]) will return the ages of the overprint rather than those of the primary ore formation. As-yet unpublished work by the present authors has shown that Pb within Pb-chalcogenides, including the clausthalite-bearing symplectites addressed here, is enriched in ^{206}Pb relative to primordial values.

The last stage of overprinting, driven by fluids percolating through the ores, is seen in the presence of vugs filled with “new” phases, such as the bellidoite documented here (Figure 17). Bellidoite, the tetragonal Cu_2Se dimorph [38], is a rare mineral formed at moderate to low temperature with other hydrothermal selenides and sulphides (e.g., [55]). The present occurrence is the first in Australia, and the first from an iron oxide copper gold system. Other occurrences of bellidoite are described by Škácha et al. [56], including a recently observed occurrence within the Příbram uranium district, Czech Republic, in which it is intergrown with berzelianite.

It is noteworthy that all study cases described here display evidence of overprinting. The nanoscale textural evidence presented here, suggesting multiple events of Pb mobilisation, as well as extended periods of reworking and recrystallization of the ore minerals, is in alignment with previous studies of ores within the Olympic Cu-Au Province. Such observations are, for example, concordant with evidence for multiple events of U dissolution and reprecipitation of U-minerals within the Olympic Dam deposit [17,18,57]. It is suggested here that remobilisation of U from U-bearing minerals led to a decoupling of Pb from at least some of the parent U- (and Th-)bearing minerals, resulting in the progressive uptake of Pb by Cu-(Fe)-sulphides and in the formation of clausthalite inclusions within them.

Altogether, this study shows the importance of using combined advanced microbeam techniques on samples extracted on a site of petrogenetic interest to address the character of ore minerals and their formation [24,40–42].

6. Conclusions and Implications

There are three main overarching conclusions that can be drawn from this study. Firstly, the results, as discussed here, challenge the classic origin of symplectites via unmixing or exsolution, suggesting that the symplectite textures could have formed by reaction between pre-existing Se present in solid solution within Cu-(Fe)-sulphides and migrating Pb (resulting from U and Th decay) from a later fluid phase. Selenium was likely present within the host Cu-(Fe)-sulphides at the time of the initial deposition of sulphide mineralisation at relatively high-temperature conditions. Secondly, the introduction of Pb from an external source implies prolonged post-crystallization hydrothermal activity. The diffusion of Pb into Cu-(Fe)-sulphides to form clausthalite preserves evidence for episodes of significant U-Pb remobilisation within the sulphide ores. Such processes may have large implications for U-Pb isotope studies within the region. Thirdly, the observed superstructuring of nanoparticles within chalcopyrite represents a link between solid solution and symplectite formation and shows that Se within the Cu-(Fe)-sulphides reacts readily with Pb, acting as a sponge for the mobilised Pb within the mineralising system. As such, the symplectite textures presented and discussed within this study represent at least two stages of Pb mobilisation and subsequent incorporation into the Cu-(Fe)-sulphides.

Acknowledgments: This research is a contribution to the ARC Research Hub for Australian Copper-Uranium. Staff at Adelaide Microscopy are thanked for instrument access and guidance. CLC acknowledges support to the “FOX” project (Trace elements in iron oxides: deportment, distribution and application in ore genesis, geochronology, exploration and mineral processing), supported by the BHP Olympic Dam and the South Australian Government Mining and Petroleum Services Centre of Excellence. We appreciate the helpful comments of three anonymous *Minerals* reviewers.

Author Contributions: Nicholas D. Owen, Cristiana L. Ciobanu, and Ashley Slattery performed all analytical work, assisted by Animesh Basak. Cristiana L. Ciobanu and Nigel J. Cook devised the project and guided the analysis and interpretation. Nicholas D. Owen, Cristiana L. Ciobanu, and Nigel J. Cook wrote the paper, assisted by the other co-authors

Conflicts of Interest: The authors declare no conflict of interest.

Appendix A

Table A1. Elements analysed, peak/background positions, count times, and standards used for sulphide analysis.

Element/Line	Diffracting Plane	Peak Count Time (Sec)	Background Type/Fit	Bkcd Points Acquired (Lo/Hi)	Background Count Time (Lo/Hi) (Sec)	Standard
S K α	LPET/1	10	Multipoint	2/2	10/10	Astimex Marcasite
Pb M α	LPET/1	200	Multipoint	4/3	20/20	P & H block Galena
Cd L α	LPET/1	10	Multipoint	2/2	10/10	P & H block Greenockite
Bi M α	LPET/1	10	Multipoint	2/2	10/10	P & H block Bi ₂ Se ₃
As L α	TAP/2	10	Multipoint	2/2	10/10	Astimex GaAs
Se L α	TAP/2	20	Multipoint	2/3	20/20	P & H block Bi ₂ Se ₃
Fe K α	LLIF/3	10	Multipoint	2/2	10/10	P & H block Chalcopyrite
Cu K α	LLIF/3	10	Linear	-	5/5	P & H block Chalcopyrite
Mn K α	LLIF/3	10	Multipoint	2/2	10/10	P & H block Rhodonite
Ag L α	LPET/4	10	Multipoint	1/2	10/10	P & H block AgTe
Sb L α	LPET/4	10	Multipoint	2/2	10/10	Astimex Stibnite
Te L α	LPET/4	10	Multipoint	2/2	10/10	P & H block AgTe
Hg L α	LLIF/5	10	Multipoint	3/3	15/15	P & H Cinnabar
Zn K α	LLIF/5	10	Multipoint	2/2	10/10	P & H Spahlerite
Ni K α	LLIF/5	10	Linear	-	5/5	Astimex Pentlandite
Co. K α	LLIF/5	10	Multipoint	2/2	10/10	Astimex Co. metal

References

1. Simon, G.; Essene, E.J. Phase relations among selenides, sulfides, tellurides, and oxides: I. Thermodynamic properties and calculated equilibria. *Econ. Geol.* **1996**, *91*, 1183–1208. [[CrossRef](#)]
2. Simon, G.; Kesler, S.E.; Essene, E.J. Phase relations among selenides, tellurides, and oxides; II, Applications to selenide-bearing ore deposits. *Econ. Geol.* **1997**, *92*, 468–484. [[CrossRef](#)]
3. Cook, N.J.; Ciobanu, C.L.; Spry, P.G.; Voudouris, P. Understanding gold-(silver)-telluride-(selenide) mineral deposits. *Episodes* **2009**, *32*, 249–263.
4. Ramdohr, P. *The Ore Minerals and Their Intergrowths*; English Translation of the 3rd Edition; Pergamon Press: Oxford, UK, 1969; p. 1174.
5. Bogdanov, K.; Filipov, A.; Kehayov, R. Au-Ag-Te-Se minerals in the Elatsite porphyry-copper deposit, Bulgaria. *Geochem. Miner. Petrol.* **2005**, *43*, 13–19.
6. Belogub, E.V.; Novoselov, K.A.; Yakovleva, V.A.; Spiro, B. Supergene sulphides and related minerals in the supergene profiles of VHMS deposits from the South Urals. *Ore Geol. Rev.* **2008**, *33*, 239–254. [[CrossRef](#)]
7. Economou-Eliopoulos, M.; Eliopoulos, D.G.; Chryssoulis, S. A comparison of high-Au massive sulfide ores hosted in ophiolite complexes of the Balkan Peninsula with modern analogues: Genetic significance. *Ore Geol. Rev.* **2008**, *33*, 81–100. [[CrossRef](#)]
8. Förster, H.J. Mineralogy of the U-Se-polymetallic deposit Niederschlema-Alberoda, Erzgebirge, Germany. IV. The continuous clausthalite-galena solid-solution series. *N. Jahrb. Mineral. Abh.* **2005**, *181*, 125–134. [[CrossRef](#)] [[PubMed](#)]
9. Cepedal, A.; Fuertes-Fuente, M.; Martin-Izard, A.; Gonzalez-Nistal, S.; Rodriguez-Pevida, L. Tellurides, selenides and Bi-mineral assemblages from the Río Narcea Gold Belt, Asturias, Spain: genetic implications in Cu-Au and Au skarns. *Mineral. Petrol.* **2006**, *87*, 277–304. [[CrossRef](#)]
10. Liu, H.; Chang, L.L.Y. Phase relations in the system PbS-PbSe-PbTe. *Mineral. Mag.* **1994**, *58*, 567–578. [[CrossRef](#)]
11. Williams, P.J.; Pollard, P.J. Australian Proterozoic iron oxide-Cu-Au deposits; an overview with new metallogenic and exploration data from the Cloncurry District, Northwest Queensland. *Explor. Min. Geol.* **2001**, *10*, 191–213. [[CrossRef](#)]
12. Piestrzynski, A.; Pieczonka, J. Low temperature ore minerals associations in the Kupferschiefer type deposit, Lubin-Sieroszowice Mining District SW Poland. *Mineral. Rev.* **2012**, *62*, 59–66.
13. Skirrow, R.G.; Bastrakov, E.N.; Barovcich, K.; Fraser, G.L.; Creaser, R.A.; Fanning, C.M.; Raymond, O.L.; Davidson, G.J. Timing of iron oxide Cu-Au-(U) hydrothermal activity and Nd isotope constraints on metal sources in the Gawler craton, South Australia. *Econ. Geol.* **2007**, *102*, 1441–1470. [[CrossRef](#)]
14. Ehrig, K.; McPhie, J.; Kamenetsky, V.S. Geology and mineralogical zonation of the Olympic Dam iron oxide Cu-U-Au-Ag deposit, South Australia. In *Geology and Genesis of Major Copper Deposits and Districts of the World, a Tribute to Richard Sillitoe*; Hedenquist, J.W., Harris, M., Camus, F., Eds.; Society of Economic Geologists: Littleton, CO, USA, 2012; Volume 16, pp. 237–268.
15. Skirrow, R.G.; Raymond, O.L.; Bastrakov, E.; Davidson, G.J.; Heithersay, P. The geological framework, distribution and controls of Fe oxide Cu-Au mineralisation in the Gawler Craton, South Australia. Part II—alteration and mineralisation. In *Hydrothermal Iron Oxide Copper-Gold & Related Deposits: A Global Perspective*; Porter, T.M., Ed.; PGC Publishing: Adelaide, Australia, 2002; Volume 2, pp. 33–48.
16. Kirchenbaur, M.; Maas, R.; Ehrig, K.; Kamenetsky, V.S.; Strub, E.; Ballhaus, C.; Münker, C. Uranium and Sm isotope studies of the supergiant Olympic Dam Cu-Au-U-Ag deposit, South Australia. *Geochim. Cosmochim. Acta* **2016**, *180*, 15–32. [[CrossRef](#)]
17. Macmillan, E.; Ciobanu, C.L.; Ehrig, K.; Cook, N.J.; Pring, A. Chemical zoning and lattice distortion in uraninite from Olympic Dam, South Australia. *Am. Mineral.* **2016**, *101*, 2351–2354. [[CrossRef](#)]
18. Macmillan, E.; Cook, N.J.; Ehrig, K.; Pring, A. Chemical and textural interpretation of late-stage coffinite and brannerite from the Olympic Dam IOCG-Ag-U deposit. *Mineral. Mag.* **2017**, *81*, 1323–1366. [[CrossRef](#)]
19. Betts, P.G.; Valenta, R.K.; Finlay, J. Evolution of the Mount Woods Inlier, northern Gawler Craton, Southern Australia: An integrated structural and aeromagnetic analysis. *Tectonophysics* **2003**, *366*, 83–111. [[CrossRef](#)]
20. Huang, Q.; Kamenetsky, V.S.; McPhie, J.; Ehrig, K.; Meffre, S.; Maas, R.; Thompson, J.; Kamenetsky, M.; Chambefort, I.; Apukhtina, O.; et al. Neoproterozoic (ca. 820–830 Ma) mafic dykes at Olympic Dam, South Australia: Links with the Gairdner Large Igneous Province. *Precambrian Res.* **2015**, *271*, 160–172. [[CrossRef](#)]

21. Cook, N.J.; Ciobanu, C.L.; Danyushevsky, L.V.; Gilbert, S. Minor elements in bornite and associated Cu-(Fe)-sulfides: A LA-ICPMS study. *Geochim. Cosmochim. Acta* **2011**, *73*, 4761–4791. [[CrossRef](#)]
22. George, L.L.; Cook, N.J.; Ciobanu, C.L. Partitioning of trace elements in co-crystallized sphalerite-galena-chalcopyrite hydrothermal ores. *Ore Geol. Rev.* **2016**, *77*, 97–116. [[CrossRef](#)]
23. George, L.L.; Cook, N.J.; Crowe, B.B.P.; Ciobanu, C.L. Trace elements in hydrothermal chalcopyrite. *Mineral. Mag.* **2018**, in press. [[CrossRef](#)]
24. Ciobanu, C.L.; Cook, N.J.; Ehrig, K. Ore minerals down to the nanoscale: Cu-(Fe)-sulphides from the iron oxide copper gold deposit at Olympic Dam, South Australia. *Ore Geol. Rev.* **2017**, *81*, 1218–1235. [[CrossRef](#)]
25. Noda, Y.; Masumoto, K.; Ohba, S.; Saito, Y.; Toriumi, K.; Iwata, Y.; Shibuya, I. Temperature dependence of atomic thermal parameters of lead chalcogenides, PbS, PbSe and PbTe. *Acta Crystallogr. Sect. C Cryst. Struct. Commun.* **1987**, *43*, 1443–1445. [[CrossRef](#)]
26. Ni, Y.; Hughes, J.M.; Mariano, A.N. Crystal chemistry of the monazite and xenotime structures. *Am. Mineral.* **1995**, *80*, 21–26. [[CrossRef](#)]
27. Hall, S.R.; Stewart, J.M. The crystal structure refinement of chalcopyrite, CuFeS₂. *Acta Cryst.* **1973**, *29*, 579–585. [[CrossRef](#)]
28. Tunell, G.; Adams, C.E. On the symmetry and crystal structure of bornite. *Am. Mineral.* **1949**, *34*, 824–829.
29. Kanazawa, Y.; Koto, K.; Morimoto, N. Bornite (Cu₅FeS₄): Stability and crystal structure of the intermediate form. *Can. Mineral.* **1978**, *16*, 397–404.
30. Ding, Y.; Veblen, D.R.; Prewitt, C.T. High-resolution transmission electron microscopy (HRTEM) study of 4a and 6a superstructure of bornite Cu₅FeS₄. *Am. Mineral.* **2005**, *90*, 1256–1264. [[CrossRef](#)]
31. Ding, Y.; Veblen, D.R.; Prewitt, C.T. Possible Fe/Cu ordering schemes in the 2a superstructure of bornite (Cu₅FeS₄). *Am. Mineral.* **2005**, *90*, 1265–1269. [[CrossRef](#)]
32. Pierce, L.; Buseck, P.R. Superstructuring in the bornite-digenite series: A high-resolution electron microscopy study. *Am. Mineral.* **1978**, *63*, 1–6.
33. Koto, K.; Morimoto, N. Superstructure investigation of bornite, Cu₅FeS₄, by the modified partial Patterson function. *Acta Crystallogr.* **1975**, *31*, 2268–2273. [[CrossRef](#)]
34. Evans, H.T. The crystal structures of low chalcocite and djurleite. *Z. Krist. Cryst. Mater.* **1979**, *150*, 299–320. [[CrossRef](#)]
35. Buerger, M.J.; Buerger, N.W. Low-chalcocite and high-chalcocite. *Am. Mineral.* **1944**, *29*, 55–65.
36. Morimoto, N.; Kullerud, G. Polymorphism in digenite. *Am. Mineral.* **1963**, *48*, 110–123.
37. Will, G.; Hinze, E.; Abdelrahman, A.R.M. Crystal structure analysis and refinement of digenite, Cu_{1.8}S, in the temperature range 20 to 500 °C under controlled sulfur partial pressure. *Eur. J. Mineral.* **2002**, *14*, 591–598. [[CrossRef](#)]
38. De Montreuil, L.A. Bellidoite, a new copper selenide. *Econ. Geol.* **1975**, *70*, 384–387. [[CrossRef](#)]
39. Ciobanu, C.L.; Cook, N.J.; Utsunomiya, S.; Pring, A.; Green, L. Focussed ion beam-transmission electron microscopy applications in ore mineralogy: Bridging micron-and nanoscale observations. *Ore Geol. Rev.* **2011**, *42*, 6–31. [[CrossRef](#)]
40. Ciobanu, C.L.; Cook, N.J.; Maunders, C.; Wade, B.P.; Ehrig, K. Focused ion beam and advanced electron microscopy for minerals: insights and outlook from bismuth sulphosalts. *Minerals* **2016**, *6*, 112. [[CrossRef](#)]
41. Ciobanu, C.L.; Kontonikas-Charos, A.; Slattery, A.; Cook, N.J.; Ehrig, K.; Wade, B.P. Short-range stacking disorder in Mixed-Layer compounds: A HAADF-STEM study of bastnäsite-parisite intergrowths. *Minerals* **2017**, *7*, 227. [[CrossRef](#)]
42. Cook, N.J.; Ciobanu, C.L.; Ehrig, K.; Slattery, A.; Verdugo-Ihl, M.R.; Courtney-Davies, L.; Gao, W. Advances and opportunities in ore mineralogy. *Minerals* **2017**, *7*, 233. [[CrossRef](#)]
43. Downs, R.T.; Hall-Wallace, M. The American mineralogist crystal structure database. *Am. Mineral.* **2003**, *88*, 247–250.
44. Yund, R.A.; Kullerud, G. Thermal stability of assemblages in the Cu-Fe-S system. *J. Petrol.* **1966**, *7*, 454–488. [[CrossRef](#)]
45. Posfai, M.; Buseck, P.R. Djurleite, digenite, and chalcocite: intergrowths and transformations. *Am. Mineral.* **1994**, *79*, 308–315.
46. Van Dyck, D.; Conde-Amiano, C.; Amelinckx, S. The diffraction pattern of crystals presenting a digenite type of disorder. II. The structure of the digenite-related phases derived by means of the Cluster Theory. *Phys. Status Solidi* **1980**, *58*, 451–468. [[CrossRef](#)]

47. Morimoto, N.; Kullerud, G. Polymorphism on the Cu_9S_5 - Cu_5FeS_4 join. *Z. Krist.* **1966**, *123*, 235–254. [[CrossRef](#)]
48. Echigoya, J.; Edington, J.W. A transmission electron microscope study of the chalcocite-djurleite transformation in topotactically grown thin films of Cu_xS . *Phys. Status Solidi* **1982**, *72*, 305–311. [[CrossRef](#)]
49. Zhao, J.; Brugger, J.; Ngothai, Y.; Pring, A. The replacement of chalcopyrite by bornite under hydrothermal conditions. *Am. Mineral.* **2014**, *99*, 2389–2397. [[CrossRef](#)]
50. Altree-Williams, A.L.; Pring, A.; Ngothai, Y.; Brugger, J. Textural and compositional complexities resulting from coupled dissolution-reprecipitation reactions in geomaterials. *Earth Sci. Rev.* **2015**, *150*, 628–651. [[CrossRef](#)]
51. Quan, Z.; Wu, D.; Zhu, J.; Evers, W.H.; Boncella, J.M.; Siebbeles, L.D.A.; Wang, Z.; Navrotsky, A.; Xu, H. Energy landscape of self-assembled superlattices of PbSe nanocrystals. *Proc. Nat. Acad. Sci. USA* **2014**, *111*, 9054–9057. [[CrossRef](#)] [[PubMed](#)]
52. Ciobanu, C.L.; Cook, N.J.; Utsunomiya, S.; Kogagwa, M.; Greem, L.; Gilbert, S.; Wade, B. Gold-telluride nanoparticles revealed in arsenic-free pyrite. *Am. Mineral.* **2012**, *97*, 1515–1518. [[CrossRef](#)]
53. Meffre, S.; Ehrig, K.; Kamenetsky, V.; Chambefort, I.; Maas, R.; McPhie, J. Pb isotopes at Olympic Dam: Constraining sulphide growth. In Proceedings of the 13th Quadrennial IAGOD Symposium 2010, Adelaide, Australia, 6–9 April 2010; pp. 78–79.
54. Maas, R.; Kamenetsky, V.; Ehrig, K.; Meffre, S.; McPhie, J.; Diemar, G. Olympic Dam U-Cu-Au deposit, Australia: New age constraints. *Mineral. Mag.* **2011**, *75*, 1375.
55. Paar, W.H.; Topa, D.; Roberts, A.C.; Criddle, A.J.; Amann, G.; Sureda, R.J. The new mineral species brodtkorbite, Cu_2HgSe_2 , and the associated selenide assemblage from Tuminico, Sierra de Cacho, La Rioja, Argentina. *Can. Mineral.* **2002**, *40*, 225–237. [[CrossRef](#)]
56. Škácha, P.; Sejkora, J.; Plášil, J. Selenide Mineralization in the Prábram Uranium and Base-Metal District (Czech Republic). *Minerals* **2017**, *7*, 91. [[CrossRef](#)]
57. Macmillan, E.; Cook, N.J.; Ehrig, K.; Ciobanu, C.L.; Pring, A. Uraninite from the Olympic Dam IOCG-U-Ag deposit: Linking textural and compositional variation to temporal evolution. *Am. Mineral.* **2016**, *101*, 1295–1320. [[CrossRef](#)]



© 2018 by the authors. Licensee MDPI, Basel, Switzerland. This article is an open access article distributed under the terms and conditions of the Creative Commons Attribution (CC BY) license (<http://creativecommons.org/licenses/by/4.0/>).

CHAPTER 4

REE-, SR-, CA-ALUMINUM-PHOSPHATE-SULFATE MINERALS OF THE ALUNITE SUPERGROUP AND THEIR ROLE AS HOSTS FOR RADIONUCLIDES

Nicholas D. Owen, Nigel J. Cook, Mark Rollog, Kathy J. Ehrig, Danielle S. Schmandt, Rahul
Ram, Joël Brugger, Cristiana L. Ciobanu, Benjamin Wade, Paul Guagliardo

Statement of Authorship

Title of Paper	REE-, Sr- Ca-aluminum-phosphate-sulfate minerals of the alunite supergroup and their role as hosts for radionuclides	
Publication Status	<input type="checkbox"/> Published <input type="checkbox"/> Submitted for Publication	<input checked="" type="checkbox"/> Accepted for Publication <input type="checkbox"/> Unpublished and Unsubmitted work written in manuscript style
Publication Details	American Mineralogist, Accepted 07-2019	

Principal Author

Name of Principal Author (Candidate)	Nicholas D. Owen	
Contribution to the Paper	Idea conception, performed analytical work, carried out data collection and analysis, wrote the the manuscript.	
Overall percentage (%)	50%	
Certification:	This paper reports on original research I conducted during the period of my Higher Degree by Research candidature and is not subject to any obligations or contractual agreements with a third party that would constrain its inclusion in this thesis. I am the primary author of this paper.	
Signature		Date 26/08/2019

Co-Author Contributions

By signing the Statement of Authorship, each author certifies that:

- i. the candidate's stated contribution to the publication is accurate (as detailed above);
- ii. permission is granted for the candidate to include the publication in the thesis; and
- iii. the sum of all co-author contributions is equal to 100% less the candidate's stated contribution.

Name of Co-Author	Nigel J. Cook	
Contribution to the Paper	Idea conception, helped define direction of research, supervised development of the work, assisted with data interpretation and writing of the manuscript. 10%	
Signature	-	Date 24/8/19

Name of Co-Author	Mark Rollog	
Contribution to the Paper	Assisted with method development and data interpretation, helped evaluate and edit the manuscript. 5%	
Signature	-	Date 28.08.19

Please cut and paste additional co-author panels here as required.

Name of Co-Author	Kathy Ehrig		
Contribution to the Paper	Provided sample material and helped evaluate and edit the manuscript.		
	5%		
Signature		Date	27 Aug 2019

Name of Co-Author	Danielle S. Schamndt		
Contribution to the Paper	Helped with data collection and analysis.		
	5%		
Signature		Date	8/29/2019

Name of Co-Author	Rahul Ram		
Contribution to the Paper	Helped with data collection and aided in manuscript preparation.		
	5%		
Signature		Date	27/08/19

Name of Co-Author	Joel Brugger		
Contribution to the Paper	Aided in idea development and manuscript preparation.		
	5%		
Signature		Date	29/8/19

Name of Co-Author	Cristiana L. Ciobanu		
Contribution to the Paper	Aided in idea development and manuscript preparation.		
	5%		
Signature		Date	27.08.19

Name of Co-Author	Benjamin Wade		
Contribution to the Paper	Aided in the operation of analytical equipment and data interpretation.		
	5%		
Signature		Date	30.8.19

Please cut and paste additional co-author panels here as required.

Name of Co-Author	Paul Guagliardo		
Contribution to the Paper	Aided in the operation of analytical equipment and data interpretation. 5%		
Signature		Date	28/08/2019

REE-, Sr-, Ca-aluminum-phosphate-sulfate minerals of the alunite supergroup and their role as hosts for radionuclides

NICHOLAS D. OWEN^{1,2,*}, NIGEL J. COOK¹, MARK ROLLOG¹, KATHY J. EHRIG³, DANIELLE S. SCHMANDT¹, RAHUL RAM², JOËL BRUGGER², CRISTIANA L. CIOBANU¹, BENJAMIN WADE⁴, AND PAUL GUAGLIARDO⁵

¹School of Chemical Engineering, The University of Adelaide, South Australia 5005, Australia

²School of Earth and Environmental Sciences, Monash University, Victoria 2800, Australia

³BHP Olympic Dam, Adelaide, South Australia 5000, Australia. Orcid 0000-0002-5381-9445

⁴Adelaide Microscopy, The University of Adelaide, South Australia 5005, Australia

⁵Centre for Microscopy, Characterisation, and Analysis, University of Western Australia, 35 Stirling Highway, Crawley, Western Australia 6009, Australia

ABSTRACT

Aluminum-phosphate-sulfate (APS) minerals of the alunite supergroup are minor components of uranium-bearing copper ores from the Olympic Dam deposit, South Australia. They typically represent a family of paragenetically late replacement phases after pre-existing REE-bearing phosphates (fluorapatite, monazite, and xenotime). Characterization with respect to textures and composition allows two groups to be distinguished: Ca-Sr-dominant APS minerals that fall within the woodhouseite and svanbergite compositional fields; and a second REE- and phosphate-dominant group closer to florencite in composition. All phases nevertheless display extensive solid solution among end-members in the broader APS clan and show extensive compositional zoning at the grain-scale. Samples representative of the deposit (flotation concentrate and tailings), as well as those that have been chemically altered during the processing cycle (acid leached concentrate), were studied for comparison. NanoSIMS isotope mapping provides evidence that the APS minerals preferentially scavenge and incorporate daughter radionuclides of the ²³⁸U decay chain, notably ²²⁶Ra and ²¹⁰Pb, both over geological time within the deposit and during ore processing. These data highlight the role played by minor phases as hosts for geologically mobile deleterious components in ores as well as during mineral processing. Moreover, Sr-Ca-dominant APS minerals exhibit preferential sorption of Pb from fluid sources, in the form of both common Pb and ²¹⁰Pb, for the first time revealing potential pathways for ²¹⁰Pb elimination and reduction from ore processing streams.

Keywords: Alunite supergroup, aluminum-phosphate-sulfates, Olympic Dam, ²³⁸U decay series radionuclides, mineral processing

INTRODUCTION

Minerals of the alunite supergroup (Jambor 1999; Bayliss et al. 2010), especially the beudantite and crandallite groups, have found extensive application in environmental remediation and storage of deleterious elements due to their broad stability and their capacity to host a wide range of contaminants via extensive solid solution with the exchange of bi- to hexavalent cations at multiple sites in their structures (Kolitsch and Pring 2001). Elements that can be incorporated include As, Pb, Bi, Hg, Tl, Sb, Cr, Se, and rare earth elements (REE) (Kolitsch and Pring 2001), as well as radioisotopes generated by decay of radioactive K, Sr, Th, and U (Dymkov et al. 1997; Kolitsch and Pring 2001). Analysis of APS mineral compositions can reveal useful information regarding local conditions of formation with respect to fluid composition, pH, and f_{O_2} (Schwab et al. 2004, 2005; Gaboreau et al. 2007).

Most beudantite- and crandallite-group minerals are stable up

to high temperatures (400–500 °C) and remain insoluble even over a wide range of pH and E_h conditions (Kolitsch and Pring 2001). These robust characteristics also make them potential hosts for daughter products of U decay (notably the radionuclides ²¹⁰Pb and ²¹⁰Po, hereafter ²¹⁰RN) in U-bearing ore deposits and in materials resulting from the processing of such ores.

Hydrothermal REE-, Ca-, and/or Sr-bearing aluminum phosphate-sulfate (APS) phases of varied composition within the alunite supergroup are reported from the giant ca. 1590 Ma (Johnson and Cross 1995) Olympic Dam Cu-U-Au-Ag deposit, South Australia (Ehrig et al. 2012). Until now, however, these phases have been inadequately characterized and despite their textural and compositional complexity, were generically categorized as “crandallite group” minerals with the general formula $(Ce,La,Nd,Ca,Sr)(Al,Fe)_3(SO_4,PO_4)_2(OH)_6$. These minerals are only present in modest amounts (modal abundance 0.109 wt%), yet are long suspected of making at least a minor contribution to the budget of U and REE in the ore (Ehrig et al. 2012).

Given their ability to incorporate a wide range of radioactive decay products, the presence of Ca- and Sr-bearing APS minerals

* E-mail: nicholas.owen@adelaide.edu.au; Orcid 0000-0002-3928-8318

within a U-bearing ore, such as Olympic Dam, makes them a viable host for the transport of ^{210}Rn throughout the processing cycle. This study sets out to document APS minerals from Olympic Dam with respect to their composition, paragenetic position, relationships with other minerals, and, not least, their potential role as natural mineral sinks for the products of radioactive decay. Evidence for uptake and incorporation of radionuclides (RN) via both geological processes in situ within the deposit and during ore processing (flotation and subsequent acid leaching) is presented and discussed.

BACKGROUND

APS crystal chemistry

APS minerals of the alunite supergroup have the general formula $[\text{AB}_3(\text{XO}_4)_2(\text{OH})_6]$, where A is a mono-, bi-, or trivalent cation, B is a trivalent cation (in this case almost exclusively Al^{3+}), and XO_4 is mainly a mixture of phosphate and sulfate groups. They are known to form in various geological environments from weathering profiles in soils, sedimentary settings (Triplehorn et al. 1991; Rasmussen 1996; Pe-Piper and Dolansky 2005) to magmatic-hydrothermal ore deposits such as the Olympic Dam Cu-U-Au-Ag deposit discussed here (Ehrig et al. 2012). The alunite supergroup contains minerals with an extensive and diverse range of compositions. Almost all crystallize within the $R\bar{3}m$ or $R\bar{3}m$ space groups and thus have almost identical crystal structures, albeit with a slight deviation of lattice parameters, thus opening up the possibility of extensive solid solution across the APS group.

The crystal structure of APS minerals (Fig. 1) is built up of sheets of AlO_6 octahedra arranged in a Kagomé network perpendicular to the parallel to the (001) plane (Kato and Miura 1977), and two phosphate and/or sulfate tetrahedra, with the A-site cation sitting in between layers (e.g., Schwab et al. 2004,

2005; Zema et al. 2012). To form the sheets, AlO_6 octahedra, with four hydroxyl groups and two oxygen ligands, corner-share hydroxyl groups with one another forming large hexagonal and small trigonal rings. The “base” of each phosphate or sulfate tetrahedra then shares three corners each of the trigonal rings, forming an overall structure in which two corners of each AlO_6 octahedra and three corners of each phosphate/sulfate tetrahedra, are made of shared oxygen atoms. Peaks formed by the remaining oxygen atom in each phosphate/sulfate tetrahedra then point in alternating sequence in the direction parallel to the *c* axis, into the hexagonal rings formed by AlO_6 octahedra in adjacent layers above and below (Kato and Miura 1977; Gaboreau and Vieillard 2004; Schwab et al. 2004, 2005). The resulting overall structure contains 12-, 6- and fourfold coordination positions, allowing cations of various charge and radius to fit within the structure (Schwab et al. 2004), aiding in the development of extensive solid solutions occurring in nature. A-site cations generally sit within the 12-fold coordination position, but disordering of cations among these positions has been recorded, resulting in a small lowering of symmetry to the monoclinic *Cm* and *C2/m* space groups (Kolitsch and Pring 2001).

Olympic Dam

The Olympic Dam mining-processing-smelting-refining operation exploits a complex, fine-grained sulfide-rich copper ore dominated by hematite, by far the most abundant gangue mineral (Ehrig et al. 2012). Economic commodities are Cu, U, Au, and Ag but the IOCG-U-Ag deposit also contains anomalous concentrations of rare earth elements (REE), P, Th, F, and many other elements. More than 100 minerals have been identified in the ore, necessitating a thorough understanding and careful control of ore mineralogy to ensure optimized processing.

In the Olympic Dam ore, the four most significant U-bearing minerals are uraninite, coffinite, brannerite, and hematite (Ehrig et al. 2012; Ciobanu et al. 2013; Macmillan et al. 2016, 2017; Verdugo-Ihl et al. 2017; Xing et al. 2018). Uranium is extracted by acid leaching of both flotation tails and flotation concentrates. In the ore, U-minerals occur intimately intergrown within mineral assemblages also containing the other economic metals Cu, Ag, and Au. Decay of the most common isotope of uranium, ^{238}U , generates daughter isotopes ^{226}Ra , ^{210}Pb , and ^{210}Po , which, due to their relatively short half-lives (1600 yr, ~22.2 yr and 138.4 days, respectively), have high activities, yet remain active for relatively long times, at least on the human timescale. As a result, the presence of these isotopes in concentrates represent cause for concern, even at very small concentrations. They thus need to be monitored, if not removed or reduced, during physical separation and subsequent hydrometallurgical treatment (Lane et al. 2016; Cook et al. 2018). It is thus essential to obtain a detailed understanding of the mineralogical deportment of ^{226}Ra , ^{210}Pb , and ^{210}Po within the deposit and to qualitatively model the behavior of these RN throughout the processing cycle.

Investigation of uraninite compositions and textures allowed Macmillan et al. (2016) to identify distinct generations of uraninite in the Olympic Dam ore. Although some early uraninite retains the full decay sequence of daughter RN within its crystal structure and may contain >10 wt% radiogenic Pb, aphanitic uraninite does not and is assumed to have formed much later as

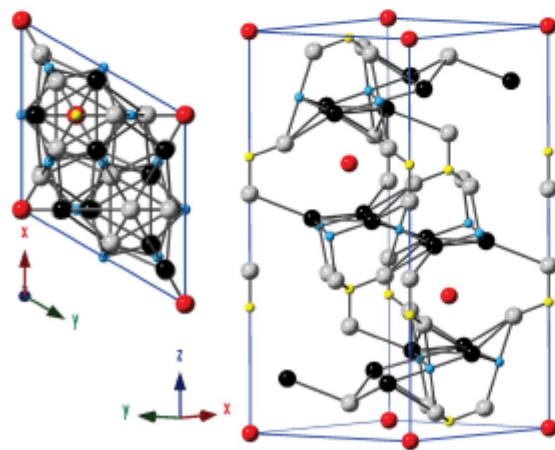


FIGURE 1. The crystal structure of APS minerals looking down the [001] zone axis (left) and just offset from [110] (right). Red atoms = A-site cations; blue atoms = Al; yellow atoms = P/S; black atoms = OH/H₂O; gray atoms = O. Note 12-fold coordination of A-site cations, electrostatically and H-bonded to OH, H₂O, and O within AlO_6 octahedra and phosphate/sulfate tetrahedra. Data from Kato (1971). (Color online.)

a result of the breakdown of early uraninite or other U-minerals and migration of released U (Xing et al. 2018, 2019). A second study, encompassing brannerite and coffinite in the deposit (Macmillan et al. 2017), shows that these minerals also contain relatively little Pb, strongly supporting the release of U and daughter RN from parent U-minerals and subsequent migration and re-concentration into existing or new minerals.

Rollog et al. (2019) have used nanoSIMS isotope mapping to directly visualize the distribution of ^{230}Ra and ^{210}Pb in representative samples from Olympic Dam. Their results demonstrate decoupling among RN (e.g., ^{230}Ra from ^{238}U) and the migration of daughter RN toward the end of the decay chain at the nanometer to micrometer scale, formation of new minerals such as galena, and also the concentration of RN at grain boundaries, in micro-fractures, and trapped in pores within mineral grains. In another Cu deposit within the Olympic Cu-Au province, Owen et al. (2018) identified at least two events in which radiogenic lead has been remobilized and separated from parent U and Th and subsequently re-concentrated within nanoscale symplectitic intergrowths of clausthalite (PbSe) within Cu-(Fe)-sulfides. Moreover, the work of Rollog et al. (2019) has suggested that spatial separation of daughter RN from parent U-bearing minerals is accelerated during the final stage of mineral processing, such that recovery of U from Cu concentrate does not equate to recovery (removal) of ^{230}Ra and ^{210}Pb .

Phosphate minerals are abundant in the Olympic Dam deposit, and include fluorapatite (Krneta et al. 2016, 2017, 2018), florencite-(Ce) and florencite-(La) (Lottermoser 1995; Schmandt et al. 2019a), and subordinate monazite-(Ce) (Lottermoser 1995) and xenotime-(Y) (Oreskes and Einaudi 1990; Ehrig et al. 2012). The deposit also contains wt% concentrations of barite (Schmandt et al. 2019b). The latter authors report uptake of Pb, during acid leaching, into barite that has reported to Cu concentrate, highlighting the potential for minor mineral components of the ores or concentrates to act as scavengers of RN.

Collectively, the above studies emphasize the critical importance of careful mineralogical study at appropriate scales of observation to identify RN carriers and assess pathways of RN mobility. Given the potential application of APS minerals in the storage of toxic metals (Kolitsch and Pring 2001), their widely variable crystal chemistry and low solubilities at high temperature (400–500 °C), and wide ranges of E_h and pH, make them excellent candidates as scavengers of products of radioactive decay.

SAMPLES AND METHODS

Three sets of finely milled samples were collected from the Olympic Dam (OD) processing plant in December 2016: a set of flotation concentrates (FC), a set from the flotation tailings (FT) and a set of concentrates following removal of the majority of uranium via sulfuric acid leaching (Concentrate Leach Discharge, CLD). At Olympic Dam, standard leach conditions are maintained at around 55 °C, pH of 1.5, E_h of ~440 mV (MacNaughton et al. 1999, 2000; Bhargava et al. 2015) for 8–12 h, depending on the mineralogy of the feed (Ehrig et al. 2015). FC and FT samples have not been chemically altered and are therefore representative of the ore mineralogy whereas CLD samples have become altered during acid leaching. The milled samples were dried and mounted as one-inch polished blocks.

Reflected-light and backscatter-electron (BSE) images were obtained to document textures and compositional zoning using a Nikon Eclipse LV100 POL Petrographic Microscope and an FEI Quanta 450 Field Emission Gun scanning electron microscope equipped with a silicon-drift energy-dispersive X-ray spectrometer (EDS), located at Adelaide Microscopy (The University of Adelaide). Energy-dispersive X-ray spectroscopy (EDS) spot analyses and element maps

were collected using an Oxford Instruments Ultim Max 170 mm SDD (silicon drift detector) EDS Detector with AZtec software. The SEM was operated in high-vacuum mode at 20 kV and a spot size of 4 μm .

Quantitative compositional data were obtained using a Cameca SX-Five electron probe microanalyzer (EPMA), located at Adelaide Microscopy, and equipped with five tunable wavelength-dispersive spectrometers. The instrument uses PeakSite software for microscope operation, and Probe for EPMA software (distributed by Probe Software Inc.) for data acquisition and processing. Initially, a suite of 40 elements (Supplemental Appendix 1[†]) were analyzed, but after ~40 analyses it was determined that the HREE elements Ho, Yb, Tm, Er, and Dy could be removed from the list to reduce overall count time as they were consistently below, or near below minimum limits of detection (mdl). Due to the measurable amounts of F (and Cl), the halogen oxygen equivalent was subtracted from the stoichiometric oxygen during processing iteration. For major to minor elements, operating conditions were 15 keV and 20 nA. Trace element counts were acquired at a higher beam current (100 nA). For all analyses, a spot size of 1 μm was used.

Isotope mapping was done with a NanoSIMS 50L (CAMECA, France) at the Centre for Microscopy, Characterization, and Analysis, at the University of Western Australia. A 16 keV primary O^+ beam, generated by a Hyperion H200 RF plasma oxygen ion source, was used for all analyses. The instrument was operated in multi-collection mode, allowing the simultaneous detection of up to seven isotopes. Positive secondary ion maps were collected for $^{40}\text{Ca}^+$, $^{44}\text{Ca}^+$, $^{86}\text{Sr}^+$, $^{206}\text{Pb}^+$, $^{208}\text{Pb}^+$, $^{232}\text{Th}^+$, $^{230}\text{Ra}^+$, $^{238}\text{U}^+$, and $^{210}\text{Pb}^+$. To avoid detector saturation, major isotopes of Ca, Sr, and U were at times substituted with minor isotopes. Mass calibration was carried out using high-purity metal standards from Astimex. For ^{230}Ra and ^{238}U , the approximate detector positions were determined from ^{105}Pd and ^{115}In , respectively. Fine-tuning of these detector positions was then carried out on uraninite grains known to contain ^{230}Ra and ^{238}U . All imaging was done with a 250 pA primary beam, rastering over 50 μm^2 areas (512 px²), with dwell times of 5.5 ms per pixel; seven planes were recorded for each area. The OpenMMS plugin (Poczek et al. 2009) for ImageJ (Schindelin et al. 2012, 2015) was used for all image analysis. All data were dead time corrected, and the seven individual planes were aligned before being summed. See Rollog et al. (2019) for discussion on isotope mass interferences.

RESULTS

Textural characterization and mineral associations

APS phases occur in close association with Cu-Fe-sulfides (bornite and chalcopyrite), hematite, and other more abundant gangue minerals, notably sericitic mica, Fe-dominant chlorites (chamosite), fluorapatite, baryte, and fluorite. Individual APS mineral grains (5–40 μm) show significant contrast variation on BSE images (Fig. 2), consistent with grain-scale compositional zonation. Different zones are variably enriched in REE, Ca, and Sr, whereby brighter zones are typically richer in REE. Several species (REE-, Ca-, and Sr-dominant) are present. BSE imaging and EDS spectra indicate that distinct zones within individual grains also show variation with respect to S and P, suggesting that some are phosphate-dominant, and others are sulfate-dominant. For the purposes of the textural characterization and mineral associations of the APS minerals, there is no discernible difference between samples from flotation and leach processing.

APS phases range from finely mottled aggregates to elongate needle-like grains (fine plates cut perpendicularly) (Figs. 2a and 2b, respectively), coarsening toward a marked tabular morphology; the latter appearing particularly strongly zoned on BSE images (Figs. 2c and 2d). Sr-Ca-dominant APS mineral phases (e.g., svanbergite, woodhouseite) are observed to replace Cu-Fe-sulfides, usually chalcopyrite, often resulting in mutual boundaries with scalloped morphology. Sr-Ca-APS minerals often contain remnants of replaced primary minerals such as the Cu-Fe-sulfides (Fig. 2b) and other gangue minerals including hematite, sericite, and chamosite (Figs. 2a–2d). Relics of replaced minerals occur as coarser, island-like inclusions (hematite; Fig. 2a) or speckled

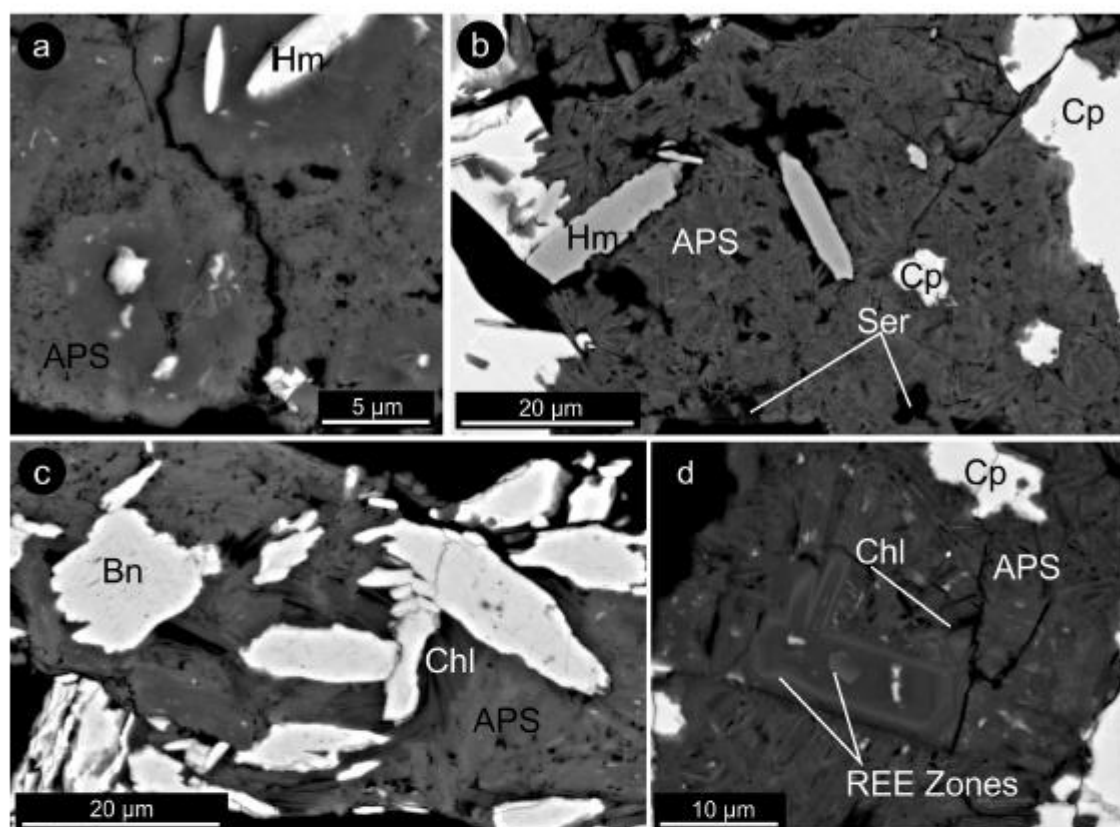


FIGURE 2. BSE images of APS and associated minerals. Images (a–d) are arranged in order of APS grain coarsening; (a) shows one of the finest-scale grained morphologies of the APS minerals observed. Note the mottled appearance of the aggregate relative to the coarser, clean surface of APS next to the replacement zones around hematite (Hm); (b, c, and d) the formation of needles (coarser in c and d) of APS as the APS replaces sericite (Ser) and chlorite (chamosite) (Chl), hematite and chalcopyrite (Cp). Relic replaced hematite and chalcopyrite are preserved within the APS grains (c and d) as indicated by the light speckling. More platy, tabular APS crystals are formed in c replacing chlorite (chamosite) (Chl) and bornite (Bn). Note that with coarsening of the APS minerals, zonation becomes more evident (c and d). (a, c, and d) from FC material, (b) from CLD material.

inclusion fields within the APS phases (Figs. 2a, 2c, and 2d).

APS minerals are also observed to replace Ca-bearing minerals, including fluorapatite (Fig. 3a) and fluorite (Fig. 4a). EDS element maps and corresponding BSE images (Figs. 3b and 2c) show relics of another Ca-bearing phase partially replaced by APS. Unfortunately, here, the phases measured within the EDS spectrum, although showing obvious peaks for Ca, Fe, and O, were too mixed to accurately determine the replaced precursor mineral, likely due to their very small grain size and relic nature. Figure 3c shows a Ca-rich zone immediately surrounding partially replaced hematite and associated with Fe-rich chlorite (chamosite), whereas Figure 3e highlights relics of almost completely replaced fluorapatite inside APS. Some coarser grains (up to 40 μm) of APS phases (Fig. 4a) are characteristically zoned, with the cores recognized as Sr-Ca-dominant and S-bearing (Fig. 4b), through to REE-dominant compositions corresponding to florencite-(Ce) at the rims (Fig. 4c). In contrast to their finer-grained analogs, the coarser-grained APS minerals show negligible replacement of surrounding minerals.

Compositional data

EPMA data (representative data shown in Tables 1 and 2 and plotted in Fig. 5, full data set in Supplemental Appendix 2') confirm the presence of two distinct compositional groups indicated by SEM observation (Fig. 4). These plot as distinct clusters but nevertheless form a broad continuum in compositional space (Fig. 5a). With respect to the APS general formula, $AB_3(XO_4)_2(OH)_6$, the two clusters, here defined as Group 1 and Group 2, are discriminated by the dominant A-site cations and the ratios of phosphate to sulfate. Both groups include analyses from FC, FT, and CLD sample types.

Group 1 represents phases with elevated Sr and Ca ($Sr > Ca$) that are enriched in sulfate [$S/(S+P) > 0.17$] relative to Group 2. Group 1 contains most of the variability within the data set (Fig. 5). In terms of calculated atom-per-formula-unit (apfu) values, Ca occupancy of the A-site ranges from 0.02 to 0.58, Sr from 0.26 to 0.67, and REE from 0.11 to 0.69. In the X-site, P ranges from 0.81 to 1.55 apfu. Sulfur is always subordinate (0.30 to 0.95 apfu). Most analyses within Group 1 thus fall within the

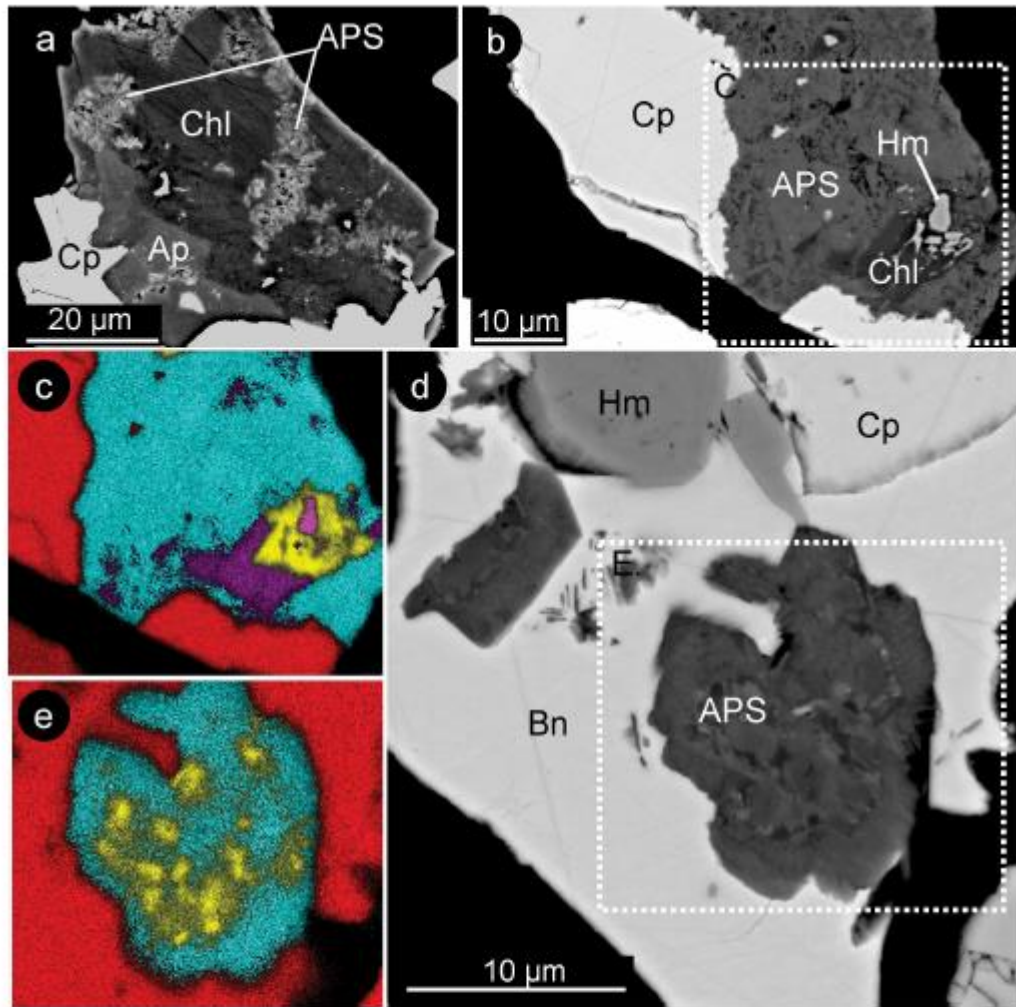


FIGURE 3. BSE images showing (a) replacement of Ca-bearing minerals such as fluorapatite (Ap) by APS phases, as well as chlorite (chamosite) (Chl) (a and b). Cu-(Fe)-sulfides chalcopyrite (Cp) and bornite (Bn) are also replaced by APS in b and d, respectively. (c and e) X-ray element distribution maps taken from the areas identified by the boxes in b and d and show the presence of remnant Ca-bearing phases encased within APS. S = red, Fe = purple, Al = blue, and Ca = yellow. All imaged grains are from FC material. (Color online.)

compositional field of *svanbergite*, albeit with strong components of Ca and REE, and with S/(S+P) ratios consistently >0.17 and therefore deviating from ideal stoichiometry. A small number of analyses included here within Group 1 have REE apfu values that exceed apfu (Sr+Ca). These can be considered as either: (1) Sr-Ca-S-bearing *florencite*; or (2) mixtures of two or more minerals below the scale of the microprobe beam.

Group 2 phases more closely resemble the composition of *florencite*-(Ce), i.e., they contain at least 80% occupation of the A site by REE (in order, Ce>La>Nd>Pr). They are also phosphate-

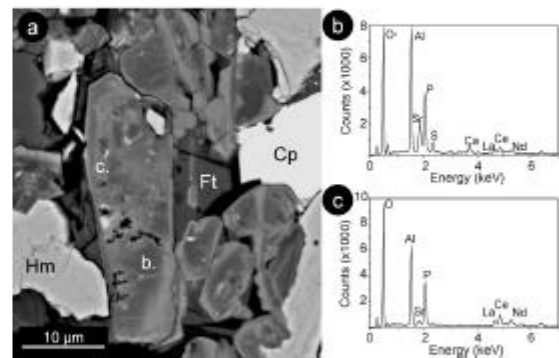


FIGURE 4. (a) BSE image of subhedral tabular APS crystals in association with fluorite (Ft), hematite (Hm), and chalcopyrite (Cp). (b and c) EDS spectra obtained from locations marked on a. Brighter zones on APS grains resemble *florencite* in composition, whereas the darker zones contain Sr, Ca, and S. Image taken from FC material.

TABLE 1. Representative EPMA data for APS minerals of Group 1 based on the ideal formula $AB_3(XO_4)_2(OH)_6nH_2O$

Material	CLD	CLD	FC	FC	CLD	FC	FC	FC	FC	FC
Oxides (wt%)										
Na ₂ O	0.035	<mdl	0.049	0.072	0.114	0.119	0.129	0.064	0.125	0.081
K ₂ O	0.189	0.018	0.134	0.085	0.169	0.340	0.303	0.362	0.340	0.274
CaO	0.26	0.26	1.29	1.60	2.54	3.16	2.20	2.37	2.37	2.80
SrO	5.10	5.79	9.58	10.60	10.80	11.23	13.86	13.42	14.22	13.32
BaO	0.160	0.101	0.420	0.508	0.522	0.412	0.477	0.363	0.578	0.296
Y ₂ O ₃	0.033	<mdl	0.230	0.377	0.192	0.037	0.154	0.047	0.132	0.027
ZrO ₂	0.063	0.069	0.052	0.058	0.071	0.073	0.066	0.075	0.070	0.055
La ₂ O ₃	7.48	7.04	3.94	4.10	2.76	1.65	1.50	1.34	1.33	1.16
Ce ₂ O ₃	10.64	11.10	8.35	6.48	5.97	3.24	2.44	2.22	2.24	2.07
Pr ₂ O ₃	0.89	0.86	0.87	0.64	0.62	0.43	0.16	0.26	0.23	0.10
Nd ₂ O ₃	1.94	2.17	1.83	1.11	1.70	1.12	0.69	0.55	0.58	0.53
Sm ₂ O ₃	<mdl	0.088	0.203	0.174	0.169	0.136	0.065	<mdl	<mdl	<mdl
Eu ₂ O ₃	0.046	0.087	0.055	0.059	0.078	0.138	<mdl	<mdl	<mdl	<mdl
Gd ₂ O ₃	<mdl	<mdl	<mdl	<mdl	0.104	0.082	<mdl	<mdl	<mdl	0.114
Tb ₂ O ₃	<mdl	<mdl	0.065	0.066	0.042	0.000	<mdl	<mdl	<mdl	<mdl
Dy ₂ O ₃	<mdl	<mdl	<mdl	<mdl	<mdl	0.062	<mdl	<mdl	<mdl	<mdl
Bi ₂ O ₃	<mdl	<mdl	0.092	<mdl	<mdl	0.032	<mdl	<mdl	<mdl	<mdl
PbO	<mdl	<mdl	<mdl	<mdl	0.250	0.315	0.233	0.454	0.292	0.270
ThO ₂	0.000	0.203	<mdl	<mdl	<mdl	<mdl	0.027	<mdl	<mdl	0.031
UO ₂	0.022	0.022	<mdl	0.027	0.023	0.024	0.019	0.021	<mdl	<mdl
MgO	<mdl	<mdl	0.026	0.012	0.029	0.027	0.067	0.040	0.018	0.016
Al ₂ O ₃	32.89	31.69	34.87	32.56	35.83	36.20	34.33	35.40	36.25	36.16
TiO ₂	0.032	0.077	0.016	0.033	0.025	0.021	<mdl	0.018	<mdl	0.015
Fe ₂ O ₃	3.28	1.86	1.44	2.18	0.89	1.55	1.27	0.90	0.84	1.28
Cu ₂ O	0.693	0.811	0.626	0.320	0.971	0.385	0.524	0.510	0.638	0.589
Nb ₂ O ₅	0.026	<mdl	<mdl	0.026	<mdl	<mdl	0.023	<mdl	0.035	<mdl
Ta ₂ O ₅	0.107	0.073	<mdl	<mdl	<mdl	<mdl	<mdl	<mdl	0.047	<mdl
WO ₃	0.109	<mdl	<mdl	0.071	<mdl	0.086	<mdl	<mdl	<mdl	<mdl
SiO ₂	0.803	0.299	0.933	0.499	0.271	0.967	0.227	0.609	0.176	0.322
P ₂ O ₅	19.17	19.25	19.96	20.61	18.01	19.79	22.13	20.78	22.02	20.06
SO ₂	3.73	4.14	3.75	3.90	6.54	8.60	5.75	9.23	6.56	9.55
As ₂ O ₃	0.070	<mdl	<mdl	<mdl	<mdl	<mdl	<mdl	<mdl	<mdl	<mdl
F	0.119	0.395	2.065	3.051	2.624	1.451	3.432	1.995	3.042	1.277
Cl	0.025	0.000	0.030	0.000	0.041	0.031	0.000	0.038	0.016	0.021
Total	87.92	86.39	90.89	89.21	91.36	91.73	90.08	91.06	92.15	90.41
APS Formula (apfu)										
A-Site										
Na	0.006	0.000	0.008	0.012	0.018	0.018	0.020	0.010	0.019	0.012
K	0.021	0.002	0.014	0.009	0.018	0.034	0.032	0.036	0.034	0.027
Ca	0.024	0.025	0.116	0.148	0.228	0.265	0.193	0.200	0.201	0.235
Sr	0.257	0.299	0.468	0.529	0.523	0.511	0.658	0.612	0.654	0.607
Ba	0.005	0.004	0.014	0.017	0.017	0.013	0.015	0.011	0.018	0.009
Y	0.002	-	0.010	0.017	0.009	0.002	0.007	0.002	0.006	0.001
Zr	0.003	0.003	0.002	0.002	0.003	0.003	0.003	0.003	0.003	0.002
La	0.239	0.232	0.122	0.130	0.085	0.048	0.045	0.039	0.039	0.034
Ce	0.338	0.363	0.258	0.204	0.183	0.093	0.073	0.064	0.065	0.059
Pr	0.028	0.028	0.027	0.020	0.019	0.012	0.005	0.007	0.007	0.003
Nd	0.060	0.069	0.055	0.034	0.051	0.031	0.020	0.015	0.016	0.015
Sm	-	0.003	0.006	0.005	0.005	0.004	0.002	-	-	-
Eu	0.001	0.003	0.002	0.002	0.002	0.004	-	-	-	-
Gd	-	-	-	-	0.003	0.002	-	-	-	0.003
Tb	-	-	0.002	0.002	0.001	-	-	-	-	-
Dy	-	-	-	-	-	0.002	-	-	-	-
Total REE	0.67	0.70	0.47	0.40	0.35	0.20	0.14	0.13	0.13	0.11
Bi	0.004	0.003	-	-	-	-	-	-	0.002	-
Pb	-	-	-	-	0.006	0.007	0.005	0.010	0.006	0.006
Th	-	0.004	-	-	-	-	-	-	-	0.001
U	-	-	-	0.001	-	-	-	-	-	-
Total	1.66	1.73	1.57	1.53	1.52	1.24	1.22	1.14	1.20	1.13

dominant, with subordinate sulfate [S/(S+P) < 0.17].

Assuming (OH+Cl+F) = 6 apfu, and knowing measured F and Cl concentrations, an estimation of OH occupancy can be made. There appears to be a negative correlation between apfu (Ca+Sr) and calculated OH⁻. Also, analyses across both groups containing negligible S tend to have higher calculated OH⁻ concentrations (Fig. 5b).

Relationships between the dominant A-site cations (Ca, Sr, and REE) are compared in ternary diagrams (Figs. 5c and 5d). An increase in Ca occupancy appears to correlate with increasing Sr content. Analyses close to, or exceeding Sr/(Sr+Ca+REE) >

TABLE 1.—CONTINUED

Material	CLD	CLD	FC	FC	CLD	FC	FC	FC	FC	FC
APS Formula (apfu)										
B-Site										
Mg	-	-	0.003	0.002	0.004	0.003	0.008	0.005	0.002	0.002
Al	3.37	3.33	3.46	3.31	3.53	3.34	3.31	3.28	3.39	3.35
Mn	-	-	-	-	-	-	-	-	0.003	-
Fe	0.32	0.19	0.14	0.21	0.08	0.14	0.12	0.08	0.07	0.11
Cu	0.045	0.055	0.040	0.021	0.061	0.023	0.032	0.030	0.038	0.035
Nb	0.001	-	-	0.001	-	-	0.001	-	0.001	-
Ta	-	-	0.001	-	-	-	-	-	-	-
W	0.002	-	-	0.002	-	0.002	-	-	-	-
Ti	0.002	0.005	0.001	0.002	0.002	0.001	-	0.001	-	0.001
Total	3.74	3.58	3.64	3.55	3.68	3.51	3.47	3.40	3.51	3.50
X-Site										
Si	0.070	0.027	0.079	0.043	0.023	0.076	0.019	0.048	0.014	0.025
P	1.41	1.45	1.42	1.50	1.27	1.31	1.53	1.38	1.48	1.33
S	0.30	0.35	0.30	0.31	0.51	0.63	0.44	0.68	0.49	0.70
Total	1.78	1.83	1.80	1.86	1.81	2.02	1.99	2.11	1.98	2.06
Anions										
O	8	8	8	8	8	8	8	8	8	8
F	0.033	0.112	0.550	0.831	0.693	0.360	0.889	0.497	0.763	0.317
Cl	0.004	-	0.004	-	0.006	0.004	-	0.005	0.002	0.003
OH	5.96	5.89	5.45	5.17	5.30	5.64	5.11	5.50	5.23	5.68

Notes: mdl = minimum limit of detection; components that were consistently below minimum detection limit (mdl) values are not given. Blank spaces indicate that no measurement was taken for the given element in that analysis (see text).

0.5, however, tend to display much wider variation in Ca content (Fig. 5c). Analytical spots that are richer in REE (~60% or more of A-site occupancy) contain only minimal Ca. Among the REE, either Ce or La is dominant (although La is most often subordinate to Ce) in both Group 1 and 2, and the relative abundance of the remaining REE is low (Fig. 5d). However, as the relative abundance of the remaining REEs (mainly Pr and Nd) increases, there is a marked decrease in La, but a corresponding slight increase in Ce.

U and Th concentrations are negligible in both groups and rarely above mdl. When present, U and Th show only very minor correlation with other elements.

Lead is a trace but nevertheless quantifiable constituent of APS minerals (Tables 1 and 2, Figs. 5e–5h). Concentrations are variable, however, and correlate with several factors. REE-enriched analyses have low Pb concentrations (<0.006 apfu). Likewise, analytical spots containing elevated P contents were among those with the lowest concentrations of Pb. In contrast, increased Ca and Sr content within the A-site (Figs. 5e and 5f, respectively) corresponds with greater Pb content. Lead content also appears to increase with decreasing OH⁻ and appears in CLD material with greater regularity.

Nanosims isotope mapping of APS and associated minerals

Investigation of selected areas containing APS minerals within the FC and CLD samples by NanoSIMS isotope mapping confirms the presence of ²²⁶Ra and ²¹⁰Rn (overwhelmingly ²¹⁰Pb due to the extreme volatility of ²¹⁰Po; Rollog et al. 2019) within Sr-Ca-dominant APS minerals (svanbergite). Within most mapped areas such as the examples shown in Figures 6 and 7, there appears to be an excess of daughter ²²⁶Ra and ²¹⁰Rn compared to the equivalent map for parent U, which is concentrated within and immediately adjacent to micrometer-sized U-bearing minerals (in most cases as uraninite). Also, ²²⁶Ra and ²¹⁰Rn are seen to be more dispersed throughout the APS minerals relative to U, and the elevated signals for ²²⁶Ra and ²¹⁰Rn do not always coincide with those of U. In addition, these radionuclides show

TABLE 2. Representative EPMA data for APS minerals of Group 2 based on the ideal formula $AB_3(XO_4)_2(OH)_6 \cdot nH_2O$

Material	FT	FT	FT	FC	FC	FT	CLD	CLD	CLD	CLD
Oxides (wt%)										
Na ₂ O	<mdl	<mdl	<mdl	<mdl	<mdl	0.035	<mdl	<mdl	<mdl	<mdl
K ₂ O	0.024	0.192	0.014	0.012	0.009	0.063	0.009	<mdl	<mdl	0.018
CaO	0.38	0.15	0.20	0.20	0.28	0.33	0.28	0.26	0.28	0.54
SrO	1.61	1.48	2.15	2.38	2.19	2.28	2.24	2.53	2.53	2.58
BaO				0.096		0.062	0.196	0.493	0.155	
Y ₂ O ₃	0.021	0.023	0.055	0.044	<mdl	0.051	<mdl	0.022	0.040	0.092
ZrO ₂	<mdl	<mdl	<mdl	<mdl	0.034	<mdl	0.040	0.028	0.057	0.054
La ₂ O ₃	8.97	8.72	6.73	9.43	11.23	13.64	7.82	11.09	11.21	9.41
Ce ₂ O ₃	15.72	13.95	14.26	14.59	13.41	12.93	11.68	12.87	12.68	13.74
Pr ₂ O ₃	1.38	1.26	1.47	1.03	0.70	0.60	0.90	0.67	0.76	1.07
Nd ₂ O ₃	3.57	3.08	4.69	2.24	1.11	0.98	2.58	1.18	1.09	1.96
Sm ₂ O ₃	0.212	0.122	0.357	<mdl	0.075	<mdl	0.189	0.082	<mdl	<mdl
Eu ₂ O ₃	0.046	0.038	0.086	<mdl	<mdl	<mdl	<mdl	0.041	<mdl	<mdl
Tb ₂ O ₃	<mdl	<mdl	<mdl	<mdl	<mdl	<mdl	<mdl	0.048	<mdl	<mdl
Dy ₂ O ₃	<mdl	<mdl	<mdl	<mdl	<mdl	<mdl	<mdl	<mdl	0.055	<mdl
Ho ₂ O ₃	<mdl	<mdl	<mdl	<mdl	<mdl	<mdl	0.203	<mdl	<mdl	<mdl
Yb ₂ O ₃	<mdl	<mdl	<mdl	<mdl	<mdl	0.327	<mdl	<mdl	<mdl	<mdl
Bi ₂ O ₃	<mdl	<mdl	<mdl	<mdl	<mdl	<mdl	<mdl	0.032	<mdl	<mdl
PbO	<mdl	<mdl	0.027	<mdl	<mdl	<mdl	<mdl	0.184	0.145	0.245
ThO ₂	<mdl	0.061	0.020	<mdl	<mdl	<mdl	<mdl	<mdl	<mdl	<mdl
UO ₂	<mdl	<mdl	<mdl	<mdl	0.019	<mdl	0.041	<mdl	<mdl	0.037
MgO				<mdl			0.015	<mdl	<mdl	0.035
Al ₂ O ₃	29.77	28.88	28.86	29.78	32.55	30.40	29.36	31.72	31.74	32.23
TiO ₂				<mdl	<mdl	<mdl	<mdl	<mdl	0.036	0.045
Fe ₂ O ₃	1.33	0.68	3.30	3.15	0.73	2.63	9.64	0.76	0.65	1.09
Cu ₂ O				0.710			0.942	0.687	0.593	0.648
Nb ₂ O ₅	<mdl	<mdl	<mdl	<mdl	<mdl	<mdl	0.023	0.028	<mdl	<mdl
Ta ₂ O ₅				<mdl	<mdl	<mdl	<mdl	0.089	<mdl	<mdl
WO ₃				0.000			<mdl	<mdl	0.115	<mdl
SiO ₂	<mdl	<mdl	<mdl	<mdl	0.399	<mdl	0.718	0.306	0.341	0.460
P ₂ O ₅	19.75	20.42	19.50	17.26	19.55	19.29	18.75	19.98	20.08	19.57
SO ₂	0.72	0.77	0.67	1.49	1.83	1.56	1.42	2.00	2.09	1.54
As ₂ O ₃	<mdl	<mdl	0.688	0.156	0.293	0.031	<mdl	0.280	0.225	0.030
F	0.265	0.064	0.061	0.218	0.235	0.219	<mdl	0.224	0.208	0.335
Cl	0.031	0.097	0.035	0.073	0.025	0.030	0.031	0.024	0.027	0.056
Total	83.80	79.99	83.18	82.06	85.49	85.41	86.75	85.42	85.51	86.00
APS Formula (apfu)										
A-Site										
Na	-	-	-	-	-	0.006	-	-	-	-
K	0.003	0.024	0.002	0.001	0.001	0.007	0.001	-	-	0.002
Ca	0.04	0.02	0.02	0.02	0.03	0.03	0.03	0.03	0.03	0.05
Sr	0.09	0.08	0.12	0.14	0.12	0.12	0.12	0.13	0.13	0.14
Ba				0.003		0.002	0.007	0.018	0.006	
Y	0.001	0.001	0.003	0.002	-	0.003	-	0.001	0.002	0.004
Zr				0.001	-	0.002	0.001	0.003	0.002	
La	0.32	0.31	0.24	0.34	0.38	0.47	0.26	0.37	0.38	0.32
Ce	0.55	0.50	0.50	0.52	0.45	0.44	0.39	0.43	0.42	0.46
Pr	0.05	0.04	0.05	0.04	0.02	0.02	0.03	0.02	0.03	0.04
Nd	0.12	0.11	0.16	0.08	0.04	0.03	0.03	0.04	0.04	0.06
Sm	0.007	0.004	0.012	-	0.002	-	0.006	0.003	-	-
Eu	0.002	0.001	0.003	-	-	-	-	-	0.001	-
Tb				-	-	-	-	-	0.001	-
Ho				-	-	-	-	-	0.006	-
Yb				-	-	0.009	-	-	-	-
Total REE	1.04	0.97	0.97	0.98	0.89	0.97	0.77	0.87	0.86	0.87
Bi				-	-	-	-	-	0.004	-
Pb			0.001	-	-	-	-	-	0.005	0.004
Th	0.000	0.001	-	-	-	-	-	-	-	-
U				-	0.000	-	0.001	-	-	0.001
Total	1.18	1.10	1.11	1.14	1.04	1.15	0.92	1.05	1.05	1.09

greater affinity to APS minerals than either Cu-Fe-sulfide or iron-oxide minerals with only limited dispersion identifiable within the latter. The distribution of ²¹⁰Rn throughout the APS minerals appears to correlate most strongly with that of Ca than the stable product of U decay, ²⁰⁶Pb (Fig. 7). Common Pb, represented by ²⁰⁴Pb, however, showed good correlation with ²¹⁰Rn, similarly mimicking Ca composition (Fig. 8). Those domains featuring elevated peak counts for ²⁰⁶Pb lack corresponding peaks on the ²¹⁰Rn map (Fig. 7). This indicates either recent fluid-mediated

TABLE 2.—CONTINUED

Material	FT	FT	FT	FC	FC	FT	CLD	CLD	CLD	CLD
APS Formula (apfu)										
B-Site										
Mg							0.002	-	-	0.005
Al	3.35	3.33	3.27	3.44	3.49	3.34	3.14	3.41	3.41	3.46
Fe	0.144	0.075	0.358	0.348	0.075	0.277	0.986	0.078	0.066	0.112
Cu				0.049			0.064	0.047	0.041	0.045
Nb	-	-	-	-	-	-	0.001	0.001	-	-
W							-	-	0.003	-
Ti							-	-	0.002	0.003
Total	3.50	3.40	3.63	3.79	3.62	3.62	4.19	3.54	3.52	3.63
X-Site										
Si	-	-	-	-	0.036	-	0.065	0.028	0.031	0.042
P	1.60	1.69	1.59	1.43	1.51	1.52	1.44	1.54	1.55	1.51
S	0.06	0.07	0.06	0.14	0.16	0.14	0.12	0.17	0.18	0.13
As	-	-	0.040	0.009	0.016	0.002	-	0.016	0.012	0.002
Total	1.66	1.76	1.69	1.58	1.72	1.66	1.62	1.76	1.77	1.69
Anions										
O	8.000	8.000	8.000	8.000	8.000	8.000	8.000	8.000	8.000	8.000
F	0.080	0.020	0.019	0.068	0.068	0.065	-	0.065	0.060	0.097
Cl	0.005	0.016	0.006	0.012	0.004	0.005	0.005	0.004	0.004	0.009
OH	5.91	5.96	5.98	5.92	5.93	5.93	6.00	5.93	5.94	5.89

Notes: mdl = minimum limit of detection; components that were consistently below minimum detection limit (mdl) values are not given. Blank spaces indicate that no measurement was taken for the given element in that analysis (see text).

dispersion of decay products away from the U-bearing minerals and throughout APS, or, alternatively in the case of the CLD samples, interaction with the RN-bearing leach solution and subsequent adsorption. Although these distribution patterns remain qualitative in the absence of suitable standards allowing quantification (Rollog et al. 2019), they nonetheless strongly suggest nanometer- to micrometer-scale migration of ²²⁶Ra and ²¹⁰Rn from parent ²³⁸U-bearing phases (either those in the immediate vicinity or possibly migrating from greater distances) and incorporation into APS minerals.

A second significant observation is that Sr-Ca-APS minerals from areas in the CLD samples mapped by nanoSIMS have greater activities of ²²⁶Ra and ²¹⁰Rn than their equivalents in the FC samples. This strongly suggests fluid-mineral interaction and, possibly, also sub-solidus diffusion of RN during the leaching process. Observed differences in ²¹⁰Rn concentrations between FC and CLD samples may also be amplified due to the recycling of Cu-sulfate-rich smelter dust (which is consequently enriched in ²¹⁰Rn) into the leach solution to maximize Cu recovery.

DISCUSSION

Composition of APS Minerals

The APS minerals examined by BSE imaging, electron microprobe, and nanoSIMS display conspicuous compositional zoning consistent with the formation of an extensive solid solution between end-member APS minerals of the beudantite group. An attempt to use focused ion beam-SEM methods to extract and thin foils for scanning transmission electron microscopy analysis of the APS phases was unsuccessful in that the APS minerals proved too beam-sensitive, even at very low ion beam currents.

Solid solution between svanbergite-woodhouseite and florencite-(REE), (REE)Al₃(PO₄)₂(OH)₆, is considered responsible for the measurable concentrations of REE within all analyses. There is complete solid solution between the end-members crandallite, CaAl₃(PO₄)₂(OH)₆, and goyazite, SrAl₃(PO₄)₂(OH)₆, and between woodhouseite, CaAl₃(PO₄)(SO₄)(OH)₆, and svanbergite, SrAl₃(PO₄)(SO₄)(OH)₆. We can also assume that the substitution

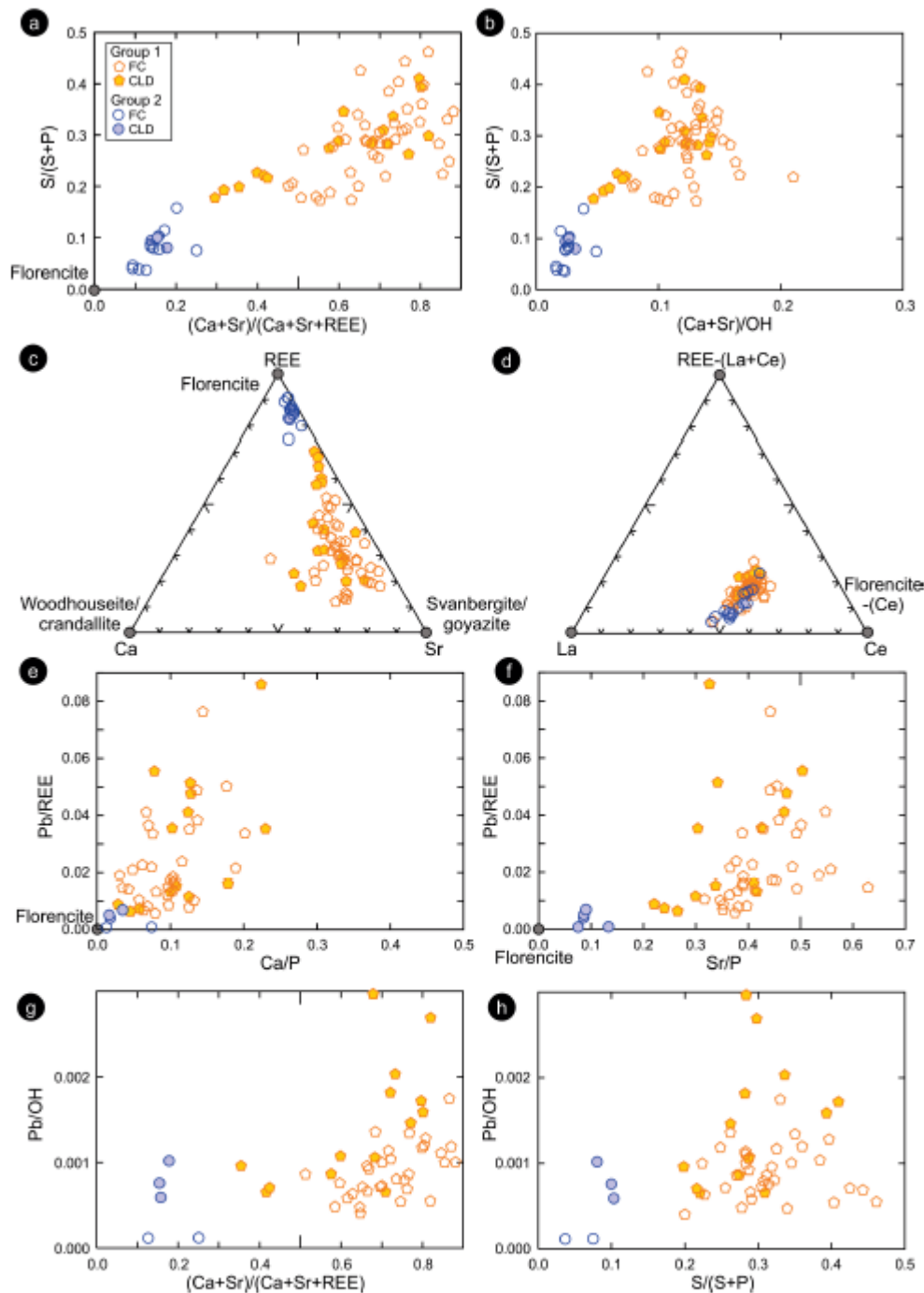


FIGURE 5. EPMA compositional data (apfu from formulas) for APS minerals plotted in terms of (a) $(Ca+Sr)/(Ca+Sr+REE)$ vs. $S/(S+P)$. Two groups are discriminated by the two variables. (b) $S/(S+P)$ vs. $(Ca+Sr)/OH$. (c and d) Ternary plots illustrating the relative abundances of A-site cations in terms of (c) Ca-Sr-REE and (d) La-Ce-[REE-(La+Ce)] where the major component of [REE-(La+Ce)] is (Pr+Nd); (e and f) Pb (apfu) as a function of $(Ca+Sr)/(Ca+Sr+REE)$ and $S/(S+P)$, respectively; (g and h) Pb/REE as a function of Ca/P and Sr/P , respectively. Note that values below mdl are not shown, resulting in fewer points on some plots. The dark gray dots mark the positions of the end-member compositions as indicated. FC and CLD material is shown by the empty and filled dots, respectively. (Color online.)

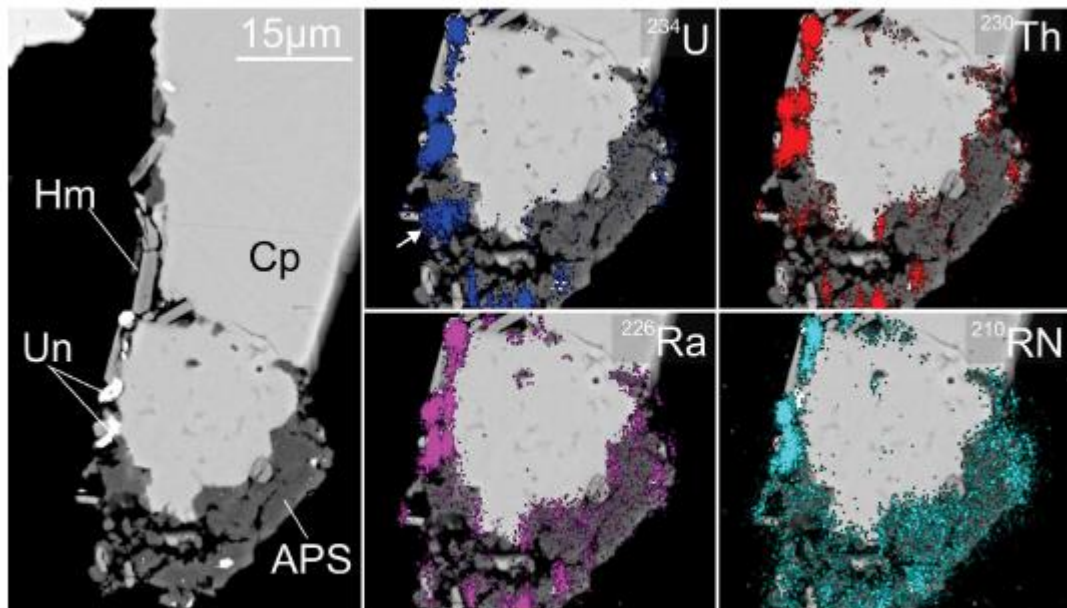


FIGURE 6. BSE image (left) of a grain from FC, with nanoSIMS maps for ^{234}U , ^{230}Th , ^{226}Ra , and ^{210}RN as overlays (see annotations). APS minerals replace chalcopyrite (Cp) and hematite (Hm). Uraninite (Un) inclusions are indicated along grain boundaries and within APS. Note the concentration of ^{234}U counts toward the bottom left side of the image (indicated by the white arrow) does not correspond to a comparable feature on the ^{226}Ra map. Note also that ^{210}RN appear restricted to the U-bearing inclusions and APS minerals only. (Color online.)

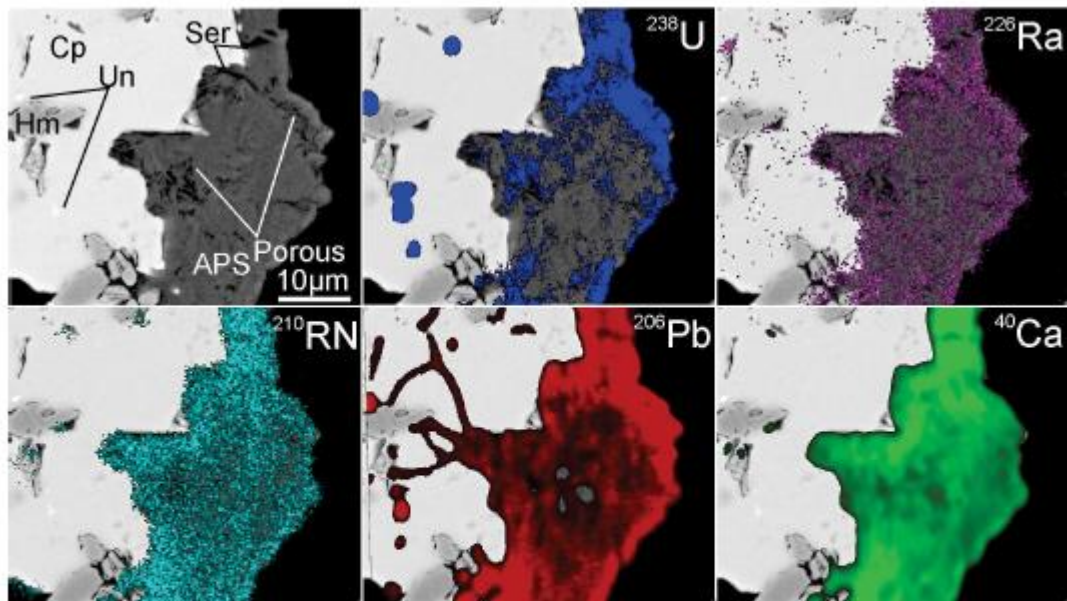


FIGURE 7. BSE image of a grain from CLD sample with nanoSIMS maps of ^{238}U , ^{226}Ra , ^{210}RN , ^{206}Pb , and ^{40}Ca as overlays (see annotations). Chalcopyrite (Cp) is undergoing replacement by APS, with grains of uraninite (Un) occurring within chalcopyrite. ^{238}U is restricted to uraninite and porous regions in APS, whereas RN become progressively more dispersed within the APS (^{226}Ra mostly overlying zones with concentrated ^{238}U counts, ^{210}RN throughout). The correspondence between "hot spots" of ^{210}RN and ^{206}Pb is relatively moderate, possibly indicating complex micrometer-scale migration of RN and/or stable radiogenic Pb. Note, however, the excellent correlation between ^{210}RN and ^{40}Ca . Also note the three spots vacant of counts in the central region of the ^{206}Pb and ^{40}Ca maps, likely resulting from the presence of sub-surface sericite within the analysis. (Color online.)

of sulfate for phosphate is continuous (Gaboreau et al. 2007) such that there is a solid solution between crandallite-goyazite and woodhouseite-svanbergite series minerals.

The Pb concentrations in the analyzed samples are minor, but solid solution can be expected to extend to the Pb-bearing analogues of the above minerals, plumbogummite, $\text{PbAl}_3(\text{PO}_4)_2(\text{OH})_6$, and hinsdalite, $\text{PbAl}_3(\text{PO}_4)(\text{SO}_4)(\text{OH})_6$, with continuous substitution of (Ca,Sr) by Pb. Note that because of its $6s^2$ lone pair of electrons, Pb causes the reduction of the crystal symmetry in some Pb-rich alunites (Kolitsch and Pring 2001), adding complexity to the Pb substitution.

The measured Pb concentrations may have been incorporated at the time of initial formation of the APS mineral assemblage. Alternatively, Pb may be introduced after crystallization via the following alternative mechanisms. First, released radiogenic Pb may interact with, and be absorbed by, the APS minerals during metamictization of, or diffusion of Pb from adjacent U-bearing minerals such as uraninite, coffinite, or brannerite. Second, Pb may have migrated in low-temperature hydrothermal fluids and interacted with existing APS minerals during the multiple tectonothermal events over the past ~1.6 Ga, which is interpreted to have impacted on the deposit. Such events are recorded by multiple mineral groups (e.g., Macmillan et al. 2017), and are also recognized from other ore systems in the Olympic Cu-Au

Province (Owen et al. 2018). Last, acidic fluids containing both Pb and other RN (notably Ra) dissolved in solution may interact with the APS minerals during the acid leach stage of mineral processing, as discussed below.

Aside from the slightly higher Pb concentrations in individual data points from the EPMA data set (Figs. 5e–5h) and the nanoSIMS isotope maps, APS analyzed from CLD material was, for all intents and purposes, identical to that from FC material, indicating negligible modification by the leach liquors. This observation highlights the robust, insoluble character of APS minerals, which remain stable over a broad range of pH and E_h conditions (Kolitsch and Pring 2001).

Radiogenic Pb from the decay of U or Th located within the crystal structure of APS minerals is likely very limited. EPMA data (Tables 1 and 2) show only negligible U and Th, barely above the detection limit in most instances (although detectable with nanoSIMS). NanoSIMS mapping also shows U and Th restricted to inclusions, porous regions within APS or along grain boundaries, even where Pb dispersion is suggested to have taken place (Figs. 6–8). There are currently no APS end-member minerals that contain significant concentrations of U (Jambor 1999; Bayliss et al. 2010), whereas a Th-bearing member of the alunite supergroup, eylettersite $[\text{Th}_{0.33}\text{Al}_3(\text{PO}_4)_2(\text{OH})_6]$, is known (Bayliss et al. 2010). Perhaps contrary to this interpretation,

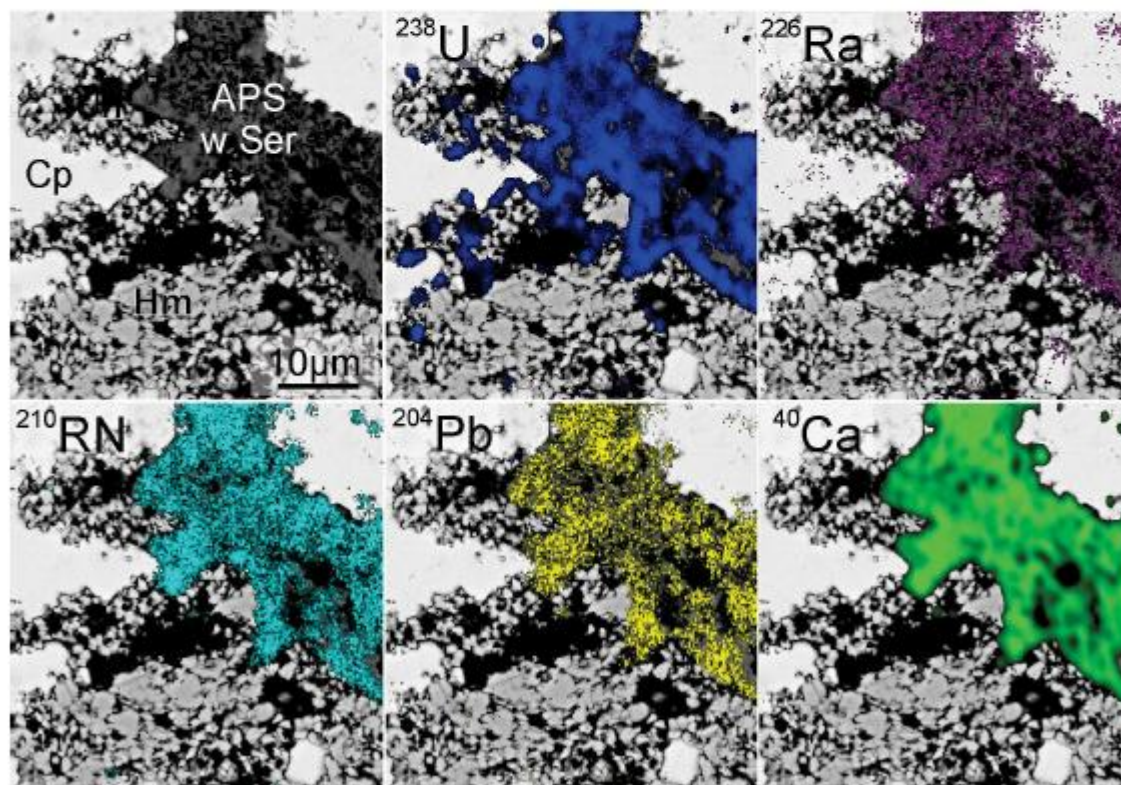


FIGURE 8. BSE image of a grain from CLD sample with nanoSIMS maps of ^{238}U , ^{226}Ra , ^{210}RN , ^{204}Pb , and ^{40}Ca as overlays (see annotations). APS replaces sericite (Ser), hematite (Hm), and chalcopyrite (Cp). Note the prevalence of U along grain boundaries between APS and hematite, and hematite and sericite. Both ^{210}RN and ^{204}Pb match well with ^{40}Ca . (Color online.)

Jerden (2007) suggests that U is sequestered by Ba-Sr-Ca-bearing Al phosphate minerals of the crandallite group (gorceixite) within an unsaturated soil zone overlying U-rich saprolites in the Coles Hill U deposit (Virginia). Additionally, EPMA compositional data revealing up to 3.44 wt% UO_2 within plumbogummite is presented by Plášil et al. (2009) from supergene altered zones of the Medvědin U deposit, Křkonoše Mountains, Czech Republic.

Relationships between the incorporation of Pb, Ca, and Sr contents are complex, as evidenced by the EPMA data (Figs. 5e–5g) and isotope mapping (Figs. 7 and 8). From the results presented here, we cannot unequivocally state whether Pb is adsorbed or absorbed by APS grains; however, Schwab et al. (2005) showed that within synthetic crandallite-group phases, thermodynamic stability increases with replacement of Ca^{2+} by Sr^{2+} and Pb^{2+} . The same trend is also recognized in phosphate-sulfate-bearing beudantite-group minerals, albeit to a lesser degree. In any case, the thermodynamic stability increases with replacement in the order of $\text{Pb} > \text{Sr} \geq \text{Ca}$, thus, absorption of Pb by Ca- and Sr-bearing APS grains seems likely. The relatively low thermodynamic stability of Ca^{2+} may be due to its small ionic radii that may cause contractions within the APS crystal structure resulting in distortions and uneven coordination within the 12-fold coordinated position (Blount 1974). Figure 9 shows the relative positions of the stability fields for each of the woodhouseite series minerals with respect to their dominant A-site cations, with the more stable species plotting closest to the field for gibbsite (Schwab et al. 2005). Studies by Schwab et al. (2004, 2005) show that crandallite and woodhouseite are intimately related and that, in complex natural systems such as Olympic Dam, it is impossible to form pure crandallite without the introduction of substituents such as Sr^{2+} and/or SO_4^{2-} . As such it is unsurprising that we see such a strong association between Ca, Sr, and S. This is an important association due to the relative stabilities of each species with respect to variation of pH, and the activities of H_2PO_4 and of HSO_4^- (Fig. 9). In this figure, plumbogummite and hinsdalite are shown to form solid-solutions with their Ca- and Sr-dominant analogs at moderately low pH, with the Pb-bearing phases, particularly hinsdalite, becoming favored as pH and $a_{\text{HSO}_4^-}$ decreases. The phase diagram indicates that there is no point at which single-phase minerals are formed (apart from a small window for hinsdalite at extreme acidity; Fig. 9). Our EPMA data support this in that they show solid-solution members within any given spot, with varying proportions of the end-member components within each analysis (Tables 1 and 2).

Alteration and APS mineralogy at Olympic Dam

Phosphate minerals are abundant in the Olympic Dam deposit and include fluorapatite (Kmetz et al. 2016, 2017, 2018), florencite-(Ce) and florencite-(La) (Lottermoser 1995; Schmandt et al. 2019a), and subordinate monazite-(Ce) (Lottermoser 1995) and xenotime-(Y) (Oreskes and Einaudi 1990; Ehrig et al. 2012). Altered mineral assemblages containing APS minerals of the alunite supergroup are interpreted to form via late-stage overprinting during alteration and replacement of paragenetically earlier minerals, observed by the systematic replacement of Cu-(Fe)-sulfides and associated gangue. Several authors (e.g., Bajnóczi et al. 2004; Hikov et al. 2010; Georgieva and Velimova 2012, 2014), report on similar replacement mechanisms within

high-sulfidation deposits occurring during advanced argillic (supergene) alteration. It is noted that while the possibility that an advanced argillic phase taking place at Olympic Dam, represented by the presence of small isolated pockets of remnant sericite + quartz \pm Al-OH assemblages, has been discussed previously (Ehrig et al. 2012), there is lack of evidence to suggest that APS is associated with such a phase. Rather, the formation of APS phases is suggested to result from reduced acidic fluids associated with the local dissolution of sulfides.

Schmandt et al. (2019a) report a similar phase of alteration and replacement of primary mineral assemblages in the Olympic Dam deposit, although focusing on florencite as the dominant REE-phosphate. The mineral associations, textures, and LREE trends of the APS minerals discussed here, however, show marked differences to the florencite-dominant compositions presented in Schmandt et al. (2019a), which were from a suite of drillcore samples anomalously rich in REE. In the present study, based on milled flotation feed and copper concentrates, APS minerals consistently replace Cu-(Fe)-sulfides (almost exclusively chalcopyrite), show distinct zonation with respect to REE, Ca, Sr, S, and P, and are variably enriched in Ce over La with increasing Pr and Nd (Fig. 5d). APS mineral textures vary, appearing to depend greatly on the morphology of the original mineral that is being replaced. Coarser grains show excellent zonation in backscatter imaging (Figs. 2c, 2d, and 3), consistently retaining Ca-, Sr-rich cores, and REE-rich rims, indicating primary zonation from alkali-earth elements (M^{2+}) to REE (M^{3+}). Replacement of ore minerals formed during the ca. ~1590 Ma onset of mineralization strongly suggests that the APS minerals identified here are paragenetically late. Additionally, the consistent preferential replacement of chalcopyrite over other Cu-(Fe)-sulfides, as confirmed via preliminary mineral liberation analysis on materials spanning multiple years of mining activity, suggests some form of association between mineralogical zonation and/or fluid pathways within the deposit and the formation

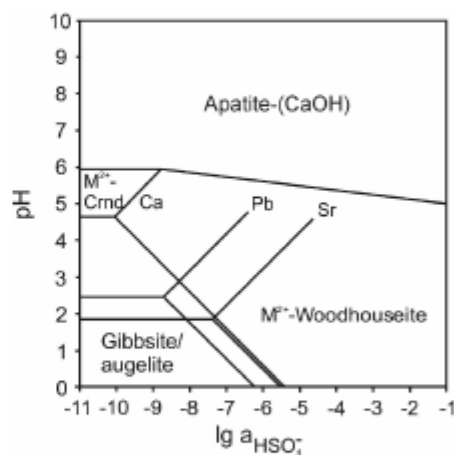


FIGURE 9. Garrel phase diagram of the system $\text{MO-Al}_2\text{O}_3\text{-P}_2\text{O}_5\text{-SO}_3\text{-H}_2\text{O}$ at 333 K. $[\text{H}_2\text{PO}_4] = 10^{-5.2}$ mol/L, $[\text{M}^{2+}] = [\text{Al}^{3+}] = 10^{-3}$ mol/L. $\text{M}^{2+} = \text{Ca}^{2+}$, Sr^{2+} , or Pb^{2+} , Crnd = crandallite, positions of gibbsite $[\text{Al}(\text{OH})_3]$, augeilite $[\text{Al}_2(\text{PO}_4)(\text{OH})_2]$, and hydroxylapatite $[\text{Ca}_5(\text{PO}_4)_3(\text{OH})]$ are shown. Modified after Schwab et al. (2005).

of the APS minerals discussed here. Alternatively, chalcopyrite may simply be more easily replaced by APS minerals than the other Cu-(Fe)-sulfides due to differences in redox potential and pH stability fields.

Florencite-(Ce) in the woodhouseite-svanbergite APS mineral assemblages discussed here fills a gap along with a REE mixing trend for minerals previously reported from Olympic Dam (Schmandt et al. 2017). This trend showed a defined separation between La/Ce-enriched florencite and Ce- (and subordinate La-) dominant bastnäsite. The Ce-dominant florencite in the woodhouseite-svanbergite APS mineral assemblages reported on here may, therefore, represent an intermediary between these two phases. It is suggested that while the Ce- and La-dominant APS mineral assemblages formed broadly simultaneously, migration of REE (likely sourced from pre-existing phosphates), Ca and Sr resulted in the formation of localized “compositional pockets” of Ce- and La-enriched florencite forming throughout the deposit.

The marked transition of REE-mineral speciation at Olympic Dam, from relatively simple REE-compounds like bastnäsite, through florencite, to the complex solid solutions represented by the alunite-supergroup minerals described here represents an illustrative example of an evolving mineralogical complexity with time in which successive mineral phases display ever greater structural and chemical complexity (Krivovichev et al. 2018).

This compositional variation is likely formed due to differences in thermodynamic stabilities of LREE end-members, indicated by their Gibbs free energies (Schwab et al. 1993) and by Goldschmidt's rule of ionic radii (Goldschmidt 1937), with thermodynamic stability of $\text{LREEAl}_3(\text{PO}_4)_3(\text{OH})_3$ end-members occurring in the order $\text{La} > \text{Nd} > \text{Ce} > \text{Sm} > \text{Pr} > \text{Eu} > \text{Gd}$. As such, the florencite previously reported from Olympic Dam (Schmandt et al. 2019a) in which the La and Ce components are roughly equal is interpreted to have formed as a combination of direct replacement of pre-existing REE bearing minerals and interaction with an acidic REE-bearing hydrothermal brine (Williams-Jones et al. 2012; Migdisov et al. 2016; Krneta et al. 2018; Schmandt et al. 2019a). Florencite-(Ce) in the APS assemblages reported here is suggested to have formed from a hydrothermal fluid that is either depleted in La or provides the conditions that favored its formation. The conditions at which florencite-(La) forms over florencite-(Ce) are accentuated at low pH with higher pH favoring increased stability of Ce-, Nd-, and Pr-florencite (Schwab et al. 1993). Additionally, Migdisov et al. (2016) have shown that the solubility of Ce, Pr, and Nd increases over that of La with the introduction of sulfate into solution indicating that the dissolution of sulfides (as mentioned above) may also play a key role in the local migration of REE.

The dominance of Sr within investigated APS minerals and the replacement of fluorapatite by svanbergite-dominant APS phases (Fig. 3) adds to evidence for formation from an acidic brine (Stoffregen and Alpers 1987) late in the evolution of the deposit. Additionally, and as discussed by Gaboreau et al. (2007), fluids with a relatively high f_{O_2} favor the incorporation of SO_4 and divalent A-site cations within APS minerals. In reducing environments, S occurs as a reduced species that cannot be incorporated into the APS structure (Gaboreau et al. 2007). Chloride salts are widely regarded as the main transport

ligand for metals in hydrothermal fluids, but while CaCl_2 and SrCl_2 are both extremely water soluble and likely available, Ca does not readily form crandallite, even in moderately acidic environments (Schwab et al. 2004, 2005). Schwab et al. (2005) have shown that decreasing pH and $a_{\text{HSO}_4^-}$ greatly favor goyazite formation, whereas woodhouseite formation is broadly favored by increasing $a_{\text{HSO}_4^-}$ (Fig. 9). Accordingly, we suggest the Sr-dominant phases discussed here formed in a moderately to strongly acidic (micro-)environment with relatively low $a_{\text{SO}_4^{2-}}$, at least relative to $a_{\text{PO}_4^{3-}}$.

APS minerals as RN scavengers

The EPMA data and nanoSIMS isotope maps represent compelling direct evidence for scavenging of RN (from ^{226}Ra down) by APS minerals, consistent with evidence presented elsewhere, both for products of radioactive decay (Kolitsch and Pring 2001, and references therein) and for removal of toxic metals from mine waste waters such as As and Ni (Monteagudo et al. 2003, 2006). Additionally, within the Oklo U deposit (Gabon), Dymkov et al. (1997) identified the migration and incorporation of ^{235}U fission products (Zr and LREE) into Ca-, Sr-, and Ba-bearing APS grains (where Sr and Ba are natural) from adjacent uraninite grains depleted in ^{235}U ($^{235}\text{U}/^{238}\text{U} = 0.0047$). The isotope maps (Figs. 6–8) also indicate that the RN is mobile at the scale of nanometers to micrometers and become separated from their U-bearing parent phases. Moreover, comparison of isotope maps for FC and CLD samples suggests that scavenging of dissolved RN, as a result of acid leaching, is achieved rapidly over a period of hours to days. These observations are critical for understanding the anomalous enrichment in ^{226}Ra and subsequent daughters relative to ^{238}U and ^{232}Th throughout Cu-(U)-ore processing. The inference is clearly that released RN are incorporated into APS phases (as well as barite; Schmandt et al. 2019b) during the leaching process, and also adsorbed onto the surfaces of other minerals, including Cu-(Fe)-sulfides (Rolloff et al. 2019). The significance of APS minerals throughout this process lies not only with their observed ability to adsorb/absorb RN, but also their insolubility, enabling them to survive and possibly even grow during leaching. Although such a statement is difficult to quantify, jarosite [$\text{KFe}_3(\text{OH})_6(\text{SO}_4)_2$], a near cousin of APS minerals, is known to form along with gypsum in leach plants, especially in tailings leach where its management can become problematic. There is also potential for formation of new Pb-bearing phases (hinsdalite and/or plumbogummite), or an increase in the hinsdalite and/or plumbogummite components of svanbergite and woodhouseite via replacement of Sr and/or Ca by Pb during acid leaching. Besold et al. (1992) suggest that the Ca^{2+} and Sr^{2+} cations may be replaced within crandallite-group minerals due to the open structure of the alunite-type crystal structure. Such a substitution mechanism is perhaps more viable between Pb and Ca than Pb and Sr and fits well with the models proposed by Schwab et al. (2004, 2005) in which crandallite and woodhouseite stability lessen with decreasing $a_{\text{HSO}_4^-}$ at pH ~2–4.

Isotope mapping shows that the correlation between ^{210}Pb and ^{206}Pb is relatively weak, particularly in CLD samples, as indicated by the mismatch of “hot spots” (Fig. 7). At the very least, this suggests distinct mechanisms and pathways for the micrometer-scale migration of late (i.e., within recent decades)

^{210}Pb throughout the APS minerals compared to the movement and concentration of ^{206}Pb over geological time. ^{210}Pb and ^{204}Pb , however, correlate well, thus indicating the sorption of common Pb via similar mechanisms to that of ^{210}Pb . Whether or not the sorption of common Pb occurred in situ or within the processing cycle remains uncertain.

IMPLICATIONS

The observed sorption properties of the Ca-Sr-dominant aluminum-phosphate-sulfate (APS) minerals and their ability to scavenge RN from the ^{238}U decay chain from ^{226}Ra onward highlights both the need to suppress natural APS phases in copper concentrates and prevent crystallization of new, anthropogenic APS phases during leaching or elsewhere during the processing-refining cycle. Alternatively, the capacity of APS minerals to scavenge radionuclides could be used in the removal of the products of U decay from processing streams, provided that these phases can be re-dissolved or otherwise removed from the final product.

ACKNOWLEDGMENTS AND FUNDING

Staff at Adelaide Microscopy are acknowledged for assistance with micro-analysis as well as referees for providing the knowledge basis for this work. We appreciate the constructive comments from Uwe Kolitsch, Frances Wall, an anonymous reviewer, and Associate Editor Daniel Harlov, which enabled us to clarify the results and interpretations. This research is a contribution of the ARC Research Hub for Australian Copper-Uranium, co-supported by BHP Olympic Dam, and the South Australian Mining and Petroleum Services Centre of Excellence.

REFERENCES CITED

- Bajnaoci, B., Serevs-Hartai, E., Molnar, F., and Nagy, G. (2004) Phosphate-bearing minerals in the advanced argillic alteration zones of high-sulphidation type ore deposits in the Carpatho-Pannonian region. *Acta Mineralogica-Petrographica, Szeged*, 45, 81–92.
- Bayliss, P., Kolitsch, U., Nickel, E.H., and Pring, A. (2010) Alunite supergroup: recommended nomenclature. *Mineralogical Magazine*, 74, 919–927.
- Beolld, E., Bieniek, D., and Ketrup, A. (1992) Synthetischer Crandallit. *Umweltwissenschaft und Schadstoff-Forschung*, 4(1), 14–16.
- Bhargava, S.K., Ram, R., Pownceby, M., Crocott, S., Ring, B., Tardio, J., and Jones, L. (2015) A review of acid leaching of uraninite. *Hydrometallurgy*, 151, 10–24.
- Blount, A.M. (1974) The crystal structure of crandallite. *American Mineralogist*, 59, 41–47.
- Ciobanu, C.L., Wade, B.P., Cook, N.J., Schmidt Mumm, A., and Giles, D. (2013) Uranium-bearing hematite from the Olympic Dam Cu-U-Au deposit, South Australia: A geochemical tracer and reconnaissance Pb-Pb geochronometer. *Precambrian Research*, 238, 129–147.
- Cook, N.J., Ehrig, K.J., Rollog, M., Ciobanu, C.L., Lane, D.J., Schmandt, D.S., Owen, N.D., Hamilton, T., and Grano, S. (2018) ^{206}Pb and ^{207}Pb in geological and related anthropogenic materials: implications for their mineralogical distribution in base metal ores. *Minerals*, 8, 211.
- Dymkov, Y., Holliger, P., Pagel, M., Gorshkov, A., and Artyukhina, A. (1997) Characterization of a La-Ce-Sr-Ca aluminous hydroxy phosphate in nuclear zone 13 in the Oklo uranium deposit (Gabon). *Mineralium Deposita*, 32, 617–620.
- Ehrig, K., McPhie, J., and Kamenetsky, V.S. (2012) Geology and mineralogical zonation of the Olympic Dam iron oxide Cu-U-Au-Ag deposit, South Australia. In F. Camus, J.W. Hedenquist, and M. Harris, Eds., *Geology and Genesis of Major Copper Deposits and Districts of the World, a Tribute to Richard Sillitoe*, 16, p. 237–267. Society of Economic Geologists Special Publication.
- Ehrig, K., Liebeseit, V., Macmillan, E., Lower, C., Kamenetsky, V.S., Cook, N.J., and Ciobanu, C.L. (2015) Uranium mineralogy versus the recovery of uranium at Olympic Dam. *Proceedings, The AusDMM International Uranium Conference 2015, Adelaide*, 75.
- Gaboreau, S., and Visillard, P. (2004) Prediction of Gibbs free energies of formation of minerals of the alunite supergroup. *Geochimica et Cosmochimica Acta*, 68, 3307–3316.
- Gaboreau, S., Cuney, M., Quirt, D., Beaufort, D., Patrier, P., and Mathieu, R. (2007) Significance of aluminum phosphate-sulfate minerals associated with U unconformity-type deposits: The Athabasca Basin, Canada. *American Mineralogist*, 92, 267–280.
- Georgieva, S., and Velinova, N. (2012) Alunite from the advanced argillic alterations in the Chelopech high-sulphidation epithermal Cu-Au deposit, Bulgaria: Chemistry, morphology and genetic significance. *Geochemistry, Mineralogy and Petrology*, 49, 17–31.
- (2014) Florencite-(Ce, La, Nd) and crandallite from the advanced argillic alteration in the Chelopech high-sulphidation epithermal Cu-Au deposit, Bulgaria. *Comptes rendus de l'Académie bulgare des sciences: sciences mathématiques et naturelles*, 67, 1669–1678.
- Goldschmidt, V.M. (1937) The principles of distribution of chemical elements in minerals and rocks. The seventh Hugo Müller Lecture, delivered before the Chemical Society on March 17, 1937. *Journal of the Chemical Society (Resumed)*, 655–673.
- Hikov, A., Lerouge, C., and Velinova, N. (2010) Geochemistry of alunite group minerals in advanced argillic altered rocks from the Atsarel porphyry copper deposit, Central Sredno-gorie. *Review of the Bulgarian Geological Society*, 71, 133–148.
- Jambor, J.L. (1999) Nomenclature of the alunite supergroup. *Canadian Mineralogist*, 37, 1323–1341.
- Jerdea, J.L. (2007) Uranium sequestration by aluminum phosphate minerals in unsaturated soils. *Materials Research Society Symposium Proceedings 985 (Scientific Basis for Nuclear Waste Management XXX)*, 461–466.
- Johnson, J.P., and Cross, K.C. (1995) U-Pb geochronological constraints on the genesis of the Olympic Dam Cu-U-Au-Ag deposit, South Australia. *Economic Geology*, 90, 1046–1063.
- Kato, T. (1971) The crystal structures of goyazite and woodhouseite. *Neues Jahrbuch für Mineralogie Monatshefte*, 241–247.
- Kato, T., and Miura, Y. (1977) The crystal structures of jarosite and svanbergite. *Mineralogical Journal*, 8(8), 419–430.
- Kolitsch, U., and Pring, A. (2001) Crystal chemistry of the crandallite, bendanite and alunite groups: a review and evaluation of the suitability as storage materials for toxic metals. *Journal of Mineralogical and Petrological Sciences*, 96, 67–78.
- Krneta, S., Ciobanu, C.L., Cook, N.J., Ehrig, K., and Kontonikas-Charos, A. (2016) Apatite at Olympic Dam, South Australia: a petrogenetic tool. *Lithos*, 262, 470–485.
- Krneta, S., Ciobanu, C.L., Cook, N.J., Ehrig, K., and Kontonikas-Charos, A. (2017) Rare earth element behaviour in apatite from the Olympic Dam Cu-U-Au-Ag deposit, South Australia. *Minerals*, 7, 135.
- Krneta, S., Ciobanu, C.L., Cook, N.J., and Ehrig, K. (2018) Numerical modeling of REE fractionation patterns in fluorapatite from the Olympic Dam deposit (South Australia). *Minerals*, 8, 342.
- Krivovichev, S.V., Krivovichev, V.G., and Hazen, R.M. (2018) Structural and chemical complexity of minerals: correlations and time evolution. *European Journal of Mineralogy*, 30, 231–236.
- Lane, D.J., Cook, N.J., Grano, S.R., and Ehrig, K. (2016) Selective leaching of penalty elements from copper concentrates: A review. *Minerals Engineering*, 98, 110–121.
- Lottermoser, B.G. (1995) Rare earth element mineralogy of the Olympic Dam Cu-U-Au-Ag deposit, Roxby Downs, South Australia; implications for ore genesis. *Neues Jahrbuch für Mineralogie, Monatshefte*, 371–384.
- Macmillan, E., Cook, N.J., Ehrig, K., Ciobanu, C.L., and Pring, A. (2016) Uraninite from the Olympic Dam IOCG-U-Ag deposit: linking textural and compositional variation to temporal evolution. *American Mineralogist*, 101, 1295–1320.
- Macmillan, E., Cook, N.J., Ehrig, K., and Pring, A. (2017) Chemical and textural interpretation of late-stage coffinite and brannerite from the Olympic Dam IOCG-Ag-U deposit. *Mineralogical Magazine*, 81, 1323–1366.
- Macnaughton, S.J., Ring, R.J., Day, A., Collier, D.E., and Tan, L.K.P. (1999) Optimization of the leach conditions for a copper/uranium ore. In B. Mishra, Ed., *Proceedings: EPD Congress 1999. The Minerals, Metals and Materials Society*, 309–322.
- Macnaughton, S.J., Tan, L., Day, A., and Ring, R.J. (2000) Modelling the leaching behaviour of an uranium ore. In E. Osberk and A.J. Oliver, Eds., *Uranium 2000: International Symposium on the Process Metallurgy of Uranium, Saskatoon*, p. 413–427. Canadian Institute of Mining, Metallurgy and Petroleum, Montreal, Quebec.
- Migdisov, A., Williams-Jones, A.E., Brugger, J., and Caporuscio, F.A. (2016) Hydrothermal transport, deposition, and fractionation of the REE: Experimental data and thermodynamic calculations. *Chemical Geology*, 439, 13–42.
- Monteagudo, J.M., Duran, A., Carmona, M.S., Schwab, R.G., and Higuera, P. (2003) Elimination of inorganic mercury from waste waters using crandallite-type compounds. *Journal of Chemical Technology and Biotechnology*, 78, 399–405.
- Monteagudo, J.M., Duran, A., Martin, I.S., and Schwab, R.G. (2006) Treatment of aqueous solutions containing nickel using crandallite-type compounds. *Journal of Chemical Technology and Biotechnology*, 81, 262–267.
- Oreskes, N., and Einaudi, M.T. (1990) Origin of rare earth element-enriched hematite breccias at the Olympic Dam Cu-U-Au-Ag deposit, Roxby Downs, South Australia. *Economic Geology*, 85(1), 1–28.
- Owen, N.D., Ciobanu, C.L., Cook, N.J., Slatery, A., and Basak, A. (2018) Nanoscale study of clausenthalite-bearing symplectites in Cu-Au-(U) ores: Implications for ore genesis. *Minerals*, 8(2), 67. doi:10.3390/min8020067.
- Pe-Piper, G., and Dolansky, L.M. (2005) Early diagenetic origin of Al phosphate-

- sulfate minerals (woodhouseite and crandallite series) in terrestrial sandstones, Nova Scotia, Canada. *American Mineralogist*, 90, 1434–1441.
- Platil, J., Sejkora, J., Čejka, J., Škoda, R., and Goliat, V. (2009) Supergene mineralization of the Měděňá uranium deposit, Krkonoše Mountains, Czech Republic. *Journal of Geosciences*, 54, 15–56.
- Poczatek, C., Kaufman, Z., and Lechene, C. (2009) OpenMIMS ImageJ Plugin Guide. Harvard Medical School, Boston, Massachusetts. <http://nrims.harvard.edu/files/nrims/files/openmims-manual.pdf>
- Rasmussen, B. (1996) Early-diagenetic REE-phosphate minerals (florenceite, gorceixite, crandallite, and xenotime) in marine sandstones; a major sink for oceanic phosphorus. *American Journal of Science*, 296, 601–632.
- Rollog, M., Cook, N.J., Gugliardo, P., Ehrig, K., and Kilburn, M. (2019) In situ spatial distribution mapping of radionuclides in minerals by nanoSIMS. *Geochemistry—Exploration, Environment, Analysis*; <https://doi.org/10.1144/geochem2018-038>.
- Schindelin, J., Arganda-Cameras, I., Frise, E., Kaynig, V., Longair, M., Pietzsch, T., Preibisch, S., Rueden, C., Saalfeld, S., Schmid, B., and Tinevez, J.Y. (2012) Fiji: an open-source platform for biological-image analysis. *Nature Methods*, 9, 676–682.
- Schindelin, J., Rueden, C.T., Hiner, M.C., and Eliceiri, K.W. (2015) The ImageJ ecosystem: An open platform for biomedical image analysis. *Molecular Reproduction and Development*, 82, 518–529.
- Schmandt, D.S., Cook, N.J., Ehrig, K., Ciobanu, C.L., Wade, B.P., Gilbert, S., and Kamensetky, V.S. (2017) Rare earth element fluorocarbonate minerals from the Olympic Dam Cu-U-An-Ag deposit, South Australia. *Minerals*, 7, 202.
- Schmandt, D.S., Cook, N.J., Ciobanu, C.L., Ehrig, K., Wade, B.P., Gilbert, S., and Kamensetky, V.S. (2019a) Rare earth element phosphate minerals from the Olympic Dam Cu-U-An-Ag deposit, South Australia: Recognizing temporal-spatial controls on REE mineralogy in an evolved IOCG system. *Canadian Mineralogist*, 57, 3–24.
- Schmandt, D.S., Cook, N.J., Ehrig, K., Gilbert, S., Wade, B.P., Rollog, M., Ciobanu, C.L., and Kamensetky, V.S. (2019b) Uptake of trace elements by baryte during copper ore processing: A case study from Olympic Dam, South Australia. *Minerals Engineering*, 135, 83–94.
- Schwab, R.G., Götz, C., Herold, H., and Pinto de Oliveira, N. (1993) Compounds of the crandallite type: thermodynamic properties of Ca-, Sr-, Ba-, Pb-, La-, Ce- to Gd-phosphates and -arsenates. *Neues Jahrbuch für Mineralogie, Monatshefte*, 551–568.
- Schwab, R.G., Pimpl, T., Schmkow, H., Stolle, A., and Breiteringer, D.K. (2004) Compounds of the crandallite type: Synthesis, properties and thermodynamic data of pure crandallite and woodhouseite. *Neues Jahrbuch für Mineralogie, Monatshefte*, 385–409.
- Schwab, R.G., Pimpl, T., Schmkow, H., Stolle, A., and Breiteringer, D.K. (2005) Compounds of the crandallite type: Synthesis, properties and thermodynamic data of Ca-Sr-Ba-Pb-(arseno)-woodhouseites. *Neues Jahrbuch für Mineralogie, Abhandlungen*, 181, 207–218.
- Stoffregen, R.E., and Alpers, C.N. (1987) Woodhouseite and svanbergite in hydrothermal ore deposits: products of apatite destruction during advanced argillic alteration. *Canadian Mineralogist*, 25, 201–211.
- Triplehorn, D.M., Stanton, R.W., Ruppert, L.F., and Crowley, S.S. (1991) Volcanic ash dispersed in the Wyodak-Anderson coal bed, Powder River basin, Wyoming. *Organic Geochemistry*, 17, 567–575.
- Verdugo-Iñal, M.R., Ciobanu, C.L., Cook, N.J., Ehrig, K., Courtney-Davies, L., and Gilbert, S. (2017) Textures and U-W-Su-Mo signatures in hematite from the Cu-U-An-Ag orebody at Olympic Dam, South Australia: defining the archetype for IOCG deposits. *Ore Geology Reviews*, 91, 173–195.
- Williams-Jones, A.E., Migdisov, A.A., and Samson, I.M. (2012) Hydrothermal mobilization of the rare earth elements—a tale of “ceria” and “yttria”. *Elements*, 8, 355–360.
- Xing, Y., Mei, Y., Etschmann, B., Liu, W., and Brugger, J. (2018) Uranium transport in F-Cl-bearing fluids and hydrothermal upgrading of U-Cu ores in IOCG deposits. *Geofluids (special issue)* (2018) Article ID 6835346, 22 pages.
- Xing, Y., Etschmann, B., Liu, W., Mei, Y., Shvarov, Y., Testemale, D., Tomkins, A., and Brugger, J. (2019) The role of fluorine in hydrothermal mobilization and transportation of Fe, U and REE and the formation of IOCG deposits. *Chemical Geology*, 504, 158–176.
- Zema, M., Collegari, A.M., Tarantino, S.C., Gasparini, E., and Ghigna, P. (2012) Thermal expansion of alunite up to dehydroxylation and collapse of the crystal structure. *Mineralogical Magazine*, 76, 613–623.

MANUSCRIPT RECEIVED MAY 14, 2019

MANUSCRIPT ACCEPTED JULY 31, 2019

MANUSCRIPT HANDLED BY DANIEL HARLOV

Endnote:

¹Deposit item AM-19-127116, Supplemental Material. Deposit items are free to all readers and found on the MSA website, via the specific issue's Table of Contents (go to http://www.minersoc.org/MSA/AmMin/TOC/2019/Dec2019_data/Dec2019_data.html).

CHAPTER 5

A SPONGE FOR RADIONUCLIDES: A STUDY ON THE DYNAMIC UPTAKE OF LEAD BY SYNTHETIC ALUMINIUM-PHOSPHATE- SULPHATES

Nicholas D. Owen, Nigel J. Cook, Rahul Ram, Barbara Etschmann, Kathy Ehrig, Danielle S.

Schmandt, Mark Rollog, Paul Guagliardo, Joël Brugger

Statement of Authorship

Title of Paper	A sponge for radionuclides: a study on the dynamic uptake of lead by synthetic aluminium-phosphate-sulphates		
Publication Status	<input type="checkbox"/> Published	<input type="checkbox"/> Accepted for Publication	
	<input checked="" type="checkbox"/> Submitted for Publication	<input type="checkbox"/> Unpublished and Unsubmitted work written in manuscript style	
Publication Details	Applied Geochemistry, submitted 11 th February 2020		

Principal Author

Name of Principal Author (Candidate)	Nicholas D. Owen		
Contribution to the Paper	Idea conception, performed analytical work, carried out data collection and analysis, wrote the the manuscript.		
Overall percentage (%)	55%		
Certification:	This paper reports on original research I conducted during the period of my Higher Degree by Research candidature and is not subject to any obligations or contractual agreements with a third party that would constrain its inclusion in this thesis. I am the primary author of this paper.		
Signature		Date	25/08/2019

Co-Author Contributions

By signing the Statement of Authorship, each author certifies that:

- the candidate's stated contribution to the publication is accurate (as detailed above);
- permission is granted for the candidate to include the publication in the thesis; and
- the sum of all co-author contributions is equal to 100% less the candidate's stated contribution.

Name of Co-Author	Nigel J. Cook		
Contribution to the Paper	Idea conception, helped define direction of research, supervised development of the work, assisted with writing of the manuscript. 5%		
Signature		Date	27/8/19

Name of Co-Author	Rahul Ram		
Contribution to the Paper	Idea conception, helped define direction of research, aided in data collection, supervised development of the work, assisted with writing of the manuscript. 10%		
Signature		Date	29/8/19

Please cut and paste additional co-author panels here as required.

Name of Co-Author	Barbara Estchmann		
Contribution to the Paper	Aided in the collection, processing and collection of analytical data. 5%		
Signature		Date	29 Aug 2019

Name of Co-Author	Kathy Ehrig		
Contribution to the Paper	Provided sample material and helped evaluate and edit the manuscript. 5%		
Signature		Date	27 Aug 2019

Name of Co-Author	Danielle Schmandt		
Contribution to the Paper	Aided in the direction of the research and conceptualization of ideas. 2.5%		
Signature		Date	8/29/2019

Name of Co-Author	Mark Rollog		
Contribution to the Paper	Assisted with method development and data interpretation. 2.5%		
Signature		Date	28 08 19

Name of Co-Author	Paul Guagliardo		
Contribution to the Paper	Aided in the operation of analytical equipment and data interpretation. 5%		
Signature		Date	28/08/2019

Name of Co-Author	Joel Brugger		
Contribution to the Paper	Idea conception, helped define direction of research, aided in data collection, supervised development of the work, assisted with writing of the manuscript. 10%		
Signature		Date	29/8/19

Please cut and paste additional co-author panels here as required.

A sponge for radionuclides: a study on the dynamic uptake of lead by synthetic aluminium-phosphate-sulphates

Nicholas D. Owen^{1,2,*}, Nigel J. Cook¹, Rahul Ram^{2,*}, Barbara Etschmann², Kathy Ehrig³,

Danielle S. Schmandt¹, Mark Rollog¹, Paul Guagliardo⁴, Joël Brugger²

¹*School of Chemical Engineering and Advanced Materials, The University of Adelaide, SA 5005,*

Australia

²*School of Earth, Atmosphere and Environment, 9 Rainforest Walk, Monash University, VIC*

2800, Australia

³*BHP Olympic Dam, Adelaide, SA 5000, Australia*

⁴*Centre for Microscopy, Characterisation, and Analysis, University of Western Australia, 35*

Stirling Highway, Crawley, WA 6009, Australia

⁵*Adelaide Microscopy, The University of Adelaide, SA 5005, Australia*

*Corresponding author email address: nicholas.owen@monash.edu; rahul.ram@monash.edu

ABSTRACT

The ability of aluminium-phosphate-sulphate (APS) phases to preferentially sorb lead and its radionuclides, particularly ²¹⁰Pb, from metallurgical processing streams has been recently recognized. This suggests that APS minerals may be suitable for the removal of radionuclides and heavy metals from environmental and anthropogenic processes. We investigated the Pb sorption capabilities of APS with different Ca:Sr and SO₄:PO₄ ratios over a range of Pb concentrations (10-1000 ppm) and pH (1.5-5.5) typical of metallurgical processes and acid drainage conditions. Through a combination of characterization techniques including electron probe microanalysis, (laser ablation-) inductively coupled plasma mass spectrometry and x-ray absorption spectroscopy, we confirm the rapid incorporation of Pb into the crystal lattice of APS phases. We also provide a mechanistic pathway for the sorption mechanism, with Pb sorption favoured at pH 3.5-5.5 via the

direct replacement of lattice-bound Ca by Pb within the APS crystal structure. The observed Pb-incorporation dynamics of APS minerals, along with their insolubility and high thermodynamic stabilities, support the use of APS minerals as a novel agent for the uptake of Pb, radiogenic and non-radiogenic, from process-, surface-, and groundwaters. Since ^{210}Pb quickly enters the crystal structure of environmentally stable APS minerals, these phases have much potential for long-term storage of ^{210}Pb waste.

Keywords: aluminium-phosphate-sulphate phases; sorption; radionuclides; lead; waste storage; remediation

1. Introduction

Aluminium phosphate sulfate (APS) minerals, members of the alunite supergroup of minerals, have the nominal formula $\text{MAl}_3(\text{PO}_4)_y(\text{SO}_4)_{2-y}(\text{OH},\text{H}_2\text{O})_6$ and form a broad range of solid solutions by varying ratios of phosphate-sulfate and incorporating mono-, di-, and trivalent cations (e.g. H_3O^+ , Na^+ , K^+ , Rb^+ , Ag^+ , Ca^{2+} , Sr^{2+} , Ba^{2+} , Pb^{2+} , Hg^{2+} , Bi^{3+} , REE^{3+}) within their M-site (Kolitsch and Pring 2001). APS minerals, both natural and synthetic, have garnered significant interest as effective sorbents of deleterious products from mine waste streams (Monteagudo et al. 2003; Owen et al. 2019) and nuclear fission (Dymkov et al. 1997).

Since 2006, the International Atomic Energy Agency (IAEA) recommends that radionuclides from the U- and Th-series be regulated for products and wastes that contain $>1 \text{ Bq.g}^{-1}$ (IAEA 2006). This includes large volumes of products and wastes from the mineral, coal, oil and gas industries that can contain higher activities (Ram et al. 2013, 2019; Cook et al. 2018), with particular reference to the relatively long half-life U-decay daughter product ^{210}Pb (half-life—21.2 y). It is thus essential to not only suppress mineral phases known to carry these radionuclides (RN) during processing, but also search for novel ways to eliminate or reduce ^{210}Pb (and ^{210}Po), e.g., via sequestration into a solid phase that can be separated, in industrial products and waste.

Presently, a number of ion exchange resins, synthetic zeolites (Dąbrowski et al. 2004; Draa et al. 2004), and mineral phases such as those in the pyrochlore supergroup (McMaster et al. 2018) have been investigated for the extraction of RN from industrial wastes within a range of operating

conditions. Their long-term stability is, however, still unknown and they also do not selectively favour Pb (and its isotopes) over other U and Th-daughter products. The use of inorganic adsorbents, namely phosphogypsum, clay, bauxite and barite, to extract RN from acid mine drainage water has been studied by Nascimento et al. (2006). The sulfate phases phosphogypsum and barite were shown to return the most promising results for ^{226}Ra , ^{228}Ra , and ^{210}Pb . RN were however partially returned to solution with freshwater reversibility experiments, indicating that these minerals may not be viable as long-term storage solutions.

Recently, Owen et al. (2019) showed that natural Ca- and Sr-bearing APS minerals act as hosts for ^{210}Pb within the Cu-U-Au-Ag metallurgical processing plant at Olympic Dam, South Australia. This work demonstrated the potential of APS minerals for radionuclide removal, however the mechanism of Pb incorporation into APS minerals remains unconstrained. Most APS minerals are stable up to 400-500 °C and remain insoluble over a wide range of pH and E_h conditions (Kolitsch and Pring 2001). As such, if Pb is shown to rapidly become lattice-bound within synthetic APS phases through a diffusion and cation exchange mechanism, APS minerals may provide a highly effective extraction and long-term storage solution for ^{210}Pb from industrial products and wastes.

This study aims to identify the optimal conditions for Pb scavenging by APS minerals under conditions relevant for industrial mineral processing, and the mechanism of sorption and subsequent crystal incorporation of Pb into APS minerals. To this end, we performed experiments involving the addition of synthetic (Pb-free) APS minerals of varying composition to Pb-bearing solutions with varying pH, and constrained the mechanism of Pb removal using synchrotron X-ray absorption spectroscopy (XAS) and additional characterisation techniques.

2. Background

2.1 APS crystallography

Only solid-solutions between Ca-, Sr- and Pb-bearing APS phases were considered in this study. Crandallite group endmembers ($\text{MA}_3\text{X}_2(\text{OH},\text{H}_2\text{O})_6$) contain PO_4 in the X-site, while woodhouseite and other beudantite group endmembers contain equal amounts of SO_4 and PO_4 .

Their crystal structure comprises hexagonal sheets of corner-sharing $\text{AlO}_2(\text{OH})_4$ octahedra (Fig. 1a,b). Phosphate/sulfate tetrahedra lie above and below the octahedral sheets, corner-sharing three oxygens with the Al-octahedra; the remaining unshared O points alternatively into the hexagonal gaps formed by the Al-octahedra (Fig. 1a,b). Between these sheets lie 4-, 6-, and 12-fold coordination M-sites (Fig. 1c) that can host cations of various ionic radii and charge, enabling the formation of a broad range of solid solutions.

Figure 1

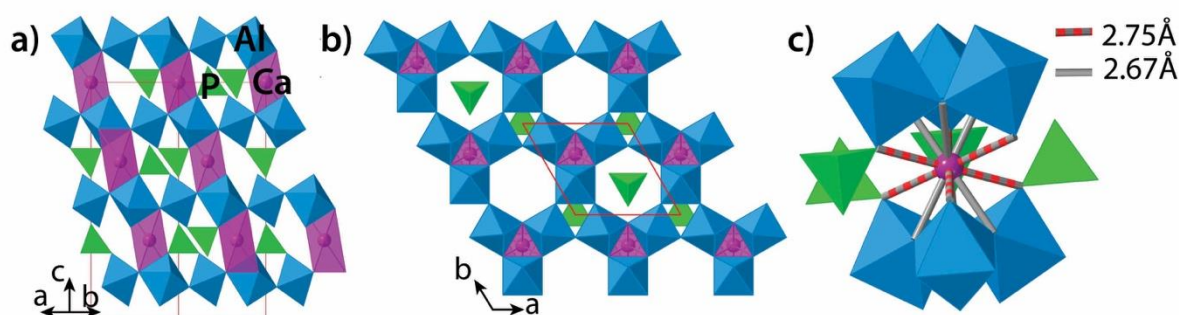


Figure 1: The crystal structure of APS minerals, down the [110] (a) and [001] (b) directions; and (c) coordination around the M-site, showing 6+6 coordination. Violet: M-site cations (Ca, Sr, Pb); maroon: Al; yellow/red: P/S; light grey: O(1); medium-grey: O(2); dark-grey: O(3) (OH/H₂O). Note 12-fold coordination of M-site cations, electrostatically and H-bonded to OH, H₂O and O within $\text{AlO}_2(\text{OH})_4$ octahedra and phosphate/sulfate tetrahedra. Data from Kato (1971).

2.2. Evidence for radionuclide scavenging by natural APS minerals

²²⁶Ra and ²¹⁰Pb incorporation into natural APS from the acid leach stage of the Olympic Dam processing circuit has recently been highlighted on the basis of nanoSIMS results (Owen et al. 2019). The giant Olympic Dam deposit currently contains the World's largest U resource and the fifth largest copper resource (Ehrig et al. 2015). The leach conditions at Olympic Dam are ~55 °C, pH -1.5, E_h of ~640 mV, contact time 8–12 h (MacNaughton et al. 1999, 2000; Bhargava et al. 2015); leaching also depends on the complex mineralogy of the initial feed (Ehrig et al. 2015). During the sulfuric acid leaching of copper sulphide concentrates, U-minerals and fluorite are dissolved. Daughter radionuclides hosted within these parent minerals are also released but become decoupled from their parent isotopes due to major differences in their chemical properties

(Cook et al. 2018). This is highlighted in Figure 2, which shows contrasting distributions of ^{238}U , ^{226}Ra , ^{210}Pb , non-radiogenic Pb represented by ^{204}Pb , and ^{40}Ca within a natural REE-Ca-Sr-bearing APS phase. The ^{210}Pb distribution, mimicked to some extent by that of ^{226}Ra , is closest to that of common Pb and Ca and unlike that of ^{238}U . The results clearly show incorporation has taken place during the 8-12 h leach step, indicating the capacity of APS minerals to rapidly and preferentially scavenge radionuclides under process conditions.

Figure 2

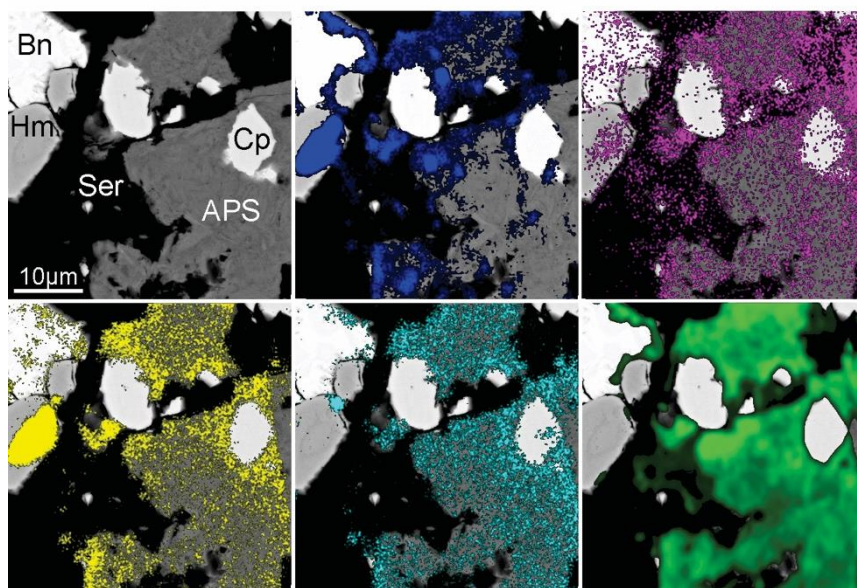


Figure 2: BSE image (top left) taken of a sample from the acid leach in the BHP Olympic Dam processing plant, showing natural APS grains surrounding grains of chalcopyrite (Cp) and sericite (Ser). Also imaged is a neighbouring bornite (Bn) grain with associated hematite (Hm). NanoSIMS data for ^{238}U (blue), ^{226}Ra (pink), ^{204}Pb (yellow), ^{210}Pb (cyan), and ^{40}Ca (green) are overlaid onto the BSE image for reference. Note the occurrence of ^{226}Ra within multiple mineral types compared to the more restricted distribution of ^{210}Pb , and presence of common ^{204}Pb within hematite and bornite where no ^{210}Pb is observed. For data acquisition methods and sample descriptions refer to Owen et al. (2019).

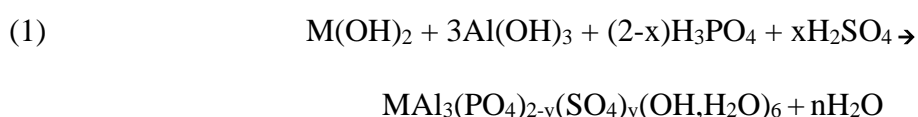
While APS phases form a broad range of solid solutions in nature, with named Ca-, Sr-, Ba-, Pb- and LREE-dominant endmembers, endmember compositions display significant differences with respect to their thermodynamic stability ($\Delta_f G$), with the Pb-bearing phases, plumbogummite ($\text{PbAl}_3(\text{PO}_4)_2(\text{OH})_5 \cdot (\text{H}_2\text{O})$) and hinsdalite ($\text{PbAl}_3(\text{PO}_4)(\text{SO}_4)(\text{OH})_6$), forming the most stable of these phases. The respective stabilities of Pb-bearing and the comparatively unstable Ca-bearing APS phases present the most significant of these differences (Schwab et al. 1993, 2005; Gaboreau

and Vieillard 2004), thus providing a ‘thermodynamic gradient’ that may be acted upon for the incorporation of Pb by Ca-bearing APS. APS crystal chemistry also explains the high selectivity of APS minerals towards Pb in Cu-rich environments; although Cu(II) can substitute on the Al-site of alunite-group minerals (e.g., mineral Beaverite-(Cu), $\text{Pb}(\text{Fe}^{3+}_2\text{Cu})(\text{SO}_4)_2(\text{OH})_6$; Bayliss et al. 2010), APS minerals at Olympic Dam incorporate less than ~1 wt% CuO (Owen et al. 2019), although the process waters contain trace Pb(II) concentrations ($\leq \sim 30$ mg/L) but are enriched in Cu(II) (≥ 5 -30 g/L).

3. Materials and methods

3.1. Synthesis of APS minerals

APS phases were synthesised by modifying existing recipes (Schwab et al. 1991, 2004) to generate crystals with varying ratios of Ca:Sr and $\text{SO}_4:\text{PO}_4$, in order to test the role of compositional variability on the sorption of Pb. Reagent grade $\text{Ca}(\text{OH})_2$, $\text{Sr}(\text{OH})_2$ and $\text{Al}(\text{OH})_3$ were added to 4 mL of 1 M $\text{H}_2\text{SO}_4 + \text{H}_3\text{PO}_4$ in order to obtain the desired product stoichiometry (Appendix D, Table 1; Equation 1). The mixtures were placed into 20 mL teflon-lined hydrothermal bombs, then diluted with milli-Q water (18.2 M Ω .cm resistivity), and placed in a 200 °C oven at water saturated pressures (~15 bar) for 6 months.



3.2. Pb-sorption experiments

Pb-sorption experiments were run via the addition of 50 mg dried APS powder into 50 mL of stock solution. Nine stock solutions with varied pH (1.5, 3.5, 5.5), prepared from reagent grade HNO_3 and milli-Q water, and Pb concentrations $[\text{Pb}_{\text{aq}}]_0$ of 10, 100, and 1000 ppm were prepared; Pb was added as $\text{Pb}(\text{NO}_3)_2$. $\text{Pb}(\text{NO}_3)_2$ was chosen because it readily dissociates, and to limit the number of complexing ligands in solution, which may affect the uptake of Pb by APS phases with varying pH (Neumann 2012). The choice of pH was based on thermodynamic calculations by Schwab et al. (2005) who suggested that a pH ranging between 1.5 and 5.5 is optimal for the

formation of Pb-bearing APS phases. The choice of Pb concentrations were typical of those encountered in a range of natural and anthropogenic environments (Jaworowski 1967). These mixtures were placed on an orbital shaker and sampled regularly up to a final time of 5 days. The sample powders were then rinsed and filtered using milli-Q water and ethanol and dried at ambient temperature (21 °C).

Further experiments were conducted using natural woodhouseite from the type locality (Champion mine, California; Lemmon 1937). Grains ~200 µm in size were hand-picked under an optical microscope. Single grains were exposed to a 1000 ppm Pb (from Pb(NO₃)₂) solution at a pH of 3.5, at ambient-T (similar conditions to synthetic APS) and hydrothermal (200°C) conditions in a teflon-lined autoclave.

Note that all experiments were conducted using stable (non-radioactive) Pb from Pb(NO₃)₂ (i.e., a mixture of 52.4% ²⁰⁸Pb, 22.1% ²⁰⁷Pb, 24.1% ²⁰⁶Pb, and 1.4% ²⁰⁴Pb). However, the results do apply equally to the highly radioactive ²¹⁰Pb isotope, as mass-dependant fractionation of Pb isotopes is negligible (<<1 per mill).

3.3.Characterisation of solids and solutions

Detailed information on analytical methods is provided in Appendix D. Solutions were analyzed by Inductively Coupled Mass Spectrometry (ICP-MS; Thermo Scientific iCAP-Q) following dilution to <1000 ppb into 50 mL vials of 2 wt% HNO₃. Isotopes analysed were ²⁷Al, ⁴⁴Ca, ⁸⁸Sr, and Pb isotopes ²⁰⁴Pb, ²⁰⁶Pb, ²⁰⁷Pb and ²⁰⁸Pb (in equal concentration from native Pb source). Multiple Pb isotopes were measured to check data quality as isotope ratios were not expected to change between analyses.

The phase purity of the solids was checked using X-ray powder diffraction (XRD; D8 Advance Eco with Co radiation source). Quantitative compositional data for Ca, Sr, Pb, Al, P and S were obtained using a Cameca SX-Five electron probe microanalyzer (EPMA), equipped with 5 wavelength-dispersive spectrometers and operated at 15 keV, 20 nA. Laser Ablation Inductively Coupled Mass Spectrometry (LA-ICP-MS), with a spot diameter of 13 µm, was used for the

quantitative analysis of trace elements within individual mineral grains. For EMPA and LA-ICP-MS analyses, samples were embedded in epoxy resin, cut, and polished.

3.4. XAS data collection and analysis

Lead L_{III}-edge (13.035 eV) X-ray Absorption Near Edge Structure (XANES) and Extended X-ray Absorption Fine Structure (EXAFS) data were collected at the XAS beamline, Australian Synchrotron, Melbourne, Australia. Where possible, measurements were conducted in transmission mode (ion chambers), however, in samples with low Pb concentrations, fluorescence data were used (100 elements Canberra solid state Ge detector). A cryogenic holder (T ~ 5 K) was used for the prevention of beam damage and to reduce thermal motion. Repeat spectra showed no significant difference. XANES and EXAFS data were analysed with the HORAE package (Ravel and Newville, 2005) using FEFF version 9 (Rehr et al., 2009).

4. Results

4.1. Composition of synthesised APS phases

XRD (Appendix D.1) confirms that the products consist predominantly of crystalline APS. Small amounts of augelite, anhydrite and celestine were present in all runs and could not be eliminated (Figure 3a,b). Based on EPMA micro-analyses (Appendix D, Tables 2, 3), the Sr-bearing phase, APS(I), regularly incorporated excess Al (up to 5.64 apfu); Sr was under-represented in the M-site (Figure 4a,c). In all APS phases, excess Al was associated with a reduction in $\sum M^{2+}$, indicating occupancy of Al within the M-site. S was also elevated within these Al-rich compositions, resulting in low P/(S+P) ratios (Figure 4b,c). Many APS grains contained Al-S-rich cores, which evolve to stoichiometric APS at the rims (Figure 3b-d). In general, APS with elevated P over S and Al values close to the stoichiometric value of 3 incorporated the highest concentrations of Ca in their M-site (Figure 4e-f).

Figure 3

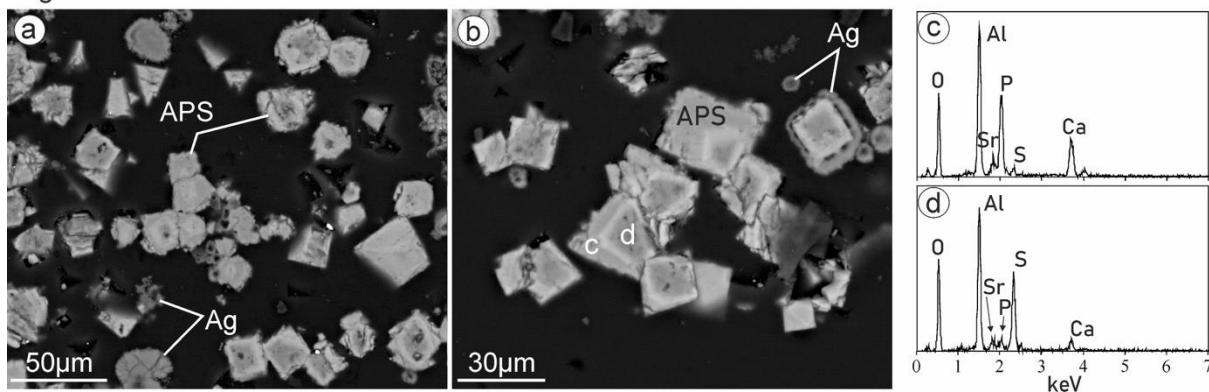


Figure 3: SEM-BSE images of synthetic APS phases showing (a) an overview of APS(I), note pseudo-cubic morphology of the APS grains formed by the trigonal-hexagonal structure, and the presence of accessory augelite (Ag); and (b) grains from APS(II) which are distinctively backscatter zoned, with composition ranging from Ca, Sr and P rich APS at the rims (c) to dark cores that are Al and S rich (d).

Figure 4

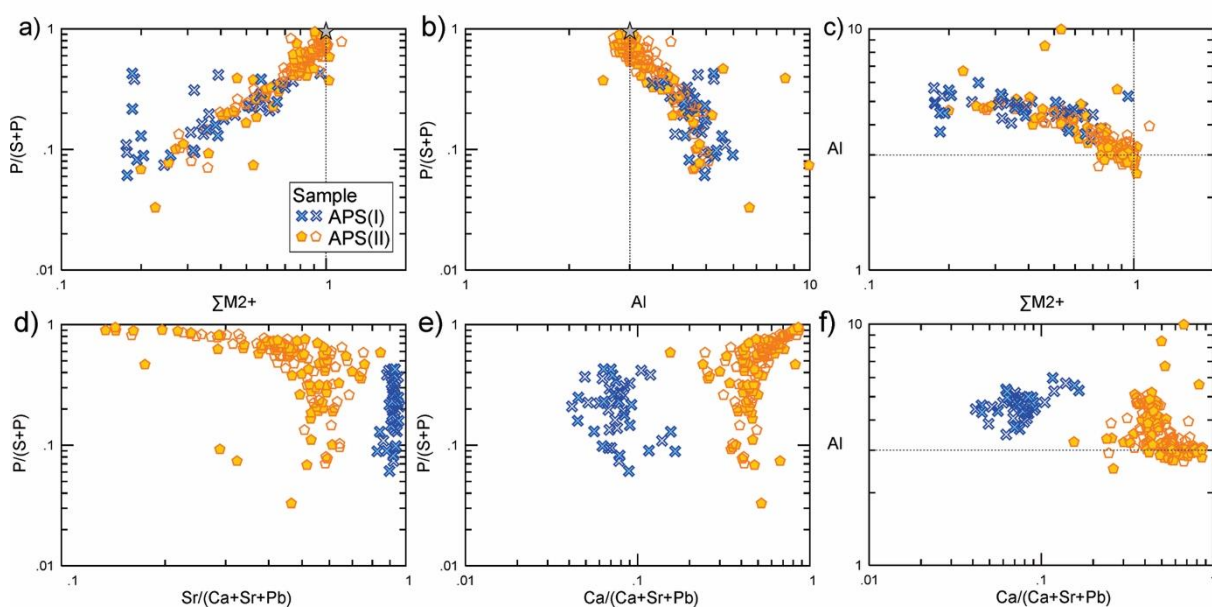


Figure 4: EPMA data for synthetic APS phases showing (a) the sum of metals in the M-site as a function of $P/(S+P)$; (b) Al concentration as a function of $P/(S+P)$; (c) the negative correlation between the sum of metals in the M-site and Al; (d) and (e) the relative concentrations Sr and Ca in the M-site (respectively) compared to $P/(S+P)$; and (f) Relative Ca concentration compared with Al concentration. Compositions which trend towards $\Sigma M^{2+} = 1$ and $Al = 3$ apfu are indicated by the dotted lines on a, b, c and f. Stoichiometric values for endmember M^{2+} -crandallite are indicated by the grey stars on (a) and (b). Symbols for sample types are provided in (a), closed symbols represent analyses that contain Pb while open symbols contained no Pb. Note APS(I) the presence of minor concentrations of Ca, likely due to contamination in the $Sr(OH)_2$ starting material.

4.2. Pb-sorption by synthetic APS phases

A series of experiments were conducted in order to examine Pb-sorption onto APS minerals as a function of Pb concentration (10-1000 ppm) and solution pH (1.5-3.5). All experiments were conducted at ambient temperature for a period of 5 days; samples of the solutions were taken at 2, 4, 8, 24 and 48 hours, 3 days, and finally after 5 days. The resulting changes in dissolved Pb concentration are compared to the initial Pb concentrations in Figure 5.

Figure 5

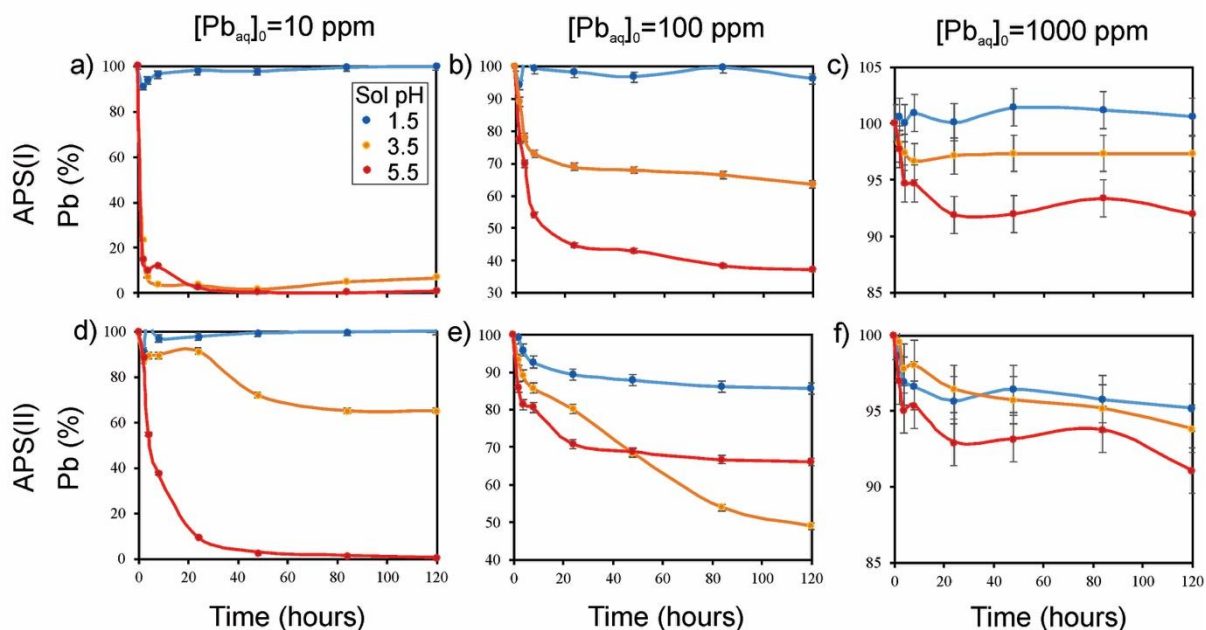


Figure 5: Solution-ICP-MS data for experiments measuring Pb-sorption by synthetic APS phases (a-c) (Sr-APS) APS(I), and (d-f) (CaSr-APS) APS(II). The experiments were run at ambient temperature with varying $[Pb_{aq}]_0$ (10, 100 and 1000 ppm) and pH (1.5, 3.5, 5.5) as indicated. Results are presented as a time series showing the percentage of Pb removed from solution. Note in experiments with initial conditions $[Pb_{aq}]_0 = 1000$ ppm and pH = 5.5, the presence of characteristic ‘humps’ following initial Pb sorption onto APS surfaces.

Experiments at pH 1.5 showed negligible scavenging of Pb onto APS(I) (Figure 5a-c), irrespective of Pb concentration. This is likely due to a positive charge (i.e. by H^+) bound to the mineral surfaces resulting in the rejection of Pb at this pH (Appendix D.2). Negligible Pb sorption took place at pH 1.5 and $[Pb_{aq}]_0=10$ ppm in the case of APS(II) (Figure 5d), but at higher $[Pb_{aq}]_0$ (100-1000 ppm) Pb sorption increased up to 10-15% (Figures 5e,f). Although the (Ca,Sr)-bearing

phases retain some capacity for Pb sorption at pH 1.5, a pH of 1.5 is generally ineffective in promoting sorption of Pb onto APS minerals.

APS(I) removed Pb from solution rapidly at pH 3.5, with most Pb-sorption occurring within the first 8 hours of contact. At $[Pb_{aq}]_0=10$ and 1000 ppm (Figure 5a,c), the rapid sorption of Pb by APS(I) was followed by a gradual return of Pb to solution, while a moderate downwards trend followed in solutions that contained 100 ppm $[Pb_{aq}]_0$ (Figure 5b), indicating in all cases a trend towards an equilibrium state between dissolved and sorbed Pb.

Pb-sorption trends for APS(II) differed from APS(I) across all $[Pb_{aq}]_0$ ranges, showing small 'humps' following the initial steep downwards trends. These 'humps' are typically observed within the first 4-24 hours of contact with Pb-bearing solution. At pH 3.5 and $[Pb_{aq}]_0=10$ ppm, APS(I) was most effective (Figure 5a), almost completely removing Pb from solution while at $[Pb_{aq}]_0=100$ ppm, APS(II) was almost twice as effective as APS(I) with 50% removal of Pb from solution (Figures 5e and b, respectively). In the experiment run at $[Pb_{aq}]_0=1000$ ppm and pH 3.5, APS(II) was still removing Pb from solution at the experiment cut-off time of 120 hours (Figure 5f).

At pH 5.5 and $[Pb_{aq}]_0=10$ ppm, <10% Pb remained in solution after 24 hours for APS(I), and 60 hours for APS(II). At 100 ppm Pb and pH 5.5, APS(I) was the most effective Pb-sorbing phase, removing ~60% of Pb compared with 30-35% for APS(II). At pH 5.5 and $[Pb_{aq}]_0=1000$ ppm, however, both APS phases performed equally, removing ~10% of Pb from solution, though APS(II)'s Pb-sorption trend was still clearly progressing downward at the experiment cut off time, indicating that the reaction had not yet come to an equilibrium state. Within pH 5.5 solution with $[Pb_{aq}]_0=1000$ ppm, Pb-sorption by APS(I/II) followed an undulating trend in which Pb is progressively sorbed by the APS phases and then returned to solution (Figure 5c,f).

4.3. Composition of Pb-sorbed APS phases

Targeted LA-ICP-MS coupled with EPMA analysis was selected as the best means for determining Pb concentration within the synthetic APS phases. Quantification via EPMA proved difficult, due to the small grain size of the synthesised crystals (15-50 μm , Figure 3), and to the

location of the highest Pb concentrations on the edges of the grains where analytical results were affected by complex interface effects in the electron-beam interaction volume. As such, EPMA data for Pb-concentration is spotty, and once bad totals had been removed, did not show clear overall trends with respect to fluid pH, aqueous Pb concentration, or host material. Nevertheless, the data (Appendix D, Table 3) showed that Pb concentrations in APS phases varied by orders of magnitude (50-1608 ppm), and formed clear trends according to concentrations of Al, P, S, Ca and Sr within individual grains (Figure 6). The highest Pb concentration, 4784 ppm Pb, occurred within (Ca,Sr)-bearing phases from $[Pb_{aq}]_0 = 1000$ ppm solution and pH 5.5. Grains from APS(I) also showed high concentrations of Pb (up to 676 ppm PbO) within samples from pH 5.5. The sorption of Pb by APS phases appeared to depend greatly on the relative concentrations of P and S, with the highest Pb concentrations recorded in samples with elevated S/P (Figure 6a). Grain with excess Al and under-representation of M^{2+} in the M site ($\sum M^{2+} < 1$) were also shown to incorporate Pb, indicating that Al^{3+} may be easily replaced from within the M-site (Figure 6b-c).

Figure 6

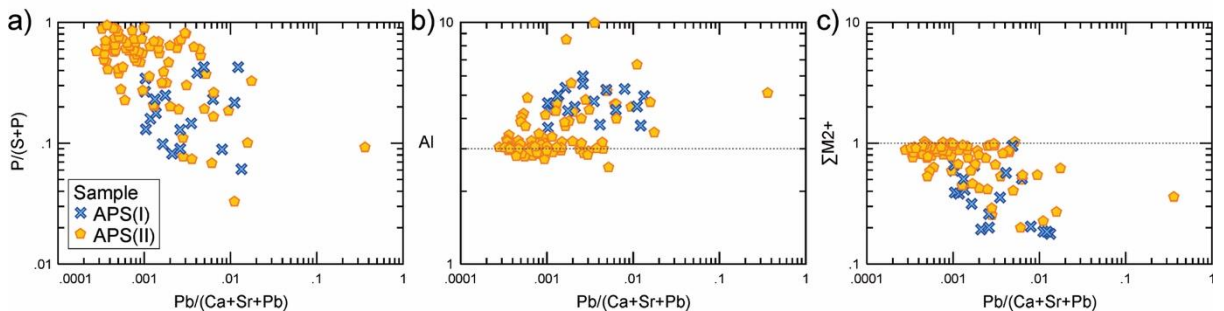


Figure 6: Plots of EPMA data showing the relationship between the relative concentration of Pb and (a) phosphate-sulfate composition; (b) Al concentration (apfu); and (c) total M^{2+} (apfu), within synthetic APS phases. Closed symbols represent analyses that contain Pb while open symbols contained no Pb. Phases with the highest purity are those with compositions which trend towards $\sum M^{2+} = 1$ and $Al = 3$ apfu (indicated by the dotted lines on b and c). Symbols for sample types are provided in (a).

A more comprehensive dataset for Pb incorporation into APS grains was obtained via LA-ICP-MS spot analyses, linking fluid compositions (pH and $[Pb_{aq}]_0$) to Pb incorporation. While Ca and Sr are present in roughly equal amounts within low Pb analyses, the Ca concentrations decrease

upon introduction of more significant Pb (Figure 7a), though Ca occurs in only trace levels within the nominally Ca-free APS(I). On the other hand, Sr concentrations within the M-site in APS phases remain largely unaffected by the introduction of Pb, except in a few analyses (Figure 7b). This trend is amplified for experiments at $\text{pH} \geq 3.5$ and higher $[\text{Pb}_{\text{aq}}]_0$, indicating that a certain threshold must be reached before the onset of rapid uptake of Pb by APS phases through cation exchange. Indeed, the majority of analyses from APS phases at pH 1.5 and any $[\text{Pb}_{\text{aq}}]_0$ show less than 1% Pb contribution of the total M-site, while APS phases at pH 3.5 and 5.5 recorded low (0.014-32.7%) and high (0.048-58.7%) values of M-site Pb occupancy, respectively.

Figure 7

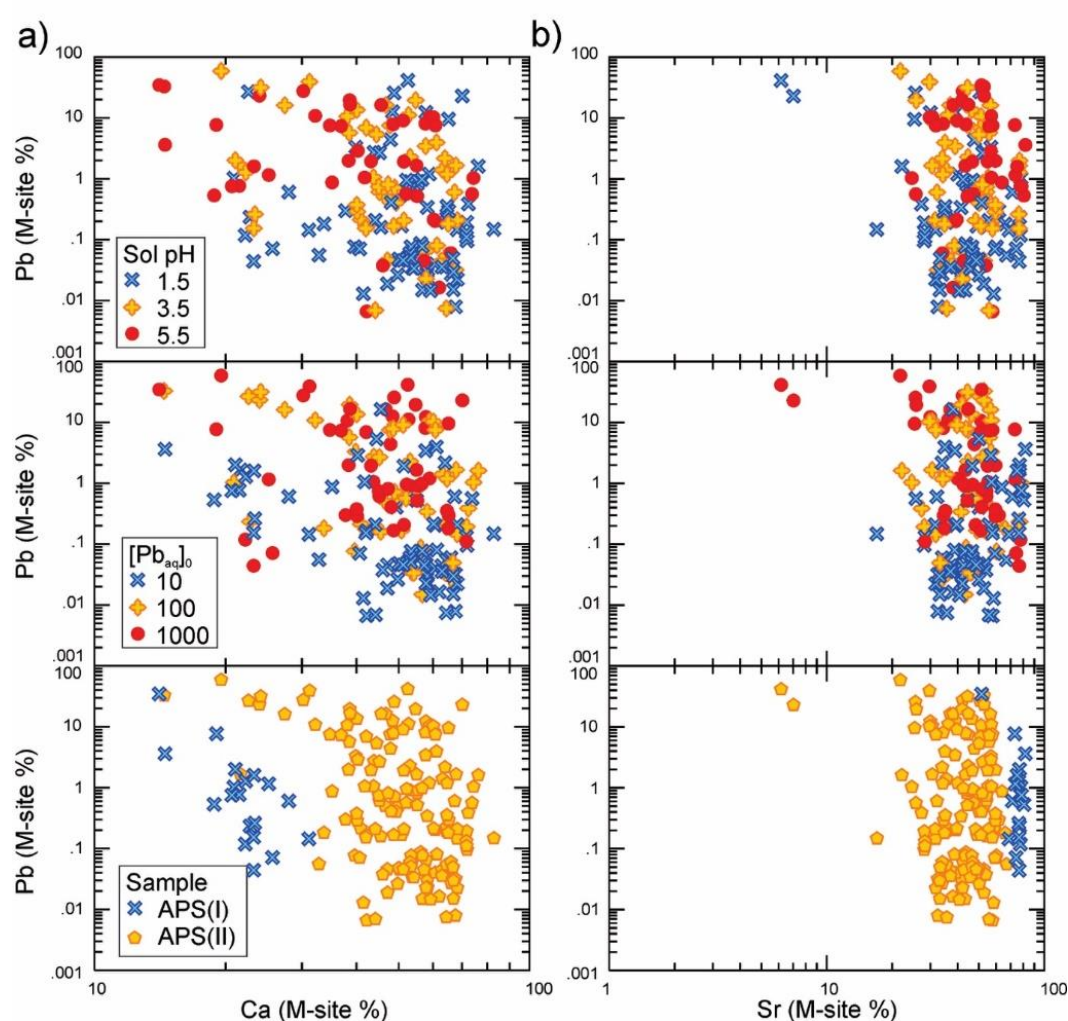


Figure 7: Graphs of targeted LA-ICP-MS spot analyses plotting the percentage of Pb incorporation in the M-site against (a) Ca % concentration in the M-site; and (b) Sr % concentration in the M-site. Symbols displaying solution pH (top row), the initial concentration of Pb in solution (middle row), and APS sample type (bottom row) are given in (a). All points are within 10% error, calculated from the 2SE value.

Relationships between Pb-incorporation into APS phases and the initial concentration of Pb within the reaction liquors ($[Pb_{aq}]_0$) were not as clear as those defined for pH, showing a broad range of compositions in each batch of experiments. Within APS grains exposed to $[Pb_{aq}]_0=10$, 100 and 1000 ppm solutions, Pb concentrations varied between 0.010-41.3, 0.004-58.7, and 0.001-34.5 % occupancy at the M-site, respectively.

Data for the (Ca,Sr)-bearing sample, APS(II), showed a clearly defined Pb incorporation trend. In solutions where $[Pb_{aq}]_0$ was 100 ppm or greater, APS(II) showed an increase of Pb sorption from solution from pH 1.5-3.5, then decreasing again at pH 5.5, indicating Pb-incorporation is maximised at pH 3.5. At $[Pb_{aq}]_0= 10$ ppm, Pb incorporation increased with pH, indicating that Pb-loading onto the crystal surfaces may be a contributing factor at low concentrations.

4.4. Pb incorporation in natural woodhouseite

To investigate the diffusion of Pb within the lattice of APS minerals, coarse-grained grains of natural woodhouseite were exposed to 1000 ppm Pb for 4 days at 25 (Grain 2) and 200°C (Grain 3) at pH 3; the distribution of Pb and other elements was mapped using LA-ICP-MS (Figure 8a-d). This element mapping approach was not possible on the fine-grained synthetic APS phases. Unprocessed samples (Grain 1) display oscillatory zoning with respect to Sr and Pb, presumably preserving changes in the mineralising fluid's composition during the growth of the mineral. In contrast, Grain 2 and 3 display distinctive Pb-rich rims. This is especially evident when the data is displayed as an empirical cumulative distribution function (ECDF) (Figure 8d, h, l). Here, the data is scaled according to a histogram of the distribution of the data, and while these maps are qualitative rather than quantitative, they reveal Pb-rich rims in both grains penetrating in the order of 10-50 μm depth. While Grain 2 predictably shows thicker Pb-rich rims than Grain 3 due to faster diffusion at elevated temperature, the chemical maps clearly indicate that Pb sorption readily occurs even at room temperature.

Figure 8

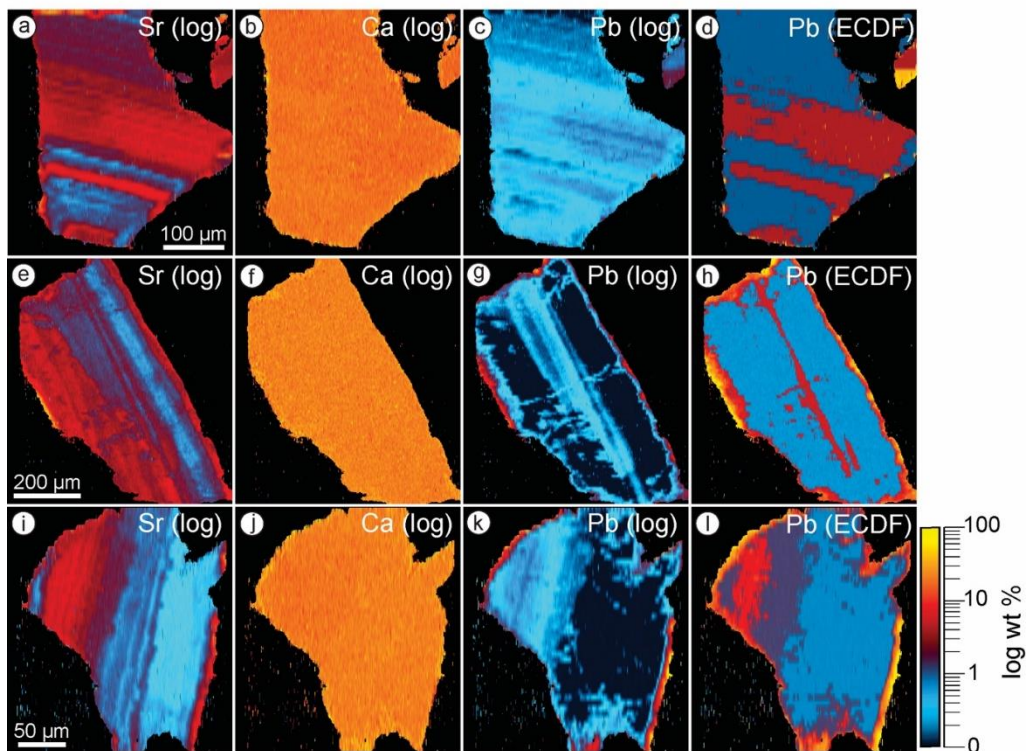


Figure 8: Laser ablation-ICP-MS maps of three natural woodhouseite grains, one without being exposed to Pb-bearing solution (Grain 1, top line); the second placed in $[\text{Pb}_{\text{aq}}]_0=1000$ ppm Pb-bearing solution at pH 3.5 in a hydrothermal bomb at 200 °C and 15 bar (Grain 2, middle line); and the third (Grain 3, bottom) placed in $[\text{Pb}_{\text{aq}}]_0=1000$ ppm solution at pH 3.5 at ambient temperature on an orbital shaker for 5 days. Note, maps (d), (h) and (l) are displayed with an empirical cumulative distribution function (ECDF) rather than log scale to highlight Pb sorption based on the data's population trend (Rittner and Müller 2012).

4.5. X-ray absorption spectroscopy of Pb in APS minerals

XANES and EXAFS data were collected to further constrain the nature of Pb in APS minerals as a function of pH and Pb concentration. XANES (Figure 9) provides information on the oxidation state and coordination geometry of the target atom (Penner-Hahn 2005; Bunker 2010; Etschmann et al. 2018), while EXAFS spectra are sensitive to the atomic number of the neighbouring atoms and their distances, and their Fourier transforms provide information on electron density distributed away from the central Pb atom (Figure 10).

The XANES spectra of the standards showed a characteristic peak for pyromorphite-like structure at 13.045 keV and hinsdalite-like at 13.049 keV (Figure 9). The XANES spectra of Pb-sorbed APS phases differ with changing pH and Pb concentration. At pH 1.5, the XANES spectra for both APS(I) and APS(II) at 100 and 1000 ppm $[\text{Pb}_{\text{aq}}]_0$ are similar to the pyromorphite standard.

The formation of pyromorphite is an artefact introduced during drying of solid residues upon completion of the experiment to the insoluble pyromorphite phase; this is consistent with the higher Pb in solution data (Figure 5) and the poor APS sorption capacity at pH 1.5 (Appendix D, Table 4). At pH 3.5, APS(I) XANES spectra at all $[Pb_{aq}]_0$ concentrations were similar to the hinsdalite standard, suggesting lattice incorporation of Pb; this is consistent with the lower Pb concentration in solution reported in Figure 5.

The XANES spectra for Pb-sorption tests at pH 5.5 showed significant change as a function of $[Pb_{aq}]_0$ concentration. In the case of APS(I), the XANES spectra showed a peak shift from hinsdalite to pyromorphite with increasing $[Pb_{aq}]_0$ from 100 to 1000 ppm, suggesting that at a pH of 5.5, the effective loading capacity of the APS(I) phase significantly decreased. This was further evident in the case of APS(II), where the XANES spectra showed a peak characteristic of hinsdalite at 10 ppm, with a consistent peak shift observed with increasing $[Pb_{aq}]_0$ to 100 ppm, where the XANES spectra showed a combined hinsdalite/pyromorphite peak, and finally, at 1000 ppm, where the XANES spectra showed a characteristic peak for pyromorphite. Therefore, the XANES spectra showed that the effective operating window for APS sorption of Pb was optimal at a pH of 3.5 for both APS(I) and APS(II), independent of [Pb] concentration.

Based on the XANES results, EXAFS spectra were fitted to either a hinsdalite or pyromorphite-like structure (Appendix D, Tables 4,5). The EXAFS fit results confirm the interpretation of the XANES data. In the pyromorphite-like structures, short Pb-Pb distances (3.60 and 2.75 Å; Dai and Hughes 1989) are identified in the fits, with close to full occupancy, consistent with a pyromorphite-like (nano)-precipitate. In hinsdalite, however, the shortest Pb-Pb distances are >6.5 Å (Kolitsch et al. 1999), and therefore beyond the range of our EXAFS data. However, the EXAFS data indicate a well-ordered shell of Al and P/S atoms around the Pb atoms (Appendix D, Table 5), consistent with Pb incorporation in the APS crystal structure rather than adsorption. Note that analysis (11) contained a relatively large bromine K-edge, likely resulting from contamination of the $Pb(NO_3)_2$ used during the sorption experiments, and low Pb-concentration. As such the data is noisier and short range, and was difficult to fit.

5. Discussion

The sorption data in Section 4.2 highlight the strong effect of pH and aqueous Pb loading on the removal of Pb from solution. In general, the Pb-removal increases with increasing pH (1.5 to 5.5). Increasing $[\text{Pb}_{\text{aq}}]_0$ from 10 to 100 ppm results in increased Pb concentrations being recorded in APS phases. There is, however, a smaller difference in the amount of Pb sorbed by APS phases when increasing $[\text{Pb}_{\text{aq}}]_0$ from 100 to 1000 ppm, indicating a loading capacity for Pb onto APS phases at ~ 1 g APS in 1 L of $[\text{Pb}_{\text{aq}}]_0=100$ ppm solution.

However, LA-ICP-MS spot analyses reveal a more complex picture of the pH dependence of Pb sorption as a function of APS composition: (Ca,Sr)-bearing APS phases incorporate large concentrations of Pb between pH 3.5 and 5.5, while APS(I) appears to be more effective at pH 5.5 (Figure 7). This suggests that the effect of the pH-dependant surface charge on adsorption of cationic Pb is not the only factor controlling Pb uptake. Thermodynamic modelling shows that the ideal formation conditions for synthetic Ca-bearing woodhouseite occur between pH 3-5 (Schwab et al. 2005; Figure 11), with Pb-bearing phases becoming preferred as solution acidity increases, in agreement with the LA-ICP-MS data showing Pb-sorption at pH 3.5 out-performing pH 5.5. Hence, there is a clear link between the thermodynamic stability of APS minerals (Schwab et al. 1993, 2005; Gaboreau and Vieillard 2004) and their capacity to incorporate Pb. A similar feature was noted by Montegudo et al. (2003) with respect to the sorption of Hg from waste waters by APS phases, which also was optimal at pH ~ 3.5 .

These complex trends of Pb sorption with pH, solution and APS mineral compositions are interpreted to arise from the interplay between initial surface sorption and subsequent incorporation into APS phases. The presence of a ‘hump’ in many of the time-resolved sorption data (Figure 5), similar to those observed during the uptake of Ra by isostructural barite and celestine (Klinkenberg et al. 2018), can be explained in this framework, whereby Pb cations entering the APS structure must either replace Ca^{2+} or Sr^{2+} , or fill otherwise unoccupied positions within the APS crystal structure, as may be the case in APS(I) in which no loss of Sr was observed with increasing Pb incorporation (Figure 7b). This observation can be explained by the relatively

weak thermodynamic gradient between Sr- and Pb-, compared with Ca- and Pb-APS endmembers. If Pb is interpreted to take the place of Ca^{2+} or Sr^{2+} within the APS structure, their displacement toward the surface of the APS grains will result in a reduction of the number of electrostatic binding sites previously available to Pb^{2+} , thus causing surface-sorbed Pb to become detached and re-enter solution, producing the observed Pb-sorption trendlines.

Figure 9

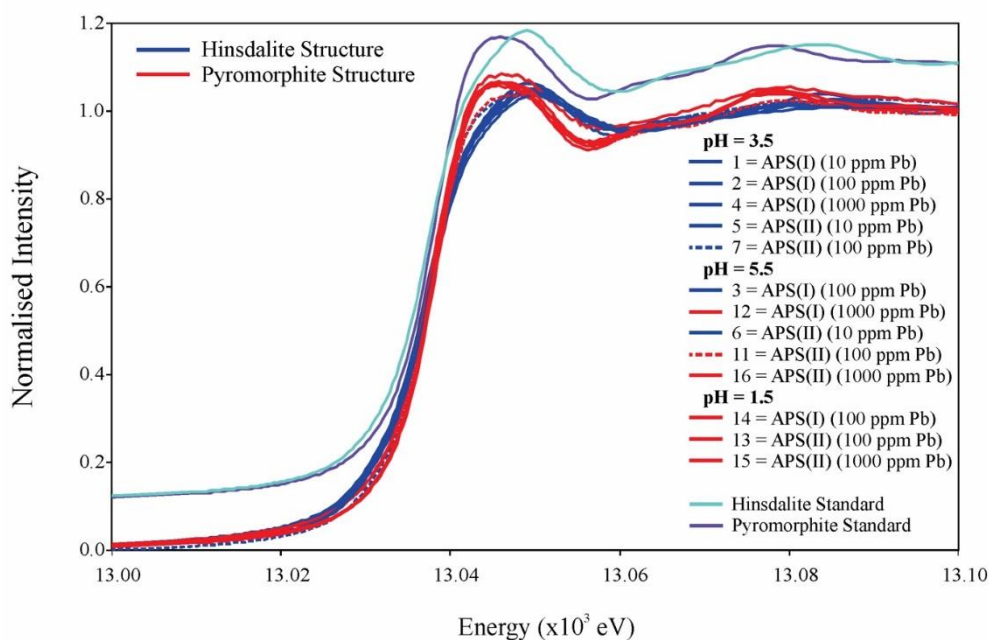


Figure 9: XANES data for Pb-sorbed synthetic APS phases. Phases correspond to either a hinsdalite or pyromorphite structure as indicated. Displayed for reference are patterns for the hinsdalite and pyromorphite standards in teal and purple respectively. Note that the normalised intensities of the standards have been shifted by 0.1.

XANES and EXAFS data confirm the prevalence of Pb incorporation on the M-site of hinsdalite-like structures in the APS products from the sorption experiments. There is a clear trend showing hinsdalite-like structures as the major Pb-bearing phase from experiments with starting pH at 3.5, and experiments with starting pH at 5.5 occasionally showed hinsdalite as the major Pb-bearing phase. None of the Pb-sorption experiments run at pH 1.5 showed hinsdalite-like features, thus indicating that the dynamic incorporation of Pb into Ca-, and Sr-bearing APS phases is preferred at pH 3.5 (Figures 9,10). As mentioned above, the data are in line with the thermodynamic modelling conducted by Schwab et al. (2005) (Figure 11): the formation

conditions of Pb-APS is likely to occur best when solution conditions are higher than pH 3.5 and less than 5.5, while residual Pb will otherwise dominate and bond to available PO_4^{3-} ligands upon drying to form the observed pyromorphite-like structures. Here, PO_4^{3-} ligands are suggested to result from partial dissolution of accessory augelite that is present within all samples. Samples (1) and (5) were exposed to the same conditions with respect to pH and $[\text{Pb}_{\text{aq}}]_0$, however sample (5) was more easily fitted with the hinsdalite structure in EXAFS, indicating that the analysed material was likely purer than that in sample (1).

Figure 10

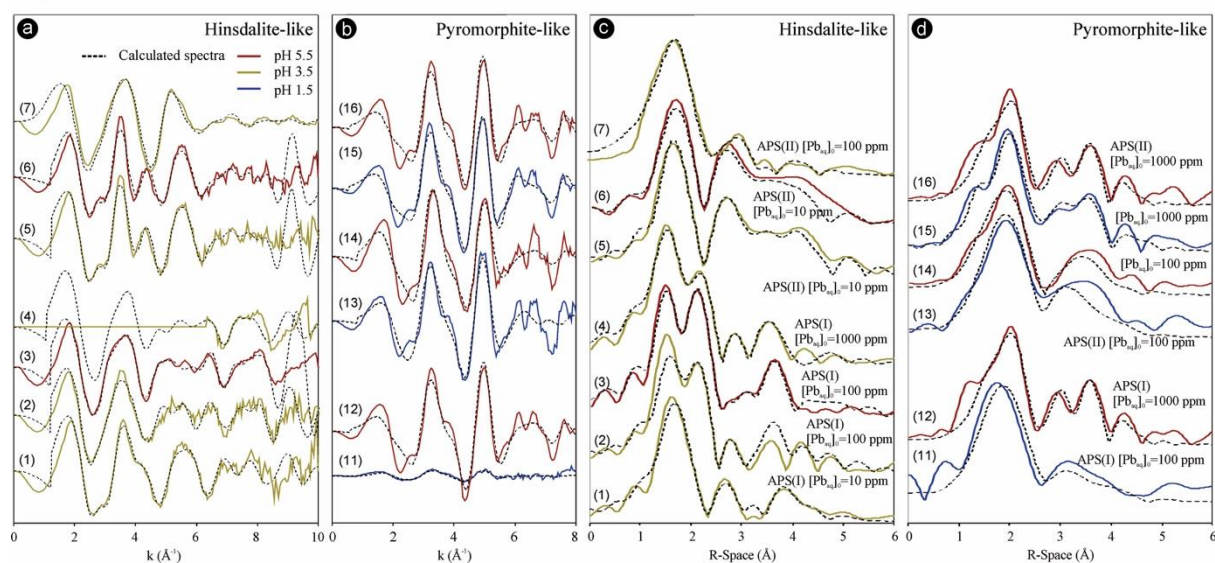


Figure 10: Modelled Pb L_{III} edge EXFAS data (dashed lines) plotted with the measured data (solid lines) of synthetic APS phases from Pb-sorption experiments (a-b); and their associated Fourier transforms (c-d). The APS phase and $[\text{Pb}_{\text{aq}}]_0$ of the solutions are listed on the figure. Dotted lines are fits corresponding to the parameters listed in Tables SUPP. 5,6. Note that differences in the R-space are due to difference in the useful data range in K-space, which depended on Pb concentrations and contamination by bromine.

The importance of structural Pb incorporation relative to surface adsorption was further demonstrated by the mapping of Pb in coarse-grained natural woodhouseite crystals, showing formation of 50 μm thick Pb-rims at 200°C, and still $\sim 10 \mu\text{m}$ thick rims at 25°C (Figure 8). Significant deviations occur along the c -axis of APS phases, depending largely upon the properties of the M-site cation whereby M^{2+} cations with larger ionic radii cause lengthening whereas smaller cations result in contraction of the structure. This is especially the case in crandallite group minerals when considering Ca^{2+} which has a relatively small ionic radius. Its small ionic radius

causes contraction of the crystal structure resulting in distortions among the sheets of $\text{AlO}_2(\text{OH})_4$ octahedra, however when Sr^{2+} and Pb^{2+} are substituted at the M-site, the structure becomes more relaxed, hence increasing stability. There is also apparent lengthening along the *c*-axis with addition of SO_4 in Ca-, Sr-, and Pb-bearing endmembers (Appendix D, Table 7) which may lead to an increase in thermodynamic stability (Schwab et al. 2005). In Pb(II) compounds the electronic configuration of Pb is $6s^2$; the resulting lone electron pair is stereochemically active in many oxy-compounds and complexes (Etschmann et al. 2018), and causes a reduction in crystal symmetry in some Pb-rich alunites (Kolitsch and Pring 2001), adding complexity to substitution of Ca and Sr by Pb, but explaining the high affinity of the APS structure for Pb^{2+} over other divalent cations. Additionally, the relative high electronegativity of Pb^{2+} cations over Ca^{2+} and Sr^{2+} (Gaboreau and Vieillard 2004) may aid in its incorporation by APS phases. The capacity of phosphate and sulfate minerals to quickly incorporate foreign ions into their structure has been illustrated recently in the case of radiobarite, $(\text{Ra},\text{Ba})\text{SO}_4$ (Vinograd et al. 2018; Klinkenberg et al. 2018), the intermobility of Sr, Ba and Pb in isostructural celestine (SrSO_4), barite and anglesite (PbSO_4) (Rollog et al. 2019), and As in apatite, $\text{Ca}_5(\text{PO}_4)_3(\text{F},\text{Cl},\text{OH})$ (Liu et al. 2017). In the latter case, fast dynamic recrystallization was driven by the distortion of the crystal structure induced by the introduction of the arsenite ion; similar dynamic recrystallization in APS minerals may be driven by the Pb^{2+} stereochemistry.

Figure 11

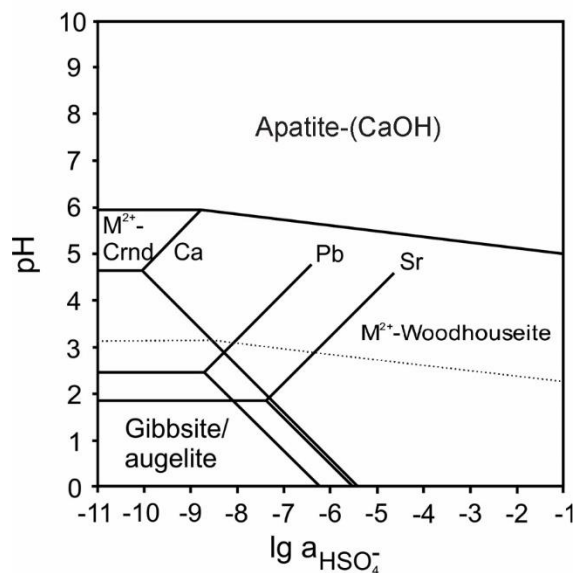


Figure 11: A slice of the hypothetical Garrel-block-diagram for the system MO-Al₂O₃-P₂O₅-SO₃-H₂O at 60°C and [H₃PO₄]= 10^{-5.2} mol.L⁻¹ and [M²⁺]=[Al]= 10⁻³ mol.L⁻¹. The dashed line marks the probable equilibrium conditions with solution (pH ~3). After Schwab et al. (2005).

6. Conclusions and implications

APS minerals are attractive materials for the removal and long-term geological storage of a range of heavy metals and radioisotopes, due to the open nature of their crystal structure (Besold et al. 1992) and their thermodynamic stabilities (Schwab et al. 1993; Gaboreau and Vieillard 2004). Indeed, synthetic APS phases have been proposed as a tool for removal of contaminants from mine waste (As, Monteagudo et al. 2003; As, Pb, Se, Te, Lazareva et al. 2019); immobilisation of radioisotopes of La, Ce and Zr from nuclear fission of ²³⁵U (Eberly et al. 1996; Janeczek and Ewing 1996; Dymkov et al. 1997); or to limit the bioavailability of toxic metals within soil horizons (Zheng et al. 2003; Dill 2001; El Agami et al. 2005).

The results presented here, showing the dynamic incorporation of Pb at between pH 3.5-5.5 combined with the insolubility of APS phases within acid leaching environments (Kolitsch and Pring 2001; Owen et al. 2019) compared with the target Cu-(Fe)-sulphides, underpins their viability as an additive to leach solutions, or elsewhere in the processing circuit, for the reduction of ²¹⁰Pb from such streams. Indeed, Pb-bearing phases are the most thermodynamically stable APS phases under such conditions (Schwab et al., 2005), increasing their potential in acting as a sink for removal of deleterious Pb from environmental processes and waste streams (Manceau et al. 2002).

The most important result from our study is the demonstration that incorporation of Pb into the crystal structure of APS-minerals, by the replacement of lattice-bound Ca (observed via EPMA and LA-ICP-MS), is the major form of Pb scavenging under conditions relevant to acid leaching. Furthermore, the bulk of Pb scavenging was observed to occur over short time scales (hours to days) with a loading capacity of ~1 g APS in 1 L of [Pb_{aq}]₀=100 ppm solution, adding relevance to their potential application as RN extractants within industrial-scale processes. In light of the environmental stability of APS minerals, this indicates their suitability not only for reducing the

load of Pb and its radioactive isotopes in processing circuits, but also for the long-term storage of these contaminants in geological waste repositories; the fact that Pb quickly enter the crystal lattice of APS minerals under process conditions, combined with the broad thermodynamic stability of the APS minerals under environmental conditions, makes them particularly attractive for waste storage (^{210}Pb has a half-life of 22.3 years). However, the viability of APS mineral phases towards industrial application are dependent on both sourcing and isolating natural mineral phases or modifying synthesis procedures of APS mineral phases (e.g. Gilkes and Palmer, 1983).

In conclusion, synthetic APS phases, if cheaply manufactured, could be used to isolate and contain such toxic heavy metals from surrounding ecosystems, and are especially effective in the case of Pb^{2+} .

Acknowledgements

This research is a contribution of the ARC Research Hub for South Australian Copper-Uranium (IH130200033). Staff at Adelaide Microscopy are acknowledged for assistance with microanalysis. Part of this research was undertaken on the XAS beamline at the Australian Synchrotron, part of ANSTO. Oskar Lindenmayer and the Melbourne Museum are thanked for assistance in supplying mineral samples.

References

- Bayliss, P., Kolitsch, U., Nickel, E.H., and Pring, A. (2010) Alunite supergroup: recommended nomenclature. *Mineral. Mag.* 74, 919-927.
- Bhargava, S.K., Ram, R., Pownceby, M., Grocott, S., Ring, B., Tardio, J., and Jones, L. (2015) A review of acid leaching of uraninite. *Hydrometallurgy*, 151, 10–24.
- Besold, E., Bieniek, D., and Kettrup, A. (1992) Synthetischer Crandallit. *Umweltwissenschaften und Schadstoff-Forschung*, 4(1), 14–16.
- Bunker, G. (2010) Introduction to XAFS: a practical guide to X-ray absorption fine structure spectroscopy. Cambridge University Press.
- Cook, N.J., Ehrig, K.J., Rollog, M., Ciobanu, C.L., Lane, D.J., Schmandt, D.S., Owen, N.D., Hamilton, T., and Grano, S.R. (2018) ^{210}Pb and ^{210}Po in geological and related anthropogenic materials: implications for their mineralogical distribution in base metal ores. *Minerals*, 8(5), 211.
- Dąbrowski, A., Hubicki, Z., Podkościelny, P., and Robens, E. (2004) Selective removal of the heavy metal ions from waters and industrial wastewaters by ion-exchange method. *Chemosphere*, 56(2), 91–106.
- Dai, Y.S. and Hughes, J.M. (1989) Crystal-structure refinements of vanadinite and pyromorphite. *Canadian Mineralogist* 27, 189–192.
- Dill, H.G. (2001) The geology of aluminium phosphates and sulphates of the alunite group minerals: a review. *Earth-Science Reviews*, 53, 35–93.
- Draa, M. T., Belaid, T., and Benamor, M. (2004) Extraction of Pb (II) by XAD7 impregnated resins with organophosphorus extractants (DEHPA, IONQUEST 801, CYANEX 272). *Separation and Purification Technology*, 40(1), 77-86.
- Dymkov, Y., Holliger, P., Pagel, M., Gorshkov, A., and Artyukhina A. (1997) Characterization of a La-Ce-Sr-Ca aluminous hydroxy phosphate in nuclear zone 13 in the Oklo uranium deposit (Gabon). *Mineralium Deposita*, 32, 617–620.
- Eberly, P.O., Ewing, R.C., Janeczek, J., and Furiano, A. (1996) Clays at the natural nuclear reactor at Bangombé, Gabon: Migration of actinides. *Radiochimica Acta*, 74, 271–276.
- Ehrig, K., Liebezeit, V., Macmillan, E., Lower, C., Kamenetsky, V.S., Cook, N.J., and Ciobanu, C.L. (2015) Uranium mineralogy versus the recovery of uranium at Olympic Dam. Proceedings, The AusIMM International Uranium Conference 2015, Adelaide, 75.

- El Agami, N.L., El Wahed, A.A., and Haroun, Y.E. (2005) Mineralogy, geochemistry and origin of aluminum-phosphate-sulfate minerals in G.Elhefuf, Baharyia Oasis, Western Desert, Egypt. Proceedings, The Fourth International Conference on the Geology of Africa, Assiut-Egypt, 2, 269–292.
- Etschmann, B., Mei, Y., Liu, W., Rae, N., Kappen, P., Testemale, D. and Brugger, J. (2018) Role of Pb(II) complexes in hydrothermal mass transfer: An X-ray absorption spectroscopic study. *Chemical Geology*, 502, 88–106.
- Gaboreau, S. and Vieillard, P. (2004) Prediction of Gibbs free energies of formation of minerals of the alunite supergroup. *Geochimica et Cosmochimica Acta*, 68, 3307–3316.
- Gilkes, R.J. and Palmer, B. (1983) Synthesis, properties, and dehydroxylation of members of the crandallite-goyazite series. *Mineralogical Magazine*, 47, 221–227.
- International Atomic Energy Agency (2006) Assessing the need for radiation protection measures in work involving minerals and raw materials. IAEA Safety Reports Series No. 49
- Janeczek, J. and Ewing, R.C. (1996) Florencite-(La) with fissionogenic REEs from a natural fission reactor at Bangombe, Gabon. *American Mineralogist*, 81, 1263–1269.
- Jaworowski, Z. (1967) Stable and radioactive lead in environment and human body. Technical Report No. NEIC-RR--29, Institute of Nuclear Research, Warsaw, Poland.
- Kato, T. (1971) The crystal structures of goyazite and woodhouseite. *Neues Jahrbuch für Mineralogie Monatshefte*, 241–247.
- Klinkenberg, M., Weber, J., Barthel, J., Vinograd, V., Poonoosamy, J., Kruth, M., Bosbach, D., and Brandt, F. (2018) The solid solution–aqueous solution system (Sr, Ba, Ra) SO_4^+ H_2O : A combined experimental and theoretical study of phase equilibria at Sr-rich compositions. *Chemical Geology*, 497, 1–17.
- Kolitsch, U., Tiekink, E.R., Slade, P.G., Taylor, M.R., and Pring, A. (1999) Hinsdalite and plumbogummite, their atomic arrangements and disordered lead sites. *European Journal of Mineralogy*, 513–520.
- Kolitsch, U. and Pring, A. (2001) Crystal chemistry of the crandallite, beudantite and alunite groups: a review and evaluation of the suitability as storage materials for toxic metals. *Journal of Mineralogical and Petrological Sciences*, 96, 67–78.
- Lazareva, E.V., Myagkaya, I.N., Kirichenko, I.S., Gustaytis, M.A., and Zhmodik, S.M. (2019) Interaction of natural organic matter with acid mine drainage: In-situ accumulation of elements. *Science of the Total Environment*, 660, 468–483.

- Lemmon, D.M. (1937) Woodhouseite, a new mineral of the beudantite group. *American Mineralogist* 22, 939–948.
- Liu, W., Mei, Y., Etschmann, B., Brugger, J., Pearce, M., Ryan, C., Borg, S., Wykes, J., Kappen, P., Paterson, D., Boesenberg, U., Garrevoet, J. and Falkenberg G. (2017) Arsenic in hydrothermal apatite: oxidation state, mechanism of uptake, and comparison between experiments and nature. *Geochimica Cosmochimica Acta* 196, 144–159.
- Macnaughton, S.J., Ring, R.J., Day, A., Collier, D.E., and Tan, L.K.P. (1999) Optimisation of the leach conditions for a copper/uranium ore. In: Mishra, B. (Ed.), *Proceedings EPD Congress 1999*. The Minerals, Metals and Materials Society, 509–522.
- Macnaughton, S.J., Tan, L., Day, A., and Ring, R.J. (2000) Modelling the leaching behaviour of an uranium ore. In: *Uranium 2000: International Symposium on the Process Metallurgy of Uranium*, Saskatoon, SK, 413–427
- Manceau, A., Marcus, M. A., and Tamura, N. (2002) Quantitative speciation of heavy metals in soils and sediments by synchrotron X-ray techniques. *Reviews in Mineralogy and Geochemistry*, 49(1), 341–428.
- McMaster, S. A., Ram, R., Faris, N., and Pownceby, M. I. (2018) Radionuclide disposal using the pyrochlore supergroup of minerals as a host matrix—A review. *Journal of Hazardous Materials*, 360, 257–269.
- Monteagudo, J.M., Durán, A., Carmona, M.S., Schwab, R.G., and Higuera, P. (2003) Elimination of inorganic mercury from waste waters using crandallite-type compounds. *Journal of Chemical Technology and Biotechnology*, 78, 399–405.
- Nascimento, M.R.L., Fukuma, H.T., Da Costa, W.C., Quinelato, A.L., Garcia Jr, O., and Gomes, H.A. (2006) Removal of radionuclides from acid mine waters by retention on adsorbing materials. *Journal of Radioanalytical and Nuclear Chemistry*, 269(3), 755–759.
- Neumann, T. (2012) Fundamentals of aquatic chemistry relevant to radionuclide behaviour in the environment. In: C. Poinssot, Geckeis, H. (Eds.), *Radionuclide Behaviour in the Natural Environment*, p. 13–43. Woodhead Publishing Series in Energy.
- Owen, N.D., Cook, N.J., Rollog, M., Ehrig, K., Schmandt, D.S., Ram, R., Brugger, J., Ciobanu, C.L., Wade, B., and Guagliardo, P. (2019) REE-, Sr- Ca-aluminum-phosphate-sulfate minerals of the alunite supergroup and their role as hosts for radionuclides. *American Mineralogist*, 104, 1806–1819.

- Penner-Hahn, J.E. (2005) Characterization of “spectroscopically quiet” metals in biology. *Coordination Chemistry Reviews*, 249(1-2), 161–177.
- Ram, R., Charalambous, F.A., McMaster, S., Pownceby, M.I., Tardio, J., and Bhargava, S.K. (2013) An investigation on the dissolution of natural uraninite ores. *Minerals Engineering*, 50, 83–92.
- Ram, R., Vaughan, J., Etschmann, B., and Brugger, J. (2019) The aqueous chemistry of Polonium (Po) in environmental and anthropogenic processes. *Journal of Hazardous Materials*, 380, doi: 10.1016/j.jhazmat.2019.06.002.
- Ravel, B. and Newville, M. (2005) ATHENA, ARTEMIS, HEPHAESTUS: data analysis for X-ray absorption spectroscopy using IFEFFIT. *Journal of Synchrotron Radiation* 12, 537–541.
- Rehr, J.J., Kas, J.J., Prange, M.P., Sorini, A.P., Takimoto, Y. and Vila, F. (2009) *Ab initio* theory and calculations of X-ray spectra. *Comptes Rendus Physique* 10, 548–559.
- Rittner, M. and Müller, W. (2012) 2D mapping of LA-ICPMS trace element distributions using R. *Computers & geosciences*, 42, 152–161.
- Rollog, M., Cook, N.J., Guagliardo, P., Ehrig, K., Gilbert, S.E., and Kilburn, M. (2019) Intermobility of barium, strontium, and lead in chloride and sulfate leach solutions. *Geochemical Transactions*, 20(1), 1–23.
- Schwab, R.G., Götz, C., Herold, H., and Pinto de Oliveira, N. (1991) Compounds of the crandallite type: synthesis and properties of pure (Ca, Sr, Ba, Pb, La, Ce to Eu)-arsenocrandallites. *Neues Jahrbuch für Mineralogie Monatshefte*, (3), 97–112.
- Schwab, R.G., Gotz, C., Herold, H., and Deoliveira, N.P. (1993) Compounds of the crandallite type: Thermodynamic properties of Ca-, Sr-, Ba-, Pb-, La-, Ce- to Gd-phosphates and -arsenates. *Neues Jahrbuch Fur Mineralogie-Monatshefte*, (12), 551–568.
- Schwab, R.G., Pimpl, T., Schukow, H., Stolle, A., and Breitingner, D.K. (2004) Compounds of the crandallite-type: Synthesis, properties and thermodynamic data of pure crandallite and woodhouseite. *Neues Jahrbuch für Mineralogie Monatshefte*, 385–409.
- Schwab, R.G., Pimpl, T., Schukow, H., Stolle, A., and Breitingner, D.K. (2005) Compounds of the crandallite-type: Synthesis, properties and thermodynamic data of Ca–Sr–Ba–Pb-(arseno)-woodhouseites. *Neues Jahrbuch für Mineralogie Abhandlungen*, 181, 207–218.

- Vinograd, V.L., Kulik, D.A., Brandt, F., Klinkenberg, M., Weber, J., Winkler, B. and Bosbach, D. (2018) Thermodynamics of the solid solution - Aqueous solution system (Ba,Sr,Ra)SO₄ + H₂O: II. Radium retention in barite-type minerals at elevated temperatures. *Applied Geochemistry* 93, 190–208.
- Zheng, M. X., Xu, J. M., Smith, L., and Naidu, R. (2003) Why a fern (*Pteris multifida*) dominantly growing on an arsenic heavy metal contaminated soil does not accumulate arsenic? *Journal de Physique IV (Proceedings)*, 107, 1409–1411.

CHAPTER 6

SUMMARY, RECOMMENDATIONS AND CONCLUDING REMARKS

1 SUMMARY

The content of this thesis crosses themes that range from microanalytical characterisation of metallurgical samples, identification of target minerals for radionuclide (RN) deportment and fundamental geochemical experimentation that can guide RN reduction in South Australian Cu-concentrates. Two main mineralogical topics were addressed.

Firstly, the formation of Pb-chalcogenides, which are frequently hosted by Cu-(Fe)-sulphides in mineralised zones of the Mt Woods Inlier (Owen et al. 2018) and in the giant Olympic Dam (OD) deposit (Schmandt 2019) were investigated, providing fundamental information on the petrography and origin of the main Pb-bearing minerals in the deposits, Pb-isotope signatures within them, and the behaviour of Pb, radiogenic or otherwise, within the deposit over geological time. The complexity of the structures the Pb-minerals form with the Cu-(Fe)-sulphides necessitated a nanoscale approach and careful isotopic evaluation so that the conditions of formation could be accurately discussed. Micron- to nanoscale analysis of ore and gangue minerals within South Australian IOCG ores and their host rocks (e.g. Macmillan et al. 2016a, 2016b; Ciobanu et al. 2013, 2017a, 2017b; Kontonikas-Charos et al. 2018; Owen et al. 2018; Courtney-Davies et al. 2019a, 2019b; Verdugo-Ihl et al. 2019a, 2019b) has revealed new evidence, allowing deposit-scale constraints on ore-formation conditions and post-mineralisation history.

Secondly, a targeted approach to RN incorporation by gangue minerals was conducted (Rollog et al. 2018, 2019; Owen et al. 2019) giving insight into the migration of radiogenic Pb and associated RN from parent ^{238}U during processing of IOCG ores. NanoSIMS isotope mapping has thus far proven to be the only method by which the grain-scale distribution of RN can be effectively observed. The recycling of Cu-sulphate rich smelter dust, which consequently contains high concentrations of RN, into the leach stage of processing (Lane et al. 2016; Cook et al. 2018) makes the nanoSIMS method particularly important as a tool to monitor the increased decoupling of ^{226}Ra and ^{210}Pb from uranium during processing. The research presented in this thesis allows for recognition of minerals such as the aluminium-phosphate-sulphates (APS) (Owen et al. 2019a, 2019b) as scavengers of RN within the processing circuit. Microanalytical characterisation of this mineral group, which had not been carried out previously, also allows for new valuable information on the post-mineralisation history of the Olympic Dam deposit. Chemical experimentation and XAS analysis on synthetic APS phases enables an understanding of the mechanism by which APS phases can incorporate RN, specifically ^{210}Pb , and highlights their potential as a novel way for reducing RN from processing streams.

1.1 Migration of radiogenic Pb within Cu-Au-(U) deposits of the Olympic Cu-Au Province

The first main question answered by this thesis was the confirmation that the Pb-chalcogenides, galena (PbS), clausthalite (PbSe) and altaite (PbTe), contain dominant radiogenic Pb generated by

decay of uranium and thorium. These results, obtained by a combination of quantitative isotope analysis and examination of mineralogical relationships at the nano- to micron-scales, imply the remobilization and migration of radiogenic Pb, consistent with the low-Pb concentrations measured in some U-minerals.

At the initiation of research reported in this thesis, radionuclides of concern (principally ^{210}Pb and ^{210}Po) were suggested to be similarly distributed to ^{206}Pb , the stable end product of ^{238}U decay. It was hoped that the more abundant, and thus measurable ^{206}Pb , would serve as a reliably proxy for ^{210}Pb and ^{210}Po , especially as all three Pb-chalcogenides are commonly hosted as inclusions within Cu-(Fe)-sulphides, highlighting their importance as potential carriers of RN into concentrates. Evidence for migration of Pb within the deposit over geological time was thus deemed relevant for assessment of RN deportment in ores.

Lead isotope values measured in-situ by laser ablation inductively coupled plasma mass spectrometry (LA-ICP-MS) suggest an overwhelmingly radiogenic origin for Pb and thus extensive decoupling of radiogenic Pb from parent U- and Th-minerals. Calculated $^{207}\text{Pb}/^{206}\text{Pb}$ ratios are indicative of Pb mobilisation during an event (or events) that postdates the initial Mesoproterozoic Fe-Cu-Au-U mineralisation event, an interpretation consistent with many other studies from across the Olympic Cu-Au province, suggesting cycles of replacement-remobilization-recrystallization (e.g., [Davidson et al. 2007](#); [McInnes et al. 2008](#); [Ciobanu et al. 2013](#); [Huang et al. 2015](#); [Apukhtina et al. 2017](#); [Bowden et al. 2017](#)). However, given the relatively short half-life of the ^{210}Pb isotope, and the inability of Pb-chalcogenides to host significant concentrations of other longer lived radionuclides from ^{238}U decay, e.g., ^{232}Th or ^{226}Ra (Rollo, unpublished nanoSIMS data), it is suggested that even if the Pb-chalcogenides were deemed to have once carried ^{210}RN during their initial formation, these unsupported concentrations have long since diminished. Nevertheless, combining data from the isotope compositional study and the nanoscale study of Pb-chalcogenides proved instructive for uncovering mechanisms of Pb incorporation by Cu-(Fe)-sulphides.

The incorporation of Pb to form the clausthalite symplectite structures analysed by [Owen et al. \(2018\)](#) were suggested to arise via migrating Pb from an external fluid source and Se which was pre-existing in solid solution in the Cu-(Fe)-sulphides. Clear diffusion textures are observed in porous zones within chalcopyrite by the formation of clausthalite nanoparticles, providing a link between diffusion of Pb and symplectite formation. The same ‘diffusion style’ textures were not visible within other Cu-(Fe)-sulphides, likely due to their ability to form superstructures during thermal overprinting episodes, thus allowing the migration of Pb from nanometres to microns within the hosting Cu-(Fe)-sulphides and the development of the spectacular symplectite textures observed. Further evidence for this formation mechanism is provided by the isotopic analysis of the different Pb-chalcogenides, whereby Pb-isotope trends for clausthalite and altaite lie along a

clear mixing trend between the pure radiogenic signature (with respect to ^{206}Pb , ^{207}Pb and ^{208}Pb) and common Pb. Included grains of galena are, in contrast, variably enriched in uraniumogenic ^{206}Pb and ^{207}Pb , thus indicating that at least a portion of them likely formed from the products of U decay, *in situ* within the Cu-(Fe)-sulphides.

1.2 Aluminium-phosphate-sulphates and RN deportment during metallurgical processing

The second part of this thesis focuses on the ability of gangue minerals, specifically aluminium-phosphate-sulphate phases within the alunite supergroup, to scavenge RN during minerals processing. Samples of Cu-concentrate were taken from the Olympic Dam Cu-processing circuit after flotation and subsequent acid leaching. Samples from the acid leach stage of processing were shown to contain significantly more RN (albeit only RN from ^{226}Ra onwards in the decay chain) than equivalent flotation concentrates that had not been acid-leached. This relationship was especially pronounced for ^{210}Pb . The recycling of Cu-sulphate rich dust from smelting of copper concentrates, which is consequently enriched in RN, into the leach stage of processing likely intensifies ^{210}Pb incorporation by APS phases. The observations emphasize that measurable RN uptake into APS minerals takes place at plant conditions ($\sim 60\text{ }^\circ\text{C}$, $\text{pH} = 1.5$) and in a matter of just 8-12 hours.

Study of the broad range of solid solutions formed by the APS phases within the Olympic Dam ore provides geological information allowing new insights into, and additional constraints on, the formation of the deposit. It was revealed that the APS minerals are Sr-, and Ca-dominant with variable amounts of rare earth elements (REE), with some analyses plotting within the compositional fields of svanbergite and woodhouseite and others plotting closer to florencite-(Ce), suggestive of an (incomplete?) solid solution, or field of solid solutions, between the two groups (Owen et al. 2019). Florencite-(Ce) and the Ca-, Sr-dominant APS phases commonly replace the REE-fluorcarbonate, bastnäsite-(Ce), previously described by Schmandt et al. (2017). The Ca- and Sr-bearing APS phases contain more sulphate than their REE-bearing equivalents, with the sulphur derived from the local dissolution and replacement of Cu-(Fe)-sulphides. The observed replacement of Cu-(Fe)-sulphides, and the suggested replacement of bastnäsite-(Ce) by APS phases indicates that they are paragenetically late, likely forming during a low-temperature hydrothermal episode late in the history of the deposit. In any case, the resulting intimate textural relationship between APS phases and Cu-(Fe)-sulphides (Owen et al. 2019), along with the insolubility of APS phases (Kolitsch and Pring 2001) make them almost impossible to completely eliminate from copper concentrate by flotation or acid leaching. This has consequences in that Pb is clearly shown, at concentrations measurably by EPMA, to partition into available Ca- and Sr-bearing phases, with a particularly strong correlation observed between Pb and Ca. The same relationship was observed by nanoSIMS isotope mapping in which the highest concentrations of

^{210}Pb showed clear spatial relationships with Ca-enriched zones, meaning that Ca- and Sr-bearing APS phases may assist in the transport of ^{210}Pb through to the very final stages of processing.

Following from the recognition that natural APS phases could play a significant, if as-yet unquantified role in the distribution of ^{210}Pb and changes in that distribution during processing, it was deemed necessary to undertake a synthetic experiment on pure, Pb-free, Ca- and Sr-bearing APS phases in order to model Pb uptake at different conditions with respect to fluid pH and concentrations of dissolved Pb (Owen et al. 2020). Synthesis of APS phases via modification of existing recipes (Schwab et al. 1991, 2004), proved difficult, taking six months equilibration time for a single batch, while always forming minor amounts of accessory augelite $\text{Al}_2(\text{OH})_3$. Nevertheless, EPMA and LA-ICP-MS analyses of sample powders exposed to solutions containing dissolved $\text{Pb}(\text{NO}_3)_2$ in dilute HNO_3 readily confirmed that the incorporation of Pb into the crystal structure of the synthetic APS phases occurred in the predicted way, whereby Pb replaces Ca within the APS crystal structure. Interestingly, compositional data did not show removal of Sr, even in phases which contained no Ca, indicating that cation exchange likely occurs between Ca and Pb only. **This likely occurred due to the formation of distortions in the APS crystal structure, caused by its contraction to accommodate the relatively smaller ionic radii of Ca^{2+} cations.** Extended X-ray absorption fine structure analysis of the resulting solids (Owen et al. 2020) reveals the nature of Pb sorption by the synthesized material. The data showed that the dynamic incorporation of Pb by APS phases occurred overwhelmingly at pH of 3.5, while the formation of pyromorphite from the dissolution of accessory augelite dominated at lower pH. The insolubility of APS phases (Kolitsch and Pring 2001) within acid leaching environments, compared with the target Cu-(Fe)-sulphides, highlights their viability as an additive to leach solutions, or elsewhere in the processing circuit, for the reduction of ^{210}Pb from such streams, provided a mechanism can be engineered to later remove the APS phases and their contained RN.

2 RECOMMENDATIONS

Due to the extraordinary diversity of the mineralogical relationships observed within ores of the Olympic Cu-Au Province, the results outlined in this thesis comprises a valuable contribution toward the understanding of radionuclide deportment within IOCG ores and concentrates and evolution of those deportments from ore to smelter feed. Further characterisation of radionuclide deportment within the Cu-Au ores is certainly necessary in order to obtain improved understanding of the physical and chemical pathways available to mobilise RN and other penalty elements. Even so, within the bounds of this research, a number of recommendations can be made for future directions of study.

2.1 Recommendations for work on natural mineral phases

The first would comprise a study of natural APS phases from Olympic Dam, and potentially the synthetic analogues, conducted at the nanoscale. Such a study was initiated during the candidature but with but poor results leading to the attempt being cut short. APS phases were discovered to be incredibly beam sensitive on the SEM, EPMA and FIB-SEM, even under very low currents and accelerating voltages. Traditional FIB milling with a Ga ion source resulted in non-representative TEM foils and mineral phases that had visibly melted during extraction and foil preparation. Similar beam sensitivity limitations are reported in studies on Ca-sulphates, anhydrite and gypsum (Lee 1993), and the Ca-phosphate hydroxyapatite (Mayer et al. 2008), in which TEM beam damage caused defragmentation of the crystalline phases within seconds of exposure. Cryo-FIB, a technique normally reserved for delicate biological samples, might thus be used to preserve mineral textural relationships and enable the extraction of foils thin enough (~20 to 50 nm) for TEM analysis. Similarly, cryo-sample holders are available for atomic-resolution STEM microscopes such as the FEI Titan with high-angle annular dark-field (HAADF STEM) imaging capability, as used in Owen et al. (2018) for element mapping.

Sample preparation permitting, such a technique would enable detailed study on the diversity of the solid solutions, in terms of crystal-structural response to compositional change, among not only the APS minerals, but also other minerals within the large alunite supergroup. In APS minerals, a relationship between higher concentrations of PO_4^{3-} and OH, and incorporation of M^{3+} cations, such as the rare earth elements, has been established (Owen et al. 2019), however, the repeating motifs that make up the structural components of APS phases have not been previously imaged at high-resolution. A fundamental, and as yet unanswered, question is whether they occur in an ordered arrangement or completely random. Atomic-scale mapping, using methods offering high Z-contrast, such as HAADF STEM (e.g., Ciobanu et al. 2017; Verdugo-Ihl et al. 2019b) could prove extraordinarily useful to understand dimensions and limits of solid solution. If perfected for such beam-sensitive compounds, such techniques might also aid identification of new mineral phases within the alunite supergroup. Additionally, the ordering of individual motifs within an APS minerals structure may provide valuable information on the mechanisms of element incorporation.

The observed diffusion textures exhibited by the uptake of Pb by Se-rich chalcopyrite (Figure 1a), and the widely observed formation of symplectite textures between the other Cu-(Fe)-sulphides and clausenthalite (Owen et al. 2018), are indicative of Pb remobilization during one or more geological events. Modelling this process via synthetic experiments on Pb uptake by Se-rich Cu-(Fe)-sulphides may prove instructive for the determination of the strength and chemical conditions of the hydrothermal fluids associated with such an event or events. As it stands, little research has been done on the fundamentals of Se behaviour within Cu-(Fe)-sulphides or the

significance for and relationships with Pb scavenging. Clausthalite-bearing symplectites hosted by chalcopyrite (Figure 1b-c) are frequently restricted to the cores of grains, indicating that for the grains in question, the first stage of growth was dominated by a Se-bearing hydrothermal fluid. Additionally, given that oxidized Se compounds tend to be isotopically heavier than reduced Se compounds (Stüeken et al. 2015, and references therein), analysis of fractionation of Se isotopes may reveal important information regarding the redox conditions that were present during initial Cu-(Fe)-sulphide formation.

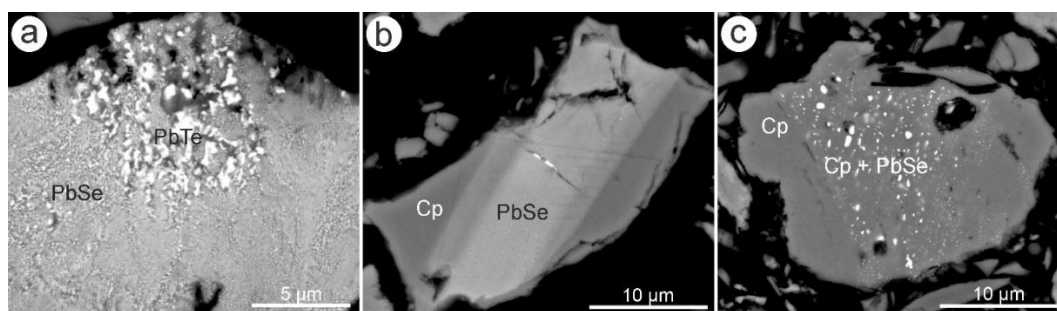


Figure 1: Backscatter electron images of (a) clausthalite (PbSe) and altaite (PbTe) symplectites hosted by a grain of chalcopyrite. Note the coarsening of the Pb-chalcogenides and more concentrated nature of altaite in the upper part of the image where the chalcopyrite grain becomes porous; and (b) and (c) clausthalite-bearing symplectites contained by zones within chalcopyrite.

Extensive methodological development for the characterisation of RN deportment within mineral phases has been demonstrated within this thesis, and in those of Rollog (2019) and Schmandt (2019). Combined with other microanalytical routines developed within the ARC Research Hub for Australian Copper Uranium, there now exists an opportunity to attempt a semi-quantitative mass balance model for RN within mineral phases of South Australian Cu-Au ores during metallurgical processing. The development of techniques, such as nanoSIMS isotope mapping for key radioisotopes which exist in minute concentrations within mineral phases, and the ongoing development of complementary techniques such as quantitative alpha tracking (Kalnins et al., 2019), combined with ‘user assisted’ mineral liberation analysis (MLA) data on the proportion of minerals may allow for such quantitative calculations. The application of synchrotron techniques such as x-ray fluorescence microscopy (XFM), which could be deployed to track U and Pb within grains quickly and at the sample scale (rather than grain by grain as was done with the SEM), may also prove useful in such an endeavour. This has proven impossible until now for two main reasons, the importance of which has become clear during the lifetime of the ARC Research Hub for Australian Copper Uranium. These are (i) the poorly constrained proportion of total RN that reside at grain boundaries, in nano- to microfractures, within pore spaces, and on mineral surfaces rather than contained within a given mineral; and (ii) the difficulty

of accurately determining the abundances of many of the finest-grained minerals that occur dominantly at the sub-micron-scale.

2.2 Recommendations for work on APS phases

Much additional work is possible to further explore the potential use of APS phases as scavengers of RN, the foremost being a simpler and faster method for their synthesis. The outline of a recipe to produce a crystalline crandallite phase, within a much shorter time frame than was needed for the synthesis of APS phases by [Owen et al. \(2020\)](#), is provided in [Gilkes and Palmer \(1983\)](#). Here, the recipe could be modified to form phosphate-sulphate bearing phases, allowing further testing of sorption dynamics and APS phase composition. A shorter method to synthesise APS phases would also make them much more commercially viable as additives to metallurgical processing streams for RN extraction. An additional method for the production of an ‘amorphous’ crandallite phase has been presented by [Monteagudo et al. \(2003\)](#), requiring only two weeks of synthesis time per batch at 70°C and atmospheric pressure. Preliminary data, not presented here, suggest that such a method could be modified for use in leach liquors for RN extraction via similar mechanisms to the crystalline APS phases.

The sorption of RN by natural APS phases within Olympic Dam Cu-processing streams was not limited to isotopes of Pb alone. Via nanoSIMS, ^{226}Ra was also observed, although with slightly different spatial distribution to that of ^{210}Pb . As such, if a clear and simple method for the synthesis of crystalline APS phases can be established, a possible next step could be to determine the competitive sorption of all of daughter RN resulting from decay of U. Such an experiment could be done simply enough, by dissolving uraninite grains containing RN from ^{235}U and ^{238}U , in secular equilibrium. Analysis of the stock solutions by ICP-MS before and after exposure to the APS phases could give a grounding of which RN are compatible within the APS crystal structure, though further microanalytical characterisation on the RN-sorbed solids, such as the methods set out in [Owen et al. \(2020\)](#), would likely be required.

The final step to validate the use of APS phases as a method for reduction of RN from mineral processing streams would involve testing them in situations which replicate processing plant conditions. Testing would be carried out within solutions that are representative of those found in the different stages of metallurgical processing. The aims of such a study would be to model the amount of synthetic APS (although naturally occurring Ca-bearing APS could be used if sourced cheaply enough) that would need to be added to metallurgical processing streams in order to cause a significant reduction in overall RN concentration, identify specific areas of the Cu-processing circuit in which addition of APS would be most effective, and, building on the results and discussions from previous studies, conduct an overall cost benefit analysis. A method for effective addition and removal of APS from the Cu-processing circuit would also have to be established.

One suggestion could be to use a permeable container, allowing solution to contact the APS while keeping it isolated from the ore material. Another method would be to crystallise APS directly onto a grid which could be lowered into Cu-processing liquors. Both cases would have to be sufficiently hardy to cope with exposure to the thick sludges and harsh solutions present in Cu-processing circuits. Alternately, an additional floatation stage could be employed to remove APS after exposure. Beyond removal, APS minerals may have value as permanent immobilisers of RN, enabling safe long-term storage and isolation from surrounding environments. Previous studies (Landa, 2003) have discussed the potential of jarosite in this respect, similar to that proposed for apatite (Rigali et al. 2016).

3 CONCLUDING REMARKS

The research outlined in this thesis adds to an ever-growing body of knowledge on the mineralogy, ore genesis and geological evolution of IOCG style deposits in the Olympic Cu-Au Province. Characterization of the extraordinary complexity of mineral relationships all the way down to the nanoscale has necessitated the use of multiple microanalytical techniques. At present rates, the giant Olympic Dam Cu-Au-U deposit will continue production for the next 100 years and beyond, highlighting the critical need for understanding not only the complex mineralogical relationships that exist within the ore, but also how individual elements deport within each mineral phase in order to allow the most efficient extraction of target metals while avoiding, isolating or eliminating penalty elements. In the quest to develop a holistic understanding of Cu-Au ores in the Olympic Cu-Au province, the data and discussions on the mineral groups contained within this thesis supplement published research on other key mineral groups within these deposits, e.g., Cu-(Fe)-sulphides (Ciobanu et al. 2017a), U-minerals (Macmillan et al. 2016a, 2016b, 2016c, 2017), apatite (Krneta et al. 2016, 2017, 2018), Fe-oxides (Ciobanu et al. 2013, 2019; Verdugo-Ihl et al. 2017, 2019a, 2019b; Courtney-Davies et al. 2019a), REE-minerals (Schmandt et al. 2017, 2019a), or baryte (Schmandt et al. 2019b).

An approach to extractive metallurgy that incorporates detailed mineralogical and geochemical characterization of an ore, has becoming increasingly recognised as one of the most important steps towards maximising recovery of economic elements while rejecting deleterious ore components. The management of deleterious components in the ore, such as the RN discussed in this thesis, can prove costly and may even present significant health and safety risks if not correctly monitored and handled with due care (IAEA 2006). The ARC Research Hub for Australian Copper Uranium, to which this research is a contribution, was established with the understanding of the need for an all-inclusive interpretation of the mineralogical, geochemical and metallurgical processes responsible for decoupling, mobilisation and deportment of RN throughout the processing circuit, and how this is ultimately controlled by mineralogy. The mineralogy and

mineralogical textures in South Australian Cu-Au ores, however, are diverse and complex down to the finest scale, necessitating integrated multi-scale, multi-technique approaches to develop this understanding. By taking a mineralogical approach, the research presented here, along with that of [Schmandt \(2019\)](#), [Rollog \(2019\)](#), and the publications contained within those theses, has had far reaching implications for metallurgical processes seeking to reduce RN from processing streams.

4 REFERENCES

- Apukhtina, O.B., Kamenetsky, V.S., Ehrig, K., Kamenetsky, M.B., McPhie, J., Maas, R., Meffre, S., Goemann, K., Rodemann, T., Cook, N.J., and Ciobanu, C.L. (2016) Postmagmatic magnetite–apatite assemblage in mafic intrusions: a case study of dolerite at Olympic Dam, South Australia. *Contributions to Mineralogy and Petrology* 171:15.
- Bowden, B., Fraser, G., Davidson, G.J., Meffre, S., Skirrow, R., Bull, S., and Thompson, J. (2017) Age constraints on the hydrothermal history of the Prominent Hill iron oxide copper-gold deposit, South Australia. *Mineralium Deposita*, 52(6), 863–881.
- Ciobanu, C.L., Wade, B.P., Cook, N.J., Mumm, A.S. and Giles, D. (2013) Uranium-bearing hematite from the Olympic Dam Cu–U–Au deposit, South Australia: A geochemical tracer and reconnaissance Pb–Pb geochronometer. *Precambrian Research*, 238, 129–147.
- Ciobanu, C.L., Cook, N.J. and Ehrig, K. (2017a) Ore minerals down to the nanoscale: Cu-(Fe)-sulphides from the iron oxide copper gold deposit at Olympic Dam, South Australia. *Ore Geology Reviews*, 81, 1218–1235.
- Ciobanu, C.L., Wade, B.P., Cook, N.J., Schmidt Mumm, A., and Giles, D. (2013) Uranium-bearing hematite from the Olympic Dam Cu–U–Au deposit, South Australia: A geochemical tracer and reconnaissance Pb–Pb geochronometer. *Precambrian Research*, 238, 129–147.
- Ciobanu, C., Kontonikas-Charos, A., Slattery, A., Cook, N., Wade, B. and Ehrig, K. (2017b) Short-range stacking disorder in mixed-layer compounds: A HAADF STEM study of bastnäsite-parisite intergrowths. *Minerals*, 7(11), 227.
- Ciobanu, C.L., Verdugo-Ihl, M.R., Slattery, A., Cook, N.J., Ehrig, K., Courtney-Davies, L. and Wade, B.P. (2019) Silician Magnetite: Si–Fe-Nanoprecipitates and Other Mineral Inclusions in Magnetite from the Olympic Dam Deposit, South Australia. *Minerals*, 9(5), 311.
- Cook, N., Ehrig, K., Rollog, M., Ciobanu, C., Lane, D., Schmandt, D., Owen, N., Hamilton, T. and Grano, S. (2018) ^{210}Pb and ^{210}Po in geological and related anthropogenic materials: implications for their mineralogical distribution in base metal ores. *Minerals*, 8(5), 211.
- Courtney-Davies, L., Tapster, S.R., Ciobanu, C.L., Cook, N.J., Verdugo-Ihl, M.R., Ehrig, K.J., Kennedy, A.K., Gilbert, S.E., Condon, D.J. and Wade, B.P. (2019a) A multi-technique

- evaluation of hydrothermal hematite U-Pb isotope systematics: Implications for ore deposit geochronology. *Chemical Geology*, 513, 54–72.
- Courtney-Davies, L., Ciobanu, C.L., Verdugo-Ihl, M.R., Slattery, A., Cook, N.J., Dmitrijeva, M., Keyser, W., Wade, B.P., Domnick, U.I., Ehrig, K. and Xu, J. (2019b) Zircon at the Nanoscale Records Metasomatic Processes Leading to Large Magmatic–Hydrothermal Ore Systems. *Minerals*, 9(6), 364.
- Davidson, G.J., Paterson, H., Meffre, S. and Berry, R.F. (2007) Characteristics and origin of the Oak Dam East breccia-hosted, iron oxide Cu-U-(Au) deposit: Olympic Dam region, Gawler craton, South Australia. *Economic Geology*, 102(8), 1471–1498.
- Gilkes, R.J. and Palmer, B. (1983) Synthesis, properties, and dehydroxylation of members of the crandallite-goyazite series. *Mineralogical Magazine*, 47, 221–227.
- Huang, Q., Kamenetsky, V.S., McPhie, J., Ehrig, K., Meffre, S., Maas, R., Thompson, J., Kamenetsky, M., Chambefort, I., Apukhtina, O., and Hu, Y. (2015) Neoproterozoic (ca. 820–830 Ma) mafic dykes at Olympic Dam, South Australia: links with the Gairdner large igneous province. *Precambrian Research*, 271, 160–172.
- International Atomic Energy Agency (2006) Assessing the need for radiation protection measures in work involving minerals and raw materials. IAEA Safety Reports Series No. 49.
- Kalnins, C.A., Spooner, N.A., Clarke, M.J. and Ottaway, D. (2019) Alpha particle autoradiography for high spatial resolution mapping of radionuclides. *Journal of Environmental Radioactivity*, 197, 9–15.
- Kolitsch, U. and Pring, A. (2001) Crystal chemistry of the crandallite, beudantite and alunite groups: a review and evaluation of the suitability as storage materials for toxic metals. *Journal of Mineralogical and Petrological Sciences*, 96(2), 67–78.
- Kontonikas-Charos, A., Ciobanu, C.L., Cook, N.J., Ehrig, K., Ismail, R., Krneta, S. and Basak, A. (2018) Feldspar mineralogy and rare-earth element (re)mobilization in iron-oxide copper gold systems from South Australia: a nanoscale study. *Mineralogical Magazine*, 82(S1), S173–S197.
- Krneta, S., Ciobanu, C.L., Cook, N.J., Ehrig, K. and Kontonikas-Charos, A. (2016) Apatite at Olympic Dam, South Australia: A petrogenetic tool. *Lithos*, 262, 470–485.
- Krneta, S., Ciobanu, C.L., Cook, N.J., Ehrig, K. and Kontonikas-Charos, A. (2017) Rare earth element behaviour in apatite from the Olympic Dam Cu–U–Au–Ag deposit, South Australia. *Minerals*, 7(8), 135.
- Krneta, S., Ciobanu, C., Cook, N. and Ehrig, K. (2018) Numerical Modeling of REE Fractionation Patterns in Fluorapatite from the Olympic Dam Deposit (South Australia). *Minerals*, 8(8), 342.

- Landa, E. (2003) Mobilization of radionuclides from uranium mill tailings and related waste materials in anaerobic environments. *Journal of Radioanalytical and Nuclear Chemistry*, 255(3), 559–563.
- Lane, D.J., Cook, N.J., Grano, S.R. and Ehrig, K. (2016) Selective leaching of penalty elements from copper concentrates: A review. *Minerals Engineering*, 98, 110–121.
- Lee, M.R. (1993) The petrography, mineralogy and origins of calcium sulphate within the Cold Bokkeveld CM carbonaceous chondrite. *Meteoritics*, 28(1), 53–62.
- Macmillan, E., Ciobanu, C.L., Ehrig, K., Cook, N.J. and Pring, A. (2016a) Chemical zoning and lattice distortion in uraninite from Olympic Dam, South Australia. *American Mineralogist*, 101(10), 2351–2354.
- Macmillan, E., Cook, N.J., Ehrig, K., Ciobanu, C.L. and Pring, A. (2016b) Uraninite from the Olympic Dam IOCG-U-Ag deposit: Linking textural and compositional variation to temporal evolution. *American Mineralogist*, 101(6), 1295–1320.
- Macmillan, E., Ciobanu, C.L., Ehrig, K., Cook, N.J. and Pring, A. (2016c) Replacement of uraninite by bornite via coupled dissolution-precipitation: Evidence from texture and microstructure. *The Canadian Mineralogist*, 54(6), 1369–1383.
- Macmillan, E., Cook, N.J., Ehrig, K. and Pring, A. (2017) Chemical and textural interpretation of late-stage coffinite and brannerite from the Olympic Dam IOCG-Ag-U deposit. *Mineralogical Magazine*, 81(6), 1323–1366.
- Mayer, I., Cuisinier, F.J.G., Gdalya, S. and Popov, I. (2008) TEM study of the morphology of Mn²⁺-doped calcium hydroxyapatite and β -tricalcium phosphate. *Journal of Inorganic Biochemistry*, 102(2), 311–317.
- McInnes, B.I.A., Keays, R.R., Lambert, D.D., Hellstrom, J., and Allwood, J.S. (2008) Re–Os geochronology and isotope systematics of the Tanami, Tennant Creek and Olympic Dam Cu–Au deposits. *Australian Journal of Earth Sciences*, 55(6-7), 967–981.
- Monteagudo, J.M., Duran, A., Carmona, M.S., Schwab, R.G. and Higuera, P. (2003) Elimination of inorganic mercury from waste waters using crandallite-type compounds. *Journal of Chemical Technology & Biotechnology: International Research in Process, Environmental & Clean Technology*, 78(4), 399–405.
- Owen, N., Ciobanu, C., Cook, N., Slattery, A. and Basak, A. (2018) Nanoscale study of clausthalite-bearing symplectites in Cu-Au-(U) ores: Implications for ore genesis. *Minerals*, 8(2), 67.
- Owen, N., Cook, N.J., Rollog, M., Ehrig, K., Schmandt, D.S., Ram, R., Brugger, J., Ciobanu, C.L., Wade, B., and Guagliardo, P. (2019) REE-, Sr-, Ca-aluminum-phosphate-sulfate minerals of the alunite supergroup and their role as hosts for radionuclides. *American Mineralogist*, 104, 1806–1819.

- Owen, N.D., Cook, N.J., Ram, R., Etschmann, B.E., Ehrig, K., Schmandt, D.S., Rollog, M., Guagliardo, P., Brugger, J. (2020) A sponge for radionuclides: a study on the dynamic uptake of lead by synthetic aluminium-phosphate-sulphates *Applied Geochemistry* (in review).
- Rigali, M.J., Brady, P.V. and Moore, R.C. (2016) Radionuclide removal by apatite. *American Mineralogist*, 101(12), 2611–2619.
- Rollog, M., Cook, N.J., Guagliardo, P., Ehrig, K. and Kilburn, M. (2018) In situ spatial distribution mapping of radionuclides in minerals by nanoSIMS. *Geochemistry: Exploration, Environment, Analysis*, 19(3), 245–254.
- Rollog, M., Cook, N.J., Guagliardo, P., Ehrig, K., Ciobanu, C.L. and Kilburn, M. (2019) Detection of trace elements/isotopes in Olympic Dam copper concentrates by nanoSIMS. *Minerals*, 9(6), 336.
- Rollog, M. (2019) Department of radionuclides in copper concentrate from Olympic Dam. Unpublished Ph.D. thesis, The University of Adelaide, Adelaide, Australia.
- Schmandt, D.S. (2019) Mineralogical distributions of radionuclides in copper-uranium ores, Olympic Dam, South Australia. Unpublished Ph.D. thesis, The University of Adelaide, Adelaide, Australia.
- Schmandt, D., Cook, N., Ciobanu, C., Ehrig, K., Wade, B., Gilbert, S., and Kamenetsky, V. (2017) Rare earth element fluorocarbonate minerals from the Olympic Dam Cu-U-Au-Ag deposit, South Australia. *Minerals*, 7(10), 202.
- Schmandt, D.S., Cook, N.J., Ciobanu, C.L., Ehrig, K., Wade, B.P., Gilbert, S., and Kamenetsky, V.S. (2019a) Rare earth element phosphate minerals from the Olympic Dam Cu-U-Au-Ag deposit, South Australia: Recognizing temporal-spatial controls on REE mineralogy in an evolved IOCG system. *The Canadian Mineralogist*, 57(1), 3–24.
- Schmandt, D.S., Cook, N.J., Ehrig, K., Gilbert, S., Wade, B.P., Rollog, M., Ciobanu, C.L., and Kamenetsky, V.S. (2019b) Uptake of trace elements by baryte during copper ore processing: A case study from Olympic Dam, South Australia. *Minerals Engineering*, 135, 83–94.
- Schwab, R.G., Götz, C., Herold, H., and Pinto de Oliveira, N. (1991) Compounds of the crandallite type: synthesis and properties of pure (Ca, Sr, Ba, Pb, La, Ce to Eu)-arsenocrandallites. *Neues Jahrbuch für Mineralogie Monatshefte*, (3), 97–112.
- Schwab, R.G., Pimpl, T., Schukow, H., Stolle, A., and Breitingner, D.K. (2004) Compounds of the crandallite-type: Synthesis, properties and thermodynamic data of pure crandallite and woodhouseite. *Neues Jahrbuch für Mineralogie Monatshefte*, 385–409.
- Stüeken, E.E., Buick, R., Bekker, A., Catling, D., Foriel, J., Guy, B.M., Kah, L.C., Machel, H.G., Montañez, I.P. and Poulton, S.W. (2015) The evolution of the global selenium cycle: Secular trends in Se isotopes and abundances. *Geochimica et Cosmochimica Acta*, 162, 109–125.

- Verdugo-Ihl, M.R., Ciobanu, C.L., Cook, N.J., Ehrig, K.J., Courtney-Davies, L., and Gilbert, S. (2017) Textures and U-W-Sn-Mo signatures in hematite from the Olympic Dam Cu-U-Au-Ag deposit, South Australia: Defining the archetype for IOCG deposits. *Ore Geology Reviews*, 91, 173–195.
- Verdugo-Ihl, M.R., Ciobanu, C.L., Cook, N.J., Ehrig, K.J., and Courtney-Davies, L. (2019a). Defining early stages of IOCG systems: Evidence from iron oxides in the outer shell of the Olympic Dam deposit, South Australia. *Mineralium Deposita*, 1–24.
- Verdugo-Ihl, M.R., Ciobanu, C.L., Slattery, A., Cook, N.J., Ehrig, K., and Courtney-Davies, L. (2019b) Copper-arsenic nanoparticles in hematite: Fingerprinting fluid-mineral interaction. *Minerals*, 9(7), 388.

CHAPTER 7

SUPPLEMENTARY MATERIAL

SUPPLEMENTARY MATERIAL A: APPENDIX FOR CHAPTER 2

Table 1: Pb isotope LA-ICP-MS analysis of Pb-chalcogenides and Cu-(Fe)-sulphides from a Cu-Au mineralised zone in the Mt Woods Inlier.

Pb Mineral	²⁰⁸ Pb/ ²⁰⁴ Pb	% error	²⁰⁷ Pb/ ²⁰⁴ Pb	% error	²⁰⁶ Pb/ ²⁰⁴ Pb	% error	²⁰⁸ Pb/ ²⁰⁶ Pb	% error	²⁰⁴ Pb/ ²⁰⁶ Pb	% error	²⁰⁷ Pb/ ²⁰⁶ Pb	% error
Alt	53.60	5	18.70	5	73.80	7	0.744	6	0.014	7	0.257	4
Alt	58.00	7	22.40	7	99.70	4	0.568	3	0.010	4	0.219	3
Cls	49.90	7	16.50	8	36.90	8	1.350	3	0.027	8	0.449	2
Cls	55.50	5	17.61	4	37.50	3	1.454	3	0.027	3	0.462	1
Cls	55.70	5	17.63	4	37.70	3	1.470	2	0.027	3	0.466	1
Cls	55.90	4	17.59	5	38.50	4	1.423	3	0.026	4	0.458	2
Cls	53.10	4	16.85	3	38.90	3	1.364	2	0.026	3	0.437	2
Cls	46.90	5	16.72	4	38.90	4	1.208	2	0.026	4	0.431	2
Cls	43.40	3	16.13	3	39.10	3	1.113	2	0.026	3	0.420	2
Cls	53.84	1	17.88	1	39.42	1	1.372	1	0.025	1	0.454	1
Cls	50.90	6	17.28	5	39.50	6	1.295	1	0.025	6	0.443	1
Cls	54.40	8	17.16	5	39.60	6	1.278	6	0.025	6	0.427	4
Cls	51.20	3	16.94	2	39.68	2	1.299	2	0.025	2	0.430	1
Cls	49.70	9	17.10	8	40.00	5	1.261	4	0.025	5	0.428	3
Cls	50.00	3	16.79	3	40.08	2	1.258	2	0.025	2	0.421	1
Cls	53.60	7	17.43	5	40.10	4	1.307	4	0.025	4	0.441	3
Cls	50.40	4	16.83	3	40.80	2	1.234	2	0.025	2	0.415	2
Cls	54.50	2	17.40	1	40.83	1	1.343	2	0.024	1	0.429	1
Cls	52.50	5	17.43	3	41.10	3	1.283	4	0.024	3	0.429	3
Cls	54.70	4	17.41	3	41.22	2	1.311	2	0.024	2	0.419	2
Cls	55.60	4	17.46	4	41.50	3	1.338	2	0.024	3	0.420	2
Cls	51.80	3	17.24	2	41.55	2	1.250	2	0.024	2	0.417	1
Cls	50.70	3	16.89	3	41.76	2	1.226	1	0.024	2	0.406	1
Cls	51.80	7	17.48	3	41.80	3	1.258	4	0.024	3	0.420	4
Cls	49.60	3	16.98	2	41.83	2	1.196	2	0.024	2	0.411	1
Cls	55.20	4	17.95	4	41.90	5	1.298	5	0.024	5	0.416	2
Cls	52.70	2	17.14	2	41.92	2	1.248	3	0.024	2	0.411	2
Cls	50.50	4	17.06	3	42.10	3	1.200	2	0.024	3	0.409	1
Cls	55.05	2	17.69	1	42.48	2	1.297	2	0.024	2	0.416	2
Cls	55.10	3	17.66	2	42.58	2	1.296	2	0.023	2	0.416	2
Cls	56.40	6	17.77	6	42.70	4	1.323	3	0.023	4	0.420	2
Cls	51.30	4	17.47	4	42.70	4	1.215	3	0.023	4	0.409	2
Cls	52.39	2	17.68	1	42.75	1	1.224	1	0.023	1	0.412	1
Cls	53.90	2	17.25	2	42.80	2	1.259	2	0.023	2	0.404	2
Cls	53.80	8	18.18	5	42.90	3	1.241	5	0.023	3	0.415	2
Cls	55.50	2	18.06	2	42.91	1	1.270	2	0.023	1	0.415	1
Cls	56.60	3	17.83	2	42.95	2	1.311	2	0.023	2	0.415	1
Cls	55.80	6	17.70	4	43.00	4	1.324	4	0.023	4	0.419	2
Cls	52.20	2	17.53	2	43.07	2	1.215	1	0.023	2	0.404	1
Cls	54.90	5	17.55	4	43.10	3	1.281	3	0.023	3	0.411	2
Cls	49.90	8	17.00	6	43.10	6	1.154	4	0.023	6	0.395	2
Cls	52.30	2	17.79	2	43.12	2	1.215	1	0.023	2	0.410	1
Cls	54.40	2	17.67	2	43.20	6	1.284	2	0.023	6	0.423	3

Cls	52.10	2	17.08	2	43.21	1	1.208	1	0.023	1	0.400	1
Cls	54.10	4	17.40	3	43.47	2	1.246	3	0.023	2	0.401	2
Cls	52.50	6	17.56	5	43.50	5	1.216	3	0.023	5	0.402	2
Cls	53.70	2	17.61	1	43.54	1	1.229	2	0.023	1	0.406	1
Cls	53.40	4	17.88	3	43.59	2	1.234	2	0.023	2	0.410	1
Cls	57.30	4	17.98	3	43.71	2	1.305	2	0.023	2	0.412	1
Cls	52.40	8	17.70	6	43.80	5	1.184	4	0.023	5	0.396	2
Cls	55.80	3	18.02	2	43.88	1	1.282	2	0.023	1	0.407	1
Cls	51.30	3	17.27	3	43.90	2	1.172	2	0.023	2	0.395	1
Cls	55.39	2	17.91	3	44.10	2	1.261	2	0.023	2	0.406	2
Cls	52.60	3	17.41	2	44.16	2	1.189	1	0.023	2	0.393	1
Cls	53.70	4	17.80	3	44.36	2	1.209	2	0.023	2	0.401	2
Cls	52.60	4	17.72	5	44.40	4	1.190	3	0.023	4	0.401	2
Cls	51.50	3	17.32	3	44.50	3	1.150	2	0.022	3	0.386	1
Cls	53.10	3	17.65	3	44.60	3	1.187	1	0.022	3	0.402	1
Cls	53.71	2	17.99	1	44.74	1	1.205	1	0.022	1	0.405	1
Cls	54.50	2	18.38	2	44.80	2	1.201	3	0.022	2	0.404	2
Cls	53.00	2	17.92	2	44.83	1	1.181	1	0.022	1	0.398	1
Cls	53.10	2	17.29	2	44.90	2	1.189	2	0.022	2	0.389	2
Cls	55.20	3	17.79	2	44.93	2	1.236	3	0.022	2	0.396	2
Cls	56.00	4	17.43	3	44.93	2	1.261	3	0.022	2	0.394	1
Cls	49.60	3	17.17	4	45.00	4	1.120	2	0.022	4	0.386	2
Cls	58.00	7	18.10	6	45.00	5	1.265	3	0.022	5	0.401	2
Cls	54.50	3	17.18	3	45.01	2	1.209	3	0.022	2	0.382	1
Cls	56.80	5	18.15	4	45.02	1	1.259	3	0.022	1	0.402	2
Cls	52.00	2	17.68	2	45.09	1	1.150	2	0.022	1	0.389	1
Cls	51.20	6	17.23	6	45.10	6	1.123	3	0.022	6	0.383	3
Cls	55.40	3	17.66	2	45.11	2	1.237	3	0.022	2	0.395	2
Cls	53.97	1	18.10	1	45.20	1	1.194	1	0.022	1	0.403	1
Cls	49.60	5	17.12	5	45.30	3	1.095	3	0.022	3	0.372	2
Cls	53.10	7	17.90	7	45.30	6	1.184	4	0.022	6	0.386	3
Cls	53.02	2	17.29	2	45.30	2	1.153	2	0.022	2	0.381	1
Cls	53.30	4	17.18	4	45.40	3	1.179	2	0.022	3	0.379	2
Cls	52.30	3	17.41	3	45.40	3	1.147	1	0.022	3	0.387	1
Cls	58.80	3	18.18	3	45.50	3	1.275	2	0.022	3	0.398	1
Cls	54.40	4	18.02	4	45.60	4	1.173	2	0.022	4	0.390	2
Cls	55.88	2	17.93	2	45.66	1	1.224	1	0.022	1	0.394	1
Cls	53.60	4	18.29	3	45.70	5	1.191	5	0.022	5	0.404	6
Cls	55.10	2	18.39	2	45.73	2	1.202	1	0.022	2	0.401	1
Cls	57.30	3	18.08	2	45.79	2	1.237	2	0.022	2	0.394	1
Cls	59.70	4	18.71	4	45.80	4	1.306	2	0.022	4	0.410	1
Cls	52.51	2	17.91	2	45.83	2	1.156	1	0.022	2	0.391	1
Cls	58.00	3	18.20	2	45.94	2	1.252	2	0.022	2	0.393	1
Cls	53.67	2	18.20	2	46.21	1	1.162	2	0.022	1	0.391	2
Cls	56.80	4	17.86	3	46.23	2	1.225	3	0.022	2	0.383	2
Cls	55.90	3	17.63	2	46.29	2	1.201	3	0.022	2	0.381	2
Cls	55.40	5	17.66	5	46.30	3	1.193	2	0.022	3	0.382	2
Cls	57.30	5	18.50	6	46.40	8	1.241	6	0.022	8	0.399	4

Cls	55.50	3	17.78	2	46.59	2	1.188	1	0.021	2	0.382	1
Cls	57.30	8	18.10	7	46.60	7	1.220	3	0.021	7	0.405	10
Cls	56.60	4	17.91	3	46.60	3	1.209	4	0.021	3	0.381	2
Cls	55.60	4	18.04	4	46.70	3	1.182	2	0.021	3	0.388	1
Cls	51.50	3	17.38	3	46.93	2	1.095	2	0.021	2	0.370	1
Cls	56.60	6	18.07	4	47.00	4	1.196	3	0.021	4	0.385	2
Cls	53.70	4	18.07	4	47.00	4	1.108	7	0.021	4	0.384	4
Cls	48.10	8	15.93	6	47.10	4	1.005	5	0.021	4	0.334	3
Cls	54.80	9	17.73	5	47.30	7	1.153	7	0.021	7	0.377	5
Cls	55.70	3	18.29	3	47.49	2	1.174	2	0.021	2	0.385	2
Cls	54.90	3	18.08	4	47.50	3	1.163	3	0.021	3	0.378	3
Cls	57.30	4	18.15	3	47.60	2	1.209	4	0.021	2	0.379	2
Cls	54.20	4	17.24	4	47.60	3	1.177	3	0.021	3	0.370	2
Cls	57.70	3	18.09	3	47.60	3	1.236	2	0.021	3	0.386	2
Cls	52.30	6	17.98	5	47.90	6	1.095	5	0.021	6	0.373	4
Cls	56.50	8	18.20	8	48.50	7	1.156	3	0.021	7	0.372	2
Cls	55.90	3	18.14	2	48.68	2	1.158	2	0.021	2	0.376	1
Cls	54.60	1	18.35	1	48.79	1	1.118	1	0.020	1	0.377	1
Cls	52.10	3	17.62	2	48.98	2	1.056	2	0.020	2	0.358	2
Cls	51.50	5	17.10	4	49.00	4	1.077	3	0.020	4	0.355	2
Cls	52.80	4	17.37	3	49.10	2	1.077	4	0.020	2	0.355	2
Cls	54.40	6	17.78	5	49.20	4	1.111	3	0.020	4	0.358	2
Cls	59.60	6	18.60	6	49.30	5	1.204	2	0.020	5	0.380	2
Cls	58.70	5	18.68	5	49.40	5	1.172	2	0.020	5	0.376	1
Cls	54.60	3	18.12	2	49.73	1	1.099	2	0.020	1	0.365	1
Cls	54.80	5	17.34	5	49.80	5	1.105	1	0.020	5	0.348	2
Cls	57.80	4	18.36	3	49.80	3	1.155	3	0.020	3	0.370	2
Cls	54.40	2	18.86	2	50.00	2	1.074	3	0.020	2	0.371	3
Cls	57.40	6	17.60	3	50.60	3	1.128	2	0.020	3	0.350	1
Cls	57.80	4	18.55	4	50.80	4	1.129	3	0.020	4	0.365	2
Cls	51.80	8	17.20	8	50.90	9	1.041	4	0.020	9	0.354	3
Cls	49.60	7	16.70	8	51.10	9	0.947	4	0.020	9	0.330	6
Cls	53.00	3	18.12	2	51.10	2	1.035	1	0.020	2	0.352	1
Cls	57.40	4	18.70	3	51.40	3	1.115	3	0.019	3	0.360	1
Cls	52.63	1	18.60	3	51.44	2	1.022	2	0.019	2	0.361	3
Cls	53.70	3	18.07	3	51.88	2	1.045	2	0.019	2	0.349	2
Cls	51.40	7	17.30	6	52.10	6	0.991	5	0.019	6	0.334	2
Cls	56.00	7	18.20	6	52.10	4	1.100	4	0.019	4	0.359	3
Cls	53.30	4	18.24	3	52.20	2	1.017	3	0.019	2	0.346	2
Cls	54.70	5	19.40	7	52.40	4	1.017	6	0.019	4	0.359	6
Cls	54.30	4	18.34	3	52.80	2	1.018	4	0.019	2	0.349	2
Cls	51.30	6	17.90	6	52.90	5	0.964	2	0.019	5	0.338	2
Cls	54.50	4	17.91	5	53.60	5	1.046	4	0.019	5	0.335	3
Cls	53.85	1	18.91	2	53.83	2	1.005	1	0.019	2	0.351	1
Cls	57.30	4	18.54	3	54.20	3	1.080	2	0.018	3	0.348	1
Cls	53.80	3	18.85	3	55.60	2	0.964	2	0.018	2	0.339	2
Cls	55.80	8	18.60	7	56.40	10	1.001	5	0.018	10	0.332	5
Cls	53.87	1	18.62	1	56.58	1	0.950	1	0.018	1	0.327	1

Cls	56.40	8	18.60	6	56.90	6	0.975	4	0.018	6	0.325	3
Cls	56.40	6	18.60	6	57.10	4	0.994	4	0.018	4	0.320	3
Cls	58.80	9	19.30	7	57.40	6	1.072	3	0.017	6	0.336	2
Cls	56.20	7	18.80	6	57.80	6	0.975	2	0.017	6	0.328	2
Cls	49.60	8	18.40	9	57.80	7	0.847	5	0.017	7	0.309	3
Cls	51.20	7	16.90	7	57.80	7	0.876	2	0.017	7	0.295	3
Cls	54.11	2	18.82	2	57.80	3	0.935	2	0.017	3	0.328	3
Cls	57.00	8	19.60	8	57.90	9	1.018	2	0.017	9	0.339	2
Cls	54.70	5	18.20	6	58.00	7	0.957	4	0.017	7	0.317	3
Cls	54.00	4	20.10	5	58.10	4	0.936	1	0.017	4	0.333	2
Cls	54.80	1	19.07	1	58.87	2	0.935	1	0.017	2	0.324	2
Cls	57.20	9	19.30	9	59.10	9	0.958	6	0.017	9	0.329	4
Cls	55.80	6	19.16	5	59.10	5	0.914	3	0.017	5	0.318	3
Cls	58.00	9	19.70	6	59.40	6	0.930	5	0.017	6	0.323	5
Cls	56.60	3	18.62	3	59.50	2	0.943	2	0.017	2	0.312	1
Cls	52.10	6	18.21	5	60.70	4	0.850	3	0.016	4	0.301	2
Cls	52.50	3	18.77	3	61.10	2	0.858	4	0.016	2	0.308	2
Cls	51.20	6	18.50	4	61.60	4	0.834	7	0.016	4	0.301	5
Cls	54.30	4	18.77	3	61.80	3	0.866	6	0.016	3	0.299	5
Cls	56.70	8	19.30	8	63.80	8	0.910	3	0.016	8	0.301	3
Cls	53.26	2	18.98	1	64.04	1	0.832	1	0.016	1	0.296	1
Cls	57.30	3	19.21	2	65.00	2	0.865	1	0.015	2	0.293	1
Cls	56.40	2	18.92	2	65.08	1	0.862	2	0.015	1	0.292	1
Cls	60.60	4	20.02	4	65.10	4	0.949	2	0.015	4	0.310	2
Cls	53.10	4	19.50	5	65.20	9	0.851	6	0.015	9	0.313	5
Cls	59.30	9	19.70	9	65.90	9	0.869	4	0.015	9	0.297	3
Cls	56.90	7	19.20	7	66.00	7	0.860	3	0.015	7	0.287	3
Cls	59.00	3	19.51	3	66.90	2	0.885	2	0.015	2	0.295	2
Cls	53.30	6	18.44	5	67.90	5	0.779	2	0.015	5	0.275	2
Cls	54.80	6	19.74	4	72.70	5	0.763	5	0.014	5	0.274	4
Cls	54.30	5	19.70	6	74.80	6	0.735	2	0.013	6	0.265	2
Cls	52.90	3	20.32	3	77.80	4	0.674	3	0.013	4	0.254	3
Cls	54.80	4	19.32	4	78.10	4	0.702	3	0.013	4	0.251	3
Cls	51.50	8	19.70	8	78.60	9	0.675	6	0.013	9	0.258	4
Cls	54.60	2	20.66	2	83.20	2	0.660	2	0.012	2	0.249	1
Cls	54.20	4	19.83	3	84.30	3	0.637	3	0.012	3	0.232	2
Cls	56.40	6	20.70	8	88.00	8	0.664	4	0.011	8	0.238	1
Cls	46.30	6	19.90	8	93.00	8	0.505	5	0.011	8	0.213	4
Cls	52.40	4	20.70	5	95.00	7	0.570	6	0.011	7	0.221	4
Cls	57.60	7	22.20	8	97.70	8	0.601	3	0.010	8	0.226	3
Cls	54.20	3	21.59	4	98.00	5	0.551	4	0.010	5	0.217	3
Cls	49.10	5	19.94	4	98.90	4	0.485	3	0.010	4	0.201	2
Cls	59.80	8	23.10	6	99.40	5	0.603	6	0.010	5	0.232	4
Cls	53.90	4	20.63	3	100.70	3	0.539	2	0.010	3	0.206	2
Cls	53.30	6	20.04	4	102.60	5	0.525	2	0.010	5	0.198	2
Cls	56.40	6	21.20	6	104.60	5	0.537	2	0.010	5	0.203	1
Cls	54.40	9	19.30	8	107.10	6	0.498	4	0.009	6	0.178	3
Cls	61.50	9	22.80	8	109.90	8	0.573	5	0.009	8	0.213	4

Cls	60.00	6	24.40	6	111.30	6	0.551	5	0.009	6	0.218	3
Cls	57.70	8	24.70	8	115.60	8	0.497	7	0.009	8	0.205	3
Cls	51.10	6	22.30	7	120.00	10	0.441	8	0.008	10	0.188	5
Cls	55.40	4	23.89	4	124.40	5	0.449	2	0.008	5	0.193	1
Cls	56.10	9	21.80	8	124.60	8	0.445	2	0.008	8	0.174	2
Cls	55.40	4	23.90	4	124.80	5	0.445	2	0.008	5	0.192	2
Cls	53.10	7	22.20	6	128.20	7	0.413	2	0.008	7	0.175	2
Cls	56.80	2	23.39	2	130.00	2	0.437	2	0.008	2	0.182	2
Cls	53.12	1	23.94	1	131.90	3	0.403	3	0.008	3	0.181	2
Cls	52.10	3	23.36	3	134.70	4	0.389	3	0.007	4	0.173	2
Cls	61.60	8	24.50	7	135.00	8	0.459	4	0.007	8	0.185	2
Cls	52.50	4	24.25	4	143.50	3	0.373	3	0.007	3	0.171	2
Cls	54.60	7	25.00	7	152.00	7	0.356	2	0.007	7	0.167	2
Cls	59.90	8	29.80	7	167.00	7	0.344	3	0.006	7	0.176	2
Cls	53.30	10	26.20	10	177.00	9	0.303	2	0.006	9	0.150	2
Cls	55.60	7	29.20	7	183.00	7	0.304	4	0.005	7	0.158	3
Cls	51.80	5	26.81	3	184.20	5	0.288	5	0.005	5	0.143	2
Cls	58.00	6	29.70	5	200.00	6	0.291	3	0.005	6	0.149	2
Cls	56.80	4	29.40	5	211.00	7	0.271	5	0.005	7	0.142	4
Cls	56.50	9	32.10	8	228.00	7	0.246	3	0.004	7	0.138	2
Cls	54.20	9	37.90	9	234.00	9	0.228	4	0.004	9	0.158	2
Cls/Alt	53.20	5	17.78	6	52.30	5	1.015	2	0.019	5	0.338	1
Cls/Alt	52.10	5	17.59	4	56.20	4	0.935	2	0.018	4	0.313	2
Gn	54.60	6	17.39	5	42.30	4	1.271	3	0.024	4	0.408	2
Gn	52.00	3	17.44	2	43.92	2	1.207	2	0.023	2	0.403	1
Gn	52.10	3	17.59	3	44.60	3	1.166	2	0.022	3	0.395	2
Gn	55.60	5	17.14	3	45.20	3	1.227	3	0.022	3	0.384	2
Gn	53.30	6	17.80	5	46.00	4	1.157	2	0.022	4	0.389	2
Gn	54.71	2	18.38	1	48.32	1	1.140	2	0.021	1	0.381	1
Gn	61.50	4	18.68	3	48.90	2	1.249	3	0.020	2	0.384	2
Gn	51.10	4	17.46	3	52.40	2	0.982	3	0.019	2	0.341	1
Gn	53.30	7	17.80	6	54.60	3	0.952	4	0.018	3	0.315	3
Gn	53.50	5	19.20	3	55.70	3	0.972	2	0.018	3	0.349	1
Gn	62.90	6	19.21	3	61.10	4	1.016	5	0.016	4	0.315	6
Gn	53.70	6	18.16	5	66.00	6	0.855	5	0.015	6	0.277	3
Gn	52.00	9	18.80	10	69.00	9	0.775	4	0.014	9	0.278	3
Gn	45.00	8	16.81	5	69.40	6	0.658	7	0.014	6	0.245	3
Gn	53.10	6	18.96	5	82.60	4	0.651	3	0.012	4	0.232	2
Gn	54.20	3	21.45	2	94.50	2	0.580	3	0.011	2	0.228	2
Gn	53.00	3	21.75	2	95.10	2	0.569	2	0.011	2	0.230	1
Gn	50.50	4	20.06	3	99.30	3	0.510	3	0.010	3	0.204	2
Gn	57.50	6	21.80	6	104.60	6	0.550	2	0.010	6	0.208	2
Gn	52.70	5	22.90	4	131.40	4	0.403	2	0.008	4	0.174	2
Gn	54.20	3	23.61	3	136.10	3	0.400	1	0.007	3	0.173	1
Gn	54.10	6	25.00	7	153.00	10	0.361	6	0.007	10	0.164	4
Gn	51.10	5	26.90	5	164.40	5	0.312	3	0.006	5	0.163	1
Gn	50.70	7	23.70	7	166.00	6	0.310	4	0.006	6	0.145	3
Gn	55.90	2	44.94	1	299.00	2	0.188	2	0.003	2	0.150	1

Gn	55.20	2	34.61	2	362.40	2	0.154	2	0.003	2	0.095	2
Gn	39.30	5	40.90	6	363.00	7	0.111	5	0.003	7	0.113	2
Gn	53.10	7	34.50	7	391.00	6	0.139	4	0.003	6	0.087	4
Gn	54.40	3	40.90	3	419.70	2	0.130	2	0.002	2	0.097	2
Gn	54.60	5	50.70	4	547.00	3	0.100	3	0.002	3	0.093	2
Gn	55.60	5	52.70	5	581.00	3	0.096	3	0.002	3	0.091	2
Gn	56.50	4	142.40	3	1627.00	4	0.034	3	0.001	4	0.087	1
Sulphide	75.00	13	24.70	13	86.00	13	0.843	4	0.012	13	0.296	3
Sulphide	56.40	9	26.30	9	136.00	9	0.415	4	0.007	9	0.188	3
Sulphide	53.00	10	23.60	11	120.00	13	0.468	5	0.008	13	0.202	4
Sulphide	87.00	25	37.50	23	217.00	24	0.377	5	0.005	24	0.176	5
Sulphide	49.90	6	23.10	6	78.60	7	0.639	2	0.013	7	0.301	2
Sulphide	56.20	9	25.70	10	144.00	9	0.386	2	0.007	9	0.174	2
Sulphide	77.00	32	35.00	34	172.00	34	0.451	4	0.006	34	0.205	4
Sulphide	56.10	7	20.00	7	70.30	8	0.799	3	0.014	8	0.290	2
Sulphide	52.00	11	18.40	10	65.90	10	0.760	3	0.015	10	0.284	3
Sulphide	54.00	19	20.80	16	76.00	20	0.725	9	0.013	20	0.272	5
Sulphide	62.10	14	22.70	14	102.00	15	0.602	4	0.010	15	0.239	5
Sulphide	53.70	5	21.70	6	73.40	8	0.775	6	0.014	8	0.299	4
Sulphide	50.70	7	17.60	6	55.80	6	0.935	3	0.018	6	0.320	3
Sulphide	57.70	14	20.50	14	69.60	14	0.852	3	0.014	14	0.307	4
Sulphide	64.00	17	31.60	16	184.00	17	0.353	3	0.005	17	0.177	4
Sulphide	65.30	11	28.20	9	142.00	24	0.429	5	0.007	24	0.189	3
Sulphide	52.60	17	22.80	15	145.00	32	0.428	6	0.007	32	0.185	6
Sulphide	59.00	34	26.00	42	177.00	40	0.327	5	0.006	40	0.159	4
Sulphide	86.00	78	40.00	80	210.00	71	0.408	5	0.005	71	0.183	5
Sulphide	85.00	40	32.00	38	150.00	35	0.539	4	0.007	35	0.214	4
Sulphide	56.70	6	25.00	6	144.80	6	0.389	2	0.007	6	0.174	3
Sulphide	72.00	24	33.00	23	212.00	25	0.339	3	0.005	25	0.158	3
Sulphide	61.20	7	25.70	6	140.70	7	0.425	3	0.007	7	0.182	2
Sulphide	58.00	29	29.40	23	153.00	31	0.388	5	0.007	31	0.172	5
Sulphide	50.00	200	44.00	157	290.00	97	0.336	9	0.003	97	0.209	6
Sulphide	60.10	7	22.70	6	105.70	6	0.561	3	0.009	6	0.217	2
Sulphide	67.00	16	29.30	19	128.00	17	0.549	4	0.008	17	0.224	4
Sulphide	62.00	95	50.00	126	470.00	106	0.123	3	0.002	106	0.121	2
Sulphide	59.20	11	23.20	12	94.00	13	0.665	3	0.011	13	0.256	3
Sulphide	68.00	25	27.10	25	137.00	26	0.463	4	0.007	26	0.200	3
Sulphide	65.00	22	25.00	24	86.00	22	0.754	3	0.012	22	0.288	4
Sulphide	59.60	10	25.50	9	148.00	10	0.400	5	0.007	10	0.173	3
Sulphide	56.70	11	22.50	11	110.00	12	0.498	4	0.009	12	0.200	5
Sulphide	54.00	20	21.70	18	130.00	18	0.386	6	0.008	18	0.167	5
Sulphide	57.90	11	25.70	11	130.00	16	0.434	10	0.008	16	0.196	8
Sulphide	69.00	39	39.00	49	146.00	20	0.382	5	0.007	20	0.169	6
Sulphide	53.30	10	26.80	10	173.00	9	0.304	3	0.006	9	0.150	2
Sulphide	64.00	34	28.70	30	147.00	30	0.491	6	0.007	30	0.202	5

SUPPLEMENTARY MATERIAL B: APPENDIX FOR CHAPTER 3

Table 1: Elements analysed, peak/background positions, count times, and standards used for sulphide analysis.

Element/line	Diffracting Crystal/Sp#	Peak count time (sec)	Background type/fit*	# bkgd points acquired (Lo/Hi)	Background count time (Lo/Hi) (sec)	Standard
S Ka	LPET/1	10	Multipoint	2/2	10/10	Astimex Marcasite
Pb Ma	LPET/1	30	Multipoint	4/3	20/15	P&H block Galena
Cd La	LPET/1	60	Multipoint	2/2	30/30	P&H block Grenockite
Bi Ma	LPET/1	30	Multipoint	2/2	20/20	P&H block Bi ₂ Se ₃
As La	TAP/2	30	Multipoint	2/2	20/20	Astimex GaAs
Se La	TAP/2	100	Multipoint	2/3	60/60	P&H block Bi ₂ Se ₃
Fe Ka	LLIF/3	10	Multipoint	2/2	10/10	P&H block Chalcopyrite
Cu Ka	LLIF/3	10	Linear	-	10/10	P&H block Chalcopyrite
Mn Ka	LLIF/3	30	Multipoint	2/2	20/20	P&H block Rhodonite
Ga Ka	LLIF/3	20	Linear	-	10/10	P&H block GaAs
Ag La	LPET/4	30	Multipoint	1/2	10/20	P&H block AgTe
Sn La	LPET/4	30	Multipoint	2/2	20/20	P&H Cassiterite
In La	LPET/4	30	Multipoint	2/1	20/10	Astimex metal Indium
Sb La	LPET/4	30	Multipoint	2/2	20/20	Astimex Stibnite
Te La	LPET/4	30	Multipoint	2/2	20/20	P&H block AgTe
Tl Ma	LPET/4	20	Linear	-	10/10	Astimex Tl metal
Hg La	LLIF/5	100	Multipoint	3/3	60/60	P&H Cinnabar
Zn Ka	LLIF/5	30	Multipoint	2/2	10/10	P&H Spahlerite
Ni Ka	LLIF/5	30	Linear	-	10/10	Astimex Pentlandite
Co Ka	LLIF/5	30	Multipoint	2/2	10/10	Astimex Co metal

Table 2: Elemental overlap corrections used in sulphide package.

Element/line	Diffracting crystal	Overlapping element/order	Overlap standard
S Ka	LPET/1	Co III, Sb II, Hg I	Astimex Co metal, Astimex Stibnite, Astimex Cinnabar
Pb Ma	LPET/1	Fe III, As V	P&H block Chalcopyrite, Astimex GaAs
Cd La	LPET/1	Pb IV, Ag I, Se IV	Astimex Galena, P&H block AgTe, Astimex Bi ₂ Se ₃
As La	TAP/2	Sb III, Fe V, Co VI	Astimex Stibnite, P&H Chalcopyrite, Astimex Co metal
Se La	TAP/2	As I, Te III, Co V, Ni IV	Astimex GaAs, P&H AgTe, Astimex Co metal, Astimex Ni metal
Fe Ka	LLIF/3	Pb II	P&H Galena
Mn Ka	LLIF/3	Hg II, As II	P&H Cinnabar, P&H GaAs
Ag La	LPET/4	Hg IV, Cu III, Mn II	P&H Cinnabar, P&H Chalcopyrite, P&H Rhodonite
Sn La	LPET/4	Co II, Hg IV	Astimex Co metal, P&H Cinnabar

In La	LPET/4	Cd I, Bi IV, Hg III	P&H Grenockite, P&H Bi ₂ Se ₃ , P&H Cinnabar
Co Ka	LLIF/5	Hg II	P&H Cinnabar
Sb La	LPET/4	Bi III	P&H Bi ₂ Se ₃
Te La	LPET/4	Sn I, Se III, Ni II	P&H Cassiterite, P&H Bi ₂ Se ₃ , Astimex Pentlandite
Bi Ma	LPET/1	Pb I	P&H Galena
Tl Ma	LPET/4	Hg I	Astimex Cinnabar
Ga Ka	LLIF/3	Pb I	P&H Galena

SUPPLEMENTARY MATERIAL C: APPENDIX FOR CHAPTER 4

Table 1: Electron Microprobe setup with element analysis conditions and standard information.

Element	Count Time (sec)	Hi (sec)	Lo (sec)	Diffraction Crystal (Sp no.)	Standard no.	Standard Name
Ca ka	20	10	10	LPET (1)	535	Astimex Plagioclase
K ka	20	10	10	LPET (1)	541	Astimex Sanidine
Ti ka	30	15	15	LPET (1)	559	Rutile
U mb	60	30	30	LPET (1)	631	UO ₂
La la	20	10	10	LPET (1)	1200	Lanthanum Phosphate (Ch)
Ce la	20	10	10	LPET (1)	1201	Cerium Phosphate (Ch)
Ba la	20	10	10	LPET (1)	554	Barite
F ka	20	40	30	PCO (2)	2001	Astimex Apatite
Fe ka	20	10	10	LIFF (3)	502	Astimex Almandine Garnet
Mn ka	20	10	10	LIFF (3)	557	Rhodonite
Cu ka	20	10	10	LIFF (3)	556	Chalcopyrite
Ho lb	20	10	10	LIFF (3)	1209	Holmium Phosphate (Ch)
Yb la	20	10	10	LIFF (3)	1212	Ytterbium Phosphate (Ch)
Tm la	20	10	10	LIFF (3)	1211	Thulium Phosphate (Ch)
Er la	20	10	10	LIFF (3)	1210	Erbium Phosphate (Ch)
Gd lb	20	10	10	LIFF (3)	1206	Gadolinium Phosphate (Ch)
Dy la	20	10	10	LIFF (3)	1208	Dysprosium Phosphate (Ch)
Tb la	20	10	10	LIFF (3)	1207	Terbium Phosphate (Ch)
Sm lb	20	10	10	LIFF (3)	1204	Samarium Phosphate (Ch)
Eu la	20	10	10	LIFF (3)	1205	Europium Phosphate (Ch)
Nd lb	20	10	10	LIFF (3)	1203	Neodymium Phosphate (Ch)
Pr lb	20	10	10	LIFF (3)	1202	Praseodymium Phosphate (Ch)
Na ka	20	10	10	TAP (4)	501	Astimex Albite
Si ka	20	10	10	TAP (4)	501	Astimex Albite
Mg ka	20	10	10	TAP (4)	502	Astimex Almandine Garnet
Al ka	20	10	10	TAP (4)	501	Astimex Albite
Sr la	20	10	10	TAP (4)	513	Astimex Celestine
As la	30	15	15	TAP (4)	562	Gallium Arsenide
P ka	20	10	10	LPET (5)	504	Astimex Apatite
S ka	20	10	10	LPET (5)	513	Astimex Celestine
Cl ka	20	10	10	LPET (5)	545	Astimex Tugtupite
Th ma	30	15	15	LPET (5)	629	Huttonite
Pb mb	20	10	10	LPET (5)	627	K227
Y la	30	15	15	LPET (5)	1214	Yttrium Phosphate (Ch)
Nb la	30	15	15	LPET (5)	616	Niobium
Zr la	30	15	15	LPET (5)	599	Zirconium

V ka	30	15	15	LIFF (3)	608	Vanadium
W la	30	15	15	LIFF (3)	596	Tungsten
Ta la	30	15	15	LIFF (3)	601	Tantalum
Bi ma	30	15	15	LPET (5)	568	Bi2Se3

Table 2: The complete Electron Microprobe dataset in weight percent concentration. Note, to allow for the composition of H₃O⁺, H₂O and OH⁻ within APS minerals, only analysis with totals summing to 75-95 wt% were used. FT=Flotation concentrate, CLD=Concentrate leach discharge.

Element/ Oxide	Concentration (wt%)												
	Material	FT	FT	FT	FT	FT	FT	FT	FT	FT	FT	FT	FT
Na2O	0.000	0.000	0.000	0.000	0.000	0.135	0.103	0.035	0.107	0.000	0.262	0.109	0.028
K2O	0.083	0.192	0.029	0.014	0.012	0.228	0.272	0.063	0.400	0.024	0.997	0.565	0.062
CaO	0.125	0.151	0.182	0.199	0.201	0.218	0.307	0.332	0.332	0.376	0.402	0.599	0.783
SrO	1.489	1.485	2.115	2.155	2.380	3.239	10.197	2.277	1.484	1.611	12.853	12.704	7.713
BaO													
Y2O3	0.000	0.023	0.026	0.055	0.044	0.051	0.000	0.051	0.000	0.021	0.000	0.000	0.000
ZrO2	0.000	0.000	0.000	0.000	0.000	0.000	0.000	0.000	0.000	0.000	0.000	0.000	0.000
La2O3	10.091	8.716	9.908	6.734	9.434	11.440	3.430	13.639	6.605	8.966	3.315	1.993	5.358
Ce2O3	13.558	13.952	11.564	14.264	14.589	10.285	4.145	12.931	8.113	15.722	3.065	2.287	8.002
Pr2O3	0.800	1.259	0.470	1.467	1.034	0.405	0.326	0.601	0.420	1.383	0.099	0.106	0.579
Nd2O3	1.890	3.082	0.618	4.688	2.241	0.632	0.868	0.983	0.782	3.570	0.224	0.291	1.834
Sm2O3	0.000	0.122	0.000	0.357	0.000	0.000	0.103	0.000	0.000	0.212	0.000	0.106	0.221
Eu2O3	0.000	0.038	0.000	0.086	0.000	0.000	0.000	0.000	0.000	0.046	0.000	0.000	0.000
Gd2O3	0.000	0.000	0.000	0.000	0.000	0.000	0.000	0.000	0.000	0.000	0.000	0.000	0.000
Tb2O3	0.000	0.000	0.054	0.000	0.000	0.000	0.000	0.000	0.072	0.000	0.000	0.039	0.000
Dy2O3	0.000	0.000	0.000	0.000	0.000	0.000	0.000	0.000	0.000	0.000	0.000	0.000	0.000
Ho2O3	0.000	0.000	0.116	0.000	0.000	0.000	0.000	0.000	0.000	0.000	0.000	0.000	0.000
Er2O3	0.000	0.000	0.069	0.000	0.000	0.000	0.000	0.000	0.000	0.000	0.000	0.000	0.000
Tm2O3	0.000	0.000	0.065	0.000	0.000	0.000	0.000	0.000	0.000	0.000	0.000	0.000	0.000
Yb2O3	0.000	0.000	0.000	0.000	0.000	0.000	0.249	0.327	0.000	0.000	0.000	0.000	0.000
Bi2O3													
PbO	0.000	0.000	0.000	0.027	0.000	0.000	0.182	0.000	0.000	0.000	0.171	0.139	0.000
ThO2	0.042	0.061	0.028	0.020	0.000	0.000	0.083	0.000	0.000	0.000	0.027	0.045	0.127
UO2	0.000	0.000	0.063	0.000	0.000	0.054	0.023	0.000	0.173	0.000	0.000	0.000	0.000
MgO													
Al2O3	28.411	28.876	29.197	28.859	29.776	25.336	30.988	30.401	29.276	29.768	32.194	33.704	31.438
TiO2													
V2O5													
MnO													
Fe2O3	0.904	0.681	0.315	3.304	3.149	3.822	14.073	2.635	2.863	1.331	0.982	0.694	7.152
Cu2O													
Nb2O5	0.023	0.000	0.000	0.000	0.000	0.000	0.000	0.000	0.000	0.000	0.000	0.023	0.000
Ta2O5													
WO3													
SiO2	0.000	0.000	0.000	0.000	0.000	2.363	3.890	0.000	2.233	0.000	2.026	1.960	0.000
P2O5	20.229	20.422	19.546	19.498	17.264	14.040	11.109	19.290	18.294	19.753	16.453	15.597	19.033
SO2	0.877	0.766	1.525	0.672	1.487	2.373	7.409	1.563	2.133	0.718	11.796	12.046	4.307
As2O3	0.182	0.000	0.435	0.688	0.156	0.000	0.000	0.031	0.020	0.000	0.037	0.000	0.022
F	0.085	0.064	0.267	0.061	0.218	0.611	0.307	0.219	0.217	0.265	1.187	1.293	0.505
Cl	0.018	0.097	0.050	0.035	0.073	0.037	0.065	0.030	0.035	0.031	0.143	0.045	0.028
Total	78.807	79.988	76.643	83.184	82.057	75.268	88.128	85.407	73.559	83.795	86.234	84.343	87.192
Material	FT	FT	FT	FT	FC	FC	FC	FC	FC	FC	FC	FC	FC
Na2O	0.143	0.133	0.181	0.135	0.000	0.000	0.131	0.061	0.035	0.058	0.082	0.047	0.139
K2O	0.216	0.258	0.294	0.150	0.009	0.044	0.258	0.108	0.102	0.359	0.202	0.071	0.271
CaO	0.876	0.936	0.950	1.241	0.276	0.532	0.615	0.852	0.953	0.958	0.980	1.006	1.052
SrO	9.004	9.961	3.145	10.810	2.244	8.680	13.027	8.707	8.723	14.447	11.946	9.469	12.607
BaO					0.062	0.177	0.182	0.174	0.516	0.328	0.459	0.557	0.331
Y2O3	0.000	0.035	0.034	0.043	0.000	0.078	0.000	0.059	0.120	0.028	0.053	0.176	0.165
ZrO2	0.000	0.000	0.000	0.000	0.040	0.028	0.039	0.064	0.051	0.000	0.047	0.071	0.050
La2O3	4.507	3.753	10.082	3.033	7.820	4.793	2.691	4.144	5.780	1.730	2.020	4.787	2.462
Ce2O3	6.288	4.846	10.985	5.904	11.685	8.238	3.652	8.046	8.684	3.207	4.989	6.680	5.152
Pr2O3	0.333	0.398	0.711	0.476	0.904	0.714	0.391	0.881	0.406	0.210	0.327	0.545	0.410
Nd2O3	0.741	1.049	1.313	1.683	2.577	2.160	0.661	2.101	1.247	0.908	1.176	0.919	0.834
Sm2O3	0.000	0.000	0.083	0.156	0.189	0.185	0.176	0.154	0.000	0.000	0.080	0.087	0.000
Eu2O3	0.000	0.000	0.000	0.079	0.000	0.103	0.000	0.122	0.000	0.000	0.040	0.081	0.000
Gd2O3	0.000	0.000	0.000	0.000	0.000	0.000	0.000	0.000	0.000	0.068	0.000	0.000	0.000
Tb2O3	0.000	0.000	0.000	0.000	0.000	0.062	0.049	0.068	0.000	0.000	0.000	0.000	0.000
Dy2O3	0.044	0.000	0.000	0.000	0.000								
Ho2O3	0.000	0.098	0.000	0.000	0.000								
Er2O3	0.000	0.000	0.000	0.000	0.000								

Tm2O3	0.000	0.000	0.000	0.000	0.000								
Yb2O3	0.000	0.000	0.000	0.000	0.000								
Bi2O3					0.000	0.000	0.081	0.000	0.000	0.000	0.000	0.046	0.000
PbO	0.110	0.112	0.027	0.090	0.000	0.000	0.146	0.220	0.000	0.340	0.267	0.000	0.262
ThO2	0.132	0.164	0.037	0.152	0.000	0.000	0.119	0.000	0.000	0.116	0.105	0.000	0.120
UO2	0.000	0.027	0.041	0.000	0.041	0.000	0.027	0.000	0.000	0.000	0.046	0.032	0.021
MgO					0.015	0.000	0.041	0.069	0.000	0.033	0.026	0.000	0.032
Al2O3	30.117	32.408	29.739	29.975	29.364	33.562	34.717	33.071	33.199	35.817	31.267	30.480	35.109
TiO2					0.000	0.028	0.042	0.018	0.013	0.000	0.000	0.025	0.000
V2O5					0.000	0.000	0.000	0.000	0.000	0.000	0.000	0.000	0.000
MnO					0.000	0.000	0.000	0.000	0.000	0.000	0.000	0.000	0.033
Fe2O3	1.083	1.604	4.444	1.389	9.642	4.553	1.229	2.471	1.360	0.879	1.573	1.674	0.947
Cu2O					0.942	0.295	0.845	0.838	0.248	0.568	0.228	0.470	0.422
Nb2O5	0.020	0.000	0.000	0.000	0.023	0.000	0.000	0.026	0.000	0.022	0.000	0.000	0.000
Ta2O5					0.000	0.000	0.126	0.078	0.000	0.000	0.063	0.000	0.000
WO3					0.000	0.071	0.092	0.000	0.000	0.000	0.000	0.000	0.000
SiO2	0.000	0.000	0.000	0.000	0.718	0.187	0.286	0.744	0.359	0.246	0.278	0.542	0.228
P2O5	17.537	17.174	16.133	19.746	18.747	19.204	18.091	18.807	19.414	18.062	20.055	20.421	17.824
SO2	6.079	7.967	1.180	4.455	1.420	4.487	11.031	6.299	3.787	10.716	7.134	4.258	10.041
As2O3	0.000	0.000	0.000	0.000	0.000	0.000	0.000	0.000	0.000	0.000	0.000	0.000	0.000
F	0.584	0.973	0.584	1.866	0.000	0.402	0.353	0.706	2.498	0.836	2.014	2.745	1.573
Cl	0.094	0.073	0.127	0.052	0.031	0.047	0.032	0.035	0.000	0.030	0.052	0.000	0.036
Total	77.908	81.969	80.092	81.434	86.747	88.626	89.131	88.923	87.497	89.968	85.508	85.188	90.121
Material	FC	FC	FC	FC	FC	FC	FC	FC	FC	FC	FC	FC	FC
Na2O	0.077	0.076	0.049	0.127	0.139	0.084	0.136	0.000	0.147	0.094	0.102	0.072	0.119
K2O	0.233	0.146	0.134	0.204	0.243	0.124	0.235	0.185	0.203	0.217	0.160	0.085	0.205
CaO	1.069	1.136	1.288	1.307	1.442	1.478	1.507	1.521	1.531	1.544	1.602	1.602	1.610
SrO	14.077	13.571	9.584	11.347	10.100	10.952	10.059	8.614	10.530	12.744	11.778	10.601	11.220
BaO	0.382	0.439	0.420	0.691	0.510	0.398	0.471	0.443	0.505	0.619	0.740	0.508	0.624
Y2O3	0.048	0.053	0.230	0.100	0.152	0.109	0.164	0.298	0.104	0.120	0.115	0.377	0.144
ZrO2	0.051	0.052	0.052	0.056	0.069	0.036	0.044	0.075	0.067	0.057	0.059	0.058	0.067
La2O3	1.544	1.983	3.941	2.640	2.782	3.287	4.947	4.332	3.230	2.616	2.806	4.096	2.941
Ce2O3	3.332	3.934	8.354	5.044	5.887	5.675	5.848	7.893	5.353	4.670	5.449	6.478	5.202
Pr2O3	0.375	0.461	0.871	0.409	0.341	0.570	0.327	0.681	0.557	0.442	0.543	0.641	0.342
Nd2O3	0.896	1.072	1.832	1.410	1.138	1.118	0.895	1.946	1.162	0.932	0.999	1.107	0.994
Sm2O3	0.000	0.000	0.203	0.000	0.000	0.095	0.000	0.132	0.113	0.129	0.128	0.174	0.000
Eu2O3	0.000	0.000	0.055	0.000	0.049	0.000	0.000	0.067	0.146	0.086	0.093	0.059	0.051
Gd2O3	0.076	0.072	0.000	0.000	0.000	0.000	0.000	0.098	0.089	0.000	0.000	0.000	0.091
Tb2O3	0.000	0.000	0.065	0.000	0.000	0.000	0.000	0.049	0.000	0.000	0.000	0.066	0.000
Dy2O3							0.000			0.042			
Ho2O3							0.000			0.000			
Er2O3							0.000			0.051			
Tm2O3							0.000			0.000			
Yb2O3							0.000			0.000			
Bi2O3	0.000	0.000	0.092	0.000	0.000	0.000	0.000	0.000	0.046	0.000	0.000	0.000	0.000
PbO	0.311	0.340	0.000	0.172	0.167	0.222	0.140	0.000	0.236	0.207	0.185	0.000	0.239
ThO2	0.082	0.107	0.000	0.082	0.107	0.000	0.077	0.000	0.098	0.084	0.139	0.000	0.095
UO2	0.000	0.000	0.000	0.000	0.038	0.059	0.035	0.076	0.020	0.036	0.000	0.027	0.000
MgO	0.034	0.034	0.026	0.019	0.070	0.088	0.040	0.000	0.093	0.047	0.047	0.012	0.055
Al2O3	35.325	34.205	34.872	33.037	34.563	32.098	32.119	34.491	33.944	34.957	34.900	32.563	32.908
TiO2	0.000	0.015	0.016	0.046	0.000	0.020	0.000	0.022	0.034	0.039	0.000	0.033	0.017
V2O5	0.000	0.000	0.000	0.000	0.000	0.000	0.000	0.000	0.000	0.000	0.000	0.000	0.000
MnO	0.000	0.000	0.000	0.000	0.000	0.000	0.000	0.000	0.000	0.000	0.000	0.000	0.000
Fe2O3	0.859	1.108	1.444	1.456	3.922	1.043	1.196	4.208	1.298	1.342	1.411	2.180	1.347
Cu2O	0.387	0.473	0.626	0.461	0.481	0.538	0.510	0.521	0.733	0.563	0.533	0.320	0.562
Nb2O5	0.000	0.000	0.000	0.000	0.000	0.000	0.000	0.034	0.000	0.000	0.000	0.026	0.000
Ta2O5	0.000	0.000	0.000	0.000	0.000	0.083	0.000	0.000	0.000	0.000	0.000	0.000	0.000
WO3	0.000	0.000	0.000	0.000	0.000	0.071	0.000	0.000	0.128	0.066	0.000	0.071	0.000
SiO2	0.206	0.220	0.933	0.268	0.457	0.644	0.567	0.507	0.489	0.353	0.402	0.499	0.391
P2O5	19.241	18.876	19.957	20.470	18.976	19.259	19.557	20.168	18.459	19.595	19.546	20.606	19.673
SO2	9.764	9.184	3.752	6.331	6.973	7.011	5.187	3.995	7.787	8.400	7.737	3.896	7.018
As2O3	0.000	0.023	0.000	0.000	0.024	0.000	0.065	0.000	0.000	0.000	0.000	0.000	0.000
F	1.537	1.279	2.065	1.977	1.584	1.661	2.797	1.336	1.727	1.602	1.395	3.051	1.744
Cl	0.045	0.038	0.030	0.089	0.092	0.068	0.040	0.016	0.059	0.065	0.092	0.000	0.097
Total	89.952	88.897	90.892	87.743	90.304	86.790	86.963	91.707	88.983	91.627	90.960	89.209	87.754
Material	FC	FC	FC	FC	FC	FC	FC	FC	FC	FC	FC	FC	FC
Na2O	0.094	0.133	0.166	0.157	0.129	0.081	0.064	0.125	0.112	0.081	0.101	0.119	0.000
K2O	0.236	0.168	0.144	0.231	0.303	0.317	0.362	0.340	0.283	0.274	0.563	0.340	0.071
CaO	1.637	1.764	1.765	1.821	2.203	2.247	2.369	2.371	2.574	2.799	2.916	3.156	6.165
SrO	12.860	9.884	10.613	8.810	13.863	13.904	13.419	14.219	11.456	13.323	10.413	11.234	9.860
BaO	0.540	0.420	0.539	0.471	0.477	0.375	0.363	0.578	0.527	0.296	0.499	0.412	0.197
Y2O3	0.058	0.095	0.119	0.161	0.154	0.114	0.047	0.132	0.085	0.027	0.085	0.037	0.158
ZrO2	0.055	0.000	0.040	0.051	0.066	0.051	0.075	0.070	0.062	0.055	0.050	0.073	0.052
La2O3	2.966	5.138	3.118	5.375	1.500	1.586	1.344	1.329	3.053	1.158	2.285	1.649	3.609
Ce2O3	3.926	6.455	5.077	6.091	2.437	2.626	2.217	2.240	4.641	2.068	3.687	3.240	7.409
Pr2O3	0.361	0.431	0.257	0.367	0.157	0.225	0.260	0.227	0.422	0.100	0.416	0.435	0.659
Nd2O3	0.791	0.956	1.561	1.027	0.686	0.677	0.549	0.582	0.804	0.526	0.896	1.124	1.649

Sm2O3	0.000	0.000	0.057	0.074	0.065	0.115	0.000	0.000	0.103	0.000	0.079	0.136	0.129
Eu2O3	0.051	0.000	0.000	0.000	0.000	0.000	0.000	0.000	0.062	0.000	0.107	0.138	0.000
Gd2O3	0.000	0.000	0.000	0.068	0.000	0.000	0.000	0.000	0.000	0.114	0.147	0.082	0.000
Tb2O3	0.000	0.000	0.000	0.000	0.000	0.000	0.000	0.000	0.000	0.000	0.000	0.000	0.054
Dy2O3			0.000								0.061	0.062	
Ho2O3			0.093								0.000	0.000	
Er2O3			0.000								0.000	0.000	
Tm2O3			0.000								0.000	0.000	
Yb2O3			0.000								0.000	0.000	
Bi2O3	0.000	0.000	0.000	0.000	0.000	0.000	0.000	0.000	0.000	0.000	0.000	0.032	0.000
PbO	0.188	0.139	0.329	0.178	0.233	0.274	0.454	0.292	0.000	0.270	0.223	0.315	0.000
ThO2	0.077	0.112	0.087	0.107	0.027	0.000	0.000	0.000	0.061	0.031	0.023	0.000	0.000
UO2	0.072	0.148	0.038	0.000	0.019	0.039	0.021	0.000	0.066	0.000	0.070	0.024	0.000
MgO	0.022	0.127	0.101	0.077	0.067	0.030	0.040	0.018	0.014	0.016	0.084	0.027	0.013
Al2O3	33.276	33.437	33.017	32.610	34.333	35.368	35.397	36.253	32.668	36.158	34.830	36.203	30.524
TiO2	0.000	0.000	0.000	0.000	0.000	0.000	0.018	0.000	0.019	0.015	0.036	0.021	0.014
V2O5	0.000	0.000	0.000	0.000	0.000	0.000	0.000	0.000	0.000	0.000	0.000	0.000	0.000
MnO	0.000	0.000	0.000	0.000	0.000	0.000	0.000	0.040	0.000	0.000	0.000	0.000	0.000
Fe2O3	2.223	1.369	1.218	1.469	1.271	1.046	0.896	0.836	1.532	1.280	1.503	1.554	2.480
Cu2O	0.315	0.714	0.376	0.522	0.524	0.622	0.510	0.638	0.251	0.589	0.415	0.385	0.303
Nb2O5	0.000	0.000	0.000	0.000	0.023	0.000	0.000	0.035	0.000	0.000	0.000	0.000	0.000
Ta2O5	0.000	0.000	0.000	0.059	0.000	0.000	0.000	0.047	0.000	0.000	0.090	0.000	0.000
WO3	0.000	0.000	0.000	0.000	0.000	0.000	0.000	0.000	0.000	0.000	0.136	0.086	0.000
SiO2	0.265	0.616	0.716	0.682	0.227	0.242	0.609	0.176	0.225	0.322	0.560	0.967	0.659
P2O5	19.463	17.768	19.257	17.423	22.127	20.763	20.782	22.017	19.756	20.059	19.515	19.789	18.460
SO2	7.801	6.581	6.170	7.211	5.753	7.378	9.234	6.563	7.330	9.551	7.966	8.601	4.681
As2O3	0.022	0.000	0.000	0.023	0.000	0.000	0.000	0.000	0.000	0.000	0.000	0.000	0.024
F	2.703	1.734	1.402	1.638	3.432	2.654	1.995	3.042	3.100	1.277	1.167	1.451	3.255
Cl	0.041	0.091	0.119	0.082	0.000	0.027	0.038	0.016	0.034	0.021	0.059	0.031	0.000
Total	90.045	88.279	86.380	86.785	90.076	90.760	91.064	92.188	89.241	90.408	88.983	91.726	90.427
Material	CLD	CLD	CLD	CLD	CLD	CLD	CLD	CLD	CLD	CLD	CLD	CLD	CLD
Na2O	0.035	0.000	0.000	0.000	0.000	0.033	0.000	0.000	0.064	0.061	0.108	0.084	0.134
K2O	0.189	0.000	0.018	0.009	0.000	0.365	0.105	0.018	0.103	0.033	0.038	0.310	0.093
CaO	0.256	0.261	0.261	0.281	0.285	0.435	0.492	0.541	0.566	0.679	0.865	1.097	1.534
SrO	5.096	2.530	5.786	2.190	2.529	6.189	11.441	2.582	6.698	7.321	6.620	13.012	11.812
BaO	0.160	0.196	0.101	0.096	0.493	0.196	0.178	0.155	0.168	0.259	0.226	0.408	0.465
Y2O3	0.033	0.022	0.000	0.000	0.040	0.000	0.062	0.092	0.047	0.053	0.041	0.036	0.052
ZrO2	0.063	0.028	0.069	0.034	0.057	0.066	0.066	0.054	0.075	0.057	0.047	0.000	0.065
La2O3	7.478	11.094	7.043	11.233	11.211	6.940	4.218	9.407	5.209	5.159	5.083	2.216	2.726
Ce2O3	10.644	12.873	11.099	13.415	12.682	10.169	6.218	13.735	9.132	9.520	8.550	3.024	4.644
Pr2O3	0.893	0.674	0.859	0.701	0.758	0.917	0.611	1.073	1.099	1.011	0.986	0.106	0.453
Nd2O3	1.943	1.182	2.168	1.106	1.092	1.885	1.133	1.960	2.564	2.719	2.434	0.732	1.340
Sm2O3	0.000	0.082	0.088	0.075	0.000	0.132	0.138	0.000	0.258	0.126	0.224	0.000	0.193
Eu2O3	0.046	0.000	0.087	0.000	0.041	0.113	0.083	0.000	0.000	0.147	0.111	0.000	0.080
Gd2O3	0.000	0.000	0.000	0.000	0.000	0.000	0.000	0.000	0.103	0.083	0.000	0.000	0.120
Tb2O3	0.000	0.000	0.000	0.000	0.048	0.000	0.046	0.000	0.000	0.000	0.059	0.000	0.000
Dy2O3	0.000	0.000	0.000	0.000	0.000	0.000		0.055	0.000	0.000	0.077		
Ho2O3	0.000	0.203	0.000	0.000	0.000	0.000		0.000	0.000	0.000	0.000		
Er2O3	0.000	0.000	0.000	0.000	0.000	0.000		0.000	0.000	0.054	0.000		
Tm2O3	0.000	0.000	0.000	0.000	0.000	0.000		0.000	0.000	0.000	0.000		
Yb2O3	0.000	0.000	0.000	0.000	0.000	0.000		0.000	0.176	0.340	0.205		
Bi2O3	0.000	0.000	0.000	0.000	0.032	0.024	0.040	0.000	0.000	0.081	0.086	0.000	0.000
PbO	0.000	0.184	0.000	0.000	0.145	0.241	0.000	0.245	0.000	0.166	0.176	0.457	0.172
ThO2	0.000	0.000	0.203	0.000	0.000	0.160	0.078	0.000	0.080	0.086	0.084	0.088	0.053
UO2	0.022	0.000	0.022	0.019	0.000	0.000	0.000	0.037	0.000	0.000	0.000	0.000	0.000
MgO	0.000	0.000	0.000	0.000	0.000	0.022	0.047	0.035	0.037	0.060	0.095	0.033	0.047
Al2O3	32.889	31.715	31.687	32.552	31.738	33.875	34.142	32.227	32.551	33.838	34.112	35.541	35.828
TiO2	0.032	0.000	0.077	0.000	0.036	0.071	0.054	0.045	0.041	0.041	0.036	0.015	0.023
V2O5	0.000	0.000	0.000	0.000	0.000	0.000	0.000	0.000	0.000	0.022	0.000	0.000	0.000
MnO	0.000	0.000	0.000	0.000	0.000	0.000	0.000	0.000	0.000	0.000	0.000	0.000	0.000
Fe2O3	3.283	0.755	1.856	0.733	0.647	0.949	1.075	1.091	1.908	1.705	1.268	1.499	1.713
Cu2O	0.693	0.687	0.811	0.710	0.593	0.850	0.951	0.648	0.760	0.957	0.782	0.548	0.699
Nb2O5	0.026	0.028	0.000	0.000	0.000	0.000	0.000	0.000	0.000	0.000	0.000	0.020	0.000
Ta2O5	0.107	0.089	0.073	0.000	0.000	0.117	0.000	0.000	0.141	0.103	0.125	0.000	0.000
WO3	0.109	0.000	0.000	0.000	0.115	0.106	0.080	0.000	0.000	0.000	0.000	0.000	0.000
SiO2	0.803	0.306	0.299	0.399	0.341	0.574	0.175	0.460	0.394	0.315	0.559	0.705	0.254
P2O5	19.172	19.982	19.248	19.552	20.083	19.216	18.823	19.575	19.212	18.909	18.897	17.702	19.422
SO2	3.734	2.002	4.140	1.833	2.089	4.295	8.956	1.541	5.075	4.830	4.705	11.073	7.837
As2O3	0.070	0.280	0.000	0.293	0.225	0.000	0.000	0.030	0.000	0.033	0.026	0.020	0.000
F	0.119	0.224	0.395	0.235	0.208	0.550	0.523	0.335	0.441	0.618	0.619	0.933	1.382
Cl	0.025	0.024	0.000	0.025	0.027	0.025	0.016	0.056	0.022	0.035	0.053	0.027	0.029
Total	87.918	85.422	86.390	85.490	85.514	88.515	89.752	85.999	86.923	89.418	87.295	89.687	91.172
Material	CLD	CLD	CLD	CLD	CLD	CLD	CLD	CLD	CLD	CLD			
Na2O	0.054	0.095	0.079	0.052	0.056	0.082	0.114	0.061	0.151				
K2O	0.040	0.605	0.198	0.066	0.067	0.176	0.169	0.286	0.267				
CaO	1.603	1.610	1.815	1.873	1.893	2.019	2.545	3.664	3.750				
SrO	9.249	12.371	12.641	12.788	8.353	10.002	10.805	8.958	10.104				

BaO	0.123	0.385	0.409	0.250	0.157	0.352	0.522	0.305	0.361				
Y2O3	0.000	0.069	0.109	0.025	0.031	0.043	0.192	0.101	0.061				
ZrO2	0.000	0.036	0.049	0.072	0.077	0.065	0.071	0.070	0.045				
La2O3	3.786	2.681	3.281	1.601	4.147	3.471	2.757	2.374	1.598				
Ce2O3	6.676	4.990	4.407	3.189	7.160	5.075	5.971	3.373	2.939				
Pr2O3	0.632	0.252	0.349	0.423	0.745	0.291	0.624	0.373	0.285				
Nd2O3	1.609	1.386	0.927	0.956	1.582	1.277	1.702	0.902	0.959				
Sm2O3	0.107	0.000	0.091	0.162	0.137	0.000	0.169	0.104	0.106				
Eu2O3	0.074	0.000	0.121	0.077	0.072	0.000	0.078	0.091	0.043				
Gd2O3	0.099	0.000	0.000	0.000	0.000	0.000	0.104	0.101	0.000				
Tb2O3	0.000	0.000	0.000	0.000	0.000	0.000	0.042	0.000	0.000				
Dy2O3		0.000	0.070			0.000		0.060	0.000				
Ho2O3		0.112	0.000			0.189		0.000	0.000				
Er2O3		0.000	0.000			0.000		0.052	0.000				
Tm2O3		0.000	0.000			0.000		0.000	0.000				
Yb2O3		0.000	0.000			0.000		0.000	0.000				
Bi2O3	0.000	0.000	0.091	0.094	0.053	0.000	0.000	0.000	0.000				
PbO	0.268	0.453	0.517	0.413	0.217	0.719	0.250	0.356	0.688				
ThO2	0.000	0.077	0.000	0.000	0.000	0.000	0.000	0.021	0.022				
UO2	0.000	0.000	0.037	0.000	0.000	0.000	0.023	0.058	0.000				
MgO	0.021	0.186	0.038	0.028	0.042	0.038	0.029	0.051	0.043				
Al2O3	32.497	35.094	35.494	32.350	32.560	34.015	35.827	34.318	34.661				
TiO2	0.037	0.046	0.065	0.021	0.049	0.048	0.025	0.014	0.016				
V2O5	0.000	0.000	0.000	0.000	0.000	0.000	0.000	0.000	0.000				
MnO	0.000	0.000	0.000	0.000	0.000	0.000	0.000	0.000	0.000				
Fe2O3	2.039	1.063	0.938	0.901	1.316	1.295	0.892	1.057	0.886				
Cu2O	0.837	0.966	0.975	0.930	0.847	0.622	0.971	0.574	0.640				
Nb2O5	0.000	0.000	0.000	0.000	0.000	0.000	0.000	0.000	0.000				
Ta2O5	0.000	0.000	0.110	0.000	0.000	0.000	0.000	0.058	0.000				
WO3	0.000	0.000	0.155	0.089	0.098	0.000	0.000	0.000	0.000				
SiO2	0.398	0.752	0.302	0.117	0.578	0.409	0.271	0.259	0.295				
P2O5	18.748	19.910	18.469	18.504	19.101	20.057	18.010	20.194	21.209				
SO2	6.843	7.055	8.434	10.826	6.505	7.161	6.537	6.479	8.119				
As2O3	0.000	0.000	0.000	0.000	0.000	0.000	0.000	0.000	0.000				
F	0.811	2.125	1.673	0.522	0.737	2.307	2.624	1.990	1.788				
Cl	0.039	0.046	0.056	0.027	0.070	0.026	0.041	0.045	0.048				
Total	86.590	92.364	91.901	86.358	86.649	89.740	91.362	86.347	89.086				

SUPPLEMENTARY MATERIAL D: APPENDIX FOR CHAPTER 5

Appendix D.1: Extended methods

Electron probe micro analysis (EPMA)

Quantitative compositional data was obtained using a Cameca SX-Five electron probe microanalyzer (EPMA), equipped with 5 tunable wavelength-dispersive spectrometers. The instrument uses PeakSite software for microscope operation, and Probe for EPMA software (distributed by Probe Software Inc.) for data acquisition and processing. Six elements (Ca, Sr, Pb, Al, P and S) were analyzed. Operating conditions were 15 keV and 20 nA, further operating parameters are listed in [Table 1](#).

Table 1: EPMA operating parameters for the analysis of synthetic APS phases.

Element	Count time (sec)	Hi (sec)	Lo (sec)	Diffracting Crystal (Sp no.)	Standard no.	Standard name
Ca Ka	15	10	10	LPET (5)	535	Astimex Plagioclase
P Ka	15	10	10	PET (2)	504	Astimex Apatite
S Ka	15	10	10	LPET (4)	513	Astimex Celestine
Al Ka	15	10	10	LTAP (1)	535	Astimex Plagioclase
Sr La	15	10	10	LTAP (1)	513	Astimex Celestine
Pb Ma	120	60	60	LPET (5)	627	K227

Laser ablation inductively coupled plasma mass spectrometry (LA-ICP-MS)

LA-ICP-MS analysis was undertaken at AM using an Agilent 7700s mass spectrometer with attached ASI M-50 laser ablation system (Adelaide Microscopy) using a spot size of 15 μm , repetition rate of 5 Hz, at 65 mJ energy, with an attenuation of 50 %T and fluence of 3.5 $\text{J}\cdot\text{cm}^{-2}$. The following isotopes were monitored for analysis: ^{27}Al , ^{31}P , ^{34}S , ^{43}Ca , ^{88}Sr , ^{208}Pb . ^{137}Ba was also measured to account for any overlapping spectral data. The standard NIST 212 was analysed using a spot size of 50 μm at the start and end of each batch run, and after every 15-20 unknown analyses. An additional GSD standard was run in parallel with the APS samples with spot sizes of 50 and 15 μm to measure any related discrepancy associated with the use of a smaller spot size. Total count times for each analysis ran for 40 sec with an additional 30 sec of background measured prior to ablation. Output data was analysed using correction software Igor and Iolite v3.4 ([Paton et al. 2011](#)). Averaged Al values, gained via EPMA, were used as an internal standard.

X-ray absorption spectroscopy (XAS) Data collection

The AS is a 3 GeV ring and was operated in top-up mode with a current of 200 mA. The XAS beamline has a Si(111) double crystal monochromator and an effective energy resolution (E/E) of

$\sim 10^{-5}$ at 10 keV. A focused beam size of FWHM $0.7 \times 0.9 \text{ mm}^2$ was used. The incident and transmitted beam intensities I_0 and I_1 were measured with Si diodes, and a Canberra 30 element solid state fluorescence detector was used for detecting fluorescence data. The beam energy was calibrated with a Pb foil, such that the maximum of the first derivative was at 13,035 eV.

X-ray absorption near edge structure (XANES) spectra were measured for Pb-bearing APS Phases to be used as standards. The respective Pb-APS standards, pyromorphite $\text{Pb}_5(\text{PO}_4)_3\text{OH}$ (synthesized) and hinsdalite $\text{PbAl}_3(\text{PO}_4)(\text{SO}_4)(\text{OH})_6$ (natural sample, donated by the Melbourne Museum), were confirmed via X-ray diffraction.

The EXAFS spectra represent a final state interference effect arising from the scattering of the outgoing photoelectron from neighbouring atoms and are therefore sensitive to the atomic number of the neighbouring atoms and their distances. Similar to the XANES, the EXAFS was obtained on the Pb-sorbed APS phases. The Fourier transforms of the EXAFS oscillations, k (\AA^{-1}), provide information on electron density distributed away from the central Pb atom in radial distance (\AA). The data was found to fit either a hinsdalite or pyromorphite-like structure within reasonable certainty, such that the EXAFS data identifies the most dominant Pb-bearing phase.

References (Appendix D.1)

Paton, C., Hellstrom, J., Paul, B., Woodhead, J., and Hergt, J. (2011) Iolite: Freeware for the visualisation and processing of mass spectrometric data. *Journal of Analytical Atomic Spectrometry*, 26(12), 2508–2518.

Appendix D.2: Supplementary tables

Table 1: The relative concentrations of reactants for synthesis of APS phases.

Starting material molar ratios				
APS	M-Site	CaOH (%)	SrOH (%)	H ₃ PO ₄ :H ₂ SO ₄
I	Sr	-	100	1:1
II	(Ca,Sr)	50	50	1:1

Table 2: Representative EPMA data of synthetic Ca- and Sr-bearing phases listed as wt% per oxide and atoms per formula unit to fit the general formula $MA_3(XO_4)_2(OH,H_2O)_6$. All values have been normalised so that P+S = 2 apfu. Averaged values are taken from the full dataset (Appendix D, Table 1).

Material	APS(I)	APS(I)	APS(I)	Ave	APS(II)	APS(II)	APS(II)	Ave
Oxides (wt%)								
CaO	0.54	0.60	0.39	0.50	4.36	6.86	5.58	4.76
SrO	15.02	12.26	7.76	12.30	13.37	6.16	7.92	8.83
P ₂ O ₅	11.35	8.85	11.31	8.92	16.03	29.12	17.70	16.03
SO ₃	23.09	28.51	28.45	27.46	19.40	6.70	16.76	15.97
Al ₂ O ₃	39.79	49.86	55.90	48.91	40.47	33.89	39.34	39.63
Total	89.79	100.09	103.81	98.09	91.47	82.74	87.30	87.94
Formula (apfu)								
Ca	0.04	0.04	0.03	0.04	0.35	0.50	0.43	0.38
Sr	0.65	0.49	0.29	0.51	0.59	0.24	0.33	0.38
∑M ²⁺	0.69	0.54	0.32	0.55	0.94	0.74	0.77	0.76
S	1.29	1.48	1.38	1.46	1.11	0.34	0.91	0.89
P	0.71	0.52	0.62	0.54	0.89	1.66	1.09	1.01
∑X	2	2	2	2	2	2	2	2
Al	3.48	4.07	4.26	4.09	3.63	2.69	3.36	3.46

Table 3: Representative averaged data from EPMA analyses of Pb-sorbed APS phases. Solution conditions for Pb-sorption experiments are given. Note, $[Pb_{aq}]_0$ is measured in ppm.

Material	AP S(I)	AP S(I)	AP S(I)	AP S(I)	AP S(I)	AP S(I)	AP S(I)	APS (II)	APS (II)	APS (II)	APS (II)	APS (II)	APS (II)	APS (II)	APS (II)	APS (II)
pH	1.5	3.5	1.5	5.5	1.5	3.5	5.5	1.5	3.5	5.5	1.5	3.5	5.5	1.5	3.5	5.5
$[Pb_{aq}]_0$ (ppm)	10	10	10	10	10	10	10	10	10	10	100	100	100	100	100	100
Oxides (wt%)																
CaO	0.36	0.35	0.44	0.40	0.21	0.26	0.44	4.86	5.75	8.34	5.56	5.87	6.85	5.51	7.05	5.02
SrO	4.06	3.47	9.34	12.06	3.76	7.76	10.40	9.38	8.94	6.93	9.65	10.46	7.50	10.23	7.56	9.97
PbO (ppm)	518	231	437	1014	1101	501	800	201	305	400	184	277	339	695	913	1109
P ₂ O ₅	2.52	3.66	6.07	7.71	4.48	7.08	7.97	24.55	19.06	25.28	18.99	21.17	20.87	18.68	21.69	18.68
SO ₃	28.96	27.74	26.69	22.41	30.56	26.77	24.71	8.95	13.56	7.65	13.22	11.65	11.31	14.51	11.34	14.26
Al ₂ O ₃	56.98	56.45	49.90	48.49	53.41	47.88	45.78	33.33	34.27	33.55	34.62	34.72	34.62	34.08	34.18	34.95
Total	92.93	91.69	92.48	91.16	92.52	89.80	89.39	81.09	81.61	81.78	82.06	83.89	81.19	83.09	81.92	83.00
Formula (atoms per formula unit)																
Ca	0.03	0.03	0.04	0.04	0.02	0.02	0.04	0.38	0.47	0.66	0.45	0.47	0.56	0.44	0.56	0.40
Sr	0.20	0.17	0.44	0.60	0.16	0.36	0.47	0.40	0.39	0.30	0.44	0.46	0.34	0.45	0.33	0.44
Pb	0.00	0.00	0.00	0.00	0.00	0.00	0.00	0.00	0.00	0.00	0.00	0.00	0.00	0.00	0.00	0.00
Total	0.23	0.20	0.48	0.68	0.18	0.34	0.51	0.78	0.86	0.92	0.89	0.93	0.89	0.89	0.89	0.84
S	1.82	1.74	1.59	1.41	1.72	1.55	1.47	0.49	0.78	0.43	0.76	0.66	0.66	0.82	0.64	0.81
P	0.18	0.26	0.41	0.59	0.28	0.45	0.53	1.51	1.22	1.57	1.23	1.34	1.34	1.18	1.36	1.19
Total	2.00	2.00	2.00	2.00	2.00	2.00	2.00	2.00	2.00	2.00	2.00	2.00	2.00	2.00	2.00	2.00
Al	5.64	5.56	4.67	4.93	4.72	4.37	4.29	2.86	3.07	2.92	3.14	3.07	3.13	3.01	3.00	3.11

Table 4: Representative LA-ICP-MS spot analyses of synthetic APS phases which have undergone Pb-sorption from Pb-loaded solutions. Conditions of the reaction solutions are given.

Material	pH	[Pb _{aq}] ⁰ (ppm)	P (wt%)	% error	Ca (wt%)	% error	Sr (wt%)	% error	Pb (wt%)	% error	Pb (% M- site)
APS(I)	3.5	10	3.708	7	3.814	6	14.251	5	0.187	12	1.025
APS(I)	3.5	10	4.614	5	3.219	8	10.873	6	0.033	8	0.234
	Average		4.161	6	3.517	7	12.562	5	0.110	10	0.679
APS(I)	5.5	10	1.825	10	3.760	8	13.143	7	0.020	9	0.118
APS(I)	5.5	10	4.614	8	2.525	12	7.308	7	0.007	6	0.071
APS(I)	5.5	10	3.571	8	2.633	17	8.700	4	0.005	10	0.044
	Average		3.336	9	2.973	13	9.717	6	0.011	8	0.087
APS(I)	1.5	100	2.652	9	3.138	18	10.252	4	0.035	15	0.261
APS(I)	5.5	1000	7.722	7	1.506	13	5.498	7	3.685	7	34.475
APS(I)	5.5	1000	3.473	12	4.491	19	13.152	5	0.206	33	1.154
APS(I)	5.5	1000	7.644	10	1.488	9	5.720	8	0.600	15	7.684
	Average		6.280	10	2.495	14	8.123	7	1.497	19	12.357
APS(II)	1.5	10	6.223	8	3.553	19	7.272	6	0.006	7	0.055
APS(II)	1.5	10	8.282	4	5.455	8	4.647	4	0.007	9	0.069
APS(II)	1.5	10	9.169	6	7.250	8	4.062	5	0.004	9	0.035
	Average		7.432	6	6.662	8	5.173	5	0.006	10	0.052
APS(II)	3.5	10	7.181	5	5.609	7	6.820	6	0.347	12	2.716
APS(II)	3.5	10	6.425	6	7.944	6	9.161	11	0.469	36	2.669
APS(II)	3.5	10	6.745	4	8.007	4	2.324	2	0.169	21	1.610
	Average		6.778	6	6.892	8	5.780	5	0.158	16	1.230
APS(II)	5.5	10	6.386	3	4.969	7	4.949	7	0.453	9	4.368
APS(II)	5.5	10	7.136	3	4.283	12	3.450	12	1.107	10	12.523
APS(II)	5.5	10	8.067	6	8.386	7	5.693	5	0.170	11	1.193
	Average		7.561	6	6.009	16	4.574	6	0.429	14	3.893
APS(II)	1.5	100	5.845	3	7.638	3	4.824	5	0.010	14	0.080
APS(II)	1.5	100	8.198	6	8.161	4	3.893	7	0.073	7	0.602
APS(II)	1.5	100	7.435	7	6.871	10	3.175	6	0.021	12	0.209
	Average		7.460	6	6.259	10	4.773	7	0.107	16	0.957
APS(II)	3.5	100	7.083	3	7.737	3	8.789	4	0.083	20	0.500
APS(II)	3.5	100	8.263	5	7.133	8	3.707	12	0.967	17	8.190
APS(II)	3.5	100	8.217	3	8.395	3	4.727	3	0.186	12	1.398
	Average		7.143	4	6.772	7	6.380	6	0.945	15	6.706
APS(II)	5.5	100	7.344	7	1.840	24	2.474	8	0.513	14	10.628
APS(II)	5.5	100	5.904	5	6.492	5	8.177	3	0.156	15	1.052
APS(II)	5.5	100	7.865	4	8.215	4	5.640	4	1.730	6	11.100
	Average		6.695	7	5.299	15	5.219	7	0.621	21	5.574
APS(II)	1.5	1000	5.624	4	7.367	4	8.638	3	0.006	9	0.037
APS(II)	1.5	1000	8.191	4	7.998	4	6.465	4	0.076	15	0.523
APS(II)	1.5	1000	7.566	4	8.079	4	5.215	4	0.027	7	0.203
	Average		7.076	4	6.484	9	5.919	5	0.083	16	0.667
APS(II)	3.5	1000	8.061	4	7.493	9	6.704	11	1.213	8	7.872
APS(II)	3.5	1000	6.125	6	6.186	11	5.631	4	0.067	22	0.564
APS(II)	3.5	1000	7.716	3	6.745	4	3.494	6	1.191	12	10.420
	Average		7.379	5	5.897	8	5.151	7	1.616	13	12.758
APS(II)	5.5	1000	8.211	13	4.689	51	6.554	11	4.288	21	27.609
APS(II)	5.5	1000	6.705	4	7.061	7	10.970	3	0.363	7	1.973
APS(II)	5.5	1000	8.830	3	8.855	4	5.268	4	1.240	23	8.071
	Average		6.655	7	6.777	14	7.771	5	1.219	22	7.731

Table 5: EXAFS data showing Pb-bond distances for peaks fitted to the hinsdalite-like structure. Bond lengths were fixed, 1-sigma errors are given in parentheses. N=2 for every distance/path.

Analysis #	R ₀₁ (Å)	R ₀₂ (Å)	R ₀₃ (Å)	R ₀₄ (Å)	R ₀₅ (Å)	R ₀₆ (Å)	R ₁₁₁ (Å)	R ₁₁₂ (Å)	R ₁₁₃ (Å)	R _{X1} (Å)	R _{X2} (Å)	R _{X3} (Å)	R _{X4} (Å)	σ ² O (Å ²)	ΔE ₀	k-range	R-range
Hinsdalite	2.631	2.66	2.768	2.815	2.872	2.987	3.35	3.463	3.573	3.894	4.087	4.271	5.17	n/a	n/a	n/a	n/a
1	2.38	2.45	2.68	2.68	2.91	3.08	3.66	3.28	4.00	4.46	4.22	4.57	5.22	0.013(1)	5.9(1)	2<k<8.5	1.0<R<5.2
2	2.40	2.61	2.75	2.75	2.99	3.35	2.93	3.27	3.64	3.44	3.85	4.26	5.39	0.011(2)	5.6(2)	2<k<8.5	1.0<R<5.2
3	2.38	2.64	2.73	2.92	2.65	3.15	2.85	3.52	3.19	3.78	4.09	4.31	5.63	0.0061(6)	5.7(2)	2<k<8.5	1.0<R<5.2
4	2.35	2.50	2.73	2.73	2.73	3.08	2.89	3.79	3.26	3.50	3.94	4.24	5.53	0.016(2)	4.5(2)	2<k<8.0	1.0<R<5.2
5	2.38	2.57	2.68	3.01	2.83	3.25	3.27	3.40	3.88	3.54	4.48	4.65	5.25	0.0030(8)	5.9(1)	2<k<8.5	1.0<R<5.2
6	2.38	2.68	2.59	3.38	2.75	3.88	3.38	2.79	3.90	3.51	4.45	4.61	5.23	0.001 (fix)	5.6(2)	2<k<7.0	1.0<R<5.2
7	2.44	2.42	2.58	2.75	3.01	3.29	3.32	3.53	3.56	3.80	3.96	4.16	5.12	0.0203(7)	0.4(2)	2<k<10.0	1.0<R<5.2

Table 6: EXAFS data for Pb-bond distances fitted to the pyromorphite-like structure.

Analysis #	n_{O1}	R_{O1} (Å)	n_{O2}	R_{O2} (Å)	n_{P1}	R_{P1} (Å)	n_{Pb1}	R_{Pb1} (Å)	n_{Pb2}	R_{Pb2} (Å)	σ^2O (Å ²)	ΔE_0	k-range	R-range
pyromorphite	3	2.569	3	2.677	3	3.381	1	3.599	1	3.739	n/a	n/a	n/a	n/a
11	0.5 (fix)	1.97	5.0 (fix)	2.62(1)	3.5 (fix)	3.55(2)	3.0 (fix)	3.67(4)	6.0 (fix)	4.34 (fix)	0.020(1)	2.6(7)	2<k<9	1.0<R<4.0
12	0.3 (fix)	1.97	4.1(6)	2.61(1)	4 (fix)	3.55(3)	6.0 (fix)	3.67(3)	6.0 (fix)	4.34 (fix)	0.013(2)	1.3(6)	2<k<10	1.5<R<4.0
13	0.5 (fix)	1.97	5.0 (fix)	2.62(7)	3.5 (fix)	3.57 (fix)	3.0 (fix)	3.74 (fix)	6.0 (fix)	4.34 (fix)	0.024(12)	2.6(7)	2<k<7	1.0<R<4.0
14	0.5 (fix)	1.97	5.0 (fix)	2.62(3)	3.5 (fix)	3.55(6)	3.0 (fix)	3.66 (fix)	6.0 (fix)	4.34 (fix)	0.023(4)	2.6(7)	2<k<8	1.0<R<4.0
15	0.3 (fix)	1.89(fix)	4.3(8)	2.63(1)	4.6(11)	3.56(2)	6.0 (fix)	3.68(3)	6.0 (fix)	4.34 (fix)	0.012(3)	1.0(6)	2<k<9	1.0<R<4.0
16	0.3 (fix)	1.97	4.0(7)	2.62(2)	4 (fix)	3.56(3)	6.0 (fix)	3.67(3)	6.0 (fix)	4.34 (fix)	0.013(2)	1.3(6)	2<k<10	1.5<R<4.0

Table 7: Cell parameters of natural Ca-, Sr-, and Pb-bearing members of the crandallite group and woodhouseite series. Note that while the *a*-axis remains fixed, the *c*-axis expands with increasing ionic radii of the M-site metal, and with the replacement of a PO₄ group with SO₄. All phases are isomorphic and crystallize in the *R3m* or *R3̄m* space group.

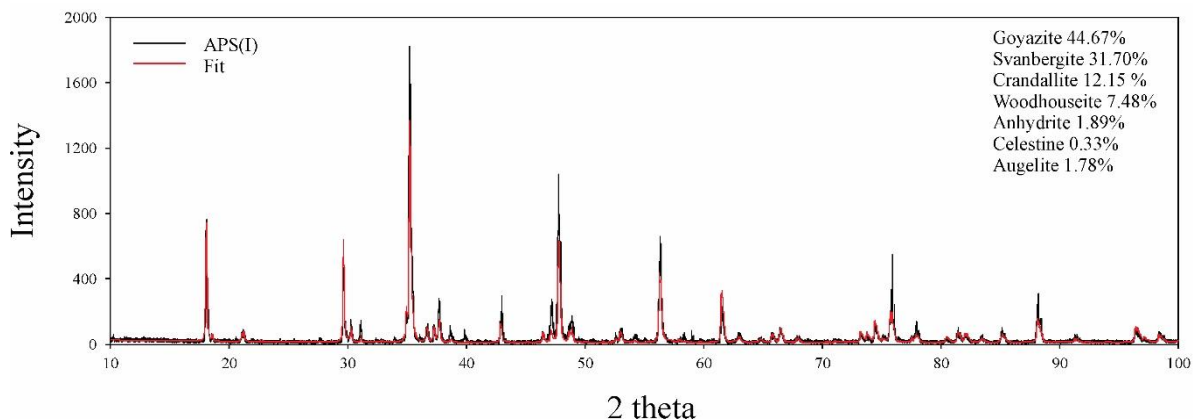
Mineral	<i>a</i> (pm)	<i>c</i> (pm)	Reference
Crandallite	700.2	1620	Owens et al. (1960)
CaAl ₃ (PO ₄) ₂ (OH) ₅ •(H ₂ O)	701.7	1625.2	Blanchard (1972)
	700.5	1619.2	Blount (1974)
	700	1619.4	Schwab et al. (2004)
	699.9	1616.4	Schwab et al. (2004)
mean	700.4	1620	
Goyazite	702.1	1650.5	Kato and Radoslovich (1968)
SrAl ₃ (PO ₄) ₂ (OH) ₅ •(H ₂ O)	698.1	1648.7	Guillemin (1955)
	698.2	1654	McKie (1962)
	mean	699.4	1651
Plumbogummite	703.9	1676.1	Kolitsch et al. (1999)
PbAl ₃ (PO ₄) ₂ (OH) ₅ •(H ₂ O)	701.8	1678.4	Botinelly (1976)
	701.9	1679.2	Frost et al. (2013)
	701.4	1675	Frost et al. (2013)
	mean	702.2	1677.1
Woodhouseite	697.9	1621.4	Blanchard (1986)
CaAl ₃ (PO ₄)(SO ₄)(OH) ₆	697.5	1630	Pabst (1947)
	697.6	1623.5	Kato and Radoslovich (1968)
	mean	697.7	1625
Svanbergite	699.6	1652.8	Schwab et al. (2005)
CaAl ₃ (PO ₄)(SO ₄)(OH) ₆	697.53	1659.7	Kato and Miura (1977)
	696	1680	Botinelly (1976)
	697.3	1654.9	Botinelly (1976)
	709.3	1685	Kato and Radoslovich (1968)
	mean	699.9	1666.5
Hinsdalite	700.6	1683.1	Botinelly (1976)
PbAl ₃ (PO ₄)(SO ₄)(OH) ₆	699	1672.5	Kato and Radoslovich (1968)
	699	1680	Nicolas and De Rosen 1963
	702.9	1678.9	Kolitsch et al. (1999)
	mean	700.4	1678.6

References (Appendix D.2)

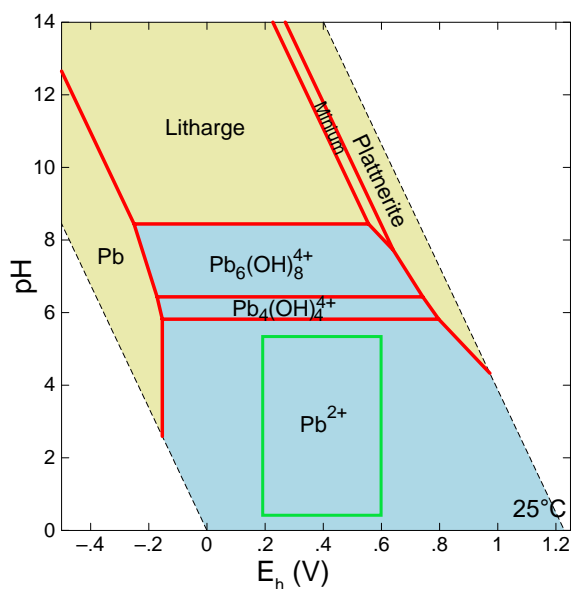
- Blanchard, F.N. (1986) The Use of Calculated Patterns as an Aid in Preparation of Powder diffraction Standards: Minuyulite, KA₁₂(PO₄)₂(OH,F)•4H₂O, as an Example. *Advances in X-ray Analysis*, 29, 225–233.
- Blount, A.M. (1974) The crystal structure of crandallite. *American Mineralogist: Journal of Earth and Planetary Materials*, 59(1-2), 41–47.
- Botinelly, T.D. (1976) A review of the minerals of the alunite-jarosite, beudantite, and plumbogummite groups. *Geologic Studies*, 4(2), 213–216.
- Frost, R.L., Palmer, S.J., Xi, Y., Čejka, J., Sejkora, J., and Plášil, J. (2013) Raman spectroscopic study of the hydroxy-phosphate mineral plumbogummite PbAl₃(PO₄)₂(OH,H₂O)₆. *Spectrochimica Acta Part A: Molecular and Biomolecular Spectroscopy*, 103, 431–434.

- Guillemin, C. (1955) Sur une variété d'hidalgoïte du Cap Garonne (Var). *Bulletin de Minéralogie*, 78(1), 27–32.
- Kato, T. and Miura, Y. (1977) The crystal structures of jarosite and svanbergite. *Mineralogical Journal*, 8(8), 419–430.
- Kato, T. and Radoslovich, E.W. (1968) Crystal structures of soil phosphates. *Transactions of the 9th International Congregation of Soil Science (Adelaide)*, 2, 725–731.
- Kolitsch, U., Tiekink, E.R., Slade, P.G., Taylor, M.R., and Pring, A. (1999) Hinsdalite and plumbogummite, their atomic arrangements and disordered lead sites. *European Journal of Mineralogy*, 513–520.
- McKie, D. (1962) Goyazite and florencite from two African carbonatites. *Mineralogical Magazine and Journal of the Mineralogical Society*, 33(259), 281–297.
- Nicolas, J., and Rosen, A. D. (1963) Phosphates hydrothermaux de basse température et kaolinisation: la gorgeixite du massif des Colettes (Allier) et les minéraux associés (hinsdalite). *Bulletin de Minéralogie*, 86(4), 379–385.
- Owens, J.P., Altschuler, Z.S., and Berman, R. (1960) Millisite in phosphorite from Homeland, Florida. *American Mineralogist* 45, 547–561.
- Pabst, A. (1947) Some computations on svanbergite, wood-houseite and alunite. *American Mineralogist* 32, 16–30.
- Schwab, R.G., Pimpl, T., Schukow, H., Stolle, A., and Breitingner, D.K. (2004) Compounds of the crandallite-type: Synthesis, properties and thermodynamic data of pure crandallite and woodhouseite. *Neues Jahrbuch für Mineralogie Monatshefte*, 385–409.
- Schwab, R.G., Pimpl, T., Schukow, H., Stolle, A., and Breitingner, D.K. (2005) Compounds of the crandallite-type: Synthesis, properties and thermodynamic data of Ca–Sr–Ba–Pb-(arseno)-woodhouseites. *Neues Jahrbuch für Mineralogie Abhandlungen*, 181, 207–218.

Appendix D.3: Supplementary figures (figures labelled as per Chapter 5)



Appendix C.1: Preliminary semi-quantitative XRD pattern showing all phases precipitated during synthesis of APS(I) as a percentage of the bulk analysis.



Appendix C.2: A simple geochemical model showing the solubility of Pb in water at varying pH. The green box indicates the conditions tested during the Pb-sorption experiments.

Appendix D.4: Complete datasets (EPMA and LA-ICP-MS)

Table 1: Complete EPMA dataset comprising of spot analysis on synthetic Sr-, and (Ca,Sr)-bearing APS phases before and after Pb sorption experiments. Analyses that were below detection limit are labelled b.d.l.

Material	pH	[Pb _{aq}] ₀ (ppm)	CaO (wt%)	P ₂ O ₅ (wt%)	SO ₃ (wt%)	Al ₂ O ₃ (wt%)	SrO (wt%)	PbO (wt%)	TOTAL
APS(I)	1.5	10	0.27	3.05	28.15	57.16	3.09	b.d.l.	91.72
APS(I)	1.5	10	0.39	2.59	30.03	55.64	3.60	0.07	92.33
APS(I)	1.5	10	0.32	2.44	27.89	58.32	4.52	0.03	93.53
APS(I)	3.5	10	0.26	11.07	20.12	54.68	3.51	b.d.l.	89.64
APS(I)	3.5	10	0.23	2.26	31.87	54.49	5.02	b.d.l.	93.86
APS(I)	3.5	10	0.35	3.66	27.74	56.45	3.47	0.02	91.69
APS(I)	5.5	10	0.66	8.65	20.16	41.93	12.34	b.d.l.	83.75
APS(I)	5.5	10	0.42	10.54	20.43	39.73	14.92	b.d.l.	86.04
APS(I)	5.5	10	0.49	12.49	19.86	51.20	7.70	b.d.l.	91.74
APS(I)	5.5	10	0.44	6.47	25.48	49.28	12.74	b.d.l.	94.41
APS(I)	5.5	10	0.30	4.95	28.78	53.84	6.99	b.d.l.	94.86
APS(I)	1.5	100	0.34	6.71	25.91	48.40	11.59	b.d.l.	92.96
APS(I)	3.5	100	0.45	8.54	23.22	47.12	11.29	b.d.l.	90.63
APS(I)	3.5	100	0.26	2.81	30.28	55.21	6.42	b.d.l.	94.98
APS(I)	3.5	100	0.39	4.50	29.62	52.07	7.22	0.06	93.86
APS(I)	3.5	100	0.49	7.64	23.76	47.73	11.45	0.03	91.10
APS(I)	5.5	100	0.28	5.78	26.74	52.28	7.26	b.d.l.	92.35
APS(I)	5.5	100	0.59	10.58	16.05	46.84	16.03	0.18	90.27
APS(I)	5.5	100	0.21	4.84	28.77	50.14	8.08	0.02	92.06
APS(I)	1.5	1000	0.52	10.80	21.97	37.87	14.30	b.d.l.	85.45
APS(I)	1.5	1000	0.28	5.83	24.83	44.40	11.92	b.d.l.	87.26
APS(I)	1.5	1000	0.29	4.18	30.49	45.55	7.31	b.d.l.	87.81
APS(I)	1.5	1000	0.19	1.85	32.17	54.03	3.53	0.11	91.89
APS(I)	1.5	1000	0.22	7.10	28.95	52.80	3.98	0.11	93.15
APS(I)	3.5	1000	0.41	6.21	24.55	48.13	9.97	b.d.l.	89.27
APS(I)	3.5	1000	0.19	15.78	23.95	49.72	4.59	0.13	94.36
APS(I)	3.5	1000	0.33	7.00	23.90	43.59	12.80	0.05	87.66
APS(I)	3.5	1000	0.33	6.02	22.61	46.48	9.01	0.03	84.48
APS(I)	3.5	1000	0.19	2.64	33.36	51.67	4.17	0.02	92.05
APS(I)	3.5	1000	0.26	3.98	30.02	47.91	8.22	0.02	90.43
APS(I)	5.5	1000	0.53	7.86	25.33	44.30	10.90	b.d.l.	88.93
APS(I)	5.5	1000	0.34	10.04	25.25	49.59	6.89	b.d.l.	92.10
APS(I)	5.5	1000	0.47	6.93	26.00	46.79	10.22	0.15	90.56
APS(I)	5.5	1000	0.49	11.75	21.46	41.71	11.81	0.11	87.33
APS(I)	5.5	1000	0.59	10.42	22.57	40.05	13.48	0.03	87.14
APS(I)	5.5	1000	0.22	2.79	28.83	54.56	6.09	0.02	92.52
APS(I)	n/a	n/a	0.49	7.76	22.88	39.57	10.57	b.d.l.	81.27
APS(I)	n/a	n/a	0.45	5.82	27.50	46.52	9.17	b.d.l.	89.46
APS(I)	n/a	n/a	0.15	2.94	31.76	54.72	3.74	b.d.l.	93.31
APS(I)	n/a	n/a	0.28	4.26	29.81	53.42	6.38	b.d.l.	94.15
APS(I)	n/a	n/a	0.39	5.03	26.31	50.95	7.79	b.d.l.	90.50
APS(II)	1.5	10	6.14	20.26	11.20	34.76	8.19	b.d.l.	80.54
APS(II)	1.5	10	5.49	17.00	15.64	37.59	7.22	b.d.l.	82.93
APS(II)	1.5	10	9.18	22.16	6.96	40.19	6.73	b.d.l.	85.22
APS(II)	1.5	10	7.59	32.22	7.41	37.50	6.82	b.d.l.	91.54
APS(II)	1.5	10	4.86	24.55	8.95	33.33	9.38	0.02	81.09
APS(II)	3.5	10	9.15	27.14	5.16	34.76	4.93	b.d.l.	81.14
APS(II)	3.5	10	5.92	19.72	12.07	34.11	10.46	b.d.l.	82.29
APS(II)	3.5	10	5.75	21.12	11.81	33.04	10.63	b.d.l.	82.35

APS(II)	3.5	10	6.84	21.37	12.01	34.63	7.98	b.d.l.	82.83
APS(II)	3.5	10	4.15	13.85	19.92	35.43	10.80	b.d.l.	84.15
APS(II)	3.5	10	2.45	6.63	25.94	43.90	5.31	b.d.l.	84.23
APS(II)	3.5	10	1.72	7.78	24.83	43.51	6.89	b.d.l.	84.71
APS(II)	3.5	10	3.10	9.59	23.55	45.11	6.14	b.d.l.	87.49
APS(II)	3.5	10	5.85	16.91	16.12	34.03	9.01	0.04	81.95
APS(II)	5.5	10	5.40	18.57	11.71	37.09	7.73	b.d.l.	80.50
APS(II)	5.5	10	4.16	13.69	17.14	39.69	6.92	b.d.l.	81.60
APS(II)	5.5	10	6.63	20.77	13.21	31.84	9.19	b.d.l.	81.63
APS(II)	5.5	10	3.97	10.97	21.80	40.55	7.85	b.d.l.	85.15
APS(II)	5.5	10	1.78	6.07	26.85	52.51	5.38	b.d.l.	92.60
APS(II)	5.5	10	2.67	7.28	26.61	49.98	6.28	b.d.l.	92.82
APS(II)	5.5	10	3.12	9.08	24.91	48.67	7.19	b.d.l.	92.96
APS(II)	5.5	10	6.36	21.36	10.79	33.66	9.44	0.07	81.68
APS(II)	5.5	10	7.62	23.99	10.00	31.98	9.93	0.05	83.57
APS(II)	5.5	10	1.82	7.78	13.78	60.99	3.36	0.02	87.76
APS(II)	5.5	10	8.74	26.17	5.80	35.23	5.04	0.02	80.99
APS(II)	5.5	10	10.62	29.60	4.03	33.33	3.30	0.02	80.90
APS(II)	1.5	100	8.28	23.63	7.07	36.49	5.72	b.d.l.	81.19
APS(II)	1.5	100	2.56	14.02	17.98	35.92	14.95	0.04	85.47
APS(II)	1.5	100	8.98	27.42	5.33	35.34	5.19	0.03	82.28
APS(II)	1.5	100	5.08	20.89	12.66	33.84	12.82	0.02	85.32
APS(II)	1.5	100	6.84	22.37	10.63	33.78	8.86	0.02	82.50
APS(II)	3.5	100	7.42	23.83	8.66	34.59	6.82	b.d.l.	81.33
APS(II)	3.5	100	2.27	6.10	26.94	50.00	5.69	0.03	91.02
APS(II)	3.5	100	1.75	16.27	12.99	32.34	17.63	0.02	81.00
APS(II)	3.5	100	7.51	20.04	13.07	34.83	7.07	0.02	82.54
APS(II)	3.5	100	6.12	20.09	12.97	34.34	10.07	0.02	83.60
APS(II)	3.5	100	8.93	28.03	4.18	34.58	4.60	0.01	80.33
APS(II)	3.5	100	3.40	11.48	21.39	44.15	5.52	0.01	85.94
APS(II)	5.5	100	7.89	20.56	10.42	35.12	6.71	b.d.l.	80.70
APS(II)	5.5	100	7.23	24.16	8.07	33.24	8.48	b.d.l.	81.17
APS(II)	5.5	100	4.24	17.77	15.32	35.73	12.06	b.d.l.	85.14
APS(II)	5.5	100	2.37	12.29	20.17	42.05	12.85	b.d.l.	89.75
APS(II)	1.5	1000	5.34	15.30	18.53	38.60	7.27	b.d.l.	85.04
APS(II)	1.5	1000	3.50	12.31	23.38	29.79	18.12	0.28	87.37
APS(II)	1.5	1000	5.61	18.34	13.84	35.04	8.93	0.18	81.94
APS(II)	1.5	1000	6.53	21.25	10.41	33.30	9.32	0.06	80.87
APS(II)	1.5	1000	6.76	20.03	13.26	33.10	7.72	0.05	80.92
APS(II)	1.5	1000	5.91	19.25	15.13	34.77	9.83	0.03	84.93
APS(II)	1.5	1000	6.41	20.26	13.27	32.22	9.65	0.03	81.85
APS(II)	3.5	1000	5.14	16.66	16.56	33.72	9.63	0.19	81.91
APS(II)	3.5	1000	3.35	8.18	25.91	44.71	6.09	0.17	88.42
APS(II)	3.5	1000	8.98	26.40	6.63	32.81	6.70	0.15	81.67
APS(II)	3.5	1000	8.42	25.67	6.80	33.37	6.39	0.14	80.80
APS(II)	3.5	1000	7.54	22.72	9.54	32.34	9.16	0.04	81.34
APS(II)	5.5	1000	1.89	5.73	27.47	43.20	5.60	0.05	83.94
APS(II)	5.5	1000	3.97	15.57	17.07	34.83	10.67	0.03	82.15
APS(II)	5.5	1000	4.59	18.89	13.70	33.60	12.22	0.03	83.03
APS(II)	5.5	1000	6.25	23.89	9.88	32.64	10.82	0.03	83.51
APS(II)	n/a	n/a	3.12	12.74	17.97	38.14	9.64	b.d.l.	81.61
APS(II)	n/a	n/a	5.45	17.27	16.35	38.39	7.73	b.d.l.	85.20
APS(II)	n/a	n/a	2.93	7.68	26.83	45.75	6.17	b.d.l.	89.37
APS(II)	n/a	n/a	1.20	3.12	30.69	51.36	4.00	b.d.l.	90.38
APS(II)	n/a	n/a	1.33	2.91	30.81	53.67	4.41	b.d.l.	93.13
APS(II)	n/a	n/a	1.83	2.19	32.63	51.82	4.74	b.d.l.	93.21
APS(II)	n/a	n/a	1.71	4.52	29.96	52.67	4.89	b.d.l.	93.75
APS(II)	n/a	n/a	1.53	2.42	31.36	55.19	4.01	b.d.l.	94.50

Table 2: Complete LA-ICP-MS dataset comprised of spot analysis on synthetic Sr-, and (Ca,Sr)-bearing APS phases before and after Pb sorption experiments.

Material	pH	[Pb _{aq}] ₀	Ca (ppm)	2SE	Sr (ppm)	2SE	Pb (ppm)	2SE
APS(I)	1.5	10	2146	780	4753	870	10	1.5
APS(I)	1.5	10	1389	660	3547	170	28	2.2
APS(I)	3.5	10	38143	2300	142514	6600	1871	220
APS(I)	3.5	10	32192	2700	108726	6600	333	26
APS(I)	5.5	10	37602	3100	131429	9100	195	17
APS(I)	5.5	10	25248	3100	73075	5000	74	4.7
APS(I)	5.5	10	26330	4500	86998	3400	55	5.4
APS(I)	1.5	100	31380	5600	102518	3900	347	51
APS(I)	1.5	100	39766	6200	136573	19000	2284	170
APS(I)	1.5	100	28855	2200	95157	6200	186	36
APS(I)	1.5	100	4202	920	15342	1400	404	86
APS(I)	1.5	1000	24798	3900	89570	15000	877	93
APS(I)	1.5	1000	18035	2400	77155	10000	511	58
APS(I)	1.5	1000	14879	2500	56491	9800	535	61
APS(I)	1.5	1000	14518	2200	46914	3500	1005	62
APS(I)	1.5	1000	2254	1000	12682	1300	561	56
APS(I)	5.5	1000	15059	1900	54984	3800	36852	2400
APS(I)	5.5	1000	44906	8700	131518	7100	2060	690
APS(I)	5.5	1000	14879	1400	57201	4500	6004	930
APS(I)	n/a	n/a	29306	2200	97641	5000	4	1.1
APS(I)	n/a	n/a	30929	6500	100390	7300	4	1.5
APS(I)	n/a	n/a	27954	14000	81411	5000	6	6.6
APS(II)	1.5	10	35528	6700	72720	4700	63	4.2
APS(II)	1.5	10	52210	6200	47268	5900	49	7.5
APS(II)	1.5	10	54555	4100	46470	1900	74	6.7
APS(II)	1.5	10	45267	3000	32636	1800	28	1.4
APS(II)	1.5	10	77909	2200	55959	1900	39	3
APS(II)	1.5	10	75745	3200	54186	2200	25	1.8
APS(II)	1.5	10	75655	2600	48953	2800	48	4.4
APS(II)	1.5	10	33995	5200	19510	2400	24	2.3
APS(II)	1.5	10	72499	5900	40617	2200	38	3.6
APS(II)	1.5	10	59965	3600	23678	1200	113	11
APS(II)	1.5	10	67449	7500	26339	1500	85	5.9
APS(II)	1.5	10	89902	13000	18455	350	163	23
APS(II)	3.5	10	12714	2000	28467	2200	15063	7900
APS(II)	3.5	10	80254	8600	114402	5500	6621	730
APS(II)	3.5	10	56088	4100	68198	3800	3475	420
APS(II)	3.5	10	79442	4600	91610	9900	4694	1700
APS(II)	3.5	10	66367	2700	65448	1900	666	140
APS(II)	3.5	10	93870	3400	90635	6300	306	36
APS(II)	3.5	10	84041	4800	67045	4000	1240	390
APS(II)	3.5	10	71327	3700	55427	3200	109	14
APS(II)	3.5	10	76376	1900	58176	1700	18	2.2
APS(II)	3.5	10	76917	5000	54806	5500	450	95
APS(II)	3.5	10	73942	5800	40706	1700	221	15
APS(II)	3.5	10	82779	4100	45317	2800	292	22
APS(II)	3.5	10	74843	2700	34764	1400	156	8.7
APS(II)	3.5	10	55907	14000	21905	1200	151	14
APS(II)	3.5	10	80705	2600	30436	750	425	50
APS(II)	3.5	10	80074	3000	23244	580	1688	350
APS(II)	5.5	10	49685	3500	49485	3300	4533	400
APS(II)	5.5	10	42832	5100	34498	4300	11069	1100
APS(II)	5.5	10	45988	23000	24069	900	24101	3000
APS(II)	5.5	10	19477	6100	2288	300	15343	3000

APS(II)	5.5	10	98649	6200	85136	4600	1674	140
APS(II)	5.5	10	58342	8500	45849	3200	946	130
APS(II)	5.5	10	16592	2200	8593	960	3517	280
APS(II)	5.5	10	83861	5900	56935	2700	1702	180
APS(II)	5.5	10	21822	2000	8496	290	3195	890
APS(II)	5.5	10	4779	3600	484	21	1559	93
APS(II)	1.5	100	5140	2700	18180	4200	386	58
APS(II)	1.5	100	48242	4500	65714	6200	195	19
APS(II)	1.5	100	62219	13000	69705	3400	58	8.6
APS(II)	1.5	100	31921	4100	32458	3300	264	47
APS(II)	1.5	100	33544	6500	22614	3100	1990	580
APS(II)	1.5	100	76286	2300	55605	3500	25	3
APS(II)	1.5	100	62580	4300	45495	3000	73	5.1
APS(II)	1.5	100	65015	3300	37158	2600	4190	860
APS(II)	1.5	100	76376	2600	48244	2300	101	14
APS(II)	1.5	100	56809	4700	33522	2700	36	4.3
APS(II)	1.5	100	71597	3100	39464	2200	62	8.7
APS(II)	1.5	100	61498	5300	30596	1600	34	3.1
APS(II)	1.5	100	81606	3500	38932	2900	735	54
APS(II)	1.5	100	63662	6600	30507	1300	32	3.6
APS(II)	1.5	100	68712	6900	31749	1800	212	25
APS(II)	3.5	100	13526	2700	27935	2700	7959	670
APS(II)	3.5	100	63392	3700	91078	6000	327	60
APS(II)	3.5	100	77368	2500	87885	3400	834	170
APS(II)	3.5	100	78901	3000	73696	2400	12380	980
APS(II)	3.5	100	55907	8800	57467	2400	823	75
APS(II)	3.5	100	78631	2400	66069	3000	3370	390
APS(II)	3.5	100	71327	5400	37070	4400	9668	1600
APS(II)	3.5	100	83951	2500	47268	1300	1857	220
APS(II)	3.5	100	84402	3600	44608	4700	1541	290
APS(II)	5.5	100	2705	1600	3015	1100	8127	1700
APS(II)	5.5	100	21371	2800	20309	1100	26763	2100
APS(II)	5.5	100	18395	4400	24743	2100	5128	700
APS(II)	5.5	100	64924	3400	81766	2400	1555	230
APS(II)	5.5	100	66728	3000	80081	2300	904	680
APS(II)	5.5	100	10640	2800	8425	1400	3713	780
APS(II)	5.5	100	74753	3300	70237	3000	302	26
APS(II)	5.5	100	82147	3600	56403	2400	17305	1000
APS(II)	5.5	100	48693	22000	22969	1200	17305	2000
APS(II)	5.5	100	64924	3400	81766	2400	1555	230
APS(II)	5.5	100	66728	3000	80081	2300	904	680
APS(II)	5.5	100	74753	3300	70237	3000	302	26
APS(II)	5.5	100	82147	3600	56403	2400	17305	1000
APS(II)	5.5	100	48693	22000	22969	1200	17305	2000
APS(II)	1.5	1000	63842	2300	87353	2100	15	2.5
APS(II)	1.5	1000	730	410	612	120	259	27
APS(II)	1.5	1000	73671	3000	86378	2500	59	5.1
APS(II)	1.5	1000	79983	3300	64650	2300	757	110
APS(II)	1.5	1000	76467	2500	57112	3900	64	9.6
APS(II)	1.5	1000	80795	3400	52146	2100	274	18
APS(II)	1.5	1000	76016	3100	46559	2000	21	4.4
APS(II)	1.5	1000	88189	4200	45415	790	84	6.1
APS(II)	1.5	1000	46078	6600	16052	1400	347	40
APS(II)	3.5	1000	29757	2800	108637	8300	67258	13000
APS(II)	3.5	1000	14608	1800	32281	3900	14152	1000
APS(II)	3.5	1000	22994	2500	40794	3000	7707	1200
APS(II)	3.5	1000	74934	6500	67045	7200	12134	990
APS(II)	3.5	1000	61859	7000	56314	2400	673	150
APS(II)	3.5	1000	67449	2700	34941	2000	11910	1400

APS(II)	3.5	1000	85664	3600	28379	1600	1191	100
APS(II)	5.5	1000	46890	24000	65537	7200	42877	9200
APS(II)	5.5	1000	70605	4700	109701	2800	3629	260
APS(II)	5.5	1000	88550	3100	52678	2300	12401	2900
APS(II)	n/a	n/a	42021	7100	87797	13000	3	1.3
APS(II)	n/a	n/a	83320	4300	112362	7200	3	0.84
APS(II)	n/a	n/a	71237	2700	95423	5100	1	0.16
APS(II)	n/a	n/a	25068	5000	28733	4000	2	0.64
APS(II)	n/a	n/a	72950	3700	82653	3700	1	0.19
APS(II)	n/a	n/a	42471	6100	31837	3800	1	0.17
APS(II)	n/a	n/a	84041	3600	55516	2100	1	0.28
APS(II)	n/a	n/a	111814	8900	62256	3300	1	0.32
APS(II)	n/a	n/a	45267	3000	23058	1300	1	0.24
APS(II)	n/a	n/a	85123	4200	39908	2000	1	0.2
APS(II)	n/a	n/a	88099	4100	39109	2100	1	0.37

SUPPLEMENTARY MATERIAL E

^{210}Pb AND ^{210}Po IN GEOLOGICAL AND RELATED ANTHROPOGENIC MATERIALS: IMPLICATIONS FOR THEIR MINERALOGICAL DISTRIBUTION IN BASE METAL ORES

Nigel J. Cook, Kathy J. Ehrig, Mark Rollog, Cristiana L. Ciobanu, Daniel J. Lane, Danielle S.
Schmandt, Nicholas D. Owen, Toby Hamilton and Stephen R. Grano



Review

^{210}Pb and ^{210}Po in Geological and Related Anthropogenic Materials: Implications for Their Mineralogical Distribution in Base Metal Ores

Nigel J. Cook ^{1,*}, Kathy J. Ehrig ², Mark Rollog ¹, Cristiana L. Ciobanu ¹, Daniel J. Lane ¹, Danielle S. Schmandt ¹, Nicholas D. Owen ¹, Toby Hamilton ³ and Stephen R. Grano ⁴

¹ School of Chemical Engineering, The University of Adelaide, Adelaide, SA 5005, Australia; mark.rollog@adelaide.edu.au (M.R.); cristiana.ciobanu@adelaide.edu.au (C.L.C.); daniel.lane@adelaide.edu.au (D.J.L.), danielle.schmandt@adelaide.edu.au (D.S.S.); nicholas.owen@adelaide.edu.au (N.D.O.)

² BHP Olympic Dam, Adelaide, SA 5000, Australia; Kathy.J.Ehrig@bhpbilliton.com

³ School of Chemical Engineering, The University of Queensland, Brisbane, QLD 4072, Australia; t.hamilton1@uq.edu.au

⁴ Institute for Mineral and Energy Resources, The University of Adelaide, Adelaide, SA 5005, Australia; stephen.grano@adelaide.edu.au

* Correspondence: nigel.cook@adelaide.edu.au; Tel.: +61-8-8313-1096

Abstract: The distributions of ^{210}Pb and ^{210}Po , short half-life products of ^{238}U decay, in geological and related anthropogenic materials are reviewed, with emphasis on their geochemical behaviours and likely mineral hosts. Concentrations of natural ^{210}Pb and ^{210}Po in igneous and related hydrothermal environments are governed by release from crustal reservoirs. ^{210}Po may undergo volatilisation, inducing disequilibrium in magmatic systems. In sedimentary environments (marine, lacustrine, deltaic and fluvial), as in soils, concentrations of ^{210}Pb and ^{210}Po are commonly derived from a combination of natural and anthropogenic sources. Enhanced concentrations of both radionuclides are reported in media from a variety of industrial operations, including uranium mill tailings, waste from phosphoric acid production, oil and gas exploitation and energy production from coals, as well as in residues from the mining and smelting of uranium-bearing copper ores. Although the mineral hosts of the two radionuclides in most solid media are readily defined as those containing parent ^{238}U and ^{226}Ra , their distributions in some hydrothermal U-bearing ores and the products of processing those ores are much less well constrained. Much of the present understanding of these radionuclides is based on indirect data rather than direct observation and potential hosts are likely to be diverse, with departments depending on the local geochemical environment. Some predictions can nevertheless be made based on the geochemical properties of ^{210}Pb and ^{210}Po and those of the intermediate products of ^{238}U decay, including isotopes of Ra and Rn. Alongside all U-bearing minerals, the potential hosts of ^{210}Pb and ^{210}Po may include Pb-bearing chalcogenides such as galena, as well as a range of sulphates, carbonates, and Fe-oxides. ^{210}Pb and ^{210}Po are also likely to occur as nanoparticles adsorbed onto the surface of other minerals, such as clays, Fe-(hydr)oxides and possibly also carbonates. In rocks, unsupported ^{210}Pb -and/or ^{210}Po -bearing nanoparticles may also be present within micro-fractures in minerals and at the interfaces of mineral grains. Despite forming under very limited and special conditions, the local-scale isotopic disequilibrium they infer is highly relevant for understanding their distributions in mineralized rocks and processing products.

Keywords: ^{210}Pb ; ^{210}Po ; uranium decay chain; radionuclides; mineral department

1. Introduction

^{210}Pb and ^{210}Po are intermediate isotopes within the ^{238}U decay-series (Figure 1) and occur in minute amounts in nature [1]. Details of the uranium (^{238}U , ^{235}U) and thorium (^{232}Th) decay-series radionuclides are concisely provided in the review by Cowart and Burnett (1994) [2].

^{210}Pb has a half-life of 22.2 years and is generated via: (i) the decay of atmospheric ^{222}Rn gas (“unsupported” ^{210}Pb); and (ii) via the continuous production of ^{222}Rn from natural ^{226}Ra contained in crustal materials (“supported” ^{210}Pb). ^{210}Pb decays to ^{210}Bi by emission of a beta particle. ^{210}Pb is useful for determining the age of a recent sediment in that, provided that the atmospheric flux is constant, the decay profile relates directly to sedimentation rate. Hence, ^{210}Pb is useful for dating sediments up to a century or so old.

Polonium has no stable isotope [3,4]. ^{210}Po is by far the longest-lived of the 7 naturally-occurring Po isotopes in the U and Th decay-series (half-life = 138.376 days). ^{210}Po is generated via beta decay from ^{210}Bi (half-life 5.01 days) and decays to ^{206}Pb by emission of an alpha particle. It has a high specific activity ($1.66 \cdot 10^{14} \text{ Bq g}^{-1}$) and is highly toxic [5] and one of the most radioactive natural radioisotopes; 1 mg of ^{210}Po emits as many alpha particles per second as 5 g ^{226}Ra . Its toxicity in nature is, however, limited by its vanishingly small mass concentration, even compared to ^{226}Ra . As an energy-generating alpha emitter, ^{210}Po has been used as a lightweight heat source to power thermoelectric cells, for example in the Russian Lunokhod lunar rovers to keep their internal components warm during the lunar nights. The principal source of both ^{210}Pb and ^{210}Po in the environment is natural ^{222}Rn gas which escapes to the atmosphere and undergoes radioactive decay. Airborne particles containing sorbed amounts of these highly particle-reactive decay products of ^{222}Rn fall to the land or water surface and either dissolve, are deposited onto soils, or become subject to sedimentation.

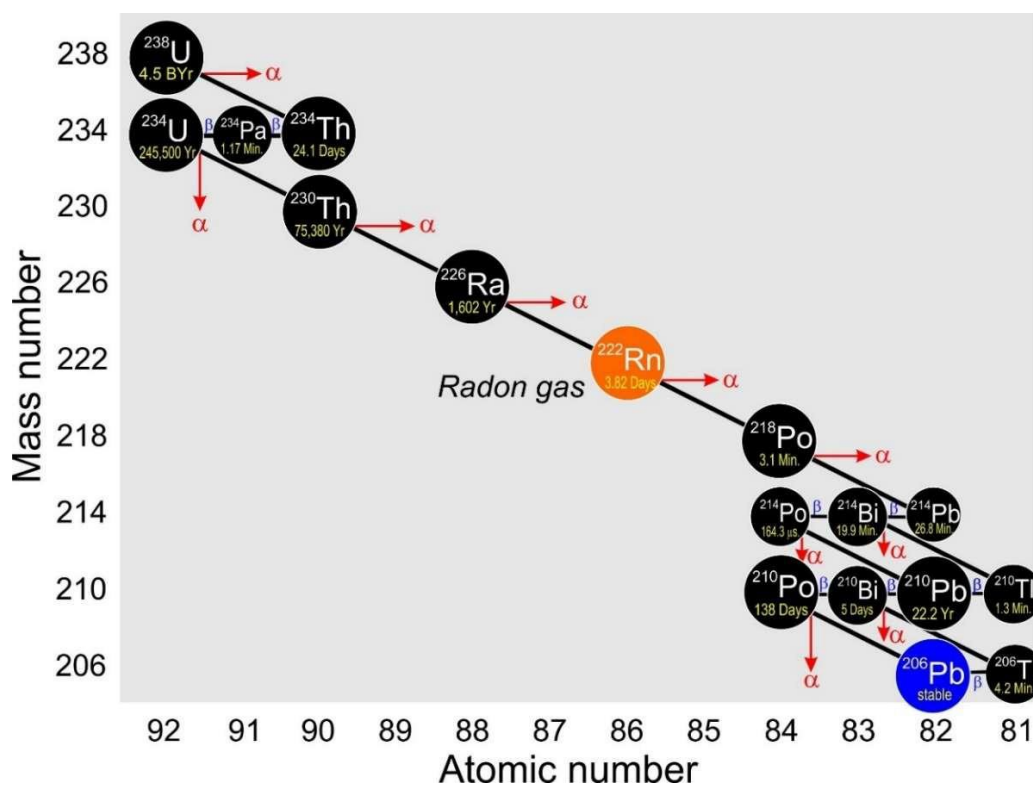


Figure 1. The uranium (radium series) decay chain, indicating half-lives, adapted from various publicly available sources.

Both radionuclides are, however, found in trace amounts in a range of solid media, both natural and anthropogenic in origin. ^{210}Pb and ^{210}Po are present in higher activity concentrations relative to crustal averages in uranium-bearing ores, and in the products of mining and processing from such deposits, including concentrates and wastes. While polonium concentrations are extremely low (< 0.1 mg/tonne even in high-grade uranium ores [6]), the presence of short half-life radionuclides (RN) can impact on the treatment, processing and transport of ore and resulting concentrates. In mining operations in which uranium is present, whether exploited or not, a knowledge of the geochemical behaviour of ^{210}Pb and ^{210}Po during mineral processing is critical to ensure that produced concentrates are as clean as possible. These radionuclides, whether occurring together with parent uranium in the mineralized rocks, or spatially decoupled from it as U-bearing minerals begin to break down, may represent a non-target element that could attract a financial penalty when sold on the open market. If present at high enough concentrations, saleability of that product may be prevented altogether (e.g., [7]). More extensive, and expensive, safety protocols and transport measures may also be required [8].

A comprehensive understanding of the geochemical behaviour and mineralogical distribution of ^{226}Ra , ^{210}Pb and ^{210}Po during ore processing is a pre-requisite for the development of methods to remove or reduce their concentration in products from minerals processing, and provides the motivation behind the present study. The following review of the distributions of ^{210}Pb and ^{210}Po (and of parent ^{226}Ra) in a broad range of geological materials builds on existing reviews of various length [9–12], many of which have emphasised the environmental and health risks that ^{210}Pb and ^{210}Po present. Our emphasis is on the concentrations and distributions of ^{210}Pb and ^{210}Po in solid media, with focus on mineralized rocks and ores, and in anthropogenic materials resulting from the exploitation of natural resources. An assessment of the likely mineral hosts for both ^{210}Pb and ^{210}Po in critical geological environments, including ores and in non-nuclear industrial sources (technologically enhanced naturally occurring radionuclide material (TENORM; [11]) follows.

2. Crustal Distribution of ^{210}Pb and ^{210}Po

^{210}Pb and ^{210}Po are widely dispersed in a large variety of natural media because they often mimic the distributions of parental ^{238}U , ^{226}Ra , or ^{222}Rn . Much of the literature on ^{210}Pb and ^{210}Po distributions in nature is focused on their concentrations in the atmosphere (e.g., [13]), in oceans (e.g., [14–17]), rivers (e.g., [18]), lakes (e.g., [19]), groundwaters (e.g., [20–23]), drinking waters (e.g., [24–26]), and soils [27–29]. Attention has also been given to mosses and lichens, which efficiently capture atmospheric ^{210}Pb and ^{210}Po , peat bogs (also anomalous with respect to ^{210}Pb and ^{210}Po), and in the animal and human food chains, e.g., milk or berries, and particularly seafood (e.g., [12,30–32]). A smaller body of data is available for some natural environments, notably hydrothermal ore deposits or active volcanic fumaroles, where there is evidence for the selective fractionation of ^{210}Pb and ^{210}Po from other ^{238}U decay products, and where ^{210}Pb and ^{210}Po are concentrated in “new” precipitates. These particle-sensitive decay product isotopes are always fractionated from gaseous parent ^{222}Rn that has extreme dispersion and mobility in the environment, particularly in the atmosphere.

There is a large body of data addressing the distribution and behaviour of ^{210}Pb and ^{210}Po in both magmatic and marine/lacustrine sedimentary environments, as well as in relation to the mining, processing and smelting of uranium-bearing ores, processing of phosphate ores for phosphoric acid production and other human activity. Somewhat less well documented are concentrations of ^{226}Ra , ^{210}Pb and ^{210}Po in other anthropogenic materials such as coal ash (e.g., [33,34]), and as scales and sludges associated with oil and gas production [35–37]. Not infrequently, observed distributions are the product of a complex interplay between natural and anthropogenic ^{226}Ra , ^{210}Pb and ^{210}Po from different mining and non-mining sources, the effects of which can only be elucidated by high-quality analysis and a good understanding of the physical and historical context of the samples in question (e.g., [38,39]). There is generally a strong link between the distributions of ^{210}Pb and ^{210}Po and that of parent ^{226}Ra in many industrial wastes (uranium mill tailings, phosphogypsum, coal fly ash, oilfield

scales and sludges) such that understanding the mode-of-occurrence of ^{226}Ra will enable prediction of ^{210}Pb and ^{210}Po behaviour. There are, however, some exceptions in which selective fractionation and concentration of ^{210}Pb and ^{210}Po takes place, as will be shown below.

A detailed treatment of analytical techniques for the determination of short-lived isotopes at concentrations of small fractions of parts-per-billion, and quantification of ^{210}Pb and ^{210}Po in rocks, minerals, concentrates and leachates, lie beyond the scope of this contribution. The reader is referred to References [1,40,41], in which comprehensive reviews of methodologies used for the determination of ^{210}Po in environmental materials are provided, building on earlier studies [42] and others. Clayton and Bradley (1995) [43] describe their methodology to measure ^{210}Pb and ^{210}Po in a range of environmental materials. In a series of papers, Jia and co-authors [44–46] have put forward procedures for analysis of ^{210}Pb and ^{210}Po in mineral, biological and soil samples. Particularly relevant to our focus on ^{210}Pb and ^{210}Po distributions in ores and ore processing residues are separation techniques outlined by Prud'homme et al. (1999) [47] for fine-grained multi-phase materials.

2.1. Magmatic Rocks and Related Hydrothermal Systems

Volcanoes represent the largest single contributor of atmospheric ^{210}Pb and ^{210}Po . For example, Allard et al. [48] document extremely high fluxes from the Ambrym basaltic volcano, Vanuatu Island Arc, in the South Pacific Ocean. Based on direct measurements, these authors maintain that this volcano is among the most powerful volcanic gas emitters on Earth, producing between 5% and 9% of current estimates for global subaerial volcanic emissions of ^{210}Pb and ^{210}Po . Data for both dissolved and emitted magmatic volatiles are used to estimate the depth, size and degassing rate of the basaltic magma reservoir that sustains the eruptive activity [48]. In the aforementioned paper, Allard et al. note radioactive disequilibrium of ^{210}Pb , ^{210}Bi and ^{210}Po in the volcanic gas phase and use this to constrain the renewal rate and dynamic time scales of the magma reservoir. Extensive radioactive disequilibrium between the three radionuclides reported in Ambrym volcanic gas is concordant with observations from other basaltic volcanoes [49,50]. The radioisotopic disequilibrium is attributed by Allard et al. [48] to the very different volatilisation rates of the three radionuclides during high-temperature basalt degassing ($^{210}\text{Po} > ^{210}\text{Bi} > ^{210}\text{Pb}$). All ^{210}Po is volatilised, whereas the emanation rate is two orders of magnitude lower. ^{210}Po – ^{210}Pb geochronology is routinely used to date recent volcanic eruptions (e.g., [51]). Measurable activity of ^{210}Pb , ^{210}Bi and ^{210}Po is not restricted to basaltic volcanoes. The volatility of all three radionuclides have been studied in andesitic gases from Merapi Volcano, Indonesia [52], although the authors note that the emanation coefficients are significantly lower than observed at basaltic volcanoes, a feature attributed to lower magma temperatures. The same authors state that the radionuclides are mainly transported in the volcanic gases as Pb-chlorides, and as “Bi- and Po-metallic species”.

The radionuclide systematics of igneous activity nevertheless differ considerably with respect to tectonic environments [53]. Enrichment of ^{210}Po and ^{226}Ra relative to ^{230}Th is noted to be more common and greater in island arcs than in continental margin subduction environments. Levels of enrichment tend to decrease with differentiation. Differences were attributed [53] to variations in the process of melt extraction, changes in bulk partition coefficients within the mantle wedge, or preferential addition of U from subducted lithosphere.

Interest in the activity of ^{210}Pb and relationships with parent radionuclides in young volcanic rocks centres on the useful geochronological information the radioisotope distributions can provide. The literature reveals substantial debate about the possible causes of observed isotopic disequilibria in many young volcanic rocks (e.g., [54]). The observed ^{210}Pb deficits relative to ^{226}Ra are attributed to magma degassing over decades rather than partial melting or interaction with cumulates [55].

Most igneous rocks contain both U and Th, with concentrations increasing as silica content increases. Granites are thus the rock type with the highest concentration of all daughter radionuclides, which remain in secular equilibrium until weathered. Uranium, Th and daughter radionuclides are important heat producers in granitic rocks [56].

Radionuclide concentrations have been examined in volcanic fumaroles from La Fossa cone, Vulcano Island, Italy [57,58]. Sulphur and sulphide incrustations show relative but variable enrichments in ^{210}Po (as high as $500 \text{ Bq}\cdot\text{g}^{-1}$), and in ^{210}Pb relative to ^{226}Ra , which are related to degassing of the fumarolic fluids. The published data record mobility of sublimates within the fumaroles. ^{210}Po is almost fully volatilised due to the relatively high velocity of the gas, even though temperatures did not exceed 280–350 °C. Much ^{210}Po may therefore be present in gaseous form within the fumarole. Sublimates at La Fossa Crater, Aeolian Islands, Italy [59] contain an abundance of rare Pb–Bi-sulphosalt mineral species (e.g., wittite, cannizzarite, mozgovaite, etc. [60,61]). Several of sulphosalts, including Cl- and Br-bearing species (e.g., vurroite [62]) have been first described from the locality.

The unusually high sulphur-reducing environments offered by deep-sea hydrothermal vents display ^{210}Pb and ^{210}Po enrichment relative to ^{226}Ra . Boisson et al. (2001) [63], for example, describe the relative enrichment in naturally-occurring ^{210}Po and ^{210}Pb associated with the high particle fluxes brought about by hydrothermal venting off the island of Milos, Aegean Sea. ^{210}Po levels in organisms living on or near the microbial mat in the vent zone were higher than from non-vent areas. It was, however, stressed [63] that input of ^{210}Po and ^{210}Pb to oceans through venting activity is probably not significant compared to that of atmospheric origin. High levels of natural radioactivity, including ^{210}Po – ^{210}Pb , in vent biota from both the East Pacific Rise and Mid-Atlantic Ridge have been confirmed [64].

2.2. Sedimentary Environments

Measurable concentrations of ^{210}Pb and ^{210}Po in sedimentary environments, whether marine, lacustrine, deltaic or fluvial have proven invaluable for understanding age relationships of sediments on the decade-scale and for calculation of rates of sedimentation. Many dozens of case studies, e.g., [65–68], document the spatial distributions of ^{210}Pb and ^{210}Po , and successfully separate natural from anthropogenic sources. Activities of ^{210}Pb and ^{210}Po have also proven valuable for studies of glaciation and the accumulation and melting rates of ice sheets [69]. Remarkably few of these studies have addressed the mineralogy of the sediments, and the likely host(s) of ^{210}Pb and ^{210}Po .

A key feature of many studies of sediments and water columns in marine or lake waters is the recognition of disequilibrium between ^{210}Pb and ^{210}Po that is linked to differential cycling patterns, rates of sequestration by sediments, as well as the contributions of atmospheric deposition, particularly for ^{210}Po . Some sedimentary rocks contain anomalous radionuclide concentrations. Of particular note are restricted marine and estuary environments supplied by organic- and clay-rich sediment. Under reducing conditions, uranium is readily adsorbed onto the organics and/or clay particles.

Sedimentary rocks are also the host for many of the World's largest and richest uranium deposits, formed via migration of dissolved U^{6+} in oxidising waters along paleoaquifers and deposited in reduced rocks. The genesis of such deposits has been amply described elsewhere [70].

3. ^{210}Pb and ^{210}Po from Anthropogenic Sources

The mining of uranium, smelting of copper and polymetallic ores, phosphoric acid and oil/gas production and combustion of coal (and peat) are the main extractive activities leading to generation of materials with high contents of ^{210}Pb , ^{210}Po , and other RN. Surveys of the generation of Naturally Occurring Radioactive Materials (NORM) from industrial operations [71–75] also cover other industrial sectors, including manufacture of zirconia, titanium dioxide pigment production, cement production and alumina and iron and steel production.

3.1. ^{210}Pb and ^{210}Po in Uranium Mill Tailings

The radiological risks associated with management of uranium mill tailings have been discussed by [76–79], among many others. Several authors have suggested that ^{226}Ra occurs in radium-bearing sulphate minerals in uranium mill tailings [80–82]. Landa et al. [83] examined uranium mill tailings from Monticello, Utah. ^{226}Ra was found to be associated with particles and colloids of alkaline-earth sulphates, alkaline-earth carbonates, and surfaces of quartz, clay, and feldspar. Landa [77] inferred from the leaching behaviour of uranium mill tailings that ^{226}Ra occurs with hydrous oxides of iron and manganese. In one study specially aimed at understanding the mineralogy of ^{210}Po [84], material from three uranium mill sites in the USA were examined to establish where contaminants reside as a prerequisite for modelling contaminant mobilisation. Four mineral hosts were suggested using a combination of electron probe microanalysis, thin-section petrography, α -emission mapping, and selective chemical extractions (although none of these techniques can identify mineral hosts for specific radioactive decay products): uranium minerals, authigenic siliceous material, Ba–Sr-sulphates, and Fe–Ti–V-oxides. These themes are explored further by Landa and Bush [79], who recognised a redistribution of radium by particle size during milling but also of the components in the tailings onto which radionuclides are adsorbed. The following potential sorbents were identified: clay minerals, Fe- and Al-oxides, feldspars, fluorite, barite, jarosite, coal, and volcanic glass. Both ^{226}Ra and ^{210}Pb showed both higher degrees of adsorption than either ^{238}U or ^{230}Th , attributable to either selective adsorption or ingrowth of ^{210}Pb daughter isotopes in minerals containing substituted radium (e.g., Ra^{2+} for Ca^{2+}).

In a review of the mineralogical controls on radionuclide mobility in uranium mill tailings [78], the importance of amorphous silica, carbonates and phosphates, and microbial reduction processes is noted. The same publication also examines radionuclide behaviour (although not mentioning ^{210}Pb and ^{210}Po in this context) during in-situ leach (ISL) recovery operations. Jarosite [$\text{KFe}_3(\text{SO}_4)_2(\text{OH})_6$], which may precipitate and severely restrict permeability along ISL aquifers, is said to be a significant host for radium. The presence of sulphides and Fe-(hydr)oxides will also impact on recovery dependent on the extracting agent used. These ideas are expanded in a more recent study of uranium mill tailings [85] that also stresses the potential role of sulphates and secondary galena as hosts for ^{210}Pb . It is reasonable to infer that these minerals scavenge ^{210}Pb dissolved within pore fluids.

Radionuclide distributions, including ^{210}Pb deposition rates and inventories, have been examined in and around the Ranger Uranium Mine, N.T., Australia [86]. Natural redistributions of ^{222}Rn and ^{210}Pb occur via atmospheric dispersion of ^{222}Rn , (seasonal) deposition of ^{210}Pb on surfaces, and eventual migration creating ^{210}Pb depth profiles prior to decay to ^{206}Pb . A net loss of ^{210}Pb from the region occurs during the dry season by attachment to aerosols.

3.2. ^{210}Pb and ^{210}Po in Copper and Polymetallic Ores and Products of Their Mining and Processing

Some copper ores contain anomalously high concentrations of RN, meaning that daughter radionuclides are present in products of mining and smelting, and within wastes resulting from those activities. Due to selective volatilization/condensation of ^{210}Pb and ^{210}Po , smelter dusts tend to be enriched in ^{210}Pb and ^{210}Po compared to ^{226}Ra , compared to their activity concentrations in the original ore feed, and compared to their activity concentrations in other solids produced during processing. Such a scenario is documented for the Olympic Dam copper mining and smelting operation, South Australia [87]. The behaviour of ^{210}Pb and ^{210}Po during concentration and smelting of copper ores, and their preferential partitioning into smelter flue dusts where they may accumulate, has been documented in several studies. One of the best studied examples is the contamination generated through centuries of exploitation of copper-bearing bituminous shales (Kupferschiefer) in the Mansfeld district of eastern Germany. A characterisation of scrubber dust slurries (*Theisenschlamm*) containing ^{210}Pb and ^{210}Po , which were produced as a by-product of the Mansfeld smelting operations, is given in [88]. Around 220,000 tonnes of these sludges are deposited at several sites and continue to represent a serious environmental risk [89–92]. The material contains: 18% Zn (as sphalerite and wurtzite);

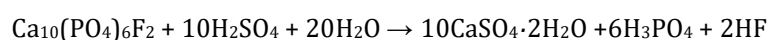
14% Pb (as galena and secondary anglesite); a wide variety of hazardous (As, Tl, Cd) elements and rare metals (Ag, Ge, Re); polycyclic aromatic hydrocarbons and other organic compounds, as well as radionuclides. ^{210}Pb and ^{210}Po are concentrated in the finest size fractions, typically of sub-micron size and combined as aggregates with mean diameter of 1.25 μm [88]. Additional characterisation of the *Theisenschlamm* is provided by Morency et al. [93], with experimental evidence in support of oxidative processes designed to immobilize elements and isotopes of concern. Of relevance to the overarching aim of the present study is the observation that almost all ^{210}Pb and ^{210}Po can be concentrated into a lead sulphate phase. Ores of comparable age and origin, albeit with generally lower associated radioactivity, are currently mined in the Lubin region, Poland [94]. The highly selective enrichment of ^{210}Pb and ^{210}Po compared to ^{226}Ra in certain wastes from copper smelting highlights the importance of understanding the distribution of these isotopes when designing plant operations or planning waste clean-up or handling.

Hypogene tin ores are generally genetically related to granites and often contain anomalous concentrations of Cu, Pb, Bi, U and Te relative to crustal averages. They may contain measurable concentrations of ^{210}Pb , ^{210}Po and ^{210}Bi . The smelter process, for which feedstock may not only comprise tin ores/concentrates but also tin-rich residues from other processes, involves a molten metal stream and separation into tin, lead and lead-bismuth alloys. ^{210}Po will rapidly volatilise, and according to Martin et al. [71], can be highly enriched in smelter fumes (200,000 $\text{Bq}\cdot\text{kg}^{-1}$). Slags will contain the non-volatile radionuclides but also some ^{210}Pb and ^{210}Po (10,000 $\text{Bq}\cdot\text{kg}^{-1}$). Within the bismuth metal, short-lived ^{210}Bi rapidly decays to ^{210}Pb , which may have activity concentrations up to 100,000 $\text{Bq}\cdot\text{kg}^{-1}$. Hipkin and Paynter (1991) [95] address activity concentrations of materials and the radiation exposures of workers in the tin industries of Bolivia and SE Asia, while background data on ^{210}Pb and ^{210}Po behaviour during the tin smelting and electro-refining process are given by Harvey et al. [96]. ^{210}Pb and ^{210}Po activities in and around a large, now-closed, tin smelter in northern England are discussed by Baxter et al. [97]. Here, over the course of ca. 55 years of tin production, about 30% of the ^{210}Po was isolated in tellurium dross, 48% decayed within the refinery, 19% went to waste slag, and 2% was released into the atmosphere.

3.3. ^{210}Pb and ^{210}Po in Mining and Processing of Phosphates

Many phosphate formations exploited for the fertiliser industry contain concentrations of naturally occurring radionuclides of the uranium and thorium decay series that exceed those in other rocks. The risks associated with mining, milling and manufacturing of phosphoric acid and phosphate fertilizers have been widely documented at different sites around the world. Solid waste products of the phosphate industry, notably gypsum ($\text{CaSO}_4 \cdot 2\text{H}_2\text{O}$), termed phosphogypsum, but also dusts generated during milling, can carry particularly high concentrations of ^{226}Rn , ^{210}Pb and ^{210}Po (e.g., [74,98–109]). Although waste from the phosphate industry has, in some cases, been disposed of in the marine environment (e.g., [101]), elsewhere, most spectacularly in Florida, where the World's largest phosphoric acid industry is centred, huge waste piles (gypstacks) have been generated, creating serious waste management issues.

In the manufacture of phosphoric acid, an important industrial chemical, phosphate rock (which typically contains U within apatite or other phosphates) is treated with sulphuric acid, resulting in by-product gypsum in volumes three times greater than the phosphoric acid (Figure 2). The reaction involved in phosphoric acid production can be simplified, after Burnett et al. [103], as:



The above reaction creates disequilibrium between U, Th and Ra. The majority of U if found in the phosphoric acid, ca. 90% of the ^{226}Ra , and effectively all the ^{210}Pb and ^{210}Po , will be preferentially concentrated within the phosphogypsum (e.g., [110]), with ^{210}Pb and ^{210}Po in secular equilibrium [111]. The ^{210}Pb and ^{210}Po activities in phosphogypsum are typically a few hundreds of $\text{Bq}\cdot\text{kg}^{-1}$. For example,

Brasilian phosphogypsum described by Mazzilli et al. [106] shows concentration ranges of 47–894 Bq·kg⁻¹ and 53–677 Bq·kg⁻¹ for ²¹⁰Pb and ²¹⁰Po, respectively. These activities depend on the uranium concentrations in the phosphate ore, which can vary over as much as an order of magnitude. For comparison, phosphate rocks in Florida, Morocco and Jordan, three important producing areas, contain 1300–1850 Bq kg⁻¹ U [112]. In the phosphate rocks, U (and Th) is present mostly within the mineral apatite. U⁴⁺ has a similar ionic radius to Ca²⁺ (0.97 and 0.99 Å, respectively) and readily substitutes into the apatite lattice, resulting in less abundant uraninite in some ores.

The physical distribution of ²²⁶Ra and ²¹⁰Pb in phosphogypsum waste piles is addressed by Rutherford et al. [100], who note heterogeneity in which ²¹⁰Pb is concentrated in the finest fraction (no more than a few microns). In studies of Florida phosphogypsum, ²¹⁰Pb/²¹⁰Po disequilibrium in mature phosphogypsum samples has been demonstrated [104], suggesting that ²¹⁰Pb was more mobile than either ²¹⁰Po or ²²⁶Ra. Although none of the phosphogypsum research has demonstrated that the mineral hosts for each radionuclide differ (phosphogypsum is, in any case essentially monomineralic with around 1% impurities), these observations are indirect evidence to the suggestion that ²¹⁰Pb may be less well bound within the crystal lattice of gypsum.

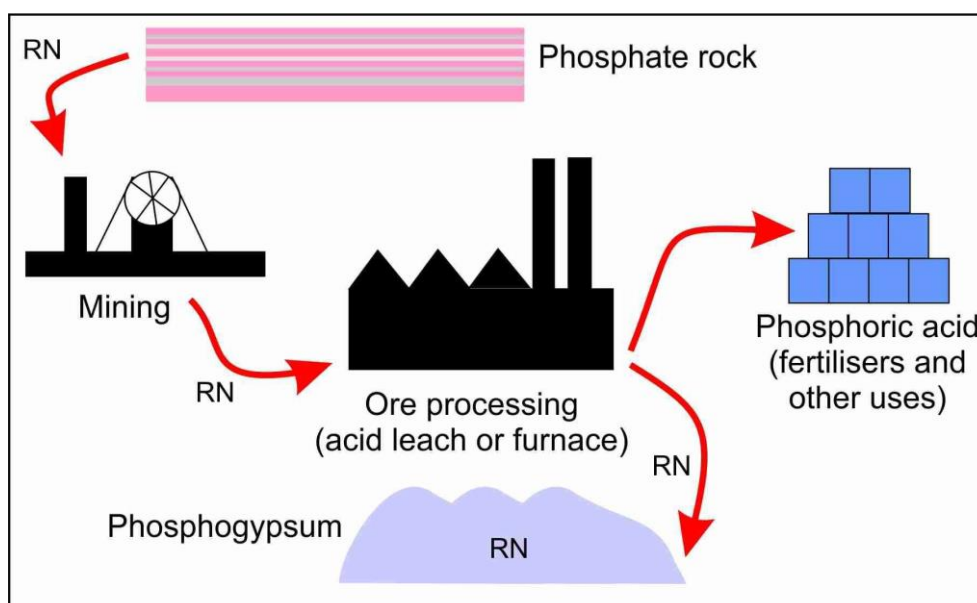


Figure 2. Schematic diagram showing RN behaviour during phosphate production.

3.4. ²¹⁰Pb and ²¹⁰Po Associated with Oil and Gas Production

Radioactive scales and sludges associated with offshore oil and gas production often contain anomalously high concentrations of ²²⁶Ra, ²¹⁰Pb and ²¹⁰Po, and have been well documented [35–37,113,114]. After the mixture of oil, gas and water is brought to the surface, and the gas and formation waters are separated from the oil, hard scales will build up on the internal surfaces of the oil field extraction and production equipment. Well fluids (saline formation waters that are co-produced with oil and gas and require separate handling) are characteristically enriched in Ca, Sr, Ba and associated Ra. Pipes and tanks that come into contact with these waters are subject to scale and sludge build-up. The relative amounts of solid waste (sludges and sands) vary with the production area due to the different geological and fluid characteristics of the reservoirs. ²²⁶Ra, ²¹⁰Pb and ²¹⁰Po-enriched scales precipitate as solids directly from the formation waters following changes in temperature, pressure and salinity.

The volumes of these materials are, however, generally rather small and typically comprise a mixture of carbonate and sulphate compounds of calcium, strontium and barium. Generation of ^{210}Pb and ^{210}Po is due to the presence of parent U and Th in the oil/gas source rocks, which decays to Ra that dissolves within the saline formation waters that also contain P, Sr, Ba and Ca. The radium isotopes, ^{226}Ra and ^{228}Ra , co-precipitate with the salts of these elements, enriching the sludges and, particularly, scales in radium and products of radium decay, including radon isotopes, ^{210}Pb and ^{210}Po . The relatively longer-lived decay products such as ^{210}Pb , will accumulate as very thin films and deposits in gas handling equipment and storage tanks.

3.5. ^{210}Pb and ^{210}Po from Combustion of Coal and Other Solid Fuels

The combustion of solid fuels such as coal for heat and power applications is an important source of atmospheric ^{210}Pb and ^{210}Po and has been studied in detail in various parts of the World. During the combustion of solid fuels, trace elements, including ^{210}Pb and ^{210}Po , partially volatilise along with organic constituents in the fuel matrix. The remaining trace elements remain in the fuel bed and are eventually collected as bottom ash. The volatilised fraction generally condenses on fly ash particles in the flue gases as the flue gases are cooled [115]. Fly ash samples collected from coal-fired power stations have been reported to contain elevated concentrations of ^{210}Pb and ^{210}Po , when compared with the original feedstocks [116], indicating that these two radionuclides volatilise to a large extent during the combustion of solid fuels. The United Nations Scientific Committee on the Effects of Atomic Radiation (UNSCEAR) provide further evidence for the enrichment of ^{210}Pb and ^{210}Po relative to precursor RN in fly ashes during solid fuel combustion in their survey on the activity concentrations of radionuclides in coal samples sourced from a wide range of geographical locations and in fly ashes sourced from various coal-fired power stations [117]. Country-averaged activity concentrations for coal were all within $50 \text{ Bq}\cdot\text{kg}^{-1}$ for both ^{210}Pb and ^{210}Po . Average concentrations of ^{210}Pb and ^{210}Po in the fly ash samples were much higher by comparison (930 Bq kg^{-1} for ^{210}Pb and 1700 Bq kg^{-1} for ^{210}Po). Studies on the size distribution of radionuclides in fly ash show ^{210}Pb and ^{210}Po to preferentially condense on fine particles below 10 microns in size [118,119]. This makes the capture of ^{210}Pb and ^{210}Po difficult, since conventional particulate control devices (e.g., electrostatic precipitators and bag filters) generally become less effective with diminishing particle size [119]. Consequently, a small but nevertheless not insignificant fraction of the ^{210}Pb and ^{210}Po in solid fuels is emitted from the stack into the atmosphere. According to Roeck et al. [120], in old coal-fired power plants, ca. 3% of the initial radioactivity will be discharged from the stack but this proportion is no more than 0.5% in modern plants. UNSCEAR [121] state that annual emissions from a "typical" 600 MW coal fired power station was 0.4 GBq for ^{210}Pb and 0.8 GBq for ^{210}Po . ^{210}Pb and ^{210}Po may also accumulate in deposits on furnace walls and on the fireside of boiler tubes.

The amounts of ^{210}Pb and ^{210}Po released into the different product streams during solid fuel combustion not only depend on processing parameters (e.g., combustion temperature and gas atmosphere) but also on the properties of the feedstock, particularly the activity concentrations of ^{210}Pb and ^{210}Po . Most coals contain small amounts of parent U and Th but their concentrations can vary over several orders of magnitude from deposit to deposit. There is a substantial volume of literature on naturally occurring radionuclide distributions in coals and fly ash [116,122–125]. Coal is formed via reduction of organic material, in which uranium is trapped or adsorbed onto clay particles, carbonaceous matter, pyrite and organic matter. In contrast, Th occurs within minerals such as monazite or apatite. Since organic matter is an effective reductant, coal horizons may accumulate additional uranium over time by extracting dissolved uranium from circulating groundwaters [126]. Lower rank sub-bituminous coals, brown coals, and lignites may contain higher concentrations of parent U and Th ([125] and references therein). Unconsolidated analogues, including peats, may also contain anomalous RN concentrations.

Enhanced atmospheric ^{210}Po in urban areas may be attributed to coal-fired power stations [127,128]. In a comparison of emissions from power plants fuelled by different hydrocarbon fuels, Häsänen et al. [129] point out that the greatest emissions of ^{210}Po per burnt volume of fuel were from combustion of peat.

3.6. ^{210}Pb and ^{210}Po from Exploitation of Mineral Sands

Anomalous concentrations of ^{210}Pb and ^{210}Po are associated with exploitation of mineral sands for production of zircon and zirconia, titanium dioxide and rare earth elements. Radiological risks associated with such ores (and corresponding products and wastes) are generally low (around $10,000 \text{ Bq}\cdot\text{kg}^{-1}$ [71]). This could, however, be an area in which ^{210}Pb and ^{210}Po release is set to increase, since demand for these commodities, especially REE, is booming, and new mineral sands operations are being established around the globe.

Mineral sands are of particular interest because of the indirect information they provide on potential mineral hosts for ^{210}Pb and ^{210}Po . The minerals within such sands (zircon, baddeleyite, monazite, xenotime, ilmenite, rutile, etc.) all host trace to minor amounts of uranium and thorium (varying up to as much as 1 wt % depending on primary source) and are all highly refractory. Despite this, there are relatively few published studies detailing ^{210}Pb and ^{210}Po geochemistry in mineral sands enabling an understanding of whether daughter radionuclides are retained in the crystal structures. The manufacture of zirconia for glazes and ceramics involves production of small volumes (~1% of feed) of highly RN-enriched waste, as well as volatilisation of ^{210}Pb and ^{210}Po .

Titanium oxide pigment production, from rutile, a mineral that also commonly contains primary minor U and Th, also results in a RN-enriched solid waste residue.

3.7. ^{210}Pb and ^{210}Po in Other Anthropogenic Materials

Most iron ores contain only low concentrations of ^{210}Pb and ^{210}Po and thus accumulation of radioactivity in waste materials produced by iron and steel production are mostly attributable to other feed materials (coal/coke and limestone). ^{210}Pb and ^{210}Po tend to accumulate in the sinter plant in dust collected from the gas cleaning systems and are generally very low or absent in saleable products. According to Martin et al. [71], for every million tonnes of steel produced, 2000 tonnes of contaminated dust will be generated. In a study of sinter plant radioactivity in the Port Kembla foundry, NSW, Australia, Brown et al., in a report cited by Martin et al. [71], report activities of 18,900 and 15,600 $\text{Bq}\cdot\text{kg}^{-1}$ for ^{210}Pb and ^{210}Po , respectively, in ductwork dust.

Production of the elements niobium and tantalum is also associated with generation of RN-rich residues. Like tin ores, Nb-Ta ores are granite-related and commonly contain minor amounts of other elements including uranium (and thorium). Pyrochlore, a primary ore mineral of niobium and tantalum, will often contain actinides at measurable concentrations. ^{210}Pb activities as high as $16,700 \text{ Bq kg}^{-1}$ in slags from a Brazilian niobium processing facility are reported [11].

Martin et al. (1997) [71] compiled information on ^{210}Pb and ^{210}Po in cement, bricks and other building materials, and provide activity concentrations for ^{226}Ra and ^{232}Th . They note that activities are only of concern if substantial amounts of waste materials in which ^{210}Pb and ^{210}Po are concentrated are added into the materials. Examples include the common addition of copper slag in concrete (in the former East Germany), phosphogypsum waste in wallboard and road construction, and fly-ash in bricks and some cements. Lightweight building blocks may contain both slag and fly-ash. Several publications detail representative ^{210}Pb and ^{210}Po activity concentration data for building materials, focussing on eastern European countries where the practice of adding smelter slags and fly-ash was commonplace [130–132]. The environmental impact of radionuclide release during processing of granite rock for ornamental stone has also been explored [133]. In this paper, Guillén et al. suggest that even basic mechanical processing of granites can lead to increased levels of ^{210}Po and ^{210}Pb in the surrounding environment, as dusts, solid waste and slurries.

Numerous studies have sought to demonstrate the impact of historical human industrial activity by monitoring the levels of lead isotopes in peat bogs, salt marsh, lakes and estuarine sediments [38,134–140].

4. Mineral Repositories for ^{210}Pb and ^{210}Po

The literature contains extensive reference to the potential mineral repositories for ^{210}Pb and ^{210}Po , although much of this evidence has been obtained indirectly. Very few studies to date have been able to provide direct confirmation that a given phase contains these RN. This is largely due to those RN with relatively short half-lives being present at minute concentrations well below minimum detection limits of conventional microanalysis.

Polonium has no non-radioactive isotope and does not occur naturally as a metal or essential component of naturally occurring compounds, although the compound PbPo has been reported [141] and has been attributed to natural alpha decay of polonium to form lead. Polonium is readily vaporised, forming Po_2 molecules even well below the melting and boiling points (254 and 962 °C, respectively) via small clusters of polonium atoms spalled off by alpha decay. These particles are readily adsorbed. Chemically, polonium displays similar behaviour to that of tellurium and bismuth [141,142]. More than 50 polonium compounds have been synthesized including metal polonides, polonium hydride, the two oxides PoO_2 and PoO_3 , halides and sulphates. Various oxidation states, including 2^+ , 4^+ and 2^- , are known.

Valuable insights into the behaviour of ^{210}Pb and ^{210}Po in polymetallic ores are provided by Golubev et al. [143]. By comparative analysis of different volumes of ore within a single vein-type uranium orebody, these authors provide critical evidence for migration of ^{238}U and, critically, of intermediate decay products within an effectively open system, creating disturbances of U–Pb systematics, expressed as local enrichments or depletions in ^{206}Pb , giving rise to discrepancies between ages based on $^{206}\text{Pb}/^{238}\text{U}$ and $^{207}\text{Pb}/^{235}\text{U}$ ratios. The authors note the presence of zones with low U contents but with excess ^{206}Pb . These contain pyrite/marcasite onto which migrating longer-lived radionuclides, including ^{210}Po and ^{210}Pb , are considered to accumulate, effectively playing the role of geochemical barriers within the system.

In a study attempting to identify the solid-phase partitioning of ^{210}Po and ^{210}Pb in anoxic marine sediments [144], the influence of early diagenetic processes on distribution patterns is documented. In sediment, ^{210}Po was found to be either bound to organic matter, sulphides such as pyrite, clay minerals or refractory oxides. ^{210}Po was found not to be significantly bound to acid volatile sulphides in sediment, even if the authors considered that ^{210}Po initially bound to acid volatile sulphides may have been redistributed by bioturbation.

Because of the extremely low concentrations and the difficulty of separating fine-grained minerals, there is a paucity of published concentration data for ^{210}Pb and ^{210}Po in individual minerals. Identification of the potential mineral repositories for either radionuclide, except for post-decay reincorporation of daughter RN into parent U-minerals is therefore reliant on indirect observation. Good indications as to potential hosts can nevertheless be made based on the literature we have summarised above (Table 1).

Table 1. Summary of potential mineral hosts for ^{210}Pb and ^{210}Po .

Mineral Group	Mineral	Formula (e)	Host for
<i>Uranium minerals</i>	Uraninite	UO_2 (ideally)	U, radiogenic Pb, minor Th
	Coffinite	$\text{U}(\text{SiO}_4)_{1-x}(\text{OH})_{4x}$	ditto -
	Brannerite	$(\text{U,Ca,REE})(\text{Ti,Fe})_2\text{O}_6$	ditto -
	Uranothorite	$(\text{Th,U})\text{SiO}_4$	Th, U, radiogenic Pb
	Carnotite	$\text{K}_2(\text{UO}_2)_2(\text{VO}_4)_2 \cdot 3\text{H}_2\text{O}$	U, (Th and Pb?)
<i>REE-, Zr- and Nb-Ta-minerals</i>	Monazite	$(\text{REE})\text{PO}_4$	Minor U, Th radiogenic Pb?)
	Bastnäsité	$\text{REE}(\text{CO}_3)\text{F}$	ditto -
	Synchysite	$\text{Ca}(\text{REE})(\text{CO}_3)_2\text{F}$	ditto -
	Xenotime	$(\text{Y,REE})\text{PO}_4$	ditto -
	Alunite Supergroup Minerals (especially crandallite and beudantite groups)	(Various minerals)	ditto -
	Baddeleyite	ZrO_2	ditto -
	Zircon	ZrSiO_4	ditto -
	Tantalite-(Fe)-tantalite-(Mn) series	$(\text{Fe,Mn,Mg})(\text{Nb,Ta})_2\text{O}_6$	Trace U,Th,Pb (?)
<i>Sulphides/selenides/tellurides</i>	Euxinite	$(\text{Y,Ca,Ce,U,Th})(\text{Nb,Ta,Ti})_2\text{O}_6$	ditto -
	Galena	PbS	Radiogenic Pb
	Clausthalite	PbSe	ditto -
	Altaite	PbTe	ditto -
	Bi-chalcogenides	$\text{Bi}_x(\text{Te,Se,S})_y$?
	Pb-Bi-sulphosalts	(various)	?
	Pyrite	FeS_2	as a sorbent (?)
<i>Carbonates</i>	Calcite, dolomite, ankerite	CaCO_3 , $\text{CaMg}(\text{CO}_3)_2$, $\text{Ca}(\text{Fe,Mg})(\text{CO}_3)_2$	Ra, minor Pb
	Strontianite	SrCO_3	ditto -
	Rhodocrosite	MnCO_3	ditto -
	Magnesite	MgCO_3	ditto -
	Witherite	PbCO_3	Pb
<i>Sulphates</i>	Barite	BaSO_4	Ra, Pb
	Celestite	SrSO_4	ditto -
	Anglesite	PbSO_4	Pb
	Gypsum	$\text{CaSO}_4 \cdot 2\text{H}_2\text{O}$	Pb (?)
<i>Fe-oxides, hydroxides</i>	Hematite	$\alpha\text{-Fe}_2\text{O}_3$	Minor/trace U, Pb, and as sorbent
	Goethite	$\text{FeO}(\text{OH})$	As sorbent
<i>Fe-Ti-oxides, Ti-oxides</i>	Ilmenite	FeTiO_3	Minor U and Th
	Rutile	TiO_2	ditto -
<i>Jarosite sub-group</i>	Jarosite	$\text{KFe}(\text{SO}_4)_2(\text{OH})_6$	Pb?
<i>Other potential hosts</i>	Apatite group	$\text{Ca}_5(\text{PO}_4)_3(\text{F,Cl,OH})$	Minor U and Th
	Fluorite	CaF_2	?
	Feldspar group	-	Pb (replacing Ca?)

4.1. Re-Incorporation of Radionuclides into Parent Minerals

All minerals originally containing uranium will host daughter RN if those products do not migrate from the parent. Plausible ^{210}Pb and ^{210}Po carriers thus include the more common uranium minerals, such as uraninite, coffinite, uranothorite and brannerite, as well as the large number of minerals which carry trace to minor amounts of uranium. The latter include REE-fluorocarbonates and phosphates (monazite, bastnäsité, synchysite, florencite, xenotime, etc.), and common accessory minerals in rocks and ores such as apatite, allanite, zircon, titanite and rutile). The assumption that ^{210}Pb and ^{210}Po can be found in these minerals, however, infers that all decay chain products, including ^{234}Th , ^{226}Ra and ^{222}Rn , are retained within the parent mineral, either within the crystal lattice, or as inclusions.

In the case of the mineral uraninite, strong supporting evidence for this emerges from our own recent research on the Olympic Dam Cu-U-Au-Ag ore deposit, South Australia, where (re-)incorporation of radiogenic lead within the crystal lattice of uraninite is recognised [145–147]. Lead concentrations in Olympic Dam uraninite can, locally exceed 10 wt % in solid solution within the uraninite structure. This contradicts the findings of Janeczek and Ewing [148], where it is maintained that Pb^{2+} is incompatible within the fluorite-type uraninite structure at concentrations greater than a few wt %. Other U-minerals will also contain Pb, albeit at lower concentrations, e.g., coffinite and

brannerite from Olympic Dam [149]. Lower Pb concentrations relative to contained U suggest these structures accommodate daughter RN less well than uraninite.

The presence of radiogenic lead is also well known in minerals such as monazite and zircon where it directly substitutes into the crystal structure (e.g., [150,151]). The ratios between parent uranium, thorium and radiogenic lead underpin U–Pb geochronology. In the Olympic Dam deposit, both U and Pb (^{206}Pb) are also noted in a characteristic oscillatory-zoned textural type of hematite [152,153]. Hematite is the most abundant gangue mineral in the deposit. Within this hematite, uranium and lead isotopes, both in solid solution and as nanoparticle inclusions [154] are in apparent secular equilibrium, indicating a closed system and providing a basis for U–Pb geochronology using hematite [152,155,156].

4.2. Migration and Precipitation as New Minerals

During radioactive decay of U-bearing minerals, metamictisation will take place. This is a natural process occurring over geological time (millions to billions of years) in which the crystal structure of the parent mineral is gradually, and ultimately completely, destroyed, rendering that mineral amorphous [157]. During that process, any impurities may be expelled from the metamict phase. Even if a portion of the ^{210}Pb and ^{210}Po is retained within the U-bearing parent mineral, migration of daughter isotopes and other trace elements initially incorporated within the parent mineral (Th, REE, Nb, etc.) is widely observed to take place following metamictisation, alteration and recrystallization. The radionuclides are either precipitated as new minerals, or alternatively, are incorporated into other existing minerals at distances ranging from microns to metres from the parent phase. Such phenomena are particularly common in hydrothermal ores, in which transport is assisted by permeability and the presence of fluids. There thus exist several potential mineral hosts for daughter RN. Obvious products resulting from ^{210}Pb and ^{210}Po migration include the common lead mineral, galena, which is often observed within, or immediately adjacent to parent U-minerals ([158,159], and many others). For example, nanometre-scale galena is documented within uraninite in parts of grains in which Cu-sulphides and fluorite fill sub-micron-scale fractures [145]. Finch and Murakami [160] have outlined how galena will form in close association with uraninite if the sulphur activity is high enough. Direct evidence for the presence of ^{210}Pb within galena is limited but has been shown within recently formed galena from burning heaps associated with coal mining in the Lower Silesian basin, Czech Republic, [161]. Migrating radiogenic lead may also combine with Se or Te, either within existing minerals or from fluid, to form clausthalite (PbSe) or altaite (PbTe). Owen et al. [162] have recently documented the formation of ^{206}Pb -enriched nanoscale inclusions of clausthalite in Cu-(Fe)-sulphides, which formed via interaction between migrating Pb in fluids with Se initially hosted in solid solution within the sulphides. These may be as small as 1–2 nm in size but display coarsening.

Rollog et al. [163] have used nanoSIMS mapping to directly observe the sub-micron-scale distributions of ^{210}RN in copper ores and flotation concentrates from Olympic Dam; measurements are the sum of ^{210}Po + ^{210}Bi + ^{210}Pb but are overwhelmingly dominated by ^{210}Pb . Although concentrated within U-bearing minerals, migration of ^{210}RN away from the parent is observed on the scale of microns, with formation of nanoinclusions of “new” phases at sulphide grain boundaries, within microfractures, and within micropores in a range of host minerals. This phenomenon leads to daughter ^{210}RN becoming readily trapped within their host phases and accompanying those hosts through processing. Figure 3 shows an example of this innovative method to visualise RN distributions within individual mineral grains.

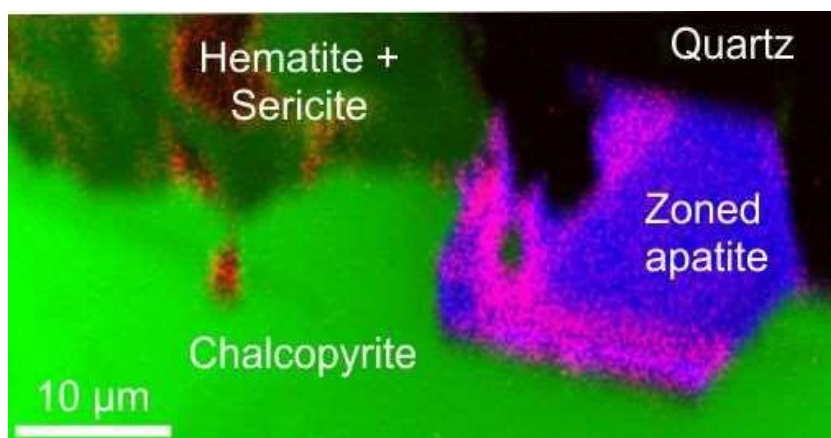


Figure 3. nanoSIMS map, modified from Rollog et al. [163] confirming the presence of ^{210}RN in apatite that is compositionally-zoned with respect to REE. Green = Fe, blue = Ca, pink = ^{210}RN .

4.3. Sulphates, Carbonates, and Other Potential Hosts

Sulphates, notably barite (BaSO_4), celestine (SrSO_4), anglesite (PbSO_4) and gypsum are commonly considered as hosts for radium and subsequent daughter radionuclides including ^{210}Pb and ^{210}Po . Prieto et al. [164] provide compelling experimental evidence for $(\text{Ba,Pb})\text{SO}_4$ solid solution. We are nevertheless unaware of empirical proof for the presence of ^{210}Pb and ^{210}Po in these sulphates.

The similarity in chemical behaviour between Ra and Ba, and to some extent also Pb, makes sulphates a good host for ^{210}Pb and, potentially, for ^{210}Po . For example, Al Attar et al. [114] report barite-strontianite solid solution and *hokutolite* [$(\text{Ba,Pb})\text{SO}_4$] as the main mineral components of radionuclide-containing scales associated with oil production. Extensive solid solution between isostructural Ba- and Ra-sulphates (so called *radiobarite*, $(\text{Ba,Ra})\text{SO}_4$ [165–174] has been modelled, and a number of natural occurrences have been documented e.g., [175,176]. In a detailed mineralogical insight into radionuclide host phases, Landa and Bush [79] document intense alpha particle activity associated with the presence of ^{210}Pb within micron-scale inclusions of anglesite within laths of gypsum.

Other possible candidates as hosts for ^{210}Pb and ^{210}Po in natural samples include common carbonates, notably the Pb-carbonate cerussite (PbCO_3). Reactions of dissolved Ra and Ba onto the surfaces of different carbonate minerals were examined by Jones et al. [177]. Calcite, dolomite, strontianite, rhodochrosite, ankerite and witherite all showed evidence of a co-precipitation reaction (increased uptake with increasing Ra concentration), siderite, magnesite and ankerite demonstrated a behaviour suggesting simple sorption. Magnesite showed a particularly high sorption capacity. An extensive treatment of the principles and mechanisms of co-precipitation with application to radionuclide incorporation within, and onto carbonate substrates, is given by Curti [178].

The role played by tellurium-bearing minerals, notably altaite (PbTe) and bismuth tellurides, as hosts for ^{210}Pb and/or ^{210}Po is unknown at the present time. These phases, as well as the selenide analogue of galena, clausthalite (PbSe) are minor yet persistent components of many hydrothermal ores, could potentially be important carriers of either radionuclide, especially given the similar chemistry of Po and Te. The environmental geochemistry of tellurium itself is only recently beginning to become better understood [179]. There may be a number of less obvious candidate hosts for ^{210}Pb and ^{210}Po . We can reasonably speculate that these will include those minerals capable of trapping gaseous radon within pore spaces during, or subsequent to growth.

4.4. Clay Minerals, Iron-Manganese-Oxides and Organics

Clay minerals, Fe–Mn oxy-hydroxides, and organic matter are well known sorbants for dissolved uranium and radium. ^{210}Pb and ^{210}Po sorption may not be primary and abundances may relate to

in-situ decay of the sorbed U and Ra. As an alternative, sorption of ^{222}Rn daughter isotopes, including ^{210}Po and ^{210}Pb may follow their generation via decay of dissolved ^{222}Rn .

In a study of a range of sites on the River Danube, preferential accumulation of ^{210}Po in sediments that are rich in clay minerals has been shown [180]. These authors invoked the ion exchange and adsorption characteristics of different types of clay minerals, suggesting that they may represent both a sink or a source for ^{210}Pb and ^{210}Po and other contaminants, as element mobilities are influenced by evolving physical, chemical and biological conditions.

A strong association between ^{210}Po and ^{210}Pb and iron oxide minerals is demonstrated in beach sands [181], even if other, far more voluminous hosts contained the majority of these and other radionuclides. Yang et al. [182] report on the adsorption properties of ^{210}Po and ^{210}Pb onto micro-particles and reported that Fe- and Mn-oxides were stronger sorbents of ^{210}Po and ^{210}Pb than SiO_2 and CaCO_3 . They did, however, note preferential adsorption of ^{210}Po over ^{210}Pb onto both SiO_2 and CaCO_3 . In the presence of the protein BSA; acid polysaccharides appeared to produce the opposite effect, enhancing ^{210}Pb adsorption.

Interaction, by both adsorption and incorporation, between Pb and Fe(III) (oxyhydr) oxide minerals, has been demonstrated by Yang et al. [183], who considered that the presence or absence of these minerals plays a major influence on the partitioning and transport of lead. They have shown how Pb is both surface-adsorbed and incorporated within ferrihydrite during crystallisation to hematite and goethite, depending on pH conditions.

Further evidence for the importance of both organic compounds and nanoparticles is given by Yang et al. [184], who have documented adsorption and fractionation of ^{210}Po and ^{210}Pb onto chemically simple oxide and carbonate nanoparticles in the presence or absence of various macromolecular organic compounds (MOCs) in natural seawater. MOCs were found to enhance sorption of selected nuclides on most nanoparticles (partition coefficients for ^{210}Po and ^{210}Pb increasing 2.9- and 5-fold, respectively), even if adsorption was largely dependent on particle composition.

In soils, ^{210}Po is adsorbed onto clay particles and organic material [9,185]. Sequential leaching techniques enable insights into the speciation of ^{210}Pb and ^{210}Po in soils to be gained [46]. Of the five fractions into which ^{210}Pb and ^{210}Po were fractionated, they found the majority of both ^{210}Pb (67.2%) and ^{210}Po (77.4%) bound to the insoluble residue. Small, but still significant fractions of the total ^{210}Pb (14.3%) and ^{210}Po (21.0%) were extracted with $\text{NH}_2\text{OH HCl}$ in 25% *v/v* acetic acid, which may indicate partial association of the radionuclides with Fe-Mn-oxides [186]. The bio-reactivity of ^{210}Pb and ^{210}Po was demonstrated by Kim and Kim [187], who asserted that colloids play a major role in their cycling within oceans.

Further supporting evidence for the affinity of ^{210}Pb and ^{210}Po for Fe-oxides comes from the Talvivaara mine, Eastern Finland, where microbe-induced heap leaching is used to recover Ni and by-product Zn, Cu, Co from a black schist [188,189]. Non-target metals in the deposit include uranium (as uraninite) and its daughter isotopes. The behaviour of ^{226}Ra , ^{210}Pb and ^{210}Po were studied in the mining process. It was found that they mostly remain in the heaps during leaching, where they are associated with jarosite, goethite and gypsum.

5. Discussion

5.1. Geochemical Behaviour of Daughter Radionuclides

Considerations of the likely mineral hosts for ^{210}Pb and ^{210}Po needs to include not only the geochemistry of each specific radionuclide, but the geochemical behaviour of the entire ^{238}U decay chain in the context of half-lives that range from fractions of a seconds (^{214}Po) to billions of years (^{238}U 4.5×10^9 years). The geochemical behaviours of each daughter radionuclide differ fundamentally from those of parent uranium, and thus, if released from the parent mineral and able to migrate, even if only at the sub-micron-scale, they will be readily incorporated, by virtue of ionic size and/or charge, into quite different minerals. They may potentially even undergo several “metamorphoses” before

accumulation of stable radiogenic lead within minerals such as galena or clausthalite that which do not necessarily coexist with the parent phases. Geochemical differences are particularly pronounced between U and Th, between Th and Ra, between Ra and Rn, and between Rn and Pb [2]. Figure 4 is a schematic diagram that attempts to illustrate how RN behaviour in different minerals may be viewed, also indicating how decoupling of RN within the decay chain might be achieved.

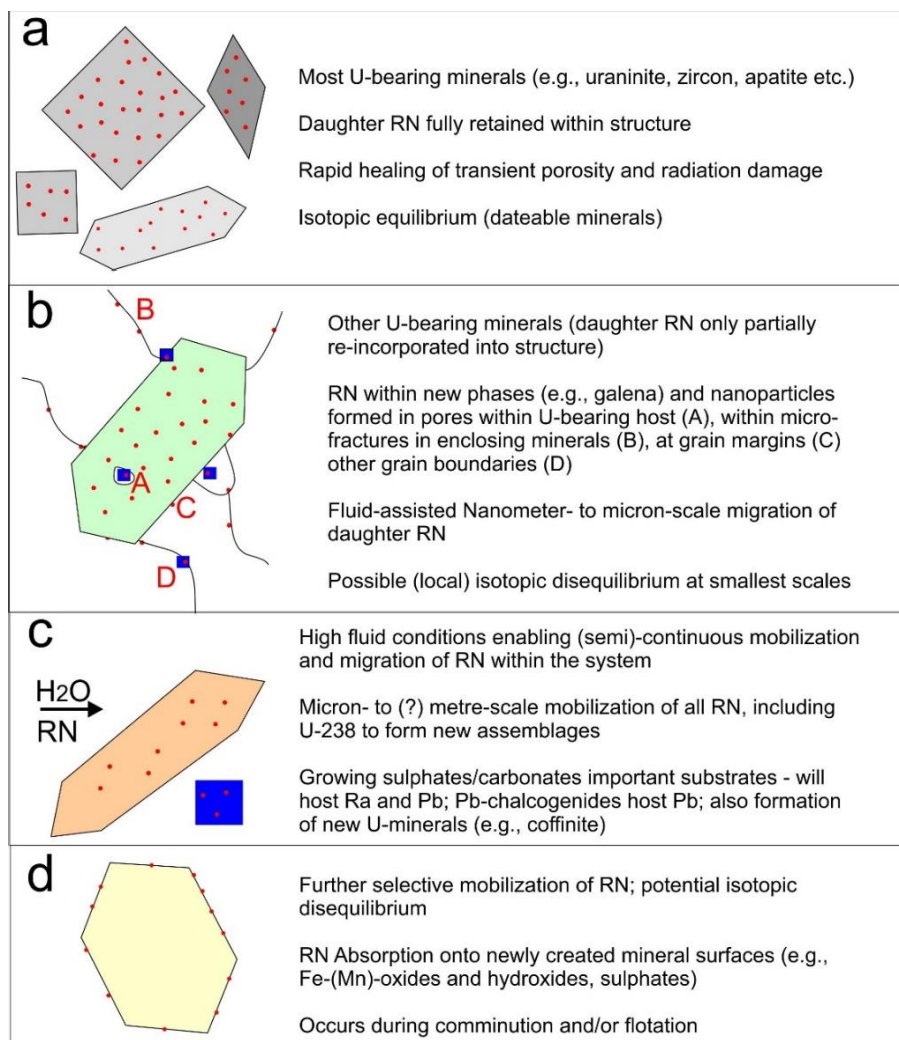


Figure 4. Schematic illustration of RN (red dots) behaviour in selected minerals within a mineralized rock, including reincorporation into parent mineral (a); grain-scale migration of daughter RN (b); fluid-assisted migration to be incorporated into new minerals (c) and potential adsorption of decoupled species (d).

Uranium can form a great variety of stable phases with different ligands. No less than 262 different uranium minerals are currently recognised, one of the largest numbers for any element in the periodic table [190]. Uranium thus belongs among a small group of elements whose mineralogical diversity is anomalous compared to its low crustal abundance. The unusual mineralogical behaviour of uranium is attributable to the unique combination of relatively large-size, high-valence and unusual coordination geometry displayed by the U^{6+} ion [191]. The hexavalent oxidation state is dominant in most U-minerals although U occurs in the tetravalent state in the most common minerals, including uraninite. Uranium mineral diversity has been amplified by Earth evolution over time with respect to oxidation state [192]. Although U^{4+} is not especially mobile, U^{6+} is highly mobile under oxidising conditions when it will readily dissolve, re-precipitating upon contact with reductants such as

sulphides or graphite. Certain minerals containing uranium undergo a process of structural breakdown (metamictisation), during which daughter radionuclides are not normally captured within the host lattice but rather migrate within or outside the mineral (e.g., [157]). In the case of uraninite, rapid annealing kinetics (e.g., [145,193]), do, however, allow for repair of radiation damage, allowing for sustained inclusion of decay product radionuclides in the mineral.

A good example of how daughter products differ geochemically from their parents is the ability for radium (^{226}Ra), unlike U or Th, to be readily enriched in the common Ba-sulphate mineral, barite. This, as examined above, takes place via direct ionic substitution (Ra^{2+} for Ba^{2+}) due to its comparable geochemical behaviour to barium with respect to charge, electronegativity and ionic size (0.143 and 0.134 nm for Ra and Ba, respectively). Although less well constrained, the potential incorporation of ^{210}Pb into galena and other Pb-bearing minerals, and of ^{210}Bi and ^{210}Po into bismuth minerals (including tellurides and other chalcogenides) may be viewed in the same way.

Decay of ^{226}Ra involves production of ^{222}Rn , a gas, which will seek to escape from the host mineral. Malczewski and Malczewski [194] have provided empirical data on ^{222}Rn and ^{220}Rn emanations from a range of metamict oxides, phosphates and silicates. These data demonstrate exponential differences in emanation rates among common minerals. Moreover, these rates vary as a function of many factors [195] closely linked to crystal structure and placing important controls on the decoupling of post- ^{222}Rn decay products from parent ^{238}U . Significantly, minerals with the highest ^{238}U concentrations, notably uraninite and brannerite, showed some of the lowest ^{222}Rn and ^{220}Rn emanation coefficients. We believe that these rates—which are closely linked to crystal structure—place important controls on the decoupling of post- ^{222}Rn daughter isotopes, including ^{210}Po and ^{210}Pb , from parent ^{238}U . This decoupling is expressed as secular disequilibrium on the small scale yet may not be noticed in bulk samples, or on the scale of a mineral deposit. The importance of the “radon stage” is illustrated in detailed mineralogical-isotopic study on a weathered aplite dyke [196], which showed significant (>40%) release of radon, leading to significant differences in the absolute concentrations of distributions of pre-Ra and post-Ra radionuclides.

Several studies cited in this review have given compelling evidence that particles of, or containing, ^{210}Pb and ^{210}Po are readily adsorbed onto the surfaces of clay minerals, Fe-oxides, and potentially also other minerals that can readily adsorb heavy atoms. This raises the possibility that the two radionuclides may not necessarily occur within the crystal structures of mineral phases. Evidence from disparate sources suggests that any study addressing the mineralogical department of ^{210}Po and ^{210}Pb must also consider that these radionuclides, or at least a significant part thereof, may not be hosted within minerals at all, but largely as nanoparticles of unknown speciation, which are adsorbed onto the surface of other minerals, such as clays, and probably, Fe-(hydr)oxides. In solid rocks, such nanoparticles may be present within micro-fractures in minerals and/or at the interfaces of mineral grains. We also believe that the affinity of ^{210}Po and ^{210}Pb for organic matter, and the potential role of organic complexes in the transport and sequestration of ^{210}Pb and ^{210}Po (e.g., biopolymers [197]), should also be taken into consideration in any effort to derive a quantitative mineralogical balance for ^{210}Pb and ^{210}Po .

The physical process involved in radionuclide decay has profound consequences for understanding the mineralogical location of each daughter radionuclide. An alpha particle comprises two protons and two neutrons, the nucleus of a helium atom. When alpha decay takes place, the energy of the nucleus recoiling from alpha decay is sufficient to break chemical bonds [198], and the newly-formed nucleus (with new geochemical behaviour) will be deposited at a different site in the damaged crystal. This new position and matrix damage may make the nucleus more vulnerable to mobilisation or leaching [2]. A newly-formed radionuclide may thus migrate and be incorporated into another mineral, although this may be limited if the half-life is short, e.g., for ^{222}Rn (3.83 days) or ^{210}Bi (5 days). Cowart and Burnett [2], citing Reference [199], also make the valuable point that, if sited close to a grain boundary, the resulting nucleus may be recoiled across the grain boundary and end up in an entirely different matrix.

Roudil et al. [200] explored the creation of “bubbles” in uranium minerals from production of radiogenic helium as a product of alpha decay. This He may be concentrated in the mineral grains, or trapped at grain boundaries, also generating matrix damage. Their measurements of He outgassing from a uranium ore showed that less than 5% of the He produced was conserved, and that one-third of the residual He is occluded in the matrix and vacancy defects, and two-thirds occurred as bubbles observable by high-resolution transmission electron microscopy.

5.2. Research Trends and Future Directions

A large part of the existing literature on ^{210}Pb and ^{210}Po and their distributions in rocks and minerals concerns radioactive contamination resulting from nuclear weapons testing, uranium mining, energy generation and industrial production of fertilisers and other products from materials containing RN. These issues remain serious but have attracted markedly less research attention in the 21st century literature as industrial practices have improved. This has been compounded no doubt by the relatively short half-lives of ^{210}Pb and ^{210}Po such that their concentrations, in at least some materials produced by human activity in the past, have declined to safer levels. The contemporary literature also reflects the many ways in which radioactive waste can be efficiently treated and immobilised ([201] and references therein). Indeed, the “benefits” of man-made contamination have been highlighted in the more recent literature, notably the potential of short-lived anthropogenic radionuclides, including ^{210}Pb and ^{210}Po , as geochemical tracers for understanding processes and rates of sedimentation (e.g., [67]).

The toxicological risks from exposure to ^{210}Pb and ^{210}Po in materials from a wide range of terrestrial and marine environments are likely to remain a research focus. As older anthropogenic sources of air- and water-borne radionuclides (e.g., nuclear testing, energy generation) begin to diminish in significance, others emerge, e.g., ^{210}Po release from large-scale burning of forest biomass (e.g., [202]), or even ingestion of ^{210}Pb from calcium dietary supplements [203]. It should, however, be borne in mind that natural sources of ^{210}Pb and ^{210}Po are more significant in scale than man-made sources, e.g., from volcanic eruption. Indeed, a study of radionuclide hazards in seafood from the NW Pacific fishing area contaminated following the 2011 Fukushima nuclear accident [204] showed that despite elevated Fukushima-derived ^{90}Sr , ^{134}Cs and ^{137}Cs , these were exponentially subordinate in dose terms to natural ^{210}Pb and ^{210}Po in the same ocean area.

Despite the relative slowdown in the construction of nuclear power stations in the aftermath of the Fukushima nuclear accident, production of uranium for power generation continues to increase. Nuclear power is currently advanced as a possible low-carbon emission “green” energy alternative among the conservationist movement (e.g., [205]). In the absence of available technology to process thorium (a potential alternative fuel; [206]), increased demand necessitates a continued supply of uranium, and inevitably, as for other commodities, a need to exploit lower-grade resources, and to optimise extraction from deposits in which uranium occurs alongside other metals, notably copper, as in giant iron-oxide copper gold deposits such as Olympic Dam, South Australia.

6. Conclusions

This review has highlighted some of the many advances made in understanding the distribution of radionuclides in the environment during the past three decades. It also highlights that although the deportment and behaviour of ^{210}Pb and ^{210}Po at the scale of individual minerals is reasonably well understood, or at least predictable to some degree, there remains a paucity of direct observational data at the nano- to micron-scales to support these models. This is particularly true for metal ores and the products of their processing, for which there is an outstanding gap in knowledge. Bridging this gap is essential for generation of clean concentrates from a range of uranium-bearing ores.

Characterisation of short half-life radionuclides down to the atomic scale is now possible via use of a combination of nanoscale techniques: nanoSIMS isotope mapping [163]; scanning transmission electron microscopy with electron energy-loss spectroscopy (e.g., [207]); and high angle annular dark-field scanning transmission electron microscopy on foils prepared in-situ using focused ion

beam methods (e.g., [162,208,209]). Valuable additional constraints on RN department may also come from the application of nanoscale analysis techniques to radioisotope dating of minerals within hydrothermal mineral deposits forming on the present-day seafloor [210,211]. Despite these crucial advances, a fully quantitative understanding of the physical form of ^{210}Pb and ^{210}Po , and the quantitative mineral department of these RN in solid media, remains elusive. Researchers can, however, expect to respond to these outstanding challenges by capitalising on micro-/nanoanalytical technology, which is rapidly advancing in terms of both spatial resolution and analytical sensitivity. This will enable reliable, predictive information on the physical state of ^{210}Pb , ^{210}Po and other RN to be communicated to stakeholders, including mining companies and environmental authorities.

Author Contributions: N.J.C. conceived and coordinated this contribution. He wrote the paper in collaboration with K.J.E. and C.L.C. All other authors (M.R., D.J.L., D.S.S., N.D.O., T.H and S.R.G.) contributed otherwise unpublished data, literature and valuable discussion.

Acknowledgments: This research is a contribution to the ARC Research Hub on Australian Copper-Uranium (project number: IH130200033), funded by the Australian Research Council, BHP Olympic Dam, OZ Minerals and the South Australian Department of State Development. The authors appreciate valuable comments from three *Minerals* reviewers as well as two anonymous reviewers of a previous incarnation of this text. These have helped us improve the clarity of this manuscript.

Conflicts of Interest: The authors declare no conflict of interest. The project sponsors approve publication of the manuscript.

References

1. Lehto, J.; Hou, X. *Chemistry and Analysis of Radionuclides—Laboratory Techniques and Methodology*; Wiley-VCH: Weinheim, Germany, 2011.
2. Cowart, J.B.; Burnett, W.C. The distribution of uranium and thorium decay-series radionuclides in the environment—A review. *J. Environ. Q.* **1994**, *23*, 651–662. [CrossRef]
3. Strominger, D.; Hollander, J.M.; Seaborg, G.T. Table of isotopes. *Rev. Mod. Phys.* **1958**, *30*, 585. [CrossRef]
4. Fry, C.; Thoennessen, M. Discovery of the thallium, lead, bismuth, and polonium isotopes. *At. Data Nucl. Data Tables* **2013**, *99*, 365–389. [CrossRef]
5. Harrison, J.; Leggett, R.; Lloyd, D.; Phipps, A.; Scott, B. Polonium-210 as a poison. *J. Radiol. Prot.* **2007**, *27*, 17–40. [CrossRef] [PubMed]
6. Figgins, P.E. *The Radiochemistry of Polonium. National Academy of Sciences Nuclear Science Series*; U.S. Atomic Energy Commission: Washington, DC, USA, 1961.
7. Lane, D.J.; Cook, N.J.; Grano, S.R.; Ehrig, K. Selective leaching of penalty elements from copper concentrates: A review. *Miner. Eng.* **2016**, *98*, 110–121. [CrossRef]
8. International Atomic Energy Agency (IAEA). *Regulations for the Safe Transport of Radioactive Material*; IAEA: Vienna, Austria, 2012.
9. Parfenov, Y.D. Polonium 210 in the environment and in the human organism. *At. Energy Rev.* **1974**, *12*, 75–143. [PubMed]
10. Coppin, F.; Roussel-Debet, S. Comportement du ^{210}Po en milieu terrestre: Revue bibliographique. *Radioprotection* **2004**, *39*, 39–58. [CrossRef]
11. Landa, E.R. Naturally occurring radionuclides from industrial sources: Characteristics and fate in the environment. *Radioact. Environ.* **2007**, *10*, 211–237.
12. Persson, B.R.R.; Holm, E. Polonium-210 and lead-210 in the terrestrial environment: A historical review. *J. Environ. Radioact.* **2011**, *102*, 420–429. [CrossRef] [PubMed]
13. Baskaran, M. Po-210 and Pb-210 as atmospheric tracers and global atmospheric Pb-210 fallout: A Review. *J. Environ. Radioact.* **2011**, *102*, 500–513. [CrossRef] [PubMed]
14. Shannon, L.V.; Cherry, R.D.; Orren, M.J. Polonium-210 and lead-210 in the marine environment. *Geochim. Cosmochim. Acta* **1970**, *34*, 701–711. [CrossRef]
15. Nozaki, Y.; Thomson, J.; Turekian, K.K. The distribution of ^{210}Pb and ^{210}Po in the surface waters of the Pacific Ocean. *Earth Plan. Sci. Lett.* **1976**, *32*, 304–312. [CrossRef]
16. Bacon, M.P.; Brewer, P.G.; Spencer, D.W.; Murray, J.W.; Goddard, J. Lead-210, polonium-210, manganese and iron in the Cariaco Trench. *Deep Sea Res. Part A Oceanogr. Res. Pap.* **1980**, *27*, 119–135. [CrossRef]

17. Bacon, M.P.; Huh, C.-A.; Fler, A.P.; Deuser, W.G. Seasonality in the flux of natural radionuclides and plutonium in the deep Sargasso Sea. *Deep Sea Res. Part A Oceanogr. Res. Pap.* **1985**, *32*, 273–286. [[CrossRef](#)]
18. González-Labajo, J.; Bolívar, J.P.; García-Tenorio, R. Natural radioactivity in waters and sediments from a Spanish mining river. *Radiat. Phys. Chem.* **2001**, *61*, 643–644. [[CrossRef](#)]
19. Balistrieri, L.S.; Murray, J.W.; Paul, B. The geochemical cycling of stable Pb, ^{210}Pb , and ^{210}Po in seasonally anoxic Lake Sammamish, Washington, USA. *Geochim. Cosmochim. Acta* **1995**, *59*, 4845–4861. [[CrossRef](#)]
20. Andrews, J.N.; Ford, D.J.; Hussain, N.; Trivedi, D.; Youngman, M.J. Natural radioelement solution by circulating groundwaters in the Stripa granite. *Geochim. Cosmochim. Acta* **1989**, *53*, 1791–1802. [[CrossRef](#)]
21. Harada, K.; Burnett, W.C.; LaRock, P.A.; Cowart, J.B. Polonium in Florida groundwater and its possible relationship to the sulfur cycle and bacteria. *Geochim. Cosmochim. Acta* **1989**, *53*, 143–150. [[CrossRef](#)]
22. Lehto, J.; Kelokaski, P.; Vaaramaa, K.; Jaakkola, T. Soluble and particle-bound ^{210}Po and ^{210}Pb in groundwaters. *Radiochim. Acta* **1999**, *85*, 149–155. [[CrossRef](#)]
23. Seiler, R.L.; Stillings, L.L.; Cutler, N.; Salonen, L.; Outola, I. Biogeochemical factors affecting the presence of ^{210}Po in groundwater. *Appl. Geochem.* **2011**, *26*, 526–539. [[CrossRef](#)]
24. Ortega, X.; Vallés, I.; Serrano, I. Natural radioactivity in drinking water in Catalonia (Spain). *Environ. Int.* **1997**, *22* (Suppl. 1), S347–S354. [[CrossRef](#)]
25. Katzlberger, C.; Wallner, G.; Irlweck, K. Determination of ^{210}Pb , ^{210}Bi and ^{210}Po in natural drinking water. *J. Radioanal. Nucl. Chem.* **2001**, *249*, 191–196.
26. Skwarzec, B.; Strumińska, D.I.; Boryło, A. Radionuclides of ^{210}Po , ^{234}U and ^{238}U in drinking bottled mineral water in Poland. *J. Radioanal. Nucl. Chem.* **2003**, *256*, 361–364. [[CrossRef](#)]
27. Simon, S.L.; Ibrahim, S.A. The plant/soil concentration ratio for calcium, radium, lead, and polonium: Evidence for non-linearity with reference to substrate concentration. *J. Environ. Radioact.* **1987**, *5*, 123–142. [[CrossRef](#)]
28. Martínez-Aguirre, A.; García-Orellana, I.; García-León, M. Transfer of natural radionuclides from soils to plants in a marsh enhanced by the operation of non-nuclear industries. *J. Environ. Radioact.* **1997**, *35*, 149–171. [[CrossRef](#)]
29. Malczewski, D.; Żaba, J. ^{222}Rn and ^{220}Rn concentrations in soil gas of Karkonosze-Izera Block (Sudetes, Poland). *J. Environ. Radioact.* **2007**, *92*, 144–164. [[CrossRef](#)] [[PubMed](#)]
30. Heyraud, M.; Cherry, R.D.; Oschadleus, H.-D.; Augustyn, C.J.; Cherry, M.I.; Sealy, J.C. Polonium-210 and Lead-210 in edible molluscs from near the Cape of Good Hope: Sources of variability in polonium-210 concentrations. *J. Environ. Radioact.* **1994**, *24*, 253–272. [[CrossRef](#)]
31. Thomas, P.A.; Gates, T.E. Radionuclides in the lichen-caribou-human food chain near uranium mining operations in northern Saskatchewan, Canada. *Environ. Health Perspect.* **1999**, *107*, 527–537. [[CrossRef](#)] [[PubMed](#)]
32. Carvalho, F.P. Polonium (^{210}Po) and lead (^{210}Pb) in marine organisms and their transfer in marine food chains. *J. Environ. Radioact.* **2011**, *102*, 462–472. [[CrossRef](#)] [[PubMed](#)]
33. Rosner, G.; Bunzl, K.; Hötzel, H.; Winkler, R. Low level measurements of natural radionuclides in soil samples around a coal-fired power plant. *Nucl. Instrum. Meth. Phys. Res.* **1984**, *223*, 585–589. [[CrossRef](#)]
34. Sahu, S.K.; Tiwari, M.; Bhangare, R.C.; Pandit, G.G. Enrichment and particle size dependence of polonium and other naturally occurring radionuclides in coal ash. *J. Environ. Radioact.* **2014**, *138*, 421–426. [[CrossRef](#)] [[PubMed](#)]
35. Schmidt, A.P. Lead precipitates from natural gas production installations. *J. Geochem. Explor.* **1998**, *62*, 193–200. [[CrossRef](#)]
36. Schmidt, A.P.; Hartog, F.A.; Van Os, B.J.H.; Schuiling, R.D. Production of ^{210}Pb from a Slochteren sandstone gas reservoir. *Appl. Geochem.* **2000**, *15*, 1317–1329. [[CrossRef](#)]
37. Al Attar, L.; Doubal, W.; Al Abdullah, J.; Khalily, H.; Abdul Ghani, B.; Safia, B. Characterization of NORM solid waste produced from the petroleum industry. *Environ. Tech.* **2015**, *36*, 1104–1113. [[CrossRef](#)] [[PubMed](#)]
38. Seen, A.; Townsend, A.; Atkinson, B.; Ellison, J.; Harrison, J.; Heijnen, H. Determining the history and sources of contaminants in sediments in the Tamar Estuary, Tasmania, using ^{210}Pb dating and stable Pb isotope analyses. *Environ. Chem.* **2004**, *1*, 49–54. [[CrossRef](#)]
39. Schindler, M.; Kamber, B.S. High-resolution lake sediment reconstruction of industrial impact in a world-class mining and smelting center, Sudbury, Ontario, Canada. *Appl. Geochem.* **2013**, *37*, 102–116. [[CrossRef](#)]

40. Matthews, K.M.; Kim, C.-K.; Martin, P. Determination of ^{210}Po in environmental materials: A review of analytical methodology. *Appl. Radiat. Isot.* **2007**, *65*, 267–279. [[CrossRef](#)] [[PubMed](#)]
41. Henricsson, F.; Ranebo, Y.; Holm, E.; Roos, P. Aspects on the analysis of ^{210}Po . *J. Environ. Radioact.* **2011**, *102*, 415–419. [[CrossRef](#)] [[PubMed](#)]
42. Flynn, W.W. The determination of low levels of polonium-210 in environmental materials. *Anal. Chim. Acta* **1968**, *43*, 221–227. [[CrossRef](#)]
43. Clayton, R.F.; Bradley, E.J. A cost effective method for the determination of ^{210}Po and ^{210}Pb in environmental materials. *Sci. Total Environ.* **1995**, *173–174*, 23–28. [[CrossRef](#)]
44. Jia, G.G.; Torri, G. Determination of ^{210}Pb and ^{210}Po in soil or rock samples containing refractory matrices. *Appl. Radiat. Isot.* **2007**, *65*, 1–8. [[CrossRef](#)] [[PubMed](#)]
45. Jia, G.G.; Belli, M.; Blasi, M.; Marchetti, A.; Rosamilia, S.; Sansone, U. Determination of ^{210}Pb and ^{210}Po in mineral and biological environmental samples. *J. Radioanal. Nucl. Chem.* **2001**, *247*, 491–499. [[CrossRef](#)]
46. Jia, G.G.; Belli, M.; Liu, S.; Sansone, U.; Xu, C.H.; Rosamilia, S.; Xiao, X.; Gaudino, S.; Chen, L.; Yang, H. The fractionation and determination procedures for the speciation of ^{210}Pb and ^{210}Po in soil samples. *Anal. Chim. Acta* **2006**, *562*, 51–58. [[CrossRef](#)]
47. Pud'homme, F.; Morency, M.; Freyer, K.; Weiss, H.; Bourne, J.; Daus, B.; Fontaine, D.; Mattusch, J.; Mineau, R.; Préda, M.; et al. Surfactant separation as a technique for physical and chemical characterization of ore processing residues. *Sci. Total Environ.* **1999**, *243/244*, 9–20.
48. Allard, P.; Aiuppa, A.; Bani, P.; Métrich, N.; Bertagnini, A.; Gauthier, P.-J.; Shinohara, H.; Sawyer, G.; Parello, F.; Bagnato, E.; et al. Prodigious emission rates and magma degassing budget of major, trace and radioactive volatile species from Ambrym basaltic volcano, Vanuatu island Arc. *J. Volc. Geotherm. Res.* **2016**, *322*, 119–143. [[CrossRef](#)]
49. Lambert, G.; Le Cloarec, M.-F.; Ardouin, B.; Le Rouley, J.-C. Volcanic emission of radionuclides and magma dynamics. *Earth Plan. Sci. Lett.* **1985**, *76*, 185–192. [[CrossRef](#)]
50. Gauthier, P.-J.; Le Cloarec, M.-F.; Condomines, M. Degassing processes at Stromboli volcano inferred from short-lived disequilibria (^{210}Pb – ^{210}Bi – ^{210}Po) in volcanic gases. *J. Volc. Geotherm. Res.* **2000**, *102*, 1–19. [[CrossRef](#)]
51. Rubin, K.H.; Macdougall, J.D.; Perfit, M.R. ^{210}Po – ^{210}Pb dating of recent volcanic eruptions on the sea floor. *Nature* **1994**, *368*, 841–844. [[CrossRef](#)]
52. Le Cloarec, M.-F.; Gauthier, P.-J. Merapi Volcano, Central Java, Indonesia: A case study of radionuclide behavior in volcanic gases and its implications for magma dynamics at andesitic volcanoes. *J. Geophys. Res.* **2003**, *108*, 2243. [[CrossRef](#)]
53. Gill, J.B.; Williams, R.W. Th isotope and U-series studies of subduction-related volcanic rocks. *Geochim. Cosmochim. Acta* **1990**, *54*, 1427–1442. [[CrossRef](#)]
54. Berlo, K.; Turner, S. ^{210}Pb – ^{226}Ra disequilibria in volcanic rocks. *Earth Plan. Sci. Lett.* **2010**, *296*, 155–164. [[CrossRef](#)]
55. Turner, S.; Reagan, M.; Vigier, N.; Bourdon, B. Origins of ^{210}Pb – ^{226}Ra disequilibria in basalts: New insights from the 1978 Asal Rift eruption. *Geochem. Geophys. Geosyst.* **2012**, *13*, Q07002. [[CrossRef](#)]
56. Artemieva, I.M.; Thybo, H.; Jakobsen, K.; Sørensen, N.K.; Nielsen, L.S.K. Heat production in granitic rocks: Global analysis based on a new data compilation GRANITE2017. *Earth-Sci. Rev.* **2017**, *172*, 1–26. [[CrossRef](#)]
57. Le Cloarec, M.-F.; Pennisi, M.; Corazza, E.; Lambert, G. Origin of fumarolic fluids emitted from a nonerupting volcano: Radionuclide constraints at Vulcano (Aeolian Islands, Italy). *Geochim. Cosmochim. Acta* **1994**, *58*, 4401–4410. [[CrossRef](#)]
58. Voltaggio, M.; Tuccimei, P.; Branca, M.; Romoli, L. U-series disequilibrium radionuclides in sulphur incrustations from the fumarolic field of Vulcano Island. *Geochim. Cosmochim. Acta* **1998**, *62*, 2111–2127. [[CrossRef](#)]
59. Garavelli, A.; Laviano, R.; Vurro, F. Sublimate deposition from hydrothermal fluids at the Fossa crater (Vulcano, Italy). *Eur. J. Miner.* **1997**, *9*, 423–432. [[CrossRef](#)]
60. Vurro, F.; Garavelli, A.; Garbarino, C.; Moëlo, Y.; Borodaev, Y.S. Rare sulfosalts from Vulcano, Aeolian Islands, Italy. II. Mozgovaite, $\text{PbBi}_4(\text{S,Se})_7$, a new mineral species. *Can. Miner.* **1999**, *37*, 1499–1506.
61. Borodaev, Y.S.; Garavelli, A.; Garbarino, C.; Grillo, S.M.; Mozgova, N.N.; Organova, N.I.; Trubkin, N.V.; Vurro, F. Rare sulfosalts from Vulcano, Aeolian Islands, Italy. III. Wittite and cannizzarite. *Can. Miner.* **2000**, *38*, 23–34. [[CrossRef](#)]

62. Garavelli, A.; Mozgova, N.N.; Orlandi, P.; Bonaccorsi, E.; Pinto, D.; Moëlo, Y.; Borodaev, Y.S. Rare sulfosalts from vulcano, Aeolian Islands, Italy. VI. Vurroite, $Pb_{20}Sn_2(Bi,As)_{22}S_{54}Cl_6$, a new mineral species. *Can. Miner.* **2005**, *43*, 703–711. [[CrossRef](#)]
63. Boisson, F.; Miquel, J.-C.; Cotret, O.; Fowler, S.W. ^{210}Po and ^{210}Pb cycling in a hydrothermal vent zone in the coastal Aegean Sea. *Sci. Total Environ.* **2001**, *281*, 111–119. [[CrossRef](#)]
64. Charmasson, S.; Sarradin, P.-M.; Le Faouder, A.; Agarande, M.; Loyen, J.; Desbruyères, D. High levels of natural radioactivity in biota from deep-sea hydrothermal vents: A preliminary communication. *J. Environ. Radioact.* **2009**, *100*, 522–526. [[CrossRef](#)] [[PubMed](#)]
65. Begy, R.C.; Dumitru, O.A.; Simon, H.; Steopoaie, I. An improved procedure for the determination of ^{210}Po by alpha spectrometry in sediments samples from Danube Delta. *J. Radioanal. Nucl. Chem.* **2015**, *303*, 2553–2557. [[CrossRef](#)]
66. Farmer, J.G.; MacKenzie, A.B.; Graham, M.C.; Macgregor, K.; Kirika, A. Development of recent chronologies and evaluation of temporal variations in Pb fluxes and sources in lake sediment and peat cores in a remote, highly radiogenic environment, Cairngorm Mountains, Scottish Highlands. *Geochim. Cosmochim. Acta* **2015**, *156*, 25–49. [[CrossRef](#)]
67. Franklin, R.L.; Fávoro, D.I.T.; Damatto, S.R. Trace metal and rare earth elements in a sediment profile from the Rio Grande Reservoir, São Paulo, Brazil: Determination of anthropogenic contamination, dating, and sedimentation rates. *J. Radioanal. Nucl. Chem.* **2015**, *307*, 99–110. [[CrossRef](#)]
68. Jones, P.; Maiti, K.; McManus, J. Lead-210 and Polonium-210 disequilibria in the northern Gulf of Mexico hypoxic zone. *Mar. Chem.* **2015**, *169*, 1–15. [[CrossRef](#)]
69. Swarzenski, P.W. ^{210}Pb Dating. In *Encyclopedia of Scientific Dating Methods*; Rink, W.J., Thompson, J.W., Eds.; Springer: Berlin, Germany, 2015; pp. 626–631.
70. Dahlkamp, F.J. *Uranium Ore Deposits*; Springer: Berlin, Germany, 1993; 460p.
71. Martin, A.; Mead, S.; Wade, B.O. *Nuclear Science and Technology: Materials Containing Natural Radionuclides in Enhanced Concentrations*; Final report for European Commission Directorate-General, Environment, Nuclear Safety and Civil Protection; Alan Martin Associates: Penetanguishene, ON, Canada, 1997; 104p.
72. Cooper, J.R.; Randle, K.; Sokhi, R.S. *Radioactive Releases in the Environment: Impact and Assessment*; John Wiley and Sons: Hoboken, NJ, USA, 2003; 773p.
73. Cooper, M.B. *Naturally Occurring Radioactive Materials (NORM) in Australian Industries—Review of Current Inventories and Future Generation: A Report Prepared for the Radiation Health and Safety Advisory Council*; EnviroRad Services Pty. Ltd.: Beaumaris, Australia, 2005; 40p.
74. García-Tenorio, R. ^{210}Po and ^{210}Pb in NORM mineral processing industries. In Proceedings of the EU-NORM 1st International Symposium, Tallinn, Estonia, 5–8 June 2012; pp. 202–209.
75. Xhixha, G.; Bezzon, G.P.; Broggin, C.; Buso, G.P.; Cacioli, A.; Callegari, I.; De Bianchi, S.; Fiorentini, G.; Guastaldi, E.; Kaçeli Xhixha, M.; et al. The worldwide NORM production and a fully automated gamma-ray spectrometer for their characterization. *J. Radioanal. Nucl. Chem.* **2013**, *295*, 445–457. [[CrossRef](#)]
76. Fernandes, H.M.; Franklin, M.R.; Veiga, L.H.S.; Freitas, P.; Gomiero, L.A. Management of uranium mill tailing: Geochemical processes and radiological risk assessment. *J. Environ. Radioact.* **1996**, *30*, 69–95. [[CrossRef](#)]
77. Landa, E.R. Leaching of radionuclides from uranium ore and mill tailings. *Uranium* **1982**, *1*, 53–64.
78. Landa, E.R. Uranium mill tailings: Nuclear waste and natural laboratory for geochemical and radioecological investigations. *J. Environ. Radioact.* **2004**, *77*, 1–27. [[CrossRef](#)] [[PubMed](#)]
79. Landa, E.R.; Bush, C.A. Geochemical hosts of solubilized radionuclides in uranium mill tailings. *Hydrometallurgy* **1990**, *24*, 361–372. [[CrossRef](#)]
80. Shearer, S.D., Jr.; Lee, G.F. Leachability of radium-226 from uranium mill solids and river sediments. *Health Phys.* **1964**, *10*, 217–227. [[CrossRef](#)] [[PubMed](#)]
81. Seeley, F.G. Problems in the separation of radium from uranium mill tailings. *Hydrometallurgy* **1977**, *2*, 249–263. [[CrossRef](#)]
82. Somot, S.; Pagel, M.; Thiry, J. Speciation of radium in uranium mill tailings from Ecarpière (Vendée, France). *Comptes Rendues Acad. Sci.* **1997**, *325*, 111–118.
83. Landa, E.R.; Stieff, L.R.; Germani, M.S.; Tanner, A.B.; Evans, J.R. Intense alpha particle emitting crystallites in uranium mill wastes. *Nucl. Geophys.* **1994**, *8*, 443–454.

84. Morrison, S.J.; Cahn, L.S. Mineralogical residence of alpha-emitting contamination and implications for mobilization from uranium mill tailings. *J. Contam. Hydrol.* **1991**, *8*, 1–21. [[CrossRef](#)]
85. Campbell, K.M.; Gallegos, T.J.; Landa, E.R. Biogeochemical aspects of uranium mineralization, mining, milling, and remediation. *Appl. Geochem.* **2015**, *57*, 206–235. [[CrossRef](#)]
86. Lawrence, C.E. Measurement of ²²²Rn Exhalation Rates and ²¹⁰Pb Deposition Rates in a Tropical Environment. Unpublished Ph.D. Thesis, Queensland University of Technology, Brisbane City, Australia, 2006.
87. BHP Billiton Olympic Dam Expansion. Draft Environmental Impact Statement 2009. Appendix S. Uranium and Radiation. Available online: www.bhp.com (accessed on 10 April 2018).
88. Weiss, H.; Morency, M.; Freyer, K.; Bourne, J.; Fontaine, D.; Ghaleb, B.; Mineau, R.; Möder, M.; Morgenstern, P.; Popp, P.; et al. Physical and chemical characterization of a complexly contaminated scrubber dust—A by-product of copper smelting in Sachsen-Anhalt, Germany. *Sci. Total Environ.* **1997**, *203*, 65–78. [[CrossRef](#)]
89. Schreck, P. Flue dust from copper shale smelting in Central Germany: Environmental pollution and its prevention. In Proceedings of the International Mine Water Association Congress, Sevilla, Spain, 13–17 September 1999; pp. 163–167.
90. Freyer, K.; Morency, M.; Weiss, H.; Treutler, H.C.; Bourne, J. High-Alpha-Active Particles in Industrial and Mining Residues. In Proceedings of the 10th International Congress of the International Radiation Protection Association on Harmonization of Radiation, Human Life and the Ecosystem, Japan Health Physics Society, Tokyo, Japan, 14–19 May 2000.
91. Schubert, M.; Morgenstern, P.; Wennrich, R.; Freyer, K.; Paschke, A.; Weiss, H. The weathering behavior of complexly contaminated ore processing residues in the region of Mansfeld/Germany. *Mine Water Environ.* **2003**, *22*, 2–6. [[CrossRef](#)]
92. Schubert, M.; Osenbrück, K.; Knöller, K. Using stable and radioactive isotopes for the investigation of contaminant metal mobilization in a metal mining district. *Appl. Geochem.* **2008**, *23*, 2945–2954. [[CrossRef](#)]
93. Morency, M.; Weiss, H.; Freyer, K.; Bourne, J.; Fontaine, D.; Mineau, R.; Möder, M.; Morgenstern, P.; Popp, P.; Preda, M.; et al. Oxidation treatment of a sulphide-bearing scrubber dust from the Mansfeld Region, Germany: Organic and inorganic phase changes and multi-element partition coefficients between liquid and solid phases. *Sci. Total Environ.* **1998**, *223*, 87–97. [[CrossRef](#)]
94. Chau, N.D.; Jodłowski, P.; Kalia, S.J.; Olko, P.; Chruściel, E.; Maksymowicz, A.; Waligórski, M.; Bilski, P.; Budzanowski, M. Natural radiation and its hazard in copper ore mines in Poland. *Acta Geophys.* **2008**, *56*, 505–517. [[CrossRef](#)]
95. Hipkin, J.; Paynter, R.A. Radiation Exposures to the Workforce from Naturally Occurring Radioactivity in Industrial Processes. *Radiat. Prot. Dosim.* **1991**, *36*, 97–100. [[CrossRef](#)]
96. Harvey, M.P.; Hipkin, J.; Simmonds, J.R.; Mayall, A.; Cabianca, T.; Fayers, C.; Haslam, I. *Radiological Consequences of Waste Arising with Enhanced Natural Radioactivity Content from Special Metal and Ceramic Processes*; European Commission: Environment, Nuclear Safety and Civil Protection; European Commission: Brussels, Belgium, 1994.
97. Baxter, M.S.; MacKenzie, A.B.; East, B.W.; Scott, E.M. Natural decay series radionuclides in and around a large metal refinery. *J. Environ. Radioact.* **1996**, *32*, 115–133. [[CrossRef](#)]
98. Rutherford, P.M.; Dudas, M.J.; Samek, R.A. Environmental impacts of phosphogypsum: A review. *Sci. Total Environ.* **1994**, *149*, 1–38. [[CrossRef](#)]
99. Rutherford, P.M.; Dudas, M.J.; Arocena, J.M. Radium in phosphogypsum leachates. *J. Environ. Q.* **1995**, *24*, 307–314. [[CrossRef](#)]
100. Rutherford, P.M.; Dudas, M.J.; Arocena, J.M. Heterogeneous distribution of radionuclides, barium and strontium in phosphogypsum by-product. *Sci. Total Environ.* **1996**, *180*, 201–209. [[CrossRef](#)]
101. Poole, A.J.; Allington, D.J.; Baxter, A.J.; Young, A.K. The natural radioactivity of phosphate ore and associated waste products discharged into the eastern Irish Sea from a phosphoric acid production plant. *Sci. Total Environ.* **1995**, *173–174*, 137–149. [[CrossRef](#)]
102. Sam, A.K.; Holm, E. The natural radioactivity in phosphate deposits from Sudan. *Sci. Total Environ.* **1995**, *162*, 173–178. [[CrossRef](#)]
103. Burnett, W.C.; Schultz, M.H.; Hull, C.D. Radionuclide flow during the conversion of phosphogypsum to ammonium sulfate. *J. Environ. Radioact.* **1996**, *32*, 33–51. [[CrossRef](#)]

104. Hull, C.D.; Burnett, W.C. Radiochemistry of Florida phosphogypsum. *J. Environ. Radioact.* **1996**, *32*, 213–238. [[CrossRef](#)]
105. Travesí, A.; Gascó, C.; Pozuelo, M.; Palomares, J.; García, M.R.; Pérez del Villar, L. Distribution of natural radioactivity within an estuary affected by releases from the phosphate industry. *Stud. Environ. Sci.* **1997**, *68*, 267–279.
106. Mazzilli, B.; Palmiro, V.; Saueia, C.; Nisti, M.B. Radiochemical characterization of Brazilian phosphogypsum. *J. Environ. Radioact.* **2000**, *49*, 113–122. [[CrossRef](#)]
107. Silva, N.C.; Fernandes, E.A.N.; Ciprianai, M.; Taddei, M.H.T. The natural radioactivity of Brazilian phosphogypsum. *J. Radioanal. Nucl. Chem.* **2001**, *249*, 251–255.
108. Beddow, H.; Black, S.; Read, D. Naturally occurring radioactive material (NORM) from a former phosphoric acid processing plant. *J. Environ. Radioact.* **2006**, *86*, 289–312. [[CrossRef](#)] [[PubMed](#)]
109. Aoun, M.; El Samrani, A.G.; Lartiges, B.S.; Kazpard, V.; Saad, Z. Releases of phosphate fertilizer industry in the surrounding environment: Investigation on heavy metals and polonium-210 in soil. *J. Environ. Sci.* **2010**, *22*, 1387–1397. [[CrossRef](#)]
110. Hurst, F.J.; Arnold, W.D. A discussion of uranium control in phosphogypsum. *Hydrometallurgy* **1982**, *9*, 69–82. [[CrossRef](#)]
111. Pennders, R.M.J.; Köster, H.W.; Lembrechts, J.F. Characteristics of ^{210}Po and ^{210}Pb in effluents from phosphate-processing industries: A first orientation. *Radiat. Prot. Dosim.* **1992**, *45*, 737–740. [[CrossRef](#)]
112. International Atomic Energy Agency (IAEA). *The Extent of Environmental Contamination by Naturally Occurring Radioactive Material (NORM) and Technological Options for Mitigation*; IAEA Draft Technical Report; IAEA: Vienna, Austria, 2002.
113. Zielinski, R.A.; Budahn, J.R. Mode of occurrence and environmental mobility of oil-field radioactive material at US Geological Survey research site B, Osage-Skiatook Project, northeastern Oklahoma. *Appl. Geochem.* **2007**, *22*, 2125–2137. [[CrossRef](#)]
114. Al Attar, L.; Safia, B.; Abdul Ghani, B.; Al Abdullah, J. Recovery of NORM from scales generated by oil extraction. *J. Environ. Radioact.* **2016**, *153*, 149–155. [[CrossRef](#)] [[PubMed](#)]
115. Clarke, L.B.; Sloss, L.L. *Trace Elements—Emissions from Coal Combustion and Gasification*; IEA Coal Research: London, UK, 1992.
116. Tadmore, J. Radioactivity from coal-fired power plants: A review. *J. Environ. Radioact.* **1986**, *4*, 177–204. [[CrossRef](#)]
117. United Nations Scientific Committee on the Effects of Atomic Radiation (UNSCEAR). *Ionizing Radiation: Sources and Biological Effects*; United Nations: New York, NY, USA, 1982.
118. Coles, D.G.; Ragain, R.C.; Ondov, J.M. Behaviour of natural radionuclides in western coal-fired power plants. *Environ. Sci. Tech.* **1978**, *12*, 442–446. [[CrossRef](#)]
119. Senior, C.L.; Helble, J.J.; Sarofim, A.F. Emissions of mercury, trace elements, and fine particles from stationary combustion sources. *Fuel Proc. Technol.* **2000**, *65–66*, 263–288. [[CrossRef](#)]
120. Roeck, D.R.; Reavey, T.C.; Hardin, J.M. Partitioning of natural radionuclides in the waste streams of coal-fired utilities. *Health Phys.* **1987**, *52*, 311–323. [[CrossRef](#)] [[PubMed](#)]
121. UNSCEAR. *Sources and Effects of Ionizing Radiation. Report to the General Assembly with Scientific Annexes*; United Nations: New York, NY, USA, 2010; Volume 1, 245p.
122. Barber, D.E.; Giorgio, H.R. Gamma-ray Activity in Bituminous, Subbituminous and Lignite Coals. *Health Phys.* **1977**, *32*, 83–88. [[CrossRef](#)] [[PubMed](#)]
123. Fardy, J.; McOrist, G.; Farrar, Y. Neutron activation analysis and radioactivity measurements of Australian coals and fly ashes. *J. Radioanal. Nucl. Chem.* **1989**, *133*, 217–226. [[CrossRef](#)]
124. Bhangare, R.; Tiwari, M.; Ajmal, P.; Sahu, S.; Pandit, G. Distribution of natural radioactivity in coal and combustion residues of thermal power plants. *J. Radioanal. Nucl. Chem.* **2014**, *300*, 17–22. [[CrossRef](#)]
125. Lauer, N.E.; Hower, J.C.; Hsu-Kim, H.; Taggart, R.K.; Vengosh, A. Naturally occurring radioactive materials in coals and coal combustion residuals in the United States. *Environ. Sci. Tech.* **2015**, *49*, 11227–11233. [[CrossRef](#)] [[PubMed](#)]
126. Zielinski, R.A.; Finkelman, R.B. Radioactive Elements in Coal and Fly Ash: Abundance, Forms and Environmental Significance. U.S. Geological Survey Fact Sheet FS-163-97; 1997; 4p. Available online: <http://greenwood.cr.usgs.gov/energy/factshts/163-97/FS-163-97.html> (accessed on 11 May 2018).

127. Długosz-Lisiecka, M. Excess of ^{210}Po polonium activity in the surface urban atmosphere. Part (1) fluctuation of the ^{210}Po excess in the air. *Environ. Sci. Process. Impacts* **2015**, *17*, 458–464.
128. Długosz-Lisiecka, M. Excess of polonium-210 activity in the surface urban atmosphere. Part 2: Origin of ^{210}Po excess. *Environ. Sci. Process. Impacts* **2015**, *17*, 465–470.
129. Häsänen, E.; Pohjola, V.; Hahkala, M.; Zilliacus, R.; Wickström, K. Emissions from power plants fuelled by peat, coal, natural gas and oil. *Sci. Total Environ.* **1986**, *54*, 29–51. [[CrossRef](#)]
130. Gallyas, M.; Török, I. Natural Radioactivity of Raw Materials and Products in the Cement Industry. *Radiat. Prot. Dosim.* **1986**, *7*, 69–71. [[CrossRef](#)]
131. Stojanovska, Z.; Nedelkovskia, D.; Ristovab, M. Natural radioactivity and human exposure by raw materials and endproduct from cement industry used as building materials. *Radiat. Meas.* **2010**, *45*, 969–972. [[CrossRef](#)]
132. Eštoková, A.; Palaščáková, L. Assessment of Natural Radioactivity Levels of Cements and Cement Composites in the Slovak Republic. *Int. J. Environ. Res. Public Health* **2013**, *10*, 7165–7179. [[CrossRef](#)] [[PubMed](#)]
133. Guillén, J.; Tejado, J.J.; Baeza, A.; Salas, A.; Muñoz-Muñoz, J.G. Environmental impact of a granite processing factory as source of naturally occurring radionuclides. *Appl. Geochem.* **2014**, *47*, 122–129. [[CrossRef](#)]
134. Harrison, J.; Heijnis, H.; Caprarelli, G. Historical pollution variability from abandoned mine sites, Greater Blue Mountains World Heritage Area, New South Wales, Australia. *Environ. Geol.* **2003**, *43*, 680–687.
135. Plater, A.J.; Appleby, P.G. Tidal sedimentation in the Tees estuary during the 20th century: Radionuclide and magnetic evidence of pollution and sedimentary response. *Estuar. Coast. Shelf Sci.* **2004**, *60*, 179–192. [[CrossRef](#)]
136. Le Roux, G.; Weiss, D.; Grattan, J.; Givélet, N.; Krachler, M.; Cheburkin, A.; Rausch, N.; Kober, B.; Shotyky, W. Identifying the sources and timing of ancient and medieval atmospheric lead pollution in England using a peat profile from Lindow bog, Manchester. *J. Environ. Monit.* **2004**, *6*, 502–510. [[CrossRef](#)] [[PubMed](#)]
137. Cloy, J.M.; Farmer, J.G.; Graham, M.C.; MacKenzie, A.B.; Cook, G.T. A comparison of antimony and lead profiles over the past 2500 years in Flanders Moss ombrotrophic peat bog, Scotland. *J. Environ. Monit.* **2005**, *7*, 1137–1147. [[CrossRef](#)] [[PubMed](#)]
138. Mayer, B.; Alpay, S.; Gould, W.D.; Lortie, L.; Rosa, F. The onset of anthropogenic activity recorded in lake sediments in the vicinity of the Horne smelter in Quebec, Canada: Sulfur isotope evidence. *Appl. Geochem.* **2007**, *22*, 397–414. [[CrossRef](#)]
139. Hansen, A.M. Lake sediment cores as indicators of historical metal(loid) accumulation—A case study in Mexico. *Appl. Geochem.* **2012**, *27*, 1745–1752. [[CrossRef](#)]
140. Gray, J.E.; Pribil, M.J.; Van Metre, P.C.; Borrok, D.M.; Thapalia, A. Identification of contamination in a lake sediment core using Hg and Pb isotopic compositions, Lake Ballinger, Washington, USA. *Appl. Geochem.* **2013**, *29*, 1–12. [[CrossRef](#)]
141. Weigel, F. Chemie des Poloniums. *Angew. Chem.* **1959**, *71*, 289–316. [[CrossRef](#)]
142. Bagnall, K.W. The Chemistry of Polonium. In *Advances in Inorganic Chemistry and Radiochemistry*; Academic Press: New York, NY, USA, 1962; Volume 4, pp. 197–226.
143. Golubev, V.N.; Chernyshev, I.V. Differential behavior of components of the ^{238}U - ^{206}Pb and ^{235}U - ^{207}Pb isotopic systems in polymineralic U ores. *Geochem. Int.* **2009**, *47*, 321–328. [[CrossRef](#)]
144. Connan, O.; Boust, D.; Billon, G.; Solier, L.; Rozet, M.; Bouderbala, S. Solid partitioning and solid-liquid distribution of ^{210}Po and ^{210}Pb in marine anoxic sediments: Roads of Cherbourg at the northwestern France. *J. Environ. Radioact.* **2009**, *100*, 905–913. [[CrossRef](#)] [[PubMed](#)]
145. Macmillan, E.; Cook, N.J.; Ehrig, K.; Ciobanu, C.L.; Pring, A. Uraninite from the Olympic Dam IOCG-U-Ag deposit: Linking textural and compositional variation to temporal evolution. *Am. Miner.* **2016**, *101*, 1295–1320. [[CrossRef](#)]
146. Macmillan, E.; Ciobanu, C.L.; Ehrig, K.; Cook, N.J.; Pring, A. Chemical zoning and lattice distortion: Uraninite from Olympic Dam, South Australia. *Am. Miner.* **2016**, *101*, 2351–2354. [[CrossRef](#)]
147. Macmillan, E.; Ciobanu, C.L.; Ehrig, K.; Cook, N.J.; Pring, A. Replacement of uraninite by bornite via coupled dissolution-precipitation: Evidence from texture and microstructure. *Can. Miner.* **2016**, *54*, 1369–1383. [[CrossRef](#)]
148. Janeczek, J.; Ewing, R.C. Mechanisms of lead release from uraninite in the natural fission reactors in Gabon. *Geochim. Cosmochim. Acta* **1995**, *59*, 1917–1931. [[CrossRef](#)]

149. Macmillan, E.; Cook, N.J.; Ehrig, K.; Pring, A. Chemical and textural interpretation of late-stage coffinite and brannerite from the Olympic Dam IOCG-Ag-U deposit. *Miner. Mag.* **2017**, *81*, 1323–1366. [CrossRef]
150. Utsunomiya, S.; Palenik, C.S.; Valley, J.W.; Cavosie, A.J.; Wilde, S.A.; Ewing, R.C. Nanoscale occurrence of Pb in an Archean zircon. *Geochim. Cosmochim. Acta* **2004**, *68*, 4679–4686. [CrossRef]
151. Kramers, J.; Frei, R.; Newville, M.; Kober, B.; Villa, I. On the valency state of radiogenic lead in zircon and its consequences. *Chem. Geol.* **2009**, *261*, 4–11. [CrossRef]
152. Ciobanu, C.L.; Wade, B.P.; Cook, N.J.; Schmidt Mumm, A.; Giles, D. Uranium-bearing hematite from the Olympic Dam Cu–U–Au deposit, South Australia: A geochemical tracer and reconnaissance Pb–Pb geochronometer. *Precambrian Res.* **2013**, *238*, 129–147. [CrossRef]
153. Verdugo-Ihl, M.R.; Ciobanu, C.L.; Cook, N.J.; Ehrig, K.; Courtney-Davies, L.; Gilbert, S. Textures and U–W–Sn–Mo signatures in hematite from the Cu–U–Au–Ag orebody at Olympic Dam, South Australia: Defining the archetype for IOCG deposits. *Ore Geology Reviews Ore Geol. Rev.* **2017**, *91*, 173–195. [CrossRef]
154. Cook, N.J.; Ciobanu, C.L.; Ehrig, K.; Slattery, A.; Verdugo-Ihl, M.R.; Courtney-Davies, L.; Gao, W. Advances and opportunities in ore mineralogy. *Minerals* **2017**, *7*, 233. [CrossRef]
155. Courtney-Davies, L.; Zhu, Z.Y.; Ciobanu, C.L.; Wade, B.P.; Cook, N.J.; Ehrig, K.; Cabral, A.R.; Kennedy, A. Matrix-matched iron-oxide laser ablation ICP-MS U–Pb geochronology using mixed solution standards. *Minerals* **2016**, *6*, 85. [CrossRef]
156. Apukhtina, O.B.; Kamenetsky, V.S.; Ehrig, K.; Kamenetsky, M.B.; Maas, R.; Thompson, J.; McPhie, J.; Ciobanu, C.L.; Cook, N.J. Early, deep magnetite-fluorapatite mineralization at the Olympic Dam Cu–U–Au–Ag deposit, South Australia. *Econ. Geol.* **2017**, *112*, 1531–1542. [CrossRef]
157. Ewing, R.C.; Meldrum, A.; Wang, L.M.; Wang, S.X. Radiation-Induced Amorphization. *Rev. Miner. Geochem.* **2000**, *39*, 319–361. [CrossRef]
158. Kerr, P.F. U-galena and uraninite in Bedford, New York cyrtolite. *Am. Miner.* **1935**, *20*, 443–450.
159. Trocki, L.K.; Curtis, D.B.; Gancarz, A.J.; Banar, J.C. Ages of Major Uranium Mineralization and Lead Loss in the Key Lake Uranium Deposit, Northern Saskatchewan, Canada. *Econ. Geol.* **1984**, *79*, 1378–1386. [CrossRef]
160. Finch, R.J.; Murakami, T. Systematics and paragenesis of uranium minerals. *Rev. Miner. Geochem.* **1999**, *38*, 91–179.
161. Čurda, M.; Goliáš, V.; Klementová, M.; Strnad, L.; Matěj, Z.; Škoda, R. Radiation damage in sulfides: Radioactive galena from burning heaps, after coal mining in the Lower Silesian basin (Czech Republic). *Am. Miner.* **2017**, *102*, 1788–1795. [CrossRef]
162. Owen, N.D.; Ciobanu, C.L.; Cook, N.J.; Slattery, A.; Basak, A. Nanoscale study of clausthalite-bearing symplectites in Cu–Au–(U) ores: Implications for ore genesis. *Minerals* **2018**, *8*, 67. [CrossRef]
163. Rollog, M.; Cook, N.J.; Guagliardo, P.; Kilburn, M.; Ehrig, K.; Ciobanu, C.L. NanoSIMS Mapping of ²¹⁰Rn and ²²⁶Ra in South Australian Copper Concentrates. Abstract, Goldschmidt Conference, Paris. 2017. Available online: <https://goldschmidtabstracts.info/2017/3392.pdf> (accessed on 9 May 2018).
164. Prieto, M.; Heberling, F.; Rodríguez-Galán, R.M.; Brandt, F. Crystallization behavior of solid solutions from aqueous solutions: An environmental perspective. *Progress Cryst. Growth Charact. Mater.* **2016**, *62*, 29–68. [CrossRef]
165. Takano, B.; Watanuki, K. Geochemical implications of the lead content of barite from various origins. *Geochem. J.* **1974**, *8*, 87–95. [CrossRef]
166. Rosenberg, Y.O.; Metz, V.; Ganor, J. Radium removal in a large scale evaporitic system. *Geochim. Cosmochim. Acta* **2013**, *103*, 121–137. [CrossRef]
167. Vinograd, V.L.; Brandt, F.; Rozov, K.; Klinkenberg, M.; Refson, K.; Winkler, B.; Bosbach, D. Solid-aqueous equilibrium in the BaSO₄–RaSO₄–H₂O system: First-principles calculations and a thermodynamic assessment. *Geochim. Cosmochim. Acta* **2013**, *122*, 398–417. [CrossRef]
168. Klinkenberg, M.; Brandt, F.; Breuer, U.; Bosbach, D. Uptake of Ra during the recrystallization of barite: A microscopic and time of flight-secondary ion mass spectrometry study. *Environ. Sci. Tech.* **2014**, *48*, 6620–6627. [CrossRef] [PubMed]
169. Brandt, F.; Curti, E.; Klinkenberg, M.; Rozov, K.; Bosbach, D. Replacement of barite by a (Ba,Ra)SO₄ solid solution at close-to-equilibrium conditions: A combined experimental and theoretical study. *Geochim. Cosmochim. Acta* **2015**, *155*, 1–15. [CrossRef]
170. Weber, J.; Barthel, J.; Klinkenberg, M.; Bosbach, D.; Kruth, M.; Brandt, F. Retention of ²²⁶Ra by barite: The role of internal porosity. *Chem. Geol.* **2017**, *466*, 722–732. [CrossRef]

171. Heberling, F.; Metz, V.; Böttle, M.; Curti, E.; Geckeis, H. Barite recrystallization in the presence of ^{226}Ra and ^{133}Ba . *Geochim. Cosmochim. Acta* **2018**. [[CrossRef](#)]
172. Rosenberg, Y.O.; Sade, Z.; Ganor, J. The precipitation of gypsum, celestine, and barite and coprecipitation of radium during seawater evaporation. *Geochim. Cosmochim. Acta* **2018**, in press. [[CrossRef](#)]
173. Vinograd, V.L.; Kulik, D.A.; Brandt, F.; Klinkenberg, M.; Weber, J.; Winkler, B.; Bosbach, D. Thermodynamics of the solid solution-Aqueous solution system $(\text{Ba,Sr,Ra})\text{SO}_4 + \text{H}_2\text{O}$: I. The effect of strontium content on radium uptake by barite. *Appl. Geochem.* **2018**, *89*, 59–74. [[CrossRef](#)]
174. Vinograd, V.L.; Kulik, D.A.; Brandt, F.; Klinkenberg, M.; Weber, J.; Winkler, B.; Bosbach, D. Thermodynamics of the solid solution-Aqueous solution system $(\text{Ba,Sr,Ra})\text{SO}_4 + \text{H}_2\text{O}$: II. Radium retention in barite-type minerals at elevated temperatures. *Appl. Geochem.* **2017**. [[CrossRef](#)]
175. Ulrych, J.; Adamovič, J.; Žák, K.; Frána, J.; Řanda, Z.; Langrová, A.; Chvátal, M. Cenozoic “radiobarite” occurrences in the Ohrře (Eger) Rift, Bohemian Massif: Mineralogical and geochemical revision. *Chemie der Erde–Geochem.* **2007**, *67*, 301–312. [[CrossRef](#)]
176. Zielinski, R.; Al-Hwaiti, M.; Budahn, J.; Ranville, J. Radionuclides, trace elements, and radium residence in phosphogypsum of Jordan. *Environ. Geochem. Health* **2011**, *33*, 149–165. [[CrossRef](#)] [[PubMed](#)]
177. Jones, M.J.; Butchins, L.J.; Charnock, J.M.; Patrick, R.A.D.; Small, J.S.; Vaughan, D.J.; Wincott, P.L.; Livens, F.R. Reactions of radium and barium with the surfaces of carbonate minerals. *Appl. Geochem.* **2011**, *26*, 1231–1238. [[CrossRef](#)]
178. Curti, E. *Coprecipitation of Radionuclides: Basic Concepts, Literature Review and First Applications*; Report 97-10; Paul Scherrer Institut: Villigen, Switzerland, 1997; 116p.
179. Belzile, N.; Chen, Y.W. Tellurium in the environment: A critical review focused on natural waters, soils, sediments and airborne particles. *Appl. Geochem.* **2015**, *63*, 83–92. [[CrossRef](#)]
180. Mihai, S.A.; Mather, J.D. Role of mineralogical structure of sediments in accumulation of radionuclides and trace elements. *J. Radioanal. Nucl. Chem.* **2003**, *256*, 425–430. [[CrossRef](#)]
181. McCubbin, D.; Leonard, K.S.; Maher, B.A.; Hamilton, E.I. Association of ^{210}Po (^{210}Pb), $^{239+240}\text{Pu}$ and ^{241}Am with different mineral fractions of a beach sand at Seascale, Cumbria, UK. *Sci. Total Environ.* **2000**, *254*, 1–15. [[CrossRef](#)]
182. Yang, W.F.; Guo, L.D.; Chuang, C.Y.; Schumann, D.; Ayrarov, M.; Santschi, P.H. Adsorption characteristics of ^{210}Pb , ^{210}Po and ^7Be onto micro-particle surfaces and the effects of macromolecular organic compounds. *Geochim. Cosmochim. Acta* **2013**, *107*, 47–64. [[CrossRef](#)]
183. Vu, H.P.; Shaw, S.; Brinza, L.; Benning, L.G. Partitioning of Pb(II) during goethite and hematite crystallization: Implications for Pb transport in natural systems. *Appl. Geochem.* **2013**, *39*, 119–128. [[CrossRef](#)]
184. Yang, W.F.; Guo, L.D.; Chuang, C.Y.; Santschi, P.H.; Schumann, D.; Ayrarov, M. Influence of organic matter on the adsorption of ^{210}Pb , ^{210}Po and ^7Be and their fractionation on nanoparticles in seawater. *Earth Plan. Sci. Lett.* **2015**, *423*, 193–201. [[CrossRef](#)]
185. Häsänen, E. Dating of sediments based on ^{210}Po measurements. *Radiochem. Radioanal. Lett.* **1977**, *31*, 207–214.
186. Tessier, A.; Campbell, P.G.C.; Bisson, M. Sequential extraction procedure for the speciation of particulate trace metals. *Anal. Chem.* **1979**, *51*, 844–851. [[CrossRef](#)]
187. Kim, T.H.; Kim, G. Important role of colloids in the cycling of ^{210}Po and ^{210}Pb in the ocean: Results from the East/Japan Sea. *Geochim. Cosmochim. Acta* **2012**, *95*, 134–142. [[CrossRef](#)]
188. Tuovinen, H. Mobilization of Natural Uranium Series Radionuclides at Three Mining Sites in Finland. Doctoral Dissertation, University of Helsinki, Helsinki, Finland, 2015.
189. Tuovinen, H.; Pohjolainen, E.; Lempinen, J.; Vesterbacka, D.; Read, D.; Solatie, D.; Lehto, J. Behaviour of radionuclides during microbially-induced mining of nickel at Talvivaara, Eastern Finland. *J. Environ. Radioact.* **2016**, *151*, 105–113. [[CrossRef](#)] [[PubMed](#)]
190. Christy, A.G. Causes of anomalous mineralogical diversity in the Periodic Table. *Miner. Mag.* **2015**, *79*, 33–49. [[CrossRef](#)]
191. Burns, P.C. The crystal chemistry of uranium. In: Burns, P.C.; Finch, R., eds., Uranium: Mineralogy, Geochemistry and the Environment. *Rev. Miner.* **1999**, *38*, 23–90.
192. Hazen, R.M.; Ewing, R.C.; Sverjensky, D.A. Evolution of uranium and thorium minerals. *Am. Miner.* **2009**, *94*, 1293–1311. [[CrossRef](#)]

193. Janeczek, J.; Ewing, R.C. X-ray powder diffraction study of annealed uraninite. *J. Nucl. Mater.* **1991**, *185*, 66–77. [[CrossRef](#)]
194. Malczewski, D.; Malczewski, M. ^{222}Rn and ^{220}Rn emanations as a function of the absorbed α -doses from select metamict minerals. *Am. Miner.* **2015**, *100*, 1378–1385. [[CrossRef](#)]
195. Krupp, K.; Baskaran, M.; Brownlee, S.J. Radon emanation coefficients of several minerals: How they vary with physical and mineralogical properties. *Am. Miner.* **2017**, *102*, 1375–1383. [[CrossRef](#)]
196. Trindade, M.J.; Prudêncio, M.I.; Burbidge, C.I.; Dias, M.I.; Cardoso, G.; Marques, R.; Rocha, F. Study of an aplite dyke from the Beira uraniferous province in Fornos de Algodres area (Central Portugal): Trace elements distribution and evaluation of natural radionuclides. *Appl. Geochem.* **2014**, *44*, 111–120. [[CrossRef](#)]
197. Chuang, C.Y.; Santschi, P.H.; Ho, Y.F.; Conte, M.H.; Guo, L.D.; Schumann, D.; Ayranov, M.; Li, Y.H. Role of biopolymers as major carrier phases of Th, Pa, Pb, Po, and Be radionuclides in settling particles from the Atlantic Ocean. *Mar. Chem.* **2013**, *157*, 131–143. [[CrossRef](#)]
198. Osmond, J.K.; Cowart, J.B. The theory and uses of natural uranium isotopic variations in hydrology. *At. Energy Rev.* **1976**, *14*, 621–679.
199. Kigoshi, K. Alpha recoil thorium-234: Dissolution into water and the uranium-234/uranium-238 disequilibrium in nature. *Science* **1971**, *173*, 47–48. [[CrossRef](#)] [[PubMed](#)]
200. Roudil, D.; Bonhoure, J.; Pik, R.; Cuney, M.; Jégou, C.; Gauthier-Lafaye, F. Diffusion of radiogenic helium in natural uranium oxides. *J. Nucl. Mater.* **2008**, *378*, 70–78. [[CrossRef](#)]
201. Ewing, R.C.; Whittleston, R.A.; Yardley, B.W.D. Geological Disposal of Nuclear Waste: A Primer. *Elements* **2016**, *12*, 233–237. [[CrossRef](#)]
202. Carvalho, F.P.; Oliveira, J.M.; Malta, M. Exposure to radionuclides in smoke from vegetation fires. *Sci. Total Environ.* **2014**, *472*, 421–424. [[CrossRef](#)] [[PubMed](#)]
203. Strumińska-Parulska, D. Radiolead ^{210}Pb and $^{210}\text{Po}/^{210}\text{Pb}$ activity ratios in calcium supplements and the assessment of their possible dose to consumers. *J. Environ. Sci. Health Part A Toxic/Hazard. Subst. Environ. Eng.* **2016**, *51*, 851–854.
204. Povinec, P.P.; Hirose, K. Fukushima radionuclides in the NW Pacific, and assessment of doses for Japanese and world population from ingestion of seafood. *Sci. Rep.* **2015**, *5*, 9016. [[CrossRef](#)] [[PubMed](#)]
205. Brook, B.W.; Bradshaw, C.J.A. Key role for nuclear energy in global biodiversity conservation. *Conserv. Biol.* **2014**, *29*, 702–712. [[CrossRef](#)] [[PubMed](#)]
206. World Nuclear Association. Thorium. 2015. Available online: <http://www.world-nuclear.org/information-library/current-and-future-generation/thorium.aspx> (accessed on 24 July 2016).
207. Utsunomiya, S.; Kogawa, M.; Kamiishi, E.; Ewing, R.C. Scanning Transmission Electron Microscopy and Related Techniques for Research on Actinide and Radionuclide Nanomaterials. In *Actinide Nanoparticle Research*; Kalmykov, S.N., Denecke, M.A., Eds.; Springer: Berlin/Heidelberg, Germany, 2011; pp. 33–62.
208. Ciobanu, C.L.; Cook, N.J.; Maunders, C.; Wade, B.P.; Ehrig, K. Focused Ion Beam and Advanced Electron Microscopy for Minerals: Insights and Outlook from Bismuth Sulphosalts. *Minerals* **2016**, *6*, 112. [[CrossRef](#)]
209. Ciobanu, C.L.; Kontonikas-Charos, A.; Slattery, A.; Cook, N.J.; Ehrig, K.; Wade, B.P. Short-Range Stacking Disorder in Mixed-Layer Compounds: A HAADF STEM Study of Bastnäsite-Parisite Intergrowths. *Minerals* **2017**, *7*, 227. [[CrossRef](#)]
210. Uchida, A.; Toyoda, S.; Ishibashi, J.; Nakai, S. ^{226}Ra - ^{210}Pb and ^{228}Ra - ^{228}Th Dating of Barite in Submarine Hydrothermal Sulfide Deposits Collected at the Okinawa Trough and the Southern Mariana Trough. In *Subseafloor Biosphere Linked to Hydrothermal Systems*; Ishibashi, J., Okino, K., Sunamura, M., Eds.; Springer: Tokyo, Japan, 2015; pp. 607–615.
211. Ditchburn, R.G.; de Ronde, C.E.J. Evidence for Remobilization of Barite Affecting Radiometric Dating Using ^{228}Ra , ^{228}Th , and $^{226}\text{Ra}/\text{Ba}$ Values: Implications for the Evolution of Sea-Floor Volcanogenic Massive Sulfides. *Econ. Geol.* **2017**, *112*, 1231–1245. [[CrossRef](#)]



SUPPLEMENTARY MATERIAL F

NANOSCALE STUDY OF CLAUSTHALITE-BEARING SYMPLECTITES IN CU-AU-(U) ORES FROM SOUTH AUSTRALIAN DEPOSITS: IMPLICATIONS FOR ORE GENESIS

Nicholas D. Owen, Cristiana L. Ciobanu, Nigel J. Cook, Animesh Basak

Nanoscale study of clausthalite-bearing symplectites in Cu-Au-(U) ores from South Australian deposits: Implications for ore genesis

NICHOLAS D. OWEN^{1,2,*}, CRISTIANA L. CIOBANU¹, NIGEL J. COOK^{1,2}, ANIMESH BASAK³

¹School of Chemical Engineering, The University of Adelaide, Adelaide, 5005 SA, Australia (correspondence; nicholas.owen@adelaide.edu.au; cristiana.ciobanu@adelaide.edu.au; nigel.cook@adelaide.edu.au)

²ARC Research Hub for Australian Copper-Uranium, The University of Adelaide, Adelaide, 5005 SA, Australia

³Adelaide Microscopy, The University of Adelaide, Adelaide, 5005 SA (animesh.basak@adelaide.edu.au)

Nanoscale investigation of symplectites comprising clausthalite (PbSe) and host Cu-(Fe)-sulfides (chalcocite, bornite and chalcopyrite) are instructive for understanding the genesis of South Australian Mesoproterozoic Cu-Au-(U) ores. High-resolution Focussed Ion Beam (FIB)-SEM imaging and Transmission Electron Microscopy study of FIB-prepared foils reveal that clausthalite 'inclusions' vary in size from a few μm to down to nm-scale ($<5\text{ nm}$), and are present as rods, blebs or needles in any of the aforementioned sulfides. The Cu-(Fe)-sulfides outside inclusion areas still contain measurable Se; these are highest in chalcopyrite. Pb is, however, absent from these areas, suggesting formation from solid solution in the system Cu-Fe-S-Se with Pb supplied from an external source. Although the orientation of swarms of smaller clausthalite inclusions is broadly congruent with the host, there is an orientation offset with host sulfide that increases with bleb coarsening, nm-scale inclusions of other phases, and with boundary corrosion/displacements. These are particularly apparent in *2a* bornite and high-T chalcocite. Such decrease in the degree of crystallographic congruency with the host sulfide indicates that the symplectites record superimposed thermal event(s). Moreover, trace element remobilisation within the ores is concordant with sulfide recrystallization within nanoscale domains during fluid percolation as observed by presence of pores, nucleation of multi-component inclusions along boundaries between low-T chalcocite and bornite, etc. Although clausthalite may have initially exsolved from Cu-(Fe)-sulfides, cyclic solid-state diffusion processes, also facilitating incorporation of mobilized radiogenic Pb released from U-(Th)-bearing minerals, have progressively modified primary structures. Such observations are concordant with preliminary LA-ICP-MS Pb-isotope data for Pb-chalcogenides, which reveal Pb-Pb ages younger than the initial ~1590 Ma mineralisation event.

SUPPLEMENTARY MATERIAL G

REE-, SR-, CA-ALUMINIUM-PHOSPHATE-SULPHATE MINERALS OF THE WOODHOUSEITE SERIES AND THEIR ROLE AS HOSTS FOR RADIONUCLIDES

Nicholas D. Owen, Nigel J. Cook, Mark Rollog, Kathy J. Ehrig, Danielle S. Schmandt, Cristiana
L. Ciobanu



REE-, Sr- Ca-ARSENATE-PHOSPHATE- SULPHATE MINERALS OF THE WOODHOUSEITE SERIES AND THEIR ROLE AS HOSTS FOR RADIONUCLIDES

A | 90

Nicholas D Owen¹, Nigel J Cook, Mark Rollog, Kathy J Ehrig, Danielle S Schmandt, Cristiana L Ciobanu

¹School of Chemical Engineering, University of Adelaide, Australia - nicholas.owen@adelaide.edu.au

BACKGROUND

Aluminium-phosphate-sulphate (APS) minerals of the alunite supergroup (Kolitsch and Pring 2001) form in geological environments ranging from sedimentary settings (Tripplehorn *et al.* 1991; Rasmussen 1996; Pe-Piper and Dolansky 2005) to hydrothermal ore deposits such as the giant Olympic Dam [OD] Cu-U-Au-Ag deposit, South Australia (Ehrig *et al.* 2012). Sulphate-free phosphate members and phosphate-free sulphate members (e.g. florencite, jarosite) have been previously identified from OD but the occurrence and composition of mixed phosphate-sulphate members such as those of the woodhouseite series (woodhouseite, svanbergite, etc.) have been inadequately characterised in prior studies. The woodhouseite series represents a broad field of solid solution between florencite, crandallite and goyazite; coupled substitutions between the 'A' and the 'X' sites preserve overall charge balance (Pe-Piper and Dolansky 2005).

Here, we report Sr-Ca-dominant APS minerals of the woodhouseite series from OD with the general formula $AB_3(PO_4)_{1-x}(SO_4)_x(OH)_6 \cdot n(H_2O)$, where A=Ca, Sr, REE, Pb, and B=Al, Fe, Ga. These phases are of interest for two reasons: the observed replacement relationships with Cu-(Fe)-sulphides that can shed light on ore evolution; and the potential ability of APS minerals in ores and copper concentrates to accommodate, within the 'A' site, ²³⁸U decay generated radionuclides (RN), notably ²²⁶Ra, ²²²Rn, ²¹⁰Po, ²¹⁰Bi and ²¹⁰Pb.

METHODS

Samples of Cu-sulphide flotation concentrates (FC) and concentrates following removal of the majority of uranium via sulphuric acid leaching (concentrate leach discharge, CLD) were collected from the Olympic Dam metallurgical processing plant. Backscatter electron (BSE) images were used to document textures and compositional zoning. Quantitative electron microprobe data allowed categorisation of APS minerals present. *In-situ* isotope mapping was attained using a Cameca NanoSIMS 50L (Centre for Microscopy, Characterisation, and Analysis, UWA; methodology described in Rollog *et al.* 2018).

RESULTS

Individual APS mineral grains show significant variation in backscatter contrast on BSE images, consistent with grain-scale compositional zonation. Different zones are variably enriched in REE, Ca and Sr, whereby brighter zones are typically richer in REE. Several species (REE-, Ca-, and Sr-dominant) are present. BSE imaging and EDAX data indicate that different zones also show variation with respect to S and P, suggesting that some are phosphate-dominant, and others are sulphate-dominant. Grains range from finely mottled in appearance through to needle-like grains and then coarsening towards those with tabular morphology, which appear particularly strongly zoned. Coarser subhedral varieties (Figure 1a) can be interpreted as having replaced pre-existing minerals such as bastnäsite (Schmandt *et al.* 2018), florencite or apatite (Stoffregen and Alpers 1987). Sr-Ca-dominant APS minerals (svanbergite, goyazite) are observed to replace Cu-Fe-sulphides (Figure 1b), often showing a modification of grain morphology within the APS minerals along interface boundaries (e.g. a fine-grained replacement zone surrounding coarser grains). Sr-Ca-APS minerals often contain remnants of replaced Cu-Fe-sulphides and gangue including Fe-oxides.

The EPMA dataset shows that REE-phosphate-dominant members are low in total Pb, with Pb concentrations increasing as Ca, Sr and S content rises (Figure 1c). The Pb content also increases with increasing (calculated) H₂O content.

NanoSIMS investigation of FC and CLD samples confirms the presence of RN within Sr-Ca-dominant APS minerals. Within most mapped areas (e.g. Figure 1d-f), there appears to be an excess of daughter ²²⁶Ra and ²¹⁰Rn (overwhelmingly ²¹⁰Pb) compared to the equivalent map for parent ²³⁸U. ²²⁶Ra and ²¹⁰Rn are also more dispersed throughout the APS minerals than ²³⁸U and elevated signals for ²²⁶Ra and ²¹⁰Rn do not always coincide with those for ²³⁸U. The distribution of ²¹⁰Rn throughout the APS minerals appears to correlate strongly with that of Ca. These qualitative distribution patterns strongly suggest micron-scale migration of ²²⁶Ra and ²¹⁰Rn from parent ²³⁸U-bearing phases, and possibly diffusion into APS. Although the number of examples mapped by nanoSIMS is currently limited, our mapping also indicates that RN activities are significantly greater within Sr-Ca-APS minerals in the CLD samples

than in the FC samples, suggesting fluid-mineral interaction and sub-solidus diffusion during leaching. The observed difference in ^{210}RN concentrations between FC and CLD samples may also be amplified due to the recycling of Cu-sulphate-rich smelter dust, which is consequently enriched in ^{210}RN , into the leach solution to maximise Cu recovery.

CONCLUSIONS

Textural relationships between Sr-Ca-dominant APS minerals and Cu-(Fe)-sulphides indicate formation at a relatively late stage in the evolution of the deposit. NanoSIMS mapping indicates these minerals carry RN within the processing cycle, especially from ^{226}Ra onwards. Further characterisation of the APS minerals and doping experiments on synthetic analogues are currently in progress to further understand cation (including RN) exchange mechanisms in APS of variable composition.

REFERENCES

- Ehrig, K., McPhie, J., Kamenetsky, V.S., 2012. Geology and Mineralogical Zonation of the Olympic Dam Iron Oxide Cu-U-Au-Ag Deposit, South Australia. In: F. Camus, J.W. Hedenquist, M. Harris (eds.), *Geology and Genesis of Major Copper Deposits and Districts of the World, a Tribute to Richard Sillitoe*, Society of Economic Geology Special Publication, 16, 237–267.
- Kolitsch, U., Pring, A., 2001. Crystal chemistry of the crandallite, beudantite and alunite groups: a review and evaluation of the suitability as storage materials for toxic metals. *Journal of Mineralogical and Petrological Sciences*, 96, 67–78.
- Pe-Piper, G., Dolansky, L.M., 2005. Early diagenetic origin of Al phosphate-sulfate minerals (woodhouseite and crandallite series) in terrestrial sandstones, Nova Scotia, Canada. *American Mineralogist*, 90, 1434–1441.
- Rasmussen, B., 1996. Early-diagenetic REE-phosphate minerals (florenceite, gorceixite, crandallite, and xenotime) in marine sandstones; a major sink for oceanic phosphorus. *American Journal of Science*, 296, 601–632.
- Rollog, M., Cook, N.J., Gugliardo, P., Ehrig, K., Kilburn, M., 2018. In situ spatial distribution mapping of radionuclides in minerals by nanoSIMS. *Geochemistry – Exploration, Environment, Analysis*, in press.
- Schmandt, D.S., Cook, N.J., Ehrig, K., Ciobanu, C.L., Wade, B.P., Gilbert, S., Kamenetsky, V.S. 2017. Rare earth element fluorocarbonate minerals from the Olympic Dam Cu-U-Au-Ag deposit, South Australia. *Minerals*, 7(10), 202; doi: 10.3390/min7100202.
- Stoffregen, R.E., Alpers, C.N., 1987. Woodhouseite and svanbergite in hydrothermal ore deposits; products of apatite destruction during advanced argillic alteration. *The Canadian Mineralogist* 25, 201–211.
- Triplehorn, D.M., Stanton, R.W., Ruppert, L.F., Crowley, S.S., 1991. Volcanic ash dispersed in the Wyodak-Anderson coal bed, Powder River basin, Wyoming. *Organic Geochemistry*, 17, 567–575.

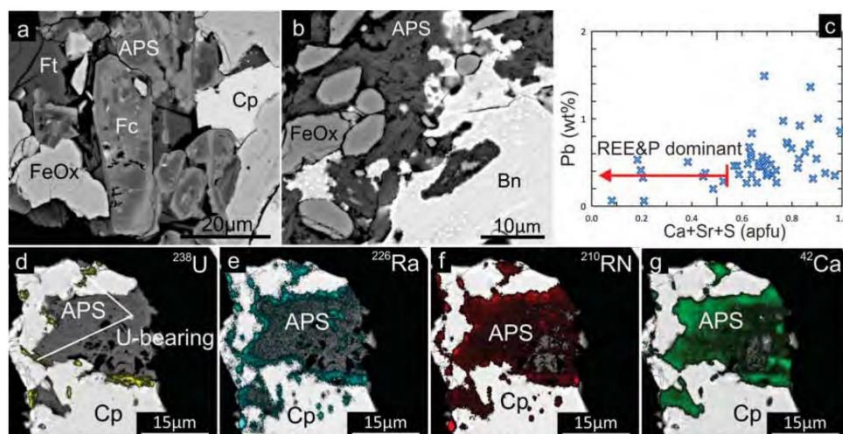


Figure 1: (a,b) BSE images showing APS mineral-bearing assemblages. (c) EPMA data showing the relationship between total Pb (wt%) and (Ca+Sr+S) (apfu). (d-g) NanoSIMS isotope maps of representative area within CLD sample showing distributions of ^{238}U , ^{226}Ra , ^{210}RN and ^{42}Ca within APS. Aluminium-phosphate-sulphate-APS, bornite-Bn, chalcopyrite-Cp, florenceite-Fc, Fe-oxide-FeOx, fluorite-Ft.

SUPPLEMENTARY MATERIAL H

NATURAL AND SYNTHETIC ALUMINIUM-PHOSPHATE-SULPHATES UNDER ACID LEACH CONDITIONS: PATHWAYS TO RADIONUCLIDE REDUCTION IN COPPER PROCESSING

Nicholas D. Owen, Nigel J. Cook, Rahul Ram, Joël Brugger, Mark Rollog, Kathy J. Ehrig,
Danielle S. Schmandt, Cristiana L. Ciobanu, Benjamin P. Wade, Paul Guagliardo

Natural and synthetic aluminium-phosphate-sulphates under acid leach conditions: Pathways to radionuclide reduction in copper processing circuits

Nicholas D. Owen^{1,2,*}, Nigel J. Cook¹, Rahul Ram², Joël Brugger², Mark Rollog¹, Kathy J. Ehrig³, Danielle S. Schmandt¹, Cristiana L. Ciobanu¹, Benjamin P. Wade⁴, Paul Guagliardo⁵

¹School of Chemical Engineering and Advanced Materials, The University of Adelaide, SA 5005, Australia

²School of Earth and Environmental Sciences, Monash University, VIC 2800, Australia

³BHP Olympic Dam, Adelaide, SA 5000, Australia

⁴Adelaide Microscopy, The University of Adelaide, SA 5005, Australia

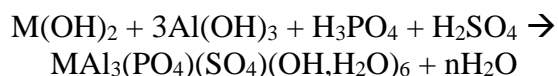
⁵Centre for Microscopy, Characterisation, and Analysis, University of Western Australia, 35 Stirling Highway, Crawley, WA 6009, Australia

Iron-oxide copper gold (IOCG) deposits such as Olympic Dam represent the primary resource for copper production in South Australia. Uranium and the daughter products of ²³⁸U decay, ²²⁶Ra, ²¹⁰Po and ²¹⁰Pb, are present in copper concentrates produced from IOCG ores. Ongoing efforts to identify novel solutions to remove or reduce concentrations of these radionuclides (RN) are benefitting from empirical mineralogical research on ores and concentrates and experimental studies targeting the geochemical behaviour of RN at conditions similar to those in the processing plant.

Aluminum-phosphate-sulfate (APS) minerals within the alunite supergroup have the general formula $MA_3(PO_4)_{2-x}(SO_4)_x(OH,H_2O)_6$, and are known to form a broad solid solution series, housing a range of mono-, di- or trivalent cations within their M-sites. Within the Olympic Dam metallurgical circuit, APS minerals of the alunite supergroup were shown to sorb products of ²³⁸U decay, notably ²²⁶Ra and ²¹⁰Pb (Rollog et al. 2019; Owen et al. in review) both over geological time within the deposit and during ore processing. Many APS phases remain stable over a wide range of pH and *Eh* and temperatures up to 450 °C (Kolitsch and Pring 2001; Schwab et al. 2005). As such synthetic APS phases present as viable candidates not only for the removal of radionuclides from metallurgical streams, but also for their safe storage and isolation from surrounding environments.

The genesis of natural APS mineral phases within the Olympic Dam deposit are shown to be paragenetically late, forming via replacement of earlier REE-bearing phosphates (fluorapatite, monazite and xenotime), and local dissolution and replacement of sulphides, with the development of two distinct compositional groups: Ca-Sr-dominant, sulfate-enriched APS minerals that lie within the woodhouseite and svanbergite compositional fields; and a REE- and phosphate-dominant group trending towards florencite in composition, similar to that reported by Schmandt et al. (2019). Of the two groups, Pb, both commonly sourced and radiogenic in origin, is shown to favor the Ca-Sr-dominated APS phases. Enrichment of these phases by Pb (including ²¹⁰Pb) is suggested to increase throughout the acid leach stages of processing, as evidenced by electron probe microanalysis and NanoSIMS isotope mapping. The data suggests that Pb-incorporation occurs with the replacement of Ca by Pb within the APS crystal structure, an interpretation in agreement with thermodynamic modelling given by Schwab et al. (2005). The same authors show that the thermodynamic stability of Ca-, Sr-, and Pb-bearing APS phases increases in the order Pb>Sr>Ca.

Ca- and Sr-bearing APS phases were synthesised by modifying existing recipes (Schwab et al. 2004) to generate mixed crystals. Ca/Sr ratios were varied according to the below reaction in order to test the role of compositional variability of mixed APS phases on the sorption of Pb via dilute PbNO₃ solution.



Phases which are Sr-, and (Ca,Sr)-bearing were produced. Accessory augelite, Al₂(PO₄)(OH)₃, was also formed within all samples, albeit in minor to moderate concentrations. APS crystals

* Corresponding author. e-mail address: nicholas.owen@adelaide.edu.au

showed compositional zoning with Al-, and S-rich cores with <1 apfu at the M-site, to stoichiometric APS at the rims with roughly equal concentrations of P and S.

Pb-sorption experiments were run by placing the synthesized APS phases in reaction vessels containing solutions of $\text{Pb}(\text{NO}_3)_2$ and diluted HNO_3 for a period of 5 days. The concentration of Pb ($[\text{Pb}_{\text{aq}}]_0$) in the reaction fluid was set at 10, 100 and 1000 ppm and a pH range of 1.5, 3.5 and 5.5 was tested.

Solution-ICP-MS, EPMA, LA-ICP-MS and EXAFS analysis confirm the sorption of Pb by the synthetic APS phases, with Pb sorption favoured at pH 3.5 and above. EPMA spot analyses indicate the preferential sorption of Pb by phases which trend towards higher S/P ratios, as well as those that deviate from ideal stoichiometry (i.e. $\text{Al} > 3$ apfu and $\sum \text{M}^{2+} < 1$). Targeted LA-ICP-MS analyses comparing the ratios of M-site cations indicate minimal change of Sr concentration with increasing Pb incorporation within both Sr-, and (Ca,Sr)-bearing APS phases, while Ca concentration within (Ca,Sr)-bearing phases subsides with increasing Pb incorporation, indicating direct replacement of Ca by Pb within the crystal structure of APS phases. Sr-bearing phases more commonly displayed non-stoichiometric values of $\sum \text{M}^{2+}$, indicating that Pb incorporation into such phases may arise via occupancy of sites that were previously vacant, or otherwise held by H^+ or excess Al within the structure.

An EXAFS study on the resulting Pb-sorbed solids was conducted, revealing the nature of Pb sorption by the synthesized APS material. The data showed that the dynamic incorporation of Pb by APS phases occurred overwhelmingly at pH 3.5. Some experiments run at pH 5.5 also favored the formation of Pb-bearing APS whereas other conditions favored dissolution and replacement of augelite to form a pyromorphite-like structure. Fairly featureless patterns in R-space were frequently observed in experiments run at high $[\text{Pb}_{\text{aq}}]_0$ (100-1000 ppm) with slightly shifted peaks indicating the prevalence of surface-sorbed Pb. Here, however, solution-ICP-MS data regularly showed undulating sorption trends, particularly in (Ca,Sr)-bearing material, indicating that equilibration between solution and solid may have not yet been achieved. Thus, synthetic APS phases may provide a novel approach to reducing radionuclides, particularly ^{210}Pb , from metallurgical streams.

Acknowledgements: This is a contribution to the ARC Research Hub for Australian Copper-Uranium.

References

- Kolitsch U, Pring A (2001) Crystal chemistry of the crandallite, beudantite and alunite groups: a review and evaluation of the suitability as storage materials for toxic metals. *J. Mineral. Petrol. Sci.* 96, 67–78.
- Owen ND, Cook NJ, Rollog M, Ehrig KJ, Schmandt DS, Ram R, Brugger J, Ciobanu CL, Wade B, Guagliardo P (2019) REE-, Sr- Ca-aluminum-phosphate-sulfate minerals of the alunite supergroup and their role as hosts for radionuclides. *Amer. Mineral.* (in review).
- Rollog M, Cook NJ, Guagliardo P, Ehrig K, Kilburn M (2019) In situ spatial distribution mapping of radionuclides in minerals by nanoSIMS. *Geochem. Explor. Environm. Analysis*; doi: 10.1144/geochem2018-038.
- Schmandt DS, Cook NJ, Ciobanu CL, Ehrig K, Wade BP, Gilbert S, Kametetsky VS (2019) Rare Earth Element Phosphate Minerals from the Olympic Dam Cu-U-Au-Ag Deposit, South Australia: Recognizing Temporal-Spatial Controls on REE Mineralogy in an Evolved IOCG System. *Can. Mineral.* 57, 3–24.
- Schwab RG, Pimpl T, Schukow H, Stolle A, Breiting DK (2004) Compounds of the crandallite-type: Synthesis, properties and thermodynamic data of pure crandallite and woodhouseite. *N. Jb. Mineral. Monatsh.*, 385–409.
- Schwab RG, Pimpl T, Schukow H, Stolle A, Breiting DK (2004) Compounds of the crandallite-type: Synthesis, properties and thermodynamic data of pure crandallite and woodhouseite. *N. Jb. Mineral. Monatsh.*, 385–409.

SUPPLEMENTARY MATERIAL I

WHY DETAILED MINERALOGY IS IMPORTANT: UNDERSTANDING EVOLUTION OF THE GIANT OLYMPIC DAM IRON-OXIDE COPPER- GOLD SYSTEM, SOUTH AUSTRALIA

Nigel Cook, Kathy Ehrig, Cristiana Ciobanu, Liam Courtney-Davies, Max Verdugo-Ihl, Mark Rollog, Danielle Schmandt, Nicholas Owen, Edeltraud Macmillan, Alkiviadis Kontonikas-Charos, Sasha Krneta, Marija Dmitrijeva

SALTA, ARGENTINA
28-31 AUGUST 2018

15th Quadrennial International Association on the Genesis of Ore Deposits Symposium

SYMPOSIUM PROCEEDINGS





WHY DETAILED MINERALOGY IS IMPORTANT: UNDERSTANDING EVOLUTION OF THE OLYMPIC DAM IRON-OXIDE COPPER-GOLD SYSTEM, SOUTH AUSTRALIA

Nigel Cook¹, Kathy Ehrig, Cristiana Ciobanu, Liam Courtney-Davies, Max Verdugo-Ihl, Mark Rollog, Danielle Schmandt, Nicholas Owen, Edeltraud Macmillan, Alkiviadis Kontonikas-Charos, Sasha Krneta, Marija Dmitrijeva
¹School of Chemical Engineering, University of Adelaide, Australia - nigelcook@adelaide.edu.au

Olympic Dam is one of the largest deposits on Earth and a significant producer of copper, uranium, gold and silver (Ehrig, *et al.*, 2013). Uranium-Pb geochronology using undisturbed magmatic and hydrothermal minerals allows interpretation of the initial and major hydrothermal ore-forming event at ~1593 Ma, associated with emplacement of the Gawler Silicic Large Igneous Province. The >10 billion-tonne resource is heterogeneous and contained within a breccia complex, itself confined to the ~1593 Ma Roxby Downs Granite. Ore textures suggest multiple episodes of replacement, remobilization and recrystallization and are supported by (radio) isotope data yielding a range of younger ages. Conceptual models for ore formation, necessary for exploration in the region, and optimised processing of complex fine-grained ores characterised by enrichment in an extraordinarily wide variety of elements are dependent on an exceptionally thorough understanding of mineralogy and geochemistry underpinned by high-quality, high-resolution assay data, extensive MLA datasets, and deportment models for multiple elements.

Micron - to nanoscale studies of feldspars and accessory phases within the alteration envelope, and of Fe-oxides, Cu-(Fe)-sulphides, sulphates, U- and REE-bearing minerals within the deposit all point to common mechanisms involved in formation of the mineral assemblages as observed today, the prevailing Mm-scale mineral textures, and measured variations in mineral compositions. Detailed mineralogical investigation has proven pivotal in establishing a framework for ore evolution.

Each of the 100 minerals in the Olympic Dam deposit has a story to tell. The complex fine-grained, intergrown, heterogeneous assemblages necessitate ultra-careful investigation on multiple representative samples and with compositional data requiring verification by examination at the nanoscale. We therefore use a combination of whole rock assay, optical and scanning electron microscopy, electron probe microanalysis (EPMA), laser-ablation inductively-coupled plasma mass spectrometry, complemented by imaging and nanoscale compositional analysis by transmission electron microscopy (TEM) on foils extracted *in-situ* by focussed ion beam SEM methods.

Investigation of feldspars from within and outside the deposit allows an understanding of the magmatic to hydrothermal transition and early Fe-metasomatism (Kontonikas-Charos, *et al.*, 2017). Nanoscale characterization of feldspars undergoing transformation from early post-magmatic (deuteric) to hydrothermal stages in granites hosting the deposit reveals complex perthitic textures, anomalously Ba, Fe, or REE-rich compositions, and REE-fluorocarbonate+molybdenite assemblages that pseudomorph feldspars (Kontonikas-Charos, *et al.*, 2018). Epitaxial orientations between (igneous) cryptoperthite, (deuteric) patch and albite replace within vein perthite support interface-mediated reactions between pre-existing alkali-feldspars and pervading fluid, irrespective of micron-scale crystal morphology. Such observations are consistent with coupled dissolution-replacement reactions (CDRR), indicating that albitization enhances rock permeability via the generation of transient pores which facilitate grain-scale element remobilization and trap elements as nanoscale inclusions. These inclusions represent the earliest stage of REE remobilization at the grain-scale, and reflect the significant role feldspar replacement reactions play in concentrating REE during hydrothermal alteration.

Hematite is by far the most abundant hydrothermal mineral and preserves oscillatory and sectorial zoning and incorporation of U, W, Mo, Sn and other trace elements, including REE (Verdugo-Ihl, *et al.*, 2017). The presence of U and Pb allows application of hematite U-Pb geochronology [e.g., Courtney-Davies, *et al.*, 2018]. These primary textures give way to repeated processes of brecciation, fluid-assisted reworking, element redistribution, recrystallization and overprinting. CDRR permits release of trace elements from the lattice to be trapped as nm- to Mm-scale inclusions (e.g., uraninite), or to form discrete minerals (e.g., scheelite molybdenite) in the near vicinity.

EPMA-scale compositional data combined with TEM investigation of chalcocite-group minerals, bornite and chalcopyrite has shown that Cu-Fe-sulphides from different ore zones feature nanoscale intergrowths, lattice defects, superstructure domains and antiphase boundary domains (Ciobanu, *et al.*, 2017). Such features can be interpreted as having originated via a combination of exsolution, coarsening, and phase transformation during cooling from high-T solid solutions (e⁺400°C) in the system Cu-Fe-S and sub-systems. A scenario of 'exsolution from primary solid-solution, corroborated by the consistency in phase relations within each zone across different scales of observation from deposit- to nanoscale, supports a model of primary hypogene ore precipitation rather than replacement, and



accounts for the observed zoning patterns at OD. Nonetheless, evidence for CDRR, replacement, phase transformation and local (Mm- to tens m-wide) remobilization is evident.

Uraninite, coffinite, brannerite and hematite are the dominant U hosts [Courtney-Davies, *et al.*, 2018, Macmillan, *et al.*, 2016, Macmillan, *et al.*, 2017). Although some uraninite and hematite retain U and daughter isotopes, breakdown and replacement can lead to release, remobilization and redistribution of radionuclides (RN) at scales from nm upwards. New minerals may be formed (late uraninite, coffinite) and U and Pb can also be incorporated into existing minerals (barite, svanbergite-woodhouseite). RN are, however, also concentrated as sub-microscopic particles within pores, microfractures and at grain boundaries in the near vicinity of altered or replaced U-bearing mineral grains (Rollog, *et al.*, 2018) attesting to fluid-mediated processes. Such redistribution carries implications for ore processing and, potentially also for the interpretation of geochronological data.

Three groups of REE-minerals are observed: REE-fluorocarbonates (bastnosite and subordinate synchysite (Schmandt, *et al.*, 2017), which appear paragenetically early; REE-phosphates (dominantly florencite of variable age and association but also minor xenotime, the main carrier of HREE); and Ca-, Sr-, REE-bearing phosphate-sulphates (svanbergite- woodhouseite), which are generally late and replace earlier-formed minerals (Owen, *et al.*, 2018). Minor REE are also contained in apatite, which displays evolving chondrite-normalized REE fractionation trends that can be explained in terms of changes in fluid parameters and speciation of REY in ore-forming fluids (Krneta, *et al.*, 2017). Under hydrothermal conditions typical of iron- oxide copper gold mineralization, a decrease in salinity, pH and temperature is associated with hematite-sericite alteration sufficient to produce a characteristic MREE-enriched apatite. However, anomalous high-pH (~7) fluids at 300 °C may account for high-grade Cu ores as modelled from apatite with strong positive Eu anomalies (Krneta, *et al.*, 2017).

Although primary assemblages are identified, a persistent narrative is offered by multiple episodes of fluid-assisted replacement, phase transition, remobilization, migration, and re- precipitation of all ore components. These processes played a major role in the modification of textural and geochemical patterns in many minerals. However, more refractory minerals, notably hematite, apatite, pyrite, some REE-minerals, and some sub-types of U-minerals, can preserve primary geochemical signatures and can also record and retain evidence of evolving and overprinting fluid signatures. Fluid regimes were likely heterogeneous given observations of texturally and geochemically distinct generations of the same mineral within single samples.

REFERENCES

- Ehrig, K., McPhie, J., Kamenetsky, V., 2013. Geology and mineralogical zonation of the Olympic Dam iron oxide Cu-U-Au-Ag deposit, South Australia. In: Hedenquist, J.W., Harris, M., Camus, F. (Eds), *Geology and Genesis of Major Copper Deposits and Districts of the World, a Tribute to Richard Sillitoe*. SEG Special Publication 16, pp. 237-268.
- Kontonikas-Charos, A., Ciobanu, C.L., Cook, N.J., Ehrig, K., Krneta, S., Kamenetsky, V.S., 2017. Feldspar evolution in the Roxby Downs Granite, host to Fe-oxide Cu-Au-(U) mineralization at Olympic Dam, South Australia. *Ore Geology Reviews*, 80, 838-859.
- Kontonikas-Charos, A., Ciobanu, C.L., Cook, N.J., Ehrig, K., Ismail, R., Krneta, S., Basak, A., 2018. Feldspar mineralogy and rare earth element (re)mobilization in iron-oxide copper gold systems from South Australia: a nanoscale study. *Mineralogical Magazine* 82 (S1), S173-S197.
- Verdugo-Ihl, M.R., Ciobanu, C.L., Cook, N.J., Ehrig, K., Courtney-Davies, L., Gilbert, S., 2017. Textures and U-W-Sn-Mo signatures in hematite from the Cu-U-Au-Ag orebody at Olympic Dam, South Australia: defining the archetype for IOCG deposits. *Ore Geology Reviews* 91, 173-195.
- Courtney-Davies, L., Ciobanu, C.L., Tapster, S.R., Cook, N.J., Ehrig, K.J., Kennedy, A.K., Condon, D.J., Verdugo-Ihl, M.R., Wade, B.S., Gilbert, S.E., 2018. The U-Pb systematics of hydrothermal hematite; insights from the IOCG system at Olympic Dam, South Australia. IAGOD Symposium, Salta (this volume).
- Ciobanu, C.L., Cook, N.J., Ehrig, K., 2017. Ore minerals down to the nanoscale: Cu-(Fe)- sulphides from the iron oxide copper gold deposit at Olympic Dam, South Australia. *Ore Geology Reviews* 81, 1218-1235.
- Macmillan, E., Cook, N.J., Ciobanu, C.L., Ehrig, E., Pring, A., 2016. Uraninite from the Olympic Dam IOCG-U-Ag deposit: linking textural and compositional variation to temporal evolution. *American Mineralogist* 101, 1295-1320.
- Macmillan, E., Cook, N.J., Ehrig, K., Pring, A., 2017. Chemical and textural interpretation of late-stage coffinite and brannerite from the Olympic Dam IOCG-Ag-U deposit. *Mineralogical Magazine* 81, 1323-1366.
- Rollog, M., Cook, N.J., Gugliardo, P., Ehrig, K., Kilburn, M., 2018. In situ spatial distribution mapping of radionuclides in minerals by nanoSIMS. *Geochemistry – Exploration, Environment, Analysis* (in press).
- Schmandt, D.S., Cook, N.J., Ciobanu, C.L., Ehrig, K., Wade, B.P., Gilbert, S., Kamenetsky, V.S., 2017. Rare earth element fluorocarbonate minerals from the Olympic Dam Cu-U-Au-Ag deposit, South Australia. *Minerals* 7(10), 202; doi: 10.3390/min7100202.
- Owen, N.D., Ciobanu, C.L., Cook, N.J., Slattery, A., Basak, A., 2018. Nanoscale study of clausenthalite-bearing symplectites in Cu-Au-(U) ores: Implications for ore genesis. *Minerals*, 8(2), 67; doi:10.3390/min8020067.
- Krneta, S., Ciobanu, C.L., Cook, N.J., Ehrig, K., Kontonikas-Charos, A., 2017. Rare earth element behaviour in apatite from the Olympic Dam Cu-U-Au-Ag deposit, South Australia. *Minerals* 7(8), 135; doi:10.3390/min7080135.

SUPPLEMENTARY MATERIAL J

RARE EARTH ELEMENT MINERALOGY AT OLYMPIC DAM, SOUTH AUSTRALIA

Danielle S. Schmandt, Nigel J. Cook, Cristiana L. Ciobanu, Kathy J. Ehrig, Nicholas D. Owen,
Benjamin P. Wade, Sarah E. Gilbert

Danielle S. Schmandt¹, Nige J. Cook¹, Cristiana L. Ciobanu¹, Kathy J. Ehrig²,
Nicholas D. Owen¹, Benjamin P. Wade², Sarah E. Gilbert²

¹School of Chemical Engineering, The University of Adelaide, ²BHP Olympic Dam, ³Adelaide Mineralogy, The University of Adelaide

Abstract

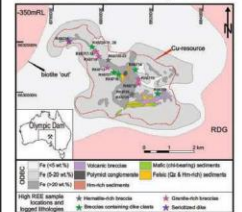
The world-class Olympic Dam breccia-hosted iron-oxide copper-gold-uranium ore deposit is enriched in light rare earth elements (LREE) by the most abundant LREE-mineral in the fluorocarbonate bastnaesite (BAST) which represents the dominant LREE mineralization stage and likely deposited during the main sulfide mineralization event at 1185 Ma. Minor Cu-bearing REE-fluorocarbonates present include synglycine (SYNG) and parisite (PAR) [CaREE₂(CO₃)₂F] which may have commenced precipitation immediately prior to bastnaesite, although these Ca-REE-fluorocarbonates are limited in occurrence, they show a greater enrichment in middle-REE than later bastnaesite, although also with considerably high LREE. The REE-Al-phosphate, florencite (FLO) [RE₂(PO₄)₂(OH)] is the second most abundant REE-mineral. Based on textural relationships, this is later than the REE-fluorocarbonates in the same samples. Cu-(Fe)-sulfides and primary hematite. Florencite is more LREE-enriched and middle- and heavy-REE-depleted than the REE-fluorocarbonates.

The REE-fluorocarbonates and florencite display progressive LREE enrichment commencing with paragenetic sequences, whereas other REE-bearing minerals in the deposit (apatite, titanite, zircon, and apatite) all show patterns of progressive LREE depletion across successive generations. This supports multiple fluid-assisted dissolution, remobilization, and re-precipitation processes that have impacted on LREE distributions. Late-stage florencite is the most L-rich of all REE-bearing phases. Such florencite forms extensive solid solutions with REE-depleted Sr-bearing phosphate-sulfate that are pervasive across the deposit, and likely formed at lower temperature and lower pH conditions under which other phosphates (e.g. monazite, apatite) are unstable.

The MHA dataset used for this analysis consists of 107 samples from the deposit, all samples are analyzed for all REE elements. The data was divided into perovskite and apatite and the lowest REE values were used for the analysis. The REE values are shown to be an indication of alteration intensity [2]. All 'host altered' with the highest Fe wt. %, up to 80 wt. % Fe.

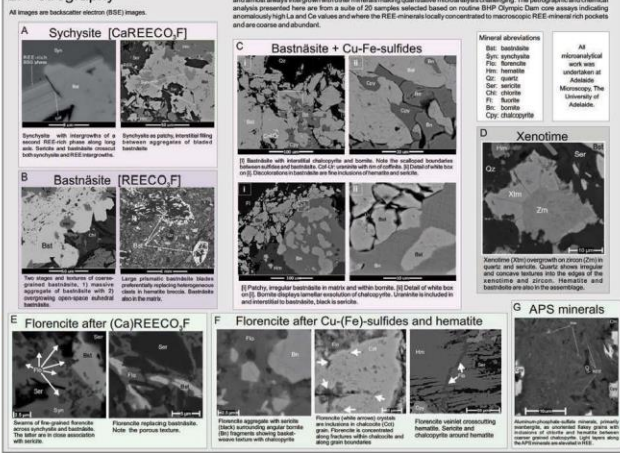
Most commonly, the REE-minerals at Olympic Dam are associated with hydrothermal fluids, and are distributed within breccia, in both matrix and clasts, indicating that the REE-minerals are highly mobile and easily transported. This analysis is particularly helpful for understanding deposit-scale trends.

1. Resource map and sample locations

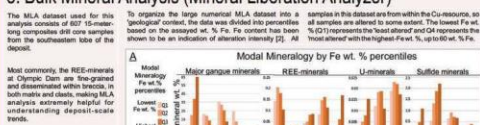


Simplified Olympic Dam deposit map at 350m RL, after Ehrig et al. [2]. Stars indicate locations of samples and are color-coded with logged lithology: RDG - Rocky Downs Granites. Average LREE grade of approximately 3,050 ppm. Heavy rare earth elements 10^{-1} ppm. The Olympic Dam is a large and complex deposit with a prolonged geological history (e.g. [1], [3]) located entirely within the RDG.

2. Petrography



3. Bulk Mineral Analysis (Mineral Liberation Analyzer)



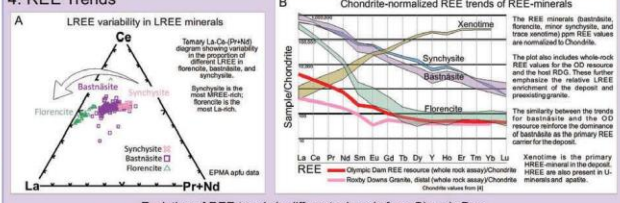
The most altered zones (up to 65 hematite) display a positive correlation between the relative abundance of synglycine, florencite, apatite, parisite, synglycine, and bastnaesite. The REE-fluorocarbonates abundance do not positively correlate with hematite abundance.

Synglycine is almost exclusive with bastnaesite, reconfirming their petrographic relationship. Bastnaesite has the strongest association with the three REE-minerals.

Bastnaesite, being the dominant REE-mineral, is best dependent on the other REE-minerals and has the strongest occurrence with hematite.

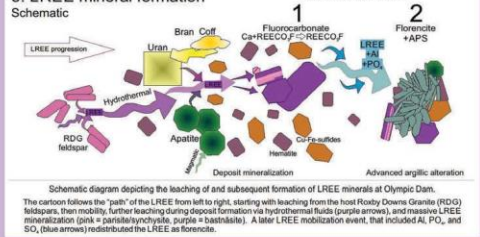
Florence shows a predictable strong relationship with its REE-depleted host group members of the aluminum phosphate-sulfate (APS) group.

4. REE Trends



The REE trends show that HREE becomes enriched relative to LREE with progression of U mineralization. This is possibly caused by REE fractionation due to transport, hydrothermal alteration, and LREE preferentially forming well-crystallized.

5. LREE mineral formation Schematic



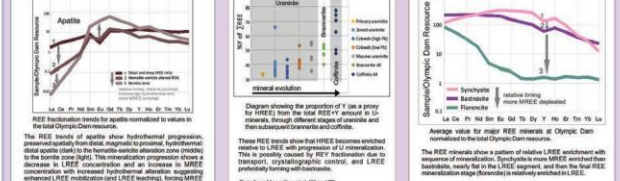
The cartoon follows the 'path' of the LREE from left to right, starting with leaching from the host Rocky Downs Granites (RDG) feldspars, then mobility, further leaching during deposition via hydrothermal fluids (purple arrows), and massive LREE mineralization (pink) in parisite/hydrolytic parisite/bastnaesite. A later LREE mobilization event, that included Al, PO₄, and SO₄ (blue arrows) redistributed the LREE as florencite.

REE mineralization summary

The formation of LREE minerals at OD can be considered in terms of a sequence of events. Minerals that formed early include Ca-REE-fluorocarbonates, including parisite (Fe-feldspar stable) [10, 12] and synglycine [6]. These were followed by the major stage of REE mineralization consisting of bastnaesite, associated with hematite and Cu-(Fe)-sulfide formation.

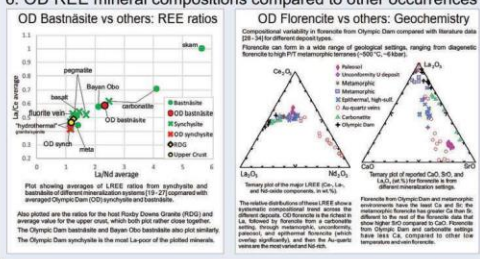
Florence is paragenetically late, representing a different stage or evolved formation conditions, which overprints the REE fluorocarbonates, hematite, and Cu-(Fe)-sulfides and replaces apatite [6]. REE-depleted APS minerals of primarily the woodhouseite-synglycine series are also an expression of the florencite event in areas without abundant REE availability or as a progression of the event after REE-mobility.

Evolution of REE trends in different minerals from Olympic Dam



The discrete REE minerals, on the other hand, show progressive LREE enrichment and MREE depletion. These REE trends of synglycine, bastnaesite, and REE-minerals are evidence of REE leaching from apatite [6] as well as a dominance of LREE across the entire deposit, which suggests enhanced LREE transport during deposit evolution.

6. OD REE mineral compositions compared to other occurrences



Plot showing averages of LREE ratios from synglycine and bastnaesite (averages of LREE ratios from synglycine and bastnaesite) compared to average Olympic Dam (OD) synglycine and bastnaesite.

7. Discussion and Conclusions

Leaching of LREE from pre-existing minerals, including but not restricted to early U-minerals, magmatic apatite, monazite, and feldspars (12 - 14) likely contributed to the LREE-dominated mineralogy of the deposit. The earliest REE phase was likely Ca-REE-fluorocarbonates, including parisite and synglycine and possibly intermediate phases. These are intimately associated with bastnaesite. The dominant REE-mineralization phase is pervasive bastnaesite, present across the deposit as the fine-grained minerals in the breccia matrix and clasts. Geological data and modeling of REE-bearing systems [15, 16], suggest that LREE preferentially formed REE-fluorocarbonates, and effectively removed LREE from solution. This then left the MREE to become concentrated in minerals such as late U-minerals and hydrothermal apatite that can more readily incorporate HREE, and that these HREE-rich mineral and/or xenotime probably formed during or after the REE-fluorocarbonates. Mixing of hydrothermal and carbonate-rich fluids, or REE-carbonate complexes precipitating from magmas degassing are both viable options for the promotion of fluorocarbonate-dominated mineralization. Florencite appears late and likely represents the result of a LREE-dominated remobilization event that took place after REE-fluorocarbonate and sulfide formation. This coincides with the REE-depleted APS-minerals as part of a late advanced argillic alteration stage or evolution of the deposit. The REE-mineral compositions are broadly similar across the expensive deposit although with localized variation. Compositional heterogeneity at the grain- and sample-scale has been observed in many other mineral species from Olympic Dam (e.g. [6], [7], [17], [18]). Such variation is typically linked to evolving fluid compositions, long-lived fluid regimes, highly heterogeneous porphyry and breccias, and to differential fluid-rock ratios driven by differences in permeability. This research is a contribution to the ARC research Hub for Australian Copper-Uranium.

References: [1] Schmandt, D.S., Cook, N.J., Ciobanu, C.L., Owen, N.D., Wade, B.P., Ehrig, K.J., Gilbert, S.E., 2019. Rare Earth Element Mineralogy at Olympic Dam, South Australia. *Journal of Mineralogical and Petrological Engineering*, 18, 1-12. [2] Ehrig, K.J., Schmandt, D.S., Cook, N.J., Ciobanu, C.L., Owen, N.D., Wade, B.P., Gilbert, S.E., 2019. The Olympic Dam deposit: A review of its geology, mineralogy, and geochemistry. *Journal of Mineralogical and Petrological Engineering*, 18, 13-24. [3] Schmandt, D.S., Cook, N.J., Ciobanu, C.L., Owen, N.D., Wade, B.P., Ehrig, K.J., Gilbert, S.E., 2019. The Olympic Dam deposit: A review of its geology, mineralogy, and geochemistry. *Journal of Mineralogical and Petrological Engineering*, 18, 25-36. [4] Schmandt, D.S., Cook, N.J., Ciobanu, C.L., Owen, N.D., Wade, B.P., Ehrig, K.J., Gilbert, S.E., 2019. The Olympic Dam deposit: A review of its geology, mineralogy, and geochemistry. *Journal of Mineralogical and Petrological Engineering*, 18, 37-48. [5] Schmandt, D.S., Cook, N.J., Ciobanu, C.L., Owen, N.D., Wade, B.P., Ehrig, K.J., Gilbert, S.E., 2019. The Olympic Dam deposit: A review of its geology, mineralogy, and geochemistry. *Journal of Mineralogical and Petrological Engineering*, 18, 49-60. [6] Schmandt, D.S., Cook, N.J., Ciobanu, C.L., Owen, N.D., Wade, B.P., Ehrig, K.J., Gilbert, S.E., 2019. The Olympic Dam deposit: A review of its geology, mineralogy, and geochemistry. *Journal of Mineralogical and Petrological Engineering*, 18, 61-72. [7] Schmandt, D.S., Cook, N.J., Ciobanu, C.L., Owen, N.D., Wade, B.P., Ehrig, K.J., Gilbert, S.E., 2019. The Olympic Dam deposit: A review of its geology, mineralogy, and geochemistry. *Journal of Mineralogical and Petrological Engineering*, 18, 73-84. [8] Schmandt, D.S., Cook, N.J., Ciobanu, C.L., Owen, N.D., Wade, B.P., Ehrig, K.J., Gilbert, S.E., 2019. The Olympic Dam deposit: A review of its geology, mineralogy, and geochemistry. *Journal of Mineralogical and Petrological Engineering*, 18, 85-96. [9] Schmandt, D.S., Cook, N.J., Ciobanu, C.L., Owen, N.D., Wade, B.P., Ehrig, K.J., Gilbert, S.E., 2019. The Olympic Dam deposit: A review of its geology, mineralogy, and geochemistry. *Journal of Mineralogical and Petrological Engineering*, 18, 97-108. [10] Schmandt, D.S., Cook, N.J., Ciobanu, C.L., Owen, N.D., Wade, B.P., Ehrig, K.J., Gilbert, S.E., 2019. The Olympic Dam deposit: A review of its geology, mineralogy, and geochemistry. *Journal of Mineralogical and Petrological Engineering*, 18, 109-120. [11] Schmandt, D.S., Cook, N.J., Ciobanu, C.L., Owen, N.D., Wade, B.P., Ehrig, K.J., Gilbert, S.E., 2019. The Olympic Dam deposit: A review of its geology, mineralogy, and geochemistry. *Journal of Mineralogical and Petrological Engineering*, 18, 121-132. [12] Schmandt, D.S., Cook, N.J., Ciobanu, C.L., Owen, N.D., Wade, B.P., Ehrig, K.J., Gilbert, S.E., 2019. The Olympic Dam deposit: A review of its geology, mineralogy, and geochemistry. *Journal of Mineralogical and Petrological Engineering*, 18, 133-144. [13] Schmandt, D.S., Cook, N.J., Ciobanu, C.L., Owen, N.D., Wade, B.P., Ehrig, K.J., Gilbert, S.E., 2019. The Olympic Dam deposit: A review of its geology, mineralogy, and geochemistry. *Journal of Mineralogical and Petrological Engineering*, 18, 145-156. [14] Schmandt, D.S., Cook, N.J., Ciobanu, C.L., Owen, N.D., Wade, B.P., Ehrig, K.J., Gilbert, S.E., 2019. The Olympic Dam deposit: A review of its geology, mineralogy, and geochemistry. *Journal of Mineralogical and Petrological Engineering*, 18, 157-168. [15] Schmandt, D.S., Cook, N.J., Ciobanu, C.L., Owen, N.D., Wade, B.P., Ehrig, K.J., Gilbert, S.E., 2019. The Olympic Dam deposit: A review of its geology, mineralogy, and geochemistry. *Journal of Mineralogical and Petrological Engineering*, 18, 169-180. [16] Schmandt, D.S., Cook, N.J., Ciobanu, C.L., Owen, N.D., Wade, B.P., Ehrig, K.J., Gilbert, S.E., 2019. The Olympic Dam deposit: A review of its geology, mineralogy, and geochemistry. *Journal of Mineralogical and Petrological Engineering*, 18, 181-192. [17] Schmandt, D.S., Cook, N.J., Ciobanu, C.L., Owen, N.D., Wade, B.P., Ehrig, K.J., Gilbert, S.E., 2019. The Olympic Dam deposit: A review of its geology, mineralogy, and geochemistry. *Journal of Mineralogical and Petrological Engineering*, 18, 193-204. [18] Schmandt, D.S., Cook, N.J., Ciobanu, C.L., Owen, N.D., Wade, B.P., Ehrig, K.J., Gilbert, S.E., 2019. The Olympic Dam deposit: A review of its geology, mineralogy, and geochemistry. *Journal of Mineralogical and Petrological Engineering*, 18, 205-216.

CHAPTER 8

REFERENCES

- Allen, S.R., McPhie, J., Ferris, G., and Simpson, C. (2008) Evolution and architecture of a large felsic Igneous Province in western Laurentia: The 1.6 Ga Gawler Range Volcanics, South Australia. *Journal of Volcanology and Geothermal Research*, 172(1-2), 132–147.
- Altree-Williams, A.L., Pring, A., Ngothai, Y., and Brugger, J. (2015) Textural and compositional complexities resulting from coupled dissolution-reprecipitation reactions in geomaterials. *Earth Science Reviews*, 150, 628–651.
- Ansoborlo, E., Berard, P., Den Auwer, C., Leggett, R., Menetrier, F., Younes, A., Montavon, G., and Moisy, P. (2012) Review of chemical and radiotoxicological properties of polonium for internal contamination purposes. *Chemical Research in Toxicology* 25, 1551–1564.
- Apukhtina, O.B., Kamenetsky, V.S., Ehrig, K., Kamenetsky, M.B., McPhie, J., Maas, R., Meffre, S., Goemann, K., Rodemann, T., Cook, N.J., and Ciobanu, C.L. (2016) Postmagmatic magnetite–apatite assemblage in mafic intrusions: a case study of dolerite at Olympic Dam, South Australia. *Contrib. Mineral. Petrol.* 171:15.
- Bajnóczi, B., Seres-Hartai, E., Molnár, F., and Nagy, G. (2004) Phosphate-bearing minerals in the advanced argillic alteration zones of high-sulphidation type ore deposits in the Carpatho-Pannonian region. *Acta Mineralogica-Petrographica*, Szeged, 45, 81–92.
- Barton, M.D. (2014) Iron Oxide(–Cu–Au–REE–P–Ag–U–Co) Systems. In: *Treatise on Geochemistry*, 2nd ed., Elsevier, 515–541.
- Bastrakov, E.N., Skirrow, R.G., and Davidson, G.J. (2007). Fluid Evolution and Origins of Iron Oxide Cu-Au Prospects in the Olympic Dam District, Gawler Craton, South Australia. *Economic Geology*, 102, 1415–1440.
- Bayliss, P., Kolitsch, U., Nickel, E.H., and Pring, A. (2010) Alunite supergroup: recommended nomenclature. *Mineralogical Magazine*, 74, 919–927.
- Beiser, A. (2003) *Concepts of Modern Physics* (Tata McGraw-Hill Education).
- Belogub, E.V., Novoselov, K.A., Yakovleva, V.A., and Spiro, B. (2008) Supergene sulphides and related minerals in the supergene profiles of VHMS deposits from the South Urals. *Ore Geology Reviews*, 33, 239–254.

- Belperio, A., Flint, R., and Freeman, H. (2007) Prominent Hill: A Hematite-Dominated, Iron Oxide Copper-Gold System. *Economic Geology*, 102, 1499–1510.
- Benavides, J. (2010) Paragenesis and Genetic Model for Prominent Hill IOCG Deposit. Implications on Exploration (OZ Minerals Ltd).
- Besold, E., Bieniek, D., and Kettrup, A. (1992) Synthetischer Crandallit. *Umweltwissenschaften und Schadstoff-Forschung*, 4(1), 14–16.
- Betts, P.G., Valenta, R.K., and Finlay, J. (2003) Evolution of the Mount Woods Inlier, northern Gawler Craton, Southern Australia: an integrated structural and aeromagnetic analysis. *Tectonophysics*, 366, 83–111.
- Bhargava, S.K., Ram, R., Pownceby, M., Grocott, S., Ring, B., Tardio, J., and Jones, L. (2015) A review of acid leaching of uraninite. *Hydrometallurgy*, 151, 10–24.
- Blanchard, F.N. (1986) The Use of Calculated Patterns as an Aid in Preparation of Powder diffraction Standards: Minuyulite, $\text{KA}_1_2(\text{PO}_4)_2(\text{OH},\text{F})\cdot 4\text{H}_2\text{O}$, as an Example. *Advances in X-ray Analysis*, 29, 225–233.
- Blount, A.M. (1974). The crystal structure of crandallite. *American Mineralogist*, 59, 41–47.
- Bogdanov, K. Filipov, A., and Kehayov, R. (2005) Au-Ag-Te-Se minerals in the Elatsite porphyry-copper deposit, Bulgaria. *Geochemistry Mineralogy and Petrology*, 43, 13–19.
- Botinelly, T.D. (1976) A review of the minerals of the alunite-jarosite, beudantite, and plumbogummite groups. *Geologic Studies*, 4(2), 213–216.
- Bowden, B., Fraser, G., Davidson, G.J., Meffre, S., Skirrow, R., Bull, S., and Thompson, J. (2017) Age constraints on the hydrothermal history of the Prominent Hill iron oxide copper-gold deposit, South Australia. *Mineralium Deposita*, 52(6), 863–881.
- Buerger, M.J. and Buerger, N.W. (1944) Low-chalcocite and high-chalcocite. *American Mineralogist*, 29, 55–65.
- Bunker, G. (2010) Introduction to XAFS: a practical guide to X-ray absorption fine structure spectroscopy. Cambridge University Press.

- Cepedal, A., Fuertes-Fuente, M., Martin-Izard, A., Gonzalez-Nistal, S., and Rodriguez-Pevida, L. (2006) Tellurides, selenides and Bi-mineral assemblages from the Río Narcea Gold Belt, Asturias, Spain: genetic implications in Cu–Au and Au skarns. *Mineralogy and Petrology*, 87, 277–304.
- Chalmers, N.C. (2007) Mount Woods Domain: proterozoic metasediments and intrusives. South Australia. Department of Primary Industries and Resources. Report Book, 20.
- Chau, N.D., Jodłowski, P., Kalita, S.J., Olko, P., Chruściel, E., Maksymowicz, A., Waligórski, M.P.R., Bilski, P., and Budzanowski, M. (2008) Natural radiation and its hazard in copper ore mines in Poland. *Acta Geophysica*, 56, 505–517.
- Cherry, A.R., Ehrig, K., Kamenetsky, V.S., McPhie, J., Crowley, J.L., and Kamenetsky, M.B. (2018) Precise geochronological constraints on the origin, setting and incorporation of ca. 1.59 Ga surficial facies into the Olympic Dam Breccia Complex, South Australia. *Precambrian Research*, 315, 162–178.
- Cherry, A.R., Kamenetsky, V.S., McPhie, J., Thompson, J.M., Ehrig, K., Meffre, S., Kamenetsky, M.B., and Krneta, S. (2018) Tectonothermal events in the Olympic IOCG Province constrained by apatite and REE-phosphate geochronology. *Australian Journal of Earth Sciences*, 65, 643–659.
- Christy, A.G. (2015) Causes of anomalous mineralogical diversity in the Periodic Table. *Mineralogical Magazine*, 79, 33–49.
- Ciobanu, C.L., Cook, N.J., Utsunomiya, S., Pring, A., and Green, L. (2011) Focussed ion beam-transmission electron microscopy applications in ore mineralogy: Bridging micron- and nanoscale observations. *Ore Geology Reviews*, 42, 6–31.
- Ciobanu, C.L., Cook, N.J., Utsunomiya, S., Kogagwa, M., Greem, L., Gilbert, S., and Wade, B. (2012) Gold-telluride nanoparticles revealed in arsenic-free pyrite. *American Mineralogist*, 97, 1515–1518.
- Ciobanu, C.L., Wade, B.P., Cook, N.J., Schmidt Mumm, A., and Giles, D. (2013) Uranium-bearing hematite from the Olympic Dam Cu–U–Au deposit, South Australia: A geochemical tracer and reconnaissance Pb–Pb geochronometer. *Precambrian Research*, 238, 129–147.

- Ciobanu, C.L., Cook, N.J., Maunders, C., Wade, B.P., and Ehrig, K. (2016) Focused Ion Beam and Advanced Electron Microscopy for Minerals: Insights and Outlook from Bismuth Sulphosalts. *Minerals*, 6, 112.
- Ciobanu, C.L., Cook, N.J., and Ehrig, K. (2017) Ore minerals down to the nanoscale: Cu-(Fe)-sulphides from the iron oxide copper gold deposit at Olympic Dam, South Australia. *Ore Geology Reviews*, 81, 1218-1235.
- Ciobanu, C., Kontonikas-Charos, A., Slattery, A., Cook, N., Wade, B., and Ehrig, K. (2017) Short-range stacking disorder in mixed-layer compounds: A HAADF STEM study of bastnäsite-parisite intergrowths. *Minerals*, 7(11), 227.
- Ciobanu, C.L., Verdugo-Ihl, M.R., Slattery, A., Cook, N.J., Ehrig, K., Courtney-Davies, L. and Wade, B.P. (2019) Silician Magnetite: Si-Fe-Nanoprecipitates and Other Mineral Inclusions in Magnetite from the Olympic Dam Deposit, South Australia. *Minerals*, 9(5), 311.
- Conor, C., Raymond, O., Baker, T., Teale, G., Say, P., and Lowe, G. (2010) Alteration and Mineralisation in the Moonta-Wallaroo Cu-Au Mining Field Region, Olympic Domain, South Australia. *Hydrothermal Iron Oxide Copper-Gold and Related Deposits: A Global Perspective*, 3, 1–24.
- Cook, N.J., Ciobanu, C.L., Spry, P.G., and Voudouris, P. (2009) Understanding gold-(silver)-telluride-(selenide) mineral deposits. *Episodes*, 32, 249–263.
- Cook, N.J., Ciobanu, C.L., Danyushevsky, L.V., and Gilbert, S. (2011) Minor elements in bornite and associated Cu-(Fe)-sulfides: A LA-ICPMS study. *Geochimica et Cosmochimica Acta*, 73, 4761–4791.
- Cook, N., Ciobanu, C., Ehrig, K., Slattery, A., Verdugo-Ihl, M., Courtney-Davies, L., and Gao, W. (2017) Advances and opportunities in ore mineralogy. *Minerals*, 7(12), 233.
- Cook, N., Ehrig, K., Rollog, M., Ciobanu, C., Lane, D., Schmandt, D., Owen, N., Hamilton, T. and Grano, S. (2018) ^{210}Pb and ^{210}Po in geological and related anthropogenic materials: implications for their mineralogical distribution in base metal ores. *Minerals*, 8(5), 211.

- Courtney-Davies, L., Zhu, Z., Ciobanu, C.L., Wade, B.P., Cook, N.J., Ehrig, K., Cabral, A.R., and Kennedy, A. (2016) Matrix-Matched Iron-Oxide Laser Ablation ICP-MS U–Pb Geochronology Using Mixed Solution Standards. *Minerals*, 6, 85–102.
- Courtney-Davies, L., Ciobanu, C.L., Verdugo-Ihl, M.R., Dmitrijeva, D., Cook, N.J., Ehrig, K., and Wade, B.P. (2019) Hematite geochemistry and geochronology resolve genetic and temporal links among iron-oxide copper gold systems, Olympic Dam district, South Australia. *Precambrian Research*, 335, 105480
- Courtney-Davies, L., Ciobanu, C.L., Verdugo-Ihl, M.R., Slattery, A., Cook, N.J., Dmitrijeva, M., Keyser, W., Wade, B.P., Domnick, U.I., Ehrig, K., and Xu, J. (2019) Zircon at the Nanoscale Records Metasomatic Processes Leading to Large Magmatic–Hydrothermal Ore Systems. *Minerals*, 9(6), 364.
- Courtney-Davies, L., Tapster, S.R., Ciobanu, C.L., Cook, N.J., Verdugo-Ihl, M.R., Ehrig, K.J., Kennedy, A.K., Gilbert, S.E., Condon, D.J., and Wade, B.P. (2019) A multi-technique evaluation of hydrothermal hematite U-Pb isotope systematics: Implications for ore deposit geochronology. *Chemical Geology*, 513, 54–72.
- Cowart, J.B. and Burnett, W.C. (1994) The Distribution of Uranium and Thorium Decay-Series Radionuclides in the Environment - A Review. *Journal of Environment Quality*, 23, 651.
- Creaser R.A. and Cooper J.A. (1993) U-Pb geochronology of middle Proterozoic felsic magmatism surrounding the Olympic Dam Cu-Au-U-Ag and Moonta Cu-Au-Ag deposits, South Australia. *Economic Geology*, 88, 186–197.
- Dai, Y.S. and Hughes, J.M. (1989) Crystal-structure refinements of vanadinite and pyromorphite. *Canadian Mineralogist*, 27, 189–192.
- Davidson, G.J., Paterson, H., Meffre, S., and Berry, R.F. (2007) Characteristics and origin of the Oak Dam East breccia-hosted, iron oxide Cu-U-(Au) deposit: Olympic Dam region, Gawler craton, South Australia. *Economic Geology*, 102, 1471–1498.
- De Montreuil, L.A. (1975) Bellidoite, a new copper selenide. *Economic Geology*, 70, 384–387.

- Dill, H.G. (2001) The geology of aluminium phosphates and sulphates of the alunite group minerals: a review. *Earth-Science Reviews*, 53, 35–93.
- Ding, Y., Veblen, D.R., and Prewitt, C.T. (2005) High-resolution transmission electron microscopy (HRTEM) study of 4a and 6a superstructure of bornite Cu_5FeS_4 . *American Mineralogist*, 90, 1256–1264.
- Ding, Y., Veblen, D.R., and Prewitt, C.T. (2005) Possible Fe/Cu ordering schemes in the 2a superstructure of bornite (Cu_5FeS_4). *American Mineralogist*, 90, 1265–1269.
- Dmitrijeva, M., Ehrig, K., Ciobanu, C.L., Cook, N.J., Verdugo-Ihl, M.R., and Metcalfe, A. (2019) Mineralization-alteration footprints in the Olympic Dam IOCG district, South Australia: The Acropolis prospect. *Journal of Geochemical Exploration*, 205, 106333.
- Dmitrijeva, M., Ehrig, K.J., Ciobanu, C.L., Cook, N.J., Verdugo-Ihl, M.R., and Metcalfe, A.V. (2019) Defining IOCG signatures through compositional data analysis: A case study of lithogeochemical zoning from the Olympic Dam deposit, South Australia. *Ore Geology Reviews*, 105, 86–101.
- Downs, R.T. and Hall-Wallace, M. (2003) The American Mineralogist Crystal Structure Database. *American Mineralogist*, 88, 247–250.
- Dymkov, Y., Holliger, P., Pagel, M., Gorshkov, A., and Artyukhina A. (1997) Characterization of a La-Ce-Sr-Ca aluminous hydroxy phosphate in nuclear zone 13 in the Oklo uranium deposit (Gabon). *Mineralium Deposita*, 32, 617–620.
- Eberly, P.O., Ewing, R.C., Janeczek, J., and Furiano, A. (1996) Clays at the natural nuclear reactor at Bangombé, Gabon: Migration of actinides. *Radiochimica Acta*, 74, 271–276.
- Echigoya, J. and Edington, J.W. (1982) A transmission electron microscope study of the chalcocite-djurleite transformation in topotactically grown thin films of Cu_xS . *Physica Status Solidi*, 72, 305–311.
- Economou-Eliopoulos, M., Eliopoulos, D.G., and Chryssoulis, S. (2008) A comparison of high-Au massive sulfide ores hosted in ophiolite complexes of the Balkan Peninsula with modern analogues: Genetic significance. *Ore Geology Reviews*, 33, 81–100.

- Ehrig, K., McPhie, J., and Kamenetsky, V.S. (2012) Geology and mineralogical zonation of the Olympic Dam Iron Oxide Cu-U-Au-Ag deposit, South Australia. In: F. Camus, J.W. Hedenquist, M. Harris (eds.), *Geology and Genesis of Major Copper Deposits and Districts of the World, a Tribute to Richard Sillitoe*. Society of Economic Geologists Special Publication, 16, 237–267.
- Ehrig, K., Liebezeit, V., Macmillan, E., Lower, C., Kamenetsky, V.S., Cook, N.J., and Ciobanu, C.L. (2015) Uranium mineralogy versus the recovery of uranium at Olympic Dam. *Proceedings, The AusIMM International Uranium Conference 2015, Adelaide*, 75.
- Ehrig, K., Kamenetsky V.S., McPhie, J., Cook, N.J., and Ciobanu, C.L. (2017) Olympic Dam iron oxide Cu-U-Au-Ag deposit. In *Australian Ore Deposits* (N. Phillips, ed.), AusIMM, Melbourne, Australia, 601–610.
- El Agami, N.L., El Wahed, A.A., and Haroun, Y.E. (2005) Mineralogy, geochemistry and origin of aluminum-phosphate-sulfate minerals in G.Elhefuf, Baharyia Oasis, Western Desert, Egypt. *Proceedings, The Fourth International Conference on the Geology of Africa, Assiut-Egypt*, 2, 269–292.
- Etschmann, B., Mei, Y., Liu, W., Rae, N., Kappen, P., Testemale, D. and Brugger, J. (2018) Role of Pb(II) complexes in hydrothermal mass transfer: An X-ray absorption spectroscopic study. *Chemical Geology*, 502, 88–106.
- Evans, H.T. (1979) The crystal structures of low chalcocite and djurleite. *Zeitschrift für Kristallographie*, 150, 299–320.
- Ewing, R.C., Meldrum, A., Wang, L.M., Weber, W.J., and Corrales, L.R. (2003) Radiation damage in zircon. *Reviews in Mineralogy and Geochemistry*, 53, 387–425.
- Fanning, C. (1997) *Geochronological Synthesis of Southern Australia, Part II, The Gawler Craton*. South Australia Department of Mines and Energy, Open File Envelope 8918.
- Fanning, C., Reid, A., and Teale, G. (2007) *A Geochronological Framework for the Gawler Craton, South Australia* (South Australia: Geological Survey).
- Ferris, G.M., Schwarz, M.P., and Heither, P. (2002) *The Geological Framework, Distribution and Controls of Fe-Oxide Cu-Au Mineralisation in the Gawler Craton, South Australia: Part I-*

Geological and Tectonic Framework. Hydrothermal iron oxide copper–gold and related deposits: a global perspective.

- Finch, R.J. and Murakami, T. (1999) Systematics and Paragenesis of Uranium Minerals. *Reviews in Mineralogy and Geochemistry*, 38, 91–180.
- Finlay, J. (1993) Structural interpretation in the Mount Woods Inlier. Honours Thesis - Monash University, Department of Earth Sciences.
- Fleischer, R.L. (1982) Alpha-recoil damage and solution effects in minerals: uranium isotopic disequilibrium and radon release. *Geochimica et Cosmochimica Acta*, 46, 2191–2201.
- Foden, J., Elburg, M.A., Dougherty-Page, J., and Burt, A. (2006) The Timing and Duration of the Delamerian Orogeny: Correlation with the Ross Orogen and Implications for Gondwana Assembly. *The Journal of Geology*, 114, 189–210.
- Forbes, C.J., Giles, D., Hand, M., Betts, P.G., Suzuki, K., Chalmers, N., and Dutch, R. (2011) Using P–T paths to interpret the tectonothermal setting of prograde metamorphism: An example from the northeastern Gawler Craton, South Australia. *Precambrian Research*, 185, 65–85.
- Förster, H.-J. (2005) Mineralogy of the U–Se-polymetallic deposit Niederschlema–Alberoda, Erzgebirge, Germany. IV. The continuous clausthalite–galena solid-solution series. *Neues Jahrbuch für Mineralogie*, 181, 125–134.
- Freeman, H. and Hart, J. (2003) Geophysics of the Prominent Hill prospect, South Australia. *ASEG Extended Abstracts 2003*, 93–100.
- Freeman, H. and Tomkinson, M. (2010) Geological setting of iron oxide related mineralisation in the Southern Mount Woods Domain, South Australia. *Hydrothermal Iron Oxide Copper–Gold and Related Deposits: A Global Perspective*, 3, 171–190.
- Frost, R.L., Palmer, S.J., Xi, Y., Čejka, J., Sejkora, J., and Plášil, J. (2013) Raman spectroscopic study of the hydroxy-phosphate mineral plumbogummite $\text{PbAl}_3(\text{PO}_4)_2(\text{OH},\text{H}_2\text{O})_6$. *Spectrochimica Acta Part A: Molecular and Biomolecular Spectroscopy*, 103, 431–434.
- Fry, C. and Thoennessen, M. (2013) Discovery of the thallium, lead, bismuth, and polonium isotopes. *Atomic Data and Nuclear Data Tables*, 99, 365–389.

- Gaboreau, S. and Vieillard, P. (2004) Prediction of Gibbs free energies of formation of minerals of the alunite supergroup. *Geochimica et Cosmochimica Acta*, 68, 3307–3316.
- Gaboreau, S., Cuney, M., Quirt, D., Beaufort, D., Patrier, P., and Mathieu, R. (2007) Significance of aluminum phosphate-sulfate minerals associated with U unconformity-type deposits: The Athabasca Basin, Canada. *American Mineralogist*, 92, 267–280.
- George, L.L., Cook, N.J., and Ciobanu, C.L. (2016) Partitioning of trace elements in co-crystallized sphalerite–galena–chalcopyrite hydrothermal ores. *Ore Geology Reviews*, 77, 97–116.
- George, L.L., Cook, N.J., Crowe, B.B.P., and Ciobanu, C.L. (2018) Trace elements in hydrothermal chalcopyrite. *Mineralogy Magazine*, 82(1), 59–88.
- Georgieva, S. and Velinova, N. (2012) Alunite from the advanced argillic alterations in the Chelopech high-sulphidation epithermal Cu-Au deposit, Bulgaria: Chemistry, morphology and genetic significance. *Geochemistry, Mineralogy and Petrology*, 49, 17–31.
- Georgieva, S. and Velinova, N. (2014) Florencite-(Ce, La, Nd) and crandallite from the advanced argillic alteration in the Chelopech high-sulphidation epithermal Cu-Au deposit, Bulgaria. *Comptes rendus de l'Académie bulgare des sciences: sciences mathématiques et naturelles*, 67, 1669–1678.
- Geoscience Australia, 2016. Copper – Geoscience Australia. URL: <http://www.ga.gov.au/scientific-topics/minerals/mineral-resources/copper> (accessed 10.09.16)
- Gilkes, R.J. and Palmer, B., 1983. Synthesis, properties, and dehydroxylation of members of the crandallite-goyazite series. *Mineralogical Magazine*, 47, 221–227.
- Goldschmidt, V.M. (1937) The principles of distribution of chemical elements in minerals and rocks. The seventh Hugo Müller Lecture, delivered before the Chemical Society on March 17th, 1937. *Journal of the Chemical Society (Resumed)*, 655–673.
- Government of South Australia Department for energy and Mining (2016) South Australia's copper strategy. URL: <http://www.energymining.sa.gov.au/minerals> (accessed 10.09.16)
- Guillemin, C. (1955) Sur une variété d'hidalgoïte du Cap Garonne (Var). *Bulletin de Minéralogie*, 78(1), 27–32.

- Hall, J.W., Glorie, S., Reid, A.J., Collins, A.S., Jourdan, F., Danišik, M., and Evans, N. (2018) Thermal history of the northern Olympic Domain, Gawler Craton; correlations between thermochronometric data and mineralising systems. *Gondwana Research*, 56, 90–104.
- Hall, S.R. and Stewart, J.M. (1973) The crystal structure refinement of chalcopyrite, CuFeS₂. *Acta Crystallographica*, 29, 579–585.
- Hand, M., Reid, A., and Jagodzinski, L. (2007) Tectonic Framework and Evolution of the Gawler Craton, Southern Australia. *Economic Geology*, 102, 1377–1395.
- Haynes, D.W., Cross, K.C., Bills, R.T., and Reed, M.H. (1995) Olympic Dam ore genesis; a fluid-mixing model. *Economic Geology*, 90, 281–307.
- Hazen, R.M., Ewing, R.C., and Sverjensky, D.A. (2009) Evolution of uranium and thorium minerals. *American Mineralogist*, 94, 1293–1311.
- Hikov, A., Lerouge, C., and Velinova, N. (2010) Geochemistry of alunite group minerals in advanced argillic altered rocks from the Asarel porphyry copper deposit, Central Sredno-gorie. *Review of the Bulgarian Geological Society*, 71, 133–148.
- Hitzman, M.W., Oreskes, N., and Einaudi, M.T. (1992) Geological characteristics and tectonic setting of Proterozoic iron-oxide (Cu–U–Au–REE) deposits. *Precambrian Research*, 58, 241–287.
- Hitzman, M.W. (2000) Iron oxide-Cu-Au deposit: What, where, when, and why, in Porter, T.M., ed., *Hydrothermal iron oxide copper-gold and related deposits a global perspective: Adelaide*, Australian Mineral Foundation, 9–26.
- Hitzman, M.W. and Valenta, R.K. (2005) Uranium in Iron Oxide-Copper-Gold (iocg) Systems. *Economic Geology*, 100, 1657–1661.
- Huang, Q., Kamenetsky, V.S., McPhie, J., Ehrig, K., Meffre, S., Maas, R., Thompson, J., Kamenetsky, M., Chambefort, I., Apukhtina, O., and Hu, Y. (2015) Neoproterozoic (ca. 820–830 Ma) mafic dykes at Olympic Dam, South Australia: links with the Gairdner large igneous province. *Precambrian Research*, 271, 160–172.
- International Atomic Energy Agency (2006) Assessing the need for radiation protection measures in work involving minerals and raw materials. IAEA Safety Reports Series No. 49

- Jagodzinski, E. (2005) Compilation of SHRIMP U-Pb geochronological data, Olympic Domain, Gawler Craton. South Australia, 2001-2003. Geoscience Australia Record 2005/020
- Jagodzinski, E., Reid, A., Chalmers, N.C., Swain, G., Frew, R.A., and Foudoulis, C. (2007) Compilation of SHRIMP U-Pb geochronological data for the Gawler craton, South Australia, 2007. Primary Industries and Resources South Australia, Division of Minerals and Energy Resources.
- Jagodzinski, E. (2014) The age of magmatic and hydrothermal zircon at Olympic Dam. Proceedings, Australian Earth Sciences Convention, Abstracts, 110, 260.
- Jambor, J.L. (1999) Nomenclature of the alunite supergroup. *The Canadian Mineralogist*, 37, 1323–1341.
- Janeczek, J. and Ewing, R.C. (1991) X-ray powder diffraction study of annealed uraninite. *Journal of Nuclear Materials*, 185, 66–77.
- Janeczek, J. and Ewing, R.C. (1996) Florencite-(La) with fissionogenic REEs from a natural fission reactor at Bangombe, Gabon. *American Mineralogist*, 81, 1263–1269.
- Janeczek, J., Ewing, R.C., Oversby, V.M., and Werme, L.O. (1996) Spent Fuels Uraninite and UO₂ in spent nuclear fuel: a comparison. *Journal of Nuclear Materials*, 238, 121–130.
- Jerden, J.L. (2007) Uranium sequestration by aluminum phosphate minerals in unsaturated soils. *Materials Research Society Symposium Proceedings 985 (Scientific Basis for Nuclear Waste Management XXX)*, 461–466.
- Johnson, J.P. and Cross, K.C. (1995) U-Pb geochronological constraints on the genesis of the Olympic Dam Cu-U-Au-Ag deposit, South Australia. *Economic Geology*, 90, 1046–1063.
- Johnson, J.P. and McCulloch, M.T. (1995) Sources of mineralising fluids for the Olympic Dam deposit (South Australia): Sm-Nd isotopic constraints. *Chemical Geology*, 121(1-4), 177–199.
- Kalnins, C.A., Spooner, N.A., Clarke, M.J., and Ottaway, D. (2019) Alpha particle autoradiography for high spatial resolution mapping of radionuclides. *Journal of Environmental Radioactivity*, 197, 9–15.

- Kanazawa, Y., Koto, K., and Morimoto, N. (1978) Bornite (Cu_5FeS_4): c the intermediate form. *Canadian Mineralogist*, 16, 397–404.
- Kato, T. and Radoslovich, E.W. (1968) Crystal structures of soil phosphates. *Transactions of the 9th International Congregation of Soil Science (Adelaide)*, 2, 725–731.
- Kato, T. (1971) The crystal structures of goyazite and woodhouseite. *Neues Jahrbuch für Mineralogie Monatshefte*, 241–247.
- Kato, T. and Miura, Y. (1977) The crystal structures of jarosite and svanbergite. *Mineralogical Journal*, 8(8), 419–430.
- Kirchenbaur, M., Maas, R., Ehrig, K., Kamenetsky, V.S., Strub, E., Ballhaus, C., and Munker, C. (2016) Uranium and Sm isotope studies of the supergiant Olympic Dam Cu–Au–U–Ag deposit, South Australia. *Geochimica et Cosmochimica Acta*, 180, 15–32.
- Klinkenberg, M., Brandt, F., Breuer, U., and Bosbach, D. (2014) Uptake of Ra during the recrystallization of barite: a microscopic and time of flight-secondary ion mass spectrometry study. *Environmental Science & Technology*, 48(12), 6620–6627.
- Kolitsch, U., Tiekink, E.R., Slade, P.G., Taylor, M.R., and Pring, A. (1999) Hinsdalite and plumbogummite, their atomic arrangements and disordered lead sites. *European Journal of Mineralogy*, 513–520.
- Kolitsch, U. and Pring, A. (2001) Crystal chemistry of the crandallite, beudantite and alunite groups: a review and evaluation of the suitability as storage materials for toxic metals. *Journal of Mineralogical and Petrological Sciences*, 96(2), 67–78.
- Kontonikas-Charos, A., Ciobanu, C.L., Cook, N.J., Ehrig, K., Krneta, S., and Kamenetsky, V.S., (2017) Feldspar evolution in the Roxby Downs Granite, host to Fe-oxide Cu-Au-(U) mineralisation at Olympic Dam, South Australia. *Ore Geology Reviews*, 80, 838–859.
- Kontonikas-Charos, A., Ciobanu, C.L., Cook, N.J., Ehrig, K., Ismail, R., Krneta, S., and Basak, A. (2018) Feldspar mineralogy and rare-earth element (re) mobilization in iron-oxide copper gold systems from South Australia: a nanoscale study. *Mineralogical Magazine*, 82(S1), 173-S197.

- Koto, K. and Morimoto, N. (1975) Superstructure investigation of bornite, Cu_5FeS_4 , by the modified partial Patterson function. *Acta Crystallographica*, B31, 2268–2273.
- Krivovichev, S.V., Krivovichev, V.G., and Hazen, R.M. (2018) Structural and chemical complexity of minerals: correlations and time evolution. *European Journal of Mineralogy*, 30, 231–236.
- Krneta, S., Ciobanu, C.L., Cook, N.J., Ehrig, K., and Kontonikas-Charos, A. (2016) Apatite at Olympic Dam, South Australia: A petrogenetic tool. *Lithos*, 262, 470–485.
- Krneta, S., Ciobanu, C.L., Cook, N.J., Ehrig, K., and Kontonikas-Charos, A. (2017) Rare earth element behaviour in apatite from the Olympic Dam Cu–U–Au–Ag deposit, South Australia. *Minerals*, 7(8), 135.
- Krneta, S., Ciobanu, C., Cook, N., and Ehrig, K. (2018) Numerical Modeling of REE Fractionation Patterns in Fluorapatite from the Olympic Dam Deposit (South Australia). *Minerals*, 8(8), 342.
- Landa, E. (2003) Mobilization of radionuclides from uranium mill tailings and related waste materials in anaerobic environments. *Journal of Radioanalytical and Nuclear Chemistry*, 255(3), 559–563.
- Lane, D.J., Cook, N.J., Grano, S.R., and Ehrig, K. (2016) Selective leaching of penalty elements from copper concentrates: A review. *Minerals Engineering*, 98, 110–121.
- Lazareva, E.V., Myagkaya, I.N., Kirichenko, I.S., Gustaytis, M.A., and Zhmodik, S.M. (2019) Interaction of natural organic matter with acid mine drainage: In-situ accumulation of elements. *Science of the Total Environment*, 660, 468–483.
- Lee, M.R. (1993) The petrography, mineralogy and origins of calcium sulphate within the Cold Bokkeveld CM carbonaceous chondrite. *Meteoritics*, 28(1), 53–62.
- Lehto, J. and Hou, X. (2011) *Chemistry and Analysis of Radionuclides: Laboratory Techniques and Methodology*, John Wiley & Sons.
- Lemmon, D.M. (1937) Woodhouseite, a new mineral of the beudantite group. *American Mineralogist*, 22, 939–948.
- Liu, H. and Chang, L.L.Y. (1994) Phase relations in the system PbS–PbSe–PbTe. *Mineralogical Magazine*, 58, 567–578.

- Liu, W., Mei, Y., Etschmann, B., Brugger, J., Pearce, M., Ryan, C., Borg, S., Wykes, J., Kappen, P., Paterson, D., Boesenberg, U., Garrevoet, J., and Falkenberg G., (2017) Arsenic in hydrothermal apatite: oxidation state, mechanism of uptake, and comparison between experiments and nature. *Geochimica Cosmochimica Acta*, 196, 144–159.
- Lottermoser, B.G. (1995) Rare earth element mineralogy of the Olympic Dam Cu-U-Au-Ag deposit, Roxby Downs, South Australia; implications for ore genesis. *Neues Jahrbuch für Mineralogie, Monatshefte*, 371–384.
- Loveless, A.J. (1975) Lead isotopes - a guide to major mineral deposits. *Geoexploration*, 13(1-4), 13–27.
- Lu, J., Plimer, I.R., Foster, D.A., and Lottermoser, B.G. (1996) Multiple post-orogenic reactivation in the Olary Block, South Australia: evidence from $^{40}\text{Ar}/^{39}\text{Ar}$ dating of pegmatitic muscovite. *International Geology Review*, 38(7), 665–685.
- Maas, R., Kamenetsky, V.S., Ehrig, K., Meffre, S., McPhie, J., and Diemar, G. (2011) Olympic Dam U-Cu-Au deposit, Australia: New age constraints: *Mineralogical Magazine, Goldschmidt Conference abstract*, 75, 1375.
- Macmillan, E., Ciobanu, C.L., Ehrig, K., Cook, N.J., and Pring, A. (2016) Chemical zoning and lattice distortion in uraninite from Olympic Dam, South Australia. *American Mineralogist*, 101, 2351–2354.
- Macmillan, E., Ciobanu, C.L., Ehrig, K., Cook, N.J., and Pring, A. (2016) Replacement of uraninite by bornite via coupled dissolution-reprecipitation: Evidence from texture and microstructure. *The Canadian Mineralogist*, 54(6), 1369–1383.
- Macmillan, E., Cook, N.J., Ehrig, K., Ciobanu, C.L., and Pring, A. (2016) Uraninite from the Olympic Dam IOCG-U-Ag deposit: Linking textural and compositional variation to temporal evolution. *American Mineralogist*, 101, 1295–1320.
- Macmillan, E., Cook, N.J., Ehrig, K., and Pring, A. (2017) Chemical and textural interpretation of late-stage coffinite and brannerite from the Olympic Dam IOCG-Ag-U deposit. *Mineralogical Magazine*, 81(6), 1323–1366.

- Macnaughton, S.J., Ring, R.J., Day, A., Collier, D.E., and Tan, L.K.P. (1999) Optimisation of the leach conditions for a copper/uranium ore. In: Mishra, B. (Ed.), Proceedings EPD Congress 1999. The Minerals, Metals and Materials Society, 509–522.
- Macnaughton, S.J., Tan, L., Day, A., and Ring, R.J. (2000) Modelling the leaching behaviour of an uranium ore. In: Uranium 2000: International Symposium on the Process Metallurgy of Uranium, Saskatoon, SK, 413–427
- Malczewski, D. and Dziurawicz, M. (2015) ^{222}Rn and ^{220}Rn emanations as a function of the absorbed α -doses from select metamict minerals. *American Mineralogist*, 100, 1378–1385.
- Maxwell, S.L., Culligan, B.K., Hutchison, J.B., Utsey, R.C., and McAlister, D.R. (2013) Rapid determination of ^{210}Po in water samples. *Journal of Radioanalytical and Nuclear Chemistry*, 298, 1977–1989.
- Mayer, I., Cuisinier, F.J.G., Gdalya, S. and Popov, I. (2008) TEM study of the morphology of Mn^{2+} -doped calcium hydroxyapatite and β -tricalcium phosphate. *Journal of Inorganic Biochemistry*, 102(2), 311–317.
- McFarlane, C.R., Soltani Dehnavi, A., and Lentz, D.R. (2016) Pb-isotopic study of galena by LA-Q-ICP-MS: Testing a new methodology with applications to base-metal sulphide deposits. *Minerals*, 6(3), 96.
- McInnes, B.I.A., Keays, R.R., Lambert, D.D., Hellstrom, J., and Allwood, J.S. (2008) Re–Os geochronology and isotope systematics of the Tanami, Tennant Creek and Olympic Dam Cu–Au deposits. *Australian Journal of Earth Sciences*, 55(6-7), 967–981.
- McKie, D. (1962) Goyazite and florencite from two African carbonatites. *Mineralogical Magazine and Journal of the Mineralogical Society*, 33(259), 281–297.
- Meffre, S., Large, R.R., Scott, R., Woodhead, J., Chang, Z., Gilbert, S.E., Danyushevsky, L.V., Maslennikov, V., and Hergt, J.M. (2008) Age and pyrite Pb-isotopic composition of the giant Sukhoi Log sediment-hosted gold deposit, Russia. *Geochimica et Cosmochimica Acta*, 72, 2377–2391.

- Meffre, S., Ehrig, K., Kamenetsky, V.S., Chambefort, I., Maas, R., and McPhie, J. (2010) Pb isotopes at Olympic Dam: Constraining sulphide growth: Giant ore deposits down under: Proceedings of 13th Quadrennial International Association on the Genesis of Ore Deposits (IAGOD) Symposium, Adelaide, South Australia, 78–79.
- Migdisov, A., Williams-Jones, A.E., Brugger, J., and Caporuscio, F.A. (2016) Hydrothermal transport, deposition, and fractionation of the REE: Experimental data and thermodynamic calculations. *Chemical Geology*, 439, 13–42.
- Monteagudo, J.M., Durán, A., Carmona, M.S., Schwab, R.G., and Higuera, P. (2003) Elimination of inorganic mercury from waste waters using crandallite-type compounds. *Journal of Chemical Technology and Biotechnology*, 78, 399–405.
- Monteagudo, J.M., Durán, A., Martín, I.S., and Schwab, R.G. (2006) Treatment of aqueous solutions containing nickel using crandallite-type compounds. *Journal of Chemical Technology and Biotechnology*, 81, 262–267.
- Morimoto, N. and Kullerud, G. (1963) Polymorphism in digenite. *American Mineralogist*, 48, 110–123.
- Morimoto, N. and Kullerud, G. (1966) Polymorphism on the Cu_9S_5 - Cu_5FeS_4 join. *Zeitschrift für Kristallographie*, 123, 235–254.
- Ni, Y., Hughes, J.M., and Mariano, A.N. (1995) Crystal chemistry of the monazite and xenotime structures. *American Mineralogist*, 80, 21–26.
- Nicolas, J., and Rosen, A. D. (1963) Phosphates hydrothermaux de basse température et kaolinisation: la gorceixite du massif des Colettes (Allier) et les minéraux associés (hinsdalite). *Bulletin de Minéralogie*, 86(4), 379–385.
- Noda, Y., Masumoto, K., Ohba, S., Saito, Y., Toriumi, K., Iwata, Y., and Shibuya, I. (1987) Temperature dependence of atomic thermal parameters of lead chalcogenides, PbS, PbSe and PbTe. *Crystallographica Section C: Crystal Structure Communications*, 43, 1443–1445.

- Oreskes, N. and Einaudi, M.T. (1990). Origin of rare earth element-enriched hematite breccias at the Olympic Dam Cu-U-Au-Ag deposit, Roxby Downs, South Australia. *Economic Geology*, 85(1), 1–28.
- Owen, N., Ciobanu, C., Cook, N., Slattery, A., and Basak, A. (2018) Nanoscale study of clausthalite-bearing symplectites in Cu-Au-(U) ores: Implications for ore genesis. *Minerals*, 8(2), 67.
- Owen, N.D., Cook, N.J., Rollog, M., Ehrig, K.J., Schmandt, D.S., Ram, R., Brugger, J., Ciobanu, C.L., Wade, B., and Guagliardo, P. (2019) REE-, Sr-, Ca-aluminum-phosphate-sulfate minerals of the alunite supergroup and their role as hosts for radionuclides. *American Mineralogist*, 104, 1806–1819.
- Owen, N.D., Cook, N.J., Ram, R., Etschmann, B.E., Ehrig, K., Schmandt, D.S., Rollog, M., Guagliardo, P., Brugger, J. (2020) A sponge for radionuclides: a study on the dynamic uptake of lead by synthetic aluminium-phosphate-sulphates. *Applied Geochemistry* (in review).
- Owens, J.P., Altschuler, Z.S., and Berman, R. (1960) Millisite in phosphorite from Homeland, Florida. *American Mineralogist* 45, 547–561.
- OZ Minerals (2018) 2018 mineral resource and ore reserve statement and explanatory notes. OZ Minerals Ltd. URL: <https://www.ozminerals.com/operations/resources-reserves/> (accessed 20.06.2019).
- Paar, W.H., Topa, D., Roberts, A.C., Criddle, A.J., Amann, G., and Sureda, R.J. (2002) The new mineral species brodtkorbite, Cu_2HgSe_2 , and the associated selenide assemblage from Tuminico, Sierra de Cacho, La Rioja, Argentina. *Canadian Mineralogist*, 40, 225–237.
- Pabst, A. (1947) Some computations on svanbergite, wood-houseite and alunite. *American Mineralogist* 32, 16–30.
- Paton, C., Hellstrom, J., Paul, B., Woodhead, J., Hergt, J. (2011) Iolite: Freeware for the visualisation and processing of mass spectrometric data. *Journal of Analytical Atomic Spectrometry*, 26, 2508–2518.
- Penner-Hahn, J.E. (2005) Characterization of “spectroscopically quiet” metals in biology. *Coordination Chemistry Reviews*, 249(1-2), 161–177.

- Pe-Piper, G. and Dolansky, L.M. (2005) Early diagenetic origin of Al phosphate-sulfate minerals (woodhouseite and crandallite series) in terrestrial sandstones, Nova Scotia, Canada. *American Mineralogist*, 90, 1434–1441.
- Pierce, L. and Buseck, P.R. (1978) Superstructuring in the bornite-digenite series: a high-resolution electron microscopy study. *American Mineralogist*, 63, 1–6.
- Piestrzynski, A. and Pieczonka, J. (2012) Low temperature ore minerals associations in the Kupferschiefer type deposit, Lubin-Sieroszowice Mining District SW Poland. *Mineralogical Reviews*, 62, 59–66.
- Plášil, J., Sejkora, J., Čejka, J., Škoda, R., and Goliáš, V. (2009): Supergene mineralization of the Medvědíň uranium deposit, Krkonoše Mountains, Czech Republic. *Journal of Geosciences*, 54, 15–56.
- Platzner, I., Ehrlich, S., and Halicz, L. (2001) Isotope-ratio measurements of lead in NIST standard reference materials by multiple-collector inductively coupled plasma mass spectrometry. *Fresenius' Journal of Analytical Chemistry*, 370, 624–628.
- Plotinskaya, O.Y., Chugaev, A.V., and Seltmann, R. (2017) Lead isotope systematics of porphyry–epithermal spectrum of the Birgilda–Tomino ore cluster in the South Urals, Russia. *Ore Geology Reviews*, 85, 204–215.
- Poczatek, C., Kaufman, Z., and Lechene, C. (2009) OpenMIMS ImageJ Plugin Guide. Harvard Medical School, Boston, Massachusetts, USA.
- Pollard, P.J. (2006) An intrusion-related origin for Cu–Au mineralization in iron oxide–copper–gold (IOCG) provinces. *Mineralium Deposita*, 41, 179.
- Posfai, M. and Buseck, P.R. (1994) Djurleite, digenite, and chalcocite: intergrowths and transformations. *American Mineralogist*, 79, 308–315.
- Quan, Z., Wu, D., Zhu, J., Evers, W.H., Boncella, J.M., Siebbeles, L.D.A., Wang, Z., Navrotsky, A., and Xu, H. (2014) Energy landscape of self-assembled superlattices of PbSe nanocrystals. *Proceedings of the National Academy of Sciences of the United States of America*, 111, 9054–9057.

- Ram, R., Charalambous, F.A., McMaster, S., Pownceby, M.I., Tardio, J., and Bhargava, S.K. (2013) Chemical and micro-structural characterisation studies on natural uraninite and associated gangue minerals. *Minerals Engineering*, 45, 159–169.
- Ramdohr, P. (1969) *The Ore Minerals and Their Intergrowths*, English translation of the 3rd edition; Pergamon Press: Oxford, UK, 1174.
- Rasmussen, B. (1996) Early-diagenetic REE-phosphate minerals (florencite, gorceixite, crandallite, and xenotime) in marine sandstones; a major sink for oceanic phosphorus. *American Journal of Science*, 296, 601–632.
- Ravel, B. and Newville, M. (2005) ATHENA, ARTEMIS, HEPHAESTUS: data analysis for X-ray absorption spectroscopy using IFEFFIT. *Journal of Synchrotron Radiation* 12, 537–541.
- Reeve, J.S. (1990). Olympic Dam copper-uranium-gold-silver deposit. *Geology of the Mineral Deposits of Australia and Papua New Guinea*, AusIMM, Melbourne, 1009–1035.
- Rehr, J.J., Kas, J.J., Prange, M.P., Sorini, A.P., Takimoto, Y., and Vila, F. (2009) Ab initio theory and calculations of X-ray spectra. *Comptes Rendus Physique* 10, 548–559.
- Reid, A.J (2019) *The Olympic Cu-Au Province, Gawler Craton: A Review of the Lithospheric Architecture, Geodynamic Setting, Alteration Systems, Cover Successions and Prospectivity*. *Minerals*, 9(6), 371.
- Reid, A.J. and Hand, M. (2012) Mesoarchean to Mesoproterozoic evolution of the southern Gawler Craton, South Australia. *Episodes*, 35, 216–225.
- Rigali, M.J., Brady, P.V., and Moore, R.C. (2016) Radionuclide removal by apatite. *American Mineralogist*, 101(12), 2611–2619.
- Rittner, M. and Müller, W. (2012) 2D mapping of LA-ICPMS trace element distributions using R. *Computers & Geosciences*, 42, 152–161.
- Rollog, M (2019). *Department of radionuclides in copper concentrate from Olympic Dam*. Unpublished Ph.D. thesis, The University of Adelaide, Adelaide, Australia.

- Rollog, M., Cook, N.J., Guagliardo, P., Ehrig, K., and Kilburn, M. (2018) In situ spatial distribution mapping of radionuclides in minerals by nanoSIMS. *Geochemistry: Exploration, Environment, Analysis*, 19(3), 245–254.
- Rollog, M., Cook, N.J., Guagliardo, P., Ehrig, K., Ciobanu, C.L., and Kilburn, M. (2019). Detection of Trace Elements/Isotopes in Olympic Dam Copper Concentrates by nanoSIMS. *Minerals*, 9(6), 336.
- Rollog, M., Cook, N.J., Gugliardo, P., Ehrig, K., and Kilburn, M. (2019) Radionuclide distributions in Olympic Dam copper concentrates: the significance of minor hosts, incorporation mechanisms, and the role of mineral surfaces. *Minerals Engineering*, 148, 106176.
- Rollog, M., Cook, N.J., Gugliardo, P., Ehrig, K., and Kilburn, M. (2019) Radionuclide-bearing minerals in Olympic Dam copper concentrates. *Hydrometallurgy*, 105, 105153.
- Schindelin, J., Arganda-Carreras, I., Frise, E., Kaynig, V., Longair, M., Pietzsch, T., Preibisch, S., Rueden, C., Saalfeld, S., Schmid, B., and Tinevez, J.Y. (2012) Fiji: an open-source platform for biological-image analysis. *Nature Methods*, 9, 676–682.
- Schindelin, J., Rueden, C.T., Hiner, M.C., and Eliceiri, K.W. (2015) The 516 ImageJ ecosystem: An open platform for biomedical image analysis. *Molecular Reproduction and Development*, 82, 518–529.
- Schlegel, T.U. and Heinrich, C.A. (2015) Lithology and Hydrothermal Alteration Control the Distribution of Copper Grade in the Prominent Hill Iron Oxide-Copper-Gold Deposit (Gawler Craton, South Australia). *Economic Geology*, 110, 1953–1994.
- Schlegel, T.U., Wagner, T., Boyce, A., and Heinrich, C.A. (2017) A magmatic source of hydrothermal sulfur for the Prominent Hill deposit and associated prospects in the Olympic iron oxide copper-gold (IOCG) province of South Australia. *Ore Geology Reviews*, 89, 1058–1090.
- Schlegel, T.U., Wagner, T., Wälle, M., and Heinrich, C.A. (2018) Hematite Breccia-Hosted Iron Oxide Copper-Gold Deposits Require Magmatic Fluid Components Exposed to Atmospheric Oxidation: Evidence from Prominent Hill, Gawler Craton, South Australia. *Economic Geology*, 113(3), 597–644.

- Schmandt, D., Cook, N., Ciobanu, C., Ehrig, K., Wade, B., Gilbert, S., and Kamenetsky, V. (2017) Rare earth element fluorocarbonate minerals from the Olympic Dam Cu-U-Au-Ag deposit, South Australia. *Minerals*, 7(10), 202.
- Schmandt, D.S. (2019) Mineralogical distributions of radionuclides in copper-uranium ores, Olympic Dam, South Australia. Ph.D. thesis, The University of Adelaide, Adelaide.
- Schmandt, D.S., Cook, N.J., Ciobanu, C.L., Ehrig, K., Wade, B.P., Gilbert, S., and Kamenetsky, V.S. (2019) Rare earth element phosphate minerals from the Olympic Dam Cu-U-Au-Ag deposit, South Australia: Recognizing temporal-spatial controls on REE mineralogy in an evolved IOCG system. *The Canadian Mineralogist*, 57(1), 3–24.
- Schmandt, D.S., Cook, N.J., Ehrig, K., Gilbert, S., Wade, B.P., Rollog, M., Ciobanu, C.L., and Kamenetsky, V.S. (2019) Uptake of trace elements by baryte during copper ore processing: A case study from Olympic Dam, South Australia. *Minerals Engineering*, 135, 83–94.
- Schwab, R.G., Götz, C., Herold, H., and Pinto de Oliveira, N. (1991) Compounds of the crandallite type: synthesis and properties of pure (Ca, Sr, Ba, Pb, La, Ce to Eu)-arsenocrandallites. *Neues Jahrbuch für Mineralogie Monatshefte*, (3), 97–112.
- Schwab, R.G., Götz, C., Herold, H., and Pinto de Oliveira, N. (1993) Compounds of the crandallite type: thermodynamic properties of Ca-, Sr-, Ba-, Pb-, La-, Ce-to Gd-phosphates and -arsenates. *Neues Jahrbuch für Mineralogie Monatshefte*, 551–568.
- Schwab, R.G., Pimpl, T., Schukow, H., Stolle, A., and Breiting, D.K. (2004) Compounds of the crandallite-type: Synthesis, properties and thermodynamic data of pure crandallite and woodhouseite. *Neues Jahrbuch für Mineralogie Monatshefte*, 385–409.
- Schwab, R.G., Pimpl, T., Schukow, H., Stolle, A., and Breiting, D.K. (2005) Compounds of the crandallite-type: Synthesis, properties and thermodynamic data of Ca–Sr–Ba–Pb-(arseno)-woodhouseites. *Neues Jahrbuch für Mineralogie Abhandlungen*, 181, 207–218.
- Semkow, T.M. (1990) Recoil-emanation theory applied to radon release from mineral grains. *Geochimica et Cosmochimica Acta*, 54, 425–440.

- Shannon, R.D. (1976) Revised effective ionic radii and systematic studies of interatomic distances in halides and chalcogenides. *Acta Crystallographica A: crystal physics, diffraction, theoretical and general crystallography*, 32(5), 751–767.
- Simon, G. and Essene, E.J. (1996) Phase relations among selenides, sulfides, tellurides, and oxides: I. Thermodynamic properties and calculated equilibria. *Economic Geology*, 91, 1183–1208.
- Simon, G., Kesler, S.E., and Essene, E.J. (1997) Phase relations among selenides, tellurides, and oxides; II, Applications to selenide-bearing ore deposits. *Economic Geology*, 92, 468–484.
- Škácha, P., Sejkora, J., and Plášil, J. (2017) Selenide Mineralization in the Příbram Uranium and Base-Metal District (Czech Republic). *Minerals*, 7, 91.
- Skirrow, R.G. and Davidson, G.J. (2007) A special issue devoted to Proterozoic iron oxide Cu-Au-(U) and gold mineral systems of the Gawler Craton: preface. *Economic Geology*, 102(8), 1373–1375.
- Skirrow, R.G., van der Wielen, S.E., Champion, D.C., Czarnota, K., and Thiel, S. (2018) Lithospheric Architecture and Mantle Metasomatism Linked to Iron Oxide Cu-Au Ore Formation: Multidisciplinary Evidence from the Olympic Dam Region, South Australia. *Geochemistry, Geophysics, Geosystems*, 19, 2673–2705.
- Skirrow, R.G., Bastrakov, E.N., Barovcich, K., Fraser, G.L., Creaser, R.A., Fanning, C.M., Raymond, O.L., and Davidson, G.J. (2007) Timing of iron oxide Cu-Au-(U) hydrothermal activity and Nd isotope constraints on metal sources in the Gawler craton, South Australia. *Economic Geology*, 102, 1441–1470.
- Skirrow, R.G., Raymond, O.L., Bastrakov, E., Davidson, G.J., and Heithersay, P. (2002) The geological framework, distribution and controls of Fe oxide Cu-Au mineralisation in the Gawler Craton, South Australia. Part II- alteration and mineralisation. In: Porter, T.M., ed., *Hydrothermal iron oxide copper-gold & related deposits: a global perspective*, vol. 2., PGC Publishing, Adelaide, 33–48.
- Stoffregen, R.E. and Alpers, C.N. (1987) Woodhouseite and svanbergite in hydrothermal ore deposits; products of apatite destruction during advanced argillic alteration. *The Canadian Mineralogist*, 25, 201–211.

- Stüeken, E.E., Buick, R., Bekker, A., Catling, D., Foriel, J., Guy, B.M., Kah, L.C., Machel, H.G., Montañez, I.P., and Poulton, S.W. (2015) The evolution of the global selenium cycle: Secular trends in Se isotopes and abundances. *Geochimica et Cosmochimica Acta*, 162, 109–125.
- Thirlwall, M.F. (2000) Inter-laboratory and other errors in Pb isotope analyses investigated using a ^{207}Pb – ^{204}Pb double spike. *Chemical Geology*, 163, 299–322.
- Triplehorn, D.M., Stanton, R.W., Ruppert, L.F., and Crowley, S.S. (1991) Volcanic ash dispersed in the Wyodak-Anderson coal bed, Powder River basin, Wyoming. *Organic Geochemistry*, 17, 567–575.
- Tunell, G. and Adams, C.E. (1949) On the symmetry and crystal structure of bornite. *American Mineralogist*, 34, 824–829.
- Van Dyck, D., Conde-Amiano, C., and Amelinckx, S. (1980) The diffraction pattern of crystals presenting a digenite type of disorder. II. The structure of the digenite-related phases derived by means of the Cluster Theory. *Physica Status Solidi*, 58, 451–468.
- Verdugo-Ihl, M.R., Ciobanu, C.L., Cook, N.J., Ehrig, K., Courtney-Davies, L., and Gilbert, S. (2017) Textures and U-W-Sn-Mo signatures in hematite from the Cu-U-Au-Ag orebody at Olympic Dam, South Australia: defining the archetype for IOCG deposits. *Ore Geology Reviews*, 91, 173–195.
- Verdugo-Ihl, M.R., Ciobanu, C.L., Cook, N.J., Ehrig, K.J., and Courtney-Davies, L. (2019). Defining early stages of IOCG systems: Evidence from iron oxides in the outer shell of the Olympic Dam deposit, South Australia. *Mineralium Deposita*, 1–24.
- Verdugo-Ihl, M.R., Ciobanu, C.L., Cook, N.J., Ehrig, K.J., Courtney-Davies, L., and Gilbert, S. (2017) Textures and UW-Sn-Mo signatures in hematite from the Olympic Dam Cu-U-Au-Ag deposit, South Australia: Defining the archetype for IOCG deposits. *Ore Geology Reviews*, 91, 173–195.
- Verdugo-Ihl, M.R., Ciobanu, C.L., Slattery, A., Cook, N.J., Ehrig, K., and Courtney-Davies, L. (2019) Copper-arsenic nanoparticles in hematite: Fingerprinting fluid-mineral interaction. *Minerals*, 9(7), 388.
- Vinograd, V.L., Kulik, D.A., Brandt, F., Klinkenberg, M., Weber, J., Winkler, B., and Bosbach, D. (2018) Thermodynamics of the solid solution - Aqueous solution system $(\text{Ba,Sr,Ra})\text{SO}_4 + \text{H}_2\text{O}$:

II. Radium retention in barite-type minerals at elevated temperatures. *Applied Geochemistry* 93, 190–208.

- Walther, C. and Gupta, D.K. (2015) Radionuclides in the environment: Influence of chemical speciation and plant uptake on radionuclide migration, Springer.
- Will, G., Hinze, E., and Abdelrahman, A.R.M. (2002) Crystal structure analysis and refinement of digenite, $\text{Cu}_{1.8}\text{S}$, in the temperature range 20 to 500 C under controlled sulfur partial pressure. *European Journal of Mineralogy*, 14, 591–598.
- Williams, P.J. and Pollard, P.J. (2001) Australian Proterozoic iron oxide-Cu-Au deposits; an overview with new metallogenic and exploration data from the Cloncurry District, Northwest Queensland. *Exploration and Mining Geology*, 10, 191–213.
- Williams-Jones, A.E., Migdisov, A.A., and Samson, I.M. (2012). Hydrothermal mobilisation of the rare earth elements—a tale of “ceria” and “yttria”. *Elements*, 8, 355–360.
- Wingate, M.T., Campbell, I.H., Compston, W., and Gibson, G.M. (1998) Ion microprobe U–Pb ages for Neoproterozoic basaltic magmatism in south-central Australia and implications for the breakup of Rodinia. *Precambrian Research*, 87(3-4), 135–159.
- Woodhead, J.A., Rossman, G.R., and Silver, L.T. (1991) The Metamictization of zircon: Radiation dose-dependent structural characteristics. *American Mineralogist*, 76, 1–2.
- Xing, Y., Etschmann, B., Liu, W., Mei, Y., Shvarov, Y., Testemale, D., Tomkins, A., and Brugger, J. (2019) The role of fluorine in hydrothermal mobilization and transportation of Fe, U and REE and the formation of IOCG deposits. *Chemical Geology*, 504, 158–176.
- Xing, Y., Mei, Y., Etschmann, B., Liu, W., and Brugger, J. (2018) Uranium transport in F-Cl-bearing fluids and hydrothermal upgrading of U-Cu ores in IOCG deposits. *Geofluids*, 22.
- Yund, R.A. and Kullerud, G. (1966) Thermal stability of assemblages in the Cu-Fe-S system. *Journal of Petrology*, 7, 454–488.
- Zema, M., Callegari, A.M., Tarantino, S.C., Gasparini, E., and Ghigna, P. (2012) Thermal expansion of alunite up to dehydroxylation and collapse of the crystal structure. *Mineralogical Magazine*, 76, 613–623.

- Zhao, J., Brugger, J., Ngothai, Y., and Pring, A. (2014) The replacement of chalcopyrite by bornite under hydrothermal conditions. *American Mineralogist*, 99, 2389–2397.
- Zheng, M. X., Xu, J. M., Smith, L., and Naidu, R. (2003) Why a fern (*Pteris multifida*) dominantly growing on an arsenic heavy metal contaminated soil does not accumulate arsenic? In *Journal de Physique IV (Proceedings)*, 107, 1409–1411.